



**HAL**  
open science

# Redox reactivity of original nickel complexes combined with divalent lanthanides

Ding Wang

► **To cite this version:**

Ding Wang. Redox reactivity of original nickel complexes combined with divalent lanthanides. Coordination chemistry. Institut Polytechnique de Paris, 2020. English. NNT : 2020IPPAX100 . tel-03362697

**HAL Id: tel-03362697**

**<https://theses.hal.science/tel-03362697v1>**

Submitted on 2 Oct 2021

**HAL** is a multi-disciplinary open access archive for the deposit and dissemination of scientific research documents, whether they are published or not. The documents may come from teaching and research institutions in France or abroad, or from public or private research centers.

L'archive ouverte pluridisciplinaire **HAL**, est destinée au dépôt et à la diffusion de documents scientifiques de niveau recherche, publiés ou non, émanant des établissements d'enseignement et de recherche français ou étrangers, des laboratoires publics ou privés.

# Redox reactivity of original nickel complexes combined with divalent lanthanides

Thèse de doctorat de l'Institut Polytechnique de Paris  
préparée à l'École polytechnique

École doctorale n°626 École Doctorale de l'Institut Polytechnique de  
Paris (ED IP Paris)  
Spécialité de doctorat: Chimie

Thèse présentée et soutenue à Palaiseau, le 11 décembre, par

**Ding Wang**

Composition du Jury :

Christophe Darcel Professeur des Universités, Université de Rennes	Président
Corinna Hess Professeur des Universités, Technische Universität München	Rapporteur
Florian Jaroschik Chargé de Recherche, École Nationale Supérieure de Chimie de Montpellier	Rapporteur
Marine Desage-El Murr Professeur des Universités, Université de Strasbourg	Examineur
Grégory Nocton Chargé de Recherche, École Polytechnique	Directeur de thèse



# Redox reactivity of original nickel complexes combined with divalent lanthanides



**Ding Wang**

Chemistry

Ecole Polytechnique, Institut Polytechnique de Paris



A thesis submitted for the degree of Doctor of Philosophy

December 2020

This work financed by



European Research Council  
Established by the European Commission





“道阻且长，行则将至；行而不辍，未来可期。”

—— 荀子《修身》

*“Road ahead is obstacle-packed and long, but we will make it if persist; Persist, and the  
future can be expected.”*

– *Xun Kuang, «Self-cultivation»*



# Acknowledgement

This PhD thesis manuscript summarizes the chemistry that I have explored, failed, and of course, accomplished with great pride, during past three years (2017 – 2020) in Laboratoire de Chimie Moléculaire at École Polytechnique. However, I myself could never ever take all the credit for the chemistry that presents in this hundred-page work, and in addition to the science, the PhD life could not be as incredible as what it has been without the people that surround me dans ce labo du bonheur.

Absolutely, my most sincere gratitude is to Greg, who offered me this PhD project after a very pleasant interview in his office in late March 2017. It entirely was a big challenge to me at the beginning of my PhD since I did not have rich background in f-element chemistry and related spectroscopic skills, but Greg was constantly there to help me better understand everything when I needed the concrete knowledge or sometimes made any mistake during the manipulations in the gloveboxes. He also let me explore anything that I was eager to give a shot with big encouragement, but more importantly, he always reminded me to wind up when there came a bite. It is Greg who trained me to behave as a more mature chemist with a more scientific brain.

I also need to thank Greg for starting to help me to think about the composition of my jury members back to early November 2019. I deeply grateful to the jury members for the evaluation of my PhD work with nice remarks and suggestions: Prof. Dr. Corinna Hess and Dr. Florian Jaroschik as reviewers, and Prof. Christophe Darcel and Prof. Marine Desage-El Murr as examiners. A special thank is to Christophe for accepting to follow up (maybe kind of “check”) what I have learned and done after I left Rennes. It truly is a pity that the defense had to be virtual due to the sanitary measures of COVID-19 pandemic and I could not have the chance to face to face with everyone to present my work and share ideas.

I would also like to thank Dr. Emmanuel Nicolas from CEA Saclay for being my thesis follow-up member (comité de suivi de thèse) and kindly providing me with a lot of valuable ideas on my chemistry during the meetings.

The completion of this work could not be possible without the help of all the group members, aka Greg's *Crazy Lanthanide Team* (© Violaine ^^). It's *mommy* Violaine who held my hand with great patience to show me how to manipulate at the beginning (e.g., the marvelous skill of canula filter preparation!) and comforted me when there was frustration with the failed chemistry. Thank you for everything with the quite- well-recognized laughter to make the life of everyone so fun in lab 1! Jules then joined the lab as a real brother to us, who made a lot of magnetism samples for we students (Grand *Jean Mich* of Lab 1!) and taught me many practical French expressions with *polite* meanings and discussed about a lot of *pleasant* jokes together... Thomas aka *le MBraun technician* repaired every problematic piece of all the gloveboxes, and it was so cool to talk about China and *practice* Chinese with you. Most importantly, thanks so much for helping me in the last minutes of

the thesis preparation. Oleh, who has a special sense of humor and kindness, joined the team just right before the first confinement of COVID-19... Good luck with your beautiful heteroleptic Ln molecules! Mathieu, aka *le Capitaine*, we shared great fun together in the lab as well as in the bars and conference (the unforgettable Brest night...) during the first year of my PhD, and he is the one that firstly made me know never ever to play with the well-blessed DCM in the presence of divalent lanthanides... Maxime and Valeriu, who helped me to measure the crystals (which are actually powder for most of times) and to perform a lot of calculations on my compounds. Maxime also helped me so much for the SQUID data and NMR analysis, and I'm so proud of you being such a great, confident and mature chemist after spending your internship with me before started your PhD! Nolwenn, I'm sure you will do great in your chemistry and enjoy preparing a lot of quartz tubes, good luck to you! I'm very looking forward to reading your first-author paper soon!... Bref, bon courage et bonne chance à tou(te)s ! I also want to thank all the interns that spent time together in the same laboratory: Max, Lamise (chère Lulu), Poonam, Lily, Jules, Sébastien, Junghan, Audrey, Zeyu (DO let me know when you wanna *quench* your next *potassium* piece...), Carla and others, including les prex.

The PhD life got incredibly enriched and joyful also with the other labmates/friends from the LCM. Céline aka la *Co-girl*, we spent three years of our PhD study and talked so much nonsense in RER and had so much fun together in and out of the lab. We shared our special weirdness when we had *Tears on the Pillow*, but we knew it's not *The End of the World* working together in Lab 1. It's wonderful to have you always around during the past three years and especially virtually ~~complain~~ exchange the feelings of our PhD life in quelle *belle année* 2020. Louis, who used the sentence *Do you drink beer* to welcome me on board the journey in LCM, you always got my back when I felt depressed and it is you who always made me feel at home with your kindness, warm care and the specific Loulou's humor. You are just an amazing man and a great friend. Yann, it was fun to do some organic synthesis with you to make some new ligands (such as the pytpy ligand!), even though some of them did not work... It's so nice to share crazy ideas with you and especially listen to you in the concerts of your Brass Band! Irene, it's so pleasant to have the ~~alcoholic~~ *vibe* with you like *Who wants to go for a beer after work...* Isabel, it was cool that we just went for running dans la forêt Palaiseau n'importe quand, and it was memorable that a wasted me stayed overnight at yours (a great night with your cat!). Emmanuel, you did great job in our LCM football team aka Cp all-stars. I wish you all the best for your chemistry! Zsuzsanna, it's impressive that you have such *business PhD* life (so jealous!), and I hope you will enjoy finishing up your thesis soon! Silvia and Radhika, it was funny to have the same French courses together and also the tea-time talking about lots of nonsense. Thibault, I am sure you will do great and take nice care of our *tasty* NMR machine... Pauline, best of luck with your beautiful cobalt complexes! And Mengyu, *jiayou!*

My big gratitude equally goes to the permanent staff of LCM. I firstly want to thank Cédric for the constantly kind help and care on my thesis and defense. I am grateful to Corinne for her nice reminders on dealing with my administrative business when I had no idea how to do it at the

beginning of PhD. I greatly thank Audrey for her rapid and timely reaction to effectively prevent the fire accident in the lab. Duncan, it was really kind of you to encourage me time to time when I met difficulties at work. Bibi, it was impressive to have a lot of frank/direct conversations with weird fun and many useful discussions on chemistry. I sincerely wish all the best with your beautiful science! I also want to thank Sophie for helping me perform Mass measurement on several my compounds that were insoluble in any solvent, although the results of Mass did not look good either... and it was really sweet that you care about me all the time with a lot of encouragement. I also thank Stéphane for holding a nice dinner at the beginning year of my PhD. Furthermore, I also appreciate Cindy, Christophe, Gilles A., Gilles F., Gilles O., Edith, Ségolène, Svetlana, Vincent, and all the interns that I met during my thesis.

I want to express my gratitude to the XRD platform staff, who played a really important role in the chemistry that I have done. I firstly thank Marie, who not only taught me basic skills and practical experience on measuring crystals, but also supported me all the time as a good friend. Wish everything goes well in Rennes! I really appreciate Nicolas for his extremely kind help on testing my crystals so many times with a lot of patience and giving me the privilege in the crystal-waiting list. Then, a special thank is to Louis R. (our dear crystallo-chemist ^^), for his curiosity in the always tricky structures of my complexes and great help in reviewing all the crystallographic data to make sure that everything we got is publishable. Hope you all the best, Louis!

The life in the lab was so well facilitated by the continuous help from Anneflo, known as the best administrative staff in the world. Thank you so much for taking care of all the administrative forms with the greatest patience that I have ever seen and thank you really a lot for the constant kindness every day. It was so nice to have such a smiling person passing by in the corridor when just failed in some reaction or crystallization. I equally want to thank Thérèse, who just retired from the lab, for also taking care of some of the paperwork for my conference, and importantly, the beverage *without any drop of alcohol aka Rhum* in the Christmas meal of lab made me *not at all drunk before* starting to eat... Enjoy your retired life with great happiness!

Finally, the most important gratitude goes to my family for supporting me all the time, especially Zijun. It's even not possible I could carry everything on in my daily life in France without you. You are my everything.



## Table of contents

<i>List of abbreviations</i> .....	9
<i>Archives for all the synthesized molecules</i> .....	11
<b>Chapter I. General introduction</b> .....	17
1. Generality of fundamental transition-metal catalysis .....	17
2. Advances in homogenous nickel catalysis: through unusual oxidation states .....	20
3. Ligands: Redox non-innocence and electron correlations.....	23
4. Why (divalent) lanthanides? .....	26
5. Objectives of the PhD thesis .....	33
<b>Chapter II. Synthesis and characterizations of original heterobimetallic complexes bridged by 2,2'-bipyrimidine and their reactivity toward small molecule activation</b> .....	49
1. Introduction: general interest in small molecule activation in organometallic nickel chemistry .....	50
2. Heterobimetallic nickel complex: synthesis and characterizations .....	54
2.1. Synthetic method and structural analysis.....	54
2.2. NMR characterizations and solid-state magnetism measurement.....	57
2.3. Theoretical Study: DFT Calculations.....	60
3. Reactivity with carbon monoxide .....	62
4. Other Reactivity Attempts .....	69
4.1. Oxidation.....	69
4.2. Reduction.....	71
5. Replacement of ytterbium: a novel samarium/nickel bimetallic complex .....	74
6. Conclusion and perspectives .....	76
<b>Chapter III. Influence of an alternative ligand at nickel center: synthesis of trifluoromethyl nickel complexes and coordination chemistry with divalent lanthanides</b> .....	87
1. Trifluoromethyl functional group: a strategy toward high valency? .....	89
1.1. [CF <sub>3</sub> ] group is not only electron-withdrawing in organometallic complexes .....	90
1.2. Selected examples in high-valent nickel compounds .....	97
2. Synthesis and characterizations of L <sub>2</sub> Ni(CF <sub>3</sub> ) <sub>2</sub> complexes .....	105
2.1. Synthesis and characterizations of (bipym)Ni(CF <sub>3</sub> ) <sub>2</sub> complex .....	105
2.2. Original dissymmetric Ni(CF <sub>3</sub> ) <sub>2</sub> complexes .....	108
3. Coordination to divalent lanthanides .....	111
4. Reactivity attempts.....	114
5. Conclusion and perspectives .....	114



**Chapter IV. Reductive C-C coupling between redox-active dissymmetric ligands in divalent organolanthanides with reactive nickel fragment** ..... 121

1. Introduction: Reversibility and irreversibility of coupling between redox-active ligands	122
1.1. Couplings in d-block transition metal complexes	122
1.2. Couplings in f-element chemistry	127
2. Synthesis and XRD analysis of the dissymmetric heterometallic framework	133
2.1. The Interest of imidazole derivatives	133
2.2. Novel organometallic frameworks: radical coupling formation on the ligand	134
2.3. Cap the active potassium ion	139
3. Characterizations and discussions	144
3.1. NMR studies	144
3.2. Magnetism	153
3.3. DFT calculations	154
4. Reactivity attempts	155
5. Replacement with samarium	159
6. Conclusion and perspectives	160

**Chapter V. Redox-active tridentate nickel complexes with divalent lanthanides: planarity and reactivity** ..... 167

1. Introduction: electron delocalization in terpyridine-based ligands	168
1.1. Ligand-based redox effects in terpyridine complexes	168
1.2. Redox activity in divalent lanthanide terpyridine-based complexes	174
2. Towards the heterobimetallic framework: synthesis and structural analysis	177
2.1. A new nickel complex with the pytpy ligand	177
2.2. Complexation with divalent organolanthanides	179
3. Characterizations in solution and discussions	187
4. Reactivity attempts	192
5. Conclusion and perspectives	193

**Chapter VI. General conclusion and perspectives** ..... 201

Appendices	203
A. Synthesis and characterization data	205
B. Crystallographic data	223
C. Published articles	233

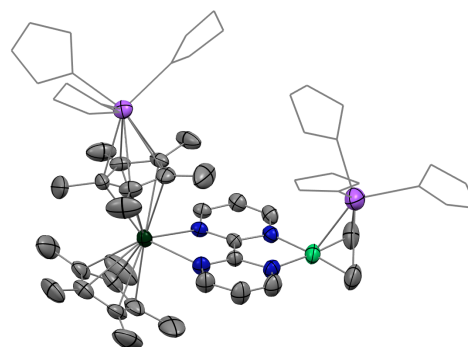
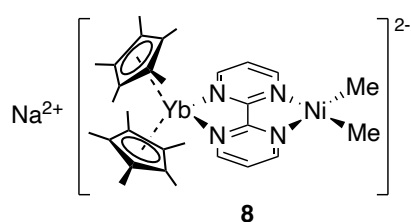
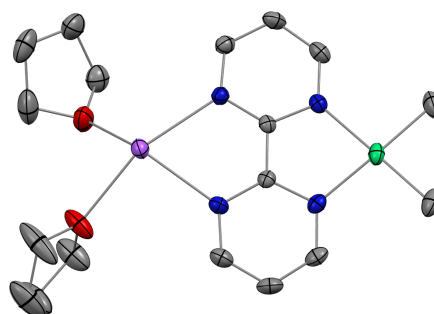
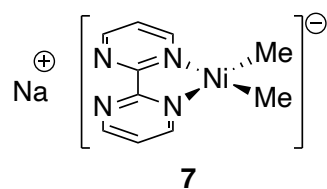
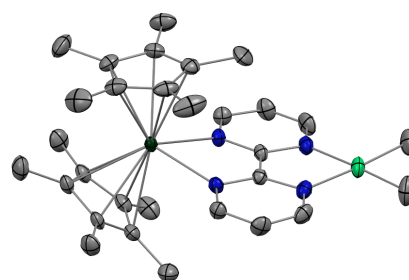
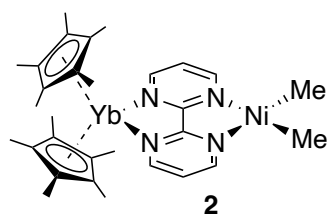
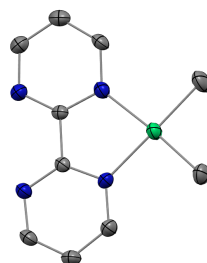
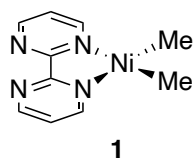
## **List of abbreviations**

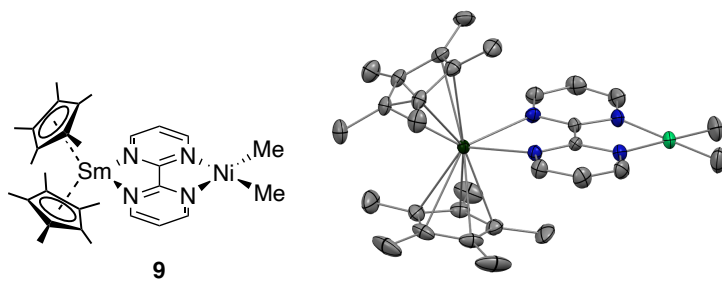
<b>acac</b>	acetylacetonate
<b>aq.</b>	aqueous
<b>a.t.</b>	ambient temperature
<b>bimpm</b>	2-pyrimidin-2-yl-benzimidazole
<b>bipy</b>	2,2'-bipyridine
<b>bipym</b>	2,2'-bipyrimidine
<b>CASSCF</b>	Complete Active Space Self Consistent Field
<b>CCDC</b>	Cambridge Crystallographic Data Centre
<b>COD</b>	1,5-cyclooctadiene
<b>Cp</b>	cyclopentadienyl
<b>Cp*</b>	pentamethylcyclopentadienyl
<b>Cp<sup>ttt</sup></b>	1,2,4-tri( <i>tert</i> -butyl)cyclopentadienyl
<b>ctr</b>	centroid
<b>d</b>	doublet
<b>DCM</b>	dichloromethane
<b>DFT</b>	Density Functional Theory
<b>DME</b>	dimethoxyethane
<b>DMSO</b>	dimethyl sulfoxide
<b>e.g.</b>	exempli grātiā ( = for example)
<b>EPR</b>	Electronic Paramagnetic Resonance
<b>equiv.</b>	equivalent
<b>Et<sub>2</sub>O</b>	diethyl ether
<b>et al.</b>	et alia ( = and others)
<b>Fc</b>	ferrocene
<b>HMDS</b>	bis(trimethylsilyl)amine
<b>HOMO</b>	Highest Occupied Molecular Orbital
<b>i.e.</b>	id est ( = that is)
<b>KHMDS</b>	potassium bis(trimethylsilyl)amide
<b>LMCT</b>	Ligand Metal Charge Transfer

<b>Ln</b>	lanthanide
<b>LUMO</b>	Lowest Unoccupied Molecular Orbital
<b>Me</b>	methyl
<b>MeCN</b>	acetonitrile
<b>nacnac</b>	1,3-diketiminato
<b>NMR</b>	Nuclear Magnetic Resonance
<b>ORTEP</b>	Oak Ridge Thermal Ellipsoid Plot
<b>Ph</b>	phenyl
<b>phen</b>	1,10-phenanthroline
<b>ppm</b>	parts per million
<b>py</b>	pyridine / pyridyl
<b>r.t.</b>	room temperature
<b>s</b>	singlet
<b>SMM</b>	Single Molecule Magnet
<b>SOMO</b>	Singly Occupied Molecular Orbital
<b>SQUID</b>	Superconducting Quantum Interference Device
<b>t</b>	triplet
<b>taphen</b>	4,5,9,10-tetraazaphenanthrene
<b><i>t</i>Bu</b>	<i>tert</i> -butyl
<b>THF</b>	tetrahydrofuran
<b>TIP</b>	Temperature-Independent Paramagnetism
<b>TfO</b>	trifluoromethanesulfonate / triflate
<b>TMS</b>	Tetramethylsilane / Trimethylsilyl
<b>TMEDA</b>	<i>N,N,N',N'</i> -tetramethylethylenediamine
<b>tpy</b>	2,2':6',2''-terpyridine
<b>tol</b>	toluene
<b>XRD</b>	X-Ray Diffraction
<b><math>\Delta H</math></b>	enthalpy of reaction
<b><math>\Delta S</math></b>	entropy of reaction
<b><math>\Delta G</math></b>	Gibbs energy of reaction

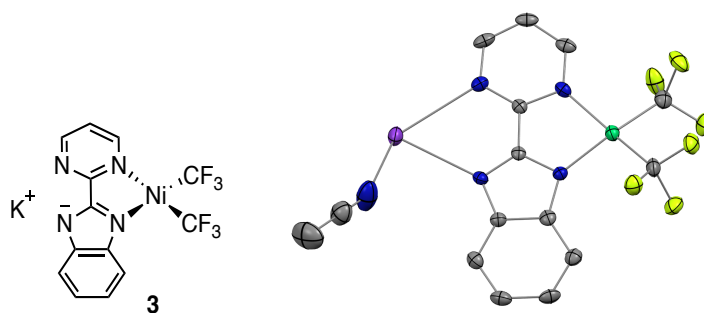
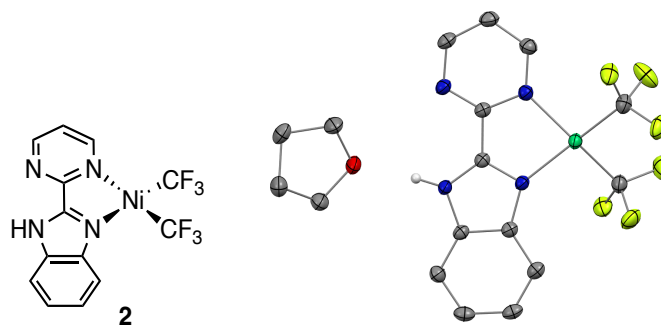
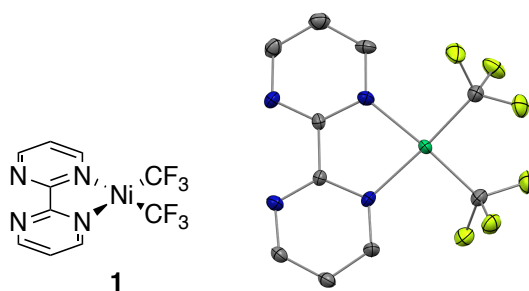
# Archives for all the synthesized molecules

## Chapter II

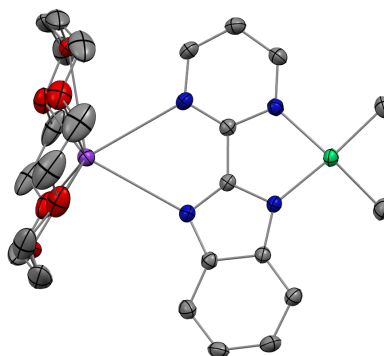
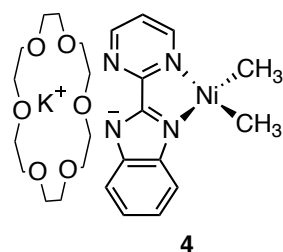
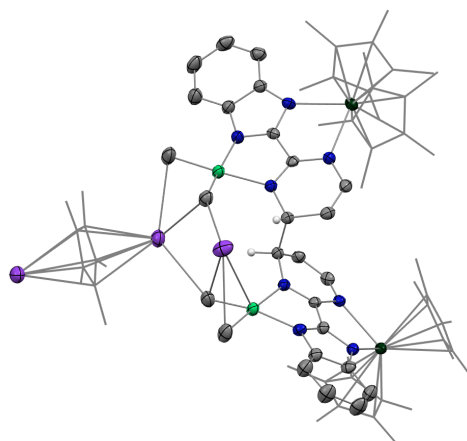
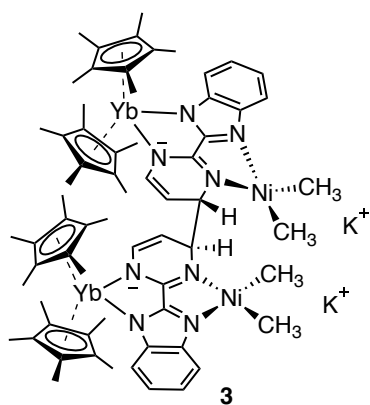
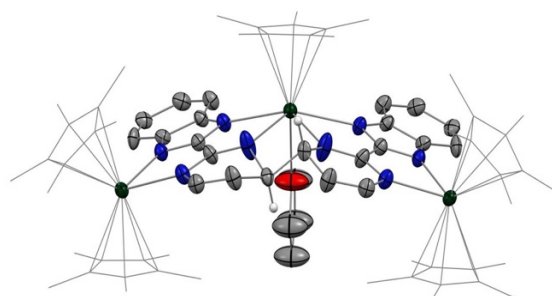
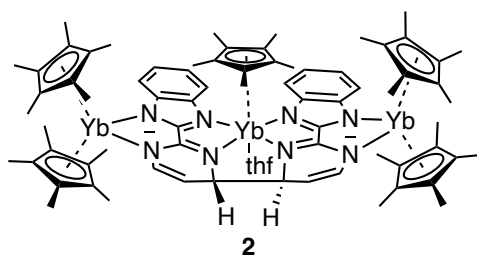
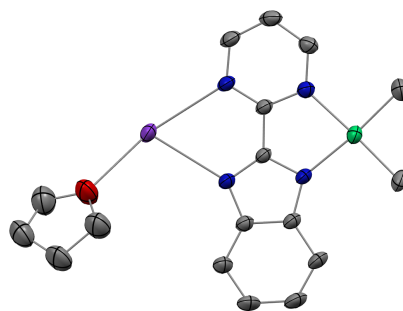
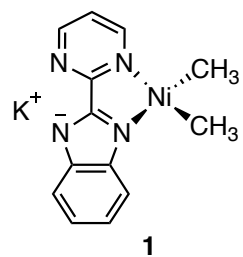


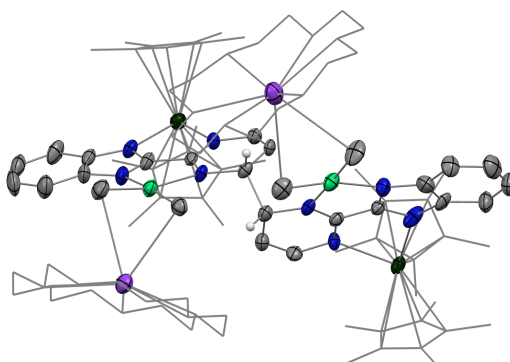
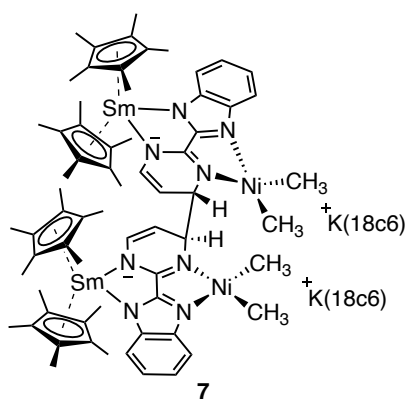
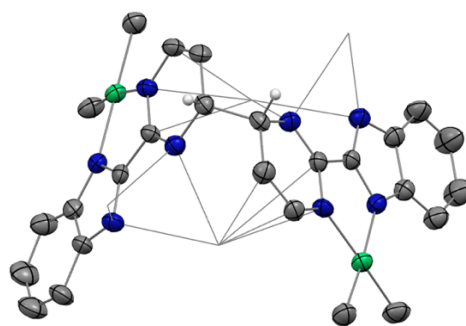
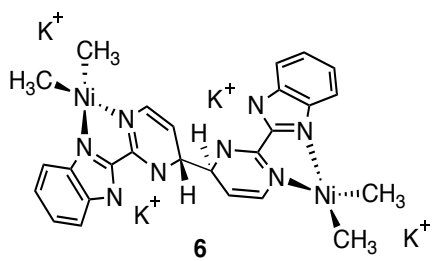
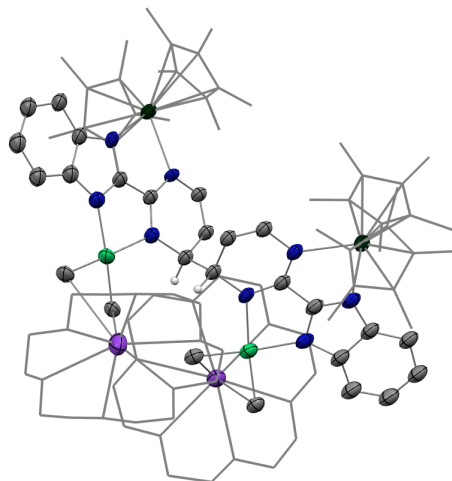
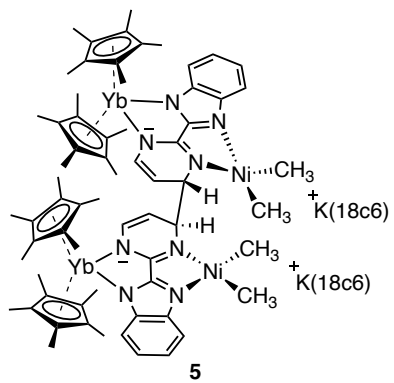


### Chapter III

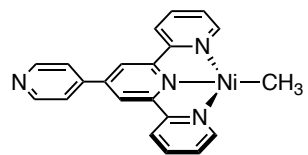


## Chapter IV

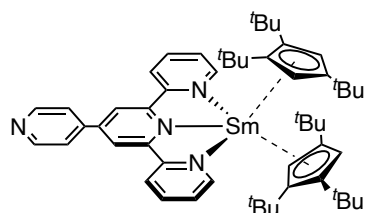
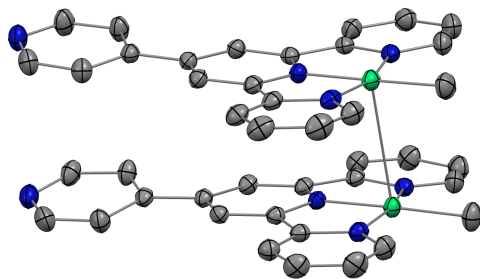




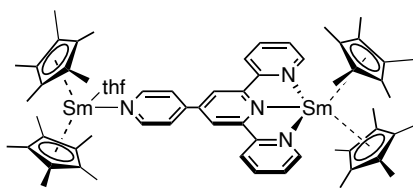
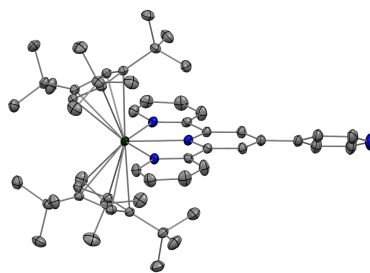
## Chapter V



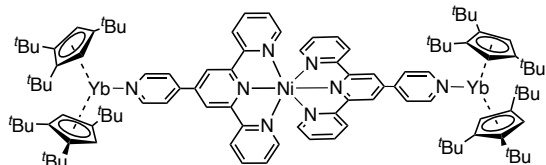
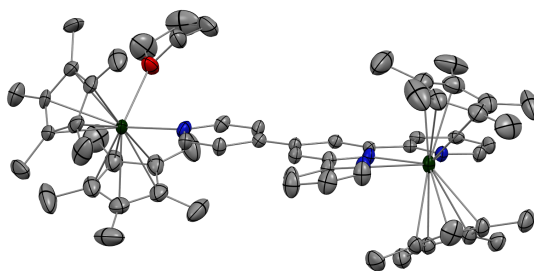
1



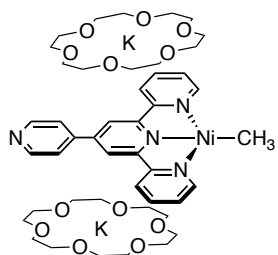
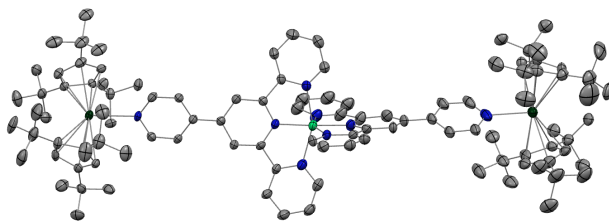
2



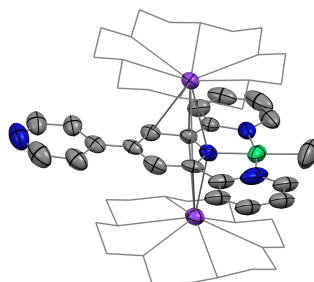
3



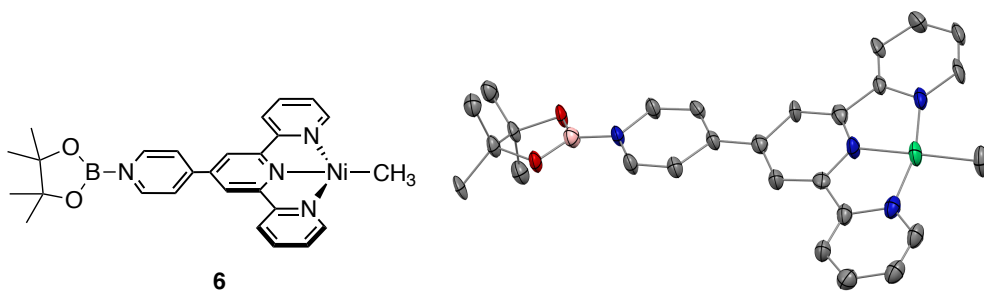
4



5









# General introduction

## 1. Generality of fundamental transition-metal catalysis

Transition metal-catalyzed homogenous processes have been broadly developed for constructing carbon-carbon/heteroatom bonds, as well as functionalizing olefins, which was also recognized with the Nobel Prize in Chemistry for the importance of “*palladium-catalyzed cross-coupling in organic synthesis*” in 2010 jointly to Richard F. Heck, Ei-ichi Negishi and Akira Suzuki.<sup>1-3</sup> The salient importance of such functionalization has mostly been shown in the direct synthesis of most organic molecules with a more efficient and atom-economical way.<sup>4-6</sup> However, the constant challenge remains the fine control of stereo- and regioselectivity,<sup>7-9</sup> as well as mechanistic insights of the synthetic strategies, which will lead to precise designs of novel, more effective catalytic systems.<sup>10,11</sup>

Generally, the critical organometallic steps in metal-catalyzed reactions, particularly cross-coupling transformations, include: (a) oxidative addition of a carbon-heteroatom bond into a transition metal center in low oxidation state, (b) transmetalation or displacement of the heteroatom group by a nucleophilic moiety, and (c) reductive elimination to form a new C-C or C-heteroatom bond.<sup>12</sup> The recent challenge and development in this field focus on the use of C(sp<sup>3</sup>) organometallic transformations, comparing to related C(sp<sup>2</sup>) cross-coupling reactions. The general mechanistic understanding reveals detailed features that would help achieve relatively satisfactory conversions, by preventing the undesired side reactions such as homo-coupling,  $\beta$ -elimination, and proto-demetalation in the presence of alkylating agents (Figure 1).<sup>13</sup> The essential use of metal catalysts in the pioneering work of palladium-mediated catalysis results in a widespread and careful selection of organometallic systems.<sup>14-17</sup> Moreover, diverse organometallics containing alkylated functionality become an accelerating development of catalytic cross-coupling procedures, mainly in the area of asymmetric catalysis.<sup>18,19</sup>

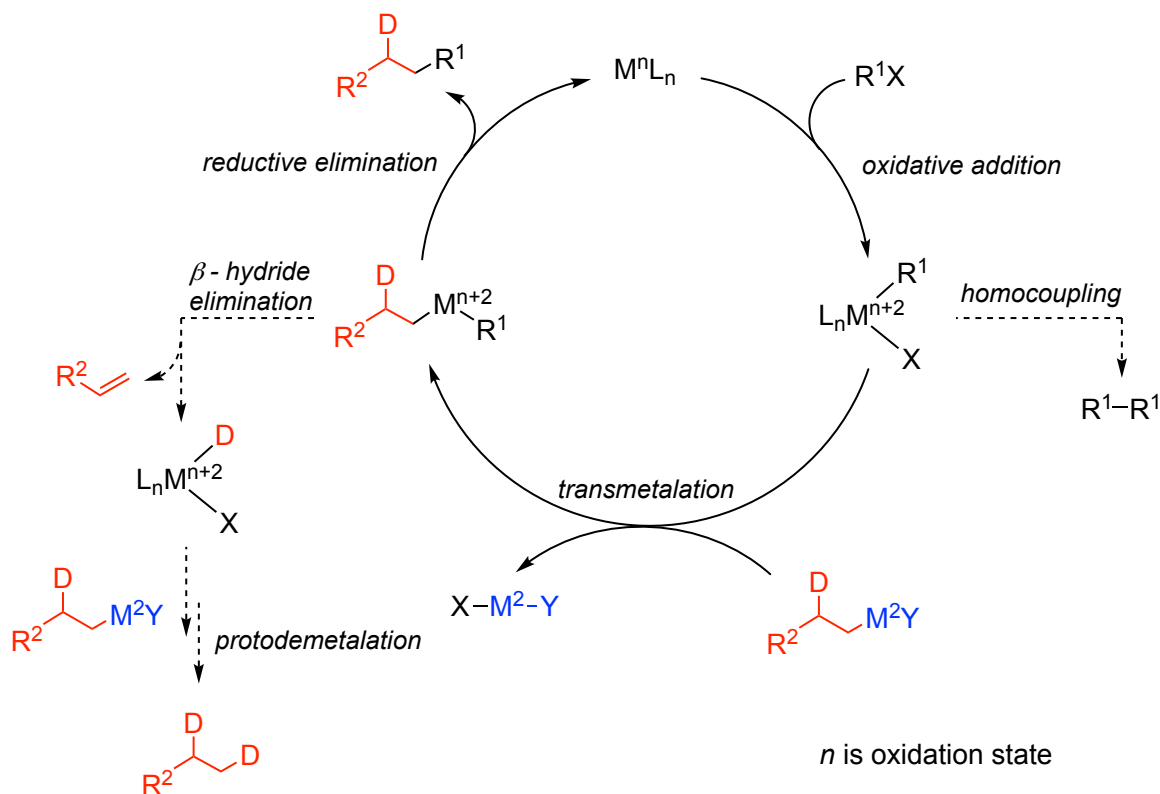


**Figure 1.** Mechanistic details for the cross-coupling reactions of C(sp<sup>3</sup>) organometallics. Figure was adapted from the ref 12. Copyright 2011 American Chemical Society.

The major advance in transition-metal catalysis, especially in coupling applications, is the utilization of later metal complexes, such as well-defined palladium catalysts, in terms of the diversity and tenability of catalyst preparation, good stability under oxidative and aqueous conditions, and facile isolation and characterization of their intermediates, which facilitates mechanistic and methodologic developments.<sup>20</sup> Nevertheless, the discovery of alternatives to these noble organometallic systems has been a significant topic in the recent development from the perspective of catalysis and green chemistry.

The seminal use of nickel catalysts could ascend to around 1897, when Paul Sabatier developed a method for causing unsaturated organic substances to absorb hydrogen and form new organic compounds, primarily mediated by nickel. In 1912, with Victor Grignard, he shared the Nobel Prize in Chemistry, "for his method of hydrogenating organic compounds in the presence of finely disintegrated metals whereby the progress of organic chemistry has been greatly advanced in recent years".<sup>21</sup> Historical contributions to organonickel chemistry from last century outlook the great potentials of nickel organometallic compounds in a wide variety of stoichiometric and, more significantly, catalytic organic syntheses in the homogeneous phase, that was reviewed by Günther Wilke,<sup>22</sup> who is also one of pioneers in dedicating to the synthesis and related reactivity investigations, including the discovery of zero-valent Ni(0)-olefin complexes, in particular Ni(COD)<sub>2</sub>, (where COD is 1,5-cyclooctadiene),<sup>23</sup> and their reactivity in the cyclooligomerizations and polymerizations of unsaturated compounds,<sup>24</sup> as known as important industrial processes.<sup>25</sup>

Nickel-based catalysts, comparing to the related, while more generally applied palladium-based systems, possess an environmentally friendly advantage of being highly abundant. In a practical way, the cost of nickel in the elemental form is roughly 2,000 times lower than palladium, and 10,000 lower than another group 10 counterpart, platinum, on a mole-for-mole basis.<sup>26</sup> Furthermore, the intrinsic properties of nickel, as a relatively electropositive metal in group 10,<sup>27</sup> results in considerable difference in catalytic performance. In the elementary steps of catalysis, oxidative additions of cross-coupling electrophiles,<sup>28</sup> such as alkyl and aromatic halides,<sup>29</sup> phenol derivatives,<sup>30</sup> and even aryl fluorides,<sup>31</sup> can be promoted by nickel catalysts, relative to less reactivity of the same process under Pd-based catalysis (Table 1).<sup>32</sup> Furthermore, recent literature has shown that nickel catalytic systems can proceed C-C bond formation by an elusive ketone decarbonylation reaction, yet without directly groups, comparing to the noble rhodium-mediated catalysis. In this creative new bond construction, the facile release of CO from a low-valent nickel center can be an intriguing application, for the affinity of low-valent metal complexes for CO as the general drawback.<sup>33</sup>

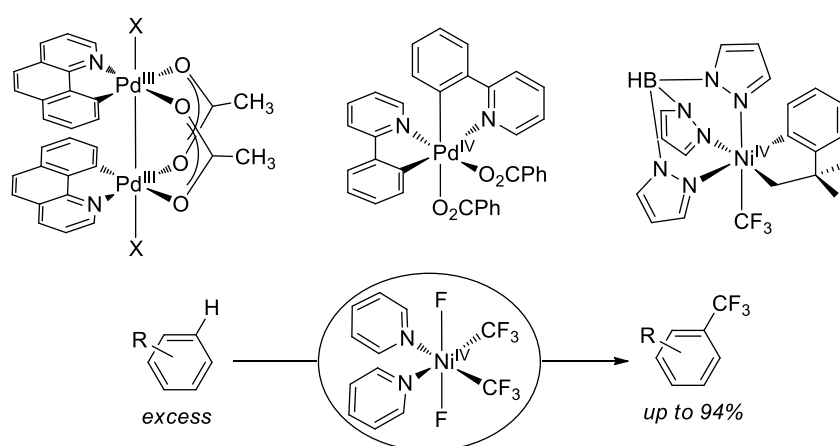
**Table 1.** Comparison of basic characteristics of Pd- and Ni-catalyzed organic cross-coupling reactions.<sup>34</sup>

Precatalyst	Advantages	Disadvantages
<b>Palladium</b>	<ul style="list-style-type: none"> <li>• Low precatalyst loading (&lt;1 mol%)</li> <li>• Reactions proceed at room temperature</li> <li>• Reaction times &lt;1 h</li> <li>• High mechanistic understanding</li> </ul>	<ul style="list-style-type: none"> <li>• Low earth abundance</li> <li>• High cost</li> <li>• Specialized ancillary ligands can cost as much as the metal</li> </ul>
<b>Nickel</b>	<ul style="list-style-type: none"> <li>• Low-cost Earth-abundant metal (~100 p.p.m.)</li> <li>• Can couple electrophiles that are not active with Pd precatalysts</li> <li>• Can undergo one-electron redox step</li> </ul>	<ul style="list-style-type: none"> <li>• High precatalyst loadings</li> <li>• High reaction temperatures</li> <li>• Reaction times &gt;1 h</li> <li>• Low mechanistic understanding</li> <li>• One-electron redox can interfere with productive catalysis</li> </ul>

Deep fundamental investigations of palladium chemistry, particularly through successful isolations characterizations and theoretical calculations of the crucial species involved in the transformations,<sup>35</sup> reveals the main accessibility of Pd<sup>0</sup>/Pd<sup>II</sup> catalytic cycles,<sup>36</sup> as well as other valency including very rarely studied Pd<sup>I</sup>/Pd<sup>III</sup> organometallics in radical processes,<sup>37</sup> and recently investigated Pd<sup>II</sup>/Pd<sup>IV</sup> systems in mediating C-H oxidation and alkene functionalization reactions.<sup>38,39</sup>

The prominent achievements of nickel catalysis are also in need of comprehensive understanding of the mechanistic details by the synthetic, spectroscopic and computational means, especially the studying of the transient organometallic species with unusual valences in the catalytic reactions.

However, as which Sabatier described as a *cheval fougueux* (“spirited horse”),<sup>40</sup> nickel chemistry emerges challenges in the recognition of elementary steps and related change of oxidation states of the metal species in the reaction manifolds. Precisely, the challenges are addressed because of the fertile development of low-cost, air-stable, and easy-to-handle nickel species,<sup>41</sup> resulting in relatively difficult features for fully characterizing the reaction intermediates; in addition, nickel has numerous readily available oxidation states invoked in catalysis.<sup>26</sup> As the majority of Pd(0)/Pd(II) catalytic cycles, Ni(0)/Ni(II) transformations are widespread, but also Ni(I)/Ni(III) and Ni(0)/Ni(II)/Ni(I) are widely accepted, thanks to the synthetic and spectroscopic accessibility to Ni(I) and Ni(III) species, which allows an extensive understanding of reactivity and radical mechanisms.<sup>42</sup> More recently, Ni(IV) species have also been reported in few examples, leading to more direct Ni-mediated catalytic reactivity (Scheme 1).<sup>43</sup>



**Scheme 1.** Selected examples in isolated high-valent Pd<sup>44,45</sup> and Ni<sup>46</sup> complexes (top); C-H trifluoromethylation of arenes mediated by a Ni<sup>IV</sup> complex<sup>47</sup> (bottom).

## 2. Advances in homogenous nickel catalysis: through unusual oxidation states

As just mentioned above, mechanistic insights of nickel catalysis in C-H bond activation and other transformations indicate that organometallic Ni(0), Ni(I), Ni(II), as well as the high-valent analogues Ni(III) and even the rarely reported Ni(IV) can all involve in the fundamental steps of the catalytic processes.<sup>48</sup> However, the exact general accessibility of nickel catalysis remains undefined, as a result of a vast of transformations that undergo through two-electron Ni(0)/Ni(II) and Ni(I)/Ni(III), and one-electron Ni(0)/Ni(I)/Ni(II) processes.<sup>49</sup> More recently, Ni(II)/Ni(IV) mechanism has been proposed in several catalytic systems for nickel-catalyzed cross-coupling reactions,<sup>50–52</sup> and few formal Ni(IV) complexes that are proven as key intermediates in carbon-carbon/carbon-heteroatom bond constructions are isolated, characterized and applied in the catalytic systems.<sup>46,47,53</sup>

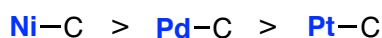
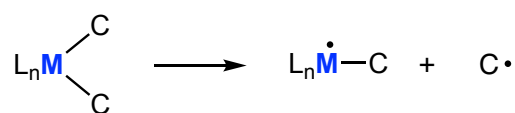
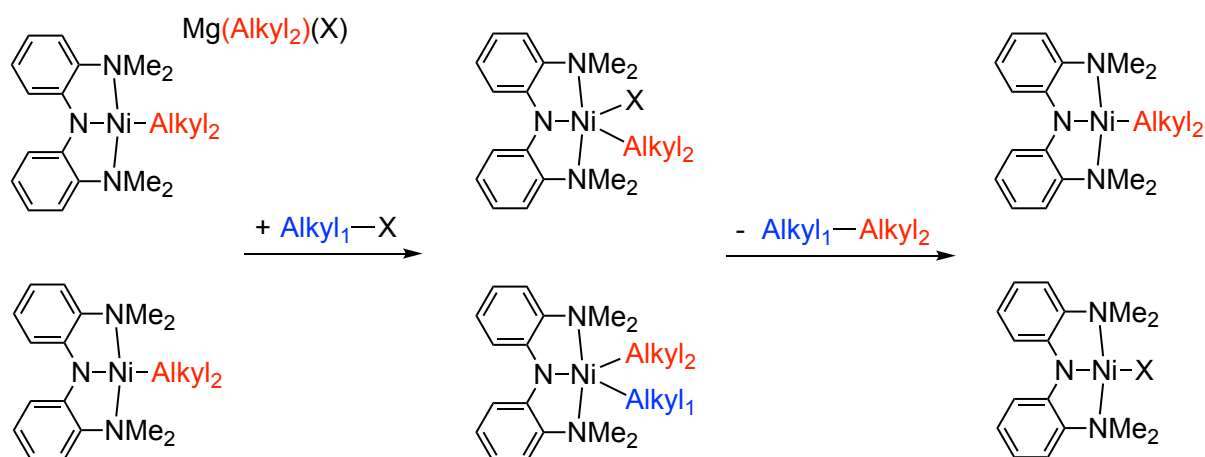


**Figure 2.** Homolytic M-C bond cleavage in the group 10 metals.

For nickel species, M(I) and M(III) oxidation states are much more feasible than those of palladium and platinum complexes. This is due to the homolytic M-C bond cleavage reactivity, so that the contribution of radical processes in nickel chemistry is relatively common, while for platinum it is the most energetically demanding (Figure 2).<sup>49</sup> Martin and co-workers reported a detailed study on the reductive cleavage of carbon-heteroatom bonds catalyzed by a catalytic system as Ni(COD)<sub>2</sub>/Cy<sub>3</sub>P with silanes as reducing agents. The reaction goes through an overall Ni(0)/Ni(II)/Ni(I) catalytic cycle, where Ni(I) species have been proved as the key reaction intermediates, which are generated *via* comproportionation of initially formed Ni(II) species.<sup>54</sup> The group of Hu reported a mechanistic investigation of alkyl-alkyl Kumada coupling reaction catalyzed by a well-defined nickel(II) pincer complex *via* a radical process with the involvement of two nickel centers for the oxidative addition of alkyl halide. A transient intermediate, [(N<sub>2</sub>N)Ni-alkyl<sub>2</sub>](alkyl<sub>2</sub>-MgCl), was identified as the key intermediate for the activation of alkyl halide. The additional interesting finding was that the oxidative addition of alkyl halide yields the formal Ni(III) species, which then readily undergoes a new bond formation by reductive elimination (Scheme 2).<sup>55</sup> Such specific transformations highlight the unique features of reactivity in nickel organometallics as well as the generality of unusual oxidation state evolution processes.<sup>56</sup>



**Scheme 2.** Oxidative addition involving radical intermediates in nickel-catalyzed alkyl-alkyl Kumada coupling reactions. Scheme was adapted from ref 55. Copyright 2013 American Chemical Society.

Endeavors in the attractive field of photoredox catalytic applications can be allowed with the intriguing properties of nickel,<sup>57</sup> especially the readily accessibility of a number of oxidation states *via* single-electron transfer (SET), as well as the related reactivity in the practical approaches, that expedite the development of novel reaction strategies in a synergetic fashion, enabling a powerful

construction of challenging chemical bonds by cross-coupling reactions.<sup>58</sup> For example, Macmillan *et al.* reported a phenomenal work on an operative visible-light-excited photoredox catalytic system applied in the development of a highly efficient carbon-oxygen bond formation reaction by using abundant alcohols and aryl bromides.<sup>59</sup> This work comprehensively demonstrates a general strategy to use an Ir(III) photocatalyst and a Ni(II) co-catalyst to employ photon energy to drive catalytic reactivity (Figure 3).<sup>60</sup> In the mechanistic study of this construction of alkyl aryl ethers, in which the redox activity of a light-activated iridium(III) catalyst is integrated with a nickel catalytic cycle, the aryl bromide reacts a nickel(0) species, generating a nickel(II) intermediate, ArNi<sup>II</sup>Br. This species reacts with the alcohol to generate an inert organo-nickel(II) alkoxide, ArNi<sup>II</sup>OR. Then, when the iridium(III) catalyst is irradiated by light the resulting excited complex (\*Ir<sup>III</sup>) oxidizes ArNi<sup>II</sup>OR through SET process to produce an iridium(II) species and access to a nickel(III) intermediate, ArNi<sup>III</sup>ORBr. This Ni(III) intermediate feasibly undergoes reductive elimination to yield the desired ether product and a nickel(I) species, Ni(I)Br. The regeneration of both catalysts is performed by the reduction of the Ni(I) complex with the reduced state of the Ir(III) photocatalyst, revealing the exceptional ability of nickel to merge Ni(0)/Ni(II)/Ni(III)/Ni(I) oxidation states in one single catalytic cycle that rendered the chemical transformation in a synergetic way.<sup>61</sup>

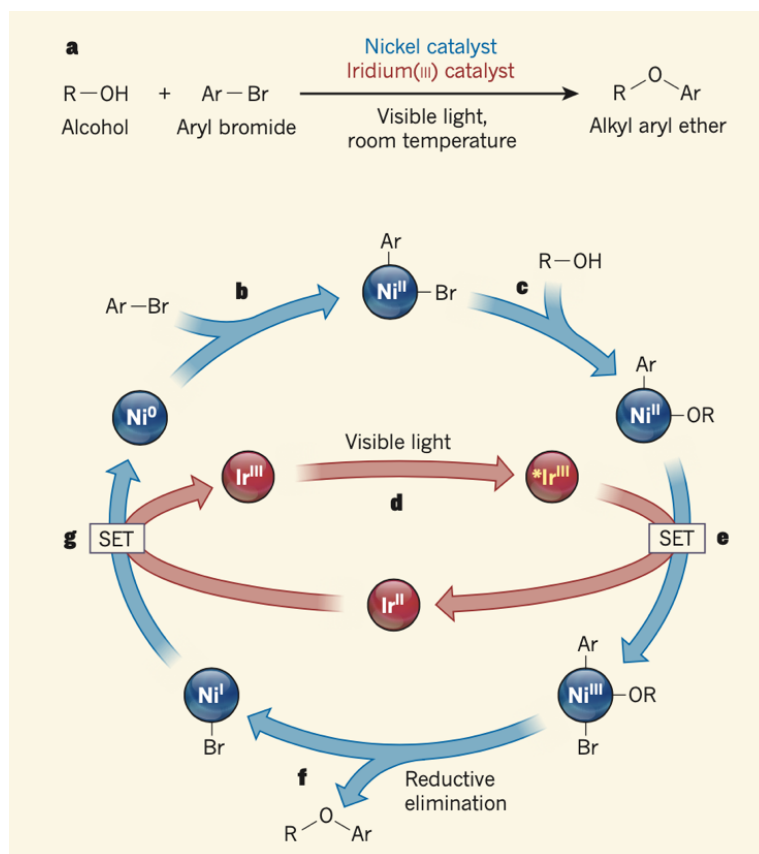


**Figure 3.** Elusive photoredox catalysis of carbon-oxygen bond couplings reported by Macmillan and co-workers by switching oxidation states for nickel. Figure was from ref 60. Copyright 2015 Macmillan Publishers Limited.

However, the transient nature of these putative intermediates has hindered definitive characterization and confirmation of their roles in the chemical transformations. Correspondingly,

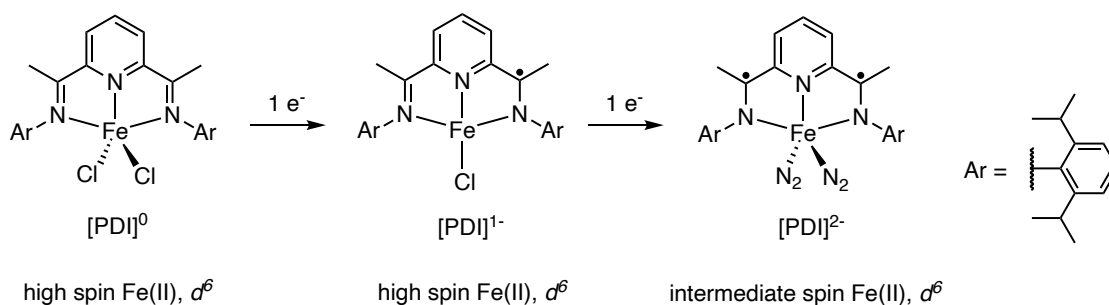
scientists have been contemplating the means to capture these elusive species, in particular with the elaborately designed ligand backbones. For example, over the past decades, redox non-innocent ligands have been used in the isolation of uncommon valent Ni species: a formally monovalent  $[\text{Ni}(\text{tpy})(\text{CH}_3)]$  complex reported by Vicić and colleagues for the mechanistic study of Ni-catalyzed cross-coupling reactions, where tpy is terpyridine, is in fact a Ni(II) bound to a radical-anion tpy ligand. This species has shown an efficient catalytic reactivity behavior in alkyl-alkyl Negishi coupling.<sup>62</sup> Likewise, Mendiola and co-workers showed a redox-active pincer-type Ni(II) complex that can be regarded as a formally high-valent Ni(III) compound.<sup>63</sup>

### 3. Ligands: Redox non-innocence and electron correlations

In 1913, the first Nobel Prize in Chemistry was awarded to Alfred Werner “*in recognition of his work on the linkage of atoms in molecules by which he has thrown new light on earlier investigations and opened up new fields of research especially in inorganic chemistry*”,<sup>64</sup> who defined the basics of coordination chemistry, by such as firstly proposing coordination compounds surrounded by neutral or anionic ligands.<sup>65</sup> After that, ancillary ligands lay the foundations in coordination and organometallic chemistry, such as affording stable metal oxidation states and tuning the reactivity properties of the metal centers with the steric and electronic effects.<sup>66</sup> The ultimate chemical transformations involved in the whole metal complexes are essentially invoked by the electronic properties of the ligands, by a cooperative,<sup>67</sup> or redox-active effect.<sup>68</sup> The former situation is also called metal-ligand cooperation,<sup>69</sup> mainly applied in bond activation of small molecules,<sup>70,71</sup> as well as sustainable chemistry in homogenous catalysis.<sup>72,73</sup> For the latter case, such ligands with redox activity are known as redox non-innocent ligands, which are particularly applied in redox reactions.<sup>74</sup>

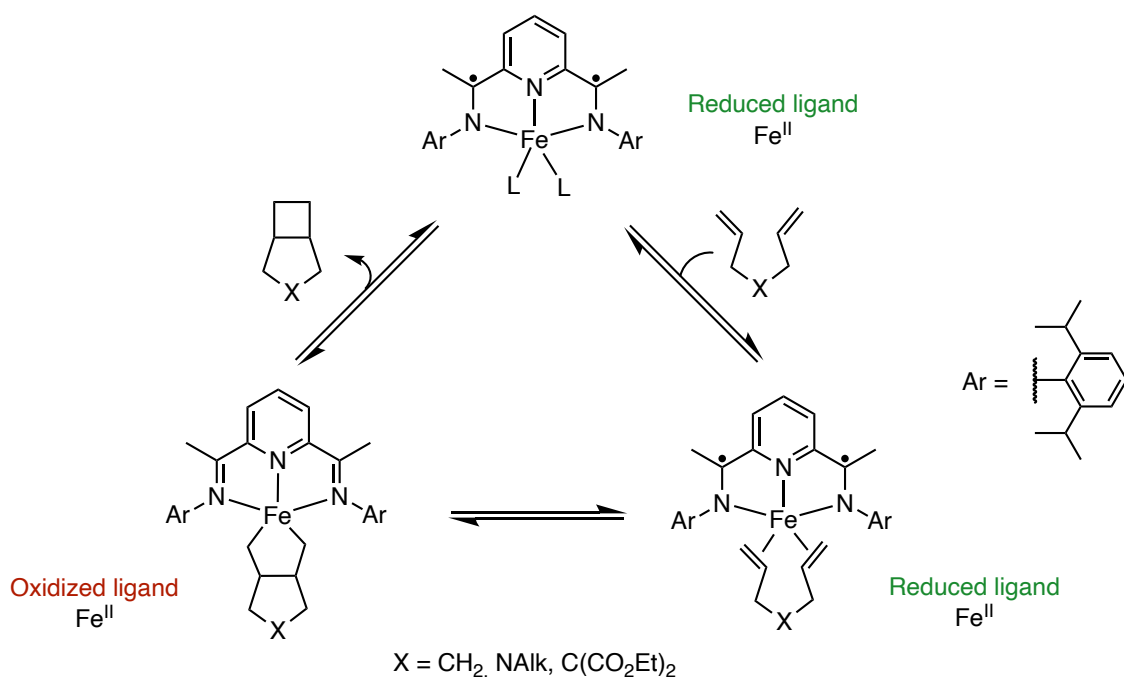
Redox non-innocent ligands, also named as redox-active ligands (RAL), are a series of ancillary ligands that dominate the electron source, with the central metal retaining its oxidation state, instead of the conventional concept of redox transformations taken place at the metal center,<sup>75</sup> which was primarily considered by Jørgensen in order to explain the oxidation state ambiguity of in the 1960s.<sup>76</sup> The metal center, generally, stays in the most stable oxidation state allowing better stability during the redox event occurring on the ligand moiety, where sequential electron transfers are energetically accessible in the oxidation and/or reduction processes.<sup>77</sup> For example, in the presence of redox-active maleonitriledithiolate (MNT) ligand, comprehensive work by Gray and co-workers on the square-planar, formally high-valent transition-metal complexes revealed that the oxidation states of the metal centers should be best described as divalence, with two radical anions on the MNT ligand moiety, rather than the metal in the tetravalent oxidation state and ligand as a dianion.<sup>78</sup> Similarly, in terms of nickel as central metal, the previously reported systems bearing toluene-3,4-dithiolate (tdt) ligands in formal +3 and +4 oxidation states were spectroscopically determined as ligand-centered radical-Ni(II) complexes.<sup>79</sup> As such, stabilization of formally unusual oxidation states of metal complexes can be feasibly attainable with this ligand-based radical system,<sup>80</sup> which can conduct specific reactivity involved in radical pathways.<sup>81</sup>





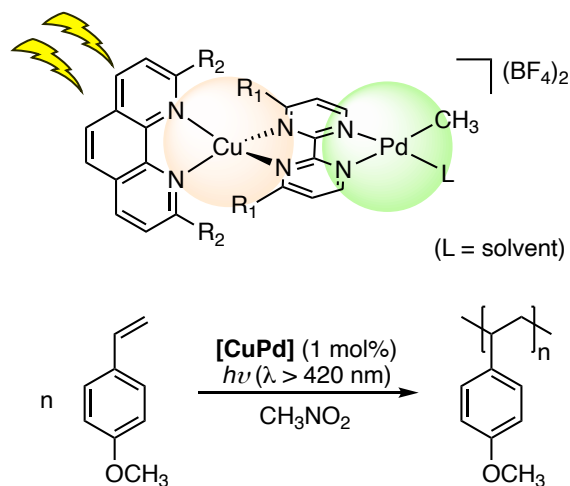
**Scheme 3.** The electronic structures of bis(imino)pyridine iron compounds.

$\pi$ -conjugation of the ligands acts a key role in storing electrons (or holes) in order to undergo the simultaneous single- or multi-electron transfers.<sup>82</sup> In this case, diimine-based ligands and other *N*-heterocycles,<sup>83</sup> have a distinctive capacity to store the internal radical(s) with their extended  $\pi$ -system, which can stabilize the radical species and facilitate radical-mediated reversible chemical transformations with the metal complexes.<sup>84</sup> The delocalized electrons (or holes) in the redox-active system can affect the electronic configurations of the complexes (Scheme 3),<sup>85</sup> which can therefore enhance the catalytic reactivity of some “less active” first-row transition metal catalysts in the catalysis involved in multiple electron-transfer processes.<sup>86</sup> Chirik *et al.* reported an elegant work demonstrating a catalytic reaction of  $[2\pi + 2\pi]$  cycloaddition of dienes and enynes mediated by an iron(II) complex bearing a redox-active bis(imino)pyridine (PDI) ligand. This transformation undergoes a two-electron process, which stems from the PDI ligand, not from the Fe center, thus remaining the energetically favorable +2 oxidation state of iron, instead of the less stable Fe(0) ion with a neutral chelate.<sup>87</sup> The ligand-based radicals facilitate the previously rarely reported reactivity with a Fe catalyst under mild conditions,<sup>88</sup> achieving 95% yield (when X = *N*-<sup>*t*</sup>Bu) with TOF > 250 h (Scheme 4).<sup>89</sup>



**Scheme 4.** Redox non-innocent 2,6-diiminepyridine ligand action as an electron-reservoir in Fe-catalyzed [2+2]-cycloaddition ring-closure reactions.

However, external reductants and oxidants, or radiation, such as photoinduction,<sup>90</sup> are mostly required in the redox-active system in order to offer the electrons (or holes). As a consequence, the reactivity of the complex can be rarely controllable and selective. A multinuclear system can likely ameliorate the selectivity in the presence of an internal electron source.<sup>91</sup> For example, a very recent published work described a heteroleptic Cu(I)-Pd(II) system with a redox-active bipyrimidine (bipym) ligand by the group of Inagaki.<sup>92</sup> The dinuclear complexes, wherein the Cu(I) unit functions as an earth-abundant photosensitizer instead of the precious metals Ru(II) and Ir(III),<sup>93</sup> are active towards styrene polymerization under visible-light irradiation *via* coordination-insertion mechanism. The reactivity at the Pd center can be controlled by the redox-active Cu-ligand moiety, which possesses the photoinduced transition, *i.e.* the copper (M)-to-bipyrimidine (L) charge transfer excited state, by the visible light (Scheme 5).<sup>94</sup>



**Scheme 5.** A Cu(I)–Pd(II) dinuclear photocatalyst reported by Inagaki and co-workers.

Based on the remarkable electronic properties supported by redox non-innocent ligands, controllable redox transformations would be intramolecularly accomplished by building up a multimetallic feature with internal electron source(s), which could lead to notable electronic structures and reactivity at the reactive metal site(s) distinguished from the redox-inactive congeners. On account of this, divalent lanthanides, as strong reductants and appealing electron-transfer sources, are thus considered.

#### 4. Why (divalent) lanthanides?

Fifteen lanthanide elements (lanthanum to lutetium) form a unique series in the Periodic Table, exhibiting a distinguishing atomic feature with the 4f electronic subshell, which results in their characteristic structural, electronic, and energetic properties.<sup>95</sup> Lanthanides (Ln), with scandium and yttrium, are also known as the “rare earths” elements because they were originally discovered together with the lanthanides in rare minerals and isolated as oxides.<sup>96</sup> However, except for promethium (Pm), which only has radioactive isotopes, the lanthanides are relatively earth-abundant; the “rare” characteristics are indicative of the difficulties in the separation of them from each other in natural ores and other mixtures, because of the high similarity in ionic size of lanthanides.<sup>97</sup>

The original separation was known as tedious processes by long-term recrystallization. Basically, the separation of lanthanide ions is industrially achieved by countercurrent solvent extraction method.<sup>98,99</sup> Nowadays, more alternative ways have been developed.<sup>100</sup> For example, redox methods, including the photo-redox process,<sup>101</sup> employ the stabilities of the lanthanide ions under certain oxidation states that can either be stable in precipitation, or stay in solution during the oxidation or reduction steps,<sup>102</sup> and subsequently be separated from the other lanthanide congeners.<sup>103</sup> Moreover, Schelter and co-workers reported an interesting work that the increasing Lewis acidity of the lanthanides can lead to kinetic differences of the irreversible oxidative electron transfer of a coordinated redox-active ligand, indicating a new approach for lanthanide separations.<sup>104</sup>

The fundamental investigation of the accessible oxidation states of lanthanides (Table 2) can help to better understand the variability in their electronic structures and then explore the related reactivity behaviors, in order to develop new paradigms of the 4f elements with diverse coordination environments by using well-designed ligand scaffolds.<sup>105</sup> All lanthanides prevalently form in their trivalence as the most stable oxidation state, regardless of the 4f subshell electrons in the metal ion.<sup>106</sup> More recently, they were also characterized as a stable fashion in solution in the divalent oxidation state,<sup>107</sup> for instance, by using cyclopentadienyl-based (Cp) ligands.<sup>108</sup> Ce<sup>IV</sup> (4f<sup>0</sup>) species are known as strong oxidizing reagents, and recently, they are additionally involved in the selective functionalization of light hydrocarbons as photocatalysts.<sup>109</sup> High-valent lanthanide complexes acquire a lot of endeavors, although the accessibility of non-trivalent oxidation states was rationalized on achieving (or approximately achieving) empty, filled, or half-filled *f* shells (*i.e.* 4f<sup>0</sup>, 4f<sup>14</sup>, or 4f<sup>7</sup>).<sup>110,111</sup> More recently, stabilization of formal tetravalent molecular lanthanide complexes,<sup>112</sup> such as praseodymium and terbium (Pr<sup>4+</sup>/Pr<sup>3+</sup> = +3.2; Tb<sup>4+</sup>/Tb<sup>3+</sup> = +3.1 V vs NHE),<sup>113</sup> are achieved in the presence of siloxide and imidophosphorane ligands,<sup>114–117</sup> which could potentially open a new horizon in the beneficiation and purification of lanthanide ores.<sup>118</sup>

**Table 2.** Commonly known oxidation states of molecular lanthanide complexes.

<sup>57</sup> La	<sup>58</sup> Ce	<sup>59</sup> Pr	<sup>60</sup> Nd	<sup>61</sup> Pm	<sup>62</sup> Sm	<sup>63</sup> Eu	<sup>64</sup> Gd	<sup>65</sup> Tb	<sup>66</sup> Dy	<sup>67</sup> Ho	<sup>68</sup> Er	<sup>69</sup> Tm	<sup>70</sup> Yb	<sup>71</sup> Lu
	+4	+4	+4					+4	+4					
+3	+3	+3	+3	+3	+3	+3	+3	+3	+3	+3	+3	+3	+3	+3
+2	+2	+2	+2		+2	+2	+2	+2	+2	+2	+2	+2	+2	+2

The coordination chemistry of lanthanide elements is being an appealing field due to the intriguing electronic structures,<sup>119</sup> resulting in interesting physical properties, for example, luminescence,<sup>120</sup> and magnetism as single molecule magnets (SMMs).<sup>121</sup> The first organolanthanides were reported by Wilkinson as formal [Cp<sub>3</sub>Ln] complexes (Cp = η<sup>5</sup>-cyclopentadienyl),<sup>122</sup> after the discovery of ferrocene.<sup>123,124</sup> However, despite such complexes were described as featuring an ionic nature of the lanthanides to Cp ring by Wilkinson,<sup>125</sup> the electronic configurations of the central lanthanide ions have been characterized by spectroscopies, revealing an intermediate valence character, instead of the formally trivalent oxidation state.<sup>126</sup> This intermediate valency is also found in the formally tetravalent cerocene,<sup>127</sup> [Ce(COT)<sub>2</sub>] (COT<sup>2-</sup> = η<sup>8</sup>-C<sub>8</sub>H<sub>8</sub>, originally from cyclooctatetraene), and derivatives,<sup>128</sup> which more likely have a trivalent oxidation state in 4f<sup>1</sup> configuration,<sup>129,130</sup> forming multiconfigurational ground states.<sup>131</sup>

The first divalent organolanthanides were reported by Fischer based on the synthesis of Eu(II, 4f<sup>7</sup>, half-filled) and Yb(II, 4f<sup>14</sup>, full-filled) complexes bearing two Cp ligands.<sup>132</sup> During the same period, more lanthanides were known to have accessible divalent oxidation states, while in solid state, mainly formed as halide compounds.<sup>133</sup> These LnX<sub>2</sub> (where X is a halide) species are, not only significant to be synthetic precursors accessing to diverse divalent lanthanide organometallic complexes,<sup>134</sup> which show exceptional reactivity based on the related highly reduced systems;<sup>135</sup>

but also greatly valuable in quantum technologies, and organic and/or organometallic synthesis. For example, they can behave slow magnetic relaxation properties as SMMs,<sup>136</sup> possess great potential in small molecule activation (SMA) reactivity by ligand substitution,<sup>137</sup> such as leading to dinitrogen reduction reactions,<sup>138</sup> and perform single-electron transfer (SET) steps in catalysis,<sup>139</sup> particularly using the Kagan reagent (Sml<sub>2</sub>).<sup>140</sup> Such SET properties prompt a state-of-the-art application of photoredox catalysis by using lanthanide photocatalysts, such as Sml<sub>2</sub>,<sup>141</sup> and those could achieve the activation of some challenging organic substrates under mild conditions.<sup>142</sup> The first catalytic use of divalent lanthanide complexes in visible-light-promoted photoredox chemistry was reported by Allen *et al.*, showing that the molecular Eu<sup>II</sup> species, as the mildest reductant of the divalent congeners, could facilitate carbon-carbon bond formation reactions from unactivated organic halides *via* single-electron transfer process, which was induced by the visible light, forming an excited state of the Eu catalyst.<sup>143</sup>

**Table 3.** Electronic configuration<sup>144</sup> and E°M(II-III) redox potentials with correlation from atomic spectroscopy<sup>113,145</sup> at 25°C with reference to the standard oxidation potential of the normal hydrogen electrode (NHE) for the Ln ions.

Lanthanide	Electronic configuration	E°(Ln <sup>III</sup> /Ln <sup>II</sup> ) (V vs. NHE)	Lanthanide	Electronic configuration	E°(Ln <sup>III</sup> /Ln <sup>II</sup> ) (V vs. NHE)
<sup>57</sup> La	4f <sup>0</sup> 5d <sup>1</sup> 6s <sup>2</sup>	-3.1	<sup>64</sup> Gd	4f <sup>7</sup> 5d <sup>1</sup> 6s <sup>2</sup>	-3.9
<sup>58</sup> Ce	4f <sup>1</sup> 5d <sup>1</sup> 6s <sup>2</sup>	-3.2	<sup>65</sup> Tb	4f <sup>9</sup> 5d <sup>0</sup> 6s <sup>2</sup>	-3.7
<sup>59</sup> Pr	4f <sup>3</sup> 5d <sup>0</sup> 6s <sup>2</sup>	-2.7	<sup>66</sup> Dy	4f <sup>10</sup> 5d <sup>0</sup> 6s <sup>2</sup>	-2.6
<sup>60</sup> Nd	4f <sup>4</sup> 5d <sup>0</sup> 6s <sup>2</sup>	-2.6	<sup>67</sup> Ho	4f <sup>11</sup> 5d <sup>0</sup> 6s <sup>2</sup>	-2.9
<sup>61</sup> Pm	4f <sup>5</sup> 5d <sup>0</sup> 6s <sup>2</sup>	-2.6	<sup>68</sup> Er	4f <sup>12</sup> 5d <sup>0</sup> 6s <sup>2</sup>	-3.1
<sup>62</sup> Sm	4f <sup>6</sup> 5d <sup>0</sup> 6s <sup>2</sup>	-1.55	<sup>69</sup> Tm	4f <sup>13</sup> 5d <sup>0</sup> 6s <sup>2</sup>	-2.3
<sup>63</sup> Eu	4f <sup>7</sup> 5d <sup>0</sup> 6s <sup>2</sup>	-0.35	<sup>70</sup> Yb	4f <sup>14</sup> 5d <sup>0</sup> 6s <sup>2</sup>	-1.15

The successful stabilization of these low-valent compounds in solution has been characterized,<sup>107</sup> in the particular presence of elaborated ligands,<sup>135</sup> even though those metal ions are relatively reductive referring to the [Ln(III, 4f<sup>n</sup>) + e<sup>-</sup> → Ln(II, 4f<sup>n+1</sup>)] standard aqueous reduction potentials (Table 3).<sup>113</sup> The commonly use of molecular Eu(II, 4f<sup>7</sup>), Yb(II, 4f<sup>14</sup>), Sm(II, 4f<sup>6</sup>),<sup>146</sup> and sometimes Tm(II, 4f<sup>13</sup>) species,<sup>135</sup> and the later increasing development of low-valent molecular lanthanide compounds in inorganic, organometallic and coordination chemistry,<sup>147</sup> shows that how important the electronic configurations can affect the physical properties as well as reactivity behaviors of the related compounds,<sup>148</sup> especially performing feasible internal SET [Ln(II, 4f<sup>n+1</sup>) → Ln(III, 4f<sup>n</sup>) + e<sup>-</sup>] when combined with redox non-innocent ligands.

For example, Andersen and co-workers have elucidated the electronic structures of a series of ytterbocenes, which are bearing two ligands, such as pentamethylcyclopentadienyl (Cp<sup>\*</sup>),<sup>149</sup> and in the presence of redox-active ligands. They particularly engaged in the study of single-electron

transfer behaviors from the divalent lanthanide (e.g. ytterbium) center to the *N*-aromatic heterocycles, such as bipyridines (bipy), phenanthrolines (phen) and diazafluorenes. The formally divalent Cp\*<sub>2</sub>Yb(bipy) complex,<sup>150</sup> was expected under two possible limit circumstances: either a divalent Yb(f<sup>14</sup>) and a neutral ligand, or a trivalent Yb(f<sup>13</sup>) and a radical-anionic bipy ligand, resulted from the SET property. Spectroscopic data, including magnetism, and computational studies were in perfect agreement with antiferromagnetic coupling between the Yb(III) center and the ligand-based radical anion, that is, a strong electron correlation in this compound, yielding a multiconfigurational ground state, that is, an open-shell singlet ground state with low-lying triplet excited state.<sup>151</sup> Both configurations of Yb(II, f<sup>14</sup>) and Yb(III, f<sup>13</sup>) are composed in the ground state, forming an intermediate valence state in this molecule.<sup>152</sup> The coordination system overcomes the energy gap between the f-orbitals of Yb and the empty π\* orbitals of the RAL,<sup>153</sup> and facilitates the electron transfer in this case, since the isolated Cp\*<sub>2</sub>Yb(thf)<sub>2</sub> fragment has a reduction potential of -1.48 V,<sup>154</sup> while the bipyridine has a reduction potential of -2.65 V (vs. Fc<sup>+</sup>/Fc).<sup>155</sup> Besides, the substituents (e.g., methyl) on the redox-active bipy ligand could interestingly affect the redox properties, which are in correlation with the relative population of the f<sup>13</sup> and f<sup>14</sup> configurations.<sup>153</sup> In parallel with the comprehensive study of Cp\*<sub>2</sub>Yb(bipy) compound, Nocton and Andersen investigated the analogous Cp\*<sub>2</sub>Yb complexes with redox-active phenanthroline adducts.<sup>156</sup> Effective electron transfer, *i.e.* reduction, on the ligand moieties from divalent lanthanide was identified by magnetic and spectroscopic analysis, including crystallographic study. The formed carbon radical on the phen ligand moiety then dimerized in solution to form a σ C-C bond, whereas the bipy analogue remained the stable radical character without further chemical reactions. In strong contrast with the case of bipyridine adduct, phenanthroline allows a triplet ground state. The difference in electronic configurations of these two decamethylytterbocene complexes possessing high symmetry, can be rationalized by the LUMO of the respective RALs in these two situations (Figure 4).<sup>156</sup> In the case of bipyridine adduct of Cp\*<sub>2</sub>Yb, a low singlet-triplet energy gap is calculated and experimentally identified. When the electron is transferred to the lowest π\* orbital, which stays in a b<sub>1</sub> symmetry and is low enough in energy to be populated, the respective half-filled ligand orbital and 4f orbital of Yb are very close in energy, that stabilizes the open-shell singlet state.

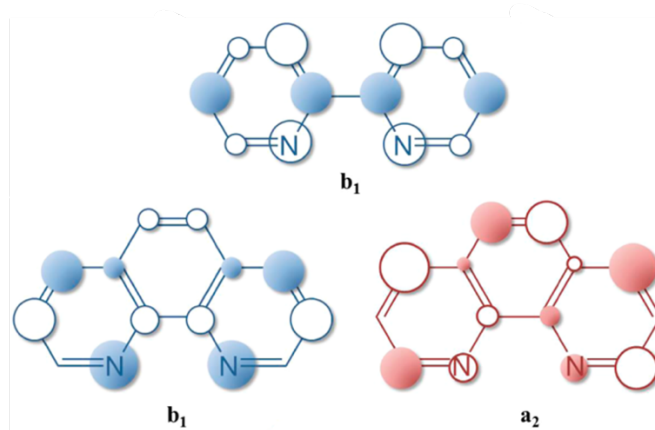


**Figure 4.** LUMO symmetry orbitals in  $C_{2v}$  for bipyridine and phenanthroline. Figure was adapted from the article of Nocton and Andersen.<sup>157</sup> Copyright 2014 American Chemical Society.

In terms of ytterbocene with phen adduct, based on the analysis of the qualitative Molecular Orbital (MO) model as well as the computational studies, the LUMO and LUMO+1 of  $b_1$  and  $a_2$  symmetry (in  $C_{2v}$  symmetry), respectively, are low enough in energy for accessibly being populated in the ground state when the charge transfer takes place. In contrast to the case of bipy, the ligand  $a_2$  orbital of phen can be stabilized by interaction with the empty Yb 5d orbital, resulting in a half-occupied  $a_2$  orbital, *i.e.* an open-shell triplet electronic configuration (Figure 5).<sup>156</sup>

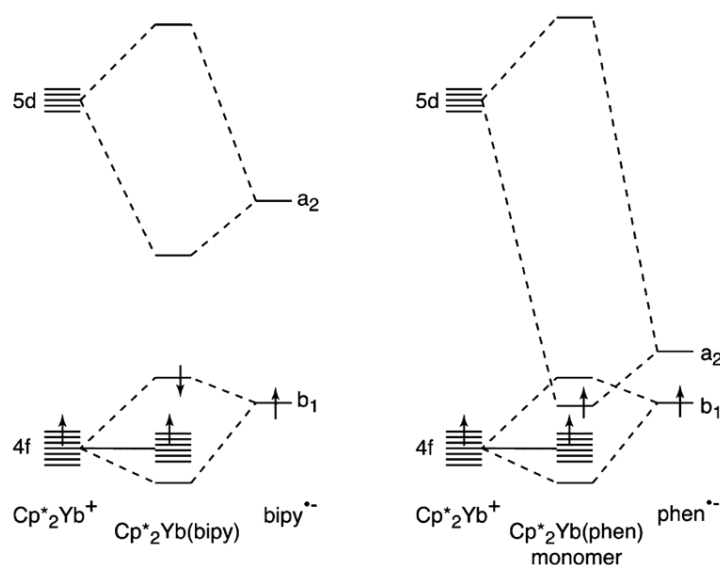
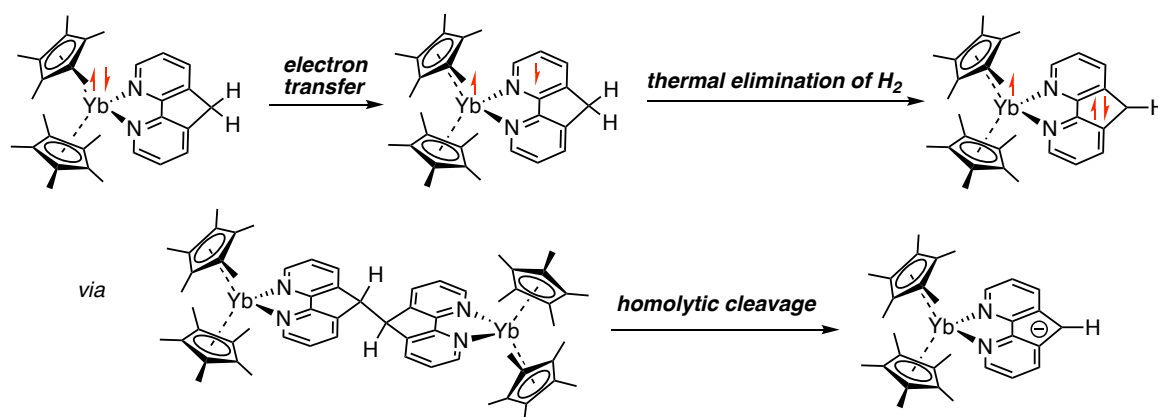


**Figure 5.** Qualitative MO diagram comparing bonding in  $Cp^*_2Yb(bipy)$  and  $Cp^*_2Yb(phen)$  monomer. Only the unpaired 4f electron is illustrated; the orbitals below those with arrows are filled. The direction of the arrows indicates the ground states of these two complexes. Figure was taken from the article of Nocton and Andersen.<sup>156</sup> Copyright 2014 American Chemical Society.

The ordering of these molecular orbitals could be therefore inverted by the substituents such as methyl groups on the phenanthroline ligand. In the further study of Nocton and Andersen, the substituted phenanthroline adducts are either triplets in the 3,8-Me<sub>2</sub>phen and 5,6-Me<sub>2</sub>phen adducts

of ytterbocenes,<sup>156</sup> or open-shell multiconfigurational singlets in  $\text{Cp}^*_2\text{Yb}(4,7\text{-Me}_2\text{phen})$  complex as the bipyridine one.<sup>157</sup> In the latter case, the resulted reactivity can be controlled by such ground-state electronic structure leading to an irreversible disproportionation in solution, forming two new species namely  $\text{Cp}^*_2\text{Yb}(4\text{-}(\text{CH}_2),7\text{-Mephen})$  and  $\text{Cp}^*_2\text{Yb}(4,7\text{-Me}_2\text{-}4\text{H}\text{-phen})$ , which lost a hydrogen atom, and gained a hydrogen atom, respectively.<sup>158</sup> This transformation involved in a C-H bond activation at one methyl substituent; while a reversible  $\sigma$ -bond formation between two ligands as the case of non-substituted  $\text{Cp}^*_2\text{Yb}(\text{phen})$  species was observed in the 3,8- $\text{Me}_2\text{phen}$  adduct.<sup>157</sup> Such multiconfigurational nature was identically observed in the 4,5-diazafluorene adduct compound, featuring two open-shell singlets lying below the triplet state. Triggered by such unusual electronic properties, this compound, in contrast to the sufficiently stable character of bipy adduct, can thermally undergo a heterolytic cleavage of C-H bond on the ligand in solution to form an Yb(III) amide species and dihydrogen, *via* an evolution of a homolytic cleavage of a coupled C-C bond resulting in formation of the 4,5-diazafluorenyl adduct (Scheme 6).<sup>159</sup>



**Scheme 6.** Thermal dihydrogen elimination from  $\text{Cp}^*_2\text{Yb}(4,5\text{-diazfluorene})$  complex.

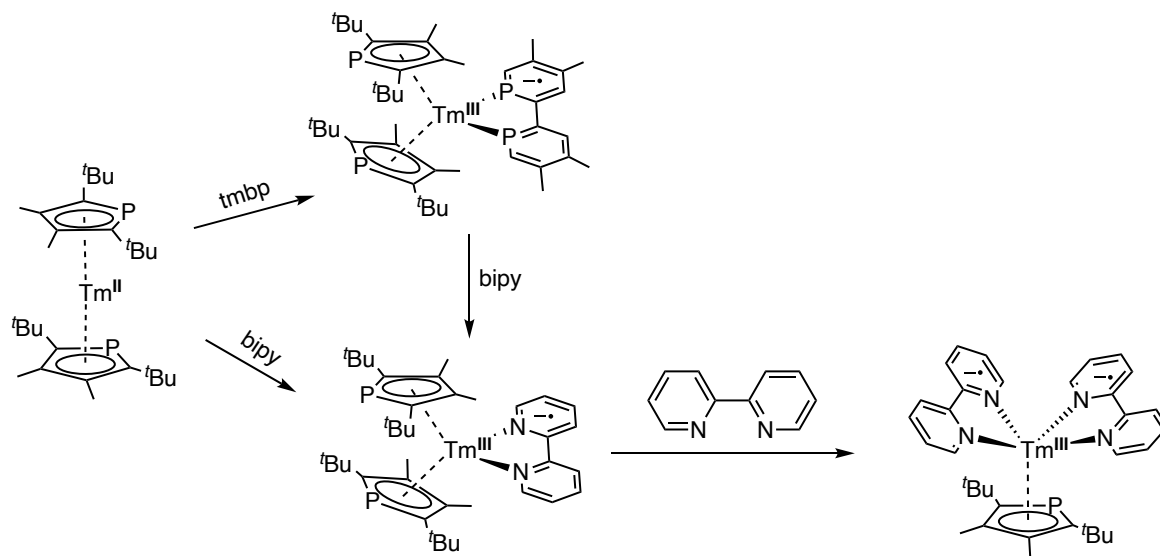
Moreover, some redox reactivity has also been observed with ytterbocenes in the presence of other bulky redox-active ligands as known as “sterically governed”,<sup>160</sup> including a series of substituted iminopyridines,<sup>161</sup> or diazabutadienes (DAD),<sup>162</sup> performing reductive transformations as a result of the  $\text{Ln}(\text{II})\text{-RAL}$  electron transfer.<sup>163</sup>

In parallel, since the isolation and characterizations of samarocenes reported by Evans and co-workers,<sup>164</sup> the reductive reactivity of these species have also been extensively explored, including dinitrogen reduction reaction yielding a planar side-on bridging of  $\text{N}_2$  complex,<sup>165</sup> but also the ligand-based radical coupling formations resulted from the efficient SET behavior from the divalent Sm center.<sup>166,167</sup> A similar example in a series of phenanthroline complexes of samarocene with different steric hinderance on the Cp analogues, was reported by our group in 2015, highlighting a reversible C-C bond coupling formation in the 4-position of phenanthroline adduct in solution despite of different thermodynamics in all studied cases.<sup>168</sup>

Divalent thulium, with a  $4f^{13}$  configuration which is “approaching” a less-stable filled shell, is regarded as not only drastically reactive in SET reactions because of the much negative estimated standard reduction potential, but also promising in the spectroscopic investigation since it is



isoelectronic to Yb(III), which features one-hole electronic structure.<sup>169</sup> However, known as the relatively low stability and propensity to disproportionate, Tm(II) complexes are very challenging to synthesize though they generally possess intriguing electronic structures.<sup>170,171</sup> In the presence of bulky ligands, especially cyclopentadienyl or phospholyl ligands bearing bulky functional groups, these highly reactive species can be prevented from the reductive side reactions.<sup>172,173</sup> The in-depth understanding of the nature of divalent thulium organometallic complexes has been in implementation, since the first successfully isolated Tm(II) complex by the group of Evans in 2002,<sup>174</sup> opening a new area of synthetic organolanthanides,<sup>175</sup> spectroscopic studies including magnetic behavior,<sup>176</sup> and electron transfer reactivity, such as N<sub>2</sub> reduction and ligand reductive coupling reactions,<sup>138,177</sup> including a reversible phenanthroline adduct coupling formation developed by our group.<sup>168</sup> This SET reactivity was also studied with a bis(phospholyl) thulium(II) complex in 2014 (Scheme 7). An effective electron transfer occurred from the highly reductive Tm(II) to a redox-active ligand, namely tetramethyl-2,2'-biphosphinine (tmbp), yielding a Dtp<sub>2</sub>Tm(tmbp) species. Another SET could take place when one equivalent of bipyridine was added, forming the analogue bipy complex with a release of tmbp ligand. Multiple single-electron transfer reactivity in this case was interestingly found when another equivalent of neutral bipyridine was added, generating a new species in which one phospholyl ligand was replaced by a bipyridine radical anion.178



**Scheme 7.** Multiple single-electron transfers in bipyridine complexes of bis(phospholyl) thulium.

Accordingly, the difference in physical properties and chemical reactivity due to the subtle changes on the series of organolanthanides can be rationalized by the investigations of electronic structures of these complexes. The comprehensive investigations on these ligand-based radical species, even some in the dimerized fashion but with reversibility in solution, resulted from the effective SET processes by divalent lanthanides, would be of great inspiration for the further design of new coordination systems, for example, a series of heterometallic complexes in order to use the transferred and stored electron(s) on the redox-active ligands. The first thought was to include

transition metal fragments where could perform further chemical transformations, while be modulated by the electron transfer(s), in the desired heteroleptic framework.

The heteroleptic complexes containing lanthanides and transition metals, have been reported in terms of multimetallic cooperativity.<sup>179</sup> These complexes behave high participation in metal-metal interaction,<sup>180</sup> single-molecule magnetism,<sup>181</sup> and catalysis. In the latter case, trivalent lanthanide ions are vastly used to promote the catalytic activity at the transition metal sites, as excellent Lewis acids. However, divalent organolanthanides are scarcely discovered as good electron sources without photo activation in multimetallic systems. Accordingly, the utilization of the SET behavior of divalent organolanthanides with *N*-aromatic ligands, in other word, that of the transferred and delocalized electron(s) on the redox non-innocent ligand system, would be of significant interest. Inspired by the efficient photo-redox processes, a multinuclear system with lanthanides and d-block metals, can be proposed, in the presence of redox-active ligand as an “on-off switch” for the transferred electron(s). Instead of using external electron sources, internal electron transfer can be accomplished by divalent lanthanide(s), acting as a remote control, in such heteroleptic molecules, and therefore, chemical transformations can selectively take place at the reactive transition metal center(s), such as olefin functionalization and C-H bond activation reactions,<sup>185–190</sup> even with relatively inert hydrocarbons in the latter case.<sup>191–194</sup> Additionally, the electronic structures of these heterometallic complexes can be intriguingly differentiated by the SET process of lanthanides as a result of the redox non-innocence,<sup>195–197</sup> that can also lead to the possible stabilization of highly reactive species as intermediates in the transformation processes, such as the isolation of organometallics in unusual oxidation states.

## 5. Objectives of the PhD thesis

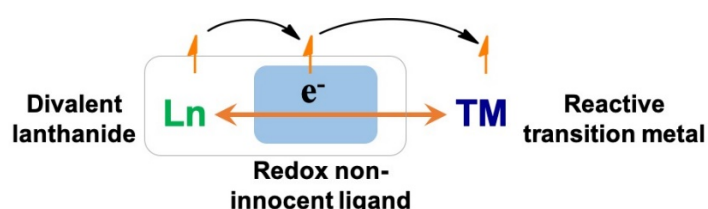
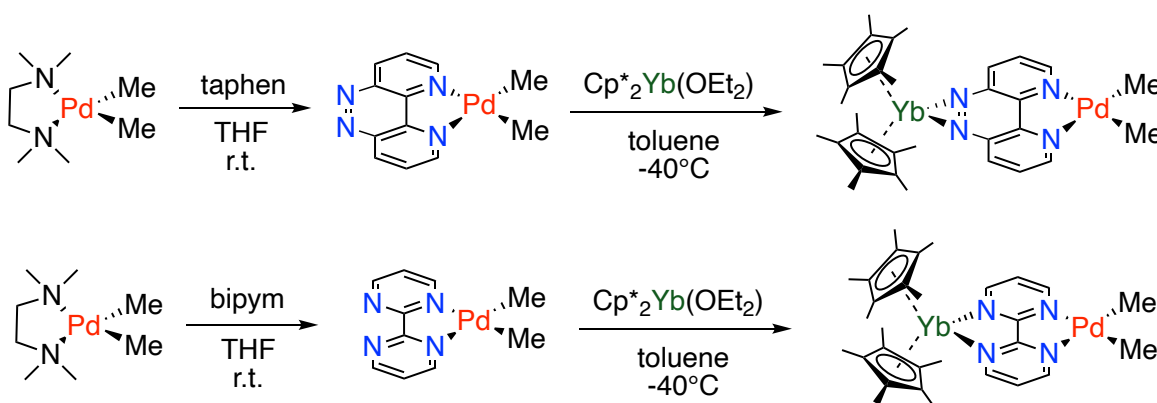


**Figure 6.** General concept for establishing heterometallic complexes with divalent lanthanides and transition metals in conjunction with redox non-innocent ligands.

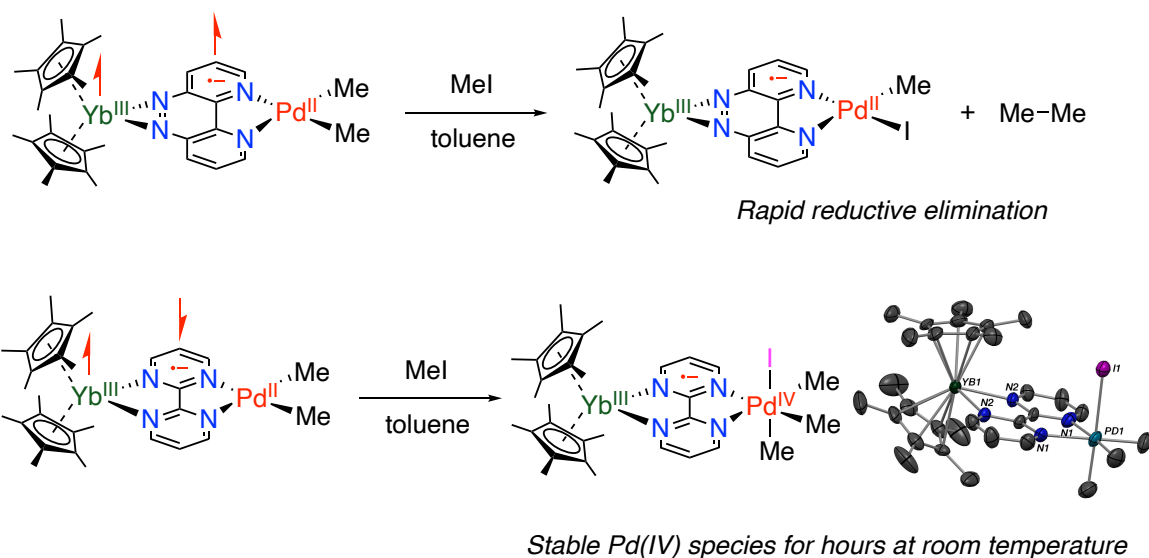
An original heterobimetallic framework bridged by redox-active ligands, combining a highly reductive divalent organolanthanide and a reactive transition metal fragment, was therefore proposed and being developed under consideration (Figure 6). For example, bimetallic complexes containing a divalent lanthanide,  $Cp^*_2Yb$ , and a palladium ion functionalized by dialkyl groups,  $PdMe_2$ , combined by redox-active ligands, 2,2'-bipyrimidine (bipym) and 4,5,9,10-tetraazaphenanthrene (taphen), which are the analogues of bipy and phen, respectively, have been recently reported, with comprehensive analysis on the electronic structures as well as unique reactivity (Scheme 8). An efficient single-electron reduction on the ligand-metal fragments of the studied complexes, as a consequence of the SET property of divalent lanthanides, was initially

identified by X-ray diffraction and NMR spectroscopy, additionally investigated by solid-state magnetism (SQUID) analysis and DFT calculations. The electronic structures of the bimetallic complexes are in significant consistence with the ones found in their respective  $\text{Cp}^*_2\text{Yb}(\text{phen})$  and  $\text{Cp}^*_2\text{Yb}(\text{bipy})$  analogues. Magnetic measurements revealed that the taphen complex,  $\text{Cp}^*_2\text{Yb}(\text{taphen})\text{PdMe}_2$ , features a triplet ground state. In strong contrast, the temperature-dependent magnetic data at low temperature agreed well with a multiconfigurational electronic configuration of the bipym analogue,  $\text{Cp}^*_2\text{Yb}(\text{bipym})\text{PdMe}_2$ , that is in which a low-lying singlet ground state with different configurations (open- and closed-shell), with a low-lying triplet state thermally populated at room temperature. Spectroscopic data, as well as theoretical studies, indicated that in the taphen complex, the transferred electron mainly lies on the taphen ligand with very limited participation on the Yb center, while in the bipym complex, there is a strong electron correlation between the Yb ion and the bipym ligand.



**Scheme 8.** Representative original heterobimetallic framework by Goudy *et al.*<sup>198</sup> reported in 2017.

The corresponding reactivity behaviors on the reactive palladium centers therefore resulted from distinct electronic ground states in these two complexes. The oxidative addition of iodomethane (1.0 equivalent) was performed on the heterometallic complexes, of which reactivity on the palladium dialkyl complexes was previously described by Canty and colleagues in forming a putative, high-valent Pd(IV) species.<sup>199</sup> Indeed, after the oxidative addition of MeI, a rapid reductive elimination process of ethane took place in the transiently formed  $\text{Cp}^*_2\text{Yb}(\text{taphen})\text{Pd}(\text{IV})\text{Me}_3\text{I}$  intermediate, as well as with the two palladium precursors,  $(\text{taphen})\text{PdMe}_2$  and  $(\text{bipym})\text{PdMe}_2$ , in great agreement with the studies of Canty and co-workers.<sup>200,201</sup> However, in the bipym ligand system, a room-temperature stable Pd(IV) was isolated and further fully characterized (Scheme 9). The prominent stability of this formed  $\text{Cp}^*_2\text{Yb}(\text{bipym})\text{Pd}(\text{IV})\text{Me}_3\text{I}$  compound enabled kinetical studies on the reductive elimination step, revealing the half-time of this Pd(IV) species being more than one hour at room temperature, and an increase reactive enthalpy barrier. This study demonstrated how the divalent lanthanides introduce electron correlations in differentiated redox-active systems, tuning the related reactivity and properties on the transition metal centers.



**Scheme 9.** Fine tuning the reactivity in oxidation addition by redox-active ligand control access to a Pd(IV) intermediate stabilization.

This well-designed heterometallic system has been and is being applied in the laboratory, with a vast combination in different divalent organolanthanides, redox-active ligands and transition metal fragments. This PhD thesis focuses on the challenging first-row late transition metal, nickel. Of particular interest nature of nickel, especially in unprecedented redox steps from Ni(0) to Ni(IV) *via* one- or two-electron processes, may impart large difference in electronic structures and specific reactivity properties of the redox-active heterobimetallic complexes with the electron correlations thanks to divalent lanthanides.

Sequential work to apply the previously studied palladium complexes into nickel will be introduced at the first place in **Chapter II**, describing a similar  $\text{Cp}^*_2\text{Yb}(\text{bipym})\text{NiMe}_2$  complex. The characterizations of this synthesized species, including magnetism, will be presented, indicating also a multiconfigurational electronic structure. As a result of SET behavior, distinct reactivity comparing to that of the corresponding nickel precursor,  $(\text{bipym})\text{NiMe}_2$ , has been found in carbon monoxide activation reaction and the related kinetics have been studied, revealing the importance of divalent lanthanide in influencing the putative migratory insertion intermediate of the reaction.<sup>202</sup> The modification on the functional groups on the nickel center will then be discussed in **Chapter III**. The considerations of replacing dialkyl into perfluoroalkyl groups are arisen from the intriguing electronic properties of the  $\text{CF}_3$  ligand, as well as the corresponding reactivity behaviors such as the isolation of high-valent species and C-F bond activation reactions. The challenges in isolating the ideal bimetallic complexes but only fluoride abstraction by divalent lanthanides from the nickel precursors would open up an additional way to study the possibly generated difluorocarbene species.

The influence of different ligand scaffolds will be next considered. A dissymmetric redox-active ligand system will be introduced in **Chapter IV**, as an unprecedented radical coupling to form a  $\sigma$  C-C bond between two ligands at the *para* positions on the pyrimidine cycle in the presence of

divalent lanthanide. An interesting transition from *dimeric* to *trimeric species* has been investigated by the isolation of the heteroleptic, transient *exo* dimer. On the contrary, in the presence of a strong reductant,  $KC_8$ , the reductive coupling takes place on the meso carbons of the pyrimidine ring, which shows the intriguing difference of electronic properties modulated by the lanthanide fragment. Furthermore, one of the original aspects in this work is to firstly introduce a dissymmetric redox-active system in divalent organolanthanides that can facilitate the ligand coupling reaction. Finally, tridentate ligand backbones are extended in **Chapter V**. It has shown that multidentate scaffold could be essential for the stabilization of organometallics in uncommon oxidation states,<sup>203</sup> which can further lead to interesting chemical transformations.<sup>62</sup> Attempts in the reduction of the additional ancillary pyridyl fragment in the redox-active terpyridine-based alkylnickel complex are applied by using strong reducing reagents such as  $KC_8$ , and more importantly by divalent lanthanides, in order to undergo the single electron transfer into the ligand system. Moreover, preliminary reactivity insights have currently been under investigation, potentially showing an interesting behavior with the inherent electron-transfer properties based on the radical anionic nature of the complex.

## References

- (1) The Nobel Prize in Chemistry 2010. <https://www.nobelprize.org/prizes/chemistry/2010/summary/>.
- (2) Negishi, E. Magical Power of Transition Metals: Past, Present, and Future (Nobel Lecture). *Angew. Chem. Int. Ed.* **2011**, *50* (30), 6738–6764. <https://doi.org/10.1002/anie.201101380>.
- (3) Suzuki, A. Cross-Coupling Reactions of Organoboranes: An Easy Way To Construct C-C Bonds (Nobel Lecture). *Angew. Chem. Int. Ed.* **2011**, *50* (30), 6722–6737. <https://doi.org/10.1002/anie.201101379>.
- (4) Trost, B. M. On Inventing Reactions for Atom Economy. *Acc. Chem. Res.* **2002**, *35* (9), 695–705. <https://doi.org/10.1021/ar010068z>.
- (5) Yamaguchi, J.; Yamaguchi, A. D.; Itami, K. C–H Bond Functionalization: Emerging Synthetic Tools for Natural Products and Pharmaceuticals. *Angew. Chem. Int. Ed.* **2012**, *51* (36), 8960–9009. <https://doi.org/10.1002/anie.201201666>.
- (6) Abrams, D. J.; Provencher, P. A.; Sorensen, E. J. Recent Applications of C–H Functionalization in Complex Natural Product Synthesis. *Chem. Soc. Rev.* **2018**, *47* (23), 8925–8967. <https://doi.org/10.1039/C8CS00716K>.
- (7) Curto, J. M.; Kozlowski, M. C. Chemoselective Activation of Sp<sup>3</sup> vs Sp<sup>2</sup> C–H Bonds with Pd(II). *J. Am. Chem. Soc.* **2015**, *137* (1), 18–21. <https://doi.org/10.1021/ja5093166>.
- (8) Sambiasco, C.; Schönbauer, D.; Blicke, R.; Dao-Huy, T.; Pototschnig, G.; Schaaf, P.; Wiesinger, T.; Zia, M. F.; Wencel-Delord, J.; Besset, T.; Maes, B. U. W.; Schnürch, M. A Comprehensive Overview of Directing Groups Applied in Metal-Catalysed C–H Functionalisation Chemistry. *Chem. Soc. Rev.* **2018**, *47* (17), 6603–6743. <https://doi.org/10.1039/C8CS00201K>.
- (9) Chen, M. S.; White, M. C. A Predictably Selective Aliphatic C–H Oxidation Reaction for Complex Molecule Synthesis. *Science* **2007**, *318* (5851), 783–787. <https://doi.org/10.1126/science.1148597>.
- (10) Xue, X.-S.; Ji, P.; Zhou, B.; Cheng, J.-P. The Essential Role of Bond Energetics in C–H Activation/Functionalization. *Chem. Rev.* **2017**, *117* (13), 8622–8648. <https://doi.org/10.1021/acs.chemrev.6b00664>.
- (11) Gutekunst, W. R.; Baran, P. S. C–H Functionalization Logic in Total Synthesis. *Chem. Soc. Rev.* **2011**, *40* (4), 1976–1991. <https://doi.org/10.1039/C0CS00182A>.
- (12) Jana, R.; Pathak, T. P.; Sigman, M. S. Advances in Transition Metal (Pd,Ni,Fe)-Catalyzed Cross-Coupling Reactions Using Alkyl-Organometallics as Reaction Partners. *Chem. Rev.* **2011**, *111* (3), 1417–1492. <https://doi.org/10.1021/cr100327p>.
- (13) Rilatt, I.; Jackson, R. F. W. Kinetic Studies on the Stability and Reactivity of  $\beta$ -Amino Alkylzinc Iodides Derived from Amino Acids. *J. Org. Chem.* **2008**, *73* (22), 8694–8704. <https://doi.org/10.1021/jo801754k>.
- (14) Negishi, E.; King, A. O.; Okukado, N. Selective Carbon-Carbon Bond Formation via Transition Metal Catalysis. 3. A Highly Selective Synthesis of Unsymmetrical Biaryls and Diarylmethanes by the Nickel- or Palladium-Catalyzed Reaction of Aryl- and Benzylzinc Derivatives with Aryl Halides. *J. Org. Chem.* **1977**, *42* (10), 1821–1823. <https://doi.org/10.1021/jo00430a041>.
- (15) Murahashi, S.; Yamamura, M.; Yanagisawa, K.; Mita, N.; Kondo, K. Stereoselective Synthesis of Alkenes and Alkenyl Sulfides from Alkenyl Halides Using Palladium and Ruthenium Catalysts. *J. Org. Chem.* **1979**, *44* (14), 2408–2417. <https://doi.org/10.1021/jo01328a016>.
- (16) Cárdenas, D. J. Advances in Functional-Group-Tolerant Metal-Catalyzed Alkyl–Alkyl Cross-Coupling Reactions. *Angew. Chem. Int. Ed.* **2003**, *42* (4), 384–387. <https://doi.org/10.1002/anie.200390123>.
- (17) Nicolaou, K. C.; Bulger, P. G.; Sarlah, D. Palladium-Catalyzed Cross-Coupling Reactions in Total Synthesis. *Angew. Chem. Int. Ed.* **2005**, *44* (29), 4442–4489. <https://doi.org/10.1002/anie.200500368>.
- (18) Hayashi, T.; Konishi, M.; Fukushima, M.; Mise, T.; Kagotani, M.; Tajika, M.; Kumada, M. Asymmetric Synthesis Catalyzed by Chiral Ferrocenylphosphine-Transition Metal Complexes.

2. Nickel- and Palladium-Catalyzed Asymmetric Grignard Cross-Coupling. *J. Am. Chem. Soc.* **1982**, *104* (1), 180–186. <https://doi.org/10.1021/ja00365a033>.
- (19) Hayashi, T. Catalytic Asymmetric Cross-Coupling. *J. Organomet. Chem.* **2002**, *653* (1), 41–45. [https://doi.org/10.1016/S0022-328X\(02\)01272-X](https://doi.org/10.1016/S0022-328X(02)01272-X).
- (20) Tsuji, J. *Palladium Reagents and Catalysts: New Perspectives for the 21st Century*, John Wiley & Sons, Ltd: New York, 2004.
- (21) Paul Sabatier – Biographical. <https://www.nobelprize.org/prizes/chemistry/1912/sabatier/biographical/>.
- (22) Wilke, G. Contributions to Organo-Nickel Chemistry. *Angew. Chem. Int. Ed. Engl.* **1988**, *27* (1), 185–206. <https://doi.org/10.1002/anie.198801851>.
- (23) Wilke, G.; Bogdanović, B.; Hardt, P.; Heimbach, P.; Keim, W.; Kröner, M.; Oberkirch, W.; Tanaka, K.; Steinrücke, E.; Walter, D.; Zimmermann, H. Allyl-Transition Metal Systems. *Angew. Chem. Int. Ed. Engl.* **1966**, *5* (2), 151–164. <https://doi.org/10.1002/anie.196601511>.
- (24) Wilke, G.; Bogdanović, B.; Borner, P.; Breil, H.; Hardt, P.; Heimbach, P.; Herrmann, G.; Kaminsky, H.-J.; Keim, W.; Kröner, M.; Müller, H.; Müller, E. W.; Oberkirch, W.; Schneider, J.; Stedefeder, J.; Tanaka, K.; Weyer, K.; Wilke, G. Cyclooligomerization of Butadiene and Transition Metal  $\pi$ -Complexes. *Angew. Chem. Int. Ed. Engl.* **1963**, *2* (3), 105–115. <https://doi.org/10.1002/anie.196301051>.
- (25) Kaminsky, W.; Arndt, M.; Böhm, L. L.; Vogt, D.; Chauvin, Y.; Olivier, H.; Henkelmann, J.; Taube, R.; Sylvester, G.; Mol, J. C.; Drent, E.; Broekhoven, J. A. M. van; Budzelaar, P. H. M.; Yoshimura, N.; Wilke, G.; Eckerle, A. Reactions of Unsaturated Compounds. In *Applied Homogeneous Catalysis with Organometallic Compounds*; John Wiley & Sons, Ltd, 2008; pp 220–273. <https://doi.org/10.1002/9783527619351.ch2c>.
- (26) Tasker, S. Z.; Standley, E. A.; Jamison, T. F. Recent Advances in Homogeneous Nickel Catalysis. *Nature* **2014**, *509* (7500), 299–309. <https://doi.org/10.1038/nature13274>.
- (27) Pauling, L. THE NATURE OF THE CHEMICAL BOND. IV. THE ENERGY OF SINGLE BONDS AND THE RELATIVE ELECTRONEGATIVITY OF ATOMS. *J. Am. Chem. Soc.* **1932**, *54* (9), 3570–3582. <https://doi.org/10.1021/ja01348a011>.
- (28) Tsou, T. T.; Kochi, J. K. Mechanism of Oxidative Addition. Reaction of Nickel(0) Complexes with Aromatic Halides. *J. Am. Chem. Soc.* **1979**, *101* (21), 6319–6332. <https://doi.org/10.1021/ja00515a028>.
- (29) Dudnik, A. S.; Fu, G. C. Nickel-Catalyzed Coupling Reactions of Alkyl Electrophiles, Including Unactivated Tertiary Halides, To Generate Carbon–Boron Bonds. *J. Am. Chem. Soc.* **2012**, *134* (25), 10693–10697. <https://doi.org/10.1021/ja304068t>.
- (30) Mesganaw, T.; Garg, N. K. Ni- and Fe-Catalyzed Cross-Coupling Reactions of Phenol Derivatives. *Org. Process Res. Dev.* **2013**, *17* (1), 29–39. <https://doi.org/10.1021/op300236f>.
- (31) Zhou, J.; Kuntze-Fechner, M. W.; Bertermann, R.; Paul, U. S. D.; Berthel, J. H. J.; Friedrich, A.; Du, Z.; Marder, T. B.; Radius, U. Preparing (Multi)Fluoroarenes as Building Blocks for Synthesis: Nickel-Catalyzed Borylation of Polyfluoroarenes via C–F Bond Cleavage. *J. Am. Chem. Soc.* **2016**, *138* (16), 5250–5253. <https://doi.org/10.1021/jacs.6b02337>.
- (32) Rosen, B. M.; Quasdorf, K. W.; Wilson, D. A.; Zhang, N.; Resmerita, A.-M.; Garg, N. K.; Percec, V. Nickel-Catalyzed Cross-Couplings Involving Carbon–Oxygen Bonds. *Chem. Rev.* **2011**, *111* (3), 1346–1416. <https://doi.org/10.1021/cr100259t>.
- (33) Somerville, R. J.; Martin, R. Forging C–C Bonds Through Decarbonylation of Aryl Ketones. *Angew. Chem. Int. Ed.* **2017**, *56* (24), 6708–6710. <https://doi.org/10.1002/anie.201702188>.
- (34) Hazari, N.; Melvin, P. R.; Beromi, M. M. Well-Defined Nickel and Palladium Precatalysts for Cross-Coupling. *Nat. Rev. Chem.* **2017**, *1* (3), 1–16. <https://doi.org/10.1038/s41570-017-0025>.
- (35) Canty, A. J. Organopalladium and Platinum Chemistry in Oxidising Milieu as Models for Organic Synthesis Involving the Higher Oxidation States of Palladium. *Dalton Trans.* **2009**, No. 47, 10409–10417. <https://doi.org/10.1039/B914080H>.
- (36) Lyons, T. W.; Sanford, M. S. Palladium-Catalyzed Ligand-Directed C–H Functionalization Reactions. *Chem. Rev.* **2010**, *110* (2), 1147–1169. <https://doi.org/10.1021/cr900184e>.

- (37) Liu, Q.; Dong, X.; Li, J.; Xiao, J.; Dong, Y.; Liu, H. Recent Advances on Palladium Radical Involved Reactions. *ACS Catal.* **2015**, *5* (10), 6111–6137. <https://doi.org/10.1021/acscatal.5b01469>.
- (38) Mei, T.-S.; Wang, X.; Yu, J.-Q. Pd(II)-Catalyzed Amination of C–H Bonds Using Single-Electron or Two-Electron Oxidants. *J. Am. Chem. Soc.* **2009**, *131* (31), 10806–10807. <https://doi.org/10.1021/ja904709b>.
- (39) Muñiz, K. High-Oxidation-State Palladium Catalysis: New Reactivity for Organic Synthesis. *Angew. Chem. Int. Ed.* **2009**, *48* (50), 9412–9423. <https://doi.org/10.1002/anie.200903671>.
- (40) Sabatier, P. Hydrogénations et Déshydrogénations Par Catalyse. *Berichte Dtsch. Chem. Ges.* **1911**, *44* (3), 1984–2001. <https://doi.org/10.1002/cber.19110440303>.
- (41) Nattmann, L.; Saeb, R.; Nöthling, N.; Cornella, J. An Air-Stable Binary Ni(0)–Olefin Catalyst. *Nat. Catal.* **2020**, *3* (1), 6–13. <https://doi.org/10.1038/s41929-019-0392-6>.
- (42) Li, Y.; Zou, L.; Bai, R.; Lan, Y. Ni(I)–Ni(III) vs. Ni(II)–Ni(IV): Mechanistic Study of Ni-Catalyzed Alkylation of Benzamides with Alkyl Halides. *Org. Chem. Front.* **2018**, *5* (4), 615–622. <https://doi.org/10.1039/C7QO00850C>.
- (43) Nebra, N. High-Valent NiIII and NiIV Species Relevant to C–C and C–Heteroatom Cross-Coupling Reactions: State of the Art. *Molecules* **2020**, *25* (5), 1141. <https://doi.org/10.3390/molecules25051141>.
- (44) Powers, D. C.; Ritter, T. Bimetallic Pd(III) Complexes in Palladium-Catalysed Carbon–Heteroatom Bond Formation. *Nat. Chem.* **2009**, *1* (4), 302–309. <https://doi.org/10.1038/nchem.246>.
- (45) Dick, A. R.; Kampf, J. W.; Sanford, M. S. Unusually Stable Palladium(IV) Complexes: Detailed Mechanistic Investigation of C–O Bond-Forming Reductive Elimination. *J. Am. Chem. Soc.* **2005**, *127* (37), 12790–12791. <https://doi.org/10.1021/ja0541940>.
- (46) Camasso, N. M.; Sanford, M. S. Design, Synthesis, and Carbon-Heteroatom Coupling Reactions of Organometallic Nickel(IV) Complexes. *Science* **2015**, *347* (6227), 1218–1220. <https://doi.org/10.1126/science.aaa4526>.
- (47) D’Accriscio, F.; Borja, P.; Saffon-Merceron, N.; Fustier-Boutignon, M.; Mézailles, N.; Nebra, N. C–H Bond Trifluoromethylation of Arenes Enabled by a Robust, High-Valent Nickel(IV) Complex. *Angew. Chem. Int. Ed.* **2017**, *56* (42), 12898–12902. <https://doi.org/10.1002/anie.201706237>.
- (48) Hu, X. Nickel-Catalyzed Cross Coupling of Non-Activated Alkyl Halides: A Mechanistic Perspective. *Chem. Sci.* **2011**, *2* (10), 1867–1886. <https://doi.org/10.1039/C1SC00368B>.
- (49) Ananikov, V. P. Nickel: The “Spirited Horse” of Transition Metal Catalysis. *ACS Catal.* **2015**, *5* (3), 1964–1971. <https://doi.org/10.1021/acscatal.5b00072>.
- (50) Aihara, Y.; Chatani, N. Nickel-Catalyzed Direct Arylation of C(sp<sup>3</sup>)–H Bonds in Aliphatic Amides via Bidentate-Chelation Assistance. *J. Am. Chem. Soc.* **2014**, *136* (3), 898–901. <https://doi.org/10.1021/ja411715v>.
- (51) Bour, J. R.; Camasso, N. M.; Sanford, M. S. Oxidation of Ni(II) to Ni(IV) with Aryl Electrophiles Enables Ni-Mediated Aryl–CF<sub>3</sub> Coupling. *J. Am. Chem. Soc.* **2015**, *137* (25), 8034–8037. <https://doi.org/10.1021/jacs.5b04892>.
- (52) Roberts, C. C.; Chong, E.; Kampf, J. W.; Canty, A. J.; Ariafard, A.; Sanford, M. S. Nickel(II/IV) Manifold Enables Room-Temperature C(sp<sup>3</sup>)–H Functionalization. *J. Am. Chem. Soc.* **2019**, *141* (49), 19513–19520. <https://doi.org/10.1021/jacs.9b11999>.
- (53) Mirica, L. M.; Smith, S. M.; Griego, L. Organometallic Chemistry of High-Valent Ni(III) and Ni(IV) Complexes. In *Nickel Catalysis in Organic Synthesis*; John Wiley & Sons, Ltd, 2019; pp 223–248. <https://doi.org/10.1002/9783527813827.ch10>.
- (54) Cornella, J.; Gómez-Bengoa, E.; Martin, R. Combined Experimental and Theoretical Study on the Reductive Cleavage of Inert C–O Bonds with Silanes: Ruling out a Classical Ni(0)/Ni(II) Catalytic Couple and Evidence for Ni(I) Intermediates. *J. Am. Chem. Soc.* **2013**, *135* (5), 1997–2009. <https://doi.org/10.1021/ja311940s>.



- (55) Breitenfeld, J.; Ruiz, J.; Wodrich, M. D.; Hu, X. Bimetallic Oxidative Addition Involving Radical Intermediates in Nickel-Catalyzed Alkyl–Alkyl Kumada Coupling Reactions. *J. Am. Chem. Soc.* **2013**, *135* (32), 12004–12012. <https://doi.org/10.1021/ja4051923>.
- (56) Lipschutz, M. I.; Tilley, T. D. Carbon–Carbon Cross-Coupling Reactions Catalyzed by a Two-Coordinate Nickel(II)–Bis(Amido) Complex via Observable NiI, NiII, and NiIII Intermediates. *Angew. Chem. Int. Ed.* **2014**, *53* (28), 7290–7294. <https://doi.org/10.1002/anie.201404577>.
- (57) McAtee, R. C.; McClain, E. J.; Stephenson, C. R. J. Illuminating Photoredox Catalysis. *Trends Chem.* **2019**, *1* (1), 111–125. <https://doi.org/10.1016/j.trechm.2019.01.008>.
- (58) Shaw, M. H.; Twilton, J.; MacMillan, D. W. C. Photoredox Catalysis in Organic Chemistry. *J. Org. Chem.* **2016**, *81* (16), 6898–6926. <https://doi.org/10.1021/acs.joc.6b01449>.
- (59) Terrett, J. A.; Cuthbertson, J. D.; Shurtleff, V. W.; MacMillan, D. W. C. Switching on Elusive Organometallic Mechanisms with Photoredox Catalysis. *Nature* **2015**, *524* (7565), 330–334. <https://doi.org/10.1038/nature14875>.
- (60) Murphy, J. J.; Melchiorre, P. Light Opens Pathways for Nickel Catalysis. *Nature* **2015**, *524* (7565), 297–298. <https://doi.org/10.1038/nature15200>.
- (61) Corcoran, E. B.; Pirnot, M. T.; Lin, S.; Dreher, S. D.; DiRocco, D. A.; Davies, I. W.; Buchwald, S. L.; MacMillan, D. W. C. Aryl Amination Using Ligand-Free Ni(II) Salts and Photoredox Catalysis. *Science* **2016**, *353* (6296), 279–283. <https://doi.org/10.1126/science.aag0209>.
- (62) Anderson, T. J.; Jones, G. D.; Vicic, D. A. Evidence for a NiI Active Species in the Catalytic Cross-Coupling of Alkyl Electrophiles. *J. Am. Chem. Soc.* **2004**, *126* (26), 8100–8101. <https://doi.org/10.1021/ja0483903>.
- (63) Adhikari, D.; Mossin, S.; Basuli, F.; Huffman, J. C.; Szilagyi, R. K.; Meyer, K.; Mindiola, D. J. Structural, Spectroscopic, and Theoretical Elucidation of a Redox-Active Pincer-Type Ancillary Applied in Catalysis. *J. Am. Chem. Soc.* **2008**, *130* (11), 3676–3682. <https://doi.org/10.1021/ja7108486>.
- (64) The Nobel Prize in Chemistry 1913 <https://www.nobelprize.org/prizes/chemistry/1913/summary/>.
- (65) Constable, E. C.; Housecroft, C. E. Coordination Chemistry: The Scientific Legacy of Alfred Werner. *Chem. Soc. Rev.* **2013**, *42* (4), 1429–1439. <https://doi.org/10.1039/C2CS35428D>.
- (66) Cotton, F. A.; Wilkinson, G.; Murillo, C. A. *Advanced Inorganic Chemistry*; Wiley-Interscience: New York; Chichester; Weinheim, 1999.
- (67) Grützmacher, H. Cooperating Ligands in Catalysis. *Angew. Chem. Int. Ed.* **2008**, *47* (10), 1814–1818. <https://doi.org/10.1002/anie.200704654>.
- (68) Luca, O. R.; Crabtree, R. H. Redox-Active Ligands in Catalysis. *Chem. Soc. Rev.* **2013**, *42* (4), 1440–1459. <https://doi.org/10.1039/C2CS35228A>.
- (69) Khusnutdinova, J. R.; Milstein, D. Metal–Ligand Cooperation. *Angew. Chem. Int. Ed.* **2015**, *54* (42), 12236–12273. <https://doi.org/10.1002/anie.201503873>.
- (70) Gunanathan, C.; Gnanaprakasam, B.; Iron, M. A.; Shimon, L. J. W.; Milstein, D. “Long-Range” Metal–Ligand Cooperation in H<sub>2</sub> Activation and Ammonia-Promoted Hydride Transfer with a Ruthenium–Acridine Pincer Complex. *J. Am. Chem. Soc.* **2010**, *132* (42), 14763–14765. <https://doi.org/10.1021/ja107770y>.
- (71) Gunanathan, C.; Milstein, D. Bond Activation and Catalysis by Ruthenium Pincer Complexes. *Chem. Rev.* **2014**, *114* (24), 12024–12087. <https://doi.org/10.1021/cr5002782>.
- (72) Gunanathan, C.; Milstein, D. Metal–Ligand Cooperation by Aromatization–Dearomatization: A New Paradigm in Bond Activation and “Green” Catalysis. *Acc. Chem. Res.* **2011**, *44* (8), 588–602. <https://doi.org/10.1021/ar2000265>.
- (73) Alig, L.; Fritz, M.; Schneider, S. First-Row Transition Metal (De)Hydrogenation Catalysis Based On Functional Pincer Ligands. *Chem. Rev.* **2019**, *119* (4), 2681–2751. <https://doi.org/10.1021/acs.chemrev.8b00555>.
- (74) Berben, L. A.; Bruin, B. de; Heyduk, A. F. Non-Innocent Ligands. *Chem. Commun.* **2015**, *51* (9), 1553–1554. <https://doi.org/10.1039/C4CC90480J>.

- (75) Chirik, P. J. Preface: Forum on Redox-Active Ligands. *Inorg. Chem.* **2011**, *50* (20), 9737–9740. <https://doi.org/10.1021/ic201881k>.
- (76) Jørgensen, Chr. K. Differences between the Four Halide Ligands, and Discussion Remarks on Trigonal-Bipyramidal Complexes, on Oxidation States, and on Diagonal Elements of One-Electron Energy. *Coord. Chem. Rev.* **1966**, *1* (1), 164–178. [https://doi.org/10.1016/S0010-8545\(00\)80170-8](https://doi.org/10.1016/S0010-8545(00)80170-8).
- (77) Ward, M. D.; McCleverty, J. A. Non-Innocent Behaviour in Mononuclear and Polynuclear Complexes: Consequences for Redox and Electronic Spectroscopic Properties. *J. Chem. Soc. Dalton Trans.* **2002**, No. 3, 275–288. <https://doi.org/10.1039/B110131P>.
- (78) Billig, E.; Williams, R.; Bernal, I.; Waters, J. H.; Gray, H. B. The Electronic Structures of Square-Planar Metal Complexes. II. The Complexes of Maleonitriledithiolate with Copper(II), Nickel(II), Palladium(II), and Platinum(II). *Inorg. Chem.* **1964**, *3* (5), 663–666. <https://doi.org/10.1021/ic50015a013>.
- (79) Stiefel, E. I.; Waters, J. H.; Billig, E.; Gray, H. B. The Myth of Nickel(III) and Nickel(IV) in Planar Complexes. *J. Am. Chem. Soc.* **1965**, *87* (13), 3016–3017. <https://doi.org/10.1021/ja01091a047>.
- (80) Büttner, T.; Geier, J.; Frison, G.; Harmer, J.; Calle, C.; Schweiger, A.; Schönberg, H.; Grützmacher, H. A Stable Aminyl Radical Metal Complex. *Science* **2005**, *307* (5707), 235–238. <https://doi.org/10.1126/science.1106070>.
- (81) Hetterscheid, D. G. H.; Kaiser, J.; Reijerse, E.; Peters, T. P. J.; Thewissen, S.; Blok, A. N. J.; Smits, J. M. M.; de Gelder, R.; de Bruin, B. Ir<sup>II</sup>(Ethene): Metal or Carbon Radical? *J. Am. Chem. Soc.* **2005**, *127* (6), 1895–1905. <https://doi.org/10.1021/ja0439470>.
- (82) Chirik, P. J.; Wieghardt, K. Radical Ligands Confer Nobility on Base-Metal Catalysts. *Science* **2010**, *327* (5967), 794–795. <https://doi.org/10.1126/science.1183281>.
- (83) de Bruin, B.; Bill, E.; Bothe, E.; Weyhermüller, T.; Wieghardt, K. Molecular and Electronic Structures of Bis(Pyridine-2,6-Diimine)Metal Complexes [ML<sub>2</sub>](PF<sub>6</sub>)<sub>n</sub> (n = 0, 1, 2, 3; M = Mn, Fe, Co, Ni, Cu, Zn). *Inorg. Chem.* **2000**, *39* (13), 2936–2947. <https://doi.org/10.1021/ic000113j>.
- (84) Lyaskovskyy, V.; de Bruin, B. Redox Non-Innocent Ligands: Versatile New Tools to Control Catalytic Reactions. *ACS Catal.* **2012**, *2* (2), 270–279. <https://doi.org/10.1021/cs200660v>.
- (85) Bart, S. C.; Chłopek, K.; Bill, E.; Bouwkamp, M. W.; Lobkovsky, E.; Neese, F.; Wieghardt, K.; Chirik, P. J. Electronic Structure of Bis(Imino)Pyridine Iron Dichloride, Monochloride, and Neutral Ligand Complexes: A Combined Structural, Spectroscopic, and Computational Study. *J. Am. Chem. Soc.* **2006**, *128* (42), 13901–13912. <https://doi.org/10.1021/ja064557b>.
- (86) Sylvester, K. T.; Chirik, P. J. Iron-Catalyzed, Hydrogen-Mediated Reductive Cyclization of 1,6-Enynes and Diynes: Evidence for Bis(Imino)Pyridine Ligand Participation. *J. Am. Chem. Soc.* **2009**, *131* (25), 8772–8774. <https://doi.org/10.1021/ja902478p>.
- (87) Budzelaar, P. H. M.; de Bruin, B.; Gal, A. W.; Wieghardt, K.; van Lenthe, J. H. Metal-to-Ligand Electron Transfer in Diiminopyridine Complexes of Mn–Zn. A Theoretical Study. *Inorg. Chem.* **2001**, *40* (18), 4649–4655. <https://doi.org/10.1021/ic001457c>.
- (88) Lautens, M.; Klute, W.; Tam, W. Transition Metal-Mediated Cycloaddition Reactions. *Chem. Rev.* **1996**, *96* (1), 49–92. <https://doi.org/10.1021/cr950016l>.
- (89) Bouwkamp, M. W.; Bowman, A. C.; Lobkovsky, E.; Chirik, P. J. Iron-Catalyzed [2π + 2π] Cycloaddition of α,ω-Dienes: The Importance of Redox-Active Supporting Ligands. *J. Am. Chem. Soc.* **2006**, *128* (41), 13340–13341. <https://doi.org/10.1021/ja064711u>.
- (90) Prier, C. K.; Rankic, D. A.; MacMillan, D. W. C. Visible Light Photoredox Catalysis with Transition Metal Complexes: Applications in Organic Synthesis. *Chem. Rev.* **2013**, *113* (7), 5322–5363. <https://doi.org/10.1021/cr300503r>.
- (91) Halpin, Y.; Pryce, M. T.; Rau, S.; Dini, D.; Vos, J. G. Recent Progress in the Development of Bimetallic Photocatalysts for Hydrogen Generation. *Dalton Trans.* **2013**, *42* (46), 16243–16254. <https://doi.org/10.1039/C3DT52319E>.

- (92) Fujiwara, T.; Nomura, K.; Inagaki, A. Cu–Pd Dinuclear Complexes with Earth-Abundant Cu Photosensitizer: Synthesis and Photopolymerization. *Organometallics* **2020**. <https://doi.org/10.1021/acs.organomet.0c00261>.
- (93) Hossain, A.; Bhattacharyya, A.; Reiser, O. Copper's Rapid Ascent in Visible-Light Photoredox Catalysis. *Science* **2019**, *364* (6439). <https://doi.org/10.1126/science.aav9713>.
- (94) Hernandez-Perez, A. C.; Collins, S. K. Heteroleptic Cu-Based Sensitizers in Photoredox Catalysis. *Acc. Chem. Res.* **2016**, *49* (8), 1557–1565. <https://doi.org/10.1021/acs.accounts.6b00250>.
- (95) Wells, W. H.; Wells, V. L. The Lanthanides, Rare Earth Elements. In *Patty's Toxicology*; American Cancer Society, 2012; pp 817–840. <https://doi.org/10.1002/0471435139.tox043.pub2>.
- (96) Bünzli, J.-C. G.; McGill, I. Rare Earth Elements. In *Ullmann's Encyclopedia of Industrial Chemistry*; American Cancer Society, 2018; pp 1–53. [https://doi.org/10.1002/14356007.a22\\_607.pub2](https://doi.org/10.1002/14356007.a22_607.pub2).
- (97) Charalampides, G.; Vatalis, K. I.; Apostoplos, B.; Ploutarch-Nikolas, B. Rare Earth Elements: Industrial Applications and Economic Dependency of Europe. *Procedia Econ. Finance* **2015**, *24*, 126–135. [https://doi.org/10.1016/S2212-5671\(15\)00630-9](https://doi.org/10.1016/S2212-5671(15)00630-9).
- (98) Kubota, F.; Goto, M.; Nakashio, F. Extraction of Rare Earth Metals with 2-Ethylhexyl Phosphonic Acid Mono-2-Ethylhexyl Ester in the Presence of Diethylenetriaminepentaacetic Acid in Aqueous Phase. *Solvent Extr. Ion Exch.* **1993**, *11*, 437–453. <https://doi.org/10.1080/07366299308918165>.
- (99) Horwitz, E. P.; McAlister, D. R.; Dietz, M. L. Extraction Chromatography Versus Solvent Extraction: How Similar Are They? *Sep. Sci. Technol.* **2006**, *41*, 2163–2182. <https://doi.org/10.1080/01496390600742849>.
- (100) Cheisson, T.; Schelter, E. J. Rare Earth Elements: Mendeleev's Bane, Modern Marvels. *Science* **2019**, *363* (6426), 489–493. <https://doi.org/10.1126/science.aau7628>.
- (101) Donohue, T. Photochemical Separation of Cerium from Rare Earth Mixtures in Aqueous Solution. *Chem. Phys. Lett.* **1979**, *61* (3), 601–604. [https://doi.org/10.1016/0009-2614\(79\)87181-X](https://doi.org/10.1016/0009-2614(79)87181-X).
- (102) Xie, F.; Zhang, T. A.; Dreisinger, D.; Doyle, F. A Critical Review on Solvent Extraction of Rare Earths from Aqueous Solutions. *Miner. Eng.* **2014**, *56*, 10–28. <https://doi.org/10.1016/j.mineng.2013.10.021>.
- (103) Uda, T.; Jacob, K. T.; Hirasawa, M. Technique for Enhanced Rare Earth Separation. *Science* **2000**, *289* (5488), 2326–2329. <https://doi.org/10.1126/science.289.5488.2326>.
- (104) Fang, H.; Cole, B. E.; Qiao, Y.; Bogart, J. A.; Cheisson, T.; Manor, B. C.; Carroll, P. J.; Schelter, E. J. Electro-Kinetic Separation of Rare Earth Elements Using a Redox-Active Ligand. *Angew. Chem. Int. Ed.* **2017**, *56* (43), 13450–13454. <https://doi.org/10.1002/anie.201706894>.
- (105) Evans, W. J. Tutorial on the Role of Cyclopentadienyl Ligands in the Discovery of Molecular Complexes of the Rare-Earth and Actinide Metals in New Oxidation States. *Organometallics* **2016**, *35* (18), 3088–3100. <https://doi.org/10.1021/acs.organomet.6b00466>.
- (106) Connick, R. E. Oxidation States of the Rare-Earth and Actinide Elements. *J. Chem. Soc.* **1949**, No. 0, S235–S241. <https://doi.org/10.1039/JR949000S235>.
- (107) MacDonald, M. R.; Bates, J. E.; Ziller, J. W.; Furche, F.; Evans, W. J. Completing the Series of +2 Ions for the Lanthanide Elements: Synthesis of Molecular Complexes of Pr<sup>2+</sup>, Gd<sup>2+</sup>, Tb<sup>2+</sup>, and Lu<sup>2+</sup>. *J. Am. Chem. Soc.* **2013**, *135* (26), 9857–9868. <https://doi.org/10.1021/ja403753j>.
- (108) Angadol, M. A.; Woen, D. H.; Windorff, C. J.; Ziller, J. W.; Evans, W. J. Tert-Butyl(Cyclopentadienyl) Ligands Will Stabilize Nontraditional +2 Rare-Earth Metal Ions. *Organometallics* **2019**, *38* (5), 1151–1158. <https://doi.org/10.1021/acs.organomet.8b00941>.
- (109) Hu, A.; Guo, J.-J.; Pan, H.; Zuo, Z. Selective Functionalization of Methane, Ethane, and Higher Alkanes by Cerium Photocatalysis. *Science* **2018**, *361* (6403), 668–672. <https://doi.org/10.1126/science.aat9750>.

- (110) Hobart, D. E.; Samhoun, K.; Young, J. P.; Norvell, V. E.; Mamantov, G.; Peterson, J. R. Stabilization of Praseodymium(IV) and Terbium(IV) in Aqueous Carbonate Solution. *Inorg. Nucl. Chem. Lett.* **1980**, *16* (5), 321–328. [https://doi.org/10.1016/0020-1650\(80\)80069-9](https://doi.org/10.1016/0020-1650(80)80069-9).
- (111) Sroor, F. M. A.; Edelmann, F. T. Lanthanides: Tetravalent Inorganic. In *Encyclopedia of Inorganic and Bioinorganic Chemistry*; American Cancer Society, 2012. <https://doi.org/10.1002/9781119951438.eibc2033>.
- (112) Gompa, T. P.; Ramanathan, A.; Rice, N. T.; Pierre, H. S. L. The Chemical and Physical Properties of Tetravalent Lanthanides: Pr, Nd, Tb, and Dy. *Dalton Trans.* **2020**. <https://doi.org/10.1039/D0DT01400A>.
- (113) Nugent, L. J.; Baybarz, R. D.; Burnett, J. L.; Ryan, J. L. Electron-Transfer and f-d Absorption Bands of Some Lanthanide and Actinide Complexes and the Standard (II-III) Oxidation Potential for Each Member of the Lanthanide and Actinide Series. *J. Phys. Chem.* **1973**, *77* (12), 1528–1539. <https://doi.org/10.1021/j100631a011>.
- (114) Willauer, A. R.; Palumbo, C. T.; Fadaei-Tirani, F.; Zivkovic, I.; Douair, I.; Maron, L.; Mazzanti, M. Accessing the +IV Oxidation State in Molecular Complexes of Praseodymium. *J. Am. Chem. Soc.* **2020**, *142* (12), 5538–5542. <https://doi.org/10.1021/jacs.0c01204>.
- (115) Willauer, A. R.; Palumbo, C. T.; Scopelliti, R.; Zivkovic, I.; Douair, I.; Maron, L.; Mazzanti, M. Stabilization of the Oxidation State +IV in Siloxide-Supported Terbium Compounds. *Angew. Chem. Int. Ed.* **2020**, *59* (9), 3549–3553. <https://doi.org/10.1002/anie.201914733>.
- (116) Palumbo, C. T.; Zivkovic, I.; Scopelliti, R.; Mazzanti, M. Molecular Complex of Tb in the +4 Oxidation State. *J. Am. Chem. Soc.* **2019**, *141* (25), 9827–9831. <https://doi.org/10.1021/jacs.9b05337>.
- (117) Rice, N. T.; Popov, I. A.; Russo, D. R.; Bacsa, J.; Batista, E. R.; Yang, P.; Telser, J.; La Pierre, H. S. Design, Isolation, and Spectroscopic Analysis of a Tetravalent Terbium Complex. *J. Am. Chem. Soc.* **2019**, *141* (33), 13222–13233. <https://doi.org/10.1021/jacs.9b06622>.
- (118) Nash, K. L. A Review of the Basic Chemistry and Recent Developments in Trivalent F-Elements Separations. *Solvent Extr. Ion Exch.* **1993**, *11* (4), 729–768. <https://doi.org/10.1080/07366299308918184>.
- (119) Parker, D.; Williams, J. A. G. Getting Excited about Lanthanide Complexation Chemistry. *J. Chem. Soc. Dalton Trans.* **1996**, No. 18, 3613–3628. <https://doi.org/10.1039/DT9960003613>.
- (120) Werts, M. H. V. Making Sense of Lanthanide Luminescence. *Sci. Prog.* **2005**, *88* (2), 101–131. <https://doi.org/10.3184/003685005783238435>.
- (121) Woodruff, D. N.; Winpenny, R. E. P.; Layfield, R. A. Lanthanide Single-Molecule Magnets. *Chem. Rev.* **2013**, *113* (7), 5110–5148. <https://doi.org/10.1021/cr400018q>.
- (122) Wilkinson, G.; Birmingham, J. M. Cyclopentadienyl Compounds of Sc, Y, La, Ce and Some Lanthanide Elements. *J. Am. Chem. Soc.* **1954**, *76* (23), 6210–6210. <https://doi.org/10.1021/ja01652a114>.
- (123) Kealy, T. J.; Pauson, P. L. A New Type of Organo-Iron Compound. *Nature* **1951**, *168* (4285), 1039–1040. <https://doi.org/10.1038/1681039b0>.
- (124) Wilkinson, G.; Rosenblum, M.; Whiting, M. C.; Woodward, R. B. The Structure of Iron Bis-Cyclopentadienyl. *J. Am. Chem. Soc.* **1952**, *74* (8), 2125–2126. <https://doi.org/10.1021/ja01128a527>.
- (125) Birmingham, J. M.; Wilkinson, G. The Cyclopentadienides of Scandium, Yttrium and Some Rare Earth Elements. *J. Am. Chem. Soc.* **1956**, *78* (1), 42–44. <https://doi.org/10.1021/ja01582a009>.
- (126) Denning, R. G.; Harmer, J.; Green, J. C.; Irwin, M. Covalency in the 4f Shell of Tris-Cyclopentadienyl Ytterbium (YbCp<sub>3</sub>)—A Spectroscopic Evaluation. *J. Am. Chem. Soc.* **2011**, *133* (50), 20644–20660. <https://doi.org/10.1021/ja209311g>.
- (127) Greco, A.; Cesca, S.; Bertolini, W. New 7r-Cyclooctate'l'raenyl and IT-Cyclopentadienyl Complexes of Cerium. *J. Organomet. Chem.* **1976**, *113* (4), 321–330. [https://doi.org/10.1016/S0022-328X\(00\)96143-6](https://doi.org/10.1016/S0022-328X(00)96143-6).

- (128) Halbach, R. L.; Nocton, G.; Booth, C. H.; Maron, L.; Andersen, R. A. Cerium Tetrakis(Tropolonate) and Cerium Tetrakis(Acetylacetonate) Are Not Diamagnetic but Temperature-Independent Paramagnets. *Inorg. Chem.* **2018**, *57* (12), 7290–7298. <https://doi.org/10.1021/acs.inorgchem.8b00928>.
- (129) Dolg, M.; Fulde, P.; Küchle, W.; Neumann, C.; Stoll, H. Ground State Calculations of Di- $\pi$ -cyclooctatetraene Cerium. *J. Chem. Phys.* **1991**, *94* (4), 3011–3017. <https://doi.org/10.1063/1.459824>.
- (130) Dolg, M.; Fulde, P.; Stoll, H.; Preuss, H.; Chang, A.; Pitzer, R. M. Formally Tetravalent Cerium and Thorium Compounds: A Configuration Interaction Study of Cerocene Ce(C<sub>8</sub>H<sub>8</sub>)<sub>2</sub> and Thorocene Th(C<sub>8</sub>H<sub>8</sub>)<sub>2</sub> Using Energy-Adjusted Quasirelativistic Ab Initio Pseudopotentials. *Chem. Phys.* **1995**, *195* (1), 71–82. [https://doi.org/10.1016/0301-0104\(94\)00363-F](https://doi.org/10.1016/0301-0104(94)00363-F).
- (131) Walter, M. D.; Booth, C. H.; Lukens, W. W.; Andersen, R. A. Cerocene Revisited: The Electronic Structure of and Interconversion Between Ce<sub>2</sub>(C<sub>8</sub>H<sub>8</sub>)<sub>3</sub> and Ce(C<sub>8</sub>H<sub>8</sub>)<sub>2</sub>. *Organometallics* **2009**, *28* (3), 698–707. <https://doi.org/10.1021/om7012327>.
- (132) Fischer, E. O.; Fischer, H. Über dicyclopentadienyleuropium und dicyclopentadienylterbium und tricyclopentadienyle des terbiums, holmiums, thuliums und lutetiums. *J. Organomet. Chem.* **1965**, *3* (3), 181–187. [https://doi.org/10.1016/S0022-328X\(00\)87500-2](https://doi.org/10.1016/S0022-328X(00)87500-2).
- (133) Meyer, G. Reduced Halides of the Rare-Earth Elements. *Chem. Rev.* **1988**, *88* (1), 93–107. <https://doi.org/10.1021/cr00083a005>.
- (134) Bochkarev, M. N. Molecular Compounds of “New” Divalent Lanthanides. *Coord. Chem. Rev.* **2004**, *248* (9), 835–851. <https://doi.org/10.1016/j.ccr.2004.04.004>.
- (135) Nief, F. Non-Classical Divalent Lanthanide Complexes. *Dalton Trans.* **2010**, *39* (29), 6589–6598. <https://doi.org/10.1039/C001280G>.
- (136) Xémard, M.; Cordier, M.; Molton, F.; Duboc, C.; Le Guennic, B.; Maury, O.; Cador, O.; Nocton, G. Divalent Thulium Crown Ether Complexes with Field-Induced Slow Magnetic Relaxation. *Inorg. Chem.* **2019**, *58* (4), 2872–2880. <https://doi.org/10.1021/acs.inorgchem.8b03551>.
- (137) Evans, W. J.; Allen, N. T.; Ziller, J. W. The Availability of Dysprosium Diiodide as a Powerful Reducing Agent in Organic Synthesis: Reactivity Studies and Structural Analysis of DyI<sub>2</sub>((DME)<sub>3</sub> and Its Naphthalene Reduction Product<sup>1</sup>. *J. Am. Chem. Soc.* **2000**, *122* (47), 11749–11750. <https://doi.org/10.1021/ja0034949>.
- (138) Evans, W. J.; Allen, N. T.; Ziller, J. W. Facile Dinitrogen Reduction via Organometallic Tm(II) Chemistry. *J. Am. Chem. Soc.* **2001**, *123* (32), 7927–7928. <https://doi.org/10.1021/ja011282l>.
- (139) Molander, G. A. Application of Lanthanide Reagents in Organic Synthesis. *Chem. Rev.* **1992**, *92* (1), 29–68. <https://doi.org/10.1021/cr00009a002>.
- (140) Nicolaou, K. C.; Ellery, S. P.; Chen, J. S. Samarium Diiodide Mediated Reactions in Total Synthesis. *Angew. Chem. Int. Ed.* **2009**, *48* (39), 7140–7165. <https://doi.org/10.1002/anie.200902151>.
- (141) Prasad, E.; Knettle, B. W.; Flowers II, R. A. Photoinduced Electron Transfer Reactions by SmI<sub>2</sub> in THF: Luminescence Quenching Studies and Mechanistic Investigations. *Chem. – Eur. J.* **2005**, *11* (10), 3105–3112. <https://doi.org/10.1002/chem.200401163>.
- (142) Qiao, Y.; Schelter, E. J. Lanthanide Photocatalysis. *Acc. Chem. Res.* **2018**, *51* (11), 2926–2936. <https://doi.org/10.1021/acs.accounts.8b00336>.
- (143) C. Jenks, T.; D. Bailey, M.; L. Hovey, J.; Fernando, S.; Basnayake, G.; E. Cross, M.; Li, W.; J. Allen, M. First Use of a Divalent Lanthanide for Visible-Light-Promoted Photoredox Catalysis. *Chem. Sci.* **2018**, *9* (5), 1273–1278. <https://doi.org/10.1039/C7SC02479G>.
- (144) Lang, P. F.; Smith, B. C. Ionization Energies of Lanthanides. *J. Chem. Educ.* **2010**, *87* (8), 875–881. <https://doi.org/10.1021/ed100215q>.
- (145) Morss, L. R. Thermochemical Properties of Yttrium, Lanthanum, and the Lanthanide Elements and Ions. *Chem. Rev.* **1976**, *76* (6), 827–841. <https://doi.org/10.1021/cr60304a007>.
- (146) Girard, P.; Namy, J. L.; Kagan, H. B. Divalent Lanthanide Derivatives in Organic Synthesis. 1. Mild Preparation of Samarium Iodide and Ytterbium Iodide and Their Use as Reducing or

- Coupling Agents. *J. Am. Chem. Soc.* **1980**, *102* (8), 2693–2698.  
<https://doi.org/10.1021/ja00528a029>.
- (147) Nief, F. Chapter 246 Molecular Chemistry of the Rare-Earth Elements in Uncommon Low-Valent States. In *Handbook on the Physics and Chemistry of Rare Earths*; Elsevier, 2010; Vol. 40, pp 241–300. [https://doi.org/10.1016/S0168-1273\(10\)40006-9](https://doi.org/10.1016/S0168-1273(10)40006-9).
- (148) Evans, W. J. Perspectives in Reductive Lanthanide Chemistry. *Coord. Chem. Rev.* **2000**, *206–207*, 263–283. [https://doi.org/10.1016/S0010-8545\(00\)00267-8](https://doi.org/10.1016/S0010-8545(00)00267-8).
- (149) Tilley, T. D.; Andersen, R. A.; Spencer, B.; Ruben, H.; Zalkin, A.; Templeton, D. H. Divalent Lanthanide Chemistry. Bis (Pentamethylcyclopentadienyl) Europium(II) and -Ytterbium(II) Derivatives: Crystal Structure of Bis (Pentamethylcyclopentadienyl) (Tetrahydrofuran Ytterbium(II) -Hemitoluene at 176 K. *Inorg. Chem.* **1980**, *19* (10), 2999–3003.  
<https://doi.org/10.1021/ic50212a031>.
- (150) Schultz, M.; Burns, C. J.; Schwartz, D. J.; Andersen, R. A. Solid-State Structures of Base-Free Ytterbocenes and Inclusion Compounds of Bis(Pentamethylcyclopentadienyl)Ytterbium with Neutral Carboranes and Toluene: The Role of Intermolecular Contacts. *Organometallics* **2000**, *19* (5), 781–789. <https://doi.org/10.1021/om990821g>.
- (151) Booth, C. H.; Walter, M. D.; Kazhdan, D.; Hu, Y.-J.; Lukens, W. W.; Bauer, E. D.; Maron, L.; Eisenstein, O.; Andersen, R. A. Decamethylytterbocene Complexes of Bipyridines and Diazabutadienes: Multiconfigurational Ground States and Open-Shell Singlet Formation. *J. Am. Chem. Soc.* **2009**, *131* (18), 6480–6491. <https://doi.org/10.1021/ja809624w>.
- (152) Booth, C. H.; Kazhdan, D.; Werkema, E. L.; Walter, M. D.; Lukens, W. W.; Bauer, E. D.; Hu, Y.-J.; Maron, L.; Eisenstein, O.; Head-Gordon, M.; Andersen, R. A. Intermediate-Valence Tautomerism in Decamethylytterbocene Complexes of Methyl-Substituted Bipyridines. *J. Am. Chem. Soc.* **2010**, *132* (49), 17537–17549. <https://doi.org/10.1021/ja106902s>.
- (153) Nocton, G.; Booth, C. H.; Maron, L.; Andersen, R. A. Influence of the Torsion Angle in 3,3'-Dimethyl-2,2'-Bipyridine on the Intermediate Valence of Yb in (C<sub>5</sub>Me<sub>5</sub>)<sub>2</sub>Yb(3,3'-Me<sub>2</sub>-Bipy). *Organometallics* **2013**, *32* (19), 5305–5312. <https://doi.org/10.1021/om400528d>.
- (154) Veauthier, J. M.; Schelter, E. J.; Carlson, C. N.; Scott, B. L.; Re, R. E. D.; Thompson, J. D.; Kiplinger, J. L.; Morris, D. E.; John, K. D. Direct Comparison of the Magnetic and Electronic Properties of Samarocene and Ytterbocene Terpyridine Complexes. *Inorg. Chem.* **2008**, *47* (13), 5841–5849. <https://doi.org/10.1021/ic8001465>.
- (155) Gore-Randall, E.; Irwin, M.; Denning, M. S.; Goicoechea, J. M. Synthesis and Characterization of Alkali-Metal Salts of 2,2'- and 2,4'-Bipyridyl Radicals and Dianions. *Inorg. Chem.* **2009**, *48* (17), 8304–8316. <https://doi.org/10.1021/ic9009459>.
- (156) Nocton, G.; Lukens, W. W.; Booth, C. H.; Rozenel, S. S.; Medling, S. A.; Maron, L.; Andersen, R. A. Reversible Sigma C–C Bond Formation Between Phenanthroline Ligands Activated by (C<sub>5</sub>Me<sub>5</sub>)<sub>2</sub>Yb. *J. Am. Chem. Soc.* **2014**, *136* (24), 8626–8641.  
<https://doi.org/10.1021/ja502271q>.
- (157) Nocton, G.; Booth, C. H.; Maron, L.; Ricard, L.; Andersen, R. A. Carbon–Hydrogen Bond Breaking and Making in the Open-Shell Singlet Molecule Cp\*<sub>2</sub>Yb(4,7-Me<sub>2</sub>Phen). *Organometallics* **2014**, *33* (23), 6819–6829. <https://doi.org/10.1021/om500843z>.
- (158) Corbin, D. R.; Willis, W. S.; Duesler, E. N.; Stucky, G. D. Intramolecular Electron-Transfer Induced Carbon-Hydrogen Bond Dissociation in Methyl-Substituted 1,10-Phenanthroline Complexes of Bis(η<sup>5</sup>-Cyclopentadienyl)Titanium. *J. Am. Chem. Soc.* **1980**, *102* (18), 5969–5971. <https://doi.org/10.1021/ja00538a074>.
- (159) Nocton, G.; Booth, C. H.; Maron, L.; Andersen, R. A. Thermal Dihydrogen Elimination from Cp\*<sub>2</sub>Yb(4,5-Diazafluorene). *Organometallics* **2013**, *32* (5), 1150–1158.  
<https://doi.org/10.1021/om300876b>.
- (160) Evans, W. J. The Expansion of Divalent Organolanthanide Reduction Chemistry via New Molecular Divalent Complexes and Sterically Induced Reduction Reactivity of Trivalent Complexes. *J. Organomet. Chem.* **2002**, *647* (1), 2–11. [https://doi.org/10.1016/S0022-328X\(01\)01462-0](https://doi.org/10.1016/S0022-328X(01)01462-0).

- (161) Trifonov, A. A.; Fedorova, E. A.; Borovkov, I. A.; Fukin, G. K.; Baranov, E. V.; Larionova, J.; Druzhkov, N. O. Steric Manipulation of the Reductive Reactivity of Ytterbocenes toward 2-(((2,6-Diisopropylphenyl)Imino)Methyl)Pyridine: Insertion of the NC Bond into the Yb–Indenyl Bond or Oxidative Cleavage of the H5 Yb–Cp (Cp = C<sub>13</sub>H<sub>9</sub>, Cp\*) Bond. *Organometallics* **2007**, *26* (10), 2488–2491. <https://doi.org/10.1021/om070073s>.
- (162) Trifonov, A. A.; Shestakov, B. G.; Lyssenko, K. A.; Larionova, J.; Fukin, G. K.; Cherkasov, A. V. Sterically Governed Redox Reactions. One-Electron Oxidation of Ytterbocenes by Diazabutadienes: Formation of Radical-Anionic Diazabutadiene vs Covalently Bonded Imino–Amido Ligand. *Organometallics* **2011**, *30* (18), 4882–4889. <https://doi.org/10.1021/om200429h>.
- (163) Meyer, G. Superbulky Ligands and Trapped Electrons: New Perspectives in Divalent Lanthanide Chemistry. *Angew. Chem. Int. Ed.* **2008**, *47* (27), 4962–4964. <https://doi.org/10.1002/anie.200801444>.
- (164) Evans, W. J.; Hughes, L. A.; Hanusa, T. P. Synthesis and Crystallographic Characterization of an Unsolvated, Monomeric Samarium Bis(Pentamethylcyclopentadienyl) Organolanthanide Complex, (C<sub>5</sub>Me<sub>5</sub>)<sub>2</sub>Sm. *J. Am. Chem. Soc.* **1984**, *106* (15), 4270–4272. <https://doi.org/10.1021/ja00327a037>.
- (165) Evans, W. J.; Ulibarri, T. A.; Ziller, J. W. Isolation and X-Ray Crystal Structure of the First Dinitrogen Complex of an f-Element Metal, [(C<sub>5</sub>Me<sub>5</sub>)<sub>2</sub>Sm]N<sub>2</sub>. *J. Am. Chem. Soc.* **1988**, *110* (20), 6877–6879. <https://doi.org/10.1021/ja00228a043>.
- (166) Evans, W. J.; Drummond, D. K. Reductive Coupling of Pyridazine and Benzaldehyde Azine and Reduction of Bipyridine by Samarium Complex (C<sub>5</sub>Me<sub>5</sub>)<sub>2</sub>Sm(THF)<sub>2</sub>. *J. Am. Chem. Soc.* **1989**, *111* (9), 3329–3335. <https://doi.org/10.1021/ja00191a034>.
- (167) Labouille, S.; Nief, F.; Le Goff, X.-F.; Maron, L.; Kindra, D. R.; Houghton, H. L.; Ziller, J. W.; Evans, W. J. Ligand Influence on the Redox Chemistry of Organosamarium Complexes: Experimental and Theoretical Studies of the Reactions of (C<sub>5</sub>Me<sub>5</sub>)<sub>2</sub>Sm(THF)<sub>2</sub> and (C<sub>4</sub>Me<sub>4</sub>P)<sub>2</sub>Sm with Pyridine and Acridine. *Organometallics* **2012**, *31* (14), 5196–5203. <https://doi.org/10.1021/om300573z>.
- (168) Nocton, G.; Ricard, L. Reversible C–C Coupling in Phenanthroline Complexes of Divalent Samarium and Thulium. *Chem. Commun.* **2015**, *51* (17), 3578–3581. <https://doi.org/10.1039/C5CC00289C>.
- (169) Goodwin, C. A. P.; Chilton, N. F.; Vettese, G. F.; Moreno Pineda, E.; Crowe, I. F.; Ziller, J. W.; Winpenny, R. E. P.; Evans, W. J.; Mills, D. P. Physicochemical Properties of Near-Linear Lanthanide(II) Bis(Silylamide) Complexes (Ln = Sm, Eu, Tm, Yb). *Inorg. Chem.* **2016**, *55* (20), 10057–10067. <https://doi.org/10.1021/acs.inorgchem.6b00808>.
- (170) Xémard, M.; Jaoul, A.; Cordier, M.; Molton, F.; Cador, O.; Le Guennic, B.; Duboc, C.; Maury, O.; Clavaguéra, C.; Nocton, G. Divalent Thulium Triflate: A Structural and Spectroscopic Study. *Angew. Chem. Int. Ed.* **2017**, *56* (15), 4266–4271. <https://doi.org/10.1002/anie.201700576>.
- (171) Xémard, M.; Zimmer, S.; Cordier, M.; Goudy, V.; Ricard, L.; Clavaguéra, C.; Nocton, G. Lanthanidocenes: Synthesis, Structure, and Bonding of Linear Sandwich Complexes of Lanthanides. *J. Am. Chem. Soc.* **2018**, *140* (43), 14433–14439. <https://doi.org/10.1021/jacs.8b09081>.
- (172) Nief, F.; Turcitu, D.; Ricard, L. Synthesis and Structure of Phospholyl- and Arsolylthulium(II) Complexes. *Chem. Commun.* **2002**, No. 15, 1646–1647. <https://doi.org/10.1039/B204337H>.
- (173) Jaroschik, F.; Nief, F.; Ricard, L. Synthesis of a New Stable, Neutral Organothulium(II) Complex by Reduction of a Thulium(III) Precursor. *Chem. Commun.* **2006**, No. 4, 426–428. <https://doi.org/10.1039/B514818A>.
- (174) Evans, W. J.; Allen, N. T.; Ziller, J. W. Expanding Divalent Organolanthanide Chemistry: The First Organothulium(II) Complex and the In Situ Organodysprosium(II) Reduction of Dinitrogen. *Angew. Chem. Int. Ed.* **2002**, *41* (2), 359–361. [https://doi.org/10.1002/1521-3773\(20020118\)41:2<359::AID-ANIE359>3.0.CO;2-A](https://doi.org/10.1002/1521-3773(20020118)41:2<359::AID-ANIE359>3.0.CO;2-A).

- (175) Izod, K. A New Era in Divalent Organolanthanide Chemistry? *Angew. Chem. Int. Ed.* **2002**, *41* (5), 743–744. [https://doi.org/10.1002/1521-3773\(20020301\)41:5<743::AID-ANIE743>3.0.CO;2-Z](https://doi.org/10.1002/1521-3773(20020301)41:5<743::AID-ANIE743>3.0.CO;2-Z).
- (176) Moutet, J.; Schleinitz, J.; La Droitte, L.; Tricoire, M.; Gendron, F.; Simler, T.; Clavaguéra, C.; Le Guennic, B.; Cador, O.; Nocton, G. Bis-Cyclooctatetraenyl Thulium(II): Highly Reducing Lanthanide Sandwich Single Molecule Magnets. *ChemRxiv* **2020**. <https://doi.org/10.26434/chemrxiv.12339614.v1>.
- (177) Jaroschik, F.; Nief, F.; Le Goff, X.-F.; Ricard, L. Synthesis and Reactivity of Organometallic Complexes of Divalent Thulium with Cyclopentadienyl and Phospholyl Ligands. *Organometallics* **2007**, *26* (14), 3552–3558. <https://doi.org/10.1021/om700316a>.
- (178) Jacquot, L.; Xémard, M.; Clavaguéra, C.; Nocton, G. Multiple One-Electron Transfers in Bipyridine Complexes of Bis(Phospholyl) Thulium. *Organometallics* **2014**, *33* (15), 4100–4106. <https://doi.org/10.1021/om500607r>.
- (179) Butovskii, M. V.; Kempe, R. Rare Earth–Metal Bonding in Molecular Compounds: Recent Advances, Challenges, and Perspectives. *New J. Chem.* **2015**, *39* (10), 7544–7558. <https://doi.org/10.1039/C5NJ00802F>.
- (180) Liddle, S. T.; Mills, D. P. Metal–Metal Bonds in f-Element Chemistry. *Dalton Trans.* **2009**, No. 29, 5592–5605. <https://doi.org/10.1039/B904318G>.
- (181) Burns, C. P.; Yang, X.; Wofford, J. D.; Bhuvanesh, N. S.; Hall, M. B.; Nippe, M. Structure and Magnetization Dynamics of Dy–Fe and Dy–Ru Bonded Complexes. *Angew. Chem. Int. Ed.* **2018**, *57* (27), 8144–8148. <https://doi.org/10.1002/anie.201803761>.
- (182) Nakajima, Y.; Hou, Z. Rare-Earth-Metal/Platinum Heterobinuclear Complexes Containing Reactive Ln-Alkyl Groups (Ln = Y, Lu): Synthesis, Structural Characterization, and Reactivity. *Organometallics* **2009**, *28* (24), 6861–6870. <https://doi.org/10.1021/om900702y>.
- (183) Ramirez, B. L.; Sharma, P.; Eisenhart, R. J.; Gagliardi, L.; Lu, C. C. Bimetallic Nickel-Lutetium Complexes: Tuning the Properties and Catalytic Hydrogenation Activity of the Ni Site by Varying the Lu Coordination Environment. *Chem. Sci.* **2019**, *10* (11), 3375–3384. <https://doi.org/10.1039/C8SC04712J>.
- (184) Ramirez, B. L.; Lu, C. C. Rare-Earth Supported Nickel Catalysts for Alkyne Semihydrogenation: Chemo- and Regioselectivity Impacted by the Lewis Acidity and Size of the Support. *J. Am. Chem. Soc.* **2020**, *142* (11), 5396–5407. <https://doi.org/10.1021/jacs.0c00905>.
- (185) Crabtree, R. H. Organometallic Alkane CH Activation. *J. Organomet. Chem.* **2004**, *689* (24), 4083–4091. <https://doi.org/10.1016/j.jorganchem.2004.07.034>.
- (186) McDonald, R. I.; Liu, G.; Stahl, S. S. Palladium(II)-Catalyzed Alkene Functionalization via Nucleopalladation: Stereochemical Pathways and Enantioselective Catalytic Applications. *Chem. Rev.* **2011**, *111* (4), 2981–3019. <https://doi.org/10.1021/cr100371y>.
- (187) Bair, J. S.; Schramm, Y.; Sergeev, A. G.; Clot, E.; Eisenstein, O.; Hartwig, J. F. Linear-Selective Hydroarylation of Unactivated Terminal and Internal Olefins with Trifluoromethyl-Substituted Arenes. *J. Am. Chem. Soc.* **2014**, *136* (38), 13098–13101. <https://doi.org/10.1021/ja505579f>.
- (188) Tang, S.; Liu, K.; Liu, C.; Lei, A. Olefinic C–H Functionalization through Radical Alkenylation. *Chem. Soc. Rev.* **2015**, *44* (5), 1070–1082. <https://doi.org/10.1039/C4CS00347K>.
- (189) Bergman, R. G. C–H Activation. *Nature* **2007**, *446* (7134), 391–393. <https://doi.org/10.1038/446391a>.
- (190) Hartwig, J. F. Carbon–Heteroatom Bond Formation Catalysed by Organometallic Complexes. *Nature* **2008**, *455* (7211), 314–322. <https://doi.org/10.1038/nature07369>.
- (191) Periana, R. A.; Taube, D. J.; Gamble, S.; Taube, H.; Satoh, T.; Fujii, H. Platinum Catalysts for the High-Yield Oxidation of Methane to a Methanol Derivative. *Science* **1998**, *280* (5363), 560–564. <https://doi.org/10.1126/science.280.5363.560>.



- (192) Periana, R. A.; Mironov, O.; Taube, D.; Bhalla, G.; Jones, C. J. Catalytic, Oxidative Condensation of CH<sub>4</sub> to CH<sub>3</sub>COOH in One Step via CH Activation. *Science* **2003**, *301* (5634), 814–818. <https://doi.org/10.1126/science.1086466>.
- (193) Cook, A. K.; Schimmler, S. D.; Matzger, A. J.; Sanford, M. S. Catalyst-Controlled Selectivity in the C–H Borylation of Methane and Ethane. *Science* **2016**, *351* (6280), 1421–1424. <https://doi.org/10.1126/science.aad9289>.
- (194) Smith, K. T.; Berritt, S.; González-Moreiras, M.; Ahn, S.; Smith, M. R.; Baik, M.-H.; Mindiola, D. J. Catalytic Borylation of Methane. *Science* **2016**, *351* (6280), 1424–1427. <https://doi.org/10.1126/science.aad9730>.
- (195) Kaim, W. Electron Transfer to Complex Ligands. Radical Anions and Organomagnesium Radical Complexes of 2,2'-Bipyridines and 1,10-Phenanthrolines. *J. Am. Chem. Soc.* **1982**, *104* (14), 3833–3837. <https://doi.org/10.1021/ja00378a010>.
- (196) Klein, A.; Kaim, W.; Waldhör, E.; Hausen, H.-D. Different Orbital Occupation by an Added Single Electron in 1,10-Phenanthroline and Its 3,4,7,8-Tetramethyl Derivative. Evidence from Electron Paramagnetic Resonance Spectroscopy of the Anion Radicals and of Their Dimesitylplatinum(II) Complexes. X-Ray Molecular Structure of Dimesityl(1,10-Phenanthroline)Platinum(II). *J. Chem. Soc. Perkin Trans. 2* **1995**, No. 12, 2121–2126. <https://doi.org/10.1039/P29950002121>.
- (197) Blanchard, S.; Derat, E.; Desage-El Murr, M.; Fensterbank, L.; Malacria, M.; Mouriès-Mansuy, V. Non-Innocent Ligands: New Opportunities in Iron Catalysis. *Eur. J. Inorg. Chem.* **2012**, *2012* (3), 376–389. <https://doi.org/10.1002/ejic.201100985>.
- (198) Goudy, V.; Jaoul, A.; Cordier, M.; Clavaguéra, C.; Nocton, G. Tuning the Stability of Pd(IV) Intermediates Using a Redox Non-Innocent Ligand Combined with an Organolanthanide Fragment. *J. Am. Chem. Soc.* **2017**, *139* (31), 10633–10636. <https://doi.org/10.1021/jacs.7b05634>.
- (199) Byers, P. K.; Canty, A. J.; Skelton, B. W.; White, A. H. The Oxidative Addition of Iodomethane to [PdMe<sub>2</sub>(Bpy)] and the X-Ray Structure of the Organopalladium(IV) Product Fac-[PdMe<sub>3</sub>(Bpy)](Bpy = 2,2'-Bipyridyl). *J. Chem. Soc. Chem. Commun.* **1986**, No. 23, 1722–1724. <https://doi.org/10.1039/C39860001722>.
- (200) Byers, P. K.; Canty, A. J.; Crespo, Margarita.; Puddephatt, R. J.; Scott, J. D. Reactivity and Mechanism in Oxidative Addition to Palladium(II) and Reductive Elimination from Palladium(IV) and an Estimate of the Palladium Methyl Bond Energy. *Organometallics* **1988**, *7* (6), 1363–1367. <https://doi.org/10.1021/om00096a021>.
- (201) Byers, P. K.; Canty, A. J.; Skelton, B. W.; White, A. H. Synthesis, Reactivity, and Structural Studies in Trimethylpalladium(IV) Chemistry, Including PdMe<sub>3</sub>(Bpy) and [MMe<sub>3</sub>((Pz)<sub>3</sub>CH)]<sup>+</sup> (M = Palladium, Platinum). *Organometallics* **1990**, *9* (3), 826–832. <https://doi.org/10.1021/om00117a044>.
- (202) Wang, D.; Moutet, J.; Tricoire, M.; Cordier, M.; Nocton, G. Reactive Heterobimetallic Complex Combining Divalent Ytterbium and Dimethyl Nickel Fragments. *Inorganics* **2019**, *7* (5), 58. <https://doi.org/10.3390/inorganics7050058>.
- (203) Khusnutdinova, J. R.; Rath, N. P.; Mirica, L. M. The Conformational Flexibility of the Tetradentate Ligand TBuN<sub>4</sub> Is Essential for the Stabilization of (TBuN<sub>4</sub>)Pd(III) Complexes. *Inorg. Chem.* **2014**, *53* (24), 13112–13129. <https://doi.org/10.1021/ic5023054>.
- (204) Jones, G. D.; Martin, J. L.; McFarland, C.; Allen, O. R.; Hall, R. E.; Haley, A. D.; Brandon, R. J.; Konovalova, T.; Desrochers, P. J.; Pulay, P.; Vicic, D. A. Ligand Redox Effects in the Synthesis, Electronic Structure, and Reactivity of an Alkyl–Alkyl Cross-Coupling Catalyst. *J. Am. Chem. Soc.* **2006**, *128* (40), 13175–13183. <https://doi.org/10.1021/ja063334i>.



# Synthesis and characterizations of original heterobimetallic complexes bridged by 2,2'-bipyrimidine and their reactivity toward small molecule activation

Small molecule activation (SMA) is an important area in point of view of chemical transformations and fossil fuel feedstocks utilization concerning environmental issues.<sup>1</sup> This fascinating topic involves massive use of transition metals,<sup>2-4</sup> including f-elements,<sup>5-9</sup> as well as a number of examples of main group compounds.<sup>10-12</sup> Earth abundant small molecules such as N<sub>2</sub>,<sup>13,14</sup> and O<sub>2</sub>,<sup>15</sup> light hydrocarbons and derivatives, H<sub>2</sub> and other H-donor derivatives<sup>16,17</sup> and more importantly, the green-house pollutants such as CO,<sup>18-21</sup> CO<sub>2</sub>,<sup>22-25</sup> N<sub>x</sub>O<sub>y</sub>,<sup>26,27</sup> and CH<sub>4</sub>,<sup>28-30</sup> are investigated in this area, and that therefore can facilitate the further transformations that would be very difficult to take place without the activations.

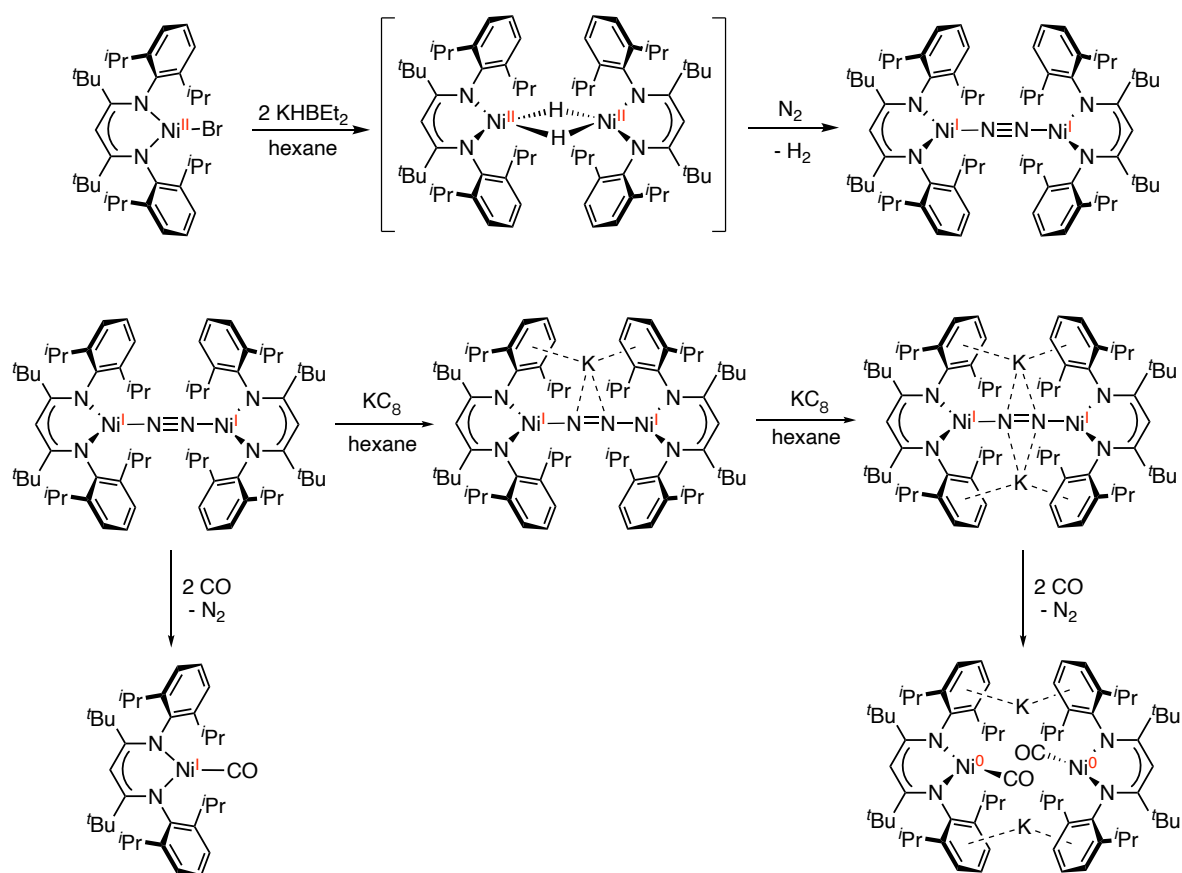
Low-valent complexes are mostly studied in SMA because they can allow undergoing multiple electron transfer processes during the activation to entirely transform the molecules. Thus, high-valent intermediates are often proposed in the mechanistic insights and related active high-valent species are isolated such as Pd<sup>III</sup>,<sup>31-33</sup> Pd<sup>IV</sup>,<sup>34-41</sup> Ni<sup>III</sup>,<sup>42-51</sup> and Ni<sup>IV</sup>,<sup>52-57</sup> further studied in new C-C bond formation or carbon-heteroatom bond formation.

In the LCM laboratory group, previous works have demonstrated the formation of heterobimetallic divalent organoytterbium and reactive palladium complex system bridged by redox non-innocent ligands, namely 2,2'-bipyrimidine (bipym) and 4,5,9,10-tetraazaphenanthrene (taphen). The divalent organolanthanide complex is an efficient single electron reductant and allows the two metallic fragments to cooperate by means of electronic correlation with the help of the ligand's redox non-innocence. The overall electronic structure of the bimetallic complex depends on the ligand used, which turns to have an impact on the modulation of the reactivity on the Pd center, such as the oxidative addition of iodomethane (MeI) to yield stable high-valent Pd<sup>IV</sup> species.<sup>58</sup>

In this context of chapter, heterometallic organolanthanide/nickel complex with bipym ligand will be presented based on the above highlighted example of the vicinage palladium. Synthesis, characterizations and reactivity studies will be described in this work.<sup>59</sup>

## 1. Introduction: general interest in small molecule activation in organometallic nickel chemistry

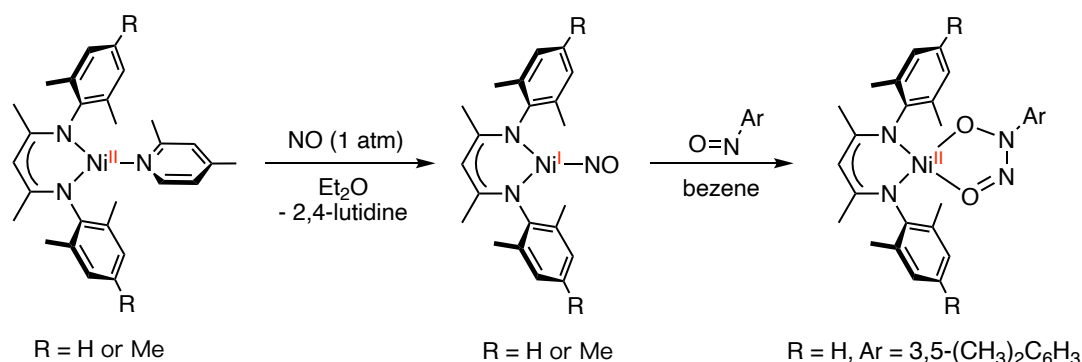
The activation of small molecules by Ni centers is a significant research interest in vast chemical transformations in catalytic and biological processes.<sup>60–63</sup> Among the enormous examples in SMA by organonickel compounds, low-valent nickel complexes as Ni<sup>I</sup> compounds (3d<sup>9</sup> electron configuration) are comparatively unusual whereas they are leading a considerably importance in the field, acting as rather strong one-electron reductants, proceeding the oxidation leading to the divalence (3d<sup>8</sup>), which is moderately stable and common in nickel chemistry.<sup>64–66</sup>



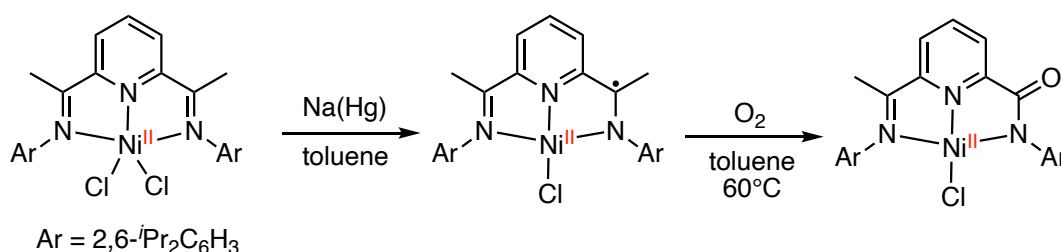
**Scheme 10.** Formation of binuclear Ni<sup>I</sup> complexes with the activation of N<sub>2</sub> in a dinitrogen atmosphere and their reactivity with CO.

In the organometallic field, a well-designed ligand system can be essential for establishing the monovalent nickel species. The  $\beta$ -diketiminato backbone is extensively utilized for the stabilization of metal complexes in unusual oxidation states,<sup>67,68</sup> and becomes an excellent ligand system to study Ni<sup>I</sup> species in their SMA reactivity.<sup>69,70</sup> One of the first examples in SMA with Ni<sup>I</sup> complexes is a binuclear complex with an activated N<sub>2</sub> ligand which is reduced by KBEt<sub>3</sub>H from a Ni<sup>II</sup> precursor in presence of dinitrogen *via* a potential hydride intermediate. Such complexes are able to retain

the monovalence of nickel with addition of carbon monoxide that replaces the chelating N<sub>2</sub> while if it further undergoes strong reduction by excess of potassium graphite (KC<sub>8</sub>): the nickel center can be reduced to zero-valent by the addition of CO (Scheme 10).<sup>71</sup>

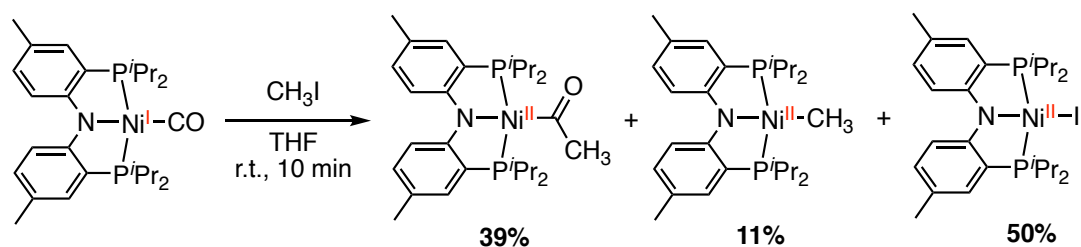


**Scheme 11.** Synthesis of three-coordinate  $\beta$ -diketiminato nickel nitrosyl complexes and the reactivity with ArN=O.

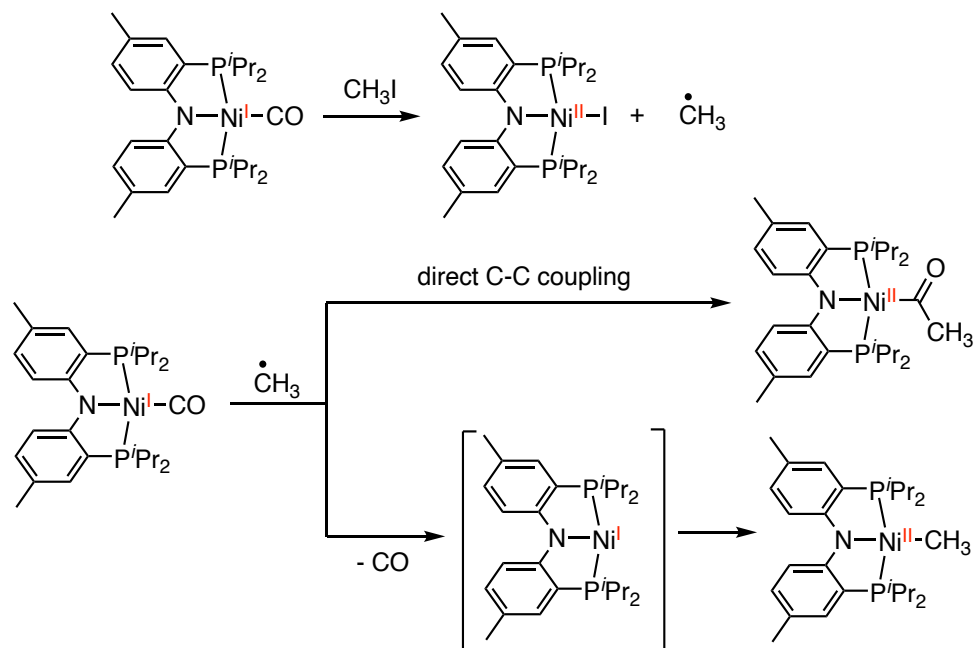


**Scheme 12.** A redox-active ligand Ni<sup>II</sup> complex with dioxygen probing ligand-radical character.

The mentioned three-coordinate Ni<sup>II</sup> precursor with the  $\beta$ -diketiminato ligand is illuminating a potential strategy in synthesizing the related Ni<sup>I</sup> complex. Warren *et al.* reported two nickel(I)  $\beta$ -diketiminato L<sub>Me2</sub>Ni(2,4-lutidine) (L<sub>Me2</sub> = HC{C(Me)NC<sub>6</sub>H<sub>2</sub>(Me)<sub>2</sub>}<sub>2</sub><sup>-</sup>) and L<sub>Me3</sub>Ni(2,4-lutidine) (L<sub>Me3</sub> = HC{C(Me)NC<sub>6</sub>H<sub>2</sub>(Me)<sub>3</sub>}<sub>2</sub><sup>-</sup>) precursors reacting with NO to form diamagnetic, three-coordinate [Ni<sup>I</sup>-NO] complexes. The L<sub>Me2</sub>Ni(NO) fragment can then undergo insertion with a nitrosobenzene derivative to form the N-aryl-N-nitrosohydroxylaminato species L<sub>Me2</sub>Ni( $\eta^2$ -O<sub>2</sub>N<sub>2</sub>Ar) (Scheme 11).<sup>72</sup> The resulting L<sub>Me3</sub>Ni(2,4-lutidine) complex can further react with AdN<sub>3</sub> (Ad = 2,6-<sup>i</sup>Pr<sub>2</sub>C<sub>6</sub>H<sub>3</sub>, adamantyl) to form a terminal Ni<sup>III</sup>-imido compound. The reactivity with selected electrophiles such as CO and CN<sup>t</sup>Bu yielding the rapid formation of AdNCO and AdNCN<sup>t</sup>Bu indicate notably that the imido group can be regarded as imidyl radical anion.<sup>44</sup> Such a redox non-innocence of the ligand can be also found in using iminopyridine-type of ligands.<sup>73</sup> The reactivity with oxygen on a one-electron reduced nickel bis(arylimino)pyridine complex to cause a cleavage of a ligand C-C bond, demonstrating a mechanism involving a direct electron transfer through a ligand-centered oxygenation (Scheme 12).<sup>74</sup> Another example of pincer systems is reported by Jung and Lee, which are describing an initial iodine radical abstraction by a Ni<sup>I</sup>-carbonyl species to undergo the direct C-C bond formation between a methyl radical and the coordinated CO ligand, generating the Ni<sup>II</sup>-COCH<sub>3</sub> acyl species (Scheme 13).<sup>75</sup>

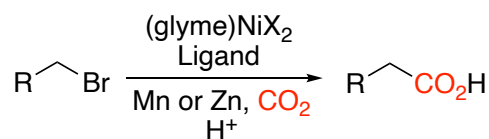


*Mechanistic insight:*

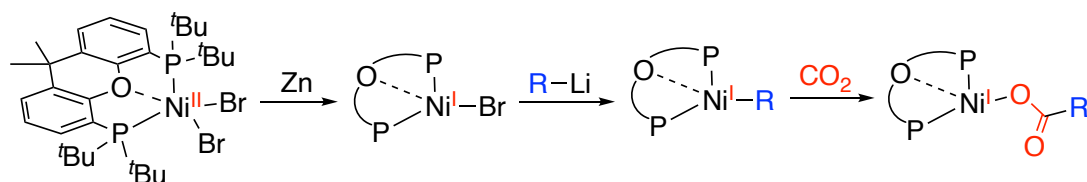


**Scheme 13.** Direct C–C bond formation of a Nickel(I) monocarbonyl pincer complex with alkyl iodides.

A practical example with pincer ligands is also reported by Diao *et al.*, demonstrating a mechanistic insight of reductive carboxylation of alkyl halides with  $\text{CO}_2$  by the (*t*Bu-Xantphos) $\text{Ni}^{\text{II}}\text{Br}_2$  precatalyst.<sup>76</sup> An insertion of  $\text{CO}_2$  into Ni<sup>I</sup>-alkyl bonds is characterized, describing the importance of Ni<sup>I</sup> intermediate relative to Ni<sup>II</sup> in the Ni-catalyzed carboxylation (Scheme 14).



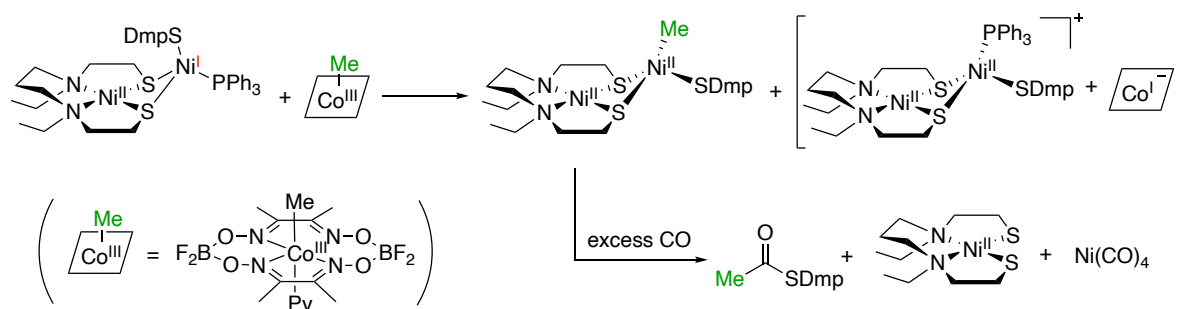
*Mechanistic insight:*



**Scheme 14.** Insertion of  $\text{CO}_2$  Mediated by a (Xantphos) $\text{Ni}^{\text{I}}$ -Alkyl Species.

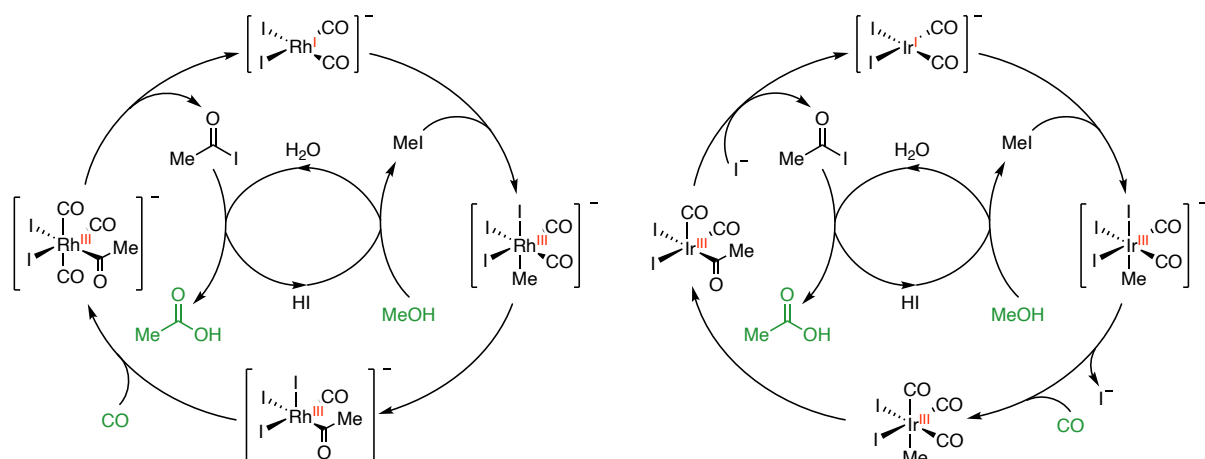
Additionally, in biology, nickel-containing enzymes are mostly involving monovalent intermediates in the mechanistic insights.<sup>77</sup> For example, nickel hydrocorphinato F<sub>430</sub>, as the active site of methyl-coenzyme M reductases (MCR), features a Ni<sup>I</sup> oxidation state that can induce the radical routes

for the methane production.<sup>78–80</sup> Another example of biological processes is the acetyl coenzyme A synthase (ACS), also involving a Ni<sup>I</sup> intermediate.<sup>81</sup> The first step is either the CH<sub>3</sub><sup>+</sup> transfer onto the formed Ni<sup>I</sup>-CO intermediate, or an oxidation by CH<sub>3</sub><sup>+</sup> transfer to generate a Ni<sup>III</sup>-CH<sub>3</sub> intermediate from the Ni<sup>I</sup> species, which react with CO that inserts into the Ni-C bond (Scheme 15). Another good example in CO migratory insertion is by using a similar dinuclear Ni<sup>II</sup>Ni<sup>I</sup> compound, namely Ni<sup>II</sup>(dadt<sup>Et</sup>)Ni<sup>I</sup>(SDmp)(PPh<sub>3</sub>), modeling of the active site Ni<sub>d</sub><sup>II</sup>-Ni<sub>p</sub><sup>I</sup> of ACS. (dadt<sup>Et</sup> = *N,N'*-diethyl-*N,N'*-diethanethiolate-1,3-diaminopropane, DmpS = 2,6-dimesitylthiophenolate) Co(dmgBF<sub>2</sub>)<sub>2</sub>(Me)(Py) is reacted with this dinuclear complex to perform the methyl group transfer to oxidate the Ni<sub>p</sub> site to afford Ni<sup>II</sup>(dadt<sup>Et</sup>)Ni<sup>II</sup>(Me)(SDmp), which can react with carbon monoxide generating the thioester *via* reductive elimination.<sup>82</sup>



**Scheme 15.** The reaction of Ni<sup>II</sup>(dadt<sup>Et</sup>)Ni<sup>I</sup>(SDmp)(PPh<sub>3</sub>) with Co(dmgBF<sub>2</sub>)<sub>2</sub>(Me)(Py) and CO.

The large interest of carbon monoxide utilization has been developed as an effective and cheap C1 source in organic chemistry, catalysis and pharmaceutical areas. One of the most related transformations is carbonylation, such as Monsanto<sup>83,84</sup> and Cativa<sup>85,86</sup> processes. Notably, organometallic Rh (Monsanto) and Ir (Cativa) complexes were originally developed and then largely investigated in the industrial carbonylative application (Scheme 16). For these particular reactions, Maitlis *et al.* investigated the oxidative addition of CH<sub>3</sub>I to [Rh(CO)<sub>2</sub>I<sub>2</sub>]<sup>-</sup>, showing that this step is more likely the rate-determining step (RDS) of the overall catalytic cycle,<sup>87,88</sup> while the migratory insertion of CO is rather fast. However, this study was not entirely conclusive since the reductive elimination of CH<sub>3</sub>I, as the back-reaction of the initial oxidative addition, is facile under the kinetic study; thus, the migratory insertion step of CO could alternatively be the RDS.<sup>88</sup> Nevertheless, this latter step plays a crucial role in the overall rhodium-catalyzed carbonylation system.<sup>85</sup> For Ir-based system, mechanistic studies described that the oxidative addition of MeI is 100 times faster than the rhodium one, whereas the migratory insertion is up to 10<sup>6</sup> times slower.<sup>85,89,90</sup> In both cases with different metals, high oxidation state of the transition-metal center is always involved in the CO migratory insertion,<sup>91,92</sup> which can be regarded as the crucial step of the overall catalytic mechanism,<sup>93</sup> after the oxidative addition of alkyl halide.



**Scheme 16.** Proposed general catalytic cycles for Monsanto (left) and Cativa (right) methanol carbonylation.

However, noble-metal catalysis still takes the majority of these applied systems.<sup>94–96</sup> More sustainable chemistry using non-noble metals, Nickel, for instance, can be one of the fascinating alternatives and that has started to be explored during the recent decades. However, the overall carbonylative reaction can also involve highly toxic nickel(0) carbonyl compounds under CO atmosphere.<sup>97</sup> In terms of mechanistic insights, few practical examples investigating CO migratory insertion into nickel-alkyl bond are reported.<sup>98</sup> It has been computationally studied that the five-coordinate mechanism for the CO reaction with methylnickel complexes is accessible kinetically and a significantly low energy pathway is calculated for the migratory insertion into the Ni-Me bond.<sup>99</sup>

Acyl complexes formed *via* the migratory CO insertion as the RDS is rarely studied for 3d metals compared to their more inert 4d and 5d congeners. It is mainly due to the stronger metal-ligand bonding leading to the stable insertion intermediate and a good preference in higher oxidation states.<sup>93</sup> Therefore, it will be of great interest to have more insights in the CO insertion into metal-alkyl bond (which will be Ni-Me bond in this work) forming the acyl active species, and performing further reactivity.<sup>98,100–102</sup> Notably, mechanistic studies have described the reversibility of CO in methylnickel complexes,<sup>103,104</sup> indicating a possibility to kinetically study the acyl intermediate formation,<sup>105</sup> as well as the possible decarbonylating process in the further investigation.<sup>106,107</sup>

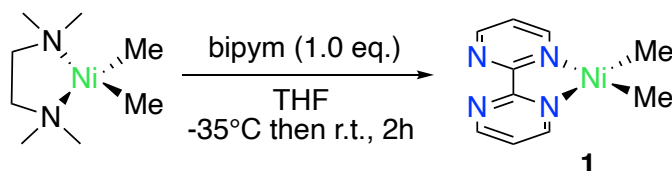
## 2. Heterobimetallic nickel complex: synthesis and characterizations

### 2.1. Synthetic method and structural analysis

The synthesis we used is similar as that of the former synthetic procedure to obtain palladium analogues.<sup>58,108</sup> (tmeda)NiMe<sub>2</sub> has been chosen as the most suitable precursor for the further ligand exchange reaction because of the excellent solubility in many polar organic solvents, for instance, THF; the only problem is the temperature sensitivity, so it requires to be stored in the freezer under inert atmosphere.

Stoichiometric amount of bipym is added to dark yellow (tmeda)NiMe<sub>2</sub> in cold THF at ambient temperature yielding a dark mixture, which can be further recrystallized at -35°C to form clean

(bipym)NiMe<sub>2</sub> (**1**) as dark crystals (73% yield) (Scheme 17). It has to be noted that the formation of the dimeric Me<sub>2</sub>Ni(bipym)NiMe<sub>2</sub> needs to be avoided at this step, in order to avoid affecting the crystalline quality of **1** with excess of free bipym ligand. Indeed this is always problematic for building up the final heterobimetallic step in this chemistry because free bipym will easily form the Cp\*<sub>2</sub>Yb(bipym)YbCp\*<sub>2</sub> dimer, which also crystallizes from the mixture as co-crystals and influence greatly the further physicochemical measurements even in small amounts.<sup>109</sup> This is the main reason why we barely set up the heterometallic synthesis firstly by the lanthanide-ligand combination.



**Scheme 17.** Synthesis of (bipym)NiMe<sub>2</sub> (**1**) complex in THF.

The X-ray suitable crystals allowed us to identify the C<sub>2v</sub> symmetry of the compound, as well as characterize some key parameters in order to compare with the ones of the further reduced complex (Figure 7).

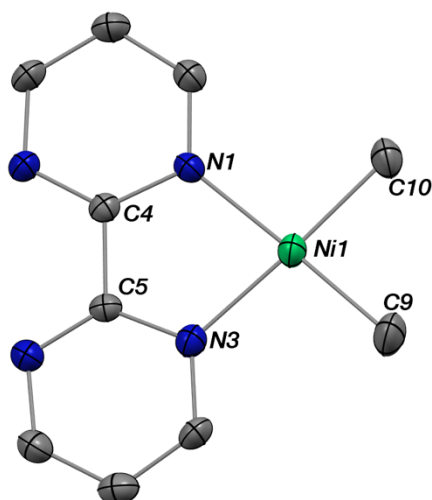
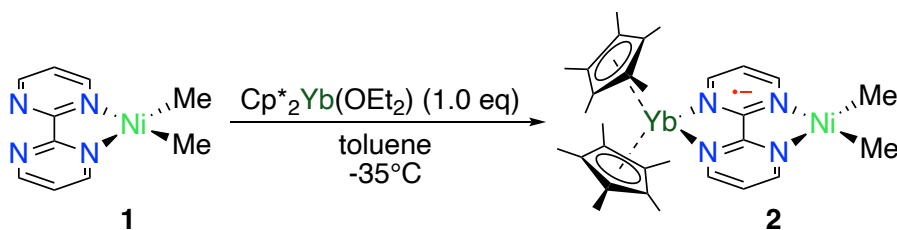


**Figure 7.** Oak Ridge Thermal Ellipsoid Plot (ORTEP) of **1**. Only one of the molecules of the cell is shown.

Thermal ellipsoids are at the 50% level; hydrogen atoms have been removed for clarity.

Compound **1** is then combined with one equivalent of Cp\*<sub>2</sub>Yb(OEt<sub>2</sub>) in cold toluene yielding the ideal heterobimetallic complex Cp\*<sub>2</sub>Yb(bipym)NiMe<sub>2</sub> (**2**) as dark-brown block crystals isolated in 58% yield, which is suitable for XRD studies (Scheme 18, Figure 8).



**Scheme 18.** Synthesis of Cp\*<sub>2</sub>Yb(bipym)NiMe<sub>2</sub> (**2**) complex in toluene.



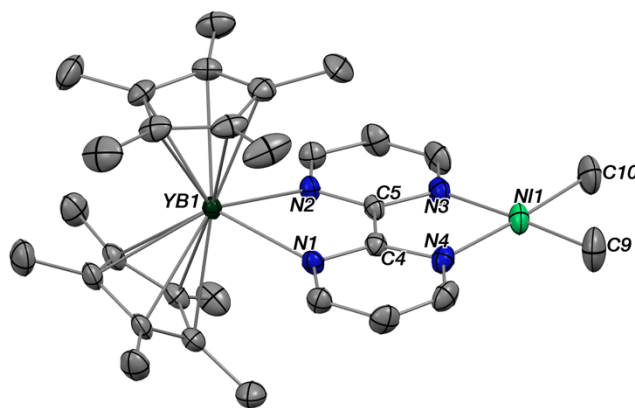


**Figure 8.** ORTEP of **2**. Only one of the molecules of the cell is shown. Thermal ellipsoids are at the 50% level; hydrogen atoms and one co-crystallized toluene solvate have been removed for clarity.

A remarkable feature is first highlighted as the different distance of C-C bridging bond that links two pyrimidine cycles in the bipym ligand by comparing the XRD structures of **1** and **2**. The C4-C5 bond has been strongly reduced in **2** comparing to the one in **1** as a neutral ligand thanks to the efficient electron transfer from divalent ytterbium, which is also noticed in the palladium analogues,<sup>58</sup> indicative of a ligand-based reduction.<sup>110–112</sup> Correspondingly, the average Cp centroid-Yb distance is indicative of the trivalent oxidation state of ytterbium atom and it is 2.31(1) Å, which is much lower than the typical range for divalent species (2.43–2.50 Å)<sup>113–117</sup> and close to the one for trivalent compounds (2.30–2.31 Å).<sup>118</sup> However, this distance range needs to be taken cautiously since these particular compounds also feature multiconfigurational energy states with intermediate valence states.<sup>114,119</sup> Moreover, similar average distances of Ni-N (1.959(2) and 1.956(3) Å) and Ni-CH<sub>3</sub> (1.930(3) and 1.925(1) Å) bonds in **1** and **2**, respectively, indicate similar oxidation state and coordination environment of the nickel center in both complexes (See these representative values in Table 4).

**Table 4.** Representative geometrical parameters: average main distances (Å) and angles (°) for **1** and **2**.

	<b>1</b>	<b>2</b>
Ni-Me	1.930(3)	1.925(1)
Ni-N	1.959(2)	1.956(3)
C-C <sub>bipym</sub>	1.482(5)	1.403(4)
Yb-N	-	2.359(1)
Yb-Cp* <sub>centroid</sub>	-	2.31(1)
Me-Ni-Me^N-Ni-N	5.34±0.24	1.80

## 2.2. NMR characterizations and solid-state magnetism measurement

The  $^1\text{H}$  NMR spectrum of **1** in THF- $d^8$  at 293 K shows three signals for bipym ligand, integrating each as two protons, and one signal as six protons for the dimethyl moiety on nickel center. The broadness of the NMR resonances is due to the solubility of **1** in THF when it is concentrated. This diamagnetic NMR is correlated with the XRD analysis as a square planar geometry of complex **1** (Figure 9).

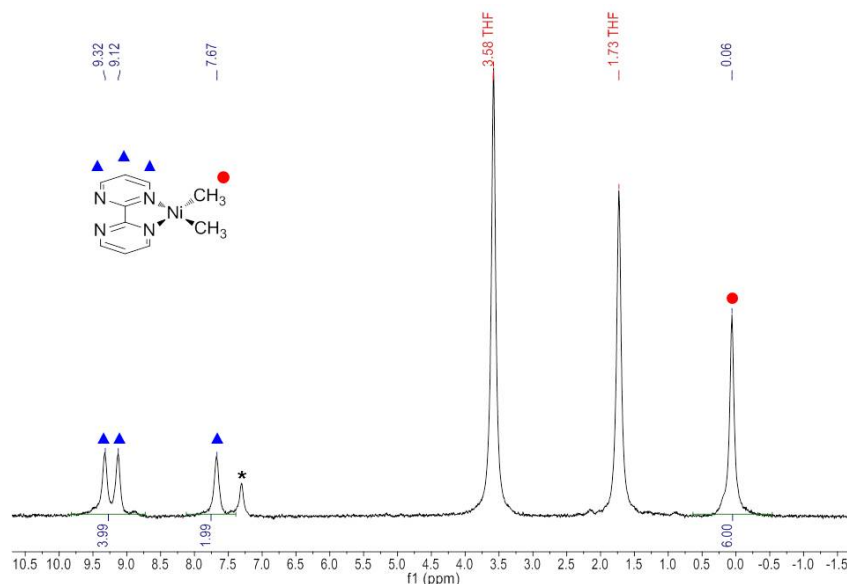


**Figure 9.**  $^1\text{H}$  NMR of **1** in THF- $d^8$  at 293 K. Benzene impurities are indicated by \*.

The  $^1\text{H}$  NMR spectrum of **2**, recorded in toluene- $d^8$  (tol- $d^8$ ) at 253 K give very different resonances compared to the one of **1**: three highly shifted signals corresponding to the protons on the bipym ligand at 272.67, 5.39 and -160.45 ppm, integrated each for two protons; one signal attributed to the Ni-Me<sub>2</sub> fragment integrated for six protons at 15.03 ppm, and one peak integrated for thirty protons corresponding to the Cp\* ligands (Figure 10, top). This is in agreement with a  $C_{2v}$  symmetry for **2** in solution and the largely shifted resonances are indicative of a clear paramagnetism of the complex. Thus, the NMR data agree with an oxidized Yb<sup>III</sup> ( $f^{13}$ ) and a reduced bipym as a radical anion, which is consistent with the observation of single electron transfer behavior from the divalent ytterbium to the ligand in solid state. *The  $^1\text{H}$  NMR of **2** in THF- $d^8$  at 293 K is also presented below. The chemical shifts are less overlapped with the solvent due to the better solubility in THF than in toluene. The further reactivity tests will be all performed in THF or THF- $d^8$  (Figure 10, bottom).*

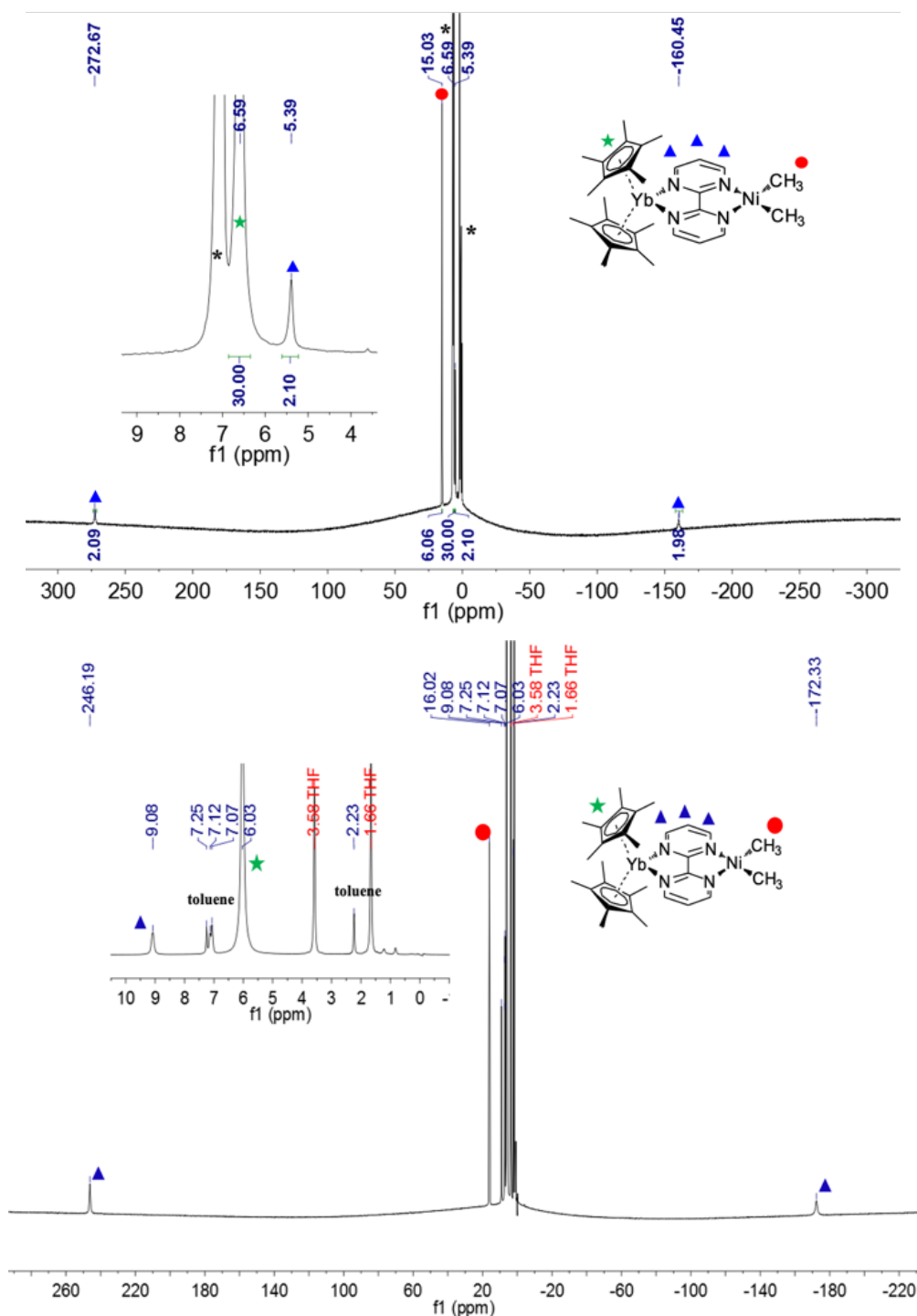


**Figure 10.**  $^1\text{H}$  NMR of **2** in  $\text{tol-d}_8$  at 253 K, solvent and grease are indicated by an asterisk (top);  $^1\text{H}$  NMR of **2** in  $\text{THF-d}_8$  at 293 K, toluene resonance is due to the co-recrystallized toluene solvate in the crystal state (bottom).

From the paramagnetic character of **2** arises several possibilities for its electronic ground state: a triplet state or a singlet state with low-lying triplet state. The variable-temperature (VT) NMR is recorded in  $\text{tol-d}_8$  and the chemical shifts of each resonance are plotted versus  $1/T$ , yielding a curved plot indicating that the magnetic behavior of **2** does not strictly follow Curie law (Figure 11). A very similar VT NMR behavior was notified in several related examples.<sup>58,113,119</sup> This can be explained by the magnetic exchange coupling between two single electrons.

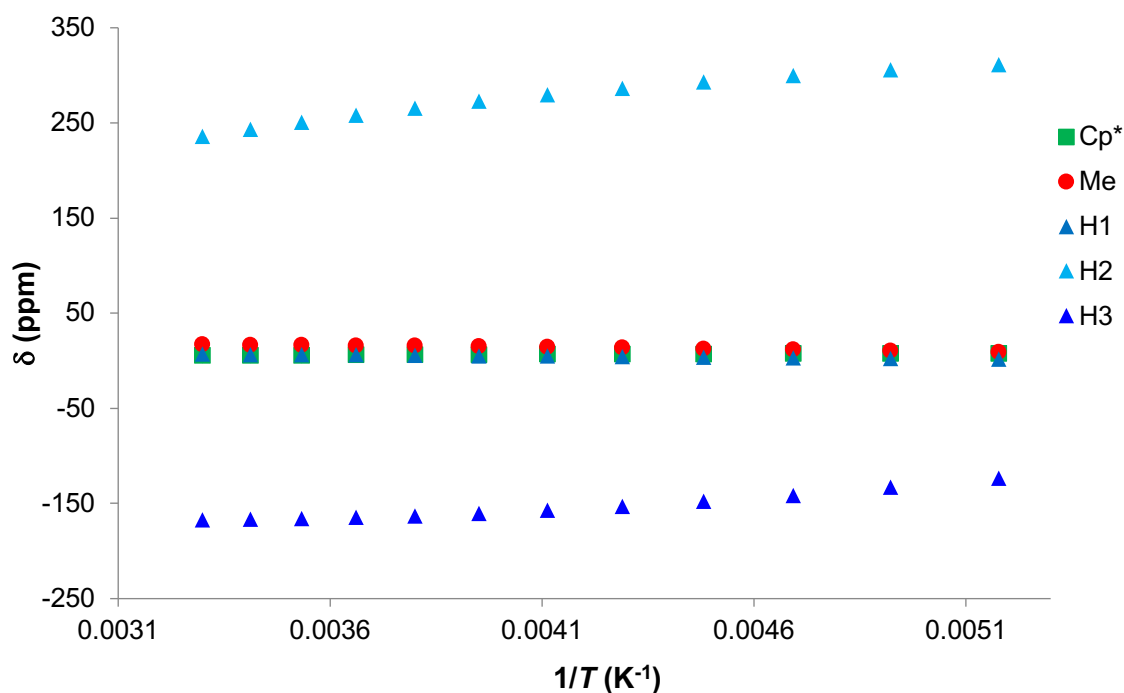


**Figure 11.** Variable temperature  $^1\text{H}$  NMR of **2** in  $\text{tol-d}^8$  plotted versus  $1/T$  between 193 K and 303 K.

Solid-state magnetism measurement was therefore performed to testify this presumption. Temperature-dependent magnetic data are recorded in the 2-300 K temperature range. Plots of  $\chi T$  versus  $T$  and  $\chi$  versus  $T$  at 0.5 T are shown in Figure 6. The  $\chi T$  value is  $2.3 \text{ emu}\cdot\text{K}\cdot\text{mol}^{-1}$  at room temperature is close to the one obtained theoretically for related bipyridine (bipy) adduct of  $\text{Cp}^*_2\text{Yb}$  compound in triplet state ( $2.36 \text{ emu}\cdot\text{K}\cdot\text{mol}^{-1}$ ) with a value of  $0.72 \text{ emu}\cdot\text{K}\cdot\text{mol}^{-1}$  as singlet state.<sup>114,120</sup> Thus, the  $\chi T$  value of **2** indicates a populated triplet state at room temperature. It then decreases significantly with decreasing the temperature, meeting two inflection points around 170 and 65 K, and eventually approaches zero at 2 K, which is in agreement with a singlet ground state. Such interesting behavior has been similarly reported for the  $\text{Cp}^*_2\text{Yb}$  analogues.<sup>113,119</sup> It can be explained by a multiconfigurational nature of **2** with two open-shell singlet states ( $S = 0$ ) and a low-lying triplet state ( $S = 1$ ), which is getting populated at room temperature.<sup>119</sup> The  $\chi$  versus  $T$  plot can provide more insight of the overall configuration of **2**. A maximum value is clearly obtained around 170 K while the values at low temperatures are low and independent of the temperature, which is following a Temperature-Independent Paramagnetism (TIP) or van Vleck paramagnetism.<sup>121,122</sup> This TIP behavior can be illustrative of an antiferromagnetic coupling between the single electrons located on the Yb center and bipym, or rather an open-shell singlet state ( $\text{Yb}^{\text{III}}, f^{13}$  and  $\text{bipym}^-$ ) mixing into the close-shell ground state ( $\text{Yb}^{\text{II}}, f^{14}$  and  $\text{bipym}^0$ ). The temperature-independent magnetic susceptibility of **2** is also indicating a low-lying triplet excited state above the singlet ground state.<sup>114</sup> In order to better understand the magnetic susceptibility curve, a modified Bleaney-Bowers equation has been used to fit to the magnetic data, with an average  $g$ -value of 3.78, which is relatively close to the one of the similar trivalent  $\text{Cp}^*_2\text{Yb}(\text{bipy})^+$  complex with 3.315,<sup>123</sup> a TIP of  $0.00602 \text{ emu}\cdot\text{mol}^{-1}$ , and a  $2J$  value of  $-275.2 \text{ cm}^{-1}$ , which can be

estimated as the singlet-triplet gap energy (Equation (1)).<sup>124</sup> The perfectly satisfactory fit is therefore acquired, which is highlighted with a red curve. However, in our system, because the values of TIP and  $g_{ave}$  are in agreement with a high anisotropy; another model need to be used to account for such high anisotropy. This model is based on Lukens *et al.* that is more adapted to highly anisotropic compounds such as the lanthanide complexes.<sup>120</sup> In their study on the multiconfigurational  $Cp^*_2Yb(bipy)$  complex, the overall wave function can be written as  $\Psi = c_1|f^{13}, bipy^{-}\rangle + c_2|f^{14}, bipy^0\rangle$ . Assuming the  $c_1^2$  approaches 1, which means the oxidation state of Yb is close to purely trivalent  $f^{13}$ , and using the  $g$ -value of the similar  $Cp^*_2Yb(bipy)^+$  complex,<sup>123</sup> the  $2J$  value is then estimated to be  $-245.7\text{ cm}^{-1}$ . Note that this value is similar as the one calculated from the Bleaney-Bowers model. This is indicative of a rather strong antiferromagnetic exchange coupling, which is well comparable to the data for the related  $Cp^*_2Yb(L)$  complexes with  $N$ -aromatic heterocycles<sup>125,126</sup> as well as other similar organotransition-metal species.<sup>110</sup>

$$\chi = \frac{2N\beta^2 g_{ave}^2 e^x}{kT(1 + 3e^x)}, \quad x = \frac{2J}{kT} \quad (1)$$

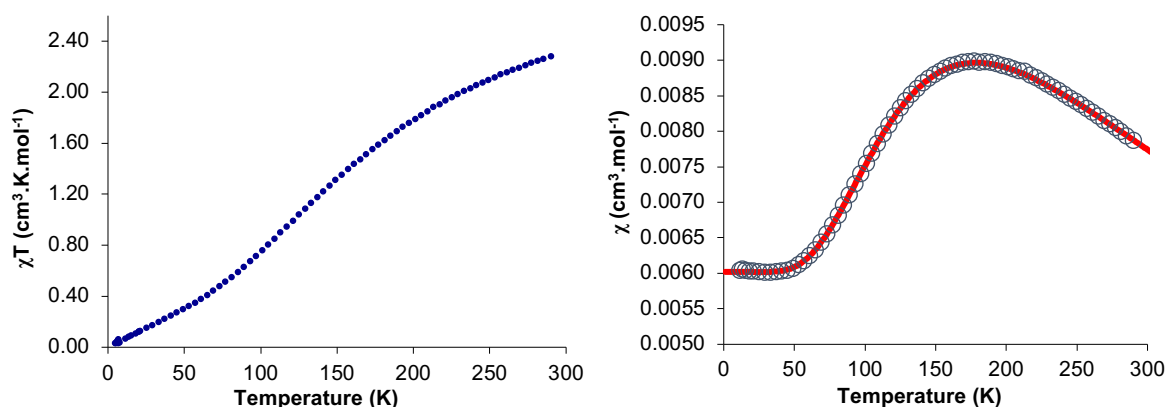


**Figure 12.** Solid-state temperature dependent magnetic data at 0.5 T: (left) plot of  $\chi T$  vs.  $T$  and of (right)  $\chi$  vs  $T$ . The solid line represents the fit of the magnetic data (see text).

Thus, the solid-state magnetism and  $^1H$  NMR data agree well with a singlet ground state ( $S = 0$ ) and a low-lying triplet state ( $S = 1$ ) which is getting populated. The maximum in the  $\chi$  vs  $T$  plot is indicative of the triplet substantial population. The magnetic exchange coupling as just mentioned above is monitored. In order to better understand the electronic structure, especially the electron density qualification on the nickel center, theoretical investigations at DFT level are consequently performed.

### 2.3. Theoretical Study: DFT Calculations

With the assistance from other group members (Maxime Tricoire), DFT calculations are firstly performed on both complexes **1** and **2** with three different functionals: PBE, PBE0, and TPSSh. For **1**, optimized geometric data by calculations are compared to the XRD data, giving minor differences (Table 5). Three different functionals lead to equivalent perspectives in the electron density of the compound. The HOMO is solely the  $dz^2$  orbital of the nickel center, whereas the

LUMO and LUMO+1 are located in the  $b_1$  symmetry orbital agreeing with of the bipym (in  $C_{2v}$ ). The LUMO has clearly much density on the C-C bridging bond between two pyrimidine rings while the LUMO+1 has a node at these positions; yet on the nickel center, there is only residual density, and the estimated atomic orbital Mulliken contribution from the nickel to LUMO and LUMO+1 are 8.3% and 4.6%, respectively (Figure 13).

**Table 5.** Average main distances (Å) and angles (°) for (bipym)NiMe<sub>2</sub> (**1**) DFT optimized geometry with three different functional (PBE, PBE0 and TPSSh) versus XRD crystallographic data.

Atoms	PBE	PBE0	TPSSH	XRD
Ni-C	1.916	1.899	1.911	1.930(3)
Ni-N	1.951	1.967	1.953	1.959(2)
C-C <sub>bipym</sub>	1.471	1.472	1.469	1.482(5) (avg)
Me-Ni-Me^N-Ni-N	9.41	16.90	13.11	5.34±0.24 (avg)
N-C-C^C-C-N <sub>bipym</sub>	4.65	12.80	7.64	2.63±1.04 (avg)

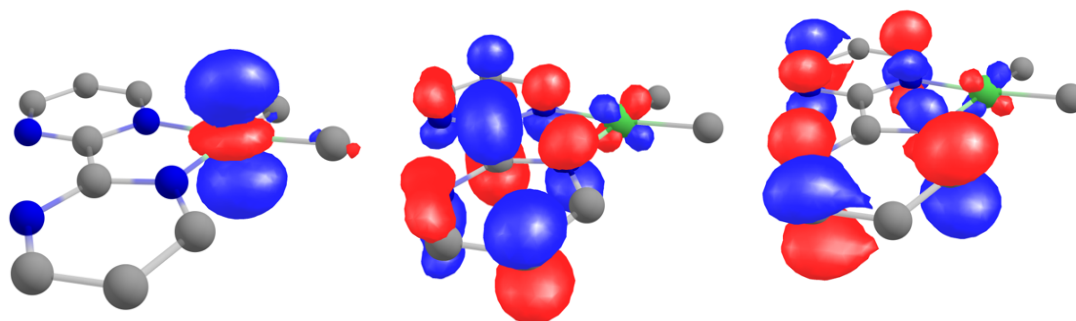


**Figure 13.** Kohn–Sham orbitals of **1** at the TPSSh level of theory calculated from PBE optimized geometry: (left) HOMO, (middle) LUMO, and (right) LUMO +1.

The computations on **2** are much more complicated because of the multiconfigurational electronic structure, which has been shown with the magnetic data. Considering the number of atoms, the multi-referential calculations become more complicated when we try to assess such electronic structure with a low-lying singlet state as well as a triplet state, which is low in energy. The multiconfigurational state is very likely to be one of the well-studied similar complexes.<sup>114–119</sup> Based on other characterizations by XRD and magnetism as well as the computational data from previous similar examples, it is indicative of electron density localizing on the linking C-C bond in the ligand, in good agreement with an electron transfer from divalent Yb to the LUMO of **1**. The HOMO remains located on the  $d_{z^2}$  orbital of the nickel center with high energy, which helps the metal prepare for the further reactivity.

### 3. Reactivity with carbon monoxide

Several organometallic examples are reported regarding unsaturated substrates (CO, imine, and/or olefins) insertion reactions, forming isolated nickel acyl or amino complexes. Nevertheless, it has barely been investigated starting with *bis*-alkylnickel precursors, probably because it is significantly difficult to stabilize the insertion intermediates, which undergo facile and fast further reductive elimination. Therefore, it becomes largely interesting to study how the lanthanide can influence the well-known mechanism and modulate the reactivity on the dimethyl nickel fragment. The reactivity studies were conducted in NMR or Schlenk tubes with J. Young valves by adding CO gas directly into a degassed frozen solution of complex **1** or **2** and letting them react at room temperature. Initially, the reaction with **1** at low pressure of CO (0.2 bar) was performed in THF- $d^8$  at 20°C (Figure 14). New signals rapidly appear within few minutes at 9.2 and 2.2 ppm, which are in the very similar range of the ones of identified acyl nickel analogues in the literature with bipyridine ligand as well as other L-type ligands (Figure 15).<sup>100,102,127,128</sup> After these are formed, fast reductive elimination occurs, leading to acetone formation as well as free bipym release (Figure 16).

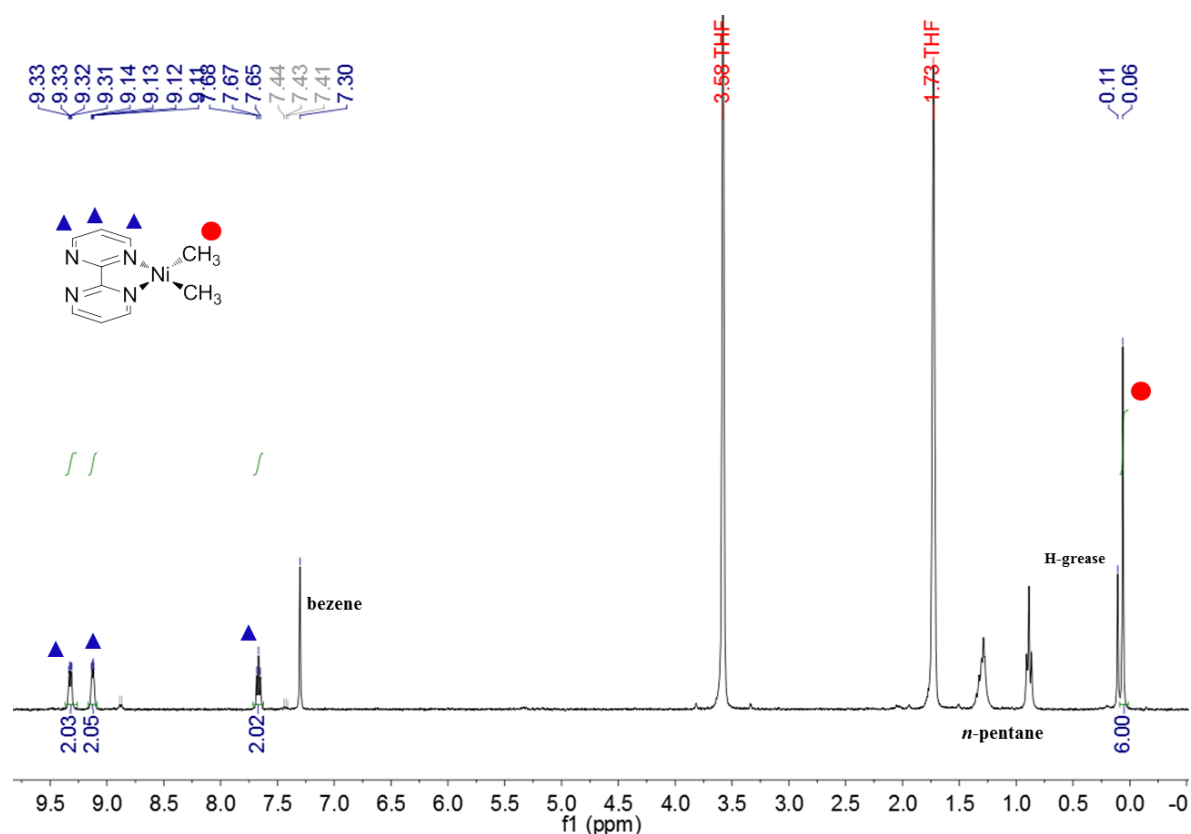


Figure 14.  $^1\text{H}$  NMR of **1** in THF- $d^8$  at 293 K before addition of CO.

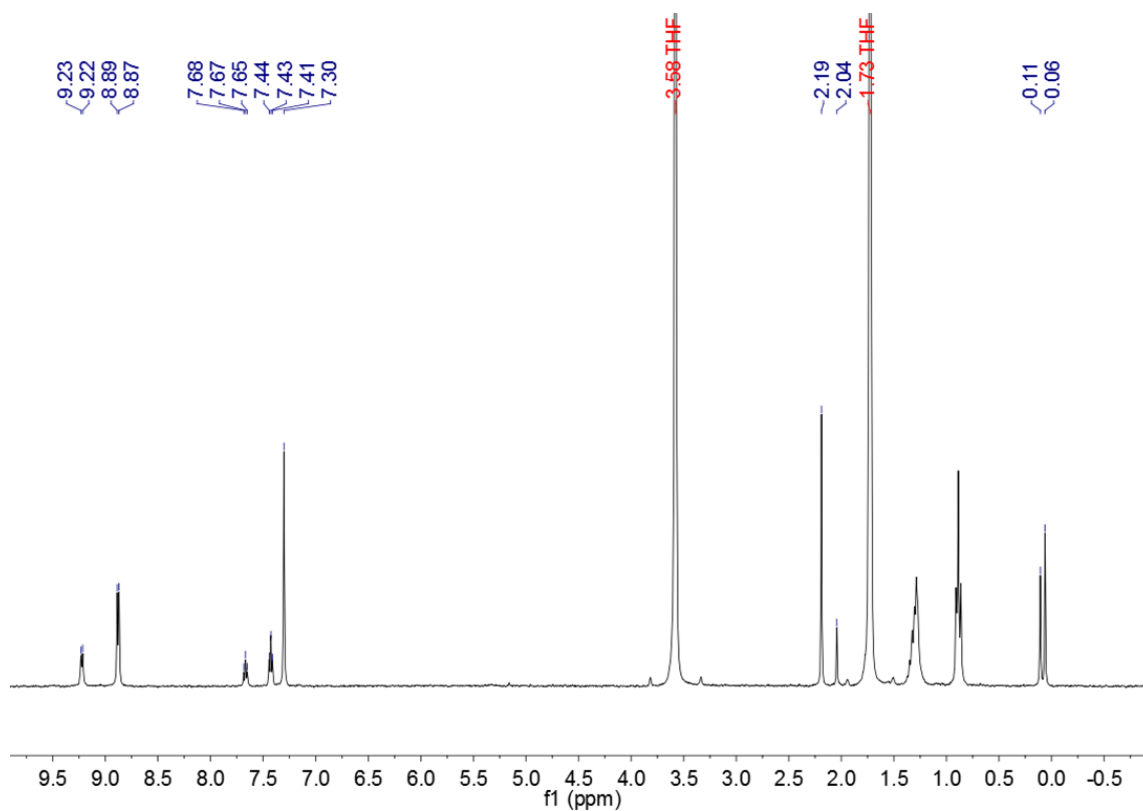


Figure 15.  $^1\text{H}$  NMR of **1** in  $\text{THF-d}_8$  at 293 K after addition of CO (0.2 bar).

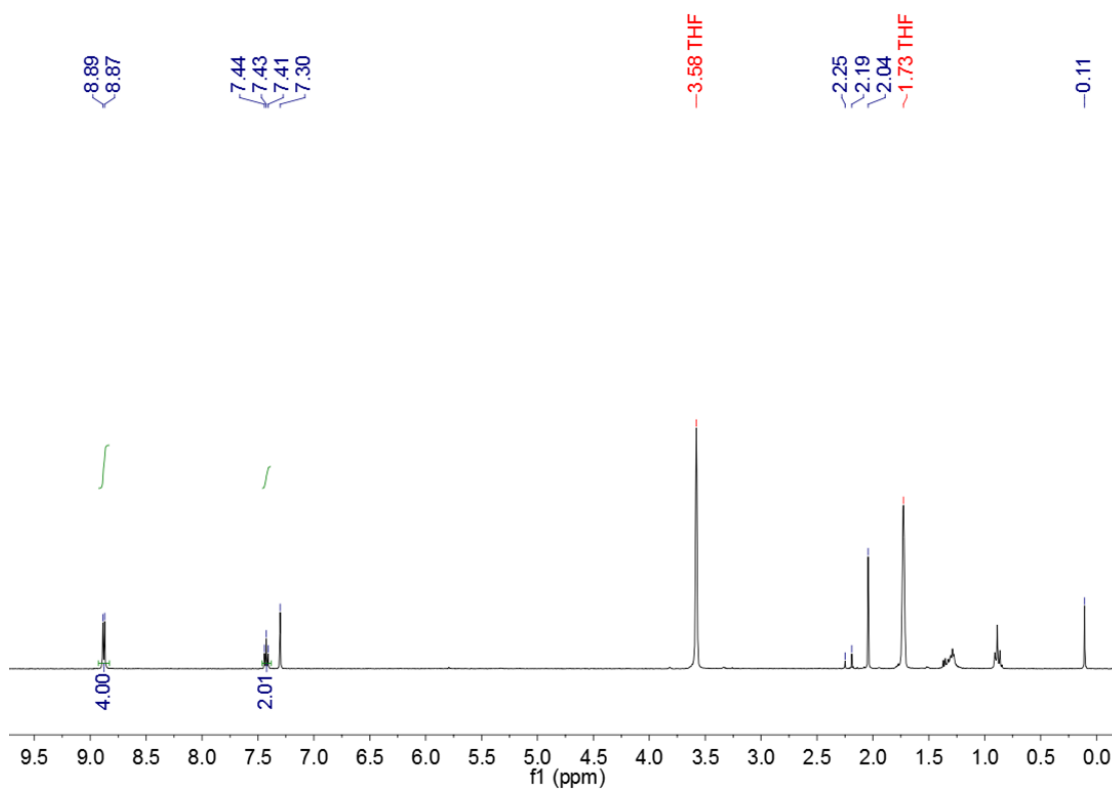
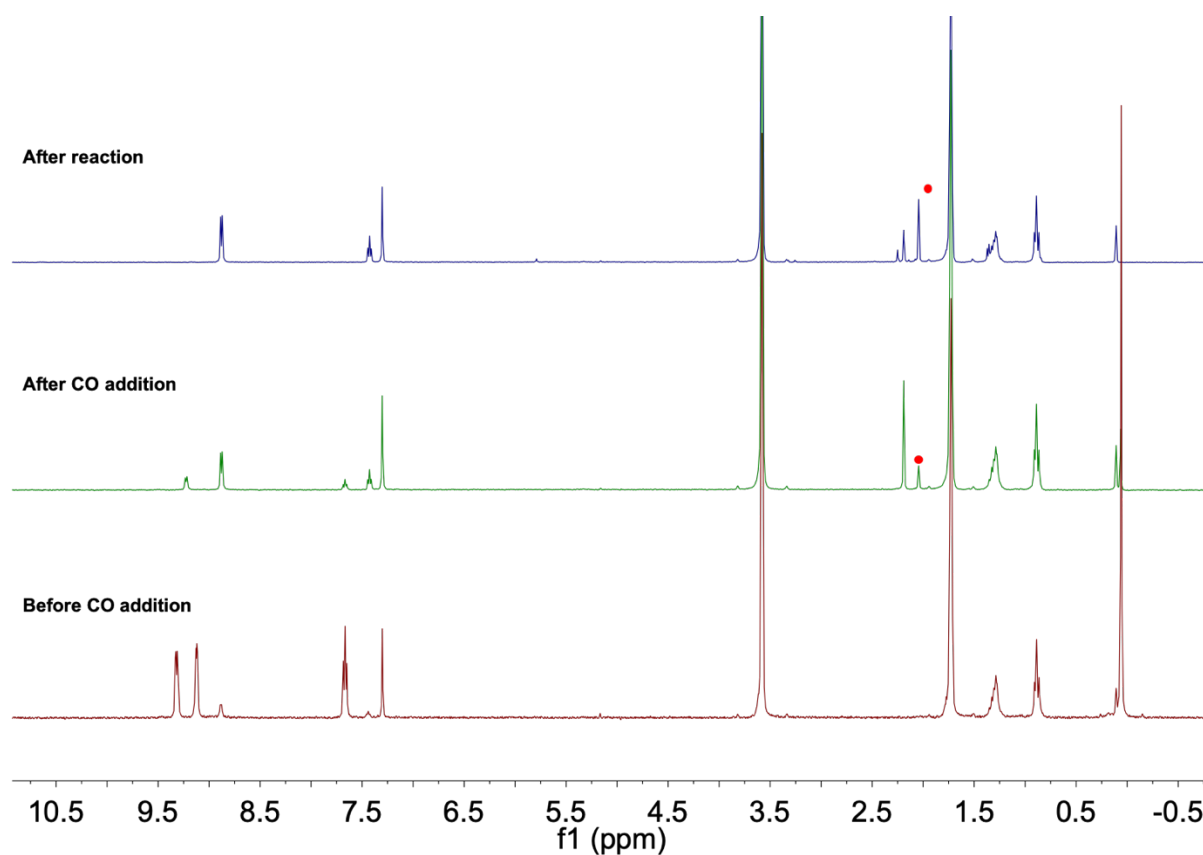


Figure 16.  $^1\text{H}$  NMR of **1** in  $\text{THF-d}_8$  at 293 K after the reaction with CO (0.2 bar).





**Figure 17.**  $^1\text{H}$  NMR of **1** in  $\text{THF-d}_8$  at 293 K of reaction with CO (0.2 bar).

The CO addition was performed under similar condition with **2** and followed by  $^1\text{H}$  NMR spectroscopy. Differently, it takes much longer time to observe several new signals appearing and growing at 259.9, 12.4 and -0.1 ppm, with a slowly decreasing quantity of **2** (Figure 19). The intensity of these new signals is increasing and then dropping to disappearance within the reaction time evolution with the formation of acetone reaching to the approximately one equivalent stoichiometry until the end of the reaction (Figure 20). The formed acetone indicates the reductive elimination step from the monitored acyl intermediate **3**, generating a  $\text{Ni}^0$  species at the same time (Scheme 19). More likely, a biscarbonyl  $\text{Ni}^0$  product is considered because of the presence of CO in excess. Unfortunately, the prior CO coordination on the nickel center through the loaded  $\text{dz}^2$  orbital to form a five coordinating system is not detected by  $^1\text{H}$  NMR. Also, the intermediate **3** or the reduced  $\text{Ni}^0$  compound **4** are not successfully isolated; yet instead, the disassociation of **4** is detected with the evidence of free bipym NMR signals as well as the crystallized  $\text{Cp}^*_2\text{Yb}(\text{bipym})\text{YbCp}^*_2$  dimer from the reaction mixture. The labelling experiments with  $^{13}\text{C}$ O should be very informative of the mechanistic investigation. However, influenced by the outbreak of the pandemics, the experiments were not performed on time, but they should be completed in the future.

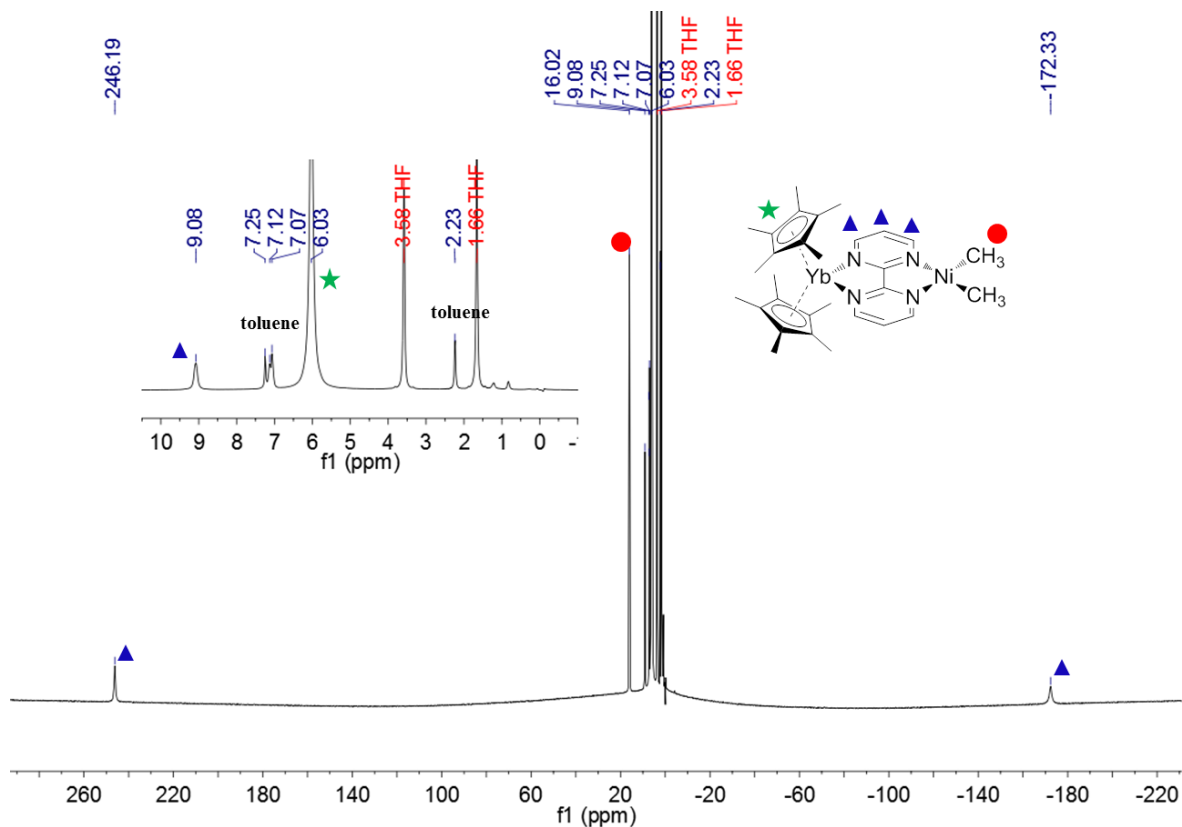


Figure 18.  $^1\text{H}$  NMR of **2** in  $\text{THF-d}_8$  at 293 K before addition of CO.

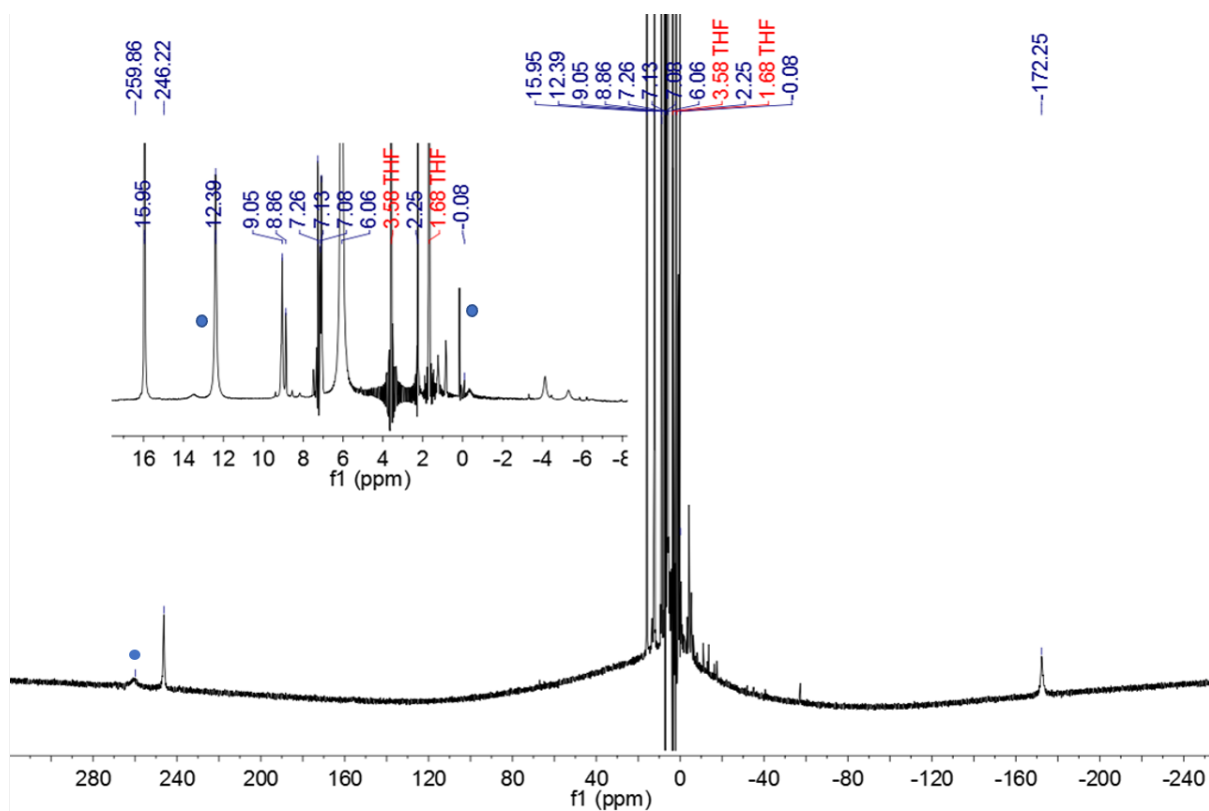
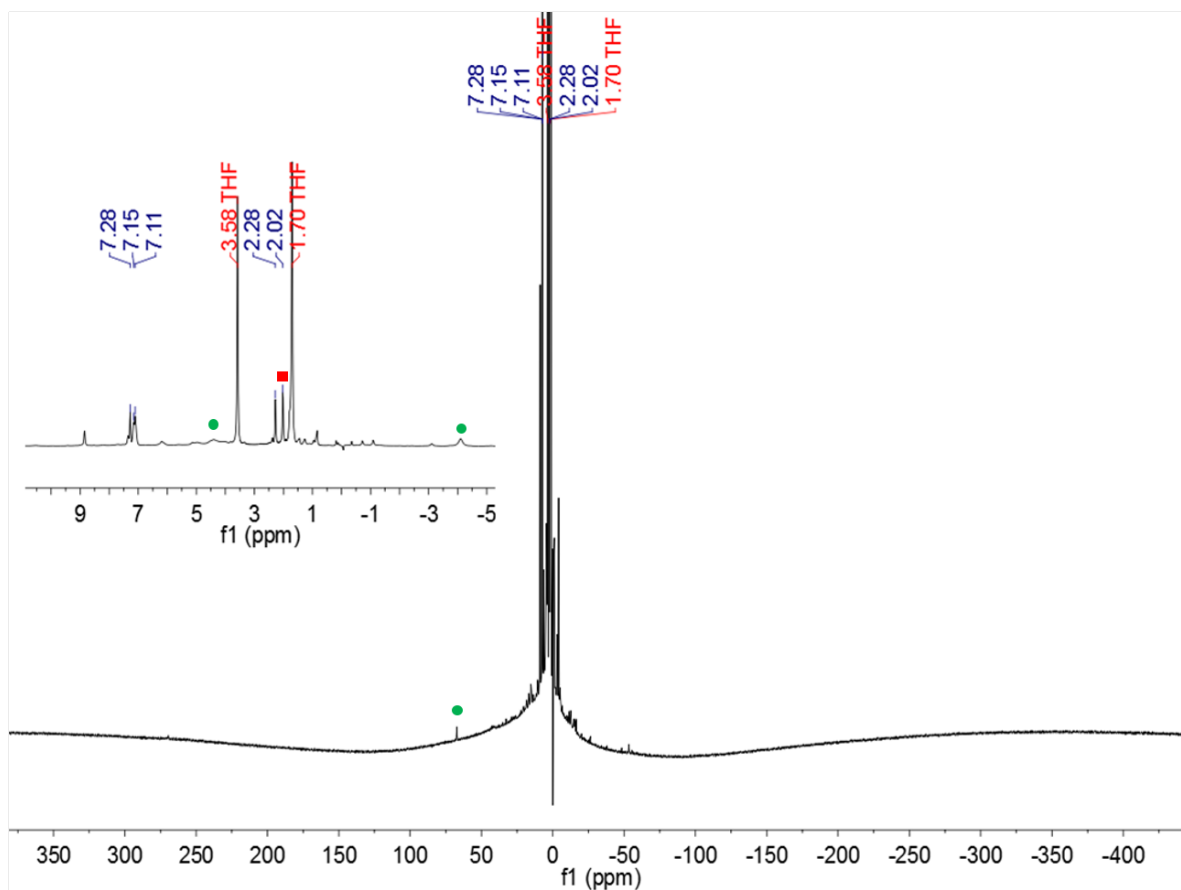
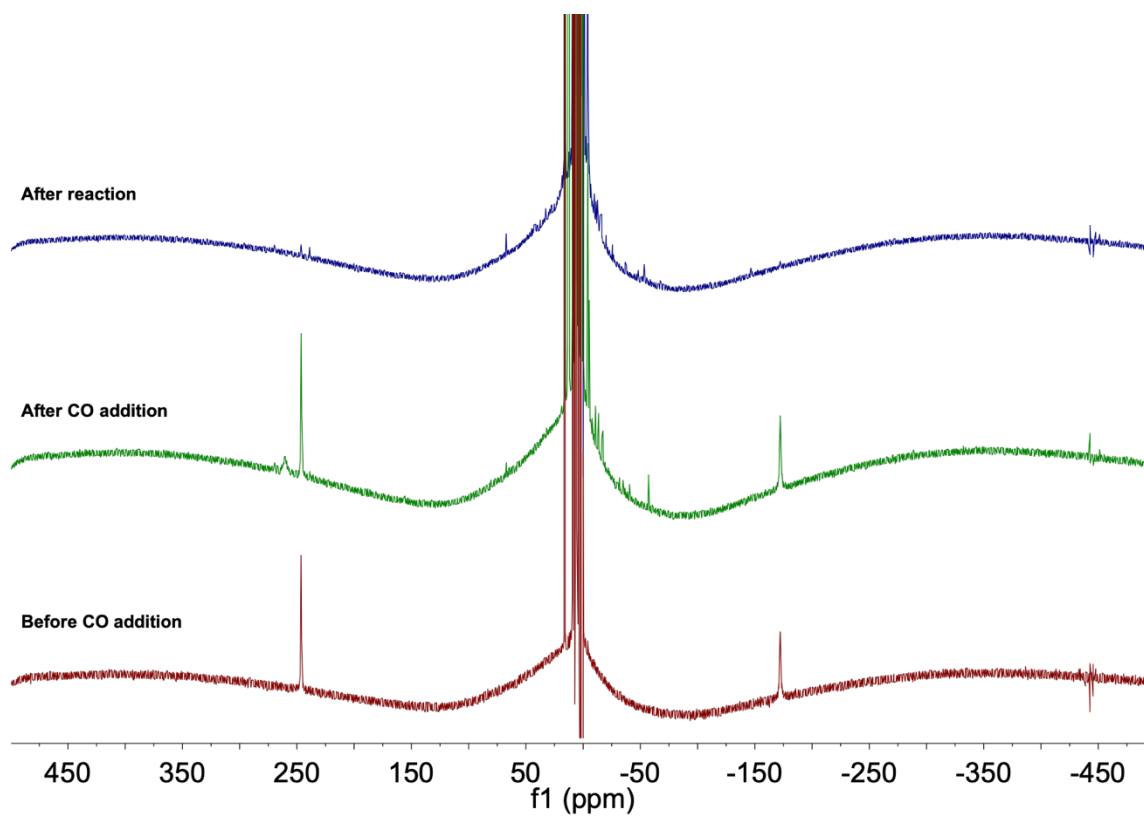


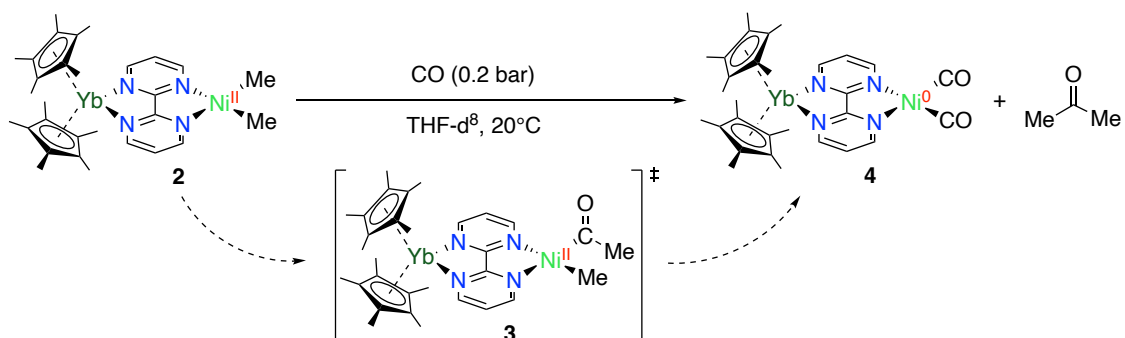
Figure 19.  $^1\text{H}$  NMR of **2** in  $\text{THF-d}_8$  at 293 K after the addition of CO. Signals of the possible generated intermediate are indicated with blue circles.



**Figure 20.**  $^1\text{H}$  NMR of **2** in  $\text{THF-d}_8$  at 293 K after the reaction with CO. Resonances of the formed acetone as well as  $\text{Cp}^*_2\text{Yb}(\text{bipym})\text{YbCp}^*_2$  are indicated with a red square and green circles, respectively.



**Figure 21.**  $^1\text{H}$  NMR of **2** in  $\text{THF-d}_8$  at 293 K of reaction with CO.



**Scheme 19.** Reactivity of **2** with CO addition and possible intermediate.

The slow evolution of the reaction helped performing the kinetical analysis of the reaction followed by NMR. The decrease of the starting material **2** concentration, which is identified by very careful integration of the  $^1\text{H}$  NMR signals, is normalized referring to the constant quantity of the co-crystallized toluene molecule from the crystal cell. The concentration of **2** is required to be in a moderate range (0.0073-0.029 mol/L) in order not to modify the observed reaction rate despite the variation of concentration at the same temperature. If the concentration of **2** goes higher, the amount of CO in the reaction system cannot be regarded as large excess any longer and the kinetics starts to evolve in a different way, making the analysis much more complicated.

Mono-exponential variation decrease of the concentration of **2** is recorded at five different temperatures and the one at  $35^\circ\text{C}$  is presented below (Figure 22).<sup>129</sup> A pseudo first-order process is then identified in the overall reaction of **2** with large excess of CO.<sup>130</sup> The rate law can be determined based on the mechanism (Scheme 20, Equation 2).

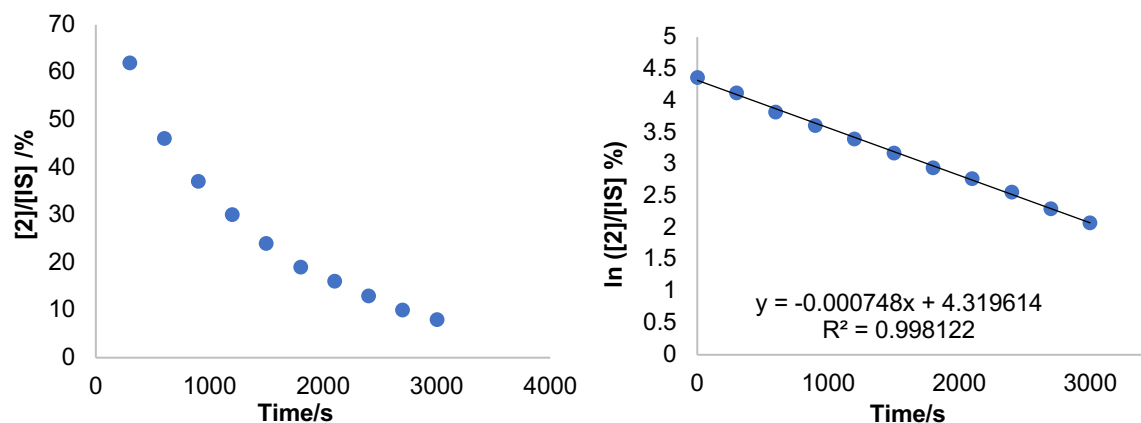
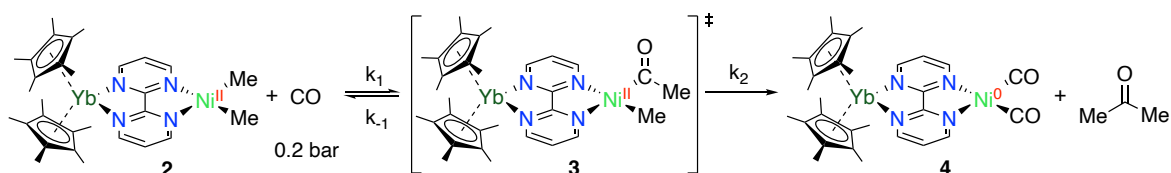


**Figure 22.** Kinetic data for **2** at  $35^\circ\text{C}$ .  $t_{1/2} = 926.7$  s.



**Scheme 20.** Reaction mechanism of **2** with CO with rate constants.

$$r = \frac{k_1 k_2 [2][CO]}{k_{-1} + k_2} \quad (2)$$

The perfectly fitted kinetic data in agreement with pseudo first-order rate law are obtained using the same NMR analysis over the temperature range from 15°C to 35°C, leading to an Eyring analysis (Table 6, Figure 23). The activation energy parameters are obtained as  $\Delta H^\ddagger = 20.7$  kcal·mol<sup>-1</sup> and  $\Delta S^\ddagger = -5.75$  cal·mol<sup>-1</sup>·K<sup>-1</sup>. The moderate value of enthalpy agrees with a rather slow reaction with a moderate activation barrier, and the small negative entropy value indicates that the reductive elimination of ketone, which is entropically favorable, is not the RDS or is likely balanced with a non-entropically favorable step with a similar rate. The migratory insertion has a more modest effect entropically (entropy decrease) and that is possibly corresponding to the RDS in this reaction. However, the overall mechanism is still not experimentally confirmed because of the deficient information of CO coordination step, hence the RDS cannot be definitely concluded at this stage.

**Table 6.** Eyring Plot data for **2**.

T (°C)	T (K)	1/T (K <sup>-1</sup> )	k (s <sup>-1</sup> )	k/T (s <sup>-1</sup> K <sup>-1</sup> )	ln (k/T)	t <sub>1/2</sub> (s)
35	308.15	0.003245173	0.000748	2.42739E-06	-12.928694	926.7
30	303.15	0.003298697	0.000385	1.27E-06	-13.576495	1800.4
25	298.15	0.003354016	0.000216	7.24468E-07	-14.137829	3209.0
20	293.15	0.003411223	0.000122	4.16169E-07	-14.692174	5681.5
15	288.15	0.003470415	0.0000648	2.24883E-07	-15.307686	10696.7

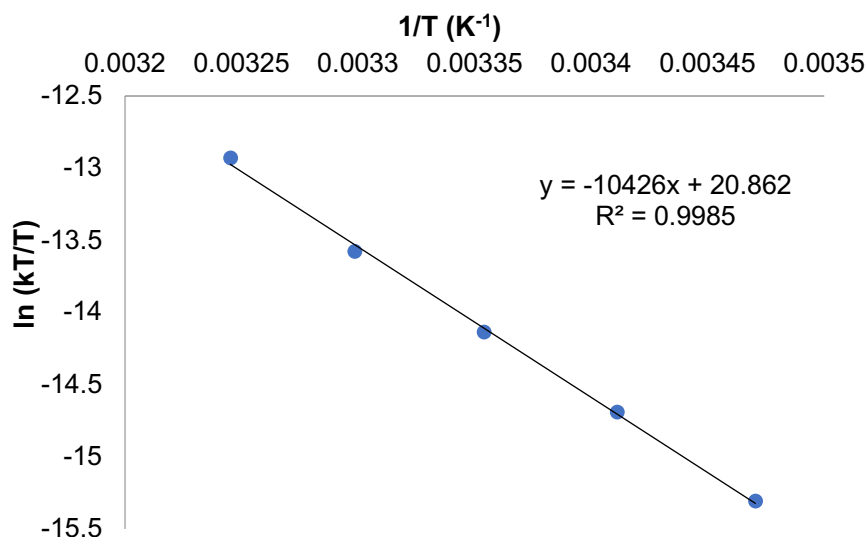
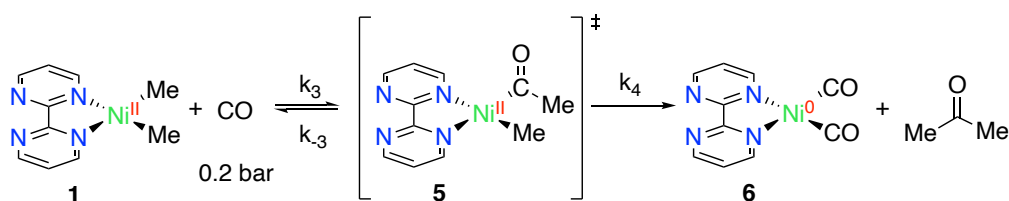


**Figure 23.** Eyring Plot and resulting  $\Delta H^\ddagger$  and  $\Delta S^\ddagger$  for **2**.

In order to evaluate the influence of the modulation of the electronic density at the Ni centre caused by the presence of the divalent ytterbium, the kinetics of **1** with CO under the same conditions were

also analyzed by  $^1\text{H}$  NMR spectroscopy. The normalization of concentration of **1** is referred to the benzene residue from the deuterated solvent. A pseudo first-order kinetics is also followed for the overall reaction, constructing an Eyring plot with the same temperature range as **2** with CO. Activation parameters  $\Delta H^\ddagger$  and  $\Delta S^\ddagger$  as  $17.06 \text{ kcal}\cdot\text{mol}^{-1}$  and  $-16.41 \text{ cal}\cdot\text{mol}^{-1}\cdot\text{K}^{-1}$  were obtained, respectively. The lesser  $\Delta H^\ddagger$  value compared to  $20.7 \text{ kcal}\cdot\text{mol}^{-1}$  of the reaction of **2** reveals a decreased reaction energy barrier, which is also proved with the different reaction half-time of **1** and **2**: for example, at  $20^\circ\text{C}$ , the reaction with CO undergoes much faster with **1** ( $t_{1/2} = 39.0 \text{ min}$ ) than with **2** ( $t_{1/2} = 94.7 \text{ min}$ ). Meanwhile, a decent negative entropy value indicates that the reductive elimination is likely the RDS of this reaction, or more precisely, the entropically favorable rate constant  $k_4$  is much larger than  $k_3$ .



**Scheme 21.** Reaction mechanism of **1** with CO with rate constants.

The comparison of the kinetic data in both cases can lead to a deducible conclusion that in the presence of lanthanide fragment, the CO migratory insertion step becomes relatively slow and the formed acyl intermediate will be much more kinetically stable. There will be various practicable extensions based on this reactivity property such as applying in carbonylative reactions with unsaturated substrates, for example, light olefins and imines.<sup>98,128</sup>

## 4. Other Reactivity Attempts

### 4.1. Oxidation

Very similar multiconfigurational ground state of **2** has been characterized as the previously studied  $\text{Cp}^*_2\text{Yb}(\text{bipym})\text{PdMe}_2$  complex, which is further oxidized to form a stable  $\text{Pd}^{\text{IV}}$  compound with MeI at room temperature. Inspired by such example, as a consequence, the addition of MeI on **2** was also performed in order to generate a  $\text{Ni}^{\text{IV}}$  species *via* straightforward oxidative addition process; however, an extremely fast ethane formation with hardly identifiable new species is only detected by  $^1\text{H}$  NMR spectroscopy at  $20^\circ\text{C}$ . Even though the reaction is performed fast in a pre-cooled NMR spectrometer at  $-60^\circ\text{C}$ , only a new product with a  $\text{C}_s$  symmetry, as well as ethane are detected. The integration of this new species implies the formation of the reductive elimination product  $\text{Cp}^*_2\text{Yb}(\text{bipym})\text{NiMeI}$  (Figure 24). However, this species in solution seems only relatively stable at low temperature because decomposition starts to occur when the temperature increases to  $0^\circ\text{C}$  (Figure 25). The signals become broader and the symmetry is being lost. In the end, a degradation can be noticed when the temperature is back to  $20^\circ\text{C}$ .

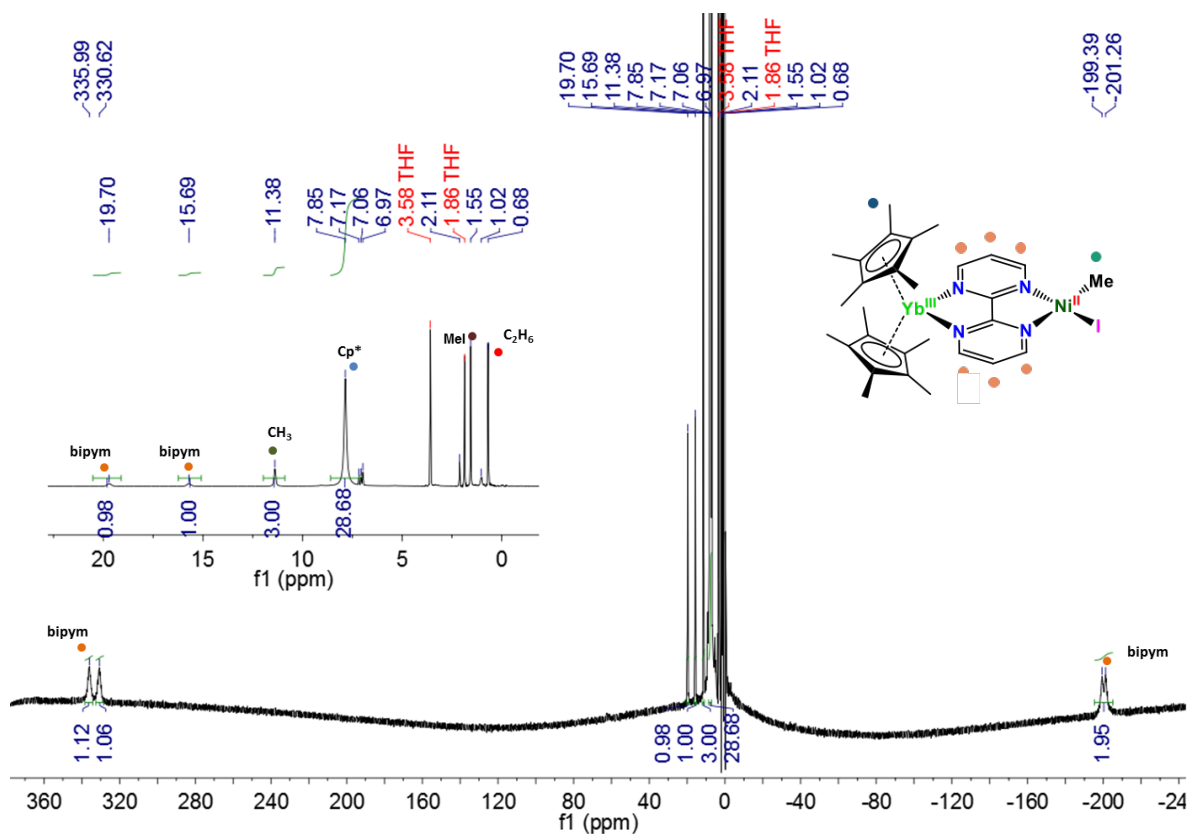


**Figure 24.**  $^1\text{H}$  NMR identification of the reductive elimination product in  $\text{THF-d}_8$  at  $-60^\circ\text{C}$  after oxidative addition of MeI (1.2 equiv.) on **2**.

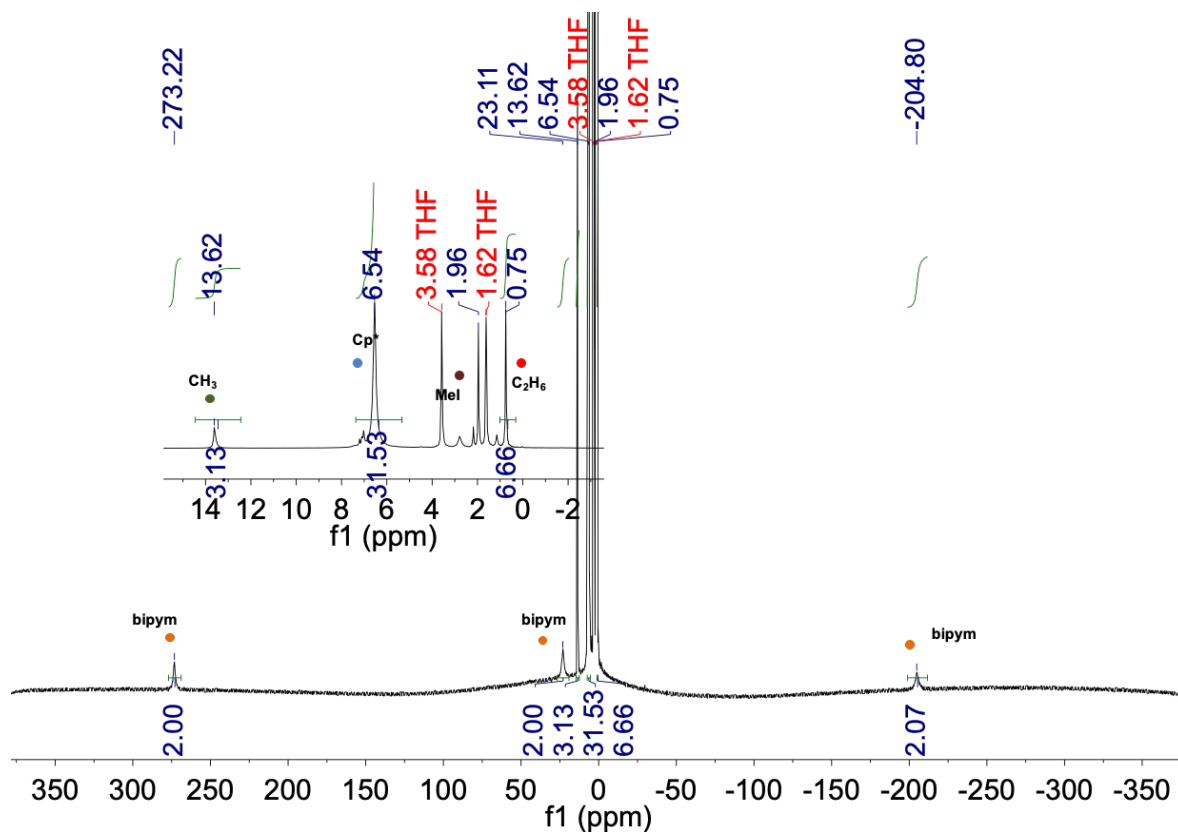


**Figure 25.**  $^1\text{H}$  NMR of the reductive elimination product in  $\text{THF-d}_8$  at  $0^\circ\text{C}$  increased from the oxidative addition of MeI (1.2 equiv.) on **2** at  $-60^\circ\text{C}$ .

Much effort is taken to crystallize this likely reductive elimination product in order to get more insights in the electronic property as well as the seemingly simple mechanism of the reaction. Indeed, contrary to the expected typical catalytic Pd<sup>II</sup>/Pd<sup>IV</sup> mechanism, nickel can undergo not only Ni<sup>II</sup>/Ni<sup>IV</sup>, but also the one electron Ni<sup>II</sup>/Ni<sup>III</sup> pathways. The nickel alkyl halide complexes are also significant intermediates in photocatalytic cross-coupling reactions.<sup>131</sup> Unfortunately, either purple crystalline Cp\*<sub>2</sub>Yb<sup>III</sup>I with thf adduct, or insoluble powder which may be the decomposed product are eventually obtained.

Similar reactivity tests were performed with MeOTf in THF, expecting a trimethylnickel or monomethylnickel triflate ionic pair formation. Also, only a reductive elimination product with ethane formation was detected at low temperature, and oligomerization or polymerization of THF takes place when the temperature is higher (20°C). When a more chelating solvent is used for the reaction, for example, pyridine, the dimeric **2** complex will dissociate and a dark green diamagnetic Cp\*<sub>2</sub>Yb(pyr)<sub>2</sub> compound can be re-crystallized.<sup>132</sup>

Several other mild to strong oxidants were used in order to achieve high valent nickel species. Particularly, silver salts, ferrocenium salts, and Umemoto reagents were selected according to their redox potential.<sup>52,133,134</sup> The reactions performed in chelating solvents (acetonitrile or pyridine) at low temperature (-40°C) all led to fast ethane formation and very broad diamagnetic NMR signals, which are probably indicating degradation occurrence, as well as the corresponding reduced compounds such as ferrocene and dibenzothiophene but not Ag<sup>0</sup> mirror after the reaction.

## 4.2. Reduction

The idea to reduce this bimetallic complex **2** is to take advantage of the electron capacity of bipym ligand, which is able to receive, store and potentially transfer two electrons maximally. Its redox property resembles the one of diiminopyridine ligands with their various diimine derivatives that have been extensively exploited in studying the electronic modularity, catalytic activity and selectivity in combination with transition metals.<sup>135-138</sup> It is rather interesting to further reduce the already radical anionic **2** to form the dianionic species and investigate its electronic configuration and study its reactivity because it can then be regarded as an intermediate-valent compound from zero to divalent oxidation states.

The preliminary test was to use Cp\*<sub>2</sub>Yb(OEt<sub>2</sub>) ( $\Delta E \sim -1.15$  eV)<sup>139</sup> to perform the one electron reduction, which is referring to the trimetallic Cp\*<sub>2</sub>Yb(taphen)PdMe<sub>2</sub>YbCp\*<sub>2</sub> complex.<sup>140</sup> Unfortunately the expected trimer in toluene does not form efficiently as observed by <sup>1</sup>H NMR spectroscopy. Instead, when using a very powerful reductant as sodium naphthalenide (NaNAP) ( $\Delta E \sim -3.0$  eV) with stoichiometric equivalent in THF-d<sup>8</sup>, a very different NMR appeared, which was rather similar as the one of trimetric Pd analogue. The oxidized naphthalene signals are also found in the spectrum (Figure 26). So far, this reduced species has not been isolated yet while the reduced precursor **7**, which is reacted with NaNAP by stoichiometric equivalence, has been recrystallized as black needles and analyzed by XRD (Figure 27). The redox-active bipym is efficiently reduced referring to the C1-C2 distance of 1.411 Å. The distances of Ni-C and Ni-N of



1.93(7) Å and 1.950(5) Å, respectively, are indicative of a divalent oxidation state of the nickel center.

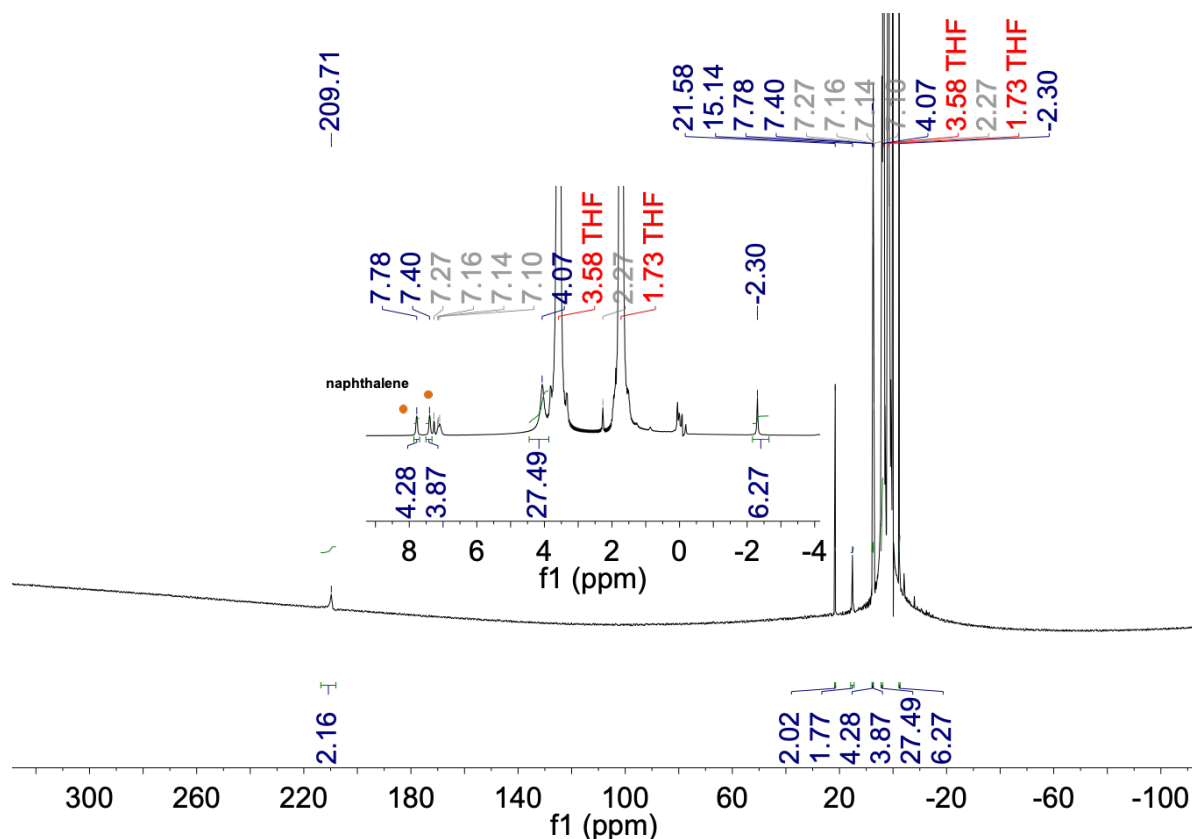


**Figure 26.**  $^1\text{H}$  NMR of *in-situ* formed product from **2** with stoichiometric equivalent NaNAP in  $\text{THF-d}^8$  at  $20^\circ\text{C}$ . Toluene resonance is highlighted in grey. The signals of generated naphthalene after reduction are indicated by orange loops.

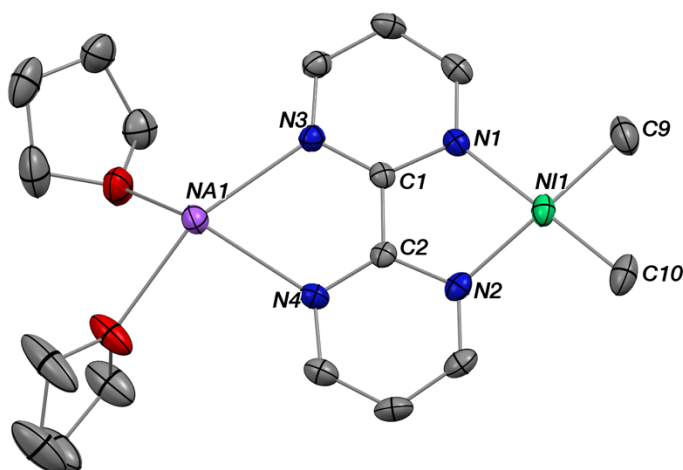


**Figure 27.** ORTEP of **7**. Only one of the molecules of the cell is shown. Thermal ellipsoids are at the 50% level. Hydrogen atoms have been removed for clarity. Selected average distances: Ni-C: 1.93(7) Å; Ni-N: 1.950(5) Å; bridging C1-C2: 1.411 Å; Na-N: 2.444(5) Å.

The complexation with  $\text{Cp}^*\text{Yb}(\text{OEt}_2)$  using crystalline **7** is performed in  $\text{THF-d}^8$  is leading to the same spectrum as the *in-situ* reduction reaction. Re-crystallization was tried in various ways but

the reduced heterobimetallic species seems very challenging to be isolated. Instead,  $\text{Cp}^*_2\text{Yb}(\text{bipym})\text{YbCp}^*_2$  is only obtained from the mixture, which is due to the trace of free bipym remaining. Note that it was the reason why it has to be mentioned at the very beginning before the divalent lanthanide fragment addition.

However, the new heterobimetallic complex **8** can be obtained *via* two-electrons reduction with excess of NaNAP or sodium metal ( $\Delta E \sim -3.0$  eV). The NMR of this compound is silent, but dark XRD-suitable crystals are isolated (Figure 28). A much shorter C-C bridging bond distance (1.350 Å) is found comparing to that (1.403(4) Å) in **2**. However, a rather shorter average bond length of Ni-N (1.94(5) Å), and an obviously longer Ni-C distance (1.94(6) Å) in **8**, comparing to those observed (1.956(3) and 1.925(1) Å, respectively) in **2**, indicate a possible transition of oxidation state of nickel center. The conclusive identification of the nature of Ni requires more physical characterizations such as EPR. The average Cp centroid-ytterbium distance (2.46(1) Å) lies in the typical range (2.43-2.50 Å) of divalence (See the description above). The crystallographic information nicely agrees with a strongly reduced bipym ligand and divalent ytterbium atom. In general, two electrons have been located inside the bipym-NiMe<sub>2</sub> fragment and one potential electron can be used from the divalent organoytterbium.

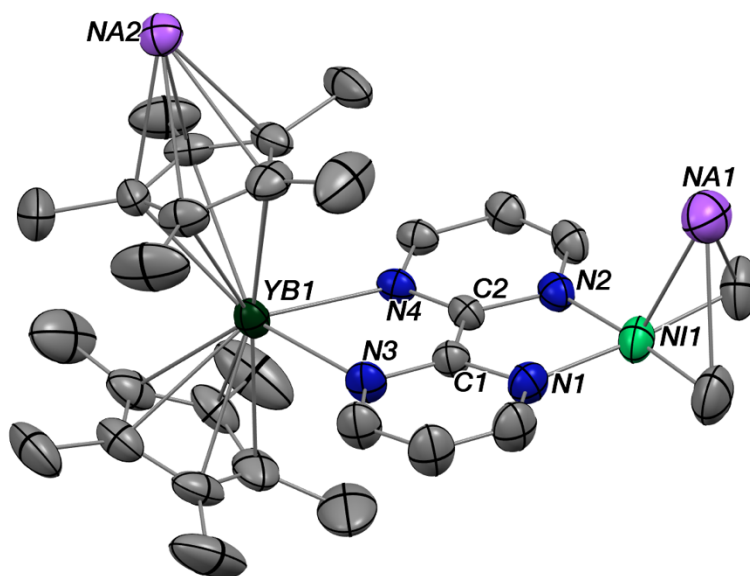


**Figure 28.** ORTEP of **8**. Thermal ellipsoids are at the 50% level. Hydrogen atoms as well as THF solvate molecules have been removed for clarity. Selected average distances: Yb-Cp<sub>ctr</sub>: 2.46(1) Å; Yb-N: 2.436(5) Å; bridging C1-C2: 1.350 Å; Ni-N: 1.94(5) Å; Ni-C: 1.94(6) Å.

**8** has effectively been double reduced by two electrons stored in the redox-active bipym, and a third electron could be potentially transferred to the ligand system from the divalent lanthanide ion. Clearly, this compound needs to be further characterized and the solid-state magnetism can be rather interesting, which can be informative of the overall electronic structure. Several reactivity tests on it have been investigated, including alkene, weak acidic terminal alkyne as well as dihydrogen addition. None of them leads to a conclusive result, since there was no obvious color change in any performed reaction, as well as the silent nature of NMR except the identical

resonances for the reagents. Besides, the oxidation with alkyl halide (MeI) and ionic oxidants (Umemoto reagents) has been tried in a possible attempt to develop a driving force by sodium inorganic salts formation. The reaction tests were performed in THF- $d^8$  with the NMR-silent **8** and MeI or Umemoto reagent in stoichiometry. Only ethane formation has been noticed as the sole product after the addition of the oxidant. The crude mixture then was tried to be crystallized after the removal of the off-white by-product (sodium salt), yet the crystallization of the products currently stays challenging. Nevertheless, more efforts are still worthwhile to be undertaken to investigate such strongly reduced species in the future.

## 5. Replacement of ytterbium: a novel samarium/nickel bimetallic complex

Samarium is utilized as a more reducing divalent organolanthanide ( $\Delta E \sim -1.55$  eV)<sup>139</sup> to build up the heterobimetallic complex in replacement of ytterbium, in order to extend the chemistry with bipym ligand. As mentioned in the general introduction, it also has an excellent ability to allow electron correlation with redox-active ligands but because it is placed at the beginning of the series, the electronic situation is significantly different. Straightforward similar synthesis as that of **2** yields a novel heterobimetallic Sm/Ni complex, **9** as XRD suitable black crystals in 76% yield (Figure 29).

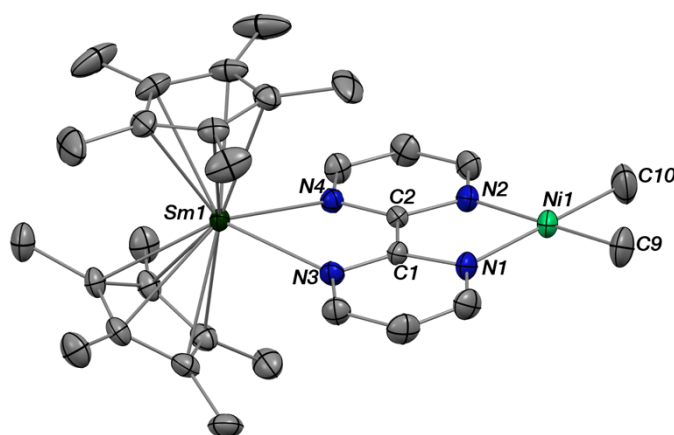


**Figure 29.** ORTEP of **9**. Only one of the molecules of the cell is shown. Thermal ellipsoids are at the 50% level; hydrogen atoms and one co-crystallized toluene solvate have been removed for clarity.

The reduction on the bipym ligand is effective referring to the much shorter C1-C2 bond than the one in **1**, thanks to the single electron transfer from divalent organosamarium. Nickel fragment remains at its divalent oxidation state as well as the coordination environment. Yet the average distance between Cp ring centroid and Sm atom center as 2.41(8) Å is 0.10(7) Å longer than the one found in **2**, which agrees with a larger ionic radius of Sm. The Sm-Cp<sub>ctr</sub> distance in **9** is very close to the one (2.42(1) Å) in its Cp\*<sub>2</sub>Sm analogue with tmbp ligand (tetramethylbiphosphinine), which is regarded as a radical anion and a trivalent Sm ion;<sup>141</sup> and also in a similar trend as the one in the [Cp\*<sub>2</sub>Sm<sup>+</sup>] analogue with tpy (terpyridine) of 2.472 Å, which is 2.504 Å when divalent,<sup>142</sup> indicating a trivalent oxidation state of samarium in **9** (See Table 7 for the comparison with **2**).<sup>143</sup>

**Table 7.** Comparison of for **9** (Ln = Sm) and **2** (Ln = Yb) in representative geometrical parameters: average main distances (Å) and angles (°).

	<b>9</b>	<b>2</b>
Ni-Me	1.927(5)	1.925(1)
Ni-N	1.954(5)	1.956(3)
C-C <sub>bipym</sub>	1.402	1.403(4)
Ln-N	2.489(5)	2.359(1)
Ln-Cp* <sub>centroid</sub>	2.41(8)	2.31(1)
Me-Ni-Me <sup>^</sup> N-Ni-N	3.11	1.80

The <sup>1</sup>H NMR of **9** is recorded in THF-d<sup>8</sup> at 20°C showing a different paramagnetism comparing to that of **2** (Figure 30). Three resonances attributed to the protons on bipym are found at 41.27, 7.86 and -332.42 ppm, and the integration of each shows two protons. Different from the chemical shifts of protons on the ligand in **2**, which are all considerably shifted comparing to the typical resonances of the free aromatic organic molecules, two signals are highly shifted in **9** and one stays at the aromatic area. One signal is corresponding to the protons on the dimethyl groups at 35.68 ppm, integrated for six protons, and one is attributed to the protons on the Cp\* ligands at 2.33 ppm, with approximate integration for thirty protons. The obvious differences in NMR behavior between **2** (Yb) and **9** (Sm) indicate the distinct magnetic performances of these two molecules. The magnetic moments and crystal field effects of the associated Ln(III) metals are very different: for Yb,  $J = 7/2$ , and  $\mu_{\text{eff}} (\text{Calcd.}) = 4.3 \mu_{\text{B}}$ ; and as for Sm,  $J = 5/2$ ,  $\mu_{\text{eff}} (\text{Calcd.}) = 1.58 \mu_{\text{B}}$ .<sup>144</sup> Based on the terpyridine system of the Yb and Sm congeners reported by John and colleagues, a more effective electron transfer was identified with the Cp\*<sub>2</sub>Sm(tpy) complex than the ytterbium analogue.<sup>142</sup> Unfortunately, in our case, the magnetism of **9** has not been well studied yet, and it should be implemented in the next step, in order to compare with that of **2**, as known as a multiconfigurational ground-state. In addition, the reactivity behavior of **9** can be interesting and different from the Yb congener in some cases, due to the intrinsically smaller spin-orbit coupling with samarium ion.

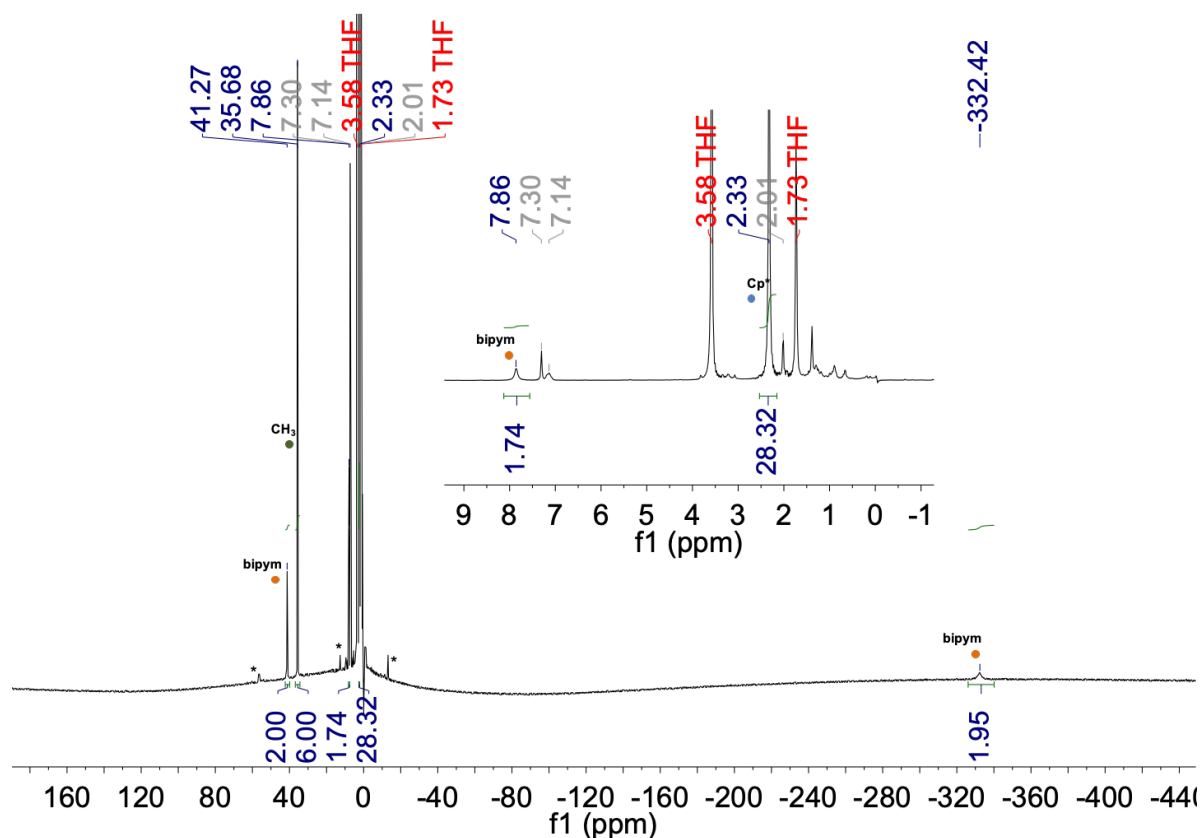


**Figure 30.**  $^1\text{H}$  NMR of **9** recorded in  $\text{THF-d}_8$  at  $20^\circ\text{C}$ . The resonance of co-crystallized toluene solvate is highlighted in grey. Trace of co-crystallized  $[\text{Cp}^*\text{Sm}(\text{bipym})\text{SmCp}^*]_2$  dimer is found and the signals of that is indicated by asterisks.

## 6. Conclusion and perspectives

In this chapter, an original heterobimetallic complex containing reductive divalent ytterbium and reactive nickel with a redox-active ligand, bipyrimidine, has been presented along with its synthesis, characterizations and reactivity tests. It has showed a multiconfigurational electronic structure caused by the strong electron correlation between the divalent organolanthanide and the ligand radical. DFT calculations show a strong spin density located on the *N*-heteroatom ligand coordinated to the reactive nickel center. The reactivity with CO describes the overall kinetics on the migratory insertion of CO into the Ni-Me bond, forming a rather stable acyl intermediate due to the impact of the lanthanide. This interesting behavior can offer us a new strategy for investigating the further CO reactivity application such as olefin functionalization by the direct and rapid carbonylation with unsaturated substrates. Moreover, the direct generation of  $^{11}\text{C}$ -radiolabelled biomolecules could possibly be applied with this rapid CO activation process.<sup>145</sup> However, a more accessible reactive fragment, such as a monoalkyl or monoaryl substituent on nickel center could be deeply considered and designed before applying into a catalytic system. In particular, an active vacant site at the metal center might be demanding to produce the functional organic molecules.<sup>146</sup> Allylbenzene, as an unsaturated substrate, was added into the reaction system of **2** and CO, while no functionalized olefin was obviously observed.

However, one of the synthetic challenges is to prevent the desired, highly reactive mono-substituted species from facile decomposition. The first trial to design a monomethyl nickel complex by performing the synthesis with Ni(COD)<sub>2</sub> and MeI *via* oxidative addition in the presence of bipyrimidine did not yield the ideal (bipym)NiMeI, but insoluble solid product instead. Nevertheless, the modifications on the functionals at the nickel center can be significantly interesting as well as necessary to extend to catalytic performance with CO activation reactivity. The great challenge to study high-valent nickel species by oxidation is leading an alternative strategy to design the heterobimetallic system. Examples on Ni<sup>III</sup> and Ni<sup>IV</sup> from Sanford,<sup>49,52,57,147</sup> Mirica,<sup>56,148</sup> and Mézailles<sup>53</sup> are good inspirations to re-design our backbone by modifying a new functional group (CF<sub>3</sub>)<sup>149</sup> or/and a new ligand system. Moreover, the great interest of reduced bimetallic complex could be another direction, due to the intriguing single-electron transfer processes involving Ni(I) chemistry mentioned in the introduction. Those considerations will be investigated, and the corresponding results will be presented in the next chapters.

## References

- (1) Milani, B.; Licini, G.; Clot, E.; Albrecht, M. Small Molecule Activation. *Dalton Trans.* **2016**, 45 (37), 14419–14420. <https://doi.org/10.1039/C6DT90140A>.
- (2) *Activation of Small Molecules: Organometallic and Bioinorganic Perspectives*; Tolman, W. B., Ed.; Wiley-VCH: Weinheim, 2006.
- (3) Lu, C. C.; Meyer, K. Small-Molecule Activation by Reactive Metal Complexes. *Eur. J. Inorg. Chem.* **2013**, 2013 (22-23), 3731–3732. <https://doi.org/10.1002/ejic.201300825>.
- (4) Crutchley, R. J. Preface. *Coord. Chem. Rev.* **2017**, 334, 1. <https://doi.org/10.1016/j.ccr.2017.01.004>.
- (5) Fagan, P. J.; Manriquez, J. M.; Marks, T. J.; Day, V. W.; Vollmer, S. H.; Day, C. S. Carbon Monoxide Activation by F-Element Organometallics. An Unusually Distorted, Carbenelike Dihaptoacyl and CO Tetramerization. *J. Am. Chem. Soc.* **1980**, 102 (16), 5393–5396. <https://doi.org/10.1021/ja00536a048>.
- (6) Fox, A. R.; Bart, S. C.; Meyer, K.; Cummins, C. C. Towards Uranium Catalysts. *Nature* **2008**, 455 (7211), 341–349. <https://doi.org/10.1038/nature07372>.
- (7) Evans, W. J. Advances in f Element Reductive Reactivity as a Paradigm for Expanding Lanthanide and Actinide Science and Technology. *J. Alloys Compd.* **2009**, 488 (2), 493–510. <https://doi.org/10.1016/j.jallcom.2009.02.018>.
- (8) Andrez, J.; Pécaut, J.; Bayle, P.-A.; Mazzanti, M. Tuning Lanthanide Reactivity Towards Small Molecules with Electron-Rich Siloxide Ligands. *Angew. Chem. Int. Ed.* **2014**, 53 (39), 10448–10452. <https://doi.org/10.1002/anie.201405031>.
- (9) Castro, L.; Kefalidis, C. E.; McKay, D.; Essa, S.; Perrin, L.; Maron, L. Theoretical Treatment of One Electron Redox Transformation of a Small Molecule Using F-Element Complexes. *Dalton Trans.* **2014**, 11.
- (10) Power, P. P. Main-Group Elements as Transition Metals. *Nature* **2010**, 463 (7278), 171–177. <https://doi.org/10.1038/nature08634>.
- (11) Martin, D.; Soleilhavoup, M.; Bertrand, G. Stable Singlet Carbenes as Mimics for Transition Metal Centers. *Chem. Sci.* **2011**, 2 (3), 389–399. <https://doi.org/10.1039/C0SC00388C>.
- (12) Stephan, D. W. The Broadening Reach of Frustrated Lewis Pair Chemistry. *Science* **2016**, 354 (6317). <https://doi.org/10.1126/science.aaf7229>.
- (13) Laplaza, C. E.; Cummins, C. C. Dinitrogen Cleavage by a Three-Coordinate Molybdenum(III) Complex. *Science* **1995**, 268 (5212), 861–863. <https://doi.org/10.1126/science.268.5212.861>.
- (14) MacKay, B. A.; Fryzuk, M. D. Dinitrogen Coordination Chemistry: On the Biomimetic Borderlands. *Chem. Rev.* **2004**, 104 (2), 385–402. <https://doi.org/10.1021/cr020610c>.
- (15) Zhang, W.; Lai, W.; Cao, R. Energy-Related Small Molecule Activation Reactions: Oxygen Reduction and Hydrogen and Oxygen Evolution Reactions Catalyzed by Porphyrin- and Corrole-Based Systems. *Chem Rev* **2017**, 81.
- (16) Kriegel, B. M.; Naested, L. C. E.; Nocton, G.; Lakshmi, K. V.; Lohrey, T. D.; Bergman, R. G.; Arnold, J. Redox-Initiated Reactivity of Dinuclear  $\beta$ -Diketiminatoniobium Imido Complexes. *Inorg. Chem.* **2017**, 56 (3), 1626–1637. <https://doi.org/10.1021/acs.inorgchem.6b02735>.
- (17) Wei, D.; Darcel, C. Iron Catalysis in Reduction and Hydrometalation Reactions. *Chem. Rev.* **2019**, 119 (4), 2550–2610. <https://doi.org/10.1021/acs.chemrev.8b00372>.
- (18) Evans, W. J.; Grate, J. W.; Hughes, L. A.; Zhang, H.; Atwood, J. L. Reductive Homologation of Carbon Monoxide to a Ketene-carboxylate by a Low-Valent Organolanthanide Complex: Synthesis and x-Ray Crystal Structure of  $[(C_5Me_5)_4Sm_2(O_2CCCO)(THF)]_2$ . *J. Am. Chem. Soc.* **1985**, 107 (12), 3728–3730. <https://doi.org/10.1021/ja00298a060>.
- (19) Summerscales, O. T.; Cloke, F. G. N.; Hitchcock, P. B.; Green, J. C.; Hazari, N. Reductive Cyclotrimerization of Carbon Monoxide to the Deltate Dianion by an Organometallic Uranium Complex. *Science* **2006**, 311 (5762), 829–831. <https://doi.org/10.1126/science.1121784>.
- (20) Nicolas, E.; Nocton, G.; Mézailles, N. CO Activation by (Diphosphane)Platinum(0): Carbonate and Acetone Formation - Experimental and Mechanistic Study. *Eur. J. Inorg. Chem.* **2013**, 2013 (22–23), 4000–4007. <https://doi.org/10.1002/ejic.201300182>.

- (21) Falcone, M.; Kefalidis, C. E.; Scopelliti, R.; Maron, L.; Mazzanti, M. Facile CO Cleavage by a Multimetallic CsU<sub>2</sub> Nitride Complex. *Angew. Chem. Int. Ed.* **2016**, *55* (40), 12290–12294. <https://doi.org/10.1002/anie.201606796>.
- (22) Davies, N. W.; Frey, A. S. P.; Gardiner, M. G.; Wang, J. Reductive Disproportionation of Carbon Dioxide by a Sm(II) Complex: Unprecedented f-Block Element Reactivity Giving a Carbonate Complex. *Chem. Commun.* **2006**, No. 46, 4853–4855. <https://doi.org/10.1039/B611784H>.
- (23) Xémard, M.; Goudy, V.; Braun, A.; Tricoire, M.; Cordier, M.; Ricard, L.; Castro, L.; Louyriac, E.; Kefalidis, C. E.; Clavaguéra, C.; Maron, L.; Nocton, G. Reductive Disproportionation of CO<sub>2</sub> with Bulky Divalent Samarium Complexes. *Organometallics* **2017**, *36* (23), 4660–4668. <https://doi.org/10.1021/acs.organomet.7b00630>.
- (24) Chauvier, C.; Cantat, T. A Viewpoint on Chemical Reductions of Carbon–Oxygen Bonds in Renewable Feedstocks Including CO<sub>2</sub> and Biomass. *ACS Catal.* **2017**, *7* (3), 2107–2115. <https://doi.org/10.1021/acscatal.6b03581>.
- (25) Goudy, V.; Xémard, M.; Karleskind, S.; Cordier, M.; Alvarez Lamsfus, C.; Maron, L.; Nocton, G. Phenylacetylene and Carbon Dioxide Activation by an Organometallic Samarium Complex. *Inorganics* **2018**, *6* (3), 82. <https://doi.org/10.3390/inorganics6030082>.
- (26) Tolman, W. B. Binding and Activation of N<sub>2</sub>O at Transition-Metal Centers: Recent Mechanistic Insights. *Angew. Chem. Int. Ed.* **2010**, *49* (6), 1018–1024. <https://doi.org/10.1002/anie.200905364>.
- (27) Anthore-Dalion, L.; Nicolas, E.; Cantat, T. Catalytic Metal-Free Deoxygenation of Nitrous Oxide with Disilanes. *ACS Catal.* **2019**, *9* (12), 11563–11567. <https://doi.org/10.1021/acscatal.9b04434>.
- (28) Labinger, J. A.; Bercaw, J. E. Understanding and Exploiting C–H Bond Activation. *Nature* **2002**, *417* (6888), 507–514. <https://doi.org/10.1038/417507a>.
- (29) Gunsalus, N. J.; Koppaka, A.; Park, S. H.; Bischof, S. M.; Hashiguchi, B. G.; Periana, R. A. Homogeneous Functionalization of Methane. *Chem. Rev.* **2017**, *117* (13), 8521–8573. <https://doi.org/10.1021/acs.chemrev.6b00739>.
- (30) Hu, A.; Guo, J.-J.; Pan, H.; Zuo, Z. Selective Functionalization of Methane, Ethane, and Higher Alkanes by Cerium Photocatalysis. *Science* **2018**, *361* (6403), 668–672. <https://doi.org/10.1126/science.aat9750>.
- (31) Cotton, F. A.; Gu, J.; Murillo, C. A.; Timmons, D. J. The First Dinuclear Complex of Palladium(III). *J. Am. Chem. Soc.* **1998**, *120* (50), 13280–13281. <https://doi.org/10.1021/ja9832313>.
- (32) Powers, D. C.; Ritter, T. Bimetallic Pd(III) Complexes in Palladium-Catalysed Carbon–Heteroatom Bond Formation. *Nat. Chem.* **2009**, *1* (4), 302–309. <https://doi.org/10.1038/nchem.246>.
- (33) Powers, D. C.; Ritter, T. Bimetallic Redox Synergy in Oxidative Palladium Catalysis. *Acc. Chem. Res.* **2012**, *45* (6), 840–850. <https://doi.org/10.1021/ar2001974>.
- (34) Byers, P. K.; Canty, A. J.; Skelton, B. W.; White, A. H. The Oxidative Addition of Iodomethane to [PdMe<sub>2</sub>(Bpy)] and the X-Ray Structure of the Organopalladium(IV) Product Fac-[PdMe<sub>3</sub>(Bpy)](Bpy = 2,2'-Bipyridyl). *J. Chem. Soc. Chem. Commun.* **1986**, No. 23, 1722–1724. <https://doi.org/10.1039/C39860001722>.
- (35) Canty, A. J. Development of Organopalladium(IV) Chemistry: Fundamental Aspects and Systems for Studies of Mechanism in Organometallic Chemistry and Catalysis. *Acc. Chem. Res.* **1992**, *25* (2), 83–90. <https://doi.org/10.1021/ar00014a005>.
- (36) Alsters, P. L.; Engel, P. F.; Hogerheide, M. P.; Copijn, M.; Spek, A. L.; van Koten, G. Rigid Five- and Six-Membered C,N,N'-Bound Aryl-, Benzyl-, and Alkylorganopalladium Complexes: Sp<sup>2</sup> vs. Sp<sup>3</sup> Carbon-Hydrogen Activation during Cyclopalladation and Palladium(IV) Intermediates in Oxidative Addition Reactions with Dihalogens and Alkyl Halides. *Organometallics* **1993**, *12* (5), 1831–1844. <https://doi.org/10.1021/om00029a045>.



- (37) Dick, A. R.; Kampf, J. W.; Sanford, M. S. Unusually Stable Palladium(IV) Complexes: Detailed Mechanistic Investigation of C–O Bond-Forming Reductive Elimination. *J. Am. Chem. Soc.* **2005**, *127* (37), 12790–12791. <https://doi.org/10.1021/ja0541940>.
- (38) Whitfield, S. R.; Sanford, M. S. Reactivity of Pd(II) Complexes with Electrophilic Chlorinating Reagents: Isolation of Pd(IV) Products and Observation of C–Cl Bond-Forming Reductive Elimination. *J. Am. Chem. Soc.* **2007**, *129* (49), 15142–15143. <https://doi.org/10.1021/ja077866q>.
- (39) Arnold, P. L.; Sanford, M. S.; Pearson, S. M. Chelating N-Heterocyclic Carbene Alkoxide as a Supporting Ligand for PdII/IV C–H Bond Functionalization Catalysis. *J. Am. Chem. Soc.* **2009**, *131* (39), 13912–13913. <https://doi.org/10.1021/ja905713t>.
- (40) Sehnal, P.; Taylor, R. J. K.; Fairlamb, I. J. S. Emergence of Palladium(IV) Chemistry in Synthesis and Catalysis. *Chem. Rev.* **2010**, *110* (2), 824–889. <https://doi.org/10.1021/cr9003242>.
- (41) Abada, E.; Zavalij, P. Y.; Vedernikov, A. N. Reductive C(Sp<sup>2</sup>)–N Elimination from Isolated Pd(IV) Amido Aryl Complexes Prepared Using H<sub>2</sub>O<sub>2</sub> as Oxidant. *J. Am. Chem. Soc.* **2017**, *139* (2), 643–646. <https://doi.org/10.1021/jacs.6b12648>.
- (42) Grove, D. M.; Van Koten, G.; Zoet, R.; Murrall, N. W.; Welch, A. J. Unique Stable Organometallic Nickel(III) Complexes; Syntheses and the Molecular Structure of [Ni{C<sub>6</sub>H<sub>3</sub>(CH<sub>2</sub>NMe<sub>2</sub>)<sub>2-2,6</sub>}]<sub>2</sub>. *J. Am. Chem. Soc.* **1983**, *105* (5), 1379–1380. <https://doi.org/10.1021/ja00343a056>.
- (43) Shimazaki, Y.; Tani, F.; Fukui, K.; Naruta, Y.; Yamauchi, O. One-Electron Oxidized Nickel(II)–(Disalicylidene)Diamine Complex: Temperature-Dependent Tautomerism between Ni(III)–Phenolate and Ni(II)–Phenoxy Radical States. *J. Am. Chem. Soc.* **2003**, *125* (35), 10512–10513. <https://doi.org/10.1021/ja035806o>.
- (44) Kogut, E.; Wiencko, H. L.; Zhang, L.; Cordeau, D. E.; Warren, T. H. A Terminal Ni(III)–Imide with Diverse Reactivity Pathways. *J. Am. Chem. Soc.* **2005**, *127* (32), 11248–11249. <https://doi.org/10.1021/ja0533186>.
- (45) Lee, C.-M.; Chiou, T.-W.; Chen, H.-H.; Chiang, C.-Y.; Kuo, T.-S.; Liaw, W.-F. Mononuclear Ni(II)–Thiolate Complexes with Pendant Thiol and Dinuclear Ni(III/II)–Thiolate Complexes with Ni···Ni Interaction Regulated by the Oxidation Levels of Nickels and the Coordinated Ligands. *Inorg. Chem.* **2007**, *46* (21), 8913–8923. <https://doi.org/10.1021/ic700719h>.
- (46) Zheng, B.; Tang, F.; Luo, J.; Schultz, J. W.; Rath, N. P.; Mirica, L. M. Organometallic Nickel(III) Complexes Relevant to Cross-Coupling and Carbon–Heteroatom Bond Formation Reactions. *J. Am. Chem. Soc.* **2014**, *136* (17), 6499–6504. <https://doi.org/10.1021/ja5024749>.
- (47) Cao, T.-P.-A.; Nocton, G.; Ricard, L.; Le Goff, X. F.; Auffrant, A. A Tetracoordinated Phosphasalen Nickel(III) Complex. *Angew. Chem. Int. Ed.* **2014**, *53* (5), 1368–1372. <https://doi.org/10.1002/anie.201309222>.
- (48) Zhou, W.; Schultz, J. W.; Rath, N. P.; Mirica, L. M. Aromatic Methoxylation and Hydroxylation by Organometallic High-Valent Nickel Complexes. *J. Am. Chem. Soc.* **2015**, *137* (24), 7604–7607. <https://doi.org/10.1021/jacs.5b04082>.
- (49) Bour, J. R.; Camasso, N. M.; Meucci, E. A.; Kampf, J. W.; Canty, A. J.; Sanford, M. S. Carbon–Carbon Bond-Forming Reductive Elimination from Isolated Nickel(III) Complexes. *J. Am. Chem. Soc.* **2016**, *138* (49), 16105–16111. <https://doi.org/10.1021/jacs.6b10350>.
- (50) Lee, H.; Börgel, J.; Ritter, T. Carbon–Fluorine Reductive Elimination from Nickel(III) Complexes. *Angew. Chem. Int. Ed.* **2017**, *56* (24), 6966–6969. <https://doi.org/10.1002/anie.201701552>.
- (51) Diccianni, J. B.; Hu, C.; Diao, T. Binuclear, High-Valent Nickel Complexes: Ni–Ni Bonds in Aryl–Halogen Bond Formation. *Angew. Chem. Int. Ed.* **2017**, *56* (13), 3635–3639. <https://doi.org/10.1002/anie.201611572>.
- (52) Camasso, N. M.; Sanford, M. S. Design, Synthesis, and Carbon–Heteroatom Coupling Reactions of Organometallic Nickel(IV) Complexes. *Science* **2015**, *347* (6227), 1218–1220. <https://doi.org/10.1126/science.aaa4526>.

- (53) D'Accriscio, F.; Borja, P.; Saffon-Merceron, N.; Fustier-Boutignon, M.; Mézailles, N.; Nebra, N. C–H Bond Trifluoromethylation of Arenes Enabled by a Robust, High-Valent Nickel(IV) Complex. *Angew. Chem. Int. Ed.* **2017**, *56* (42), 12898–12902. <https://doi.org/10.1002/anie.201706237>.
- (54) Carnes, M.; Buccella, D.; Chen, J. Y.-C.; Ramirez, A. P.; Turro, N. J.; Nuckolls, C.; Steigerwald, M. A Stable Tetraalkyl Complex of Nickel(IV). *Angew. Chem. Int. Ed.* **2009**, *48* (2), 290–294. <https://doi.org/10.1002/anie.200804435>.
- (55) Martinez, G. E.; Ocampo, C.; Park, Y. J.; Fout, A. R. Accessing Pincer Bis(Carbene) Ni(IV) Complexes from Ni(II) via Halogen and Halogen Surrogates. *J. Am. Chem. Soc.* **2016**, *138* (13), 4290–4293. <https://doi.org/10.1021/jacs.5b12827>.
- (56) Schultz, J. W.; Fuchigami, K.; Zheng, B.; Rath, N. P.; Mirica, L. M. Isolated Organometallic Nickel(III) and Nickel(IV) Complexes Relevant to Carbon–Carbon Bond Formation Reactions. *J. Am. Chem. Soc.* **2016**, *138* (39), 12928–12934. <https://doi.org/10.1021/jacs.6b06862>.
- (57) Bour, J. R.; Ferguson, D. M.; McClain, E. J.; Kampf, J. W.; Sanford, M. S. Connecting Organometallic Ni(III) and Ni(IV): Reactions of Carbon-Centered Radicals with High-Valent Organonickel Complexes. *J. Am. Chem. Soc.* **2019**, *141* (22), 8914–8920. <https://doi.org/10.1021/jacs.9b02411>.
- (58) Goudy, V.; Jaoul, A.; Cordier, M.; Clavaguéra, C.; Nocton, G. Tuning the Stability of Pd(IV) Intermediates Using a Redox Non-Innocent Ligand Combined with an Organolanthanide Fragment. *J. Am. Chem. Soc.* **2017**, *139* (31), 10633–10636. <https://doi.org/10.1021/jacs.7b05634>.
- (59) Wang, D.; Moutet, J.; Tricoire, M.; Cordier, M.; Nocton, G. Reactive Heterobimetallic Complex Combining Divalent Ytterbium and Dimethyl Nickel Fragments. *Inorganics* **2019**, *7* (5), 58. <https://doi.org/10.3390/inorganics7050058>.
- (60) Kieber-Emmons, M. T.; Riordan, C. G. Dioxygen Activation at Monovalent Nickel. *Acc. Chem. Res.* **2007**, *40* (7), 618–625. <https://doi.org/10.1021/ar700043n>.
- (61) Anderson, J. S.; Iluc, V. M.; Hillhouse, G. L. Reactions of CO<sub>2</sub> and CS<sub>2</sub> with 1,2-Bis(Di-Tert-Butylphosphino)Ethane Complexes of Nickel(0) and Nickel(I). *Inorg. Chem.* **2010**, *49* (21), 10203–10207. <https://doi.org/10.1021/ic101652e>.
- (62) Kundu, S.; Stieber, S. C. E.; Ferrier, M. G.; Kozimor, S. A.; Bertke, J. A.; Warren, T. H. Redox Non-Innocence of Nitrosobenzene at Nickel. *Angew. Chem. Int. Ed.* **2016**, *55* (35), 10321–10325. <https://doi.org/10.1002/anie.201605026>.
- (63) Krüger, M.; Meyerdierks, A.; Glöckner, F. O.; Amann, R.; Widdel, F.; Kube, M.; Reinhardt, R.; Kahnt, J.; Böcher, R.; Thauer, R. K.; Shima, S. A Conspicuous Nickel Protein in Microbial Mats That Oxidize Methane Anaerobically. *Nature* **2003**, *426* (6968), 878–881. <https://doi.org/10.1038/nature02207>.
- (64) Yao, S.; Driess, M. Lessons from Isolable Nickel(I) Precursor Complexes for Small Molecule Activation. *Acc. Chem. Res.* **2012**, *45* (2), 276–287. <https://doi.org/10.1021/ar200156r>.
- (65) Garduño, J. A.; Arévalo, A.; García, J. J. Bond and Small-Molecule Activation with Low-Valent Nickel Complexes. *Dalton Trans.* **2015**, *44* (30), 13419–13438. <https://doi.org/10.1039/C5DT01516B>.
- (66) Zimmermann, P.; Limberg, C. Activation of Small Molecules at Nickel(I) Moieties. *J. Am. Chem. Soc.* **2017**, *139* (12), 4233–4242. <https://doi.org/10.1021/jacs.6b12434>.
- (67) Bourget-Merle, L.; Lappert, M. F.; Severn, J. R. The Chemistry of  $\beta$ -Diketiminatometal Complexes. *Chem. Rev.* **2002**, *102* (9), 3031–3066. <https://doi.org/10.1021/cr010424r>.
- (68) Camp, C.; Arnold, J. On the Non-Innocence of “Nacnacs”: Ligand-Based Reactivity in  $\beta$ -Diketimate Supported Coordination Compounds. *Dalton Trans.* **2016**, 37.
- (69) Mindiola, D. J. Nacnac ... Are You Still There? The Evolution of  $\beta$ -Diketimate Complexes of Nickel. *Angew. Chem. Int. Ed.* **2009**, *48* (34), 6198–6200. <https://doi.org/10.1002/anie.200901400>.
- (70) Yi-Chou, T. The Chemistry of Univalent Metal  $\beta$ -Diketimates. *Coord. Chem. Rev.* **2012**, *256* (5–8), 722–758. <https://doi.org/10.1016/j.ccr.2011.12.012>.

- (71) Pfirrmann, S.; Limberg, C.; Herwig, C.; Stößer, R.; Ziemer, B. A Dinuclear Nickel(I) Dinitrogen Complex and Its Reduction in Single-Electron Steps. *Angew. Chem. Int. Ed.* **2009**, *48* (18), 3357–3361. <https://doi.org/10.1002/anie.200805862>.
- (72) Puiu, S. C.; Warren, T. H. Three-Coordinate  $\beta$ -Diketiminato Nickel Nitrosyl Complexes from Nickel(I)–Lutidine and Nickel(II)–Alkyl Precursors. *Organometallics* **2003**, *22* (20), 3974–3976. <https://doi.org/10.1021/om034041q>.
- (73) Chirik, P. J.; Wieghardt, K. Radical Ligands Confer Nobility on Base-Metal Catalysts. *Science* **2010**, *327* (5967), 794–795. <https://doi.org/10.1126/science.1183281>.
- (74) Manuel, T. D.; Rohde, J.-U. Reaction of a Redox-Active Ligand Complex of Nickel with Dioxygen Probes Ligand-Radical Character. *J. Am. Chem. Soc.* **2009**, *131* (43), 15582–15583. <https://doi.org/10.1021/ja9065943>.
- (75) Yoo, C.; Ajitha, M. J.; Jung, Y.; Lee, Y. Mechanistic Study on C–C Bond Formation of a Nickel(I) Monocarbonyl Species with Alkyl Iodides: Experimental and Computational Investigations. *Organometallics* **2015**, *34* (17), 4305–4311. <https://doi.org/10.1021/acs.organomet.5b00548>.
- (76) Diccianni, J. B.; Hu, C. T.; Diao, T. Insertion of CO<sub>2</sub> Mediated by a (Xantphos)Ni(II)–Alkyl Species. *Angew. Chem. Int. Ed.* **2019**, *58* (39), 13865–13868. <https://doi.org/10.1002/anie.201906005>.
- (77) Rospert, S.; Böcher, R.; Albracht, S. P. J.; Thauer, R. K. Methyl-Coenzyme M Reductase Preparations with High Specific Activity from H<sub>2</sub>-Preincubated Cells of Methanobacterium Thermoautotrophicum. *FEBS Lett.* **1991**, *291* (2), 371–375. [https://doi.org/10.1016/0014-5793\(91\)81323-Z](https://doi.org/10.1016/0014-5793(91)81323-Z).
- (78) Dey, M.; Telser, J.; Kunz, R. C.; Lees, N. S.; Ragsdale, S. W.; Hoffman, B. M. Biochemical and Spectroscopic Studies of the Electronic Structure and Reactivity of a Methyl–Ni Species Formed on Methyl-Coenzyme M Reductase. *J. Am. Chem. Soc.* **2007**, *129* (36), 11030–11032. <https://doi.org/10.1021/ja074556z>.
- (79) Scheller, S.; Goenrich, M.; Boecher, R.; Thauer, R. K.; Jaun, B. The Key Nickel Enzyme of Methanogenesis Catalyses the Anaerobic Oxidation of Methane. *Nature* **2010**, *465* (7298), 606–608. <https://doi.org/10.1038/nature09015>.
- (80) Wongnate, T.; Sliwa, D.; Ginovska, B.; Smith, D.; Wolf, M. W.; Lehnert, N.; Raugei, S.; Ragsdale, S. W. The Radical Mechanism of Biological Methane Synthesis by Methyl-Coenzyme M Reductase. *Science* **2016**, *352* (6288), 953–958. <https://doi.org/10.1126/science.aaf0616>.
- (81) Can, M.; Armstrong, F. A.; Ragsdale, S. W. Structure, Function, and Mechanism of the Nickel Metalloenzymes, CO Dehydrogenase, and Acetyl-CoA Synthase. *Chem. Rev.* **2014**, *114* (8), 4149–4174. <https://doi.org/10.1021/cr400461p>.
- (82) Matsumoto, T.; Ito, M.; Kotera, M.; Tatsumi, K. A Dinuclear Nickel Complex Modeling of the Ni(II)–Ni(I) State of the Active Site of Acetyl CoA Synthase. *Dalton Trans* **2010**, *39* (12), 2995–2997. <https://doi.org/10.1039/B924915J>.
- (83) Paulik, F. E.; Roth, J. F. Novel Catalysts for the Low-Pressure Carbonylation of Methanol to Acetic Acid. *Chem. Commun. Lond.* **1968**, No. 24, 1578a. <https://doi.org/10.1039/c1968001578a>.
- (84) Robinson, K. K.; Hershman, A.; Craddock, J. H.; Roth, J. F. Kinetics of the Catalytic Vapor Phase Carbonylation of Methanol to Acetic Acid. *J. Catal.* **1972**, *27* (3), 389–396. [https://doi.org/10.1016/0021-9517\(72\)90175-3](https://doi.org/10.1016/0021-9517(72)90175-3).
- (85) Maitlis, P. M.; Haynes, A.; Sunley, G. J.; Howard, M. J. Methanol Carbonylation Revisited: Thirty Years On. *J. Chem. Soc. Dalton Trans.* **1996**, No. 11, 2187. <https://doi.org/10.1039/dt9960002187>.
- (86) Sunley, G. J.; Watson, D. J. High Productivity Methanol Carbonylation Catalysis Using Iridium The Cativa™ Process for the Manufacture of Acetic Acid. *Catal. Today* **2000**, *15*.

- (87) Haynes, A.; Mann, B. E.; Gulliver, D. J.; Morris, G. E.; Maitlis, P. M. Direct Observation of  $\text{MeRh}(\text{CO})_2\text{I}_3^-$ , the Key Intermediate in Rhodium-Catalyzed Methanol Carbonylation. *J. Am. Chem. Soc.* **1991**, *113* (22), 8567–8569. <https://doi.org/10.1021/ja00022a079>.
- (88) Haynes, A.; Mann, B. E.; Morris, G. E.; Maitlis, P. M. Mechanistic Studies on Rhodium-Catalyzed Carbonylation Reactions: Spectroscopic Detection and Reactivity of a Key Intermediate,  $[\text{MeRh}(\text{CO})_2\text{I}_3]^-$ . *J. Am. Chem. Soc.* **1993**, *115* (10), 4093–4100. <https://doi.org/10.1021/ja00063a030>.
- (89) Ellis, P. R.; Pearson, J. M.; Haynes, A.; Adams, H.; Bailey, N. A.; Maitlis, P. M. Oxidative Addition of Alkyl Halides to Rhodium(I) and Iridium(I) Dicarbonyl Diiodides: Key Reactions in the Catalytic Carbonylation of Alcohols. *Organometallics* **1994**, *13* (8), 3215–3226. <https://doi.org/10.1021/om00020a039>.
- (90) Cheong, M.; Ziegler, T. Density Functional Study of the Oxidative Addition Step in the Carbonylation of Methanol Catalyzed by  $[\text{M}(\text{CO})_2\text{I}_2]^-$  (M = Rh, Ir). *Organometallics* **2005**, *24* (13), 3053–3058. <https://doi.org/10.1021/om049383q>.
- (91) Gonsalvi, L.; Adams, H.; Sunley, G. J.; Ditzel, E.; Haynes, A. A Dramatic Steric Effect on the Rate of Migratory CO Insertion on Rhodium. *J. Am. Chem. Soc.* **1999**, *121* (48), 11233–11234. <https://doi.org/10.1021/ja992891k>.
- (92) Ghaffar, T.; Adams, H.; Maitlis, P. M.; Haynes, A.; Ghaffar, T.; Adams, H.; Sunley, G. J.; Baker, M. J. Spectroscopic Identification and Reactivity of  $[\text{Ir}(\text{CO})_3\text{I}_2\text{Me}]$ , a Key Reactive Intermediate in Iridium Catalysed Methanol Carbonylation. *Chem. Commun.* **1998**, No. 9, 1023–1024. <https://doi.org/10.1039/A800659H>.
- (93) Haynes, A.; Maitlis, P. M.; Morris, G. E.; Sunley, G. J.; Adams, H.; Badger, P. W.; Bowers, C. M.; Cook, D. B.; Elliott, P. I. P.; Ghaffar, T.; Green, H.; Griffin, T. R.; Payne, M.; Pearson, J. M.; Taylor, M. J.; Vickers, P. W.; Watt, R. J. Promotion of Iridium-Catalyzed Methanol Carbonylation: Mechanistic Studies of the Cativa Process. *J. Am. Chem. Soc.* **2004**, *126* (9), 2847–2861. <https://doi.org/10.1021/ja039464y>.
- (94) Brennführer, A.; Neumann, H.; Beller, M. Palladium-Catalyzed Carbonylation Reactions of Aryl Halides and Related Compounds. *Angew. Chem. Int. Ed.* **2009**, *48* (23), 4114–4133. <https://doi.org/10.1002/anie.200900013>.
- (95) Franke, R.; Selent, D.; Börner, A. Applied Hydroformylation. *Chem. Rev.* **2012**, *112* (11), 5675–5732. <https://doi.org/10.1021/cr3001803>.
- (96) Wu, X.-F.; Fang, X.; Wu, L.; Jackstell, R.; Neumann, H.; Beller, M. Transition-Metal-Catalyzed Carbonylation Reactions of Olefins and Alkynes: A Personal Account. *Acc. Chem. Res.* **2014**, *47* (4), 1041–1053. <https://doi.org/10.1021/ar400222k>.
- (97) Li, Y.; Hu, Y.; Wu, X.-F. Non-Noble Metal-Catalysed Carbonylative Transformations. *Chem. Soc. Rev.* **2018**, *47* (1), 172–194. <https://doi.org/10.1039/C7CS00529F>.
- (98) Tjutrins, J.; Shao, J. L.; Yempally, V.; Bengali, A. A.; Arndtsen, B. A. A Nickel-Based, Tandem Catalytic Approach to Isoindolinones from Imines, Aryl Iodides, and CO. *Organometallics* **2015**, *34* (10), 1802–1805. <https://doi.org/10.1021/acs.organomet.5b00215>.
- (99) Macgregor, S. A.; Neave, G. W. Theoretical Study of CO Migratory Insertion Reactions with Group 10 Metal-Alkyl and -Alkoxide Bonds. *Organometallics* **2003**, *22* (22), 4547–4556. <https://doi.org/10.1021/om030459c>.
- (100) Matsunaga, P. T.; Hess, C. R.; Hillhouse, G. L. Reactions of Organoazides with Nickel Alkyls. Syntheses and Reactions of Nickel(II) Amido Complexes. *J. Am. Chem. Soc.* **1994**, *116* (8), 3665–3666. <https://doi.org/10.1021/ja00087a089>.
- (101) Han, R.; Hillhouse, G. L. Sulfur-Atom Transfer from Elemental Sulfur to Nickel-Carbon Bonds as a New Route to Reactive Nickel(II) Thiolates. *J. Am. Chem. Soc.* **1998**, *120* (30), 7657–7658. <https://doi.org/10.1021/ja981266x>.
- (102) Davis, J. L.; Arndtsen, B. A. Comparison of Imine to Olefin Insertion Reactions: Generation of Five- and Six-Membered Lactams via a Nickel-Mediated CO, Olefin, CO, Imine Insertion Cascade. *Organometallics* **2011**, *30* (7), 1896–1901. <https://doi.org/10.1021/om1011566>.

- (103) Klein, H.-F.; Karsch, H. H. Stabile Methylnickelverbindungen, VII: Reversible Überführung in Acetylnickelverbindungen. *Chem. Ber.* **1976**, *109* (7), 2524–2532. <https://doi.org/10.1002/cber.19761090721>.
- (104) Ito, M.; Kotera, M.; Matsumoto, T.; Tatsumi, K. Dinuclear Nickel Complexes Modeling the Structure and Function of the Acetyl CoA Synthase Active Site. *Proc. Natl. Acad. Sci.* **2009**, *106* (29), 11862–11866. <https://doi.org/10.1073/pnas.0900433106>.
- (105) Tan, X.; Surovtsev, I. V.; Lindahl, P. A. Kinetics of CO Insertion and Acetyl Group Transfer Steps, and a Model of the Acetyl-CoA Synthase Catalytic Mechanism. *J. Am. Chem. Soc.* **2006**, *128* (37), 12331–12338. <https://doi.org/10.1021/ja0627702>.
- (106) Maleckis, A.; Sanford, M. S. Synthesis of Fluoroalkyl Palladium and Nickel Complexes via Decarbonylation of Acylmetal Species. *Organometallics* **2014**, *33* (14), 3831–3839. <https://doi.org/10.1021/om500535x>.
- (107) Malapit, C. A.; Bour, J. R.; Brigham, C. E.; Sanford, M. S. Base-Free Nickel-Catalysed Decarbonylative Suzuki–Miyaura Coupling of Acid Fluorides. *Nature* **2018**, *563* (7729), 100–104. <https://doi.org/10.1038/s41586-018-0628-7>.
- (108) Kaschube, W.; Pörschke, K. R.; Wilke, G. tmeda-Nickel-Komplexe: III. (N,N,N',N'-Tetramethylethylenediamin)-(dimethyl)nickel(II). *J. Organomet. Chem.* **1988**, *355* (1), 525–532. [https://doi.org/10.1016/0022-328X\(88\)89050-8](https://doi.org/10.1016/0022-328X(88)89050-8).
- (109) Berg, D. J.; Boncella, J. M.; Andersen, R. A. Preparation of Coordination Compounds of Cp\*<sub>2</sub> Yb with Heterocyclic Nitrogen Bases: Examples of Antiferromagnetic Exchange Coupling across Bridging Ligands. *Organometallics* **2002**, *21* (22), 4622–4631. <https://doi.org/10.1021/om020477e>.
- (110) Scarborough, C. C.; Wieghardt, K. Electronic Structure of 2,2'-Bipyridine Organotransition-Metal Complexes. Establishing the Ligand Oxidation Level by Density Functional Theoretical Calculations. *Inorg. Chem.* **2011**, *50* (20), 9773–9793. <https://doi.org/10.1021/ic2005419>.
- (111) Irwin, M.; Doyle, L. R.; Kram, T.; Goicoechea, J. M. A Homologous Series of First-Row Transition-Metal Complexes of 2,2'-Bipyridine and Their Ligand Radical Derivatives: Trends in Structure, Magnetism, and Bonding. *Inorg Chem* **2012**, *12*.
- (112) Wolff, C.; Gottschlich, A.; England, J.; Wieghardt, K.; Saak, W.; Haase, D.; Beckhaus, R. Molecular and Electronic Structures of Mononuclear and Dinuclear Titanium Complexes Containing π-Radical Anions of 2,2'-Bipyridine and 1,10-Phenanthroline: An Experimental and DFT Computational Study. *Inorg. Chem.* **2015**, *54* (10), 4811–4820. <https://doi.org/10.1021/acs.inorgchem.5b00285>.
- (113) Schultz, M.; Boncella, J. M.; Berg, D. J.; Tilley, T. D.; Andersen, R. A. Coordination of 2,2'-Bipyridyl and 1,10-Phenanthroline to Substituted Ytterbocenes: An Experimental Investigation of Spin Coupling in Lanthanide Complexes. *Organometallics* **2002**, *21* (3), 460–472. <https://doi.org/10.1021/om010661k>.
- (114) Booth, C. H.; Walter, M. D.; Kazhdan, D.; Hu, Y.-J.; Lukens, W. W.; Bauer, E. D.; Maron, L.; Eisenstein, O.; Andersen, R. A. Decamethylytterbocene Complexes of Bipyridines and Diazabutadienes: Multiconfigurational Ground States and Open-Shell Singlet Formation. *J. Am. Chem. Soc.* **2009**, *131* (18), 6480–6491. <https://doi.org/10.1021/ja809624w>.
- (115) Nocton, G.; Booth, C. H.; Maron, L.; Andersen, R. A. Thermal Dihydrogen Elimination from Cp\*<sub>2</sub> Yb(4,5-Diazafluorene). *Organometallics* **2013**, *32* (5), 1150–1158. <https://doi.org/10.1021/om300876b>.
- (116) Nocton, G.; Lukens, W. W.; Booth, C. H.; Rozenel, S. S.; Medling, S. A.; Maron, L.; Andersen, R. A. Reversible Sigma C–C Bond Formation Between Phenanthroline Ligands Activated by (C<sub>5</sub>Me<sub>5</sub>)<sub>2</sub> Yb. *J. Am. Chem. Soc.* **2014**, *136* (24), 8626–8641. <https://doi.org/10.1021/ja502271q>.
- (117) Nocton, G.; Booth, C. H.; Maron, L.; Ricard, L.; Andersen, R. A. Carbon–Hydrogen Bond Breaking and Making in the Open-Shell Singlet Molecule Cp\*<sub>2</sub> Yb(4,7-Me<sub>2</sub> Phen). *Organometallics* **2014**, *33* (23), 6819–6829. <https://doi.org/10.1021/om500843z>.

- (118) Nocton, G.; Booth, C. H.; Maron, L.; Andersen, R. A. Influence of the Torsion Angle in 3,3'-Dimethyl-2,2'-Bipyridine on the Intermediate Valence of Yb in  $(C_5Me_5)_2Yb(3,3'-Me_2-Bipy)_2$ . *Organometallics* **2013**, *32* (19), 5305–5312. <https://doi.org/10.1021/om400528d>.
- (119) Booth, C. H.; Kazhdan, D.; Werkema, E. L.; Walter, M. D.; Lukens, W. W.; Bauer, E. D.; Hu, Y.-J.; Maron, L.; Eisenstein, O.; Head-Gordon, M.; Andersen, R. A. Intermediate-Valence Tautomerism in Decamethylytterbocene Complexes of Methyl-Substituted Bipyridines. *J. Am. Chem. Soc.* **2010**, *132* (49), 17537–17549. <https://doi.org/10.1021/ja106902s>.
- (120) Lukens, W. W.; Magnani, N.; Booth, C. H. Application of the Hubbard Model to  $Cp^*2Yb(Bipy)$ , a Model System for Strong Exchange Coupling in Lanthanide Systems. *Inorg. Chem.* **2012**, *51* (19), 10105–10110. <https://doi.org/10.1021/ic300037q>.
- (121) Van Vleck, J. H. *The Theory of Electric and Magnetic Susceptibilities*; Oxford University Press: London, UK, 1932.
- (122) Nocton, G.; Ricard, L. N-Aromatic Heterocycle Adducts of Bulky  $[1,2,4-(Me_3C)_3C_5H_2]_2Sm$ : Synthesis, Structure and Solution Analysis. *Dalton Trans* **2014**, *43* (11), 4380–4387. <https://doi.org/10.1039/C3DT52641K>.
- (123) Lukens, W. W.; Walter, M. D. Quantifying Exchange Coupling in F-Ion Pairs Using the Diamagnetic Substitution Method. *Inorg. Chem.* **2010**, *49* (10), 4458–4465. <https://doi.org/10.1021/ic100120d>.
- (124) O'Connor, C. J. Magnetochemistry—Advances in Theory and Experimentation. In *Progress in Inorganic Chemistry*; John Wiley & Sons, Ltd, 2007; pp 203–283. <https://doi.org/10.1002/9780470166307.ch4>.
- (125) Walter, M. D.; Berg, D. J.; Andersen, R. A. Coordination Complexes of Decamethylytterbocene with 4,4'-Disubstituted Bipyridines: An Experimental Study of Spin Coupling in Lanthanide Complexes. *Organometallics* **2006**, *25* (13), 3228–3237. <https://doi.org/10.1021/om051051d>.
- (126) Walter, M. D.; Berg, D. J.; Andersen, R. A. Coordination of 1,4-Diazabutadiene Ligands to Decamethylytterbocene: Additional Examples of Spin Coupling in Ytterbocene Complexes. *Organometallics* **2007**, *26* (9), 2296–2307. <https://doi.org/10.1021/om0610142>.
- (127) Komiya, Sanshiro.; Akai, Yasushi.; Tanaka, Kohkichi.; Yamamoto, Takakazu.; Yamamoto, Akio. Reductive Elimination of Aryl Carboxylates from Acyl(Aryloxy)Nickel(II) and -Palladium(II) Complexes. *Organometallics* **1985**, *4* (6), 1130–1136. <https://doi.org/10.1021/om00125a033>.
- (128) Curley, J. J.; Kitiachvili, K. D.; Waterman, R.; Hillhouse, G. L. Sequential Insertion Reactions of Carbon Monoxide and Ethylene into the Ni–C Bond of a Cationic Nickel(II) Alkyl Complex. *Organometallics* **2009**, *28* (8), 2568–2571. <https://doi.org/10.1021/om900023y>.
- (129) Anslyn, E.; Dougherty, D. *Modern Physical Organic Chemistry*; University Science Books: Sausalito, 2005.
- (130) Meek, S. J.; Pitman, C. L.; Miller, A. J. M. Deducing Reaction Mechanism: A Guide for Students, Researchers, and Instructors. *J. Chem. Educ.* **2016**, *93* (2), 275–286. <https://doi.org/10.1021/acs.jchemed.5b00160>.
- (131) Shields, B. J.; Kudisch, B.; Scholes, G. D.; Doyle, A. G. Long-Lived Charge-Transfer States of Nickel(II) Aryl Halide Complexes Facilitate Bimolecular Photoinduced Electron Transfer. *J. Am. Chem. Soc.* **2018**, *140* (8), 3035–3039. <https://doi.org/10.1021/jacs.7b13281>.
- (132) Tilley, T. Don.; Andersen, R. A.; Spencer, Brock.; Zalkin, Allan. Crystal Structure of Bis(Pentamethylcyclopentadienyl)Bis(Pyridine)Ytterbium(II). *Inorg. Chem.* **1982**, *21* (7), 2647–2649. <https://doi.org/10.1021/ic00137a023>.
- (133) Umemoto, T. Electrophilic Perfluoroalkylating Agents. *Chem. Rev.* **1996**, *96* (5), 1757–1778. <https://doi.org/10.1021/cr941149u>.
- (134) Connelly, N. G.; Geiger, W. E. Chemical Redox Agents for Organometallic Chemistry. *Chem. Rev.* **1996**, *96* (2), 877–910. <https://doi.org/10.1021/cr940053x>.
- (135) de Bruin, B.; Bill, E.; Bothe, E.; Weyhermüller, T.; Wieghardt, K. Molecular and Electronic Structures of Bis(Pyridine-2,6-Diimine)Metal Complexes  $[ML_2](PF_6)_n$  ( $n = 0, 1, 2, 3$ ; M = Mn, Fe, Co, Ni, Cu, Zn)<sup>†</sup>. *Inorg. Chem.* **2000**, *39* (13), 2936–2947. <https://doi.org/10.1021/ic000113j>.

- (136) Da Re, R. E.; Kuehl, C. J.; Brown, M. G.; Rocha, R. C.; Bauer, E. D.; John, K. D.; Morris, D. E.; Shreve, A. P.; Sarrao, J. L. Electrochemical and Spectroscopic Characterization of the Novel Charge-Transfer Ground State in Diimine Complexes of Ytterbocene. *Inorg. Chem.* **2003**, *42* (18), 5551–5559. <https://doi.org/10.1021/ic030069i>.
- (137) Obligacion, J. V.; Chirik, P. J. Earth-Abundant Transition Metal Catalysts for Alkene Hydrosilylation and Hydroboration. *Nat. Rev. Chem.* **2018**, *2* (5), 15–34. <https://doi.org/10.1038/s41570-018-0001-2>.
- (138) Regenauer, N. I.; Settele, S.; Bill, E.; Wadehohl, H.; Rosc, A. Bis(Imino)Pyrazine-Supported Iron Complexes: Ligand-Based Redox Chemistry, Dearomatization, and Reversible C–C Bond Formation. *Inorg Chem* **2020**, *9*.
- (139) Morss, L. R. Thermochemical Properties of Yttrium, Lanthanum, and the Lanthanide Elements and Ions. *Chem. Rev.* **1976**, *76* (6), 827–841. <https://doi.org/10.1021/cr60304a007>.
- (140) Jaoul, A.; Tricoire, M.; Moutet, J.; Cordier, M.; Clavaguéra, C.; Nocton, G. Reversible Electron Transfer in Organolanthanide Chemistry. *Chem. Squared* **2019**, *3*, 1. <https://doi.org/10.28954/2019.csq.06.001>.
- (141) Jaoul, A.; Clavaguéra, C.; Nocton, G. Electron Transfer in Tetramethylbiphosphinine Complexes of Cp\*2Yb and Cp\*2Sm. *New J. Chem.* **2016**, *40* (8), 6643–6649. <https://doi.org/10.1039/C6NJ00527F>.
- (142) Veauthier, J. M.; Schelter, E. J.; Carlson, C. N.; Scott, B. L.; Re, R. E. D.; Thompson, J. D.; Kiplinger, J. L.; Morris, D. E.; John, K. D. Direct Comparison of the Magnetic and Electronic Properties of Samarocene and Ytterbocene Terpyridine Complexes. *Inorg. Chem.* **2008**, *47* (13), 5841–5849. <https://doi.org/10.1021/ic8001465>.
- (143) Evans, W. J.; Foster, S. E. Structural Trends in Bis(Pentamethylcyclopentadienyl)Lanthanide and Yttrium Complexes. *J. Organomet. Chem.* **1992**, *433* (1), 79–94. [https://doi.org/10.1016/0022-328X\(92\)80131-G](https://doi.org/10.1016/0022-328X(92)80131-G).
- (144) Boudreaux, E. A.; Mulay, L. N. *Theory and Applications of Molecular Paramagnetism*; Wiley: New York, 1976.
- (145) Buscemi, G.; Miller, P. W.; Kealey, S.; Gee, A. D.; Long, N. J.; Passchier, J.; Vilar, R. Rapid Carbonylative Coupling Reactions Using Palladium(I) Dimers: Applications to <sup>11</sup>C- Radiolabelling for the Synthesis of PET Tracers. *Org. Biomol. Chem.* **2011**, *9* (9), 3499–3503. <https://doi.org/10.1039/C1OB05268C>.
- (146) Kuganathan, N.; Veal, E.; Green, M. L. H.; Green, J. C.; Pascu, S. I. Exploring Pathways for Activation of Carbon Monoxide by Palladium Iminophosphines. *ChemPlusChem* **2013**, *78* (11), 1413–1420. <https://doi.org/10.1002/cplu.201300214>.
- (147) Bour, J. R.; Camasso, N. M.; Sanford, M. S. Oxidation of Ni(II) to Ni(IV) with Aryl Electrophiles Enables Ni-Mediated Aryl–CF<sub>3</sub> Coupling. *J. Am. Chem. Soc.* **2015**, *137* (25), 8034–8037. <https://doi.org/10.1021/jacs.5b04892>.
- (148) Watson, M. B.; Rath, N. P.; Mirica, L. M. Oxidative C–C Bond Formation Reactivity of Organometallic Ni(II), Ni(III), and Ni(IV) Complexes. *J. Am. Chem. Soc.* **2017**, *139* (1), 35–38. <https://doi.org/10.1021/jacs.6b10303>.
- (149) Rovira, M.; Roldán-Gómez, S.; Martin-Diaconescu, V.; Whiteoak, C. J.; Company, A.; Luis, J. M.; Ribas, X. Trifluoromethylation of a Well-Defined Square-Planar Aryl-Ni(II) Complex Involving Ni(III)/CF<sub>3</sub> and Ni(IV)–CF<sub>3</sub> Intermediate Species. *Chem. – Eur. J.* **2017**, *23* (48), 11662–11668. <https://doi.org/10.1002/chem.201702168>.



# Influence of an alternative ancillary ligand at nickel center: synthesis of trifluoromethyl nickel complexes and coordination chemistry with divalent lanthanides

In the previous chapter, a synthetic trial to high-valent nickel species was investigated by direct oxidative addition of iodomethane with stoichiometric amount to  $\text{Cp}^*_2\text{Yb}(\text{bipym})\text{NiMe}_2$  complex. Unlike the one with its binuclear  $\text{Cp}^*_2\text{Yb}(\text{bipym})\text{PdMe}_2$  congener, this reaction only led to a very fast reductive elimination of ethane and eventual decomposition of the compound, instead of an accessible oxidized product.

Examples in the accessibility towards well-studied organonickel complexes with high valency, such as  $\text{Ni}^{\text{IV}}$ , are relatively rare, as a result of the highly transient features. Mentioned in the general introduction in *Chapter 1*, nickel-catalyzed transformations are usually considered as a  $\text{Ni}^0/\text{Ni}^{\text{II}}$  mechanism and lately invoked in odd-electron states of  $\text{Ni}^{\text{I}}$  and  $\text{Ni}^{\text{III}}$  species undergoing radical processes.  $\text{Ni}^{\text{IV}}$  species as critical intermediates in the catalytic cycles have been also often proposed,<sup>1-5</sup> while until recently by Sanford *et al.*, a series of those were thoroughly investigated and accessibly underwent highly selective carbon-heteroatom coupling reactions with exogenous nucleophiles.<sup>6</sup>

The isolation of high-valent  $\text{Ni}^{\text{IV}}$  species has become an intriguing and certainly extremely challenging topic and limited examples were reported over the last few years (*vide infra*) (Figure 31). Representative work done by Sanford and co-workers described tridentate nickel(IV) systems, in which they notably introduced the trifluoromethyl functional group. In contrast, the double oxidation on the methylated organonickel scaffold to yield high-valent nickel species only generated a transient  $\text{Ni}^{\text{IV}}$  intermediate, while the trivalent nickel species *via* single oxidation was isolated by Mirica and co-workers.<sup>7</sup> Indeed, facial tridentate or tetradentate ligands plausibly play a remarkably effective role in supporting the high oxidation states of isolable nickel complexes in most of the known examples. The function of trifluoromethyl ligand is likewise significant, not only dedicating to the development of new catalytic strategy in trifluoromethylation,<sup>8</sup> but also affecting



the electronic structures of the complexes, as which is previously introduced as electrophilic sources (*i.e.*,  $\text{CF}_3^+$ , from Umemoto reagent, otherwise being called “TDTT” reagent by Sanford, for example).<sup>9</sup> An elegant study by Mézailles and Nebra has shown a straightforward route to enable direct aryl- $\text{CF}_3$  bond formation from inert Ar-H derivatives in quantitative conversions by an exceptionally stable, high-valent Ni(IV) complex  $[(\text{py})_2\text{Ni}^{\text{IV}}\text{F}_2(\text{CF}_3)_2]$  (Scheme 22). This complex was accessed from the oxidation of  $[(\text{py})_2\text{Ni}^{\text{II}}(\text{CF}_3)_2]$  with  $\text{XeF}_2$ , in the absence of any polydentate ancillary ligands, showing the feasibility of the  $[\text{CF}_3]$  moiety to stabilize high oxidation states of nickel ion.<sup>10</sup> In our case, we consider to extend the bimetallic system by modifying the  $\text{CH}_3$  into  $\text{CF}_3$  groups on the nickel center. Few examples showed that with bidentate ancillary ligand such as bipyridine,  $\text{Ni}^{\text{IV}}$  species could be accessed *via* the 2e oxidation whereas the isolation of such intermediates remains difficulties. Hence, it is of great interest to attempt such chemistry with our concept.

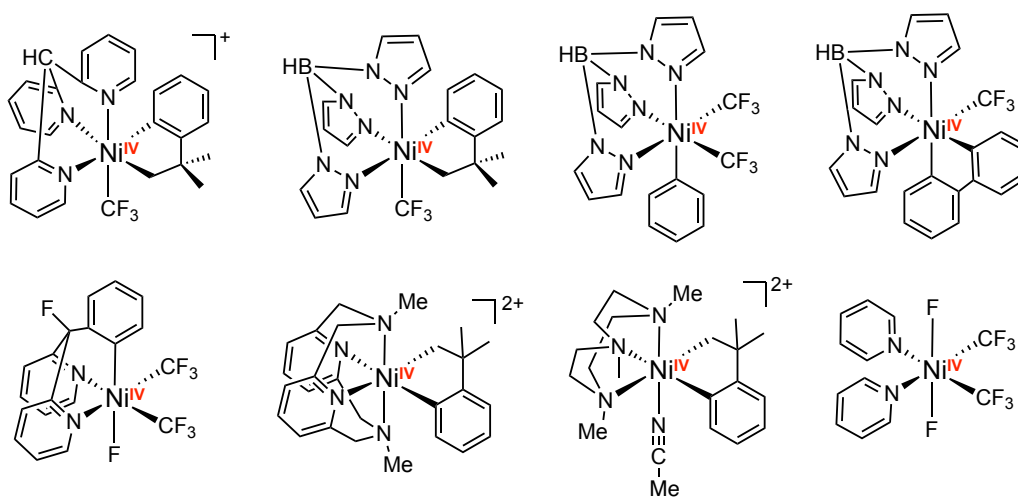
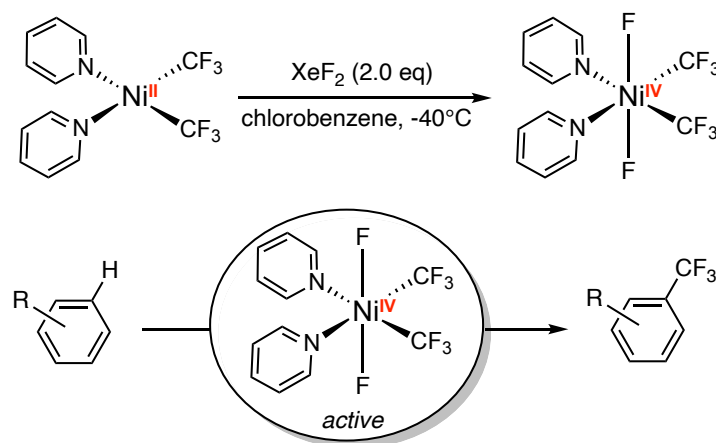


**Figure 31.** Selected examples in well-defined Ni<sup>IV</sup> organometallic complexes which facilitate coupling reactions.



**Scheme 22.** Synthesis of an isolable, well-defined Ni<sup>IV</sup> complex and its application in C-H trifluoromethylation reaction of aromatic compounds.

In the context of this chapter, the replacement of the functional group on the nickel center from methyl to trifluoromethyl will be presented. Several nickel precursors with a general formula as

$L_2Ni(CF_3)_2$  ( $L$  = redox-active  $N$ -ligand) have been synthesized and characterized by NMR spectroscopy. The complexation with divalent lanthanide remains challenging up to now, mainly because of the concomitant and facile C-F bond activation induced by divalent lanthanide fragment, whereas such “side-reaction” could be applied to synthesize novel nickel species in the future study.

### 1. Trifluoromethyl functional group: a strategy toward high valency?

Trifluoromethyl compounds and other fluorinated substituents have considerable significance in influencing the functions of natural products and electronic properties of organometallic complexes. Remarkable interest in fluorinated organic molecules has a variety of applications, of particular in medicinal chemistry, over the decades (Figure 32).<sup>11</sup> The specific impact from fluorinated substituents includes enhanced binding interaction (such as  $F \cdots Protein$  interaction), metabolic stability (mostly by reducing the susceptibility of the adjacent groups to attack, *i.e.*, enzymatic oxidation by cytochrome P450),<sup>12</sup> changes in physical properties and reactivity selectivity.<sup>13</sup> Trifluoromethyl ( $CF_3$ ) group has been described as larger functional group (Van der Waals radius of 2.7 Å) comparing to methyl ( $CH_3$ ), as 2.0 Å for its Van der Waals radius. However, it has been suggested that there is little or no effect on bond length difference attaching to a carbon atom when replacing  $CH_3$  to  $CF_3$  group, resulting in minimal disruption to an enzyme-substrate complex.<sup>14</sup> Other properties of  $CF_3$  functional group imparts the ability to traverse lipid membrane as well as confers extra molecule stability.<sup>15</sup>

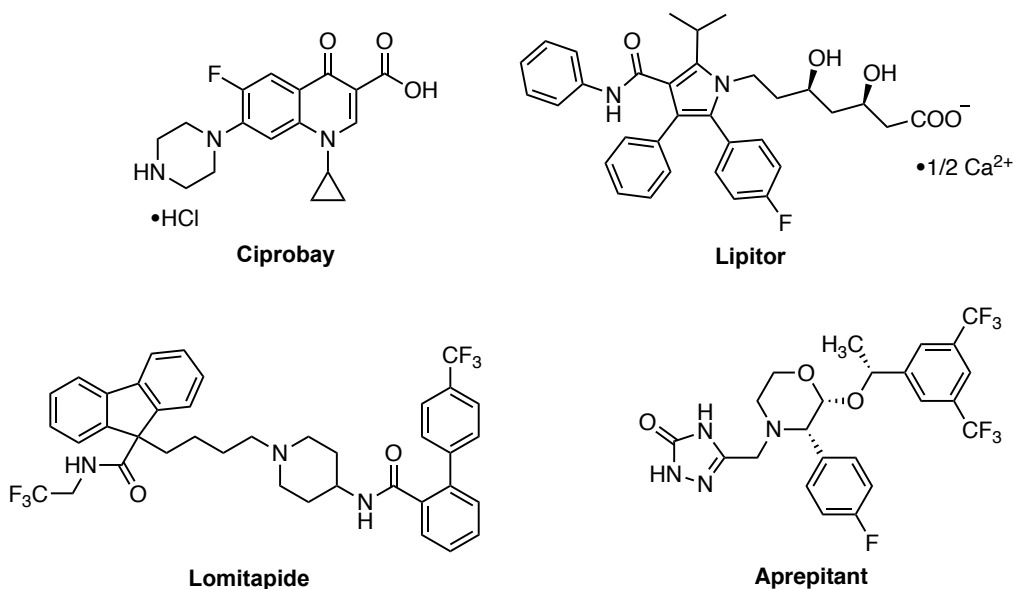


**Figure 32.** Selected common fluorinated drugs: cholesterol-lowering drug Lipitor; quinolone antibiotic Ciprobay; microsomal triglyceride transfer protein inhibitor Lomitapide, and chemotherapy-caused antiemetic Aprepitant.

Consequently, the major success of fluorinated drugs increases the synthetic advances of (asymmetric) fluorination, including trifluoromethylation transformation since last century.<sup>16–18</sup> A wide variety of fluorine and fluoroalkyl groups reagents for selective transformations into the target molecules have been developed (Figure 33).<sup>19–22</sup> As such, the blossom of catalytic

trifluoromethylation mediated by transition metals arises increasing interest in the development of fluorinated and fluoroalkyl organometallic complexes.<sup>23–26</sup> One example in this rich chemistry of perfluoroalkyl metal complexes was reported by Grushin and co-worker. The authors intriguingly found a Ph-X activation (X = I, Cl) by [(dppe)Pd(Ph)(CF<sub>3</sub>)] cleanly producing biphenyl, instead of PhCF<sub>3</sub> as previously expected, in the presence of adventitious water. The mechanism of this reactivity was remarkable, involving H<sub>2</sub>O-induced reduction of a small quantity of the initial Pd(II) complex to Pd(0). When in the absence of H<sub>2</sub>O and PhX, this stable (dppe)Pd(Ph)(CF<sub>3</sub>) complex underwent slow reductive elimination of PhCF<sub>3</sub> under reinforcing conditions (xylenes, 145°C)<sup>27</sup> (Scheme 23).

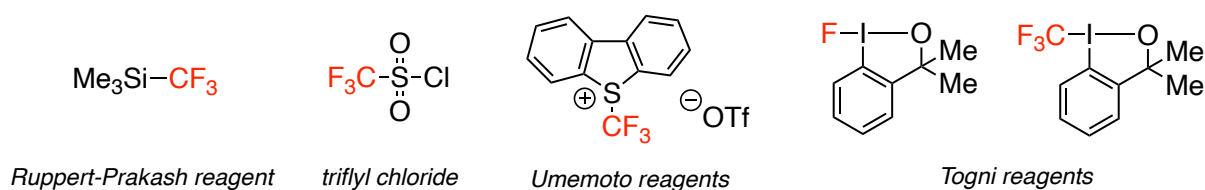
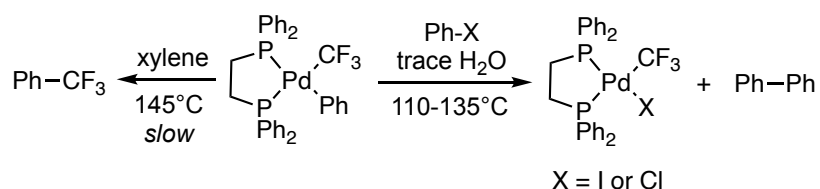


**Figure 33.** Selected examples of common reagents for fluorination and trifluoromethylation reactions.



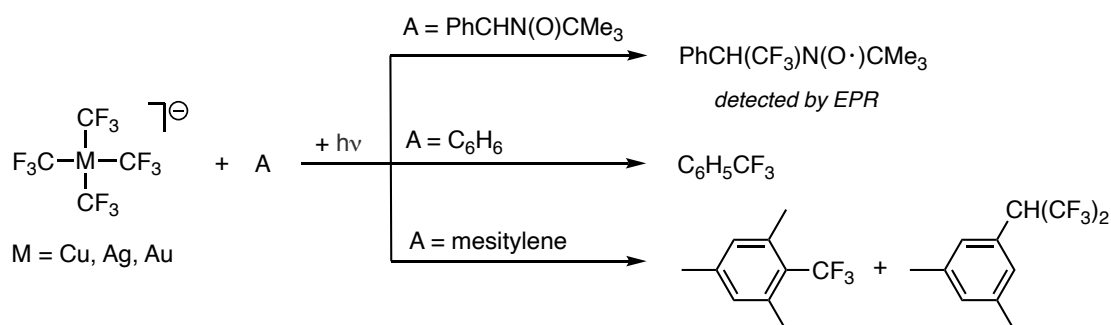
**Scheme 23.** H<sub>2</sub>O-induced Ar-X activation with Pd<sup>II</sup>CF<sub>3</sub> aryl complex reported by Grushin and co-workers.

Fluoroalkyl functional groups are mainly considered as a class of electron-withdrawing group. For example, high CO stretching frequency (2180 cm<sup>-1</sup>) is found in the study of a carbonyl gold complex, when bearing a trifluoromethyl group; while the CO stretch for its analogue [AuCl(CO)] appears at 2162 cm<sup>-1</sup>. This example also highlighted the importance in using CF<sub>3</sub> functional group in the preparation of intermediately formed, short-lived species.<sup>28</sup> Extra electrochemical stability of some fluoroalkyl organometallic complexes also indicates the impact of strong electronegativity of the fluoroalkyl groups, reflected by a dramatical increase in oxidation potential comparing to their nonfluorinated counterparts.<sup>29</sup> Yet to date, fluoroalkyl groups in organometallic complexes are also regarded as possessing “inverted ligand fields”, or known as more likely electron-donating groups. Such behavior can help stabilize high-valent metal complexes with perfluoroalkyl ligands.

### 1.1. [CF<sub>3</sub>] group is not only electron-withdrawing in organometallic complexes

One of the most known model examples in high-valent metal complexes is the stable [Cu(CF<sub>3</sub>)<sub>4</sub>]<sup>1-</sup> ion discovered by Naumann in 1993.<sup>30</sup> Snyder then investigated the electronic structure of this [Cu(CF<sub>3</sub>)<sub>4</sub>]<sup>1-</sup> species as being formed by the interaction of a linear organocopper(I) species [CF<sub>3</sub>CuCF<sub>3</sub>]<sup>1-</sup> ascribed to a d<sup>10</sup> configuration with two additional ionic ligands bearing opposite charges: CF<sub>3</sub><sup>+</sup> and CF<sub>3</sub><sup>-</sup>.<sup>31</sup> Snyder’s assertion was criticized by Kaupp, based on their perceptions in electronegative and covalent bonding nature of Cu-C bond as well as the formally perfect

square-planar geometry supported by a  $\text{Cu}^{\text{III}}$  ion.<sup>32</sup> However, more evidence provided by recent studies, for example, experimental electron density analysis, reveals that the atomic charge of Cu is approximately +1.<sup>33</sup> In sharp contrast to Snyder's ionic model, experimental including spectroscopic studies and theoretical investigations imparted a marked covalent character of the Cu-CF<sub>3</sub> bond in such high oxidation state. Menjón and co-workers reported their contributions in a comparative study of M-C bond homolysis in  $[\text{M}(\text{CF}_3)_4]^-$  complexes (M = Cu, Ag, Au), which was favored in each case upon excitation, generating C<sub>2</sub>F<sub>6</sub> and the corresponding  $[\text{CF}_3\text{MCF}_3]^-$  ions. Unlike the non-fluorinated congener  $[\text{Ag}(\text{CH}_3)_4]^-$ , which underwent a concerted elimination of ethane,<sup>34</sup> the trifluoromethylated compounds featured a detected three-coordinate  $[\text{Cu}(\text{CF}_3)_3]^-$  species, resulted from homolytic cleavage of the Cu-C bond. Therefore, the formation of C<sub>2</sub>F<sub>6</sub> would rather be the result of the stepwise dissociation of CF<sub>3</sub>• radicals, which were confirmed by spin trapping (EPR) (Scheme 24).<sup>35</sup>



**Scheme 24.** The formation of CF<sub>3</sub>• radicals upon irradiation confirmed by spin trapping (EPR) and its transfer to typical arenes reported by Menjón and co-workers.

The assignment of the interesting character of Cu-C bond and particularly the oxidation state of Cu center remains highly controversial, even there was a friendly disagreement among the coauthors in a review article.<sup>36</sup> Indeed, Snyder originally described  $[\text{Cu}(\text{CF}_3)_4]^{1-}$  as featuring an “inverted” ligand field, in which the LUMO exhibited dominantly ligand orbital admixture, contrary to the classical ligand field in which the frontier orbitals are dominated by metal d-orbital admixture (Figure 34).<sup>37</sup>

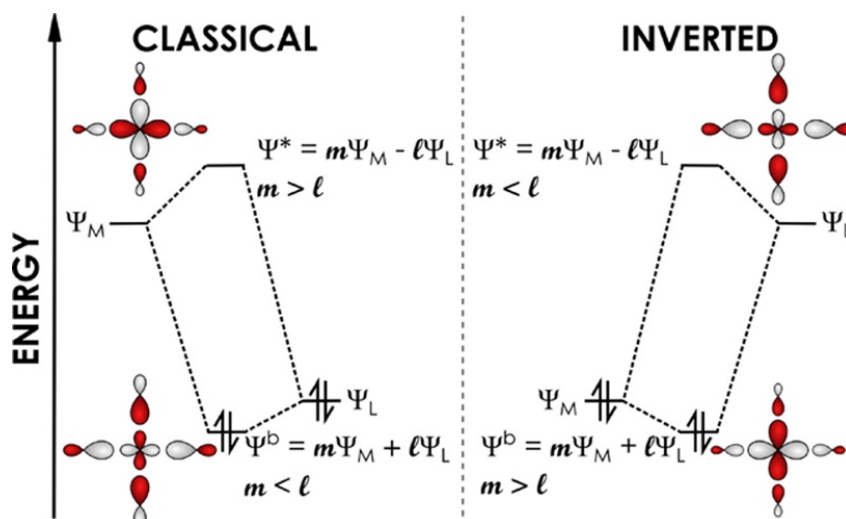


**Figure 34.** In a classical Werner-type ligand field, the antibonding orbital  $\Psi^*$  is dominated by metal d-orbital character. An inverted ligand field arises when  $\Psi^*$  has predominantly ligand orbital character. Figure was created by Lancaster *et al.*<sup>38</sup> Copyright 2016 American Chemical Society.

In the review by Hoffmann and co-workers, they demonstrated the historical theoretical developments in understanding the so-called “The Snyder Imbroglio” with the concept of inverted ligand fields. Three types of inverted ligand-field splitting in octahedron ( $O_h$ ), tetrahedron ( $T_d$ ) and square-planar ( $D_{4h}$ ) coordination were discussed by the authors. The inverting ligand field does exhibit in the former two ligand environments, resulting in longer metal-ligand bonds, for example, although in mild magnitude comparing to the square-planar one. The authors debated on the connection between coordination environment (geometry) and oxidation state (electron configuration), but they eventually agreed with each other on the fact that a certain orbital might be substantially populated who should be relatively empty ( $x^2-y^2$  orbital in a 16-electron complex, for example).<sup>36</sup> Generally, a four-coordinate ion with a  $d^{10}$  electron configuration should exhibit tetrahedral and not square-planar geometry, however, in the presence of an inverted ligand field, it will result in unfilled ligand  $\sigma$  orbitals, whose splitting causes the square-planar geometry to be energetically favored.<sup>33</sup> Snyder's calculations indicated four ligand orbitals of the average  $CF_3^{0.5-}$  ligands pointing toward Cu with four molecular orbitals, of which two were symmetric (SS) and the other were antisymmetric (AS). SS2 and the same symmetry as  $d_{x^2-y^2}$  on Cu possess the highest energy and are empty in the configuration. The interaction between  $d_{x^2-y^2}$  with SS2 resulted in electron transfer from the metal to the ligand, while electrons were back-donated from the fully occupied and symmetrical SS1 of the ligands to the empty 4s orbital of the Cu atom. These interactions resulted in a depletion of  $d_{x^2-y^2}$ , as well as the possibility for nonzero population in the formally empty 4s and SS2 orbitals (Figure 35).

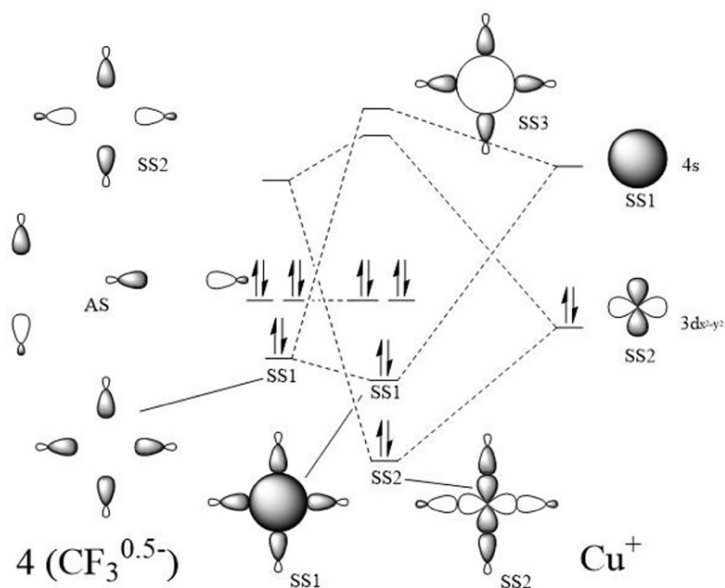


**Figure 35.** Idealized MO correlation diagram for the Cu–C bonding. Figure was adapted from the ref of Snyder<sup>31</sup> by Overgaard.<sup>33</sup> Copyrights 1995 Wiley-VCH Verlag GmbH & Co. KGaA, Weinheim and 2019 American Chemical Society.

The group of Lancaster recently reported a comprehensive study about the electronic configuration of the monoanionic  $[\text{Cu}(\text{CF}_3)_4]^{1-}$  species by a variety of spectroscopic measurements and theoretical studies that support  $d^{10}$  as the ground state electronic configuration of  $[\text{Cu}(\text{CF}_3)_4]^{1-}$  in agreement with Snyder's discovery. Lancaster and co-workers firstly confirmed that the  $D_{4h}$  geometry is favored in an inverted ligand field despite the  $d^{10}$  configuration when comparing with inverted  $D_{4h}$  and  $T_d$  ligand field diagrams. The subsequent studies based on different spectroscopy studies and theoretical calculations revealed a better described  $d^{10}$  rather than the formally  $d^8$  configuration as well as a largely  $\text{CF}_3$ -centered LUMO, that is, the consensus  $d^{10}$  configuration features an inverted ligand field, in which all five metal-localized molecular orbitals are located at lower energy relative to the trifluoromethyl-centered  $\sigma$  orbitals.<sup>38</sup> Additionally, the authors indicated the ligand field inversion in extended species exhibiting electronic vacancy of  $\text{CF}_3$ -centered molecular orbitals with diverse coordination environments, of particular in other high-valent species of transition metal complexes, not only in the originally discovered inverted nature of  $[\text{Cu}(\text{CF}_3)_4]^{1-}$ .<sup>39</sup> Very recently, Lancaster and Vicic discovered that the nickel anions  $[(\text{MeCN})\text{Ni}(\text{CF}_3)_3]^{1-}$  and  $[\text{Ni}(\text{CF}_3)_4]^{2-}$  should be better described as  $d^9$  metal complexes, instead of the most common oxidation state of divalence ( $3d^8$ ), revealing an electron vacancy on the  $\text{CF}_3$  ligands and resulting in the metal to a more reduced state. Evidently, in the presence of bis(4-*tert*-butylphenyl)iodonium hexafluorophosphate as oxidant, trifluoromethylated arene was yielded in this trifluoromethylation reaction, involving a high-valent formally  $[\text{Ar-Ni}^{\text{IV}}(\text{CF}_3)_3(\text{MeCN})_2]$  intermediate. Moreover, further experiments showed very facile oxidation towards a high-valent, unsupported, and formally organonickel(IV) species could be directly achieved *via* two-electron oxidation (potassium persulfate) of  $[\text{Ni}(\text{CF}_3)_4]^{2-}$ .<sup>40</sup>

Indeed, the concept of inverted ligand field indicates ligand oxidation and a highly covalent metal-ligand  $\sigma$ -bonds hence rendering a formal electrophilic “ $\text{CF}_3^+$ ”. Accordingly,  $\sigma$ -noninnocence of certain metal-ligand bonds has been described, notably mentioned in the review of Hoffmann in order to discuss the attribution of oxidation states of  $[\text{Cu}(\text{CF}_3)_4]^{1-}$ . The work of Mézailles and Nebra mentioned above also implicated the inverted ligand fields as well as possible  $\sigma$ -noninnocence in their stable high-valent Ni(IV) species. The “actual” oxidation state of such high-valent Ni- $\text{CF}_3$  complexes may therefore remain ambiguity. Klein and co-workers thus started a computational study to investigate the intriguing electronic configuration and the related reactivity in Ar- $\text{CF}_3$  reductive elimination of a formally Ni<sup>IV</sup> complex reported by Sanford *et al.* in 2015, which were bearing two  $\text{CF}_3$  ligands and one aryl moiety on the nickel center.<sup>41</sup> In such six-coordinate, less symmetric system of Sanford’s Ni<sup>IV</sup> complexes, a cationic aryl ligand and anionic  $\text{CF}_3$  groups were proposed by the authors using the intrinsic bond orbital (IBO) method. This finding revealed that the formation of Ar- $\text{CF}_3$  would be rather based on the transfer of an aryl cation to a  $\text{CF}_3$  anion instead of the transfer of an electrophilic  $\text{CF}_3$  group experimentally reported by Sanford. As such, this elimination process should approach redox neutrality, that is, a nucleophilic attack by the  $\text{CF}_3$  ligand on an electrophilic aryl ligand, rather than behave a strictly reductive fashion. Originating from the high-covalency of the Ni- $\text{C}_{\text{Ar}}$  bond, the cationic character of the aryl group resulted from Ni-aryl  $\sigma$  interaction was also described by the authors as a “ $\sigma$ -noninnocence-induced masked aryl-cation transfer”.<sup>42</sup> Consequently, the Ni(IV) species could better be described to feature an approaching Ni(II) in physically  $d^8$  electronic configuration, with a noninnocent aryl ligand.<sup>43</sup>

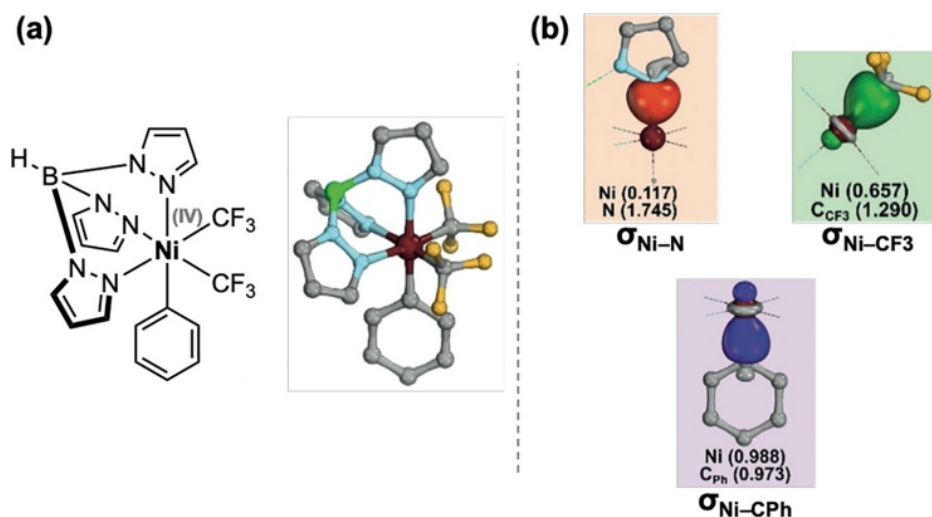


**Figure 36.**  $\sigma$ -Noninnocence in high-valent Ni(IV) complex of Sanford.<sup>41</sup> (a) Structure of the Ni(IV) complex. (b) Intrinsic bonding orbital (IBO) for different coordination. Figure was from the ref of Ye,<sup>43</sup> adapted from Klein.<sup>42</sup>  
Copyrights 2019 Wiley-VCH Verlag GmbH & Co. KGaA, Weinheim and 2020 Elsevier B.V..

Evidently, perfluoroalkyl ligands including  $\text{CF}_3$  moiety in the transition metal complexes may manifest distinctive electronic properties from their analogous non-fluorinated congeners. Based on the fact that square-planar nickel complexes of 2,2'-bipyridine show intense metal-to-ligand ( $d$ -to- $\pi^*$ ) charge transfer properties, the group of Vicic studied the electronic differences between the

well-known non-fluorinated  $[(bpy)Ni(CH_3)_2]$  and a well-defined  $[(bpy)Ni(CF_3)_2]$  complex by the means of optical spectroscopy as well as theoretical investigations. Observed higher energies in the visible absorption for the  $CF_3$  derivative than that for the *bis*- $CH_3$  analogue revealed the involvement of orbitals with  $CF_3$  contributions (or  $Ni-CF_3$   $\sigma$  bonds) for  $[(bpy)Ni(CF_3)_2]$ , and seemingly no contributions to the transitions of  $[(bpy)Ni(CH_3)_2]$  from the  $CH_3$  ligand. The calculations including bond analysis indicated a more positively charged C-Ni bond in the  $CF_3$  complex, whereas a more negatively charged C-Ni bond in the *bis*- $CH_3$  one (Figure 37).<sup>44</sup> Additionally, a much larger stabilization of the HOMO of the  $CF_3$  complex, which was also observed in the Pt analogues by Puddephatt *et al.*,<sup>45</sup> indicated a thermal stability and thus a increased difficulty in the oxidation of the complex, as shown by electrochemistry studies (quasi-reversible at +0.90 V vs  $Fc^+/Fc$  in THF solution compared to -0.60 V vs  $Fc^+/Fc$  in THF solution for  $[(bpy)Ni(CH_3)_2]$ ).<sup>46</sup>

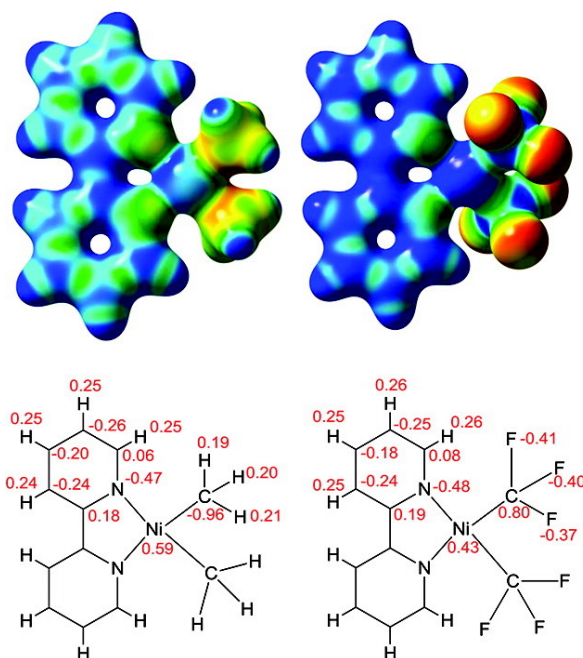


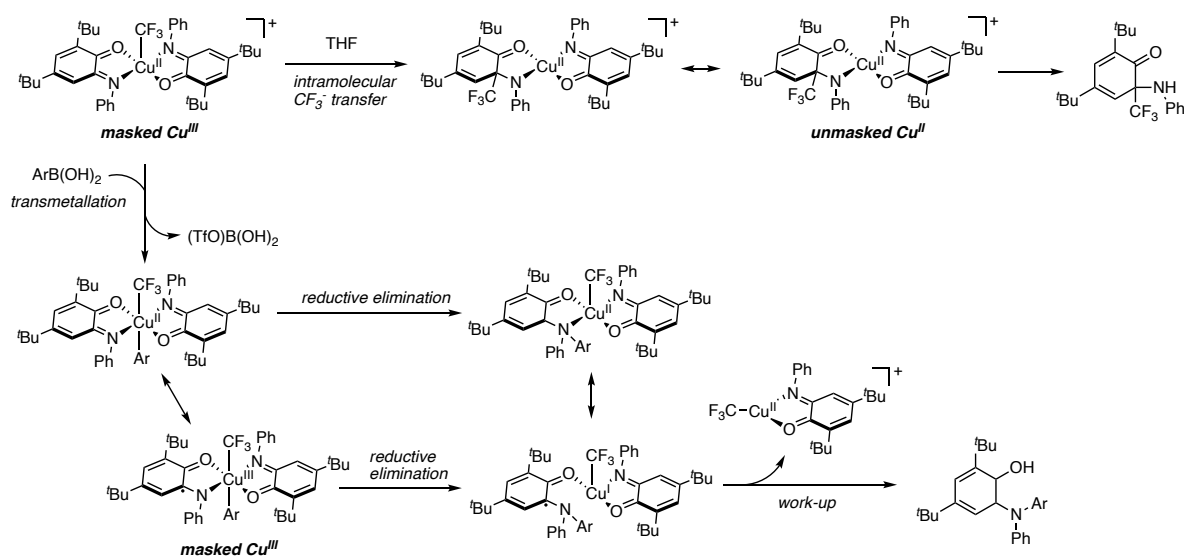
**Figure 37.** (top) DFT-calculated electrostatic surface potentials of complexes  $[(bpy)Ni(CH_3)_2]$  and  $[(bpy)Ni(CF_3)_2]$ . Red indicates regions of negative charge, while blue indicates regions of positive charge. (bottom) Calculated natural atomic charge distributions from a Natural Bond Orbital analysis. Figure was from the ref of Vicic.

Copyright 2012 American Chemical Society.

A broad perspective in the reactivity investigations of the metal-trifluoromethyl bonds, notably intrinsic trifluoromethylation from well-defined complexes have been explored based on the intriguing electronic behaviors of  $CF_3$  ligand. For instance, in the presence of a redox-active system, the generation of reactive  $CF_3\cdot$  radical can be accessibly realized with an electrophilic  $CF_3^+$  source. Desage-Ei Murr and Fensterbank described a series of studies based on a well-defined Cu(II) complex featuring a redox-active iminosemiquinone ligand ( $L_{SQ}$ ) motif. This ligand motif can be involved in two successive single-electron redox steps with three distinct oxidation states, *i.e.*, amidophenolate (AP), iminosemiquinone (SQ) and iminobenzoquinone (BQ). An electrophilic  $CF_3^+$  source (Umamoto reagent) was introduced onto a redox-active ligand-based

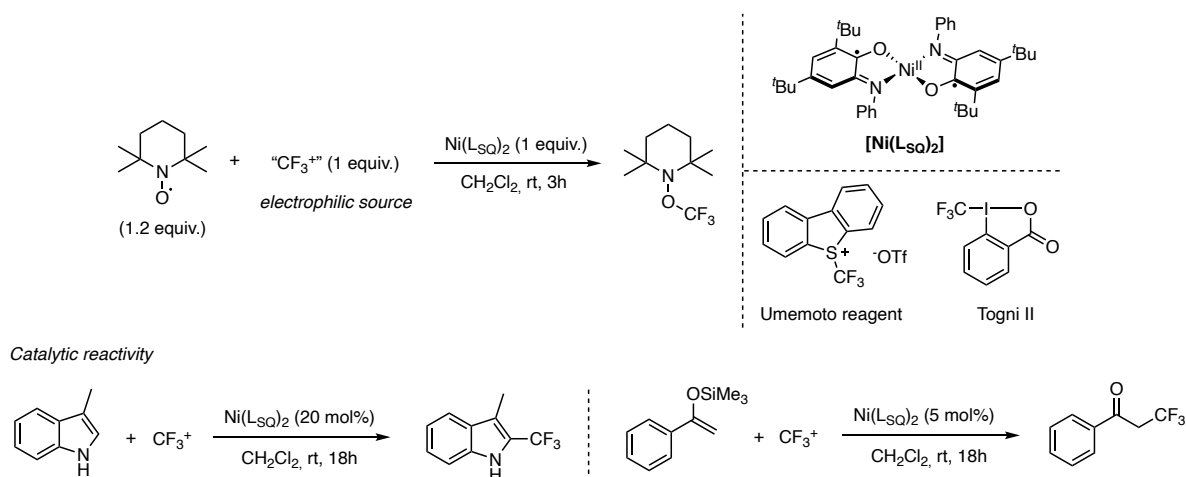


radical  $[\text{Cu}^{\text{II}}(\text{L}_{\text{SQ}}\bullet)_2]$  complex, forming a well-defined, paramagnetic  $[\text{Cu}^{\text{II}}(\text{L}_{\text{BQ}})_2\text{CF}_3]^+$  species, in which the +II oxidation state of Cu center was preserved and the two anti-ferromagnetic coupled SQ ligands were already oxidized into the corresponding diamagnetic BQ manner. Such  $\text{Cu}^{\text{II}}\text{CF}_3$  complex enabled an intramolecularly nucleophilic trifluoromethylation selectively at the electrophilic sites of the BQ ligand depending on the reaction time and temperature, resulting from a formal umpolung reactivity of the initial  $\text{CF}_3^+$  source caused by the redox-active system.<sup>47</sup> The electronic interplay of  $\text{CF}_3$  moiety from electrophilicity to radical fashion was found from the reaction of  $[\text{Cu}^{\text{II}}(\text{L}_{\text{SQ}}\bullet)_2]$  with a  $\text{CF}_3^+$  source in the presence of TEMPO (2,2,6,6-tetramethylpiperidine-*N*-oxyl radical). The mono-oxidized  $[\text{Cu}^{\text{II}}(\text{L}_{\text{SQ}}\bullet)(\text{L}_{\text{BQ}})]^+$  species from  $[\text{Cu}^{\text{II}}(\text{L}_{\text{SQ}}\bullet)_2]$  as intermediate of the reaction *via* a single-electron transfer process was confirmed by spectroscopic and computational studies, of which the divalent Cu center featured one unpaired charge while only one electron was lied inside the ligands, forming an anti-ferromagnetic coupling between these two unpaired electrons. This SET-induced  $\text{CF}_3$  radical formation property cooperated with the redox-active Cu complex led to prominently catalytic reactivity in trifluoromethylation of some “radical accepters” containing unsaturated bonds, such as silyl enol ethers and heteroaromatics, as well as in hydrotrifluoromethylation of alkynes.<sup>48</sup> The authors then described an efficient *N*-arylation of  $\text{L}_{\text{BQ}}$  and derivatives with carbon nucleophiles by the previously reported  $[\text{Cu}^{\text{II}}(\text{L}_{\text{BQ}})_2\text{CF}_3]^+$  complex. This reactivity was also originally arisen from initial oxidation of  $[\text{Cu}^{\text{II}}(\text{L}_{\text{SQ}}\bullet)_2]$  complex with a  $\text{CF}_3^+$  source. A masked Cu(III) species with a radical  $\text{L}_{\text{SQ}}$  as intermediate, instead of a Cu(II) with closed-shell  $\text{L}_{\text{BQ}}$ , was proposed in the mechanistic insights by DFT calculations. Also, the geometry of the possibly formed  $[\text{ArCu}^{\text{III}}(\text{L}_{\text{BQ}})(\text{L}_{\text{SQ}}\bullet)\text{CF}_3]$  after transmetalation with  $\text{ArB}(\text{OH})_2$  remained *trans* position, which prevented the unfavored *O*-arylation (Scheme 25).<sup>49</sup> This work additionally demonstrated that, in the presence of redox-active ligand scaffold, a high-valent species could be well-stabilized and exhibit unprecedented reactivity that the low-valent ones limitedly enable.



**Scheme 25.** Proposed mechanisms rationalizing the masked high-valent reactivity of  $[\text{Cu}^{\text{II}}(\text{L}_{\text{BQ}})_2\text{CF}_3]^+$  species in an intramolecular  $\text{CF}_3$  transfer as well as C-N bond formation reactions by Desage-El Murr and co-workers.

The group of Desage-EI Murr sequentially explored a similar catalytic reactivity in the  $\text{CF}_3^\bullet$  radical formation through a single-electron transfer process to an external  $\text{CF}_3^+$  source with a redox-active Ni complex supported by iminosemiquinone ligands. The observation of TEMPO- $\text{CF}_3$  adduct from the preliminary test on  $\text{Ni}(\text{L}_{\text{SQ}})_2$  with an electrophilic  $\text{CF}_3^+$  reagent (Umemoto or Togni reagent) implied the radical  $\text{CF}_3^\bullet$  formation in the reaction. Theoretical studies on the putative intermediate from  $\text{Ni}(\text{L}_{\text{SQ}})_2$  precursor with  $\text{CF}_3^+$  source showed a delocalized  $\pi$ -system principally distributed on the iminosemiquinone moieties, in good consistence with a ligand-based radical species ( $S = 1/2$ ). Combined with the experimental data in adsorption spectroscopy, the reaction was described by the authors as a single-electron transfer to  $\text{CF}_3^+$ , as well as a ligand-centered oxidized intermediate species, namely  $\text{Ni}^{\text{II}}(\text{L}_{\text{SQ}})(\text{L}_{\text{BQ}})^+$ . This  $\text{CF}_3^\bullet$  radical generating system was applied, as similarly as in the case of the copper congener, in catalytic trimethylation reaction of a silyl enol ether or 3-methylindole mediated by  $\text{Ni}(\text{L}_{\text{SQ}})_2$  (0.5% and 20%, respectively) with a  $\text{CF}_3^+$  source (1.5 equiv.) forming corresponding trifluoromethylated products in 42% and 78% yield, respectively (Scheme 26).<sup>50</sup>



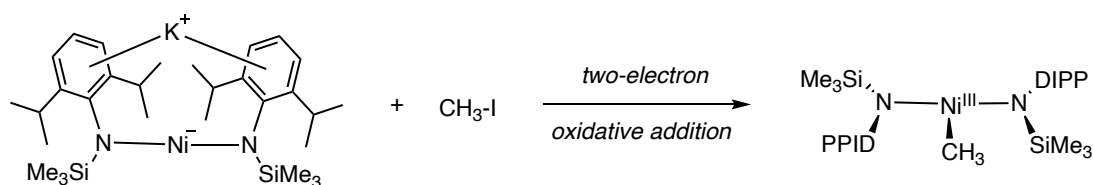
**Scheme 26.**  $\text{CF}_3^\bullet$  radical generation with a redox-active Ni complex leading to catalytic reactivity in trifluoromethylation reported by Desage-EI Murr and co-workers.

## 1.2. Selected examples in high-valent nickel compounds

Based on the fundamental studies above, routes to access stable high-valent nickel ( $\text{Ni}^{\text{III}}$  or  $\text{Ni}^{\text{IV}}$ ) species seem to be feasibly achieved by introducing  $[\text{CF}_3]$  ligand(s). Since a seminal work reported by Kochi *et al.*, who spectroscopically (ESR) studied a metastable paramagnetic  $\text{Ni}^{\text{III}}$  species that was capable to undergo carbon( $\text{sp}^2$ )-halogen coupling *via* reductive elimination,<sup>51</sup> state-of-the-art strategies towards the preparation or/and spectroscopical identification of  $\text{Ni}^{\text{III}}$  and  $\text{Ni}^{\text{IV}}$  complexes have been developed in the following decades.<sup>52</sup> As mentioned in *Chapter 1*, high-valent nickel species have intrinsic properties in extremely readily undergoing single- or two-electron redox sequences, that resulting in novel reaction approaches and unprecedented chemical transformations in nickel-mediated catalysis.

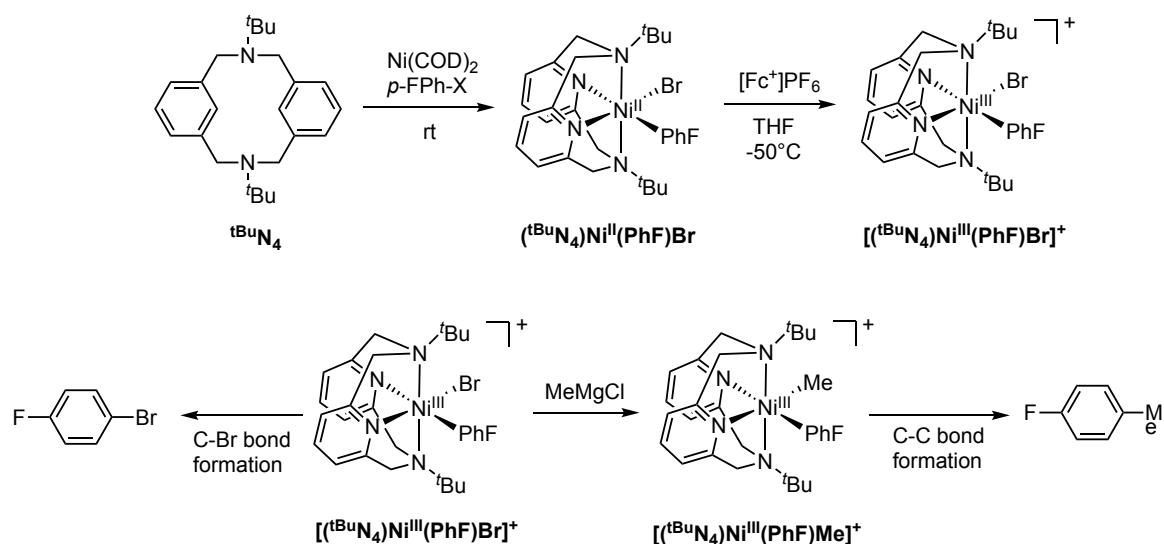
The group of Tilley reported an isolable three coordinate, T-shaped  $\text{Ni}^{\text{III}}$ -methyl complex prepared by oxidative addition of  $\text{MeI}$ , analyzed as one unpaired electron and a low spin,  $d^7$  electronic

configuration. However, this complex is thermally unstable in solution, decomposing at ambient temperature to its stable Ni<sup>I</sup> precursor, accompanied by the formation of ethane (Scheme 27).<sup>53</sup> A well-defined catalytic system for the C-C coupling of aryl halides with Grignard reagents involved by this complex was also identified and evaluated mechanistically by the same group.<sup>54</sup> A proposed two-electron Ni<sup>I</sup>/Ni<sup>III</sup> scenario in such system showed that a new class of nickel catalysts promote novel metal-mediated transformations.



**Scheme 27.** A T-shaped bis(amido) Ni(III) methyl complex obtained by oxidative addition reported by Tilley *et al.*

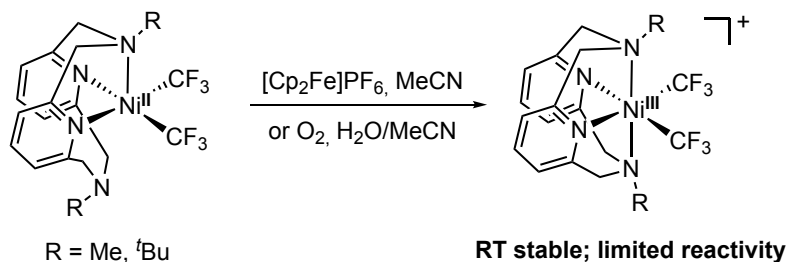
Coordination of polydentate *N*-donor ligands also invokes the possibility in the stabilization of reactive high-valent nickel species. For example, Mirica and co-workers reported a series of isolated Ni(III) and Ni(IV) complexes in the presence of flexible multidentate ligands with direct relevance to C-H functionalization and carbon-carbon/heteroatom bond formation reactions.<sup>55</sup> Their very first contribution in this field was the isolation of Ni<sup>III</sup>(aryl)halide complexes stabilized by a tetradentate ligand *N,N'*-di-*tert*-butyl-2,11-diaza[3.3](2,6)pyridinophane (<sup>t</sup>BuN<sub>4</sub>). They initially prepared a (<sup>t</sup>BuN<sub>4</sub>)Ni<sup>II</sup>(aryl)halide via oxidative addition of arylhalide with Ni(0) precursor, then used ferrocenium hexafluorophosphate [Fc<sup>+</sup>][PF<sub>6</sub><sup>-</sup>] to access to the Ni<sup>III</sup> species by 1e<sup>-</sup> oxidation. These Ni(III) species readily underwent transmetalation and/or reductive elimination to form new C-C or C-heteroatom bonds at room temperature and were also competent catalysts for Kumada and Negishi cross-coupling reactions (Scheme 28).<sup>56</sup>



**Scheme 28.** Mirica *et al.* reported the synthesis of a Ni(III) complex and the relevance to carbon-carbon and carbon-heteroatom bond formation reactions.

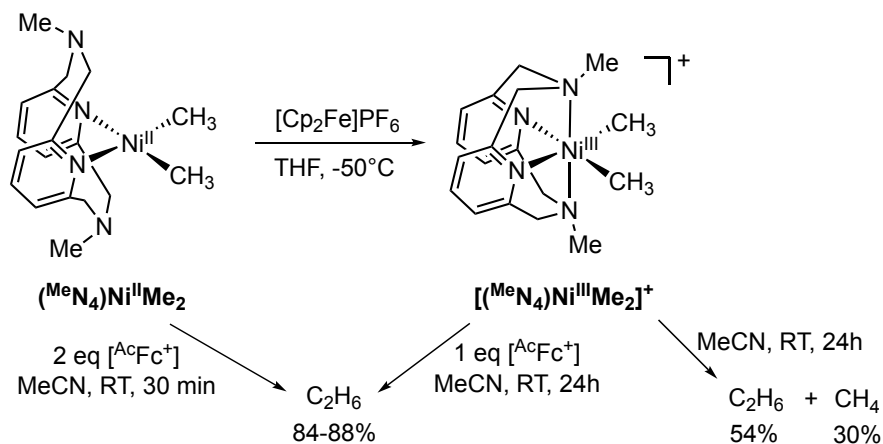
Importantly, the same group then reported a stable Ni<sup>III</sup> complex that contains two trifluoromethyl ligands and is supported by the same <sup>t</sup>BuN<sub>4</sub> ligand. This compound was generated from by facile

oxidation, including aerobic oxidation, and it exhibits a very limited reactivity in reductive elimination process (Scheme 29).<sup>57</sup>



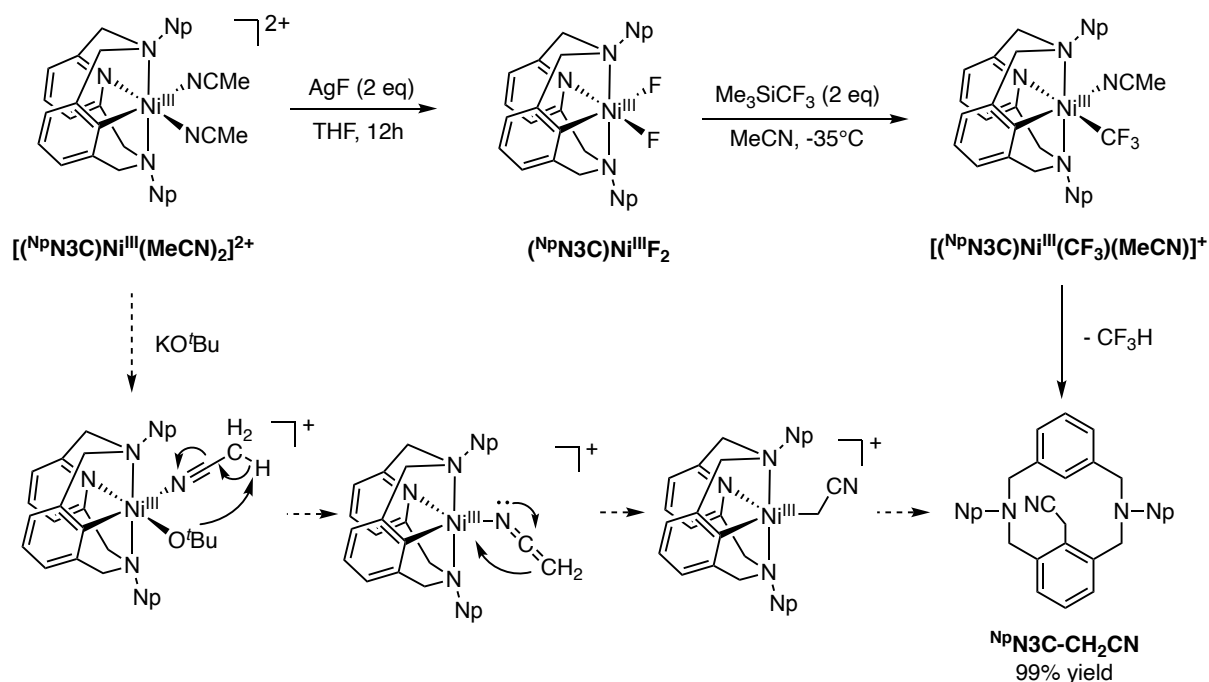
**Scheme 29.** Stable bis(trifluoromethyl)nickel(III) complexes reported by Mirica and co-workers.

In parallel with this *bis*-trifluoromethyl complex, Mirica confirmed that the same tetradentate ligand system enabled the isolation of the first Ni<sup>III</sup>-dialkyl complex, which was achieved from 1e<sup>-</sup> oxidation by [Fc<sup>+</sup>][PF<sub>6</sub>]. Different from its *bis*-CF<sub>3</sub> congener, this Ni(III) complex was reactive enough to slowly undergo reductive elimination of ethane and methane at room temperature in solution, yet it was relatively stable under inert atmosphere. Ethane production rate was enhanced in the presence of an oxidant, pointing to an involvement of transient Ni(IV) intermediate, which could decompose rapidly to the Ni<sup>II</sup> precursor as well as produce ethane.<sup>58</sup> Such species was also involved in catalytic C-C bond formations, suggesting an importance of corresponding high-valent species in a range of Ni-catalyzed cross-coupling reaction with alkyl substrates (Scheme 30).<sup>7</sup>



**Scheme 30.** Isolated Ni(III) complex relevant to C-C bond formation via Ni(IV) intermediate reported by Mirica.

Unlike the high stability of the *bis*-CF<sub>3</sub> congener, another Ni(III) species in a family of Mirica's work bearing one CF<sub>3</sub> ligand, generated a cyanomethylation product quantitatively at room temperature in MeCN. This species was only spectroscopically observed by ESI-MS and EPR. The Ni<sup>III</sup> precursor underwent aromatic cyanoalkylation assisted by an intramolecular (with CF<sub>3</sub> ligand) or external base (<sup>t</sup>BuOK) that cleaves the C(sp<sup>3</sup>)-H bond. This work described an example in aromatic cyanoalkylation reactions that employed nitriles as building blocks and proceeded through C-H bond activation mediated by Ni<sup>III</sup> species (Scheme 31).<sup>59</sup>



**Scheme 31.** Mirica *et al.* reported aromatic cyanoalkylation mediated by Ni(III), through C(sp<sup>3</sup>)-H bond activation of MeCN and subsequent C-C bond formation reactions by reductive elimination.

The first approach to high-valent NiCF<sub>3</sub> species was reported by Vicic *et al.* about an in-situ formed cationic [(<sup>t</sup>Bupty)Ni<sup>III</sup>(CF<sub>3</sub>)<sub>2</sub>][PF<sub>6</sub>] species characterized by EPR. Such highly active species underwent CF<sub>3</sub> radical elimination and yielded complex [(<sup>t</sup>Bupty)Ni<sup>II</sup>(CF<sub>3</sub>)]<sup>+</sup> rapidly at room temperature.<sup>60</sup> Yet, bearing a perfluoroalkyl ligand, a stable trivalent nickelacycle complex was successfully isolated by the same group (Figure 38).<sup>61</sup> In *Chapter 5*, several examples by Vicic will be also detailed and the chemistry with terpyridine-type ligand will be discussed.

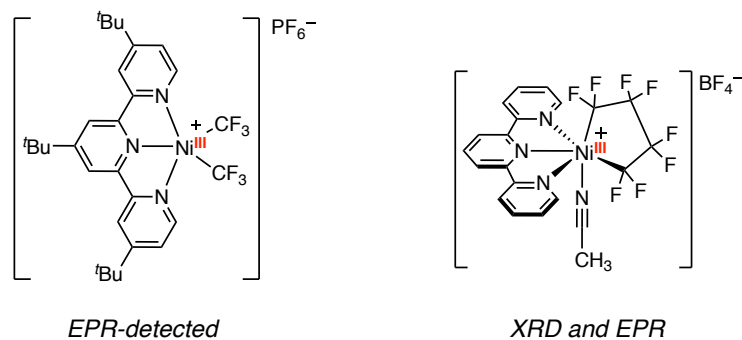
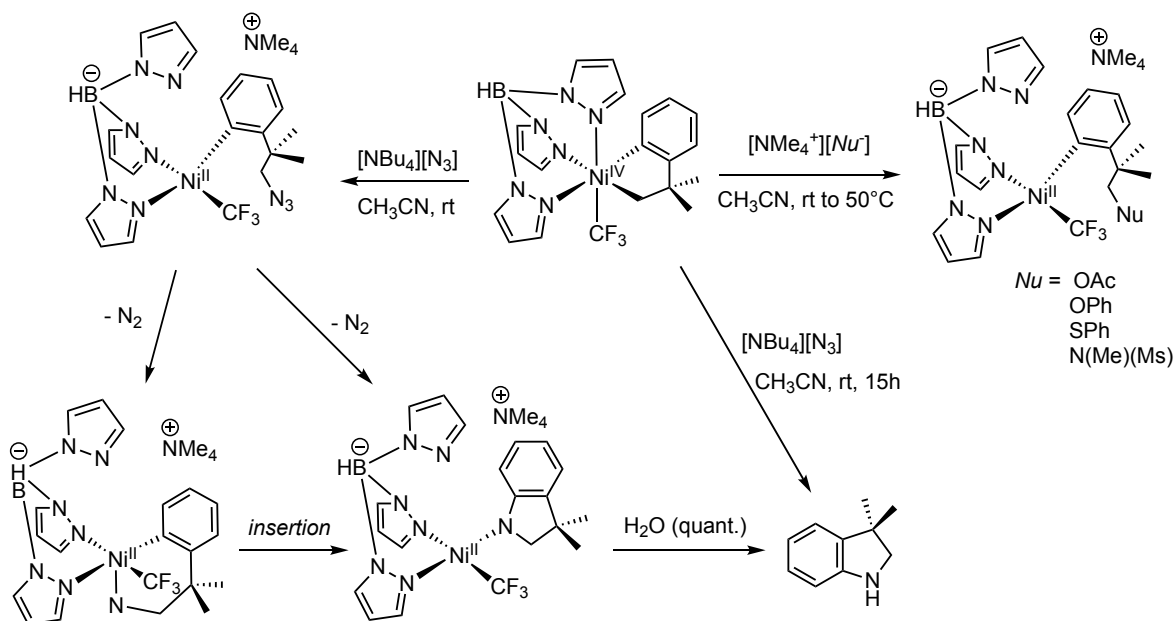


**Figure 38.** Ni(III) perfluoroalkyl complexes bearing terpyridine ligand scaffold reported by Vicic and co-workers.

In a variety of recent examples in the identifications of high-valent nickel complexes, the group of Sanford reported a pioneering example in the isolation of octahedral Ni<sup>IV</sup>(cyclo-neophyl) complexes bearing tridentate scorpionate ligand scaffolds, *i.e.*, tris(pyrazolyl)borate (Tp) and tris(2-pyridyl)methane (Py<sub>3</sub>CH), which were engaged in the mechanistic study of cross-coupling reactions. A highly stable, diamagnetic Ni(IV) cationic complex was obtained by the addition of Umemoto reagent and it underwent reductive elimination to form quantitatively dimethylbenzocyclobutene when heating up to 95°C in solution. In the presence of heteroatom-

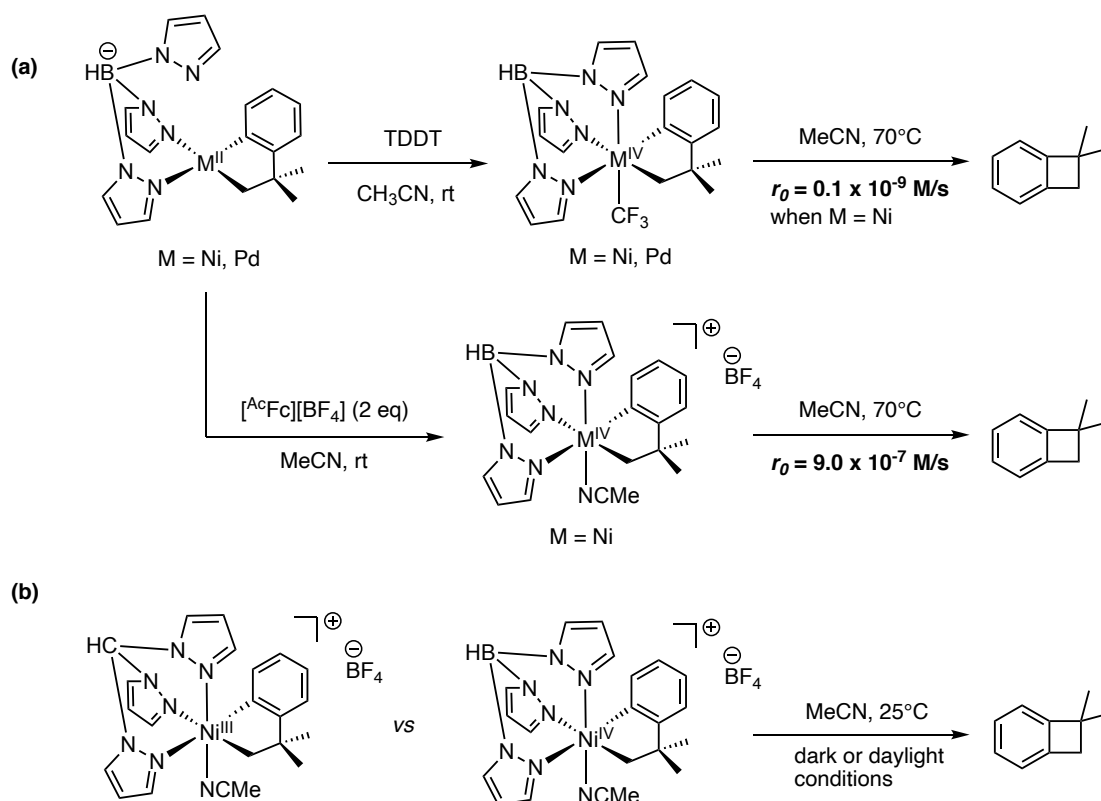
based exogenous nucleophiles, the neutral  $\text{TpNi}^{\text{IV}}$  analogue underwent  $\text{C}(\text{sp}^3)$ -heteroatom formation, affording relatively stable  $\text{C}(\text{sp}^3)$ -heteroatom coupled  $\text{Ni}(\text{II})$  complexes. Whereas with  $[\text{NBu}_4][\text{N}_3]$ , the reaction intriguingly in succession underwent  $\text{C}(\text{sp}^3)$ -N coupling,  $\text{N}_2$  elimination from the azide intermediate resulting in the insertion into  $\text{C}(\text{sp}^2)$ -Ni bond, and protonation of the Ni-N bond by adventitious water releasing the produced 3,3'-dimethylindoline. Preliminary mechanistic insights in the coupling reactivity were collected under the kinetic studies, in a correlation with the Swain-Scott nucleophilicity parameters, indicating a  $\text{S}_{\text{N}}2$  mechanism of nucleophilic attack into the Ni- $\text{C}(\text{sp}^3)$  bond in this system (Scheme 32).<sup>6</sup>



**Scheme 32.** Sanford *et al.* reported the reactivity of isolated  $\text{Ni}(\text{IV})$  complexes in selective  $\text{C}(\text{sp}^3)$ -heteroatom bond formation reactions.

In order to better understand the participation of high-valent species involved in cross-coupling reactions, Sanford and co-workers then evaluated that how the nature of central metals (Ni and Pd) as well as the surrounding chelates ( $\text{MeCN}$  and  $\text{CF}_3$ ) impacts the feasibility of their developed reactivity in C-C and C-heteroatom bond formation. A class of high-valent nickel and palladium model complexes bearing the same Tp and cycloneophyl ligands were prepared from their divalent anionic salts  $[(\text{Tp})\text{M}^{\text{II}}(\text{cyclo-neophyl})]$  ( $\text{M} = \text{Ni}, \text{Pd}$ ) *via* selective  $1\text{e}^-$  or  $2\text{e}^-$  oxidation processes. The  $\text{Ni}^{\text{II}}$  precursor readily underwent both  $1\text{e}^-$  and  $2\text{e}^-$  oxidations to afford stable  $\text{Ni}^{\text{III}}$  and  $\text{Ni}^{\text{IV}}$  products, while the  $\text{Pd}^{\text{II}}$  analogue exclusively went through  $2\text{e}^-$  oxidation reaction to generate  $\text{Pd}^{\text{IV}}$ . Though mechanistic studies implicated outer-sphere  $\text{S}_{\text{N}}2$  pathways for these coupling processes, the significant kinetic difference in reactivity in  $\text{C}(\text{sp}^3)$ -heteroatom coupling reactions between  $\text{Ni}^{\text{IV}}$  and  $\text{Pd}^{\text{IV}}$  was reflected by the approximately 2 orders of magnitude faster reactions at  $\text{Ni}^{\text{IV}}$  than those at  $\text{Pd}^{\text{IV}}$ ; also, a higher propensity of the  $\text{Ni}^{\text{IV}}$  species towards  $\text{C}(\text{sp}^3)$ -OAc coupling was found comparing to their  $(\text{Tp})\text{Pd}^{\text{IV}}\text{CF}_3$  analogues. Remarkable similarities in the  $\text{Ni}^{\text{IV}}$  and  $\text{Pd}^{\text{IV}}$  chemistry were overall investigated but a distinction from palladium was shown by the role for  $\text{Ni}^{\text{III}}$  species in enabling reactivity, which could readily promote one-electron transfer processes. Another

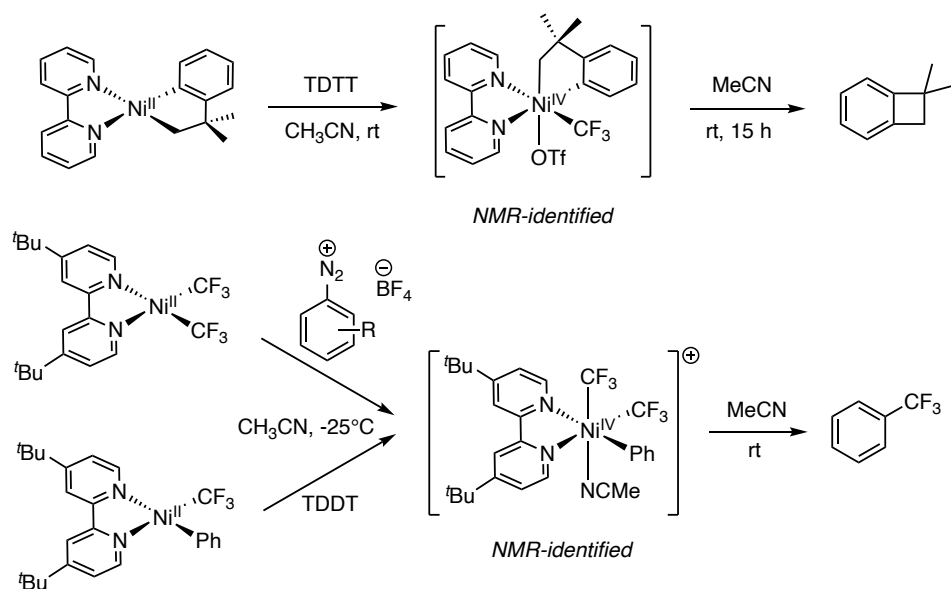
interesting conclusion from this work was the demonstration of a higher stability of the  $(\text{Tp})\text{Ni}^{\text{IV}}(\text{cyclo-neophyl})(\text{CF}_3)$  complex than that of its anionic  $(\text{Tp})\text{Ni}^{\text{IV}}(\text{cyclo-neophyl})(\text{MeCN})$  analogue by kinetic studies in the elimination of dimethylbenzocyclobutene molecule, revealing the strong  $\sigma$ -donation of the  $\text{CF}_3$  functional group (Scheme 33a).<sup>62</sup> Additionally, the authors described a systematic comparison of several factors impacting the relative reaction rates and selectivities of  $\text{C}(\text{sp}^3)\text{-C}(\text{sp}^2)$  and  $\text{C}(\text{sp}^3)\text{-O}$  formation reactions at the cationic octahedral  $(\text{Py}_3\text{CH})\text{Ni}^{\text{III}}$  and  $(\text{Tp})\text{Ni}^{\text{IV}}$  complexes. Interestingly, based on the electrophilicity of the respective  $\text{Ni-C}(\text{sp}^3)$  bonds, the relative reactivity of both complexes towards outer-sphere  $\text{S}_{\text{N}}2$  bond formation pathways behaved distinctly. The  $\text{C}(\text{sp}^3)\text{-C}(\text{sp}^2)$  cyclization proceeded more easily (up to 300-fold faster) from the  $\text{Ni}^{\text{III}}$  in dark conditions or exposed to daylight. In contrast, the  $\text{Ni}^{\text{IV}}$  complex exclusively underwent selective  $\text{C}(\text{sp}^3)\text{-OAc}$  bond formation. Such behavior at  $\text{Ni}^{\text{IV}}$  was explained as an enhanced electrophilicity towards a more favorable nucleophilic attack to yield the  $\text{C}(\text{sp}^3)\text{-OAc}$  bonded product (Scheme 33b).<sup>63</sup>



**Scheme 33.** Sanford *et al.* reported the factors in impacting of cross-coupling reactivity by comparing (a) central metals (Ni and Pd) and ancillary ligands (MeCN and  $\text{CF}_3$ ), as well as (b) the oxidation state of Ni center.

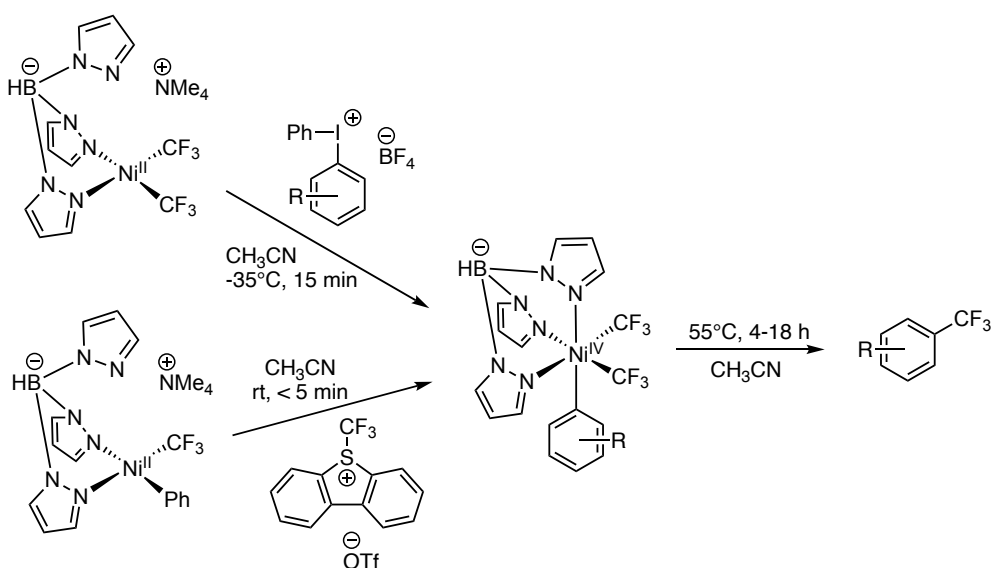
The Sanford group continued to describe the reactivity of two different types of  $\text{Ni}^{\text{IV}}(\text{aryl})(\text{CF}_3)_2$  species supported by trispyrazolylborate (Tp) and 4,4'-di-*tert*-butyl-bipyridine (dtbpy) ligands. With less donating dtbpy ligand, putative  $\text{Ni}^{\text{IV}}(\text{CF}_3)_2$  species were observed by NMR at low temperature, and such intermediates accessed rapid benzotrifluoride formation via reductive elimination when warmed up to the room temperature, whose reactivity was similar to the one of the presumable  $(\text{bipy})\text{Ni}^{\text{IV}}(\text{aryl})\text{CF}_3$  species (Scheme 34).<sup>6</sup> Stable high-valent  $(\text{Tp})\text{Ni}^{\text{IV}}(\text{CF}_3)_2$  complexes were

accessed *via* the net  $2e^-$  oxidation of  $Ni^{II}$ - $CF_3$  precursors (aryliodonium salts or umemoto reagent), and underwent high yielding aryl- $CF_3$  bond-forming reductive elimination of the corresponding benzotrifluorides when heated to  $55^\circ C$ . This reactivity behavior was then kinetically analyzed by Hammett plot, showing a  $\rho$  value of  $-0.91$ , indicating that reductive elimination is fastest with electron-enriched arenes. The electronic effect was explained by the authors as the larger trans-effect of electron-rich  $\sigma$ -aryl groups facilitating ligand dissociation to generate a reactive five-coordinate  $Ni^{IV}$  intermediate, and/or the electron donor substituents accelerating a nucleophilic attack by the  $\sigma$ -aryl ligand onto the electrophilic  $CF_3$  group in the transition state (Scheme 35).<sup>41</sup> However, as already mentioned above, Klein *et al.* revealed the  $\sigma$ -noninnocent nature in these complexes as a result of an inverted ligand field occasion, and the  $Ni^{IV}$  should be better described as approaching  $Ni^{II}$  species. As a consequence, the Ph- $CF_3$  bond formation step was not as reductive, but as essentially redox-neutral.<sup>42</sup>



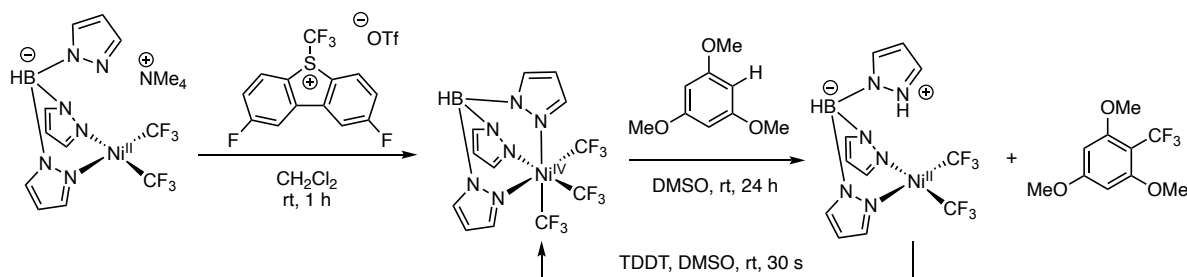
**Scheme 34.** Identification of transient  $Ni^{IV}$ - $CF_3$  species bearing bpy and dtbpy ancillary ligands and subsequent reductive elimination process.





**Scheme 35.** Different synthetic strategies to approach the Ni(IV) species  $[\text{Ni}^{\text{IV}}(\text{Tp})(\text{aryl})(\text{CF}_3)_2]$  and reactivity in the formation of benzotrifluorides via reductive elimination, reported by Sanford and co-workers.

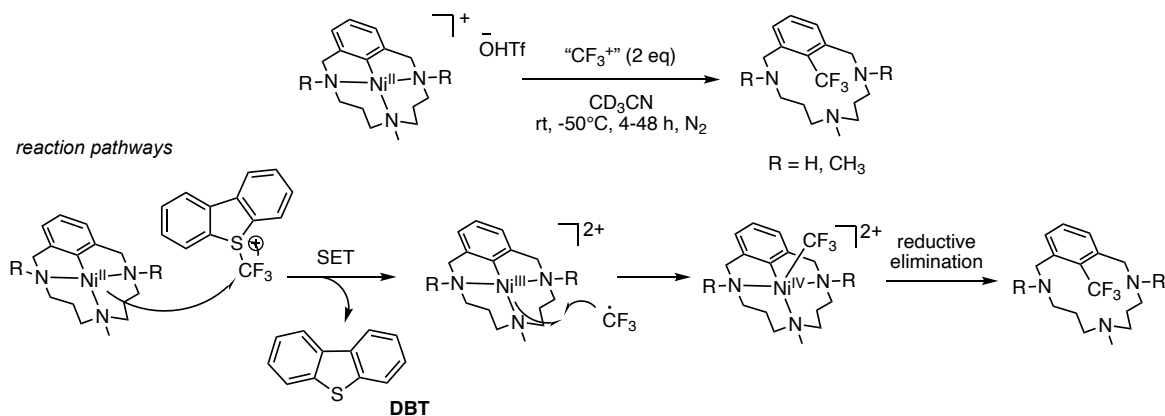
Another recent example in Sanford's exceptional contributions in the study of high-valent nickel chemistry was the first isolated Ni<sup>IV</sup> complex supported by three CF<sub>3</sub> groups. The authors described the stoichiometric reactivity of such complex with 2,4,6-trimethoxybenzene (TMB) to yield the corresponding benzotrifluoride TMB-CF<sub>3</sub> accompanied by the Ni<sup>II</sup>-CF<sub>3</sub> precursor. More remarkably, this work highlighted the first authenticated Ni<sup>IV</sup> complex as an effective catalyst in C(sp<sup>2</sup>)-H bond trifluoromethylation of (hetero)arenes (turnover number up to 5), in the presence of an electrophilic trifluoromethylating reagent. Detailed mechanistic studies revealed a CF<sub>3</sub> radical chain pathway proceeding through a Ni<sup>II/III/IV</sup> cycle, in which this Ni<sup>IV</sup> species played a role in both the initiation and propagation regimes (Scheme 36).<sup>64</sup>



**Scheme 36.** Catalytic C-H trifluoromethylation of (hetero)arenes by Ni(IV) species *via* Ni<sup>II-IV</sup> redox manifold, described by Sanford and co-workers.

Luis and Ribas reported that trifluoromethylation of a square-planar Ni<sup>II</sup>-aryl complex by CF<sub>3</sub><sup>+</sup> sources such as 5-(trifluoromethyl)dibenzothiophenium trifluoromethanesulfonate (Umemoto reagent) and 3,3-dimethyl-1-(trifluoromethyl)-1,2-benziodoxole (Togni reagent) afforded the quantitative formation of trifluoromethylated products. This transformation involved a putative Ni<sup>IV</sup>-aryl intermediate, while the corresponding high-valent species was not isolated but characterized theoretically. They proposed that a feasible single electron transfer (SET) initially took place, forming a CF<sub>3</sub> radical and Ni<sup>III</sup>-aryl species, that recombined to generate an aryl-Ni<sup>IV</sup>CF<sub>3</sub>

intermediate. Such intermediate rapidly underwent facile reductive elimination affording the final trifluoromethylated products (Scheme 37).<sup>65</sup> This example well explained a plausible  $\text{CF}_3^+$  and  $\text{CF}_3\cdot$  transition as well as the rich redox chemistry of nickel complexes in an experimental and theoretical point of view.



**Scheme 37.** Oxidative trifluoromethylation *via* SET process through an elusive  $\text{Ni}^{\text{IV}}\text{-CF}_3$  intermediate reported by Luis and Ribas.

Hence, inspired by these related examples in fluoroalkyl Ni complexes with of particular interest in the identifications of high-valent nickel species, the attempt to the corresponding novel bimetallic complexes with divalent lanthanides from redox-active nickel complexes bearing  $\text{CF}_3$  ligand is worth to be considered. Possible multielectron transfer onto nickel center would take place in the overall heterometallic scaffold when regarding intrinsic  $\text{CF}_3$  ligand as  $\sigma$ -noninnocent, leading to an extreme interest in the investigations of special electronic structures and reactivity of the designed complexes as well as their congeners in high oxidation states.

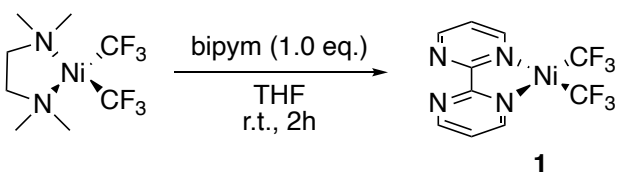
## 2. Synthesis and characterizations of $\text{L}_2\text{Ni}(\text{CF}_3)_2$ complexes

A synthetic strategy of trifluoromethyl nickel complexes is based on the similarly described procedure by Vicic and co-workers, utilizing  $\text{L}_2\text{Ni}(\text{CF}_3)_2$  precursors, such as  $(\text{MeCN})_2\text{Ni}(\text{CF}_3)_2$  or  $(\text{tmeda})\text{Ni}(\text{CF}_3)_2$ , with a liable to be exchanged L-type ligand.<sup>60</sup> In order to obtain clean, yellow solid of  $(\text{MeCN})_2\text{Ni}(\text{CF}_3)_2$  and  $(\text{tmeda})\text{Ni}(\text{CF}_3)_2$ , which was not detailed in the referring paper of Vicic, necessary purification step has to be performed *via* recrystallization of the reaction residue in DCM. This step can remove the adjoint monosubstituted analogue, which could be an orange by-product, that will strong influence the further reaction trials with divalent lanthanides.

### 2.1. Synthesis and characterizations of (bipym)Ni(CF<sub>3</sub>)<sub>2</sub> complex

A straightforward synthesis of (bipym)Ni(CF<sub>3</sub>)<sub>2</sub> is similar to that of (bipym)Ni(CH<sub>3</sub>)<sub>2</sub> described in Chapter 2 (Scheme 38). To an orange color THF solution of (tmeda)Ni(CF<sub>3</sub>)<sub>2</sub> compound, bipym (1.0 equivalent) was added and the orange mixture was stirred at room temperature for 2 hours. The volatile material was evaporated, and an orange oil was obtained. The crude product was then extracted by DCM/Et<sub>2</sub>O mixed solvent, yielding a yellow solid as the final product (**1**) in 62% yield.

The XRD-suitable single crystals of **1** can be obtained *via* DCM-Et<sub>2</sub>O vapor diffusion at room temperature (Figure 39).



**Scheme 38.** Synthesis of (bipym)Ni(CF<sub>3</sub>)<sub>2</sub> (**1**) from (tmeda)Ni(CF<sub>3</sub>)<sub>2</sub> precursor.

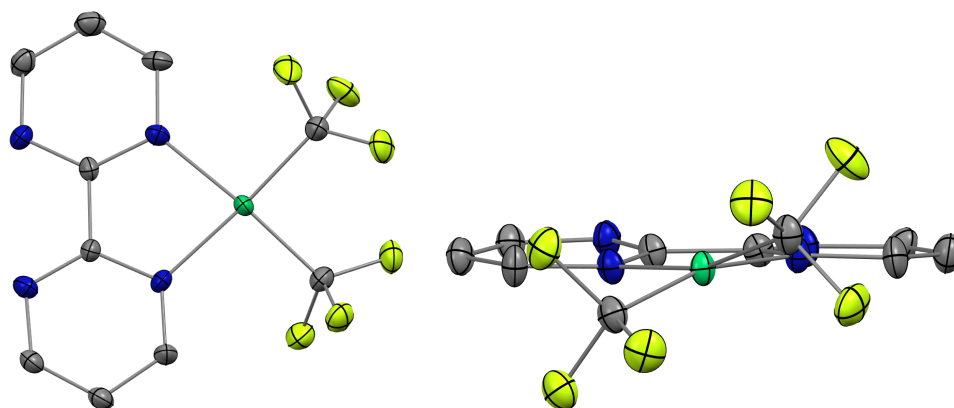


**Figure 39.** ORTEP of **1**. Thermal ellipsoids are at 50 % level. Two different orientations of the structure are presented. Carbon atoms are in grey, nitrogen in blue, fluorine in yellow and nickel atoms are in green. Hydrogen atoms are removed for clarity.

Main geometrical data (bond distances and angles) of **1** and the other complexes in this section are presented in Table 8. In **1**, an extremely distorted geometry, as 21°, from ideal square planarity can be identified as a result of the steric interaction of the *bis*-trifluoromethyl ligands. The average distances of Ni-N and Ni-CF<sub>3</sub> are 1.97(5) and 1.89(2) Å, respectively, indicating the divalent oxidation state of nickel center. The bond length of Ni-C in **1** is substantially shorter than the one found in the nonfluorinated (bipym)Ni(CH<sub>3</sub>)<sub>2</sub> analogue, whose distance is 1.930(3) Å. In comparison, the average Ni-N bond length in (bipym)Ni(CH<sub>3</sub>)<sub>2</sub> compound is 1.959(2) Å, which is slightly shorter than the one in **1**. These data are in good consistence with those in the reported (dtbpy)Ni(CF<sub>3</sub>)<sub>2</sub> analogue by Vicic, while differently, the largely asymmetric Ni-N and Ni-C bonds as they described is not observed in **1**.<sup>46</sup> The linkage C-C bond between two pyrimidine rings is 1.47(6) Å, similar to the one in (bipym)Ni(CH<sub>3</sub>)<sub>2</sub> congener as 1.482(5) Å.

<sup>1</sup>H NMR spectrum of **1** was recorded in THF-d<sup>8</sup> at 20°C, showing two signals for the bipym ligand, integrating four protons at 9.05 ppm as a multiplet and two at 7.67 ppm as a triplet (Figure 40). The spectrum nicely indicates a symmetric species (C<sub>2v</sub>) in solution. <sup>19</sup>F NMR of **1** recorded in THF-d<sup>8</sup> showed one signal at -28 ppm for the two equivalent CF<sub>3</sub> ligands on the nickel center (Figure 41).

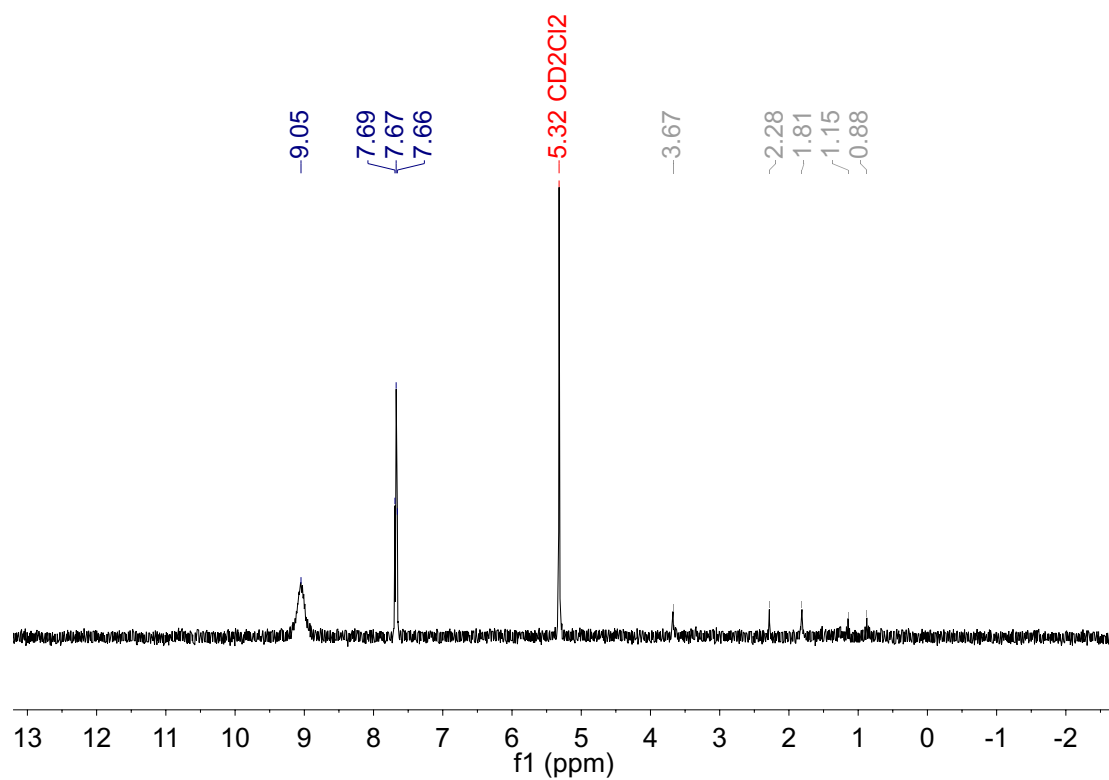


**Figure 40.** <sup>1</sup>H NMR of **1** in CD<sub>2</sub>Cl<sub>2</sub> at 20°C. Resonances of THF, n-pentane and tmeda impurities from the synthesis are indicated in grey.

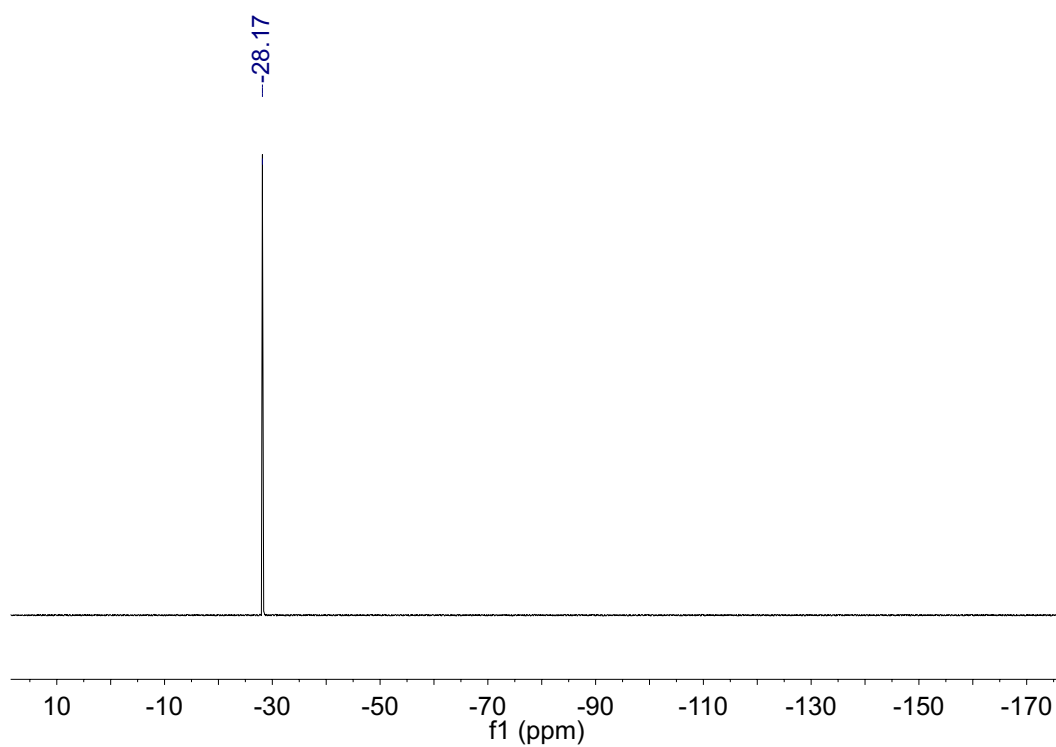
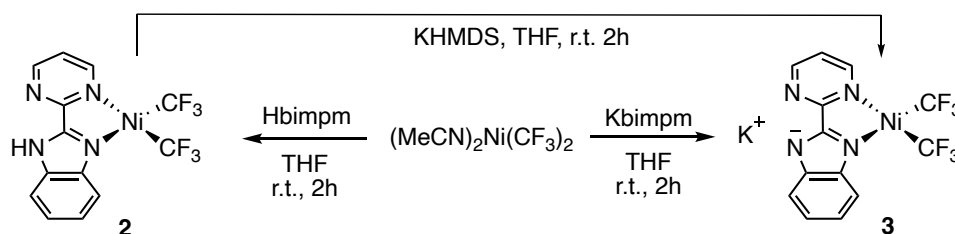


**Figure 41.** <sup>19</sup>F NMR of **1** in CD<sub>2</sub>Cl<sub>2</sub> at 20°C.

## 2.2. Original dissymmetric Ni(CF<sub>3</sub>)<sub>2</sub> complexes

In parallel, two other complexes were synthesized in attempt to differentiate the redox-active ligand system effect by using a dissymmetric ligand, namely 2-pyrimidin-2-yl-1H-benzimidazole, or Hbimp, as an abbreviation. The chemistry with this ligand and NiMe<sub>2</sub> fragments will be expatiated in *Chapter 4*.



**Scheme 39.** Synthesis of **2** and **3** from (MeCN)<sub>2</sub>Ni(CF<sub>3</sub>)<sub>2</sub> precursor.

Facile synthesis of dissymmetric CF<sub>3</sub> complexes **2** and **3** was performed by direct combination of the (MeCN)<sub>2</sub>Ni(CF<sub>3</sub>)<sub>2</sub> precursor with Hbimpm ligand in THF and with Kbimp<sup>-</sup>m, deprotonated by KHMDS prior to use, in MeCN, respectively (Scheme 39). Recrystallization by slow evaporation in THF at -40°C gave yellow crystals of **2**, which are suitable for XRD study (Figure 42). In **2**, noticeable asymmetry of Ni-N bonds as 1.96(8) and 2.00(5) Å, respectively. The difference between two Ni-C bonds is not remarkable (less than 0.01 Å). The average distance of Ni-C is 1.89(0) Å. A largely distorted geometry from the ideal planar structure is also noticed with an angle between the N-Ni-N and C-Ni-C planes of 21.4°. Moreover, a hydrogen bonding N-H···O between (Hbimpm)Ni(CF<sub>3</sub>)<sub>2</sub> and one co-crystallized THF solvate is found in the structure as 1.85(9) Å.

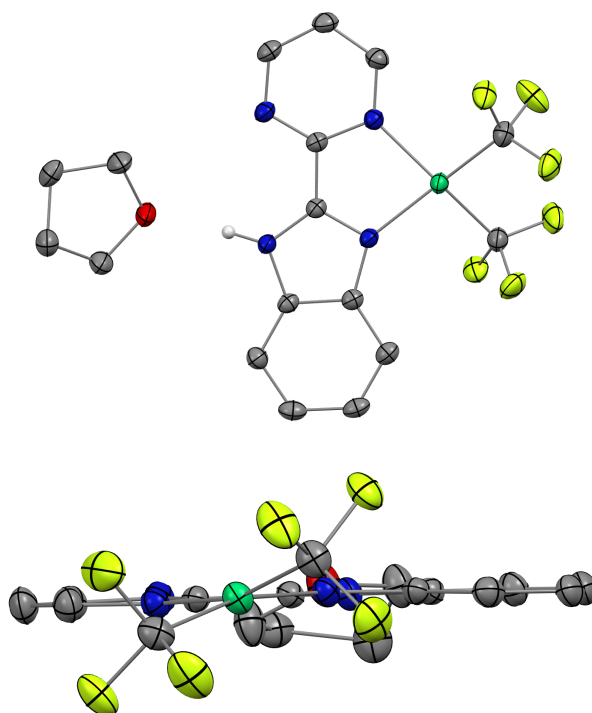


**Figure 42.** ORTEP of **2**. Thermal ellipsoids are at 50 % level. Two different orientations of the structure are presented. Carbon atoms are in grey, nitrogen in blue, oxygen in red, fluorine in yellow and nickel atoms are in green. Hydrogen atoms are in grey and removed for clarity except the one in the hydrogen bond.

The crystal structure of **3** was obtained from the bright yellow crystals, which can be isolated *via* CH<sub>3</sub>CN/Et<sub>2</sub>O vapor diffusion at room temperature (Figure 43). Likewise, a remarkable distortion to the planarity caused by the steric interaction of the trifluoromethyl groups is observed (20°). Considerably asymmetric Ni-N bond distances of 1.92(3) and 2.00(1) Å, respectively, are noticed; whereas the two nickel-carbon bonds are relatively equivalent, as the average distance of 1.884(5) Å.

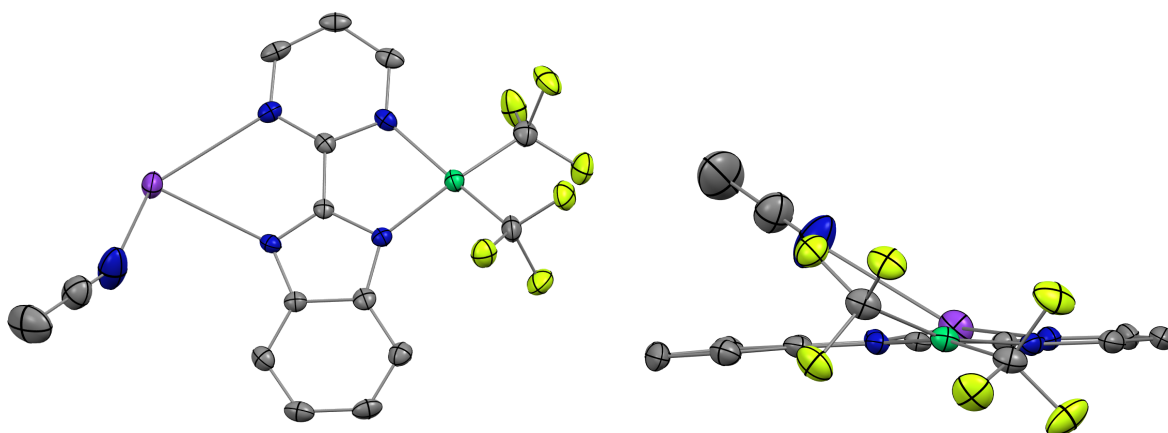


**Figure 43.** ORTEP of **3**. Thermal ellipsoids are at 50 % level. Two different orientations of the structure are presented. Carbon atoms are in grey, nitrogen in blue, fluorine in yellow, potassium in purple and nickel atoms are in green. Hydrogen atoms are removed for clarity.

**Table 8.** Representative geometrical parameters: average main distances (Å) and angles (°) for **1**, **2** and **3**.

	<b>1</b>	<b>2</b>	<b>3</b>
Ni-CF <sub>3</sub>	1.89(2)	1.89(0)	1.884(5)
Ni-N	1.986(5)	1.986(5)	1.96(2)
C-C <sub>in</sub> kage	1.47(6)	1.45(4)	1.45(6)
F <sub>3</sub> C-Ni-CF <sub>3</sub> <sup>^</sup> N-Ni-N	21	21	20

<sup>1</sup>H NMR spectra of **2** and **3** were recorded in THF-d<sup>8</sup> at 20°C. In the spectrum of **2**, it gives five signals for the bimpm ligand from 9.0 to 7.3 ppm, integrating as six protons. A remarkable signal at 13.61 ppm is attributed to the proton on the imidazole moiety, which is found in the XRD structure as a hydrogen bonding with one THF solvate. The co-crystallized THF molecule is also observed in the spectrum (Figure 44). Unfortunately, a clean <sup>19</sup>F NMR spectrum of the yellow crystalline **2** has not been obtained and it will be completed in the future.

<sup>1</sup>H NMR spectrum of **3** nicely shows six resonances in the range of 8.7 – 6.9 ppm, for the deprotonated bimpm ligand, integrating for seven protons (Figure 45). <sup>19</sup>F NMR spectrum of **3** shows two signals for two CF<sub>3</sub> ligands at -17.0 and -24.6 ppm, respectively, indicating a dissymmetric character of the molecule in solution (Figure 46).

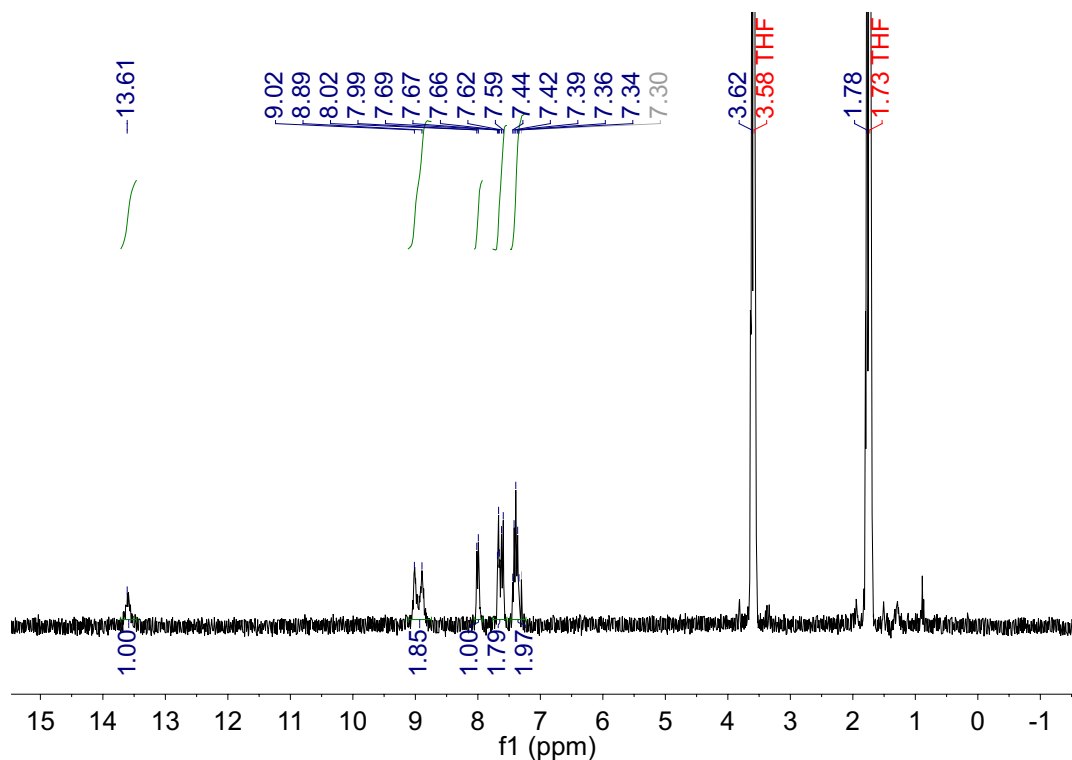


**Figure 44.** <sup>1</sup>H NMR of **2** in THF-d<sup>8</sup> at 20°C. Benzene impurity is indicated in grey.

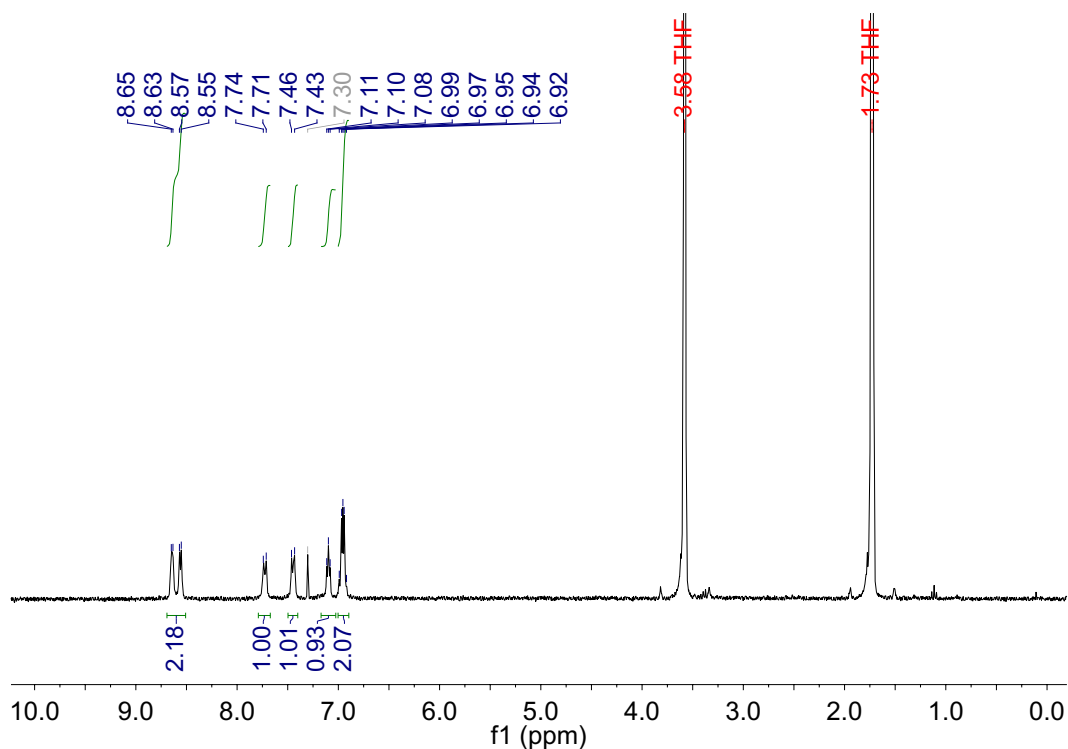


**Figure 45.**  $^1\text{H}$  NMR of **3** in  $\text{THF-d}_8$  at  $20^\circ\text{C}$ . Benzene impurity is indicated in grey.

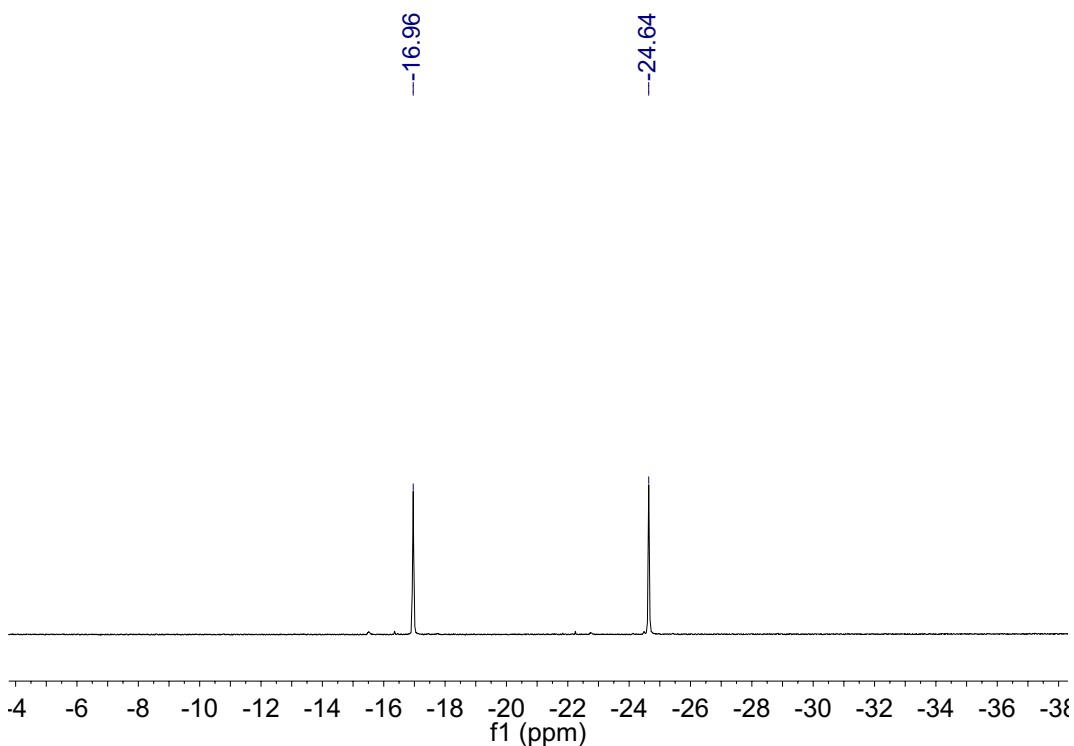


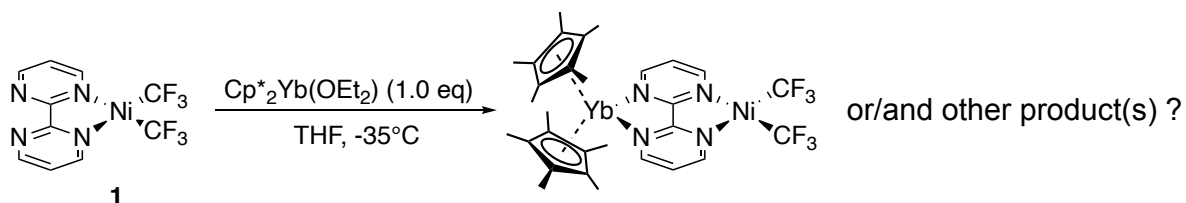
**Figure 46.**  $^{19}\text{F}$  NMR of **3** in  $\text{THF-d}_8$  at  $20^\circ\text{C}$ .

### 3. Coordination to divalent lanthanides

Similarly, as what was described in *Chapter 2* for nonfluorinated Ni complexes, it is expected that the addition of divalent lanthanide fragment leads to an efficient single electron transfer process. Thus, a brownish mixture was obtained instantly when combining a yellow solution of **1** (which has



less good solubility in THF than in DCM) and a red solution  $\text{Cp}^*_2\text{Yb}$  in THF. *In-situ*  $^1\text{H}$  NMR in THF- $d^8$  did not show decent resonances corresponding to the desired product, although there are no signals of the starting materials in the spectrum. The NMR of the brownish solid obtained from the reaction mixture after evaporation of the volatile and washing by  $\text{Et}_2\text{O}$ , was also silent (solely the resonances of deuterated solvent appeared).

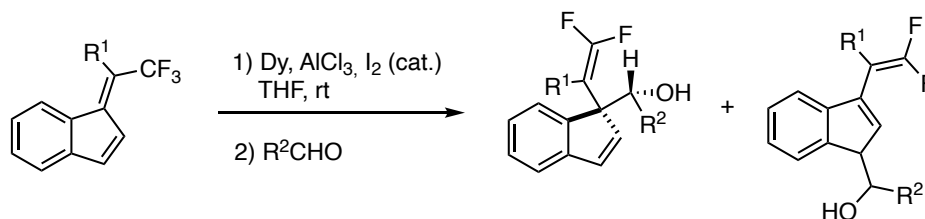


**Scheme 40.** Complexation of **1** with  $\text{Cp}^*_2\text{Yb}(\text{OEt}_2)$ .

The surprising fact silent nature in NMR of the crude mixture triggered us to hard try to crystallize the possible product. A lot of efforts were made in order to crystallize the crude product from such complexation reaction, such as using different solvents/mixed solvents, recrystallization speed control, or different temperatures; however, unfortunately, only brownish powder-like solid was obtained under any circumstances. After washing by  $\text{Et}_2\text{O}$  in order to remove the possibly unreacted  $\text{Cp}^*_2\text{Yb}$  species and removing the volatile material under reduced pressure, a brown crystalline-like solid could be obtained. “Blind” elemental analysis (found: C, 44.76; H, 4.82; N, 6.22; F, 10.4) on this product was performed under inert atmosphere, indicating a possible mixture of the desired  $\text{Cp}^*_2\text{Yb}(\text{bipym})\text{Ni}(\text{CF}_3)_2$  (expected: C, 45.13; H, 4.55; N, 7.02; F, 14.28),  $\text{Cp}^*_2\text{YbF}$  (expected: C, 51.94; H, 6.54; F, 4.11), which could be from the fluorine abstraction of lanthanide ion, and other by-product in the minimal amount. A proper way to isolate and recrystallize the seeming bimetallic product needs to be figured out and this challenging compound indeed is worth to take more effort in the future.

The coordination of  $\text{Cp}^*_2\text{Yb}(\text{OEt}_2)$  molecule with **3**, or with **2** in the presence of a strong base (such as KHMDS) was studied at the same time, in attempt to isolate a dissymmetric dinuclear complex. The reaction was performed in different solvents except the ones that are very good ligands for the ytterbocene fragment, such as MeCN and pyridine. A very deep brown reaction mixture was formed in both cases. The lack of solubility of **3** in many solvents required a long stirring (16 h) of the mixture at room temperature to ensure a complete reaction from a yellow suspension of **3** to the dark brown mixture. Recrystallization of this dark brownish product in toluene did not yield any crystalline solid but powder; however, in THF, brownish crystals were isolated and suitable by XRD. Instead of the desired bimetallic product, a  $\text{K}[\text{Cp}^*_2\text{YbF}_2]$  molecule was obtained, plausibly undergoing C-F activation mediated by divalent ytterbium, which then has been oxidized to trivalence, with an average Cp ring centroid to Yb center distance of 2.35(6) Å (Figure 47). This reactivity of C-F activation of polyfluorinated arenes not only with divalent ytterbium but also other f-elements, has been comprehensively described over the decades, mostly forming polynuclear or cluster Ln-F complexes.<sup>66–73</sup> More recently, Jaroschik *et al.* reported the first example in selective

C-F activation of trifluoromethylated benzofulvenes mediated by zero-valent lanthanide towards the formation of  $\epsilon,\epsilon$ -difluorinated lanthanide-pentadienyl species. In the presence of Lewis acidic  $\text{AlCl}_3$  salt, such dienyl-metal species as intermediates could react with aldehydes in high regio- and diastereoselectivity to generate fluorinated heterocyclic spiroindenes (Scheme 41).<sup>74</sup>



**Scheme 41.** Lanthanide(0)-mediated C-F activation via  $\epsilon,\epsilon$ -difluorinated metal-dienyl species in high regio- and diastereoselectivity reported by Jaroschik and co-workers.

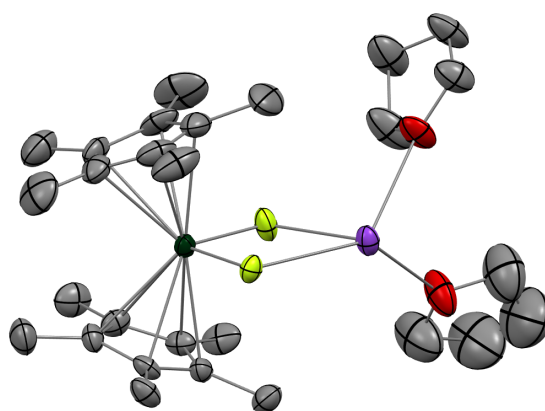
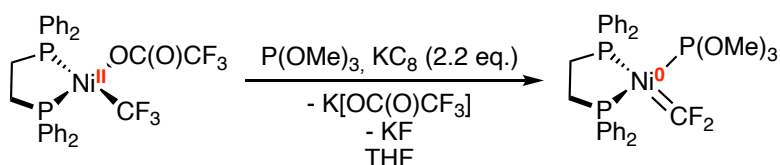


**Figure 47.** ORTEP of the crystallized product  $\text{Cp}^*_2\text{YbF}\cdot\text{KF}$  from the reaction mixture of **3** and  $\text{Cp}^*_2\text{Yb}(\text{OEt}_2)$  in THF. Thermal ellipsoids are at 50 % level. Only one of the molecules of the cell is shown. Carbon atoms are in grey, oxygen atoms in red, fluorine in yellow, potassium atom in purple and ytterbium in deep green. Hydrogen atoms have been omitted for clarity.

Following the stoichiometry, a nickel difluorocarbene species can be possibly generated from this reaction. This type of difluorocarbene compounds with nickel as well as cobalt was reported by Baker *et al.*, demonstrating potential relevance to fluoroalkene metathesis and polymerization.<sup>75,76</sup> This discovery could give another possible explanation for the C-F bond activation in our case. According to the study from Baker's group, they used potassium graphite in the presence of  $\text{P}(\text{OMe})_3$  to reduce a  $\text{Ni}(\text{II})\text{-CF}_3$  species to form a  $\text{Ni}(\text{0})=\text{CF}_2$  complex (Scheme 42). In our case, divalent ytterbium is a good reductant, even though not as strong as  $\text{KC}_8$ , and able to transfer an electron onto the ligand. Therefore, likely what Baker and co-workers described, this reduced  $\text{bimpm-Ni}(\text{CF}_3)_2$  fragment might undergo  $\alpha$ -fluorine elimination to give the possible perfluoroalkylidene complexes.<sup>77</sup> Also, the example of Baker's work is a good inspiration to continue getting insight into the mechanistic study of such reaction. The corresponding work, in particular the isolation of the possible difluorocarbene product from the stoichiometric reaction, is currently under study.



**Scheme 42.** Synthesis of a nickel difluorocarbene complex reported by Baker and co-workers.

#### 4. Reactivity attempts

Several reactivity tests were undertaken on **1** and **3**. Inspired by the above-mentioned examples of the synthetic approach to high-valent Ni species, electrophilic  $\text{CF}_3^+$  or  $\text{F}^+$  fluorinating reagents were considered to attempt. Stoichiometric amount of Umemoto reagent was added to **1** in THF at room temperature led to a hardly identified *in-situ*  $^1\text{H}$  NMR spectrum, and an eventual polymerization. Such polymerized product can be attributed to the high Lewis acidity of the ambiguously formed Ni(IV) species, leading to the ring-opening of THF solvent which could be more likely bonded to the metal center than the triflate anion. The same reaction was also performed in  $\text{CH}_2\text{Cl}_2$  yielded yellow-green mixture and an evolution to black precipitate at the end, even at  $-40^\circ\text{C}$ . The crude  $^1\text{H}$  NMR indicated barely no conclusion for the formed mixture in  $\text{CD}_2\text{Cl}_2$ . However, such reactivity attempts should be reconsidered with  $^{19}\text{F}$  NMR (at  $20^\circ\text{C}$  and low temperatures in parallel) in the important comparison with the desired heterobimetallic species in the future.

The anionic character of **3** would potentially lead to the generation of a neutral oxidized high-valent Ni species. Indeed, a yellow solid was formed immediately when combining **3** and fluorinating reagents, either the Umemoto reagent or NFTPT, with 1:1 ratio. However, this yellow solid is scarcely soluble in any solvent including acetone and methanol, but transiently solubilized in acid and fast decomposed in the end. Mass spectrometry (ESI-MS) analysis did not indicate the intense signal dedicated to the expected Ni(IV) species due to the very poor solubility in used solvents such as acetonitrile and methanol for analysis. It has also been observed of poor solubility with such bimp ligand in the following *Chapter 4*, mainly owing to the benzimidazole fragment in bimp. Modification of such ligand skeleton should be considered in order to increase the solubility.

#### 5. Conclusion and perspectives

In this chapter, three nickel complexes bearing redox-active ligands and two trifluoromethyl moieties were synthesized and characterized by XRD and  $^1\text{H}$  NMR. Unfortunately, the complexation towards the desired heterobimetallic species with divalent lanthanides led to either unidentified product or a C-F bond activation of  $\text{CF}_3$  ligand on the nickel center. Nevertheless, based on the rich chemistry in high-valent metal complexes as well as attracting electronic properties of trifluoromethyl ligands, this study should be continued and optimized into some interesting attempts.

Additionally, modification of the  $\text{CF}_3$  functional groups into other perfluoroalkyl ligand such as the chelating  $[\text{C}_4\text{F}_8]$  unit mentioned above by Vicic, could be prospectively considered for the further investigation in attempt to the synthesis of high-valent Ni species. The challenge of concomitant C-F bond activation would not minimize at this step; however, it could also bring a new cyclo-perfluorocarbene species as product. Although the hypothesized Ni difluorocarbene species clearly requires more experimental insights, such difluorocarbene species, in the presence of labile ligands,<sup>78</sup> could be applied into an important field of fluoro-organic chemistry,<sup>79</sup> such as accessing to diversified fluoroalkylated arenes.<sup>80</sup>

## References

- (1) Aihara, Y.; Tobisu, M.; Fukumoto, Y.; Chatani, N. Ni(II)-Catalyzed Oxidative Coupling between C(Sp<sup>2</sup>)-H in Benzamides and C(Sp<sup>3</sup>)-H in Toluene Derivatives. *J. Am. Chem. Soc.* **2014**, *136* (44), 15509–15512. <https://doi.org/10.1021/ja5095342>.
- (2) Aihara, Y.; Chatani, N. Nickel-Catalyzed Direct Arylation of C(Sp<sup>3</sup>)-H Bonds in Aliphatic Amides via Bidentate-Chelation Assistance. *J. Am. Chem. Soc.* **2014**, *136* (3), 898–901. <https://doi.org/10.1021/ja411715v>.
- (3) Omer, H. M.; Liu, P. Computational Study of Ni-Catalyzed C-H Functionalization: Factors That Control the Competition of Oxidative Addition and Radical Pathways. *J. Am. Chem. Soc.* **2017**, *139* (29), 9909–9920. <https://doi.org/10.1021/jacs.7b03548>.
- (4) Li, Y.; Zou, L.; Bai, R.; Lan, Y. Ni(I)-Ni(III) vs. Ni(II)-Ni(IV): Mechanistic Study of Ni-Catalyzed Alkylation of Benzamides with Alkyl Halides. *Org. Chem. Front.* **2018**, *5* (4), 615–622. <https://doi.org/10.1039/C7QO00850C>.
- (5) Beattie, D. D.; Grunwald, A. C.; Perse, T.; Schafer, L. L.; Love, J. A. Understanding Ni(II)-Mediated C(Sp<sup>3</sup>)-H Activation: Tertiary Ureas as Model Substrates. *J. Am. Chem. Soc.* **2018**, *140* (39), 12602–12610. <https://doi.org/10.1021/jacs.8b07708>.
- (6) Camasso, N. M.; Sanford, M. S. Design, Synthesis, and Carbon-Heteroatom Coupling Reactions of Organometallic Nickel(IV) Complexes. *Science* **2015**, *347* (6227), 1218–1220. <https://doi.org/10.1126/science.aaa4526>.
- (7) Schultz, J. W.; Fuchigami, K.; Zheng, B.; Rath, N. P.; Mirica, L. M. Isolated Organometallic Nickel(III) and Nickel(IV) Complexes Relevant to Carbon-Carbon Bond Formation Reactions. *J. Am. Chem. Soc.* **2016**, *138* (39), 12928–12934. <https://doi.org/10.1021/jacs.6b06862>.
- (8) Furuya, T.; Kamlet, A. S.; Ritter, T. Catalysis for Fluorination and Trifluoromethylation. *Nature* **2011**, *473* (7348), 470–477. <https://doi.org/10.1038/nature10108>.
- (9) Umemoto, T. Electrophilic Perfluoroalkylating Agents. *Chem. Rev.* **1996**, *96* (5), 1757–1778. <https://doi.org/10.1021/cr941149u>.
- (10) D'Accriscio, F.; Borja, P.; Saffon-Merceron, N.; Fustier-Boutignon, M.; Mézailles, N.; Nebra, N. C-H Bond Trifluoromethylation of Arenes Enabled by a Robust, High-Valent Nickel(IV) Complex. *Angew. Chem. Int. Ed.* **2017**, *56* (42), 12898–12902. <https://doi.org/10.1002/anie.201706237>.
- (11) Purser, S.; Moore, P. R.; Swallow, S.; Gouverneur, V. Fluorine in Medicinal Chemistry. *Chem. Soc. Rev.* **2008**, *37* (2), 320–330. <https://doi.org/10.1039/B610213C>.
- (12) Park, B. K.; Kitteringham, N. R.; O'Neill, P. M. Metabolism of Fluorine-Containing Drugs. *Annu. Rev. Pharmacol. Toxicol.* **2001**, *41* (1), 443–470. <https://doi.org/10.1146/annurev.pharmtox.41.1.443>.
- (13) Müller, K.; Faeh, C.; Diederich, F. Fluorine in Pharmaceuticals: Looking Beyond Intuition. *Science* **2007**, *317* (5846), 1881–1886. <https://doi.org/10.1126/science.1131943>.
- (14) Hagmann, W. K. The Many Roles for Fluorine in Medicinal Chemistry. *J. Med. Chem.* **2008**, *51* (15), 4359–4369. <https://doi.org/10.1021/jm800219f>.
- (15) McClinton, M. A.; McClinton, D. A. Trifluoromethylations and Related Reactions in Organic Chemistry. *Tetrahedron* **1992**, *48* (32), 6555–6666. [https://doi.org/10.1016/S0040-4020\(01\)80011-9](https://doi.org/10.1016/S0040-4020(01)80011-9).
- (16) Liang, T.; Neumann, C. N.; Ritter, T. Introduction of Fluorine and Fluorine-Containing Functional Groups. *Angew. Chem. Int. Ed.* **2013**, *52* (32), 8214–8264. <https://doi.org/10.1002/anie.201206566>.
- (17) Charpentier, J.; Früh, N.; Togni, A. Electrophilic Trifluoromethylation by Use of Hypervalent Iodine Reagents. *Chem. Rev.* **2015**, *115* (2), 650–682. <https://doi.org/10.1021/cr500223h>.
- (18) Alonso, C.; Martínez de Marigorta, E.; Rubiales, G.; Palacios, F. Carbon Trifluoromethylation Reactions of Hydrocarbon Derivatives and Heteroarenes. *Chem. Rev.* **2015**, *115* (4), 1847–1935. <https://doi.org/10.1021/cr500368h>.
- (19) Kirsch, P. *Modern Fluoroorganic Chemistry: Synthesis, Reactivity, Applications*; John Wiley & Sons, 2013.

- (20) Hiyama, T.; Yamamoto, H. Reagents for Fluorination. In *Organofluorine Compounds: Chemistry and Applications*; Hiyama, T., Yamamoto, H., Eds.; Springer: Berlin, Heidelberg, 2000; pp 25–76. [https://doi.org/10.1007/978-3-662-04164-2\\_2](https://doi.org/10.1007/978-3-662-04164-2_2).
- (21) Prakash, G. K. S.; Yudin, A. K. Perfluoroalkylation with Organosilicon Reagents. *Chem. Rev.* **1997**, *97* (3), 757–786. <https://doi.org/10.1021/cr9408991>.
- (22) Singh, R. P.; Shreeve, J. M. Nucleophilic Trifluoromethylation Reactions of Organic Compounds with (Trifluoromethyl)Trimethylsilane. *Tetrahedron* **2000**, *56* (39), 7613–7632. [https://doi.org/10.1016/S0040-4020\(00\)00550-0](https://doi.org/10.1016/S0040-4020(00)00550-0).
- (23) Cho, E. J.; Senecal, T. D.; Kinzel, T.; Zhang, Y.; Watson, D. A.; Buchwald, S. L. The Palladium-Catalyzed Trifluoromethylation of Aryl Chlorides. *Science* **2010**, *328* (5986), 1679–1681. <https://doi.org/10.1126/science.1190524>.
- (24) Lundgren, R. J.; Stradiotto, M. Transition-Metal-Catalyzed Trifluoromethylation of Aryl Halides. *Angew. Chem. Int. Ed.* **2010**, *49* (49), 9322–9324. <https://doi.org/10.1002/anie.201004051>.
- (25) Ye, Y.; Lee, S. H.; Sanford, M. S. Silver-Mediated Trifluoromethylation of Arenes Using TMSCF<sub>3</sub>. *Org. Lett.* **2011**, *13* (20), 5464–5467. <https://doi.org/10.1021/ol202174a>.
- (26) Tomashenko, O. A.; Grushin, V. V. Aromatic Trifluoromethylation with Metal Complexes. *Chem. Rev.* **2011**, *111* (8), 4475–4521. <https://doi.org/10.1021/cr1004293>.
- (27) Grushin, V. V.; Marshall, W. J. Unexpected H<sub>2</sub>O-Induced Ar–X Activation with Trifluoromethylpalladium(II) Aryls. *J. Am. Chem. Soc.* **2006**, *128* (14), 4632–4641. <https://doi.org/10.1021/ja0602389>.
- (28) Martínez-Salvador, S.; Forniés, J.; Martín, A.; Menjón, B. [Au(CF<sub>3</sub>)(CO)]: A Gold Carbonyl Compound Stabilized by a Trifluoromethyl Group. *Angew. Chem. Int. Ed.* **2011**, *50* (29), 6571–6574. <https://doi.org/10.1002/anie.201101231>.
- (29) Kieltch, I.; Dubinina, G. G.; Hamacher, C.; Kaiser, A.; Torres-Nieto, J.; Hutchison, J. M.; Klein, A.; Budnikova, Y.; Vivic, D. A. Magnitudes of Electron-Withdrawing Effects of the Trifluoromethyl Ligand in Organometallic Complexes of Copper and Nickel. *Organometallics* **2010**, *29* (6), 1451–1456. <https://doi.org/10.1021/om901122z>.
- (30) Naumann, D.; Roy, T.; Tebbe, K.-F.; Crump, W. Synthesis and Structure of Surprisingly Stable Tetrakis(Trifluoromethyl)Cuprate(III) Salts. *Angew. Chem. Int. Ed. Engl.* **1993**, *32* (10), 1482–1483. <https://doi.org/10.1002/anie.199314821>.
- (31) Snyder, J. P. Elusiveness of Cu(III) Complexation; Preference for Trifluoromethyl Oxidation in the Formation of [Cu(CF<sub>3</sub>)<sub>4</sub>]<sup>–</sup> Salts. *Angew. Chem. Int. Ed. Engl.* **1995**, *34* (1), 80–81. <https://doi.org/10.1002/anie.199500801>.
- (32) Kaupp, M.; Schnering, H. G. von. Formal Oxidation State versus Partial Charge—A Comment. *Angew. Chem. Int. Ed. Engl.* **1995**, *34* (9), 986–986. <https://doi.org/10.1002/anie.199509861>.
- (33) Gao, C.; Macetti, G.; Overgaard, J. Experimental X-Ray Electron Density Study of Atomic Charges, Oxidation States, and Inverted Ligand Field in Cu(CF<sub>3</sub>)<sub>4</sub><sup>–</sup>. *Inorg. Chem.* **2019**, *58* (3), 2133–2139. <https://doi.org/10.1021/acs.inorgchem.8b03226>.
- (34) Weske, S.; Hardin, R. A.; Auth, T.; O’Hair, R. A. J.; Koszinowski, K.; Ogle, C. A. Argentate(I) and (III) Complexes as Intermediates in Silver-Mediated Cross-Coupling Reactions. *Chem. Commun.* **2018**, *54* (40), 5086–5089. <https://doi.org/10.1039/C8CC01707G>.
- (35) Baya, M.; Joven-Sancho, D.; Alonso, P. J.; Orduna, J.; Menjón, B. M–C Bond Homolysis in Coinage-Metal [M(CF<sub>3</sub>)<sub>4</sub>]<sup>–</sup> Derivatives. *Angew. Chem. Int. Ed.* **2019**, *58* (29), 9954–9958. <https://doi.org/10.1002/anie.201903496>.
- (36) Hoffmann, R.; Alvarez, S.; Mealli, C.; Falceto, A.; Cahill, T. J.; Zeng, T.; Manca, G. From Widely Accepted Concepts in Coordination Chemistry to Inverted Ligand Fields. *Chem. Rev.* **2016**, *116* (14), 8173–8192. <https://doi.org/10.1021/acs.chemrev.6b00251>.
- (37) Snyder, J. P. Distinguishing Copper D<sub>8</sub> and D<sub>10</sub> Configurations in a Highly Ionic Complex; A Nonformal Metal Oxidation State. *Angew. Chem. Int. Ed. Engl.* **1995**, *34* (9), 986–987. <https://doi.org/10.1002/anie.199509862>.
- (38) Walroth, R. C.; Lukens, J. T.; MacMillan, S. N.; Finkelstein, K. D.; Lancaster, K. M. Spectroscopic Evidence for a 3d<sup>10</sup> Ground State Electronic Configuration and Ligand Field

- Inversion in [Cu(CF<sub>3</sub>)<sub>4</sub>]<sup>1-</sup>. *J. Am. Chem. Soc.* **2016**, *138* (6), 1922–1931. <https://doi.org/10.1021/jacs.5b10819>.
- (39) DiMucci, I. M.; Lukens, J. T.; Chatterjee, S.; Carsch, K. M.; Titus, C. J.; Lee, S. J.; Nordlund, D.; Betley, T. A.; MacMillan, S. N.; Lancaster, K. M. The Myth of D<sub>8</sub> Copper(III). *J. Am. Chem. Soc.* **2019**, *141* (46), 18508–18520. <https://doi.org/10.1021/jacs.9b09016>.
- (40) Shreiber, S. T.; DiMucci, I. M.; Khrizanforov, M.; Titus, C. J.; Nordlund, D.; Dudkina, Y. B.; Cramer, R. E.; Budnikova, Y.; Lancaster, K. M.; Vivic, D. [(MeCN)Ni(CF<sub>3</sub>)<sub>3</sub>]<sup>1-</sup> and [Ni(CF<sub>3</sub>)<sub>4</sub>]<sup>2-</sup>: Foundations Towards the Development of Trifluoromethylations at Unsupported Nickel. **2020**. <https://doi.org/10.26434/chemrxiv.12071673.v1>.
- (41) Bour, J. R.; Camasso, N. M.; Sanford, M. S. Oxidation of Ni(II) to Ni(IV) with Aryl Electrophiles Enables Ni-Mediated Aryl–CF<sub>3</sub> Coupling. *J. Am. Chem. Soc.* **2015**, *137* (25), 8034–8037. <https://doi.org/10.1021/jacs.5b04892>.
- (42) Steen, J. S.; Knizia, G.; Klein, J. E. M. N. σ-Noninnocence: Masked Phenyl-Cation Transfer at Formal NiIV. *Angew. Chem. Int. Ed.* **2019**, *58* (37), 13133–13139. <https://doi.org/10.1002/anie.201906658>.
- (43) Mondal, B.; Ye, S. Hidden Ligand Noninnocence: A Combined Spectroscopic and Computational Perspective. *Coord. Chem. Rev.* **2020**, *405*, 213115. <https://doi.org/10.1016/j.ccr.2019.213115>.
- (44) Algarra, A. G.; Grushin, V. V.; Macgregor, S. A. Natural Bond Orbital Analysis of the Electronic Structure of [LnM(CH<sub>3</sub>)] and [LnM(CF<sub>3</sub>)] Complexes. *Organometallics* **2012**, *31* (4), 1467–1476. <https://doi.org/10.1021/om2011003>.
- (45) Yang, D. S.; Bancroft, G. M.; Dignard-Bailey, L.; Puddephatt, R. J.; Tse, J. S. Electronic Structure of Cis-Dimethylplatinum(II) Complexes from UV Photoelectron Spectra and SCF-MS-X.Alpha. Calculations. *Inorg. Chem.* **1990**, *29* (13), 2487–2495. <https://doi.org/10.1021/ic00338a020>.
- (46) Yamaguchi, Y.; Ichioka, H.; Klein, A.; Brennessel, W. W.; Vivic, D. A. Linear Bis(Perfluoroalkyl) Complexes of Nickel Bipyridine. *Organometallics* **2012**, *31* (4), 1477–1483. <https://doi.org/10.1021/om2012776>.
- (47) Jacquet, J.; Salanouve, E.; Orio, M.; Vezin, H.; Blanchard, S.; Derat, E.; Murr, M. D.-E.; Fensterbank, L. Iminosemiquinone Radical Ligands Enable Access to a Well-Defined Redox-Active CuI–CF<sub>3</sub> Complex. *Chem. Commun.* **2014**, *50* (72), 10394–10397. <https://doi.org/10.1039/C4CC04487H>.
- (48) Jacquet, J.; Blanchard, S.; Derat, E.; Murr, M. D.-E.; Fensterbank, L. Redox-Ligand Sustains Controlled Generation of CF<sub>3</sub> Radicals by Well-Defined Copper Complex. *Chem. Sci.* **2016**, *7* (3), 2030–2036. <https://doi.org/10.1039/C5SC03636D>.
- (49) Jacquet, J.; Chaumont, P.; Gontard, G.; Orio, M.; Vezin, H.; Blanchard, S.; Desage-El Murr, M.; Fensterbank, L. C–N Bond Formation from a Masked High-Valent Copper Complex Stabilized by Redox Non-Innocent Ligands. *Angew. Chem. Int. Ed.* **2016**, *55* (36), 10712–10716. <https://doi.org/10.1002/anie.201605132>.
- (50) Jacquet, J.; Cheaib, K.; Ren, Y.; Vezin, H.; Orio, M.; Blanchard, S.; Fensterbank, L.; Desage-El Murr, M. Circumventing Intrinsic Metal Reactivity: Radical Generation with Redox-Active Ligands. *Chem. – Eur. J.* **2017**, *23* (60), 15030–15034. <https://doi.org/10.1002/chem.201704049>.
- (51) Tsou, T. T.; Kochi, J. K. Reductive Coupling of Organometals Induced by Oxidation. Detection of Metastable Paramagnetic Intermediates. *J. Am. Chem. Soc.* **1978**, *100* (5), 1634–1635. <https://doi.org/10.1021/ja00473a067>.
- (52) Nebra, N. High-Valent NiIII and NiIV Species Relevant to C–C and C–Heteroatom Cross-Coupling Reactions: State of the Art. *Molecules* **2020**, *25* (5), 1141. <https://doi.org/10.3390/molecules25051141>.
- (53) Lipschutz, M. I.; Yang, X.; Chatterjee, R.; Tilley, T. D. A Structurally Rigid Bis(Amido) Ligand Framework in Low-Coordinate Ni(I), Ni(II), and Ni(III) Analogues Provides Access to a Ni(III)

- Methyl Complex via Oxidative Addition. *J. Am. Chem. Soc.* **2013**, *135* (41), 15298–15301. <https://doi.org/10.1021/ja408151h>.
- (54) Lipschutz, M. I.; Tilley, T. D. Carbon–Carbon Cross-Coupling Reactions Catalyzed by a Two-Coordinate Nickel(II)–Bis(Amido) Complex via Observable NiI, NiII, and NiIII Intermediates. *Angew. Chem. Int. Ed.* **2014**, *53* (28), 7290–7294. <https://doi.org/10.1002/anie.201404577>.
- (55) Mirica, L. M.; Smith, S. M.; Griego, L. Organometallic Chemistry of High-Valent Ni(III) and Ni(IV) Complexes. In *Nickel Catalysis in Organic Synthesis*; John Wiley & Sons, Ltd, 2019; pp 223–248. <https://doi.org/10.1002/9783527813827.ch10>.
- (56) Zheng, B.; Tang, F.; Luo, J.; Schultz, J. W.; Rath, N. P.; Mirica, L. M. Organometallic Nickel(III) Complexes Relevant to Cross-Coupling and Carbon–Heteroatom Bond Formation Reactions. *J. Am. Chem. Soc.* **2014**, *136* (17), 6499–6504. <https://doi.org/10.1021/ja5024749>.
- (57) Tang, F.; Rath, N. P.; Mirica, L. M. Stable Bis(Trifluoromethyl)Nickel(III) Complexes. *Chem. Commun.* **2015**, *51* (15), 3113–3116. <https://doi.org/10.1039/C4CC09594D>.
- (58) Smith, S. M.; Rath, N. P.; Mirica, L. M. Axial Donor Effects on Oxidatively Induced Ethane Formation from Nickel–Dimethyl Complexes. *Organometallics* **2019**, *38* (19), 3602–3609. <https://doi.org/10.1021/acs.organomet.9b00438>.
- (59) Zhou, W.; Zheng, S.; Schultz, J. W.; Rath, N. P.; Mirica, L. M. Aromatic Cyanoalkylation through Double C–H Activation Mediated by Ni(III). *J. Am. Chem. Soc.* **2016**, *138* (18), 5777–5780. <https://doi.org/10.1021/jacs.6b02405>.
- (60) Zhang, C.-P.; Wang, H.; Klein, A.; Biewer, C.; Stirnat, K.; Yamaguchi, Y.; Xu, L.; Gomez-Benitez, V.; Vivic, D. A. A Five-Coordinate Nickel(II) Fluoroalkyl Complex as a Precursor to a Spectroscopically Detectable Ni(III) Species. *J. Am. Chem. Soc.* **2013**, *135* (22), 8141–8144. <https://doi.org/10.1021/ja4030462>.
- (61) Yu, S.; Dudkina, Y.; Wang, H.; Kholin, K. V.; Kadirov, M. K.; Budnikova, Y. H.; Vivic, D. A. Accessing Perfluoroalkyl Nickel(II), (III), and (IV) Complexes Bearing a Readily Attached [C4F8] Ligand. *Dalton Trans.* **2015**, *44* (45), 19443–19446. <https://doi.org/10.1039/C5DT01771H>.
- (62) Camasso, N. M.; Canty, A. J.; Ariafard, A.; Sanford, M. S. Experimental and Computational Studies of High-Valent Nickel and Palladium Complexes. *Organometallics* **2017**, *36* (22), 4382–4393. <https://doi.org/10.1021/acs.organomet.7b00613>.
- (63) Roberts, C. C.; Camasso, N. M.; Bowes, E. G.; Sanford, M. S. Impact of Oxidation State on Reactivity and Selectivity Differences between Nickel(III) and Nickel(IV) Alkyl Complexes. *Angew. Chem. Int. Ed.* **2019**, *58* (27), 9104–9108. <https://doi.org/10.1002/anie.201903638>.
- (64) Meucci, E. A.; Nguyen, S. N.; Camasso, N. M.; Chong, E.; Ariafard, A.; Canty, A. J.; Sanford, M. S. Nickel(IV)-Catalyzed C–H Trifluoromethylation of (Hetero)Arenes. *J. Am. Chem. Soc.* **2019**, *141* (32), 12872–12879. <https://doi.org/10.1021/jacs.9b06383>.
- (65) Rovira, M.; Roldán-Gómez, S.; Martin-Diaconescu, V.; Whiteoak, C. J.; Company, A.; Luis, J. M.; Ribas, X. Trifluoromethylation of a Well-Defined Square-Planar Aryl-NiIII Complex Involving NiIII/CF<sub>3</sub> and NiIV–CF<sub>3</sub> Intermediate Species. *Chem. – Eur. J.* **2017**, *23* (48), 11662–11668. <https://doi.org/10.1002/chem.201702168>.
- (66) Deacon, G. B.; Harris, S. C.; Meyer, G.; Stellfeldt, D.; Wilkinson, D. L.; Zelesny, G. Organolanthanoids: XXII.1Part XX, [1], Part XXI, Aust. J. Chem. 50 (1997) 959.1 The Synthesis and X-Ray Structure of Dimeric [YbCp<sub>2</sub>F(THF)]<sub>2</sub> (Cp=cyclopentadienyl; THF=tetrahydrofuran). *J. Organomet. Chem.* **1998**, *552* (1), 165–170. [https://doi.org/10.1016/S0022-328X\(97\)00584-6](https://doi.org/10.1016/S0022-328X(97)00584-6).
- (67) Burns, C. J.; Berg, D. J.; Andersen, R. A. Preparation and Crystal Structure of the Mixed-Valence (YbIII,II) Tetranuclear Complex, (Me<sub>5</sub>C<sub>5</sub>)<sub>6</sub>Yb(μ-F)<sub>4</sub>. *J. Chem. Soc. Chem. Commun.* **1987**, No. 4, 272–273. <https://doi.org/10.1039/C39870000272>.
- (68) Watson, P. L.; Tulip, T. H.; Williams, I. Defluorination of Perfluoroolefins by Divalent Lanthanoid Reagents: Activating Carbon–Fluorine Bonds. *Organometallics* **1990**, *9* (7), 1999–2009. <https://doi.org/10.1021/om00157a006>.



- (69) Deacon, G. B.; Meyer, G.; Stellfeldt, D. Syntheses and Structures of Bis(Aryloxo)Fluoroytterbium(III) Complexes,  $[\text{Yb}(\text{OAr})_2\text{F}(\text{THF})]_2$  (OAr = OC<sub>6</sub>H<sub>2</sub>-2,6-TBu<sub>2</sub>-4-R; R = H, Me, TBu), and Bis(Cyclopentadienyl)Fluoroytterbium(III) Complexes,  $[\text{YbCp}_2\text{F}]_3$ ,  $[\text{Yb}(\text{MeCp})_2\text{F}]_4$ ,  $[\text{YbCp}_2\text{F}(\text{OPPh}_3)]_2$ , and  $[\text{Yb}(\text{MeCp})_2\text{F}(\text{THF})]_2$ . *Eur. J. Inorg. Chem.* **2000**, 2000 (5), 1061–1071. [https://doi.org/10.1002/\(SICI\)1099-0682\(200005\)2000:5<1061::AID-EJIC1061>3.0.CO;2-7](https://doi.org/10.1002/(SICI)1099-0682(200005)2000:5<1061::AID-EJIC1061>3.0.CO;2-7).
- (70) Cole, M. L.; Deacon, G. B.; Junk, P. C.; Konstas, K. Steric Engineering of C–F Activation with Lanthanoid Formamidinates. *Chem. Commun.* **2005**, No. 12, 1581–1583. <https://doi.org/10.1039/B419047E>.
- (71) Deacon, G. B.; Forsyth, C. M.; Junk, P. C.; Wang, J. Intramolecular Metal–Fluorocarbon Coordination, C–F Bond Activation and Lanthanoid–Fluoride Clusters with Tethered Polyfluorophenylamide Ligands. *Chem. – Eur. J.* **2009**, 15 (13), 3082–3092. <https://doi.org/10.1002/chem.200802294>.
- (72) Dorn, H.; Murphy, E. F.; Shah, S. A. A.; Roesky, H. W. Organometallic Fluorides of the Lanthanide and Actinide Elements. *J. Fluor. Chem.* **1997**, 86 (2), 121–125. [https://doi.org/10.1016/S0022-1139\(97\)00081-X](https://doi.org/10.1016/S0022-1139(97)00081-X).
- (73) Kiplinger, J. L.; Richmond, T. G.; Osterberg, C. E. Activation of Carbon–Fluorine Bonds by Metal Complexes. *Chem. Rev.* **1994**, 94 (2), 373–431. <https://doi.org/10.1021/cr00026a005>.
- (74) Kumar, T.; Massicot, F.; Harakat, D.; Chevreux, S.; Martinez, A.; Bordolinska, K.; Preethalayam, P.; Kokkuvayil Vasu, R.; Behr, J.-B.; Vasse, J.-L.; Jaroschik, F. Generation of  $\epsilon,\epsilon$ -Difluorinated Metal–Pentadienyl Species through Lanthanide-Mediated C–F Activation. *Chem. – Eur. J.* **2017**, 23 (65), 16460–16465. <https://doi.org/10.1002/chem.201704322>.
- (75) Harrison, D. J.; Daniels, A. L.; Korobkov, I.; Baker, R. T. D10 Nickel Difluorocarbenes and Their Cycloaddition Reactions with Tetrafluoroethylene. *Organometallics* **2015**, 34 (24), 5683–5686. <https://doi.org/10.1021/acs.organomet.5b00808>.
- (76) Harrison, D. J.; Lee, G. M.; Leclerc, M. C.; Korobkov, I.; Baker, R. T. Cobalt Fluorocarbenes: Cycloaddition Reactions with Tetrafluoroethylene and Reactivity of the Perfluorometallacyclic Products. *J. Am. Chem. Soc.* **2013**, 135 (49), 18296–18299. <https://doi.org/10.1021/ja411503c>.
- (77) Bourgeois, C. J.; Hughes, R. P.; Yuan, J.; DiPasquale, A. G.; Rheingold, A. L.  $\alpha$ - and  $\beta$ -Fluorine Elimination Reactions Induced by Reduction of Iridium–Fluoroalkyl Complexes. Selective Formation of Fluoroalkylidene and Hydrofluoroalkene Ligands. *Organometallics* **2006**, 25 (12), 2908–2910. <https://doi.org/10.1021/om060243l>.
- (78) Harrison, D. J.; Daniels, A. L.; Guan, J.; Gabidullin, B. M.; Hall, M. B.; Baker, R. T. Nickel Fluorocarbene Metathesis with Fluoroalkenes. *Angew. Chem. Int. Ed.* **2018**, 57 (20), 5772–5776. <https://doi.org/10.1002/anie.201802090>.
- (79) Fu, X.-P.; Xue, X.-S.; Zhang, X.-Y.; Xiao, Y.-L.; Zhang, S.; Guo, Y.-L.; Leng, X.; Houk, K. N.; Zhang, X. Controllable Catalytic Difluorocarbene Transfer Enables Access to Diversified Fluoroalkylated Arenes. *Nat. Chem.* **2019**, 11 (10), 948–956. <https://doi.org/10.1038/s41557-019-0331-9>.
- (80) Jaroschik, F. Picking One out of Three: Selective Single C–F Activation in Trifluoromethyl Groups. *Chem. – Eur. J.* **2018**, 24 (55), 14572–14582. <https://doi.org/10.1002/chem.201801702>.

# Reductive C-C coupling between redox-active dissymmetric ligands in divalent organolanthanides with reactive nickel fragment

Complexes with redox-active ligands have been extensively studied in recent years. This class of ligands is known to possess a large delocalization extent added to a low-lying  $\pi^*$  system in using *N*-heterocyclic ligands.<sup>1</sup> The ligand noninnocence can not only affect the spin state of the complex by electron transfer capacity, ultimately the reactivity of the metal center, but also that at the ligand site, mainly undergoing radical reactions with the stored electron(s). One of the consequentially redox transformations for the latter situation involves bond coupling formation between ligands intra- or intermolecularly with or without reversibility. Nevertheless, the concomitant bond formation within ligands does not affect the redox noninnocence in the further reactivity based on multielectron redox systems.<sup>2,3</sup>

In divalent organolanthanides, redox-active ligand coupling reactivity has been specifically investigated while studying the role of the symmetry orbitals as well as the electronic structure. This is notably illustrated with the examples of phenanthroline complexes with decamethylterbocene,<sup>4</sup> decamethylsamarocene and the related divalent samarium and thulium analogues.<sup>5</sup> Proceeding to use dissymmetric redox-active ligands, for instance, LX-types ones, in establishing a heterometallic framework to extend such type of reactivity not only still at the ligand site but also at the transition metal center, is of great interest. Nickel is currently considered and studied in this work with a dissymmetric LX-type ligand, namely 2-pyrimidin-2-yl-1H-benzimidazole (Hbimpm). Particularly, LX-type ligands are widely used in nickel-catalyzed cross-coupling reactions to enhance the catalytic efficiency,<sup>6-9</sup> regarded as significantly facilitating the activation of unreactive carbon-halogen bonds.<sup>10</sup> Furthermore, the bite angle as well as the ligand dissymmetry would also be important parameters to have effects on the electronic structure of the complexes and reactivity at the metal center.<sup>11,12</sup>

Hence, in this chapter, the synthesis and characterization of organometallic complexes with a dissymmetric *N*-aromatic ligand, which combines a divalent organolanthanide and a dimethyl

nickel fragment, will be demonstrated. Dimerization in carbon-carbon  $\sigma$  bond formation between two ligands occurs in *exo* position due to the effective electron transfer from the divalent lanthanide fragment. The evolution of a transient, heterometallic species to a stable, homoleptic organometallic complex can be explained by the lack of stability of the dimethyl nickel fragment. Meanwhile, the radical coupling between two ligands also occur in the presence of  $\text{KC}_8$ , however, on an opposite site of the ligand, that can be indicative of the intriguing modulation of electronic behavior by divalent lanthanides.

## 1. Introduction: Reversibility and irreversibility of coupling between redox-active ligands

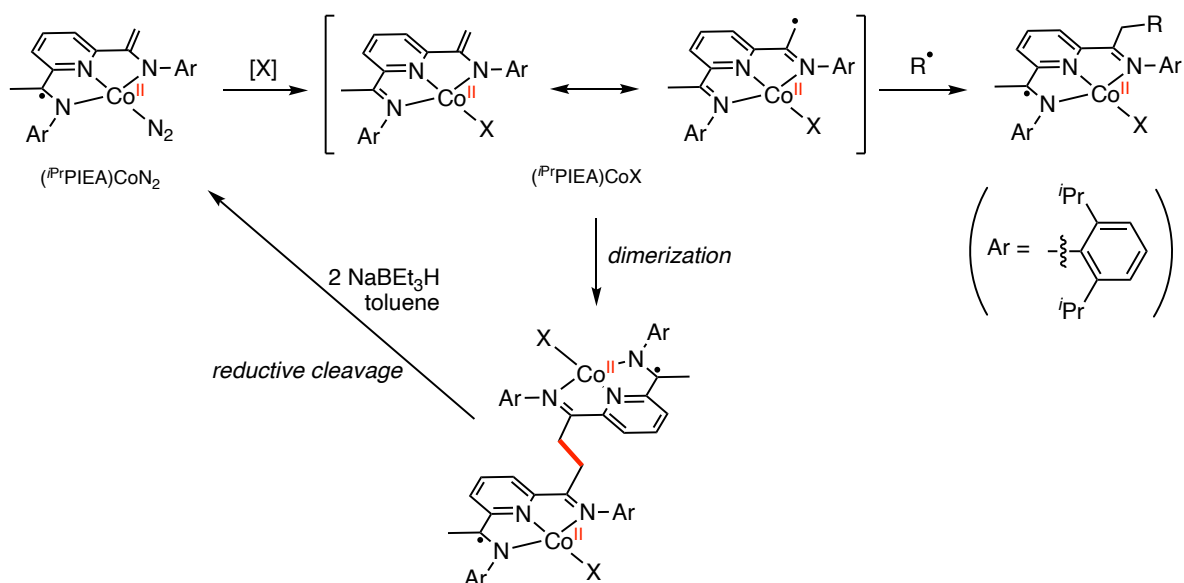
### 1.1. Couplings in d-block transition metal complexes

Organic radicals are usually very active because of their unpaired electrons, which often results in specific reactivity behaviors, for example, dimerization reactions, forming closed-shell compounds from the characteristic open-shell electronic structures.<sup>13</sup> As it has been mentioned in the general introduction in *Chapter 1*, radical-based organometallic systems can be easily achieved using redox non-innocent *N*-aromatic ligands with readily accessible  $\pi$ -conjugation.<sup>13,14</sup> Reversible or irreversible dimerization between the radicals located on the ligands usually occurs with the low-valence of the metal centers, exhibiting the reductive properties.<sup>15-17</sup> One of the related early studies was reported by Tilley *et al.* in 1992 in the investigation of ruthenium complexes containing unsaturated silicon-based ligands, which were described as stabilized silylynes ( $\equiv\text{SiR}$ ) by *N*-heterocyclic bases (bipyridine and phenanthroline in their case). The study demonstrated the reductive dimerization of the complex via coupling of two phenanthroline rings in presence of sodium amalgam.<sup>18</sup> This irreversible formation was also informative of the possible conversion of one of the  $\text{Si}\rightarrow\text{N}$  dative bonds to a Si-N covalent bond in the phenanthroline compound during the reduction. Such external reduction leading to reductive coupling can be accomplished not only by chemical reductants but also by other physicochemical methods, such as electro-inducement. One example of this type of electro-activated system is based on a cationic 2,2'-bipyridyl tungsten alkylidyne complex, formulated as  $[\text{W}(\equiv\text{CC}_6\text{H}_4\text{NMe}_{2-4})(\text{NCMe})(\text{CO})_2\{\kappa^2\text{-}2,2'\text{-(NC}_5\text{H}_4)_2\}][\text{PF}_6]$ .<sup>19</sup> This complex was described as electroactive in MeCN solution ( $E \approx -1.0$  V vs. ferrocene) leading to an intermolecular reductive dimerization between the bipyridine ligands. Molecular orbital analysis was then performed by the authors, indicating an energy-accessible LUMO almost entirely located on the 2,2'-bipyridyl ligand of the tungsten precursor. It was thus suggested that occupation of this orbital upon the reduction leads to a short-lived metastable precursor to 2,2'-bipyridyl ring coupling. Therefore, the reduced complex might better be described as a metastable  $\text{W}^{\text{IV}}$  ( $d^2$ )/bipy<sup>-</sup> species rather than a formally metal-reduced  $\text{W}^{\text{III}}$  ( $d^3$ )/bipy<sup>0</sup> moiety.

Such redox non-innocence has been largely demonstrated by so-called diimine-based ligands series with their derivatives.<sup>20-22</sup> One of the well-established classes is the redox-active bis(imino)pyridine (PDI) ligand system, which has been mentioned in *chapter 1* as a largely

delocalized  $\pi$ -system with two low-lying  $\pi^*$  orbitals on the imine moieties. The central pyridine ring also participates in the success of the overall system by stabilizing the radical species and by facilitating the reversible transformations that involve radical process.<sup>23-26</sup> By deprotonation of one (or both) of the imine methyl groups, ligand-centered reactivity as C-C bond formation between two PDI ligands at the terminal =CH<sub>2</sub> group can be observed. The related study in such reductive coupling was reported earlier by Gambarotta and Budzelaar.<sup>27</sup> They described a dinuclear manganese derivative, which proceeds to a reductive coupling between the deprotonated terminal methyl group. This reaction was accompanied by a formal reduction of the manganese complex with alkylating agents from a (PDI)MnCl<sub>2</sub> precursor. Very similar dimerization formations through the deprotonated alkyl substituents were also investigated by some of them in the case of vanadium,<sup>28</sup> iron,<sup>29</sup> cobalt,<sup>30</sup> and furthermore f-elements such as lanthanum and neodymium.<sup>31</sup> Another unprecedented reactivity was described by the same group in the case of the trivalent chromium, which triggered a complex rearrangement and alkylation at the *para*-position of the central pyridine ring, followed by a [3+3] cycloaddition linking the pyridine *meta*-carbon atoms.<sup>27</sup> They also reported such a dimerization at *meta*-pyridine with *p*-block elements such as aluminum.<sup>32,33</sup> A similar research in terms of iron species bearing a  $\pi$ -acidic bis(imino)pyrazine ligand was recently reported by Roşca and co-workers: a reductive (Cp<sub>2</sub>Co) C-C bond coupling between the pyrazinium rings at one of the *meso*-carbon atoms was followed by the *N*-methylation of the pyrazine. The C-C bond that is formed can then be cleaved under mild oxidative conditions by FcPF<sub>6</sub>, achieving a reversibility of the dimerization.<sup>34</sup>

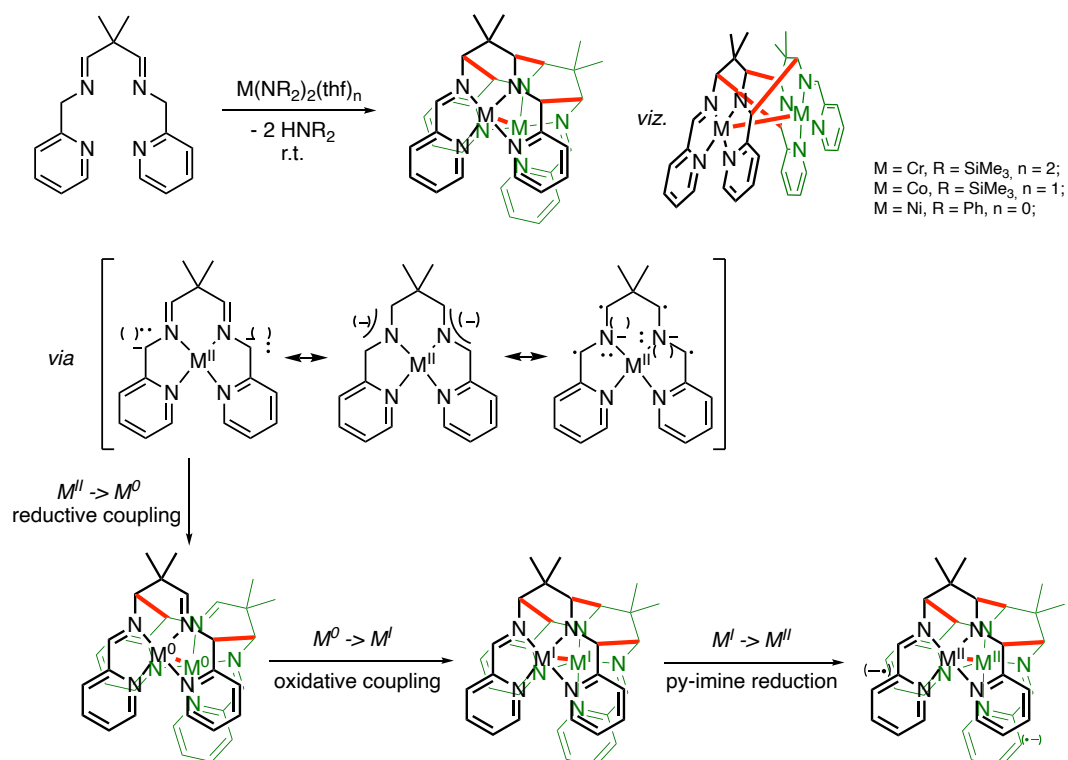
A representative example of the possible reversibility in a coupling involving the PDI ligand was demonstrated by Chirik and co-workers. A pyridine imine enamide cobalt(II) dinitrogen complex, which features a low spin configuration antiferromagnetically coupled to a ligand-centered radical, (<sup>*i*</sup>PrPIEA)CoN<sub>2</sub>, can be obtained from (<sup>*i*</sup>PrPDI)CoCl by deprotonation of *t*-BuONa.<sup>35</sup> Addition of potential radical sources [X] such as organic halides, PhSSPh, or NO resulted in C-C coupling at the enamide positions to form dimeric cobalt species. However, when the same complex was treated with certain halocarbons, it yielded long-lived radicals such as allyl or benzyl radicals, resulting to a monomeric, C<sub>s</sub> symmetric (PDI)CoX complexes with homologated enamide backbone. The reversibility of this dimerization was demonstrated by reduction with NaBEt<sub>3</sub>H leading back to quantitative formation of (<sup>*i*</sup>PrPIEA)CoN<sub>2</sub>. (Scheme 43)



**Scheme 43.** Reversible carbon–carbon coupling induced by oxidation and reduction at a cobalt complex bearing a redox-active bis(imino)pyridine ligand.

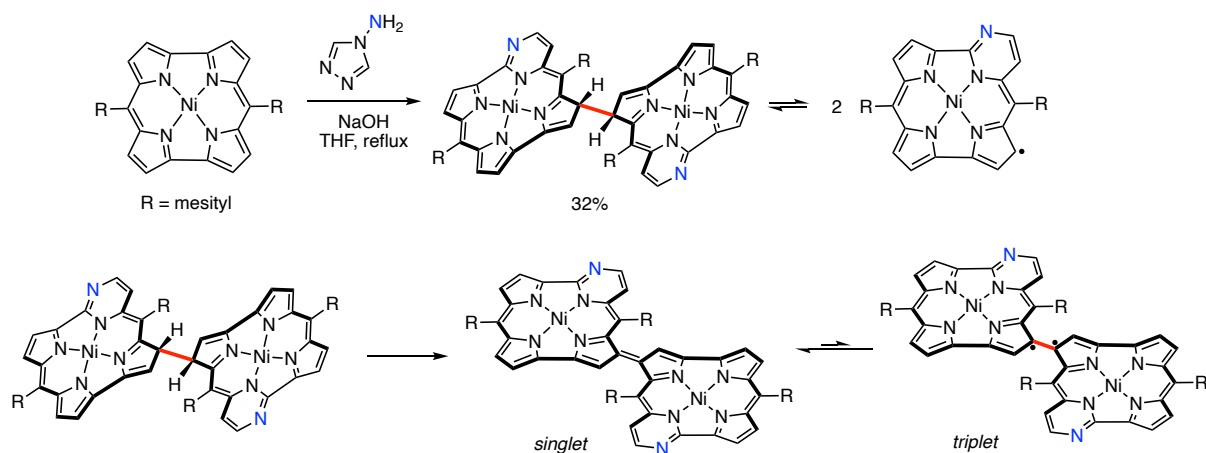
The diversity of iminopyridine-based ligand systems conduces to more investigations on reversible dimerization formation. The dipyritylazaallyl ligand (smif), (2-py)CHNCH(2-py), which was demonstrated by Wolczanski *et al.* also revealed redox-active properties in the chemistry of iron, cobalt and nickel. Notably, this redox activity was identified by the reversible dimerization *via* the C–C bond formation of the azaallyl backbone of  $(smif)FeN(TMS)_2$ , converting it to  $(smif)_2\{FeN(TMS)_2\}_2$  when crystallized, while remaining principally to its monomeric form in solution.<sup>36</sup>

More interestingly, the same group described reductive coupling at the two imino CH positions of bis-pyridine-imine ligands *via* transient azaallyl radical generation, forming two C–C bonds while a third C–C bond is formed *via* dinuclear bis-imine oxidative coupling, resulting from the redox non-innocence of the ligand. Meanwhile, a unique metal-metal bond forms as a consequence of the chelation (Scheme 44). The possible reaction mechanism was proposed by *ab initio* calculations. The basic  $NR_2^-$  was construed as deprotonating the chelate, forming the azaallyl subunits. Similarly, as for the smif ligand, the azaallyl species can be considered nonbonding, with valid ionic ( $-HC=N-CH^-$ ) or “singlet diradical” ( $-HC^{\cdot}-N-C^{\cdot}(H)-$ ) depictions. This yielded two reductive bond formations undergoing radical coupling processes. In this step, a  $M^{II}/M^0$  reduction occurred, and corresponding oxidative coupling of the imines derived from the prior reaction to generate  $M^I$  species. Eventually, the reduction of the pyridine-imine units to radical anions afforded  $M^{II}$  cores as the redox non-innocence. However, the authors also mentioned that the overall mechanistic pathways remained under consideration.<sup>37</sup>



**Scheme 44.** Binuclear C-C bond formation involving the generation of transient radicals based on a redox-active bis-pyridine-imine ligand system.

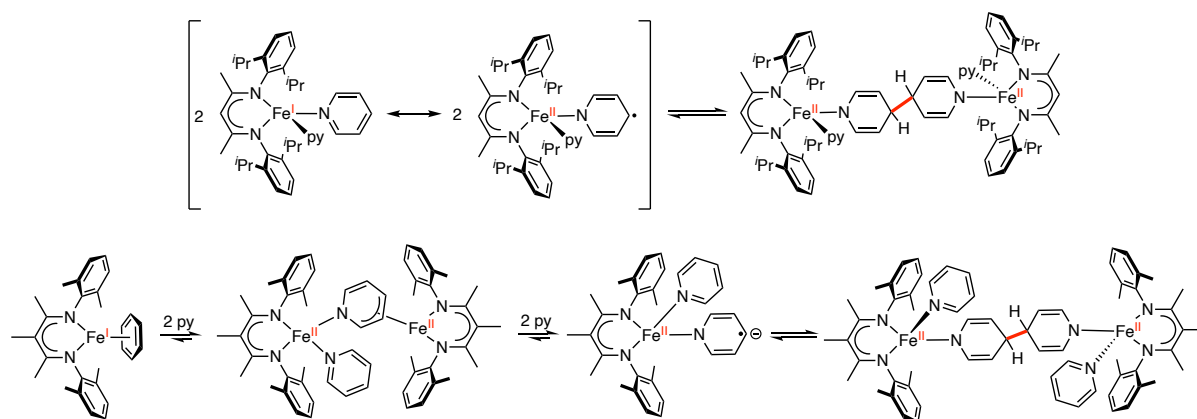
Indeed, carbon-centered radicals can be readily stabilized by large  $\pi$ -conjugated systems, offered by macro-*N*-heterocycles such as porphyrinoids as a result of their remarkable spin delocalization abilities. Generally, these  $\pi$ -cation radicals can further undergo intramolecular<sup>2,38–42</sup> or intermolecular<sup>41,43–45</sup> coupling under oxidative conditions. For example, Li and Chmielewski described an unprecedented ring expansion of norcorrole that can undergo reversible homolytic C-C bond cleavage of the bis(pyrimidinenorcorrole)  $\sigma$ -dimer. This dimeric species provided a straightforward access to another dimer via dehydrogenation displaying a singlet–triplet equilibrium in polar solution, consisting of a reversible homolytic  $\pi$ -bond dissociation.<sup>46</sup>



**Scheme 45.** Reversible carbon–carbon bond coupling and spin equilibria in bis(pyrimidinenorcorrole).

In 2012, Holland and co-workers comprehensively reported the spontaneously reversible coupling of pyridine ligands in iron diketiminate complexes  $L^{Me}Fe(py-R)_2$  ( $L^{Me}$  = bulky  $\beta$ -diketiminato;  $R = H$ , or  $4-tBu$ ). Structural, spectroscopic and computational studies on these complexes demonstrated significant radical character on the basal pyridine ligand with a balance between high spin  $Fe^I$  and  $Fe^{II}$  with antiferromagnetic coupling to the pyridine radical ( $S = 3/2$ ). Without a  $tBu$  protecting group, the  $L^{Me}Fe(py)_2$  complex resulted in a rapid and reversible C-C bond formation at the *para*-position between the pyridine ligands, in which the dimer was present in the solid state, and the monomer was present in solutions. It was relatively interesting that the electrons stored in the newly formed C-C bond can still be used to perform further reactivity in solutions as the  $Fe^I$  species does. For example, the addition of 1-adamantyl azide ( $AdN_3$ ), the dimeric species still generates an iron(III) imido complex  $L^{Me}Fe(NAd)(Py)$ , while the monomeric species was trapped with a triphenylmethyl radical, leading to a complex with a  $[Ph_3C]$  substituent in the *para*-position of the pyridine cycle. These reactions well demonstrated the reversibility of such dimerization formation.<sup>47</sup>

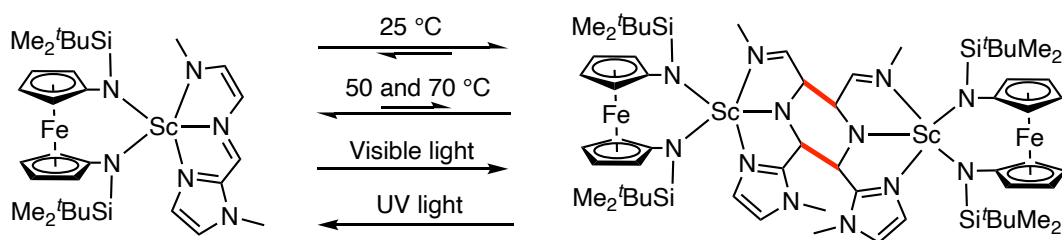
Subsequently, the authors furthermore quantitatively explored the monomer-dimer equilibrium through solution NMR analysis. Decreasing the size of the supporting ligand as 2,4-bis(2,6-dimethylimino)-3-methylpentyl chelate on  $Fe^I$  center led to solid-state XRD characterization of the dimer. Such smaller diketiminate ligand revealed either the known one electron reduction of the pyridine ring, yielding the reversible coupling; or more surprisingly, a doubly reduced bridging pyridine ligand with an unprecedented  $\mu-\eta^1:\eta^3$  binding mode in the formed bimetallic iron(II) complex. The latter was assigned by the Mössbauer spectrum analysis and eventually underwent the dimerization favored by a larger amount of pyridine. The latter discovery showed the great flexibility of pyridine in its ability to accept charge and undergo bond distortion, formation, and cleavage (Scheme 46).<sup>48</sup>



**Scheme 46.** Reversible interconversion of  $L^{Me}Fe(py)_2$  through radical coupling, and pyridine binding and reduction in this system depends on the amount of pyridine added.

This type of reductive coupling of pyridine adduct *via* its radical anion species by low-valent transition metal complexes requires highly reductive organometallic systems due to the very cathodic potential of  $-2.7$  V vs SCE. Diaconescu *et al.* also reported such similar reductive coupling between pyridine ligands, generating two  $sp^3$ -hybridized carbons at 4,4'-positions, in their study of

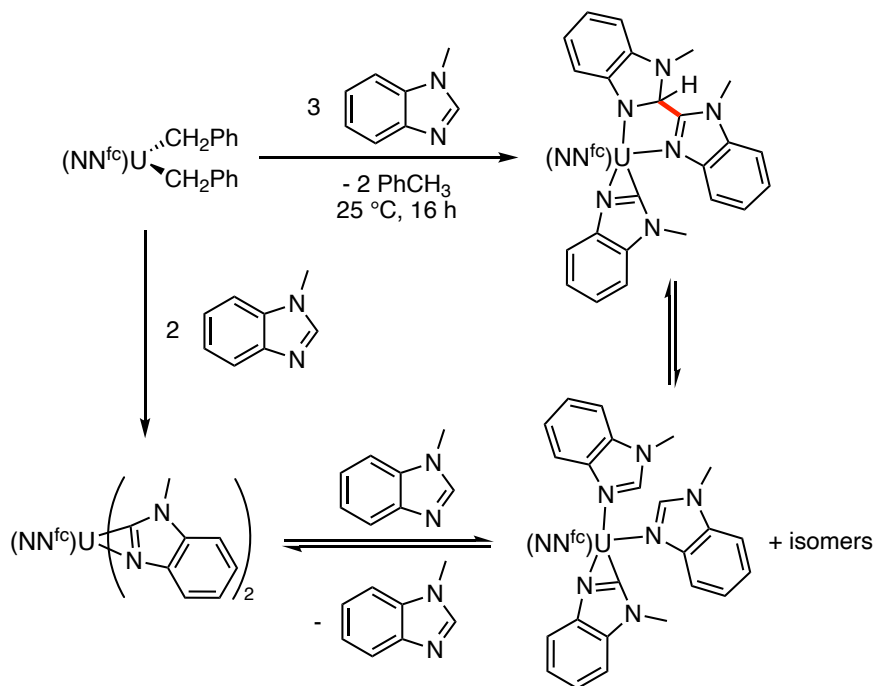
highly reductive arene inverted-sandwich complexes supported by a ferrocene diamide ligand ( $\text{NN}^{\text{fc}}$ ) of scandium metal ion.<sup>49</sup> Sc features the smallest ionic radius among the rare-earth metals, *i.e.*, the early transition metals of Group 3 and lanthanides.<sup>50</sup> The same group also described a visible-light-induced scandium system, leading to a reversible [3+3] cycloaddition between two ( $\text{NN}^{\text{fc}}$ )Sc complexes formed by the ring-opening of 1-methylimidazole. A higher temperature or UV light is necessary to induced the ligand bond cleavage, while the dimerization was favored in the presence of visible light (Scheme 47).<sup>51</sup> The example of scandium organometallics can raise significant interest in accounting similar and other related reactivity in reductive coupling between the chelates of the system in the chemistry of reductive lanthanides as well as actinides.



**Scheme 47.** Reversible [3+3] cycloaddition between two scandium complexes formed by the ring-opening of 1-methylimidazole with light and temperature dependence.

## 1.2. Couplings in f-element chemistry

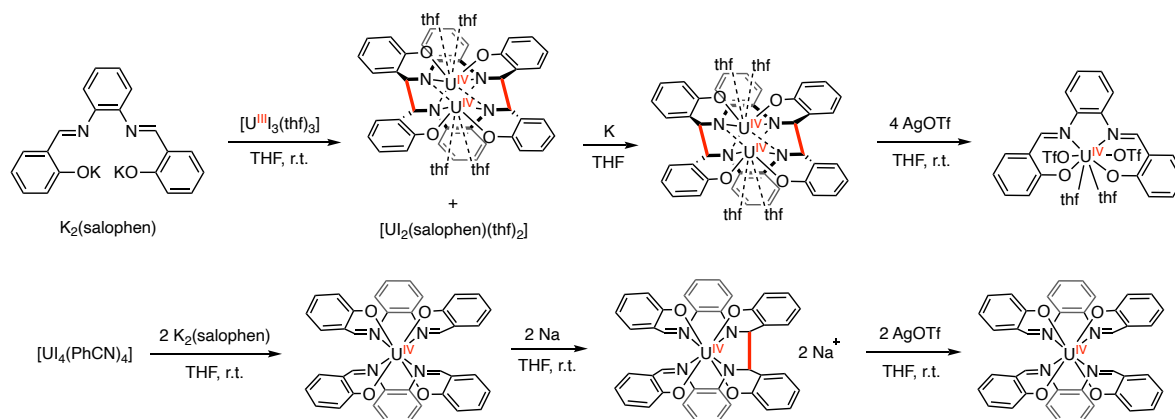
The group of Diaconescu also demonstrated a reversible C-C coupling of two  $\eta^2$ -N,C-imidazolyl fragment fragments of coordinated 1-methylbenzimidazole molecules in a low-valent  $\text{NN}^{\text{fc}}$  uranium(IV) complex *via* C-H activation of two heterocycles. The reversibility of such coupling was supported by variable-temperature NMR studies as well as reactivity with the precursor ( $\text{NN}^{\text{fc}}$ ) $\text{U}(\text{CH}_2\text{Ph})_2$ , indicating the equilibria in solution of this system (Scheme 48).<sup>52</sup>



**Scheme 48.** Solution Equilibria of C-C coupling in a uranium  $\text{NN}^{\text{fc}}$  complex with 1-methylbenzimidazole.



Representative work in redox-active uranium chemistry that resulted in  $\pi$ -radical coupling between the chelating ligands was reported by Mazzanti and co-workers. They demonstrated that the reaction of trivalent uranium salt with a tetradentate Schiff base (salophen) directly led to a dinuclear tetravalent uranium complex with a macrocyclic octaanionic amido ligand *via* a reductive coupling between the imino groups on the Schiff base, instead of forming the expected U(III) species. By the reduction of co-produced  $[\text{U}_2(\text{salophen})_2]$  salt with potassium, this reaction eventually generated the pure unexpected  $[\text{U}_2(\text{cyclo-salophen})(\text{THF})_4]$  complex, whose coupled bonds can be oxidatively cleaved to restore the imino groups of the Schiff ligand without influencing the oxidation state of uranium center. Alternatively, an intramolecular reductive coupling between two coordinated Schiff bases can be achieved by the reduction of a tetravalent  $[\text{U}(\text{salophen})_2]$  complex and dissociated by oxidation of AgOTf leading to the reversibility (Scheme 49).<sup>53</sup> Similar work was also extended to trivalent lanthanides, resulting in the same coupling reactivity.<sup>54</sup>

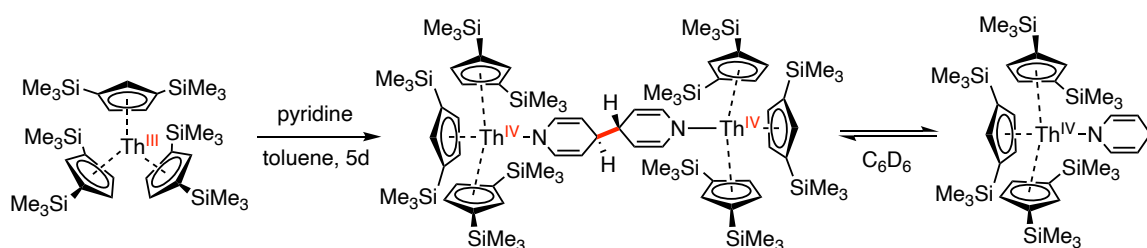


**Scheme 49.** Multielectron redox reactions involving C–C coupling and cleavage in uranium Schiff complexes.

The formation of C–C coupling promoted by U(IV) complexes with a reducing agent was also reported for other redox-active systems. For example, Berthet and Ephritikhine reported that by the reaction of 2,4,6-tris(2-pyridyl)-1,3,5-triazine (tptz) with  $\text{U}(\text{py})_4$ , a reductive dimerization of a polycyclic azine took place, involving  $\text{U}^{\text{III}} \rightarrow \text{U}^{\text{IV}}$  oxidation with the generation of tptz anion-radical.<sup>55</sup> Meyer and coworkers described the reaction of a triazacyclononane-anchored trisaryloxy uranium(III) complex with benzophenone affording a ketyl radical species, which resulted in the formation of a U(IV) diphenyl methoxide complex *via* H-abstraction and a head-to-tail reductive *para*-coupling of two benzophenone ketyl ligands.<sup>56</sup> This similar ketyl radical coupling *via*  $\text{U}^{\text{III}}/\text{U}^{\text{IV}}$  was also reported by Schelter *et al.* in the reactivity study of  $\text{U}[\text{N}(\text{SiMe}_3)_2]_3$  complex in 2017.<sup>57</sup> Another example of uranium(IV) chemistry was about a uranium cluster containing an isopolyoxometalate  $[\text{U}_6\text{O}_{13}]$  core reported by Duval and colleagues.  $[\text{Cp}^{\text{III}}_2\text{UCl}_2]$  ( $\text{Cp}^{\text{III}} = 1,2,4\text{-}^t\text{Bu}_3\text{C}_5\text{H}_2$ ) as the uranium(VI) precursor was firstly reduced with two equivalents of  $\text{KC}_8$  in THF, followed by an addition of two equivalents of pyridine N-oxide, yielding a cluster compound  $[\text{Cp}^{\text{III}}_4(\text{bpy})_2][\text{U}_6\text{O}_{13}]$  instead of the expected organometallic dioxo species  $[\text{Cp}^{\text{III}}_2\text{UO}_2]$ . The formation of the bipyridine adduct was plausibly from the irreversible coupling between two pyridyl radicals which were generated from an  $\alpha$ -H abstraction of pyridine released by pyridine N-oxide.

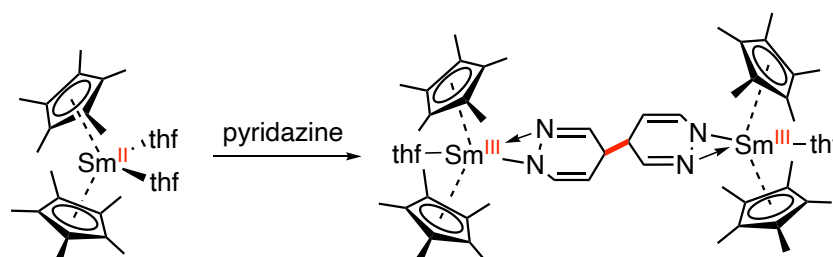
This step was induced by a Cp<sup>III</sup> radical reductive homolytic Cp<sup>III</sup>-U cleavage of intermediate [Cp<sup>III</sup><sub>2</sub>UO<sub>2</sub>], as proposed by the magnetic and electrochemical analysis.<sup>58</sup>

Because thorium(III) is supposed to be more reducing than uranium(III) ( $E^0 \text{Th}^{\text{IV}} \rightarrow \text{Th}^{\text{III}}: -3.7 \text{ V}$ , cf.  $\text{U}^{\text{IV}} \rightarrow \text{U}^{\text{III}}: -0.6 \text{ V}$ ), it led to several differences in their redox reactivity.<sup>59</sup> For instance, trivalent uranium complexes are rarely reported to perform the reductive coupling of pyridine ligands, as mentioned with low-valent iron complexes presented earlier. However, reduction of other *N*-heterocycles such as pyrazine is possible.<sup>60</sup> On the other hand, Mills *et al.* reported that [Th(Cp'')<sub>3</sub>] (Cp''={C<sub>5</sub>H<sub>3</sub>(SiMe<sub>3</sub>)<sub>2</sub>-1,3}) with pyridine gave [Th(Cp'')<sub>3</sub>]<sub>2</sub>[μ-(NC<sub>5</sub>H<sub>5</sub>)<sub>2</sub>] containing an equilibrium in solution (Scheme 50).<sup>61</sup>



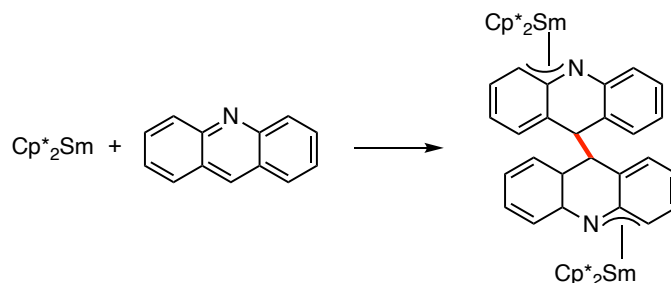
**Scheme 50.** Single-electron transfer induced reversible reductive coupling of pyridine by a thorium(III) complex.

Similar to their actinides neighbors in reductive chemistry, highly reductive divalent organolanthanides have been deeply studied for the reductive coupling of *N*-aromatic heterocycles, mainly with ytterbium (II), samarium (II) and thulium (II). For example, the group of Evans reported a rather early research based on the reaction with reductive decamethylsamarocene and pyridazine, yielding a dimeric species with a bipyridazine unit coupled at the 4-position (Scheme 51).<sup>62</sup> This new dimeric samarium compound contains an inversion center at the midpoint of the formed  $\sigma$  C-C bond, in agreement with a  $C_{2h}$  symmetry instead of  $C_{2v}$  since the two pyridazine cycles are no longer planar once coupled. The coupling was induced from the formation a stable radical anion of pyridazine at the 4-position due to the reduction by divalent samarium. The reductive coupling at the certain position is consistent with the molecular orbitals of pyridazine whose most electron density at the 1- and 4-positions based on Hückel theory.<sup>63</sup> Moreover, the authors found that the nitrogen double-bond character in coupled pyridazine was lost. The nitrogen that binds to samarium center has a single-bond character as that of the Sm-NR<sub>2</sub> type, while the other nitrogen to samarium center is regarded as a dative bond, coordinating *via* its lone pair as a Sm←NR<sub>3</sub> donor bond.



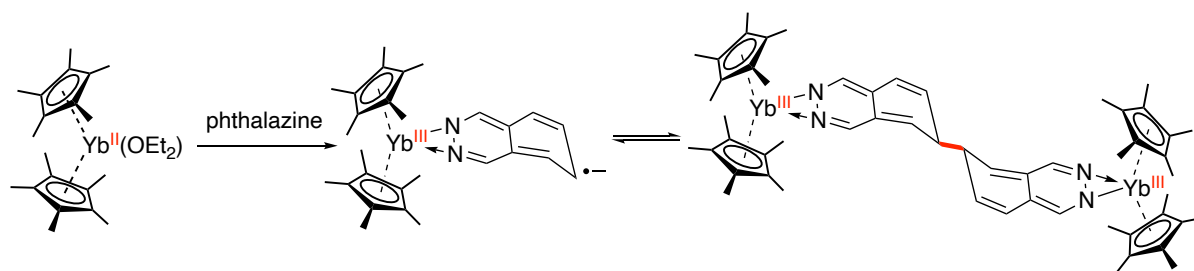
**Scheme 51.** Reductive coupling of pyridazine by Cp\*<sub>2</sub>Sm(thf)<sub>2</sub> reported by Evans and co-workers.

The same group continued to report the study in reactivity of decamethylsamarocene with several polycyclic aromatic hydrocarbons, such as a reductive coupling of acridine adduct.<sup>64</sup> In this formation, the planarity of reduced acridine unit is likely maintained by an allylic bonding to the samarium center (Scheme 52).



**Scheme 52.** Reductive dimerization of acridine reacted by  $\text{Cp}^*_2\text{Sm}$ .

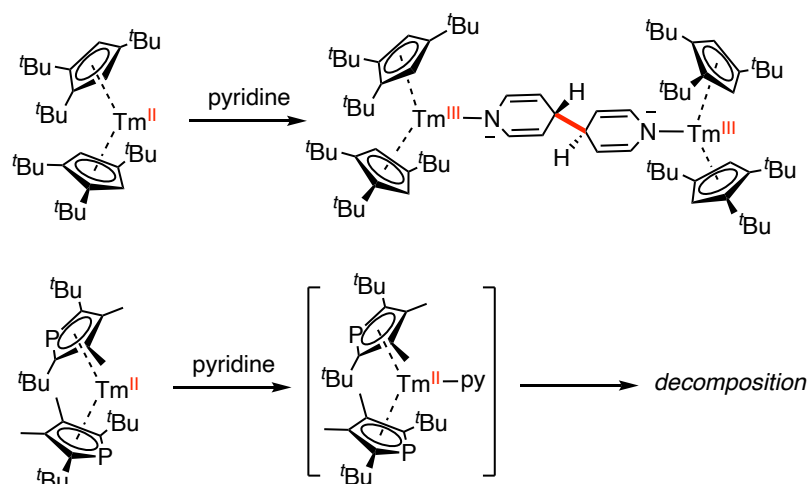
Later on, Andersen and coworkers demonstrated a series of paramagnetic compounds of  $\text{Cp}^*_2\text{Yb}$  with *N*-heterocyclic adducts.<sup>65</sup> In their study, adducts (L) of six-membered rings with two nitrogen atoms such as pyrazine, pyridazine and phthalazine were reacted with divalent  $\text{Cp}^*_2\text{Yb}$ , forming  $\text{Cp}^*_2\text{Yb}^{\text{III}}(\text{L}^{\cdot-})$  ( $\text{L}^{\cdot-}$  = radical anionic ligand), which leading to different reactivity based on their redox potentials. The adduct with pyrazine formed an insoluble product, which was presumed to be a polymeric structure. The reaction with pyridazine solely yielded a stable paramagnetic compound  $\text{Cp}^*_2\text{Yb}(\text{pyridazine})_2$ , differently from the case of samarium in reductive coupling just mentioned above. It can be presumably explained that the spin density at the *para*-position of pyridazine is higher in the case of samarium than ytterbium. Yet, the phthalazine, as a derivative of pyridazine, with decamethylytterbocene can lead to a reversible dimerization between two ligands. The coupling formation was characterized by NMR analysis, agreeing with a  $\text{C}_{2h}$  symmetric product in solution (Scheme 53).



**Scheme 53.** Reversible dimerization of  $\text{Cp}^*_2\text{Yb}(\text{phthalazine})$  adduct in solution.

Consequently, the authors concluded that divalent  $\text{Cp}^*_2\text{Yb}$  can reduce the ligands with the reduction potentials on the order of -2.2 V and less, yielding the trivalent  $\text{Cp}^*_2\text{Yb}$  fragment. When it comes to the reaction between divalent  $\text{Cp}^*_2\text{Yb}$  with pyridine ( $E^0 = -2.6$  V), it only yielded a diamagnetic  $\text{Cp}^*_2\text{Yb}(\text{py})_2$  compound.<sup>66</sup> Likewise, a sterically equivalent phospholyl analogue  $\text{Dtp}_2\text{Tm}$  ( $\text{Dtp} = 2,5\text{-}t\text{Bu}_2\text{-}3,4\text{-Me}_2\text{C}_4\text{P}$ ) was reported by Nief *et al.*<sup>67</sup> and was treated with pyridine. Initially, the pyridine coordinated to the thulium(II) ion center, as analyzed by NMR but after a short period of time, the reaction evolved into an intractable mixture, presumably through eventual

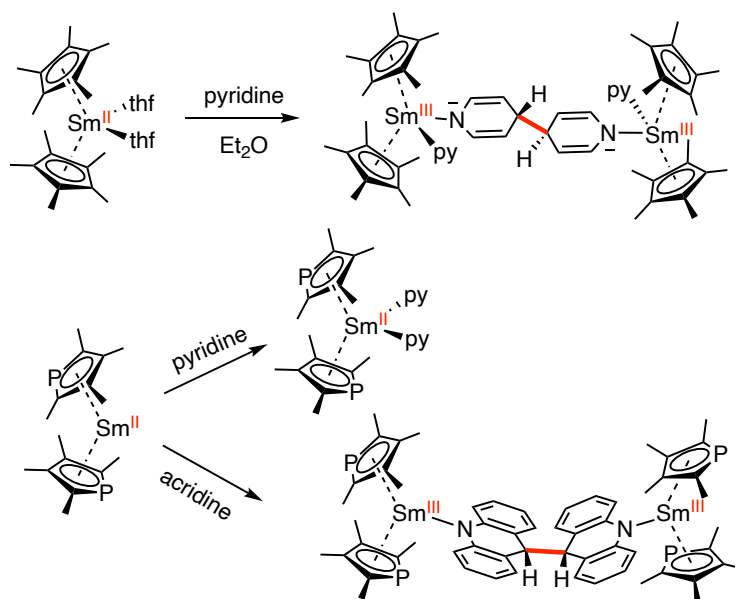
oxidation of thulium(II). This can be explained by a less electron-donating character of phospholyl ligands than the similar bulky ligands such as cyclopentadienyl analogues.<sup>68</sup> The parallel study of radical dimerization of pyridine adduct in the presence of divalent  $\text{Cp}^{\text{tBu}}_2\text{Tm}^{\text{II}}$  complex [ $\text{Cp}^{\text{tBu}} = 1,2,4\text{-}(\text{tBu})_3\text{C}_5\text{H}_2$ ] in solution was described in the same work. The reaction instantaneously went through electron transfer from thulium(II) to the pyridine to form the intermediate pyridinyl radical species,<sup>69</sup> and subsequent coupling at the *para*-position. (Scheme 54) A similar reductive coupling of pyridine was also previously described with thulium diiodide by Bochkarev and Schumann.<sup>70</sup>



**Scheme 54.** Reactions of substituted cyclopentadienyl- and phospholylthulium(II) complexes with pyridine.

Accordingly, the different reactivity with cyclopentadienyl and phospholyl analogue ligands in divalent organosamarium in the presence of pyridine was studied by Nief and Evans.<sup>71</sup> With  $\text{Cp}^*_2\text{Sm}(\text{thf})_2$ , pyridine was reductively dimerized with concomitant oxidation of Sm(II), which is comparable with the reactivity of the same complex with acridine. On the other hand,  $\text{Tmp}_2\text{Sm}$  ( $\text{Tmp} = \eta^5\text{-C}_4\text{Me}_4\text{P}$ ) with pyridine only yielded a stable divalent  $\text{Tmp}_2\text{Sm}(\text{py})_2$  product without any reduction on the pyridine adduct. However, the reaction of  $\text{Tmp}_2\text{Sm}$  with acridine resulted in a reductive coupling formation of  $(\text{Tmp}_2\text{Sm})_2[\mu\text{-(NC}_{13}\text{H}_9\text{-C}_{13}\text{H}_9\text{N})]$ , and unlikely the  $(\text{Cp}^*_2\text{Sm})_2[\mu\text{-(NC}_{13}\text{H}_9\text{-C}_{13}\text{H}_9\text{N})]$  analogue, the conformation of the bridging ligand is in the *gauche* conformation (or *endo*) in the former compound and in the *anti*-conformation (or *exo*) in the latter one (Scheme 55).

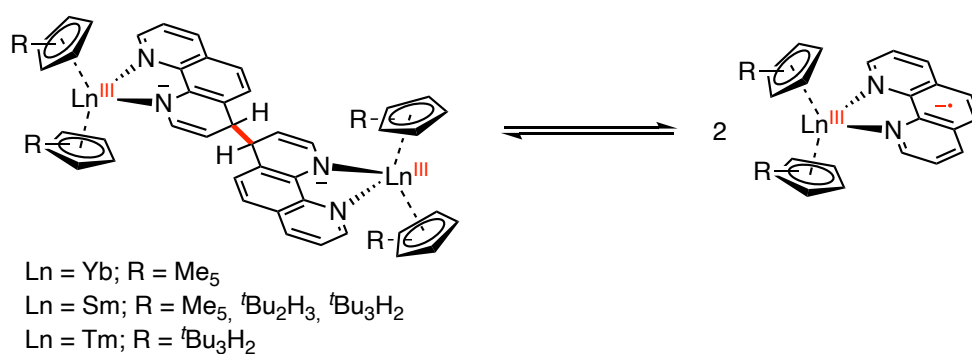
The authors also demonstrated, using theoretical tools, that the different electronic properties of the Tmp and  $\text{Cp}^*$  ligands are the reason for the different reactivity that is observed. In both cases, strong f-orbital character can be found in the six highest molecular orbitals; however, the energy levels of the f manifold are around  $-0.6$  eV more negative in Tmp than  $\text{Cp}^*$  ligands. This is indicative of the better negative charge distribution on the Tmp ligand. Therefore, the reduction of pyridine by  $\text{Tmp}_2\text{Sm}$  complex did not take place but when substituted with a more conjugated as  $\text{Cp}^*_2\text{Sm}$  analogue or the more delocalized derivative as acridine, the reduction can be efficient with the lower LUMO and higher HOMO in energy.



**Scheme 55.** Ligand influence on the redox reactivity of  $\text{Cp}^*_2\text{Sm}(\text{thf})_2$  and  $\text{Tmp}_2\text{Sm}$  with pyridine and acridine.

The adduct of decamethylsamarocene with pyridine (1:2 stoichiometry) led to a reductive dimerization, while the one with one equivalent of bipyridine yielded a radical anionic bipyridyl complex with a trivalent samarium.<sup>62</sup> A similar observation was found in decamethylytterbocene:  $\text{Cp}^*_2\text{Yb}(\text{py})_2$  is diamagnetic, while  $\text{Cp}^*_2\text{Yb}(\text{bipy})$  is paramagnetic, although they have the same general molecular structures. It has been mentioned in previous chapters that  $\text{Cp}^*_2\text{Yb}(\text{bipy})$  is forming a stable  $\text{Cp}^*_2\text{Yb}^{\text{III}}(\text{bipy}^{\cdot-})$  species in solution, which was firstly reported and has been thoroughly studied by Andersen *et al.*,<sup>72</sup> while the 1,10-phenanthroline adduct with  $\text{Cp}^*_2\text{Yb}$  was investigated by our group, showing a different behavior in solution.<sup>4</sup> The reaction between  $\text{Cp}^*_2\text{Yb}$  and phenanthroline yielded a dimerization between two carbons at the 4-position of phen ligand. This coupling formation is thermodynamically reversible in solution, which means that there is an equilibrium between the dimeric  $[\text{Cp}^*_2\text{Yb}^{\text{III}}(\text{phen})]_2$  and the monomeric  $\text{Cp}^*_2\text{Yb}^{\text{III}}(\text{phen}^{\cdot-})$  species. Both species have been isolated by crystallization and sublimation, respectively. The thermodynamics are then of significant interest because the enthalpy  $\Delta H$  in this reaction is actually the bond dissociation enthalpy (BDE) for the new formed  $\sigma$  C-C bond in equilibrium. In order to investigate this point, a more soluble system was studied with 3,8-Me<sub>2</sub>phen derivative, which possesses a similar electronic structure and similar reactivity to that of the original phen system. A Van't Hoff analysis allowed the extraction of the thermodynamic parameters as  $-5.8 \text{ kcal}\cdot\text{mol}^{-1}$  and  $-8.1 \text{ kcal}\cdot\text{mol}^{-1}$  in THF and toluene, respectively, of  $\Delta H$  values; and  $-26 \text{ cal}\cdot\text{mol}^{-1}\cdot\text{K}^{-1}$  and  $-31 \text{ cal}\cdot\text{mol}^{-1}\cdot\text{K}^{-1}$  in THF and toluene, respectively, of the  $\Delta S$  values. This allow to determine  $\Delta G$  values at 298 K at  $1.1 \text{ kcal}\cdot\text{mol}^{-1}$  and  $1.9 \text{ kcal}\cdot\text{mol}^{-1}$  in THF and toluene, respectively. The small free energy value can be explained by a compensation between the radical coupling, which is favorable in enthalpy, and the entropically unfavorable process in dimerization from two radicals. It agrees with the momic form being present in solution at room temperature.

Similar reversibility in solution was also studied in the cases of complexes of divalent samarium and thulium with phenanthroline.<sup>5</sup> The NMR studies showed that in all cases of samarium with Cp<sup>\*</sup>, Cp<sup>tt</sup>, and Cp<sup>ttt</sup> ligands, the values of  $\Delta G$  lie between  $-4.5$  and  $-3.2$  kcal $\cdot$ mol<sup>-1</sup>. Any relation between the steric bulk and the thermodynamics of the complexes was difficult to make, while it was noted that the majority in samarium series is the dimeric form at room temperature in solution, in agreement with negative  $\Delta G$  of the dimerization while it is positive for the Cp<sup>\*</sup><sub>2</sub>Yb<sup>III</sup>(phen) analogue. Additionally, a reversible reductive coupling was found in the reaction of Cp<sup>ttt</sup><sub>2</sub>Tm with phenanthroline, displaying similar redox behavior with this more reductive divalent lanthanide fragment comparing to Yb and Sm (Scheme 56). It is in consistent with the study of Morris *et al.* in the redox properties of the ligands, which are not largely affected by the reduction potentials of the metal center, in different divalent organolanthanides.<sup>73</sup>



**Scheme 56.** Thermodynamically reversible C-C coupling in phenanthroline complexes of divalent lanthanides. In general, the work involving reversible or irreversible radical coupling is mainly utilizing a redox-active L-type ligand with high symmetry, for example, C<sub>2v</sub> symmetry in the phenanthroline systems. Under all circumstances, it will be of fundamental interest to study a redox system with a dissymmetric ligand with excellently accessible delocalization, in combination with a divalent lanthanide. Electron transfer would occur then through the ligand forming a new radical anionic species. Instantaneous radical coupling can take place depending on the systems and in our case, a heterometallic system with a transition metal (here, it will be nickel) will be explored to study the electronic structures as well as modulated reactivity of this new framework.

## 2. Synthesis and XRD analysis of the dissymmetric heterometallic framework

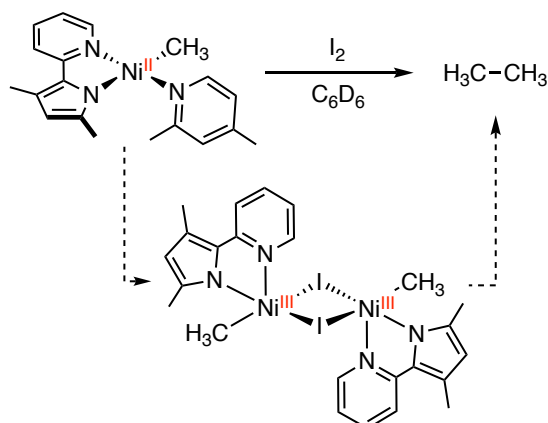
### 2.1. The Interest of imidazole derivatives

To design a novel dissymmetric heterometallic system, the difference in chelating sites was firstly considered. For example, in this work, an LX-type coordination site can be towards the nickel center, while the L<sub>2</sub>-type of chelation to the divalent lanthanides would rather be maintained; however, the bite angles in this case will be totally different from the ones in other symmetric molecule, such as the Cp<sup>\*</sup><sub>2</sub>Yb(bipym)NiMe<sub>2</sub> complex in *Chapter 2*.

Inspired by some examples in photo- or electro-induced mixed-valent complexes by using redox-active benzimidazole and derivatives,<sup>74,75</sup> especially the work from Haga and Bond in the study of electron correlation properties in bibenzimidazole-bridged dinuclear Ru and/or Os complexes,<sup>76,77</sup>

we considered that a benzimidazole-based ligand, which has good  $\sigma/\pi$ -donor property, combined with the excellent  $\pi$ -accepter pyrimidine would be applicable to enable the effective electron transfer from lanthanide to the ligand-transition metal fragment.<sup>78</sup> In the example of the mix-valent dinuclear ruthenium complex bridged by Hbimpm, the HOMO/LUMO energy orbitals of bimpm are higher than that of bipym, while the electron density distribution in the former case is relatively interesting. The electron density of the HOMO is concentrated only on the benzimidazolate part, whereas the LUMO possesses the main electron density on the pyrimidine moiety. A synergetic effect can be illustrated in the interaction between the  $d\pi(\text{Ru}^{\text{II}})-\pi(\text{bimpm})$  and  $d\pi(\text{Ru}^{\text{III}})-\pi(\text{bimpm})$  as a result of the mixed valency.<sup>79</sup>

Besides, an interesting work reported by Diao and coworkers described mechanistic insights in Ni-catalyzed cross-coupling reactions *via* bimolecular pathways.<sup>80</sup> They experimentally highlighted the complexity of high-valent nickel-mediated  $sp^3-sp^3$  and  $sp^2-sp^2$  C-C bond formation by means of spectroscopic and computational ways, in the presence of an LX-type pyridine-pyrrolyl ligand (Scheme 57). Therefore, a similar pyrimidine-benzimidazolate adduct in our case would be interesting to help investigate the reactivity behavior of nickel metal center in the ideal heterobimetallic complexes with divalent lanthanides.

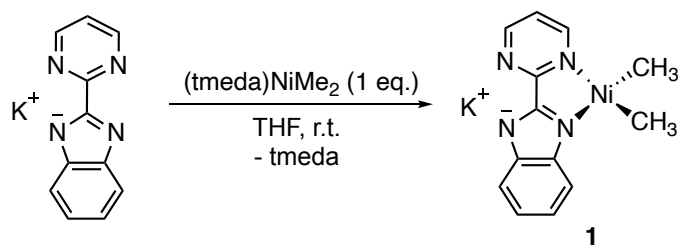


**Scheme 57.** Dinuclear (pyridine-pyrrolyl)Ni<sup>III</sup>-mediated C-C formation of ethane reported by Diao and colleagues.

## 2.2. Novel organometallic frameworks: radical coupling formation on the ligand

The preliminary attempt in synthesizing an expected monomethyl nickel complex by combining (tmeda)NiMe<sub>2</sub>, and Hbimpm in chelating solvents such as pyridine or acetonitrile at room temperature only led to insoluble solids that were hardly characterizable. When heating up the mixture to higher temperature, the reaction only yielded to decomposition products, which were very also difficult to identify, probably due to the temperature sensitivity of (tmeda)NiMe<sub>2</sub>, as well as the bad solubility of the Hbimpm ligand in aprotic solvents caused by the benzimidazole fragment.<sup>81</sup> However, when Hbimpm (pK<sub>a</sub> ≈ 12.3) was prior deprotonated with a strong base (potassium hexamethyldisilane) before addition of (tmeda)NiMe<sub>2</sub> in THF at room temperature, dark red microcrystalline solid K(bimpm)NiMe<sub>2</sub> (**1**) was isolated in good yield of 60% (Scheme 58). Complex **1** can be further re-crystallized from THF-pentane vapor diffusion in moderate yield (40%) as purple crystals, which were suitable for X-ray diffraction (Figure 48).





**Scheme 58.** Synthesis of **1** from deprotonated Hbimpm ligand.

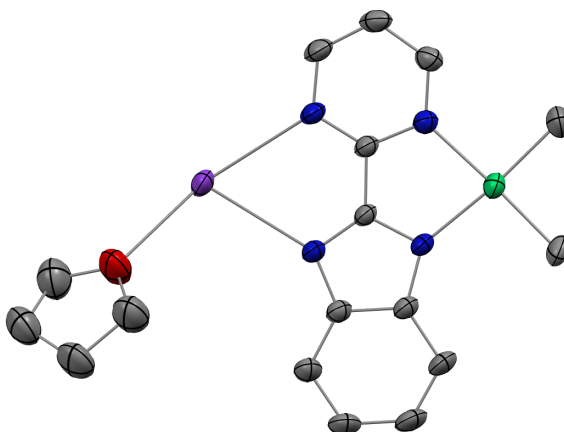


**Figure 48.** ORTEP of **1**. Thermal ellipsoids are at 50 % level. Carbon atoms are in grey, oxygen in red, potassium in purple, nitrogen in blue, and nickel in bright green. Hydrogen atoms are omitted for clarity.

The addition of  $\text{Cp}^*_2\text{Yb}(\text{OEt}_2)$  to **1** in THF in a 1:1 stoichiometric ratio led to the formation of a red suspension that was stirred for 1 h. After evaporation of the volatile and extraction in  $\text{Et}_2\text{O}$ , bright red crystals were obtained *via* slow evaporation at  $-35^\circ\text{C}$  of the  $\text{Et}_2\text{O}$  solution in moderate yield (51%). Interestingly, instead of the formation of expected dimeric Yb-bimpm-Ni anionic complex, a homo-trimetallic neutral Yb-bimpm complex (**2**) was generated. In **2**, a carbon-carbon bond formation has happened between two bimpm ligands at the 4-pyrimidine fragments. The coupling fashion is similar to the examples in some *N*-heteroaromatic ligands, such as pyrazine and pyridazine adduct coupling systems described above, in *exo*-position. A third ytterbium ion is coordinated in the pocket formed by four of the nitrogen atoms from two bimpm ligands, with only one pentamethylcyclopentadienyl ligand remaining on the ytterbium center (Scheme 59(a) and Figure 49).



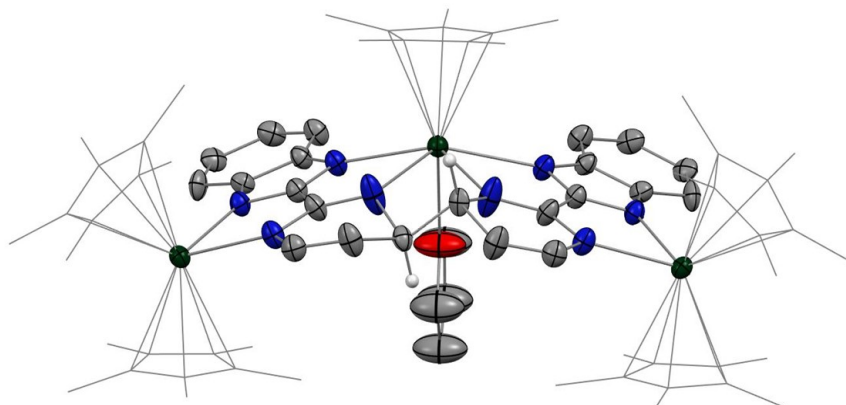


**Figure 49.** ORTEP of **2**. Thermal ellipsoids are at 50 % level. Carbon atoms are in grey, hydrogen atoms are in white and have been removed for clarity except the ones on the coupled carbons of the ligands, potassium in purple, nitrogen in blue, and ytterbium atoms in deep green. Co-recrystallized solvent molecules of Et<sub>2</sub>O in **2** are omitted. Cp\* ligands on ytterbium are presented in wireframe style for clarity.

Main distances and angles of these two and other complexes are shown in Table 9 according to the XRD analysis. In **2**, the average distance between Cp\* centroid and ytterbium atom is in the range of 2.33-2.34 Å. It is lower than the typical values (2.43–2.50 Å) found in divalent Yb complexes with Cp ligands.<sup>82</sup> This value is indicative of the trivalent oxidation state of Yb and it means that the Yb-ligand (*i.e.*, Yb-pyrimidinyl, in this case) fragment firstly undergoes the transition from Yb<sup>II</sup>(f<sup>14</sup>, L<sup>0</sup>) to Yb<sup>III</sup>(f<sup>13</sup>, L<sup>-</sup>) before coupling.<sup>72,83</sup> Then, the dimerization takes place between the same *meso*-position of pyrimidinyl moieties on bimpm ligands, causing the dearomatization of pyrimidine and forming a new Csp<sup>3</sup>-Csp<sup>3</sup> bond.<sup>4,5</sup> This behavior is explained by the efficient electron transfer from ytterbium fragment to the LUMO of pyrimidine heterocycle, then undergoing the radical coupling process. The latter has been investigated by Haga *et al.* on the bimpm ligand system *via ab initio* molecular orbital calculations.<sup>79</sup> The effective reduction of the ligand also features a longer C-C bond distance linking the pyrimidine and benzimidazole heterocycles in **2** (1.476 Å) than in **1** (1.451 Å), indicating a loss of the conjugation in the ligand and charge localization on the nitrogen of the pyrimidine.

This unexpected complex **2** could plausibly be the result of the easy formation of KCp\* which is well soluble in THF; yet not in the extraction solvent Et<sub>2</sub>O. Thus, the formation of the salt could be explained by the ionic bonding nature of the lanthanide to the Cp ring.<sup>84</sup> It also demonstrates the relative lability of the highly reactive nickel dimethyl fragment once the ligand is reduced. As a result, **2** is likely to be the thermodynamic product of the reaction by rearrangement of the expected heterobimetallic Yb-Ni dimer.

In order to get some insights in this singular rearrangement, another reaction was performed in a similar fashion but that was let to react only for several seconds at room temperature before it was dried, dissolved in Et<sub>2</sub>O and cooled to -35°C for the crystallization. A clear brown solution formed during this reaction without any precipitation and the crystallization of this brown mixture yielded

brown X-ray suitable crystals of an anionic Yb-bimpm-Ni fragment **3** in which two bimpm ligands are coupled and one molecule of  $\text{KCp}^*$  is co-crystallized (Figure 50). However, when the same initial reaction was performed in  $\text{Et}_2\text{O}$ , no matter the reaction time, it only yielded to the red crystalline product of rearrangement **2** (Scheme 59(b)).

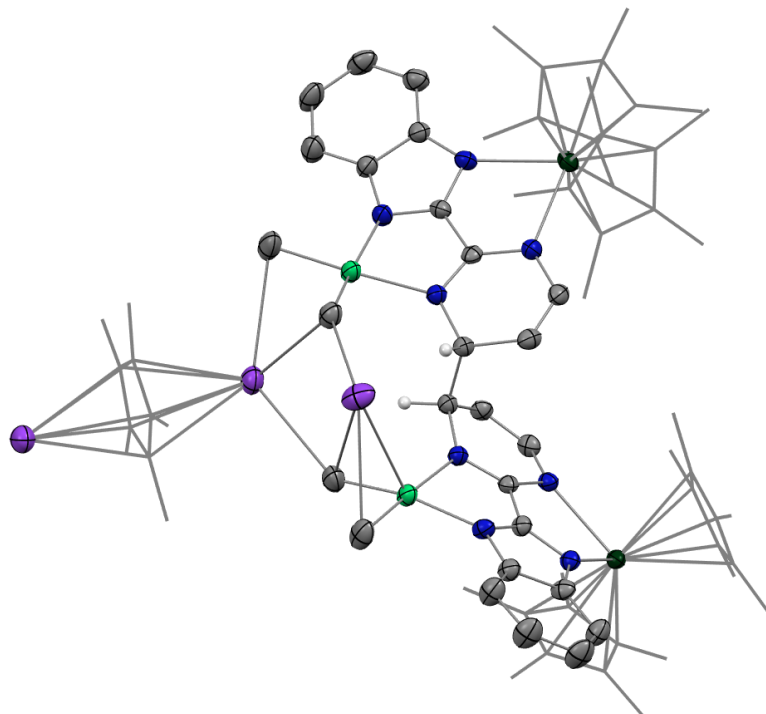
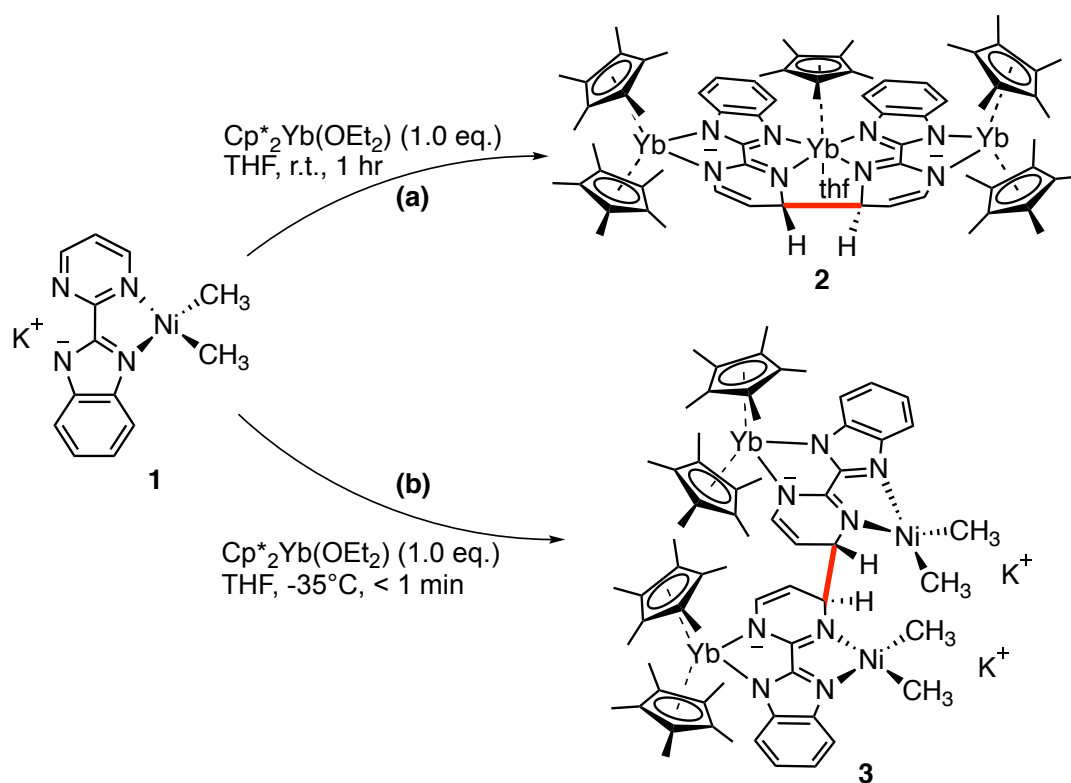


**Figure 50.** ORTEP of **3**. Thermal ellipsoids are at 50 % level. Carbon atoms are in grey, hydrogen atoms are in white and have been removed for clarity except the ones on the coupled carbons of the ligands, potassium in purple, nitrogen in blue, nickel in bright green and ytterbium atoms in deep green. Co-recrystallized solvate molecules of  $\text{Et}_2\text{O}$  are removed and pentamethylcyclopentadienyl ligands on ytterbium are presented in wireframe style for clarity.



**Scheme 59.** Synthetic routes for complexes **2** and **3**.

The average Yb-Cp\* centroid and Yb-N distances in **3** are 2.33(2) and 2.330(8) Å, respectively, and are slightly shorter than the ones in **2** as 2.342(2) and 2.364(2) Å. Thus, the data agree well with a trivalent Yb fragment. A longer bimpm bridging bond length of 1.459(5) Å is observed in **3** in comparison to that in **1**, following a similar trend of the ligand reduction as that in **2**. The distance of the coupled  $\sigma$ -bond (1.56 Å) between two pyrimidine cycles is much longer than the one in **2** (1.520 Å). This could be due to the less compressed coordination environment found in **3** than in **2**. Moreover, in comparison with **1**, the average distances in **3** of the Ni-N (1.987(2) Å in **3**, 1.97(5) Å in **1**) and Ni-CH<sub>3</sub> bonds (1.928(5) Å in **3**, 1.922(5) Å in **1**) are rather similar. It indicates that both complexes possess a similar divalent coordination system around the nickel center. Importantly, the presence of one co-crystallized KCp\* molecule is an evident evidence of the *dimeric* to *trimeric* transition from **3** to **2**, indicating that the KCp\* formation in solution can be regarded as a clear driving force leading to the rearrangement. Another interesting structural observation in **3** is the noticeable distortion of the nickel fragment (Figure 51). The nearly planar angle (1°) between the bimpm ligand plane and NiMe<sub>2</sub> fragment in **1** became largely bent (31°) in **3**. This is clearly indicative of the liable disassociation of the NiMe<sub>2</sub> moiety in the formation of the coupled ligand system. It has also been observed that a facile decomposition of **3** occurs under the inert atmosphere in solid-state at room temperature compared to **2**, which is stable in these conditions. This probably indicates that the dimethyl-nickel moiety is ready for disassociation from the bimpm ligand to generate ethane and Ni(0) species.

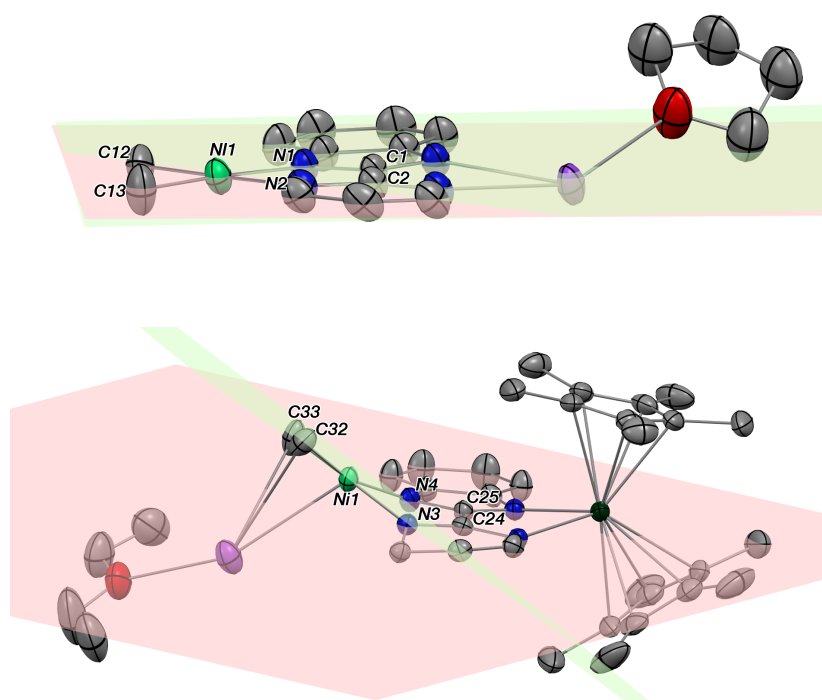
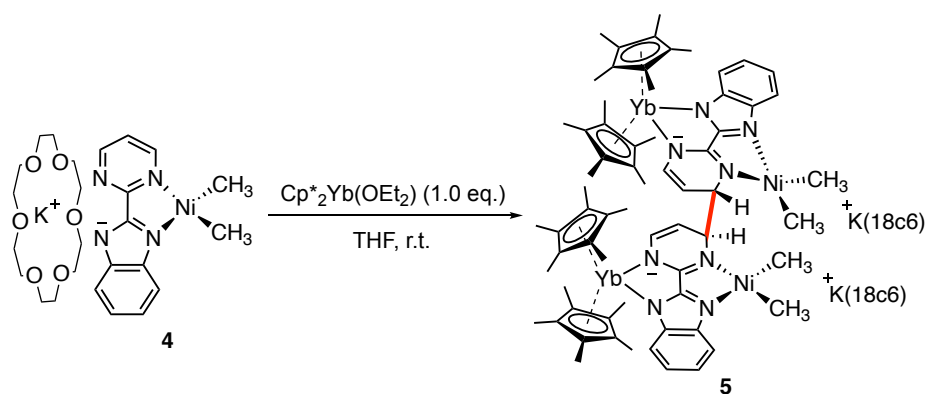


**Figure 51.** Comparison of distortion of the NiMe<sub>2</sub> fragment in **1** (top) and **3** (bottom) presented by ORTEP. N-C-C-N is regarded as the overall ligand plane (red) and atoms are labelled; C-Ni-C is NiMe<sub>2</sub> plane (green) and also labelled. Thermal ellipsoids are at 50 % level. Carbon atoms are in grey, potassium in purple, nitrogen in blue, nickel in bright green and ytterbium atoms in deep green. Half structure of the coupled **3** is presented. Hydrogen atoms have been removed for clarity.

Based on these observations so far, although the fate of NiMe<sub>2</sub> fragment remains uncertain, it is relatively obvious that the formation of KCp\* salt helps the rearrangement from **3** to **2**. Accordingly, the addition of crown ether (18-crown-6) in solution was considered to cap the active potassium ion and reduced its driving force.<sup>85</sup>

### 2.3. Cap the active potassium ion

The analogous nickel precursor K(18-c-6)(bimpm)NiMe<sub>2</sub> (**4**) was synthesized by straightforward stoichiometric addition of 18-crown-6, isolated as deep blue crystalline product (Figure 52) in good yield (91%). The combination with Cp\*<sub>2</sub>Yb(OEt<sub>2</sub>) was performed in both THF and Et<sub>2</sub>O with different reaction times at room temperature yielding indifferently an anionic heterobimetallic species containing the Yb-bimpm-Ni fragment (**5**), in which two pyrimidine cycles on bimpm ligands are also coupled in *exo*-position and the potassium counter ions are capped by 18-crown-6. (Scheme 60 and Figure 53) *Even though the crystals of 5 are still not perfectly suitable for X-ray diffraction (final R-factor as 12.11%) with the best effort has been made, the crystallographic data are indicative enough of all the parameters concerning this work.*



**Scheme 60.** Synthesis of complexes **5** from **4**.

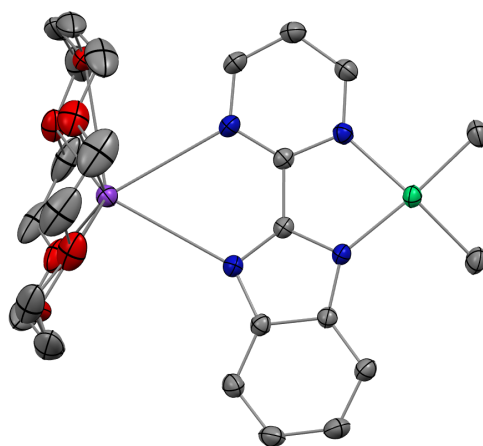


**Figure 52.** ORTEPs of **4** (only one of the molecules of the cell is shown). Thermal ellipsoids are at 50 % level. Carbon atoms are in grey, nitrogen atoms in blue, oxygen atoms in red, nickel atom in green and potassium atom in purple. Hydrogen atoms have been removed for clarity.

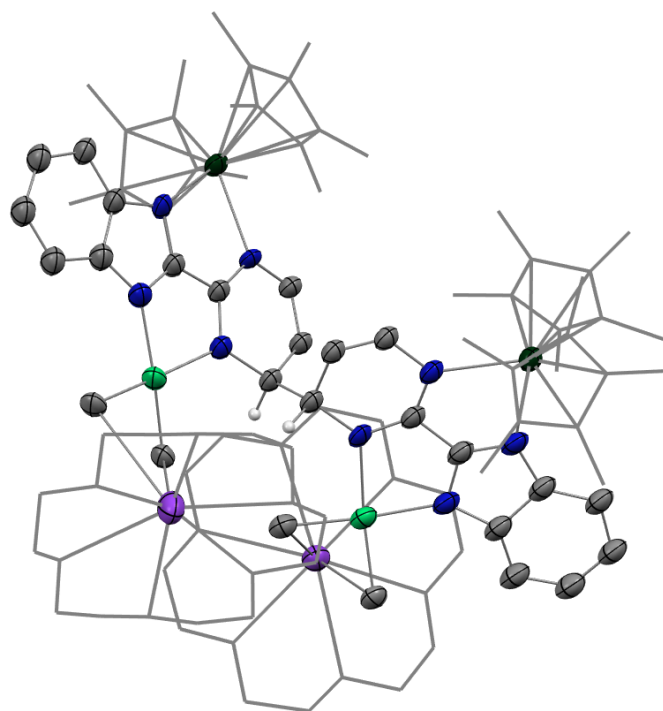


**Figure 53.** ORTEPs of **5**. Thermal ellipsoids are at 50 % level. Carbon atoms are in grey, hydrogen atoms are in white and have been removed for clarity except the ones on the coupled carbons of the ligands, potassium in purple, nitrogen in blue, nickel in bright green and ytterbium atoms in deep green. Co-recrystallized solvate molecules of Et<sub>2</sub>O are removed and pentamethylcyclopentadienyl ligands on ytterbium and 18-crown-6 molecules are presented in wireframe style for clarity.

The average distance Yb-Cp\*<sub>ctr</sub> in **5** is 2.340(2) Å indicating an Yb<sup>III</sup> fragment. A reduction has taken place in the ligand, which can be noticed by a longer ligand linker bond length (1.464(5) Å) comparing to the one in **4** as 1.45(6) Å. Similar parameters based on the comparison in Ni-CH<sub>3</sub> and Ni-N distances of **4** and **5** indicate the remaining divalent nickel center. The distortion angle of bimpm and NiMe<sub>2</sub> difference in **4** and **5** is only nearly 6°, indicating a more stable coordination environment, compared to than found in **3**.

**Table 9.** Main distances (Å) and angles (°) for **1-6**.

	<b>1</b>	<b>4</b>	<b>2</b>	<b>3</b>	<b>5</b>	<b>6</b>
Ni-CH <sub>3</sub>	1.922(5)	1.92(4)	-	1.928(5)	1.913(5)	1.930(5)
Ni-N	1.97(5)	1.970(5)	-	1.987(2)	2.013(2)	1.973(5)
Yb-N	-	-	2.364(2)	2.330(8)	2.328(2)	-
Yb-Cp* <sub>centr</sub>	-	-	2.342(2)	2.33(2)	2.340(2)	-
Bridging C-C <sub>bimpm</sub>	1.451	1.45(6)	1.476	1.459(5)	1.464(5)	1.46(8)
Coupled C-C <sub>bimpm</sub>	-	-	1.520	1.56	1.556	1.537
bimpm^NiMe <sub>2</sub>	1	12	-	31	18	17

As discussed before, it is rather interesting to compare the distortion angles between the bimpm ligand plane and the dimethyl nickel fragment plane in **3** and **5** (Figure 54). In **5**, the average angle is 18°, which is similar to that of 12° in **4**. Thus, the small increase in **5** compare to **1** is likely due to steric hindrance because of the 18-crown-6 chelation. Additionally, **5** was found to be more stable at room temperature in the solid-state than **3** under the same conditions. Thus, the fast decomposition of the nickel fragment in **3** is likely to be the reason for the easy formation of **2** as a thermodynamically stable, homoleptic trimer.

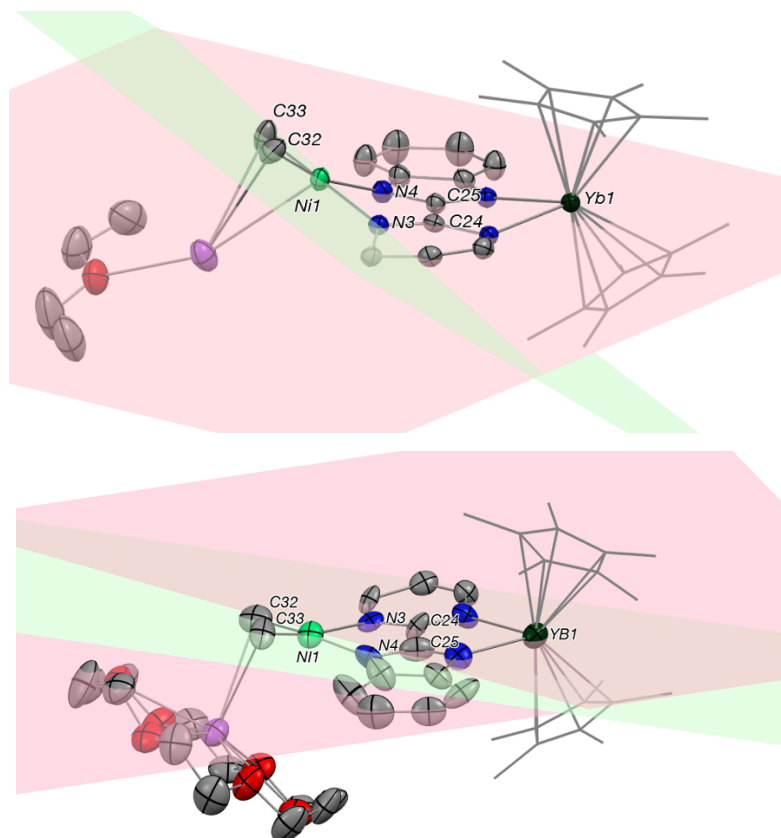
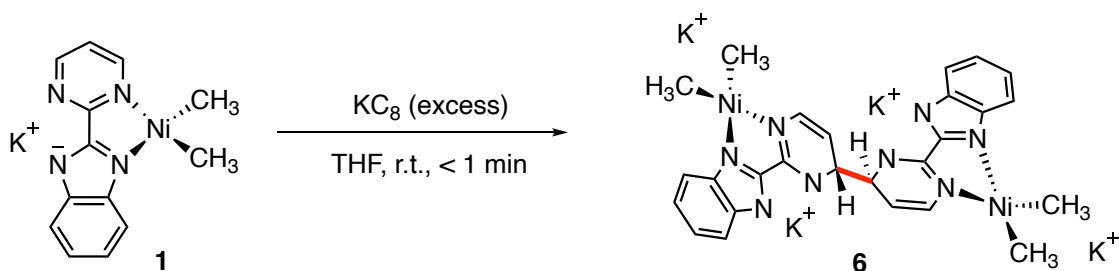


**Figure 54.** Comparison of the bimpm-NiMe<sub>2</sub> distortion angle between **3** and **5**. ORTEPs of **3** (left) and **5** (right).

Thermal ellipsoids are at 50 % level. Carbon atoms are in grey, hydrogen atoms are in white and have been omitted for clarity except the ones on the coupled carbons of the ligands, potassium in purple, nitrogen in blue, nickel in bright green and ytterbium atoms in deep green. Co-recrystallized solvate molecules of Et<sub>2</sub>O in both complexes are removed and pentamethylcyclopentadienyl ligands on ytterbium are presented in wireframe style for clarity.

The radical coupling nature of **2**, **3**, and **5** resulted from single-electron transfer, which was induced by divalent lanthanides, led to a sequential study by a direct reduction on **1**, in order to estimate the impact of the reductive lanthanide ions. A reduction by using KC<sub>8</sub>, which is in excess, was performed on **1** (Scheme 61) and XRD-suitable brown-orange crystals of the reaction product, **6**, were isolated *via* slow diffusion of pentane into THF solution at -35°C after several days. An ORTEP of **6** and main bond distances and angle are presented in Figure 55 and Table 9.



**Scheme 61.** Synthesis of **6** from **1** by  $\text{KC}_8$  reduction.

In **6**, the average distances of the Ni-N and Ni-CH<sub>3</sub> bonds are 1.973(5) and 1.930(5) Å, respectively, which are indicative of the divalent oxidation state of nickel center. A longer distance of C-C linkage bond between pyrimidine and benzimidazole of 1.46(8) Å compared to that of 1.451 Å in **1**, indicates an efficient reduction on the ligand moiety by potassium graphite. The torsion angle between the ligand plane and the NiMe<sub>2</sub> fragment is 17°, which is similar to the one in **5** (19°), yet much smaller than the one in **3** (31°). Correspondingly, **6** was found to be thermally stable for several days in solution at room temperature under inert atmosphere, without eliminating ethane or forming Ni(0) species. What is comparatively interesting in **6** is that, a coupled C-C bond between two pyrimidine rings was also observed but in a completely different position than that in **2**, **3** and **5**. In **6**, the coupling occurs on the *para* carbon of the Ni-coordinated nitrogen atom, while in other structures with the divalent lanthanide, the coupling is at the *ortho* site. The length of the coupled C(sp<sup>3</sup>)-C(sp<sup>3</sup>) bond is 1.537 Å, which is similar to the ones in **2**, **3** and **5**.

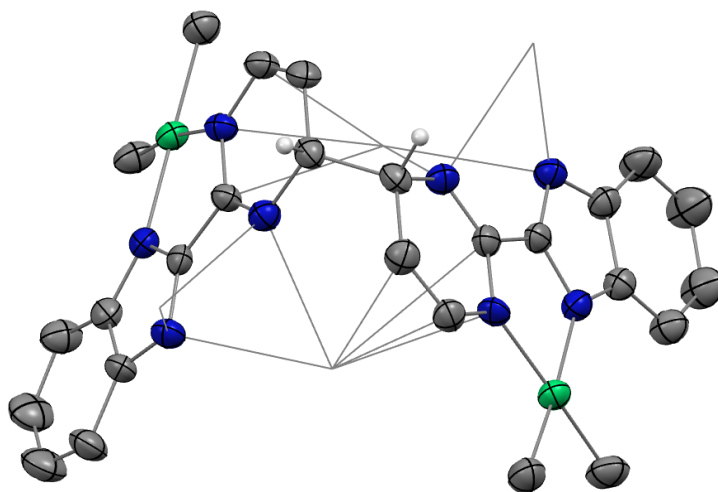


**Figure 55.** ORTEPs of **6**. Thermal ellipsoids are at 50 % level. Carbon atoms are in grey, hydrogen atoms in white and have been removed for clarity except the ones on the coupled carbons of bimpm ligands, nitrogen in blue and nickel in bright green. Co-recrystallized solvate molecules of THF have been omitted and potassium atoms are presented in wireframe style for clarity.

This opposite coupling fashion on bimpm ligand in **3** and **6** is intriguing and it then is plausible that the coordination of the divalent lanthanide ions could subtly modulate the electron density on the redox-active ligand fragment because of strong electron correlation. The steric hinderance effect of the Cp\* ligands on the lanthanide moiety might also participate in regulating the position at which



the coupling occurs. Therefore, further study on the electronic structures and spin density of these molecules should be required, in order to investigate the intriguing roles of the lanthanide fragments in the heterometallics.

### 3. Characterizations and discussions

#### 3.1. NMR studies

The dissymmetric bimpm ligand imposes a  $C_s$  symmetry in the precursor **1** and **4**.  $^1\text{H}$  NMR of **1** in THF- $d^8$  at 293 K shows two resonances for the methyl (6 protons) at 0.02 and -0.40 ppm, and five signals are found in the range of 8.6 – 6.8 ppm for the seven protons on bimpm ligand (Figure 56). The spectrum of **4** was recorded in  $\text{CD}_3\text{CN}$  at 293 K, showing six resonances for the bimpm ligands (7 protons), found in 8.8 – 6.9 ppm range, one signal for 18-crown-6 (24 protons) at 3.55 ppm, as well as two signals for the dimethyl fragment at -0.10 and -0.54 ppm (Figure 57).

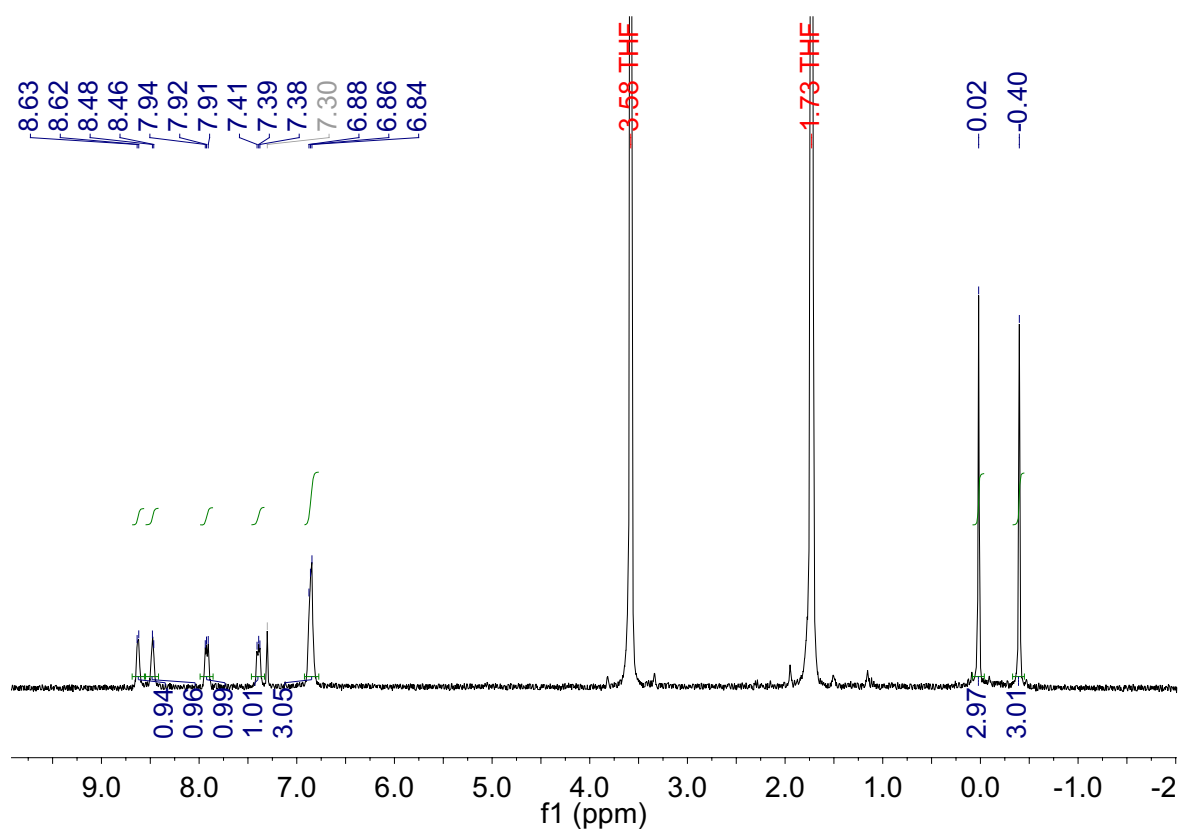


**Figure 56.**  $^1\text{H}$  NMR of **1** in THF- $d^8$  at 20°C. Benzene impurities are indicated in grey.

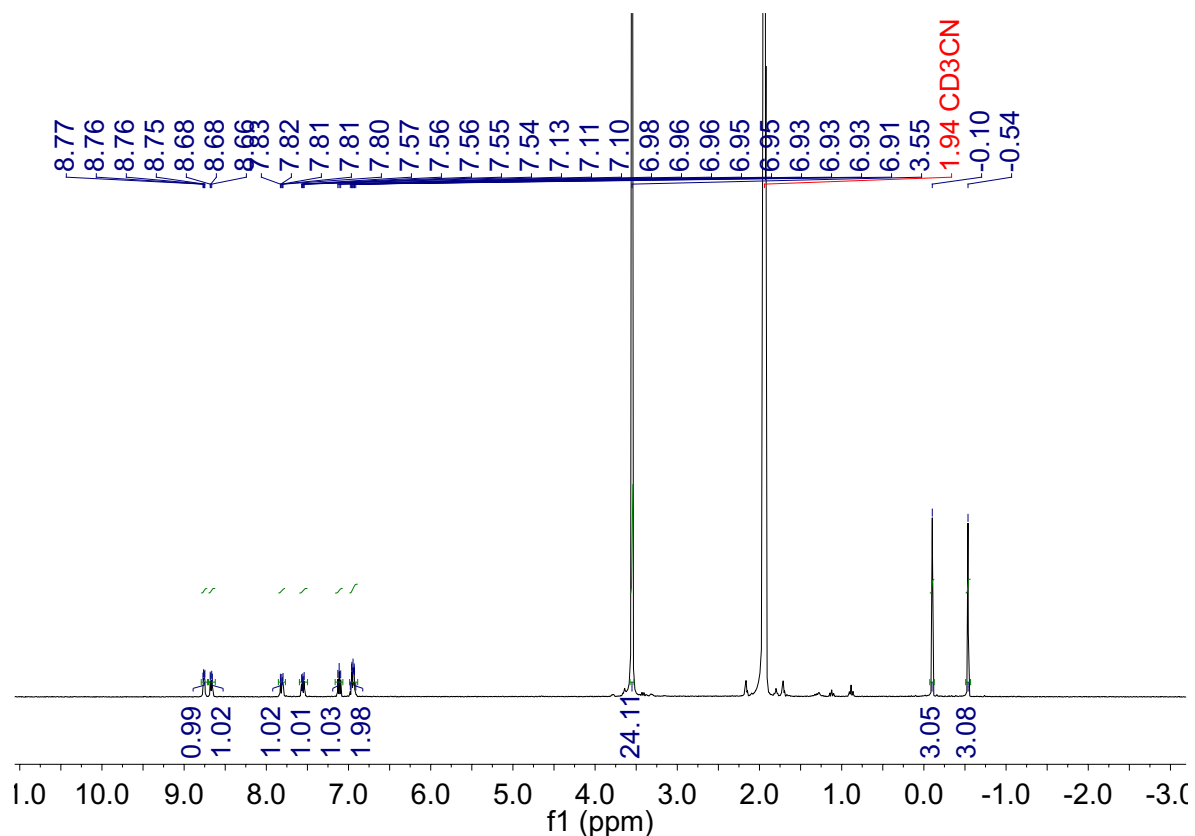


**Figure 57.** <sup>1</sup>H NMR of **4** in CD<sub>3</sub>CN at 20°C.

The addition of the divalent ytterbium fragment can drastically shift these protons in **1** and **4**, agreeing with the presence of a paramagnetic Yb<sup>III</sup> center when the electron transfer takes place. The <sup>1</sup>H NMR of **2** was recorded in THF-d<sup>8</sup> at 293 K and it shows nicely 14 signals of two bimpm ligands with each integration of 1 proton, and 5 signals of Cp\* moieties on ytterbium ions with integration of 15 protons (Figure 58). This spectrum is in good agreement with a coupled ligand and no symmetry, other than the identity, *i.e.* a C<sub>1</sub> symmetric molecule in solution. The strong paramagnetism well indicates the presence of the paramagnetic trivalent ytterbium ion in this complex.

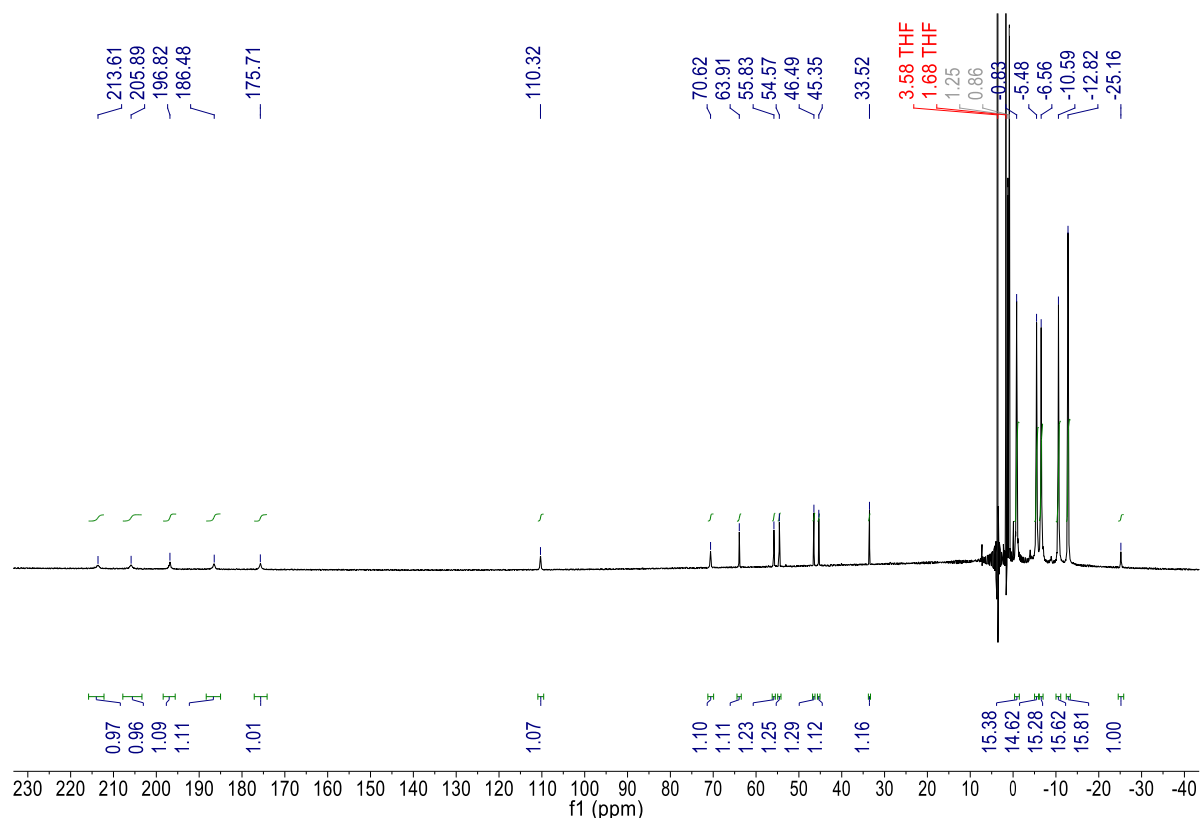


**Figure 58.**  $^1\text{H}$  NMR of **2** in THF- $d_8$  at 20°C. *n*-Pentane impurities are indicated in grey.

Similarly,  $^1\text{H}$  NMR spectra of **3** and **5** (recorded values in bracket) due to the similar coordination environment were recorded in THF- $d_8$  and in  $\text{CD}_3\text{CN}$ , respectively at 293 K, with seven protons for the bimpm ligand at 187.66 (186.25), 181.49 (176.11), 50.43 (53.04), 27.46 (30.55), 19.17 (23.32), 4.91 (-0.03) and -8.27 (-4.50) ppm. Additionally, two non-equivalent Cp\* signals are found at 12.28 (7.91) and 2.93 (2.29) ppm and non-equivalent methyl signals at -4.81 (-0.86) and -18.17 (-14.03) ppm (Figure 59 and 60). Differently from **2**, the presence of only seven signals for the ligand but two different signals for the methyl and Cp\* moieties is in good agreement with a dimeric species with a  $\text{C}_2$  symmetry, which means an inversion center at the center position of the formed *exo*-C-C bond. However, the NMR data actually cannot identify the exact stereochemical nature of the C-C coupling, while they provide much information of such dimeric species in solution, fitting the bond formations that are found in the solid-state XRD structure. Again, the paramagnetism of **3** and **5** is indicative of effective electron transfer from divalent lanthanide to the redox-active bimpm- $\text{NiMe}_2$  fragment.

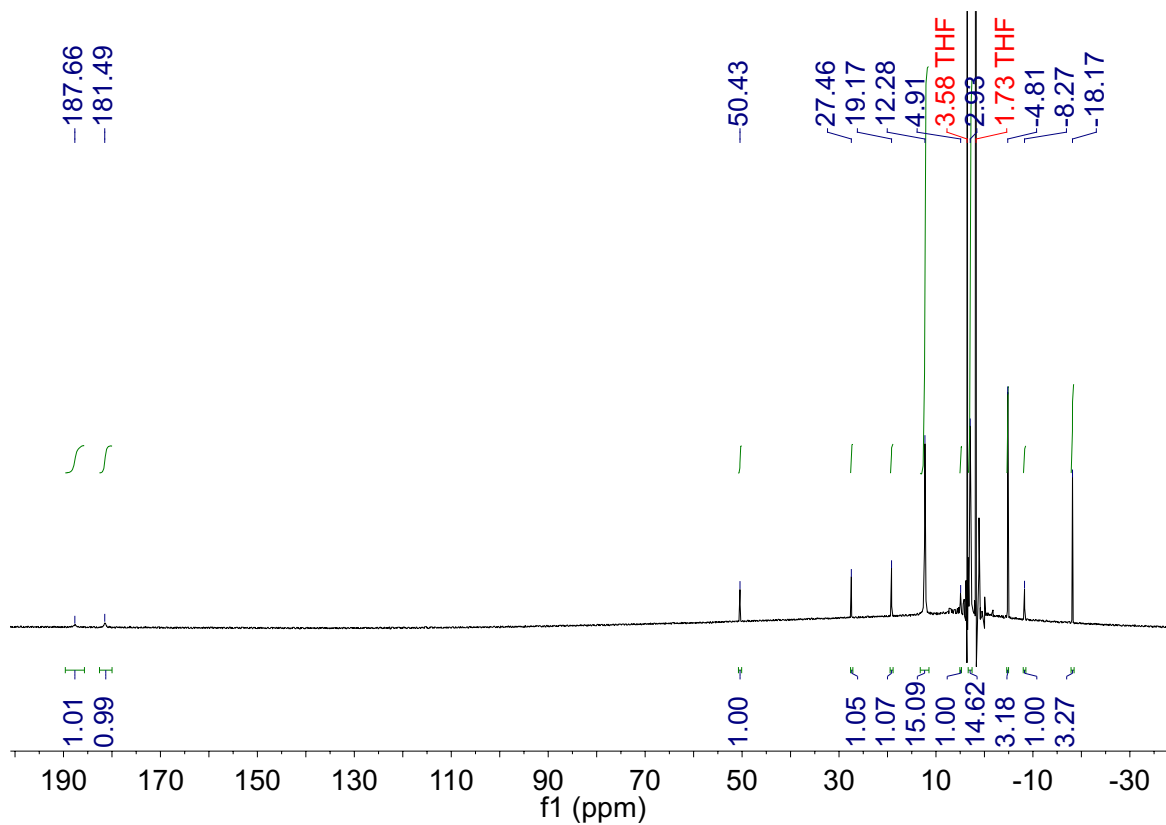


Figure 59.  $^1\text{H}$  NMR of **3** in  $\text{THF-d}_8$  at  $20^\circ\text{C}$ .

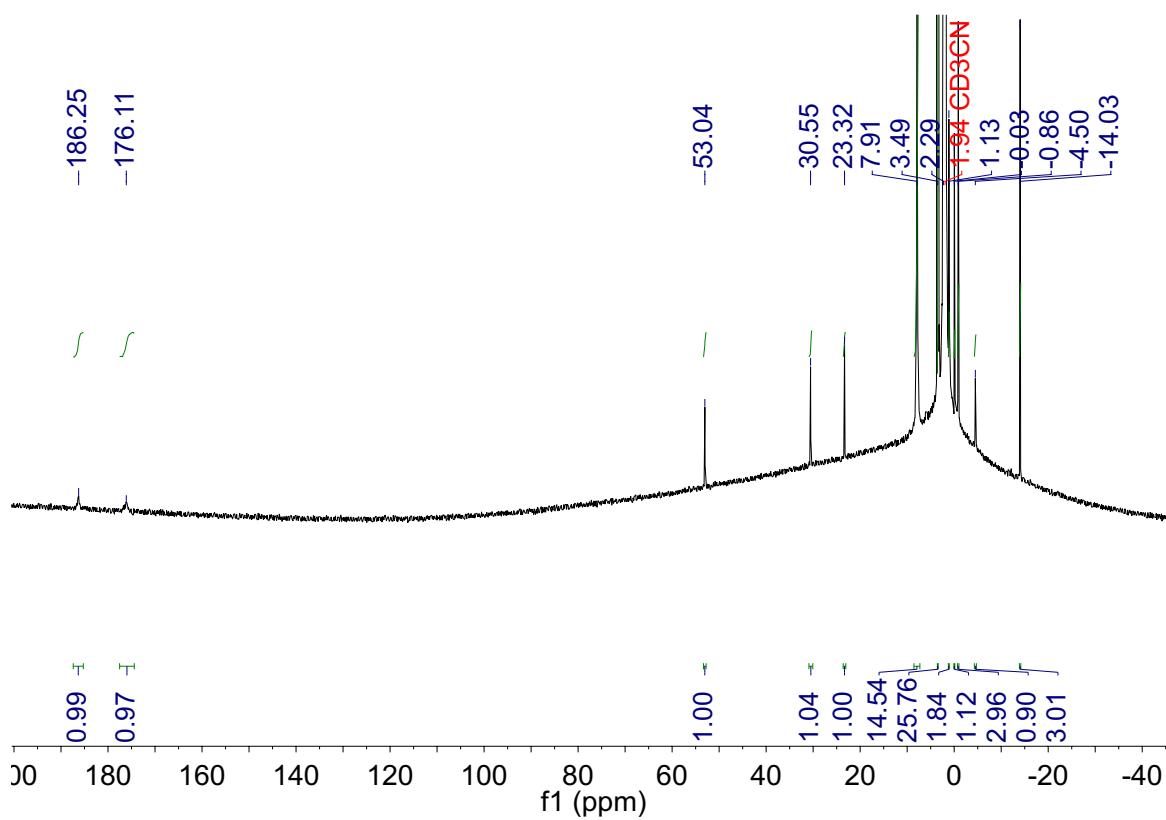
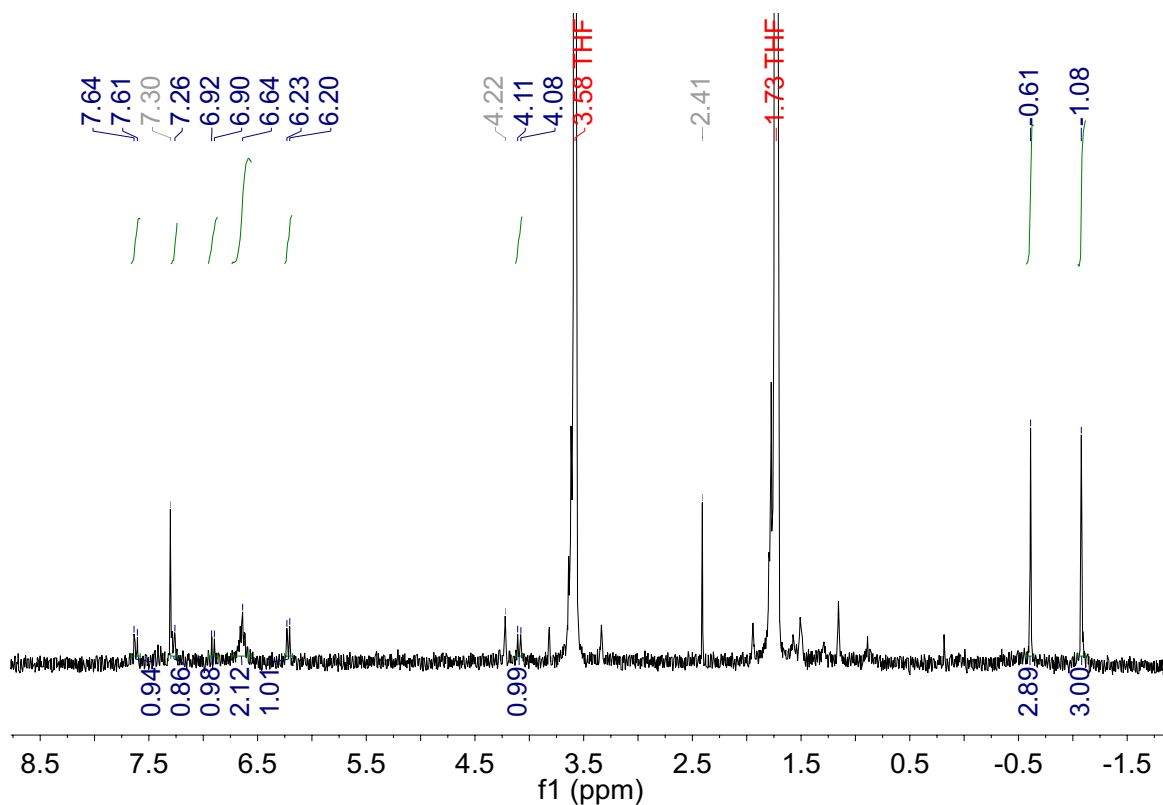
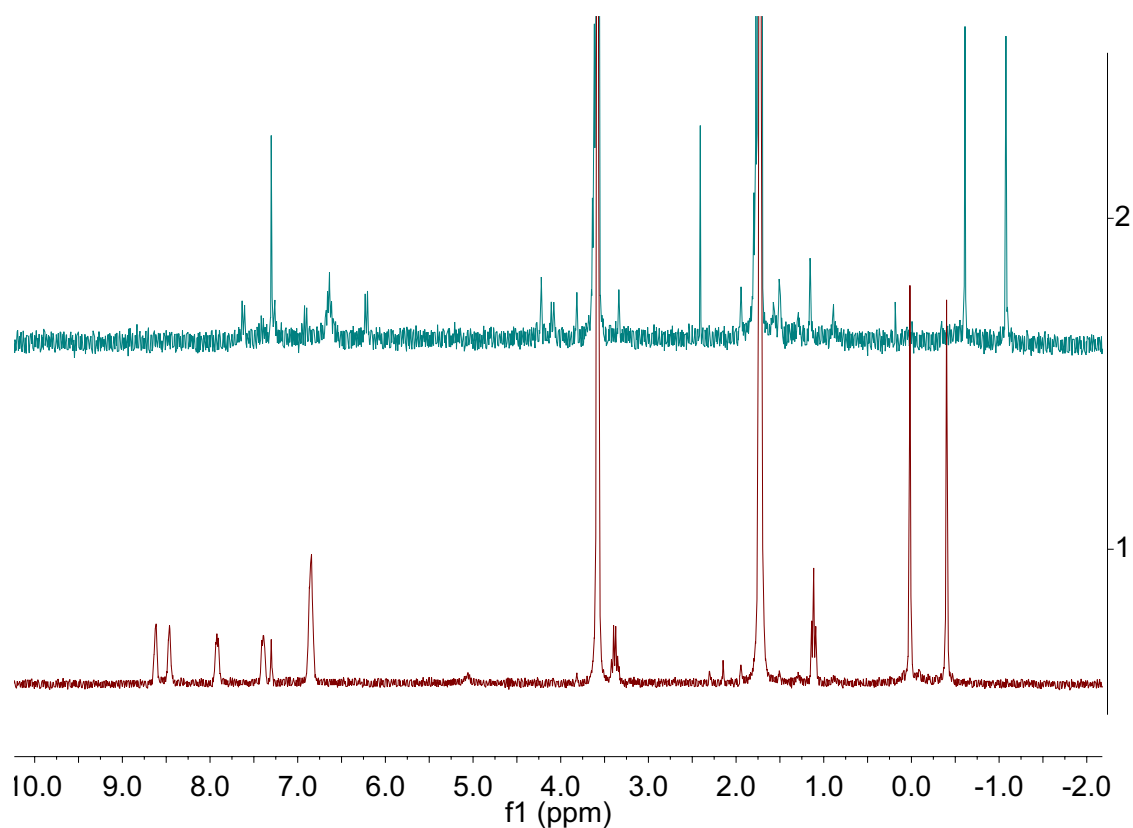


Figure 60.  $^1\text{H}$  NMR of **5** in  $\text{CD}_3\text{CN}$  at  $20^\circ\text{C}$ .

$^1\text{H}$  NMR of **6** was recorded in  $\text{THF-d}^8$  at 293 K, showing two resonances for the methyl (6 protons) at -0.61 and -1.08 ppm, and five signals are found in the range of 7.6 – 6.2 ppm for the six protons on the  $\text{sp}^2$  carbons of the bimpm ligand, and one doublet signal for one proton on the  $\text{sp}^3$  coupled carbon (Figure 61). The thorough purification was unfortunately not successful due to the hardly removed, orange residue impurity accompanied with the isolated crystals of **6**. Nevertheless, a clearly different, reduced species of **6** from **1** can be identified in solution (Figure 62).



**Figure 61.**  $^1\text{H}$  NMR (300 MHz,  $\text{THF-d}^8$ , 20°C) spectrum of  $[\text{K}_2(\text{bimpm})\text{NiMe}_2]_2$  (**6**). Residue impurity, which is hardly removed from crystallization, as well as benzene solvate from deuterated solvent are indicated in grey.



**Figure 62.**  $^1\text{H}$  NMR (300 MHz,  $\text{THF-d}^8$ ,  $20^\circ\text{C}$ ) comparison between **6** (top, in green) and **1** (bottom, in red).

In order to get insights on their electronic structures, VT  $^1\text{H}$  NMR of the paramagnetic complexes **2**, **3** and **5** were then recorded in  $\text{THF-d}^8$  and  $\text{CD}_3\text{CN}$ , respectively. The chemical shifts of each resonance in these three compounds are plotted respectively versus  $1/T$  (Figure 64, 65 and 66), and one example of  $\delta$  vs  $T$  plot of **2** is also shown in Figure 63. A linear  $\delta$  vs  $1/T$  plot over the set-up temperature range for each reveals a typical Curie behavior, in good agreement with the recorded solid-state temperature-dependent magnetic data as following.

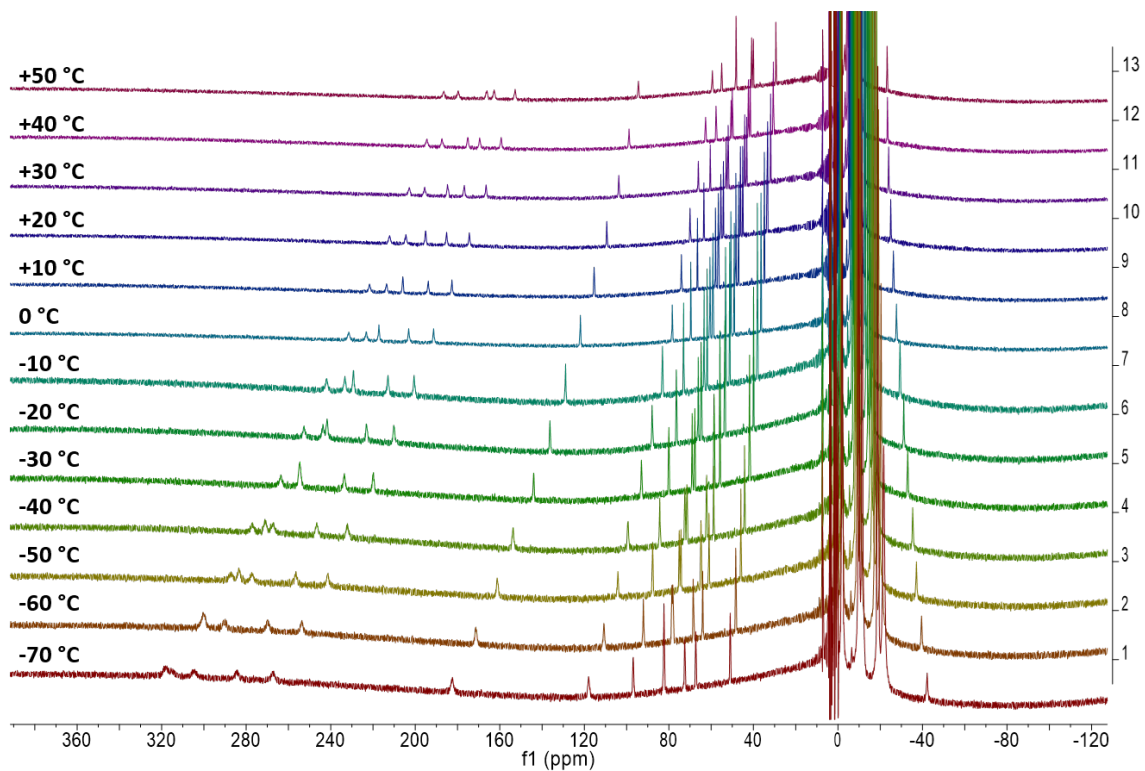


Figure 63. Variable Temperature  $^1\text{H}$  NMR of **2** in  $\text{THF-d}_8$  from  $-70^\circ\text{C}$  to  $50^\circ\text{C}$ :  $\delta$  vs  $T$ .

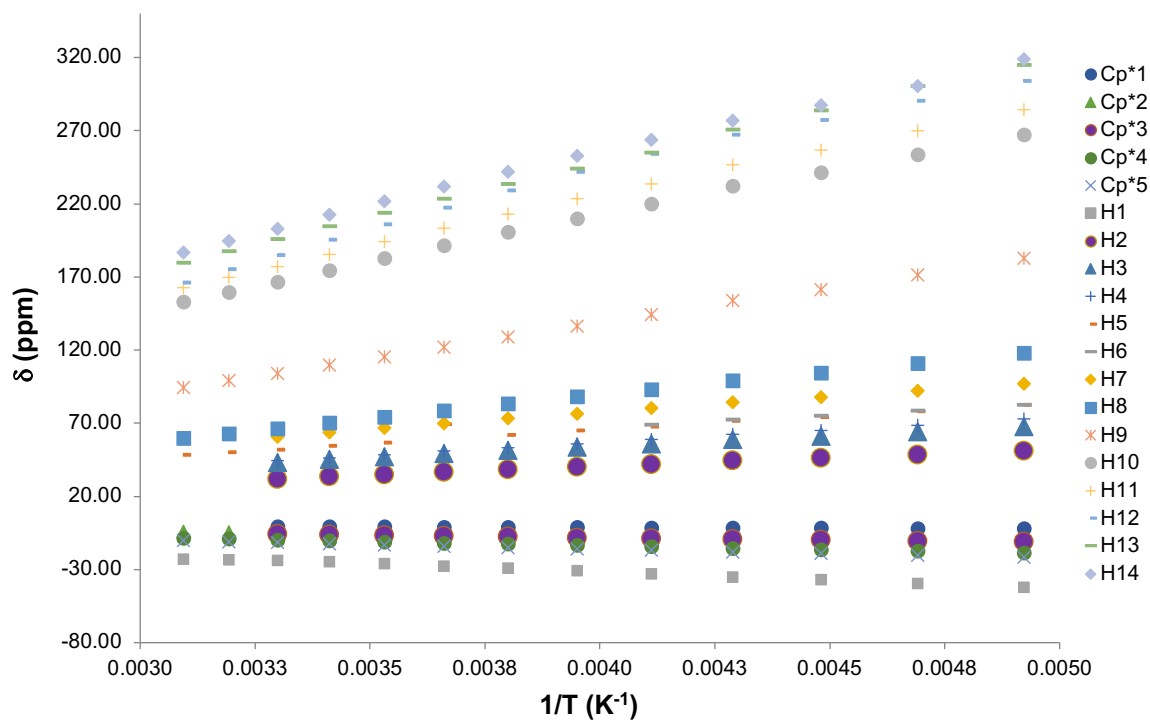
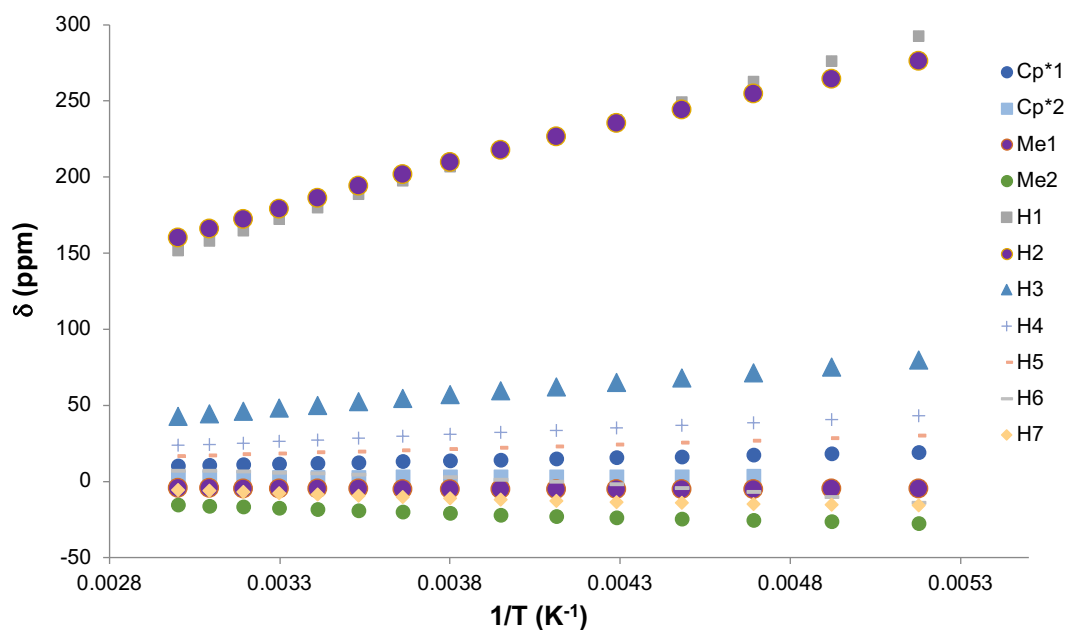
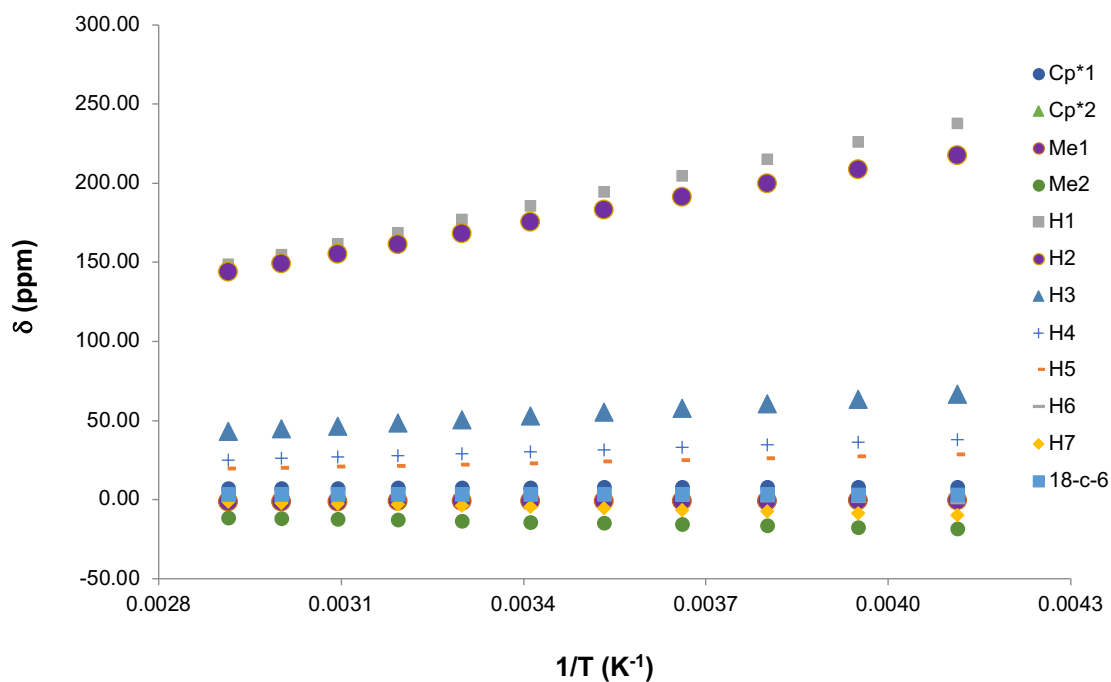


Figure 64. Variable Temperature  $^1\text{H}$  NMR of **2** in  $\text{THF-d}_8$  from  $-70^\circ\text{C}$  to  $50^\circ\text{C}$ :  $\delta$  vs  $1/T$ .



**Figure 65.** Variable Temperature  $^1\text{H}$  NMR of **3** in  $\text{THF-d}_8$  from  $-80^\circ\text{C}$  to  $60^\circ\text{C}$ :  $\delta$  vs  $1/T$ . (Note: Some proton signals are overlapped in the temperature range with the  $\text{THF-d}_8$  signals.)



**Figure 66.** Variable Temperature  $^1\text{H}$  NMR of **5** in  $\text{CD}_3\text{CN}$  from  $-30^\circ\text{C}$  to  $70^\circ\text{C}$ :  $\delta$  vs  $1/T$ . (Note: Most of resonances of one  $\text{Cp}^*$  protons as well as one proton on the bimpm ligand are overlapped in the temperature range with the  $\text{CD}_3\text{CN}$  signal.)

Meanwhile, the reversible or irreversible character of the dimerized C-C bond which is induced by divalent lanthanides, was studied by  $^1\text{H}$  NMR at high temperatures. In fact, different from the relatively stable nature of the  $\text{Cp}^*_2\text{Yb}(\text{phen})$  analogue, **2**, **3** and **5** are rather thermosensitive. An eventual dimer-monomer equilibrium was not efficiently observed when dissolving the crystals of



**2**, **3** and **5** in THF-d<sup>8</sup> at room temperature, comparing to the case of the phen adduct. The possible formation of monomer might take place at higher temperatures, by observing several new signals, such as at 60°C (Figure 67). However, the concomitant decomposition of the dimers also occurred when heating up the solutions for extended periods of time, resulting in a number of hardly identifiable signals (Figure 68). Thus, the reversibility of C-C dimerization in **2**, **3** and **5** remains equivocal.

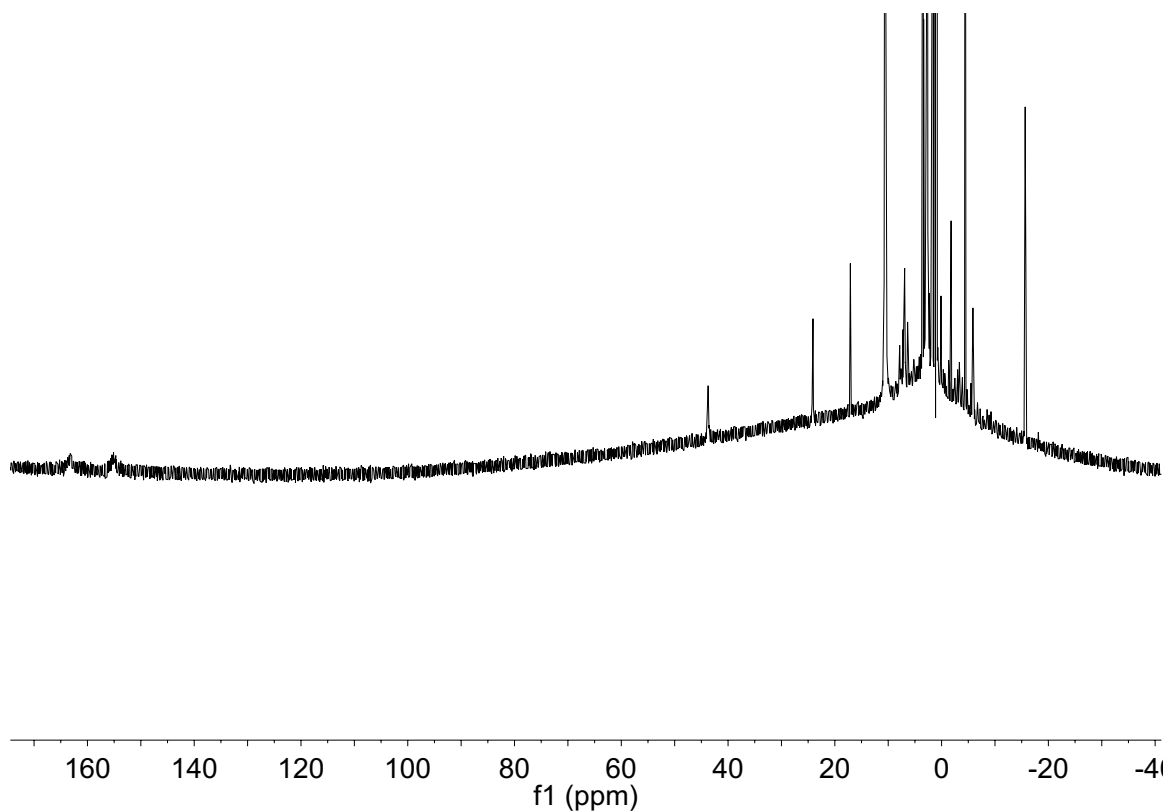


**Figure 67.** <sup>1</sup>H NMR (300 MHz, THF-d<sup>8</sup>, 60°C) spectrum of **3**.

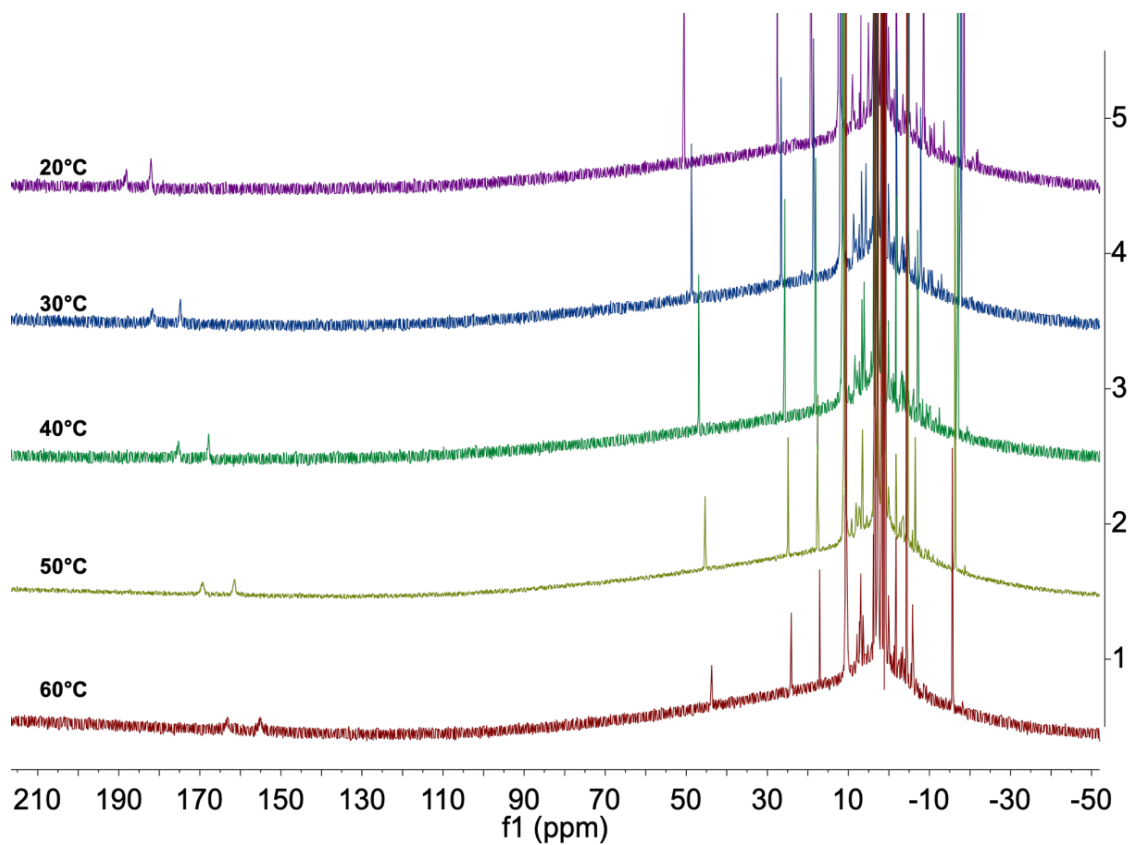


Figure 68. Variable temperature  $^1\text{H}$  NMR (300 MHz,  $\text{THF-d}_8$ ) spectra of **3** from 60°C to 20°C:  $\delta$  vs T.

### 3.2. Magnetism

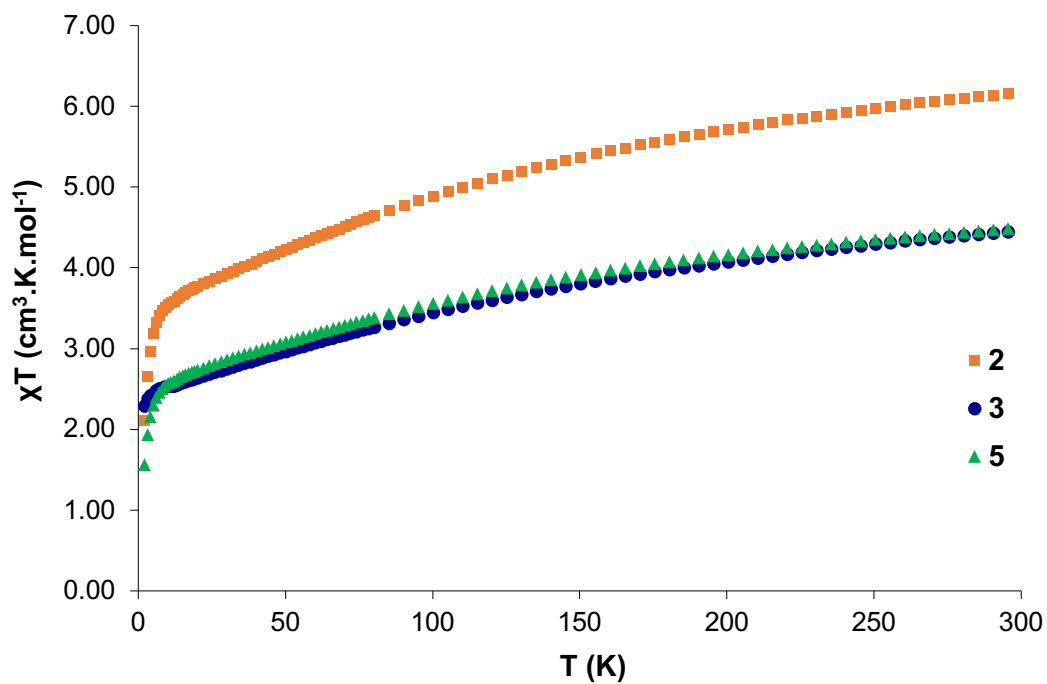


Figure 69. Solid-state temperature-dependent magnetic data for **2** (squares), **3** (circles) and **5** (triangles) at 2 T: plot of  $\chi T$  versus T.

In **2**, **3** and **5**, the coupling character of bimpm ligands indicates that the electron has been transferred from the coordinated divalent ytterbium, which results in the trivalent ytterbium center. Solid-state temperature-dependent magnetic data are recorded in the temperature range of 2-300 K (Figure 69). The solid-state data of all three organometallic compounds at 300 K, indicate  $\chi T$  values of 6.17, 4.45 and 4.45 emu.K.mol<sup>-1</sup> for **2**, **3** and **5**, respectively. The experiment values are in good agreement with the theoretical ones of 2.54 emu.K.mol<sup>-1</sup> for uncorrelated <sup>2</sup>F<sub>7/2</sub> ground-states for each ytterbium center, which reveals three ytterbium centers in **2** and two ytterbium centers in both **3** and **5**. Then, when the temperature constantly decreases, the  $\chi T$  values monotonously decreases up to 6 K with 3.32, 2.42 and 2.44 emu.K.mol<sup>-1</sup> for **2**, **3** and **5**, respectively, and then drops below 6 K. The decreasing behavior of the  $\chi T$  values is due to the depopulation of the higher energy crystal-field states. Additionally, a very similar behavior of **3** and **5** is indicative of a very similar crystal field, which well agrees with their very similar structural characters.

### 3.3. DFT calculations

In order to better understand how the lanthanide fragments impact the spin density on the redox-active ligand systems, theoretical investigations have been undertaken on the anionic bimpm species, **1**, and the monomeric form of **3**, at the DFT level using the PBE density functional.

The optimized geometry of the anionic ligand reveal that the LUMO is delocalized equally across the C<sub>2</sub> axis of symmetrical ligand, while the spin density is more localized in the pyrimidine cycle (Figure 70). In the presence of the Ni fragment, the electronic density of the LUMO is significantly modified with strong density localized on the pyrimidine nitrogen atom that coordinates the nickel ion and on the carbon in *para* position to the latter. On the contrary, the *ortho* position to the coordinated nitrogen atom possesses much little electron density (Figure 71). This is consistent with the coupling fashion observed in **6** that when electron transfer occurs, a strong spin density will be localized in the *para* position.

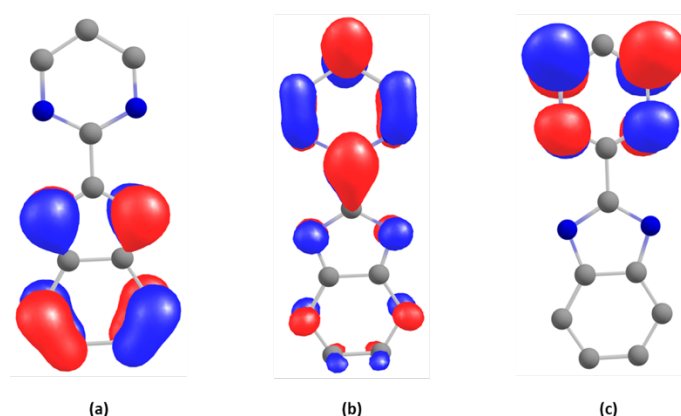


**Figure 70.** Main Kohn-Sham orbitals of the [bimpm] anion molecule obtained with PBE0 functional starting from a geometry optimized in PBE: (a) HOMO, (b) LUMO, and (c) LUMO +1.

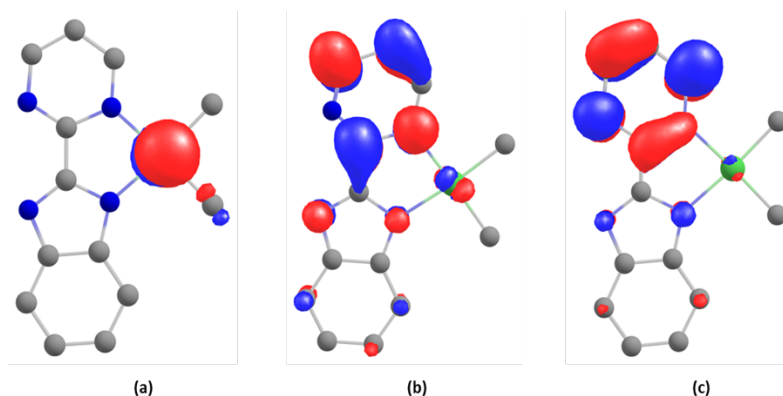


**Figure 71.** Main Kohn-Sham orbitals of the anionic **1** obtained with PBE0 functional starting from a geometry optimized in PBE: (a) HOMO, (b) LUMO, and (c) LUMO +1.

The addition of Cp\*<sub>2</sub>Yb fragment is accompanied by an electron transfer to the bimpm ligand (Figure 72). The SOMO is now delocalized on the ligand while the LUMO is majorly centered on the pyrimidine moiety of the ligand. In the SOMO, the spin density has virtually no contribution on the *para* carbon of the Ni-coordinated pyrimidine nitrogen atom, while little contribution on the *ortho* carbon where the coupling occurs in **2**, **3** and **5**. Only based on the study at DFT level, it will be complicated to well explain why the spin delocalization towards the distinct coupling site can be significantly influenced by the lanthanide ion in **3** comparing to the case in **6**. A more sophisticated method should be applied to this multiconfigurational system in the presence of lanthanide moiety, such as CASSCF, in the future study.

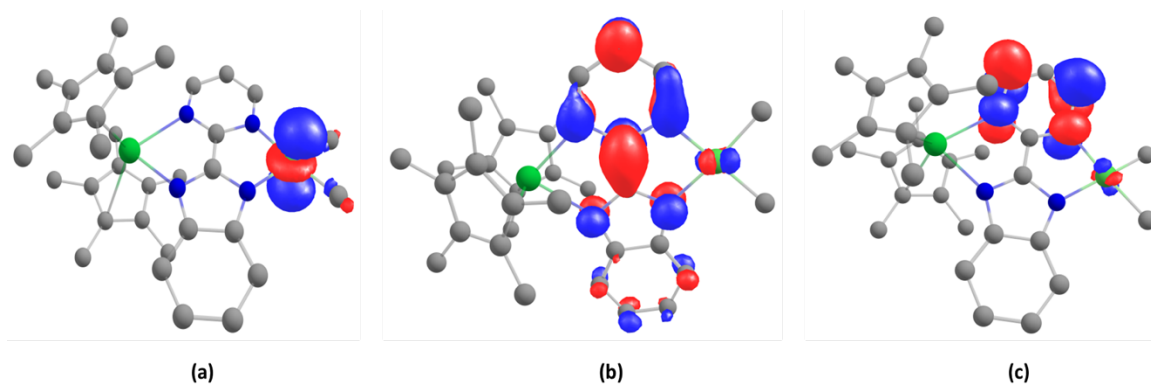
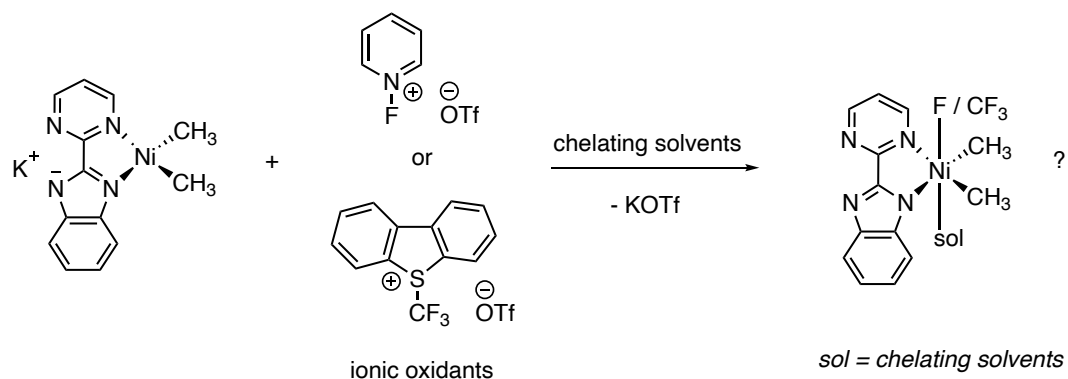


**Figure 72.** Main Kohn-Sham alpha orbitals of the anion of the monomeric form of **3** obtained with PBE0 functional starting from a geometry optimized in PBE: (a) SOMO-1, (b) SOMO, and (c) LUMO.

#### 4. Reactivity attempts

Several reactivity tests were performed on the nickel precursors **1** and **4** with mild and strong oxidants. The presence of the potassium counter ion could be considered as a good driving force towards the desired high-valent Ni species by forming potassium salts from the reaction mixture when using ionic oxidants. Umemoto reagents, as well as 1-fluoropyridinium derivatives, were applied in the deuterated chelating solvents (CD<sub>3</sub>CN and pyridine-d<sup>5</sup>) for the preliminary trials (Scheme 62). Ethane formation did not observe from <sup>1</sup>H NMR, however, newly formed, yellow solid went into precipitation immediately during the *in-situ* addition of oxidants, and this caused a

difficulty in performing the proper NMR study. The insoluble, formed yellow solid was then analyzed by mass spectroscopy. However, the signals corresponding to the desired high-valent nickel species were not found even though isotopic patterns with Ni could be identified. This trial is worth to be mentioned because of the rather stability of the questionable crude product, but a certain modification on the ligand moiety should surely be considered in order to increase the solubility, so that the further attempt to the possible high-valent species can be proceeded.



**Scheme 62.** Reactivity trials of **1** with some ionic oxidants performed in chelating solvents.

To further probe the reversibility of the C-C coupling formation in **2**, **3** and **5**, a hydrogen donor such as 9,10-dihydroanthracene (DHA), which can undergo relatively facile dehydrogenation to form the aromatic anthracene, was considered.<sup>86,87</sup> Stoichiometric equivalence of DHA was added to the *in situ* reaction mixture towards **3** in THF-*d*<sup>8</sup> at room temperature and NMR study was then followed. The expected C-C cleavage did not observe by <sup>1</sup>H NMR in the beginning of the reaction (Figure 73 and 74). Then the degradation of **3** as well as the possible transition from **3** to **2** (Figure 75) was observed by NMR after 24 h, and no obvious consumption of DHA was identified even though the internal standard was lacking in this whole test (Figure 76).

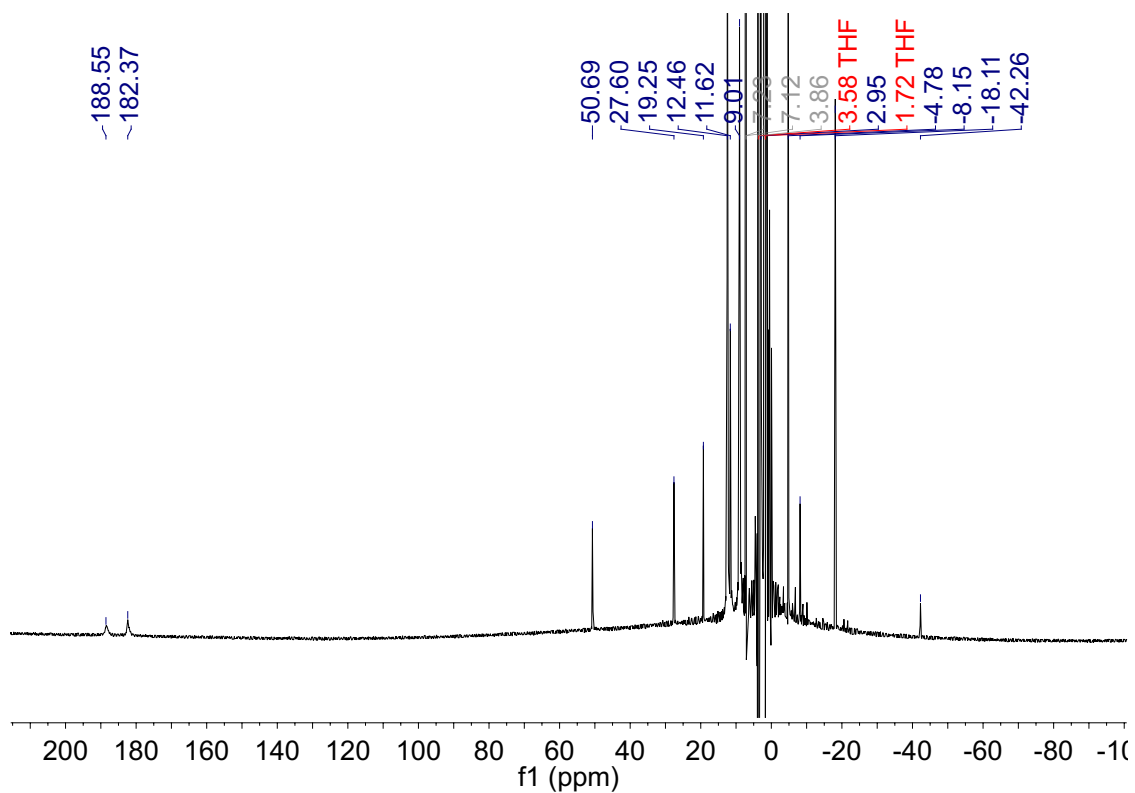


**Figure 73.**  $^1\text{H}$  NMR (300 MHz,  $\text{THF-d}_8$ ,  $20^\circ\text{C}$ ) spectrum of the cleavage trial of **3** in the presence of DHA (1 equiv.) at  $t = 0$ . Resonances of DHA are indicated in grey.

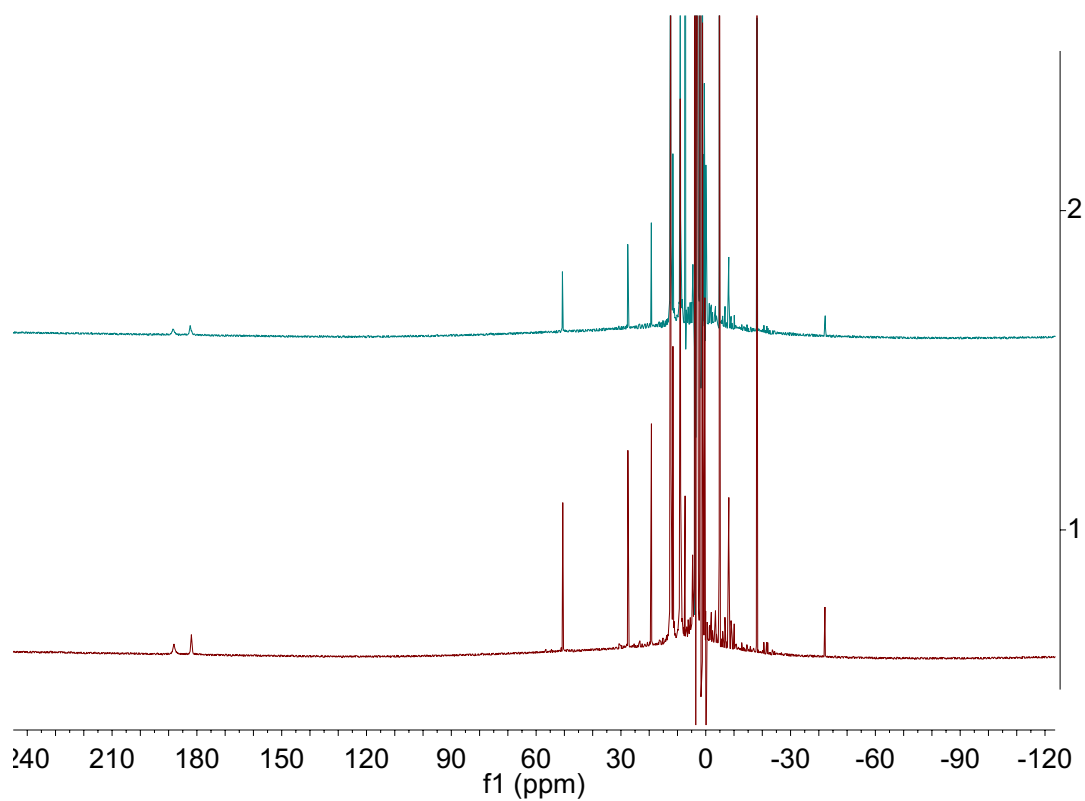


**Figure 74.**  $^1\text{H}$  NMR (300 MHz,  $\text{THF-d}_8$ ,  $20^\circ\text{C}$ ) comparison between **3** in the presence of DHA ( $t = 0$ , top, in green) and *in situ* formed **3** without DHA (bottom, in red).

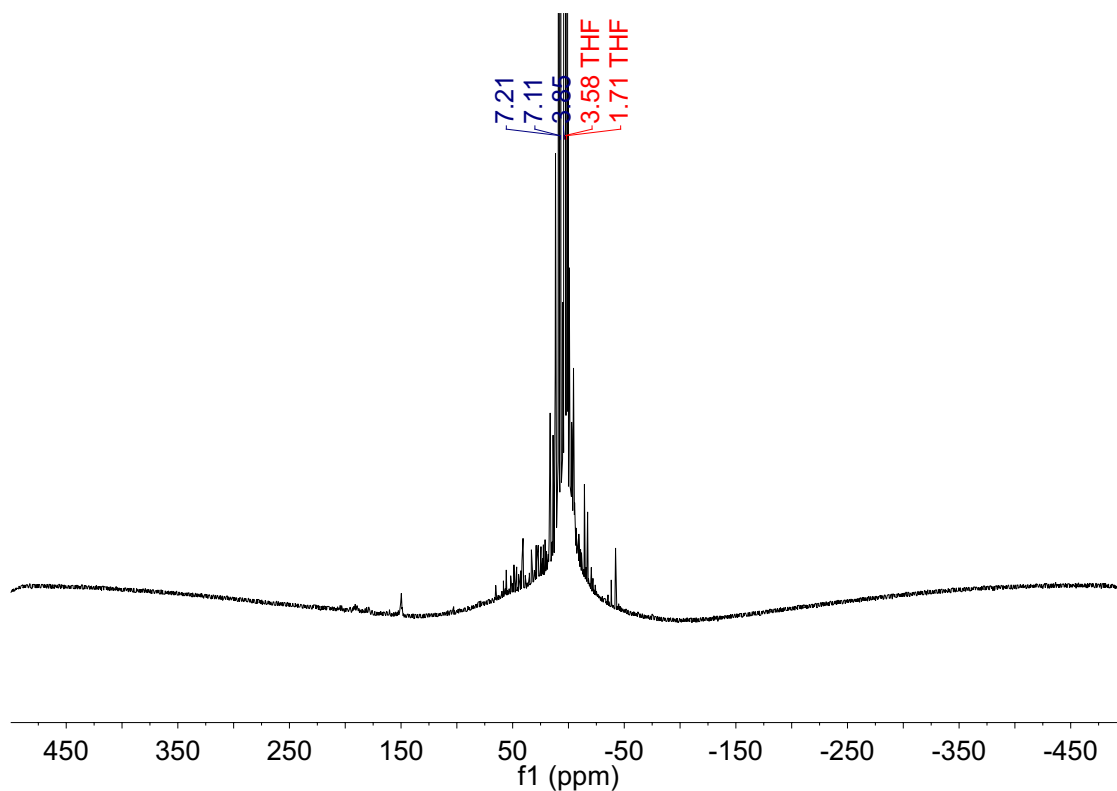


**Figure 75.**  $^1\text{H}$  NMR (300 MHz, THF- $d_8$ , 20°C) spectrum of the cleavage trial of **3** with DHA (1 equiv.) after 24 hours at room temperature. Resonances of DHA are only indicated.

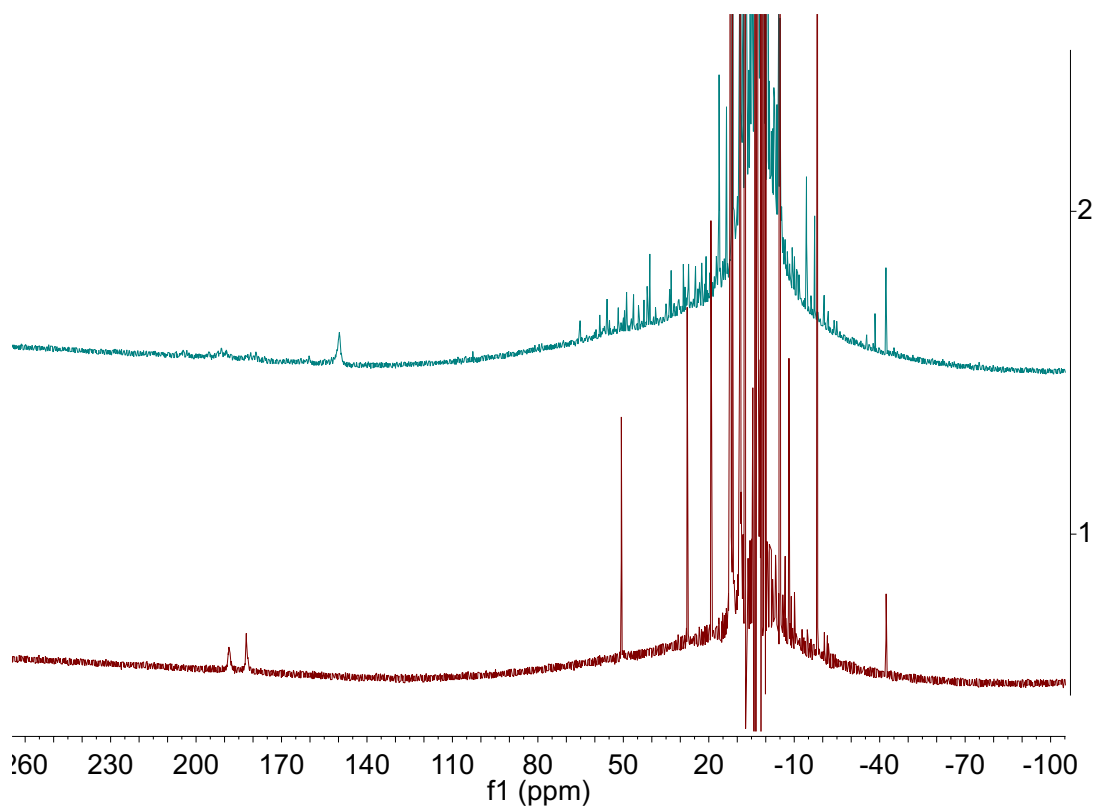
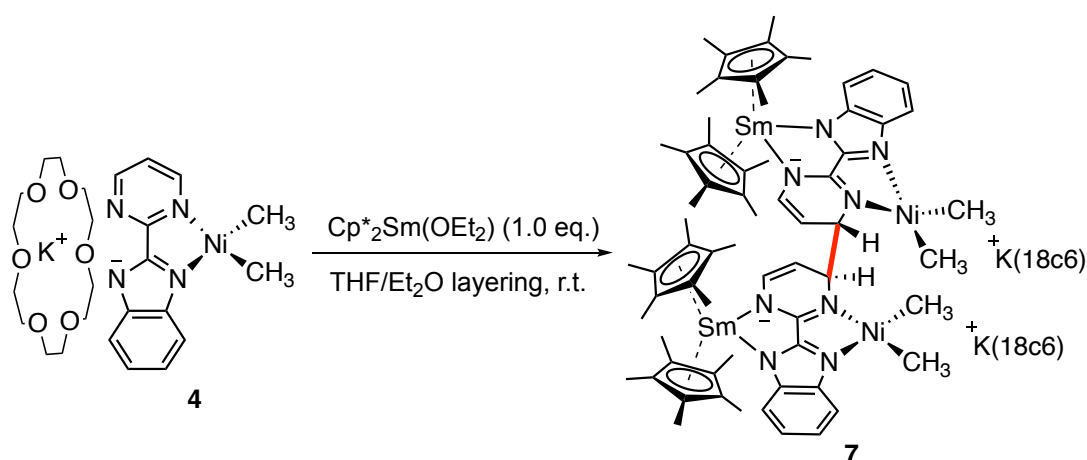


**Figure 76.**  $^1\text{H}$  NMR (300 MHz, THF- $d_8$ , 20°C) comparison of **3** with dihydroanthracene between  $t = 24$  h (top, in green) and  $t = 0$  (bottom, in red).

## 5. Replacement with samarium

Extending this work by modifying elements in the framework of “Ln-RAL-TM”, a different organolanthanide fragment was considered,  $\text{Cp}^*_2\text{Sm}$ . This would notably allow getting more insights into such coupling formation, for instance, the thermodynamics for the dimerization reaction.

It was expected that the dimerization can more readily happen because of the more reducing potential of divalent samarium than ytterbium.<sup>59</sup> The preliminary reaction between  $\text{Cp}^*_2\text{Sm}(\text{OEt}_2)$  and the precursor **4** was performed to testify liable disassociation of the  $\text{NiMe}_2$  fragment in this more reductive case. Dark brown crystals of the same ligand-coupled complex **7** as an anionic Sm-bimpm-Ni species were obtained by a slow liquid/liquid diffusion method from  $\text{Cp}^*_2\text{Sm}(\text{OEt}_2)$  in diethyl ether to a THF solution of **4** (Scheme 63).



**Scheme 63.** Synthesis of compound **7** in the presence of divalent samarium.

The limit of the single crystal size led the final *R*-factor to 8.69%, while the refined data are qualified enough to analyze the main parameters to compare with complex **3** and **5** (Figure 77). The average distances of Sm-Cp centroid and Sm-N in **7** are 2.45(2) and 2.42(4) Å, respectively, which are in agreement with a trivalent samarium ion in this species.<sup>73,88</sup> A much longer C-C linking bond average length in the bimpm ligand in **7** as 1.47(0) Å than the one in **4** as 1.45(6) Å, indicating the effective reduction in the ligand fragment from the divalent samarium. A C-C coupling between the two pyrimidine cycles in the ligand formed and its distance as 1.571 Å is longer than the one in its Yb analogue **5** as 1.556 Å. This can be probably explained as a steric effect in **7**, due to the bigger ion size of samarium compared to ytterbium. The average Ni-N and Ni-CH<sub>3</sub> distances in **7** are 2.01(4) and 1.916(5) Å, respectively, as similar as the ones as 1.970(5) and 1.92(4) Å, respectively, in its precursor **4**, showing that the nickel center remains the divalent oxidation state. Importantly, the average bimpm-NiMe<sub>2</sub> distortion angle is 16°, slightly smaller than the one in **5** as 18°, and also very close to the one in **4** as 12°, agreeing with the fact of a stable coordination system in **7**.



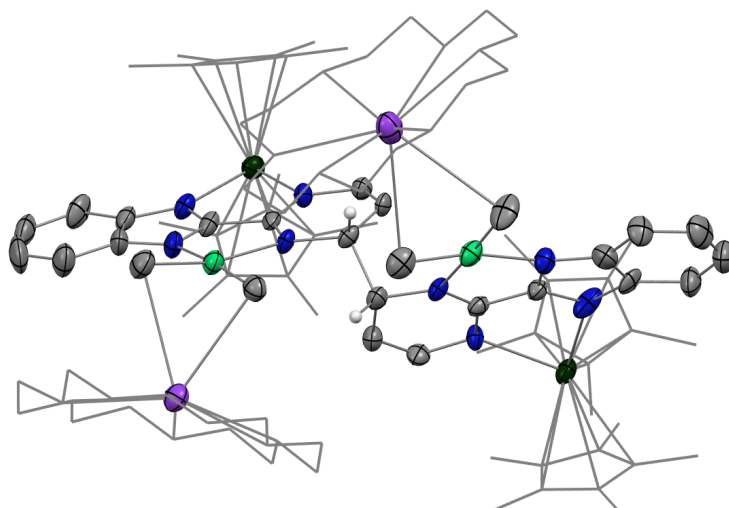


**Figure 77.** ORTEPs of **7**. Thermal ellipsoids are at 50 % level. Carbon atoms are in grey, hydrogen atoms are in white and have been removed for clarity except the ones on the coupled carbons of the ligands, potassium in purple, nitrogen in blue, nickel in bright green and samarium atoms in deep green. Co-recrystallized Et<sub>2</sub>O molecule is removed and Cp\* ligands on ytterbium and 18-c-6 are presented in wireframe style for clarity.

**7** needs more characterizations such as NMR study in the future to probe the reversibility behavior in solution. The extending work with samarocene and **1** has not been investigated yet, while the more reductive event of divalent samarium analogue should bring some more information on this reductive coupling formation, especially the reversibility of the C-C bond in solution. The *dimeric-trimeric* evolution in the case of ytterbium could be different in the case of samarium ion with a larger size due to lanthanide contraction.

## 6. Conclusion and perspectives

To summarize, the chemistry of a redox-active, dissymmetric *N*-heteroaromatic ligand, bimpm, leading to a radical coupling to form an intermolecular  $\sigma$  C-C bond induced by divalent lanthanide, has been presented in this chapter. The interesting fact of the stereochemistry of the coupling as *exo* position and an evolution from a transient, heteroleptic *dimeric* species to a stable, homoleptic *trimeric* compound due to a reactive NiMe<sub>2</sub> fragment, has been described. This work strongly supports the concept and related application of electron transfer property in divalent lanthanides, providing a new example in radical coupling reactions with a dissymmetric ligand, which has been rarely reported not only in transition metals but also rare-earth ones. However, the reversibility of this bond formation remains ambiguous.

The cleavage of the C-C bond formation could be achieved by mild oxidative steps, such as silver salts. The idea to cleave the formed  $\sigma$  bond is to consider to further utilize the transferred electron(s) from the lanthanide fragment(s) to undergo other chemical transformations *via* radical process. Meanwhile, the subtle modification of the bimpm ligand such as by blocking the para-position on the pyrimidine ring might help the ligand reserve the radical or undergo different reactivity.

## References

- (1) Suarez, A. I. O.; Lyaskovskyy, V.; Reek, J. N. H.; van der Vlugt, J. I.; de Bruin, B. Complexes with Nitrogen-Centered Radical Ligands: Classification, Spectroscopic Features, Reactivity, and Catalytic Applications. *Angew. Chem. Int. Ed.* **2013**, *52* (48), 12510–12529. <https://doi.org/10.1002/anie.201301487>.
- (2) Bachmann, J.; Nocera, D. G. Multielectron Chemistry of Zinc Porphyrinogen: A Ligand-Based Platform for Two-Electron Mixed Valency. *J. Am. Chem. Soc.* **2004**, *126* (9), 2829–2837. <https://doi.org/10.1021/ja039617h>.
- (3) Bachmann, J.; Hodgkiss, J. M.; Young, E. R.; Nocera, D. G. Ground- and Excited-State Reactivity of Iron Porphyrinogens. *Inorg. Chem.* **2007**, *46* (3), 607–609. <https://doi.org/10.1021/ic0616636>.
- (4) Nocton, G.; Lukens, W. W.; Booth, C. H.; Rozenel, S. S.; Medling, S. A.; Maron, L.; Andersen, R. A. Reversible Sigma C–C Bond Formation Between Phenanthroline Ligands Activated by  $(C_5Me_5)_2Yb$ . *J. Am. Chem. Soc.* **2014**, *136* (24), 8626–8641. <https://doi.org/10.1021/ja502271q>.
- (5) Nocton, G.; Ricard, L. Reversible C–C Coupling in Phenanthroline Complexes of Divalent Samarium and Thulium. *Chem. Commun.* **2015**, *51* (17), 3578–3581. <https://doi.org/10.1039/C5CC00289C>.
- (6) Ghosh, R.; Sarkar, A. Bidentate P, N–P Ligand for Nickel-Catalyzed Cross-Coupling of Aryl or Benzyl Chlorides with  $ArMgX$ . *J. Org. Chem.* **2010**, *75* (23), 8283–8286. <https://doi.org/10.1021/jo1016458>.
- (7) Magano, J.; Dunetz, J. R. Large-Scale Applications of Transition Metal-Catalyzed Couplings for the Synthesis of Pharmaceuticals. *Chem. Rev.* **2011**, *111* (3), 2177–2250. <https://doi.org/10.1021/cr100346g>.
- (8) Handa, S.; Mathota Arachchige, Y. L. N.; Slaughter, L. M. Access to 2'-Substituted Binaphthyl Monoalcohols via Complementary Nickel-Catalyzed Kumada Coupling Reactions under Mild Conditions: Key Role of a P,O Ligand. *J. Org. Chem.* **2013**, *78* (11), 5694–5699. <https://doi.org/10.1021/jo400349r>.
- (9) Han, F.-S. Transition-Metal-Catalyzed Suzuki–Miyaura Cross-Coupling Reactions: A Remarkable Advance from Palladium to Nickel Catalysts. *Chem. Soc. Rev.* **2013**, *42* (12), 5270–5298. <https://doi.org/10.1039/C3CS35521G>.
- (10) Yoshikai, N.; Mashima, H.; Nakamura, E. Nickel-Catalyzed Cross-Coupling Reaction of Aryl Fluorides and Chlorides with Grignard Reagents under Nickel/Magnesium Bimetallic Cooperation. *J. Am. Chem. Soc.* **2005**, *127* (51), 17978–17979. <https://doi.org/10.1021/ja056327n>.
- (11) Kranenburg, M.; Kamer, P. C. J.; van Leeuwen, P. W. N. M.; Vogt, D.; Keim, W. Effect of the Bite Angle of Diphosphine Ligands on Activity and Selectivity in the Nickel-Catalysed Hydrocyanation of Styrene. *J. Chem. Soc. Chem. Commun.* **1995**, No. 21, 2177–2178. <https://doi.org/10.1039/C39950002177>.
- (12) van Leeuwen, P. W. N. M.; Kamer, P. C. J.; Reek, J. N. H.; Dierkes, P. Ligand Bite Angle Effects in Metal-Catalyzed C–C Bond Formation. *Chem. Rev.* **2000**, *100* (8), 2741–2770. <https://doi.org/10.1021/cr9902704>.
- (13) Kato, K.; Osuka, A. Platforms for Stable Carbon-Centered Radicals. *Angew. Chem. Int. Ed.* **2019**, *58* (27), 8978–8986. <https://doi.org/10.1002/anie.201900307>.
- (14) Chirik, P. J.; Wieghardt, K. Radical Ligands Confer Nobility on Base-Metal Catalysts. *Science* **2010**, *327* (5967), 794–795. <https://doi.org/10.1126/science.1183281>.
- (15) Morris, W. D.; Wolczanski, P. T.; Sutter, J.; Meyer, K.; Cundari, T. R.; Lobkovsky, E. B. Iron and Chromium Complexes Containing Tridentate Chelates Based on Nacnac and Imino- and Methyl-Pyridine Components: Triggering C–X Bond Formation. *Inorg. Chem.* **2014**, *53* (14), 7467–7484. <https://doi.org/10.1021/ic500807y>.
- (16) Shen, X.; Zhang, Y.; Xue, M.; Shen, Q. Reduction of Sterically Hindered  $\beta$ -Diketiminato Europium(III) Complexes by the  $\beta$ -Diketiminato Anion: A Convenient Route for the Synthesis of

- $\beta$ -Diketiminato Europium(II) Complexes. *Dalton Trans.* **2012**, 41 (13), 3668–3674. <https://doi.org/10.1039/C2DT12176J>.
- (17) Camp, C.; Arnold, J. On the Non-Innocence of “Nacnacs”: Ligand-Based Reactivity in  $\beta$ -Diketiminato Supported Coordination Compounds. *Dalton Trans.* **2016**, 45 (37), 14462–14498. <https://doi.org/10.1039/C6DT02013E>.
- (18) Grumbine, S. D.; Chadha, R. K.; Tilley, T. D. Transition Metal Complexes Containing Donor-Stabilized Silylyne Ligands. Reductive Dimerization to a Silylene Complex. *J. Am. Chem. Soc.* **1992**, 114 (4), 1518–1520. <https://doi.org/10.1021/ja00030a079>.
- (19) Duplessis, E. A.; Jelliss, P. A.; Kirkpatrick, C. C.; Minter, S. D.; Wampler, K. M. Electrocatalytic Reductive Dimerization of the 2,2'-Bipyridyl Tungsten Alkylidyne Complex  $[W(CC_6H_4NMe_2-4)(NCMe)(CO)_2\{\kappa^2-2,2'-(NC_5H_4)_2\}]^+$ . *J. Organomet. Chem.* **2006**, 691 (22), 4660–4666. <https://doi.org/10.1016/j.jorganchem.2006.07.029>.
- (20) Bourget-Merle, L.; Lappert, M. F.; Severn, J. R. The Chemistry of  $\beta$ -Diketiminato-metal Complexes. *Chem. Rev.* **2002**, 102 (9), 3031–3066. <https://doi.org/10.1021/cr010424r>.
- (21) Grützmacher, H. Cooperating Ligands in Catalysis. *Angew. Chem. Int. Ed.* **2008**, 47 (10), 1814–1818. <https://doi.org/10.1002/anie.200704654>.
- (22) Caulton, K. G. Systematics and Future Projections Concerning Redox-Noninnocent Amide/Imine Ligands. *Eur. J. Inorg. Chem.* **2012**, 2012 (3), 435–443. <https://doi.org/10.1002/ejic.201100623>.
- (23) de Bruin, B.; Bill, E.; Bothe, E.; Weyhermüller, T.; Wieghardt, K. Molecular and Electronic Structures of Bis(Pyridine-2,6-Diimine)Metal Complexes  $[ML_2](PF_6)_n$  ( $n = 0, 1, 2, 3$ ; M = Mn, Fe, Co, Ni, Cu, Zn)<sup>†</sup>. *Inorg. Chem.* **2000**, 39 (13), 2936–2947. <https://doi.org/10.1021/ic000113j>.
- (24) Budzelaar, P. H. M.; de Bruin, B.; Gal, A. W.; Wieghardt, K.; van Lenthe, J. H. Metal-to-Ligand Electron Transfer in Diiminopyridine Complexes of Mn–Zn. A Theoretical Study. *Inorg. Chem.* **2001**, 40 (18), 4649–4655. <https://doi.org/10.1021/ic001457c>.
- (25) Knijnenburg, Q.; Gambarotta, S.; Budzelaar, P. H. M. Ligand-Centred Reactivity in Diiminepyridine Complexes. *Dalton Trans.* **2006**, No. 46, 5442–5448. <https://doi.org/10.1039/B612251E>.
- (26) Gibson, V. C.; Redshaw, C.; Solan, G. A. Bis(Imino)Pyridines: Surprisingly Reactive Ligands and a Gateway to New Families of Catalysts. *Chem. Rev.* **2007**, 107 (5), 1745–1776. <https://doi.org/10.1021/cr068437y>.
- (27) Sugiyama, H.; Aharonian, G.; Gambarotta, S.; Yap, G. P. A.; Budzelaar, P. H. M. Participation of the  $\alpha,\alpha'$ -Diiminopyridine Ligand System in Reduction of the Metal Center during Alkylation. *J. Am. Chem. Soc.* **2002**, 124 (41), 12268–12274. <https://doi.org/10.1021/ja020485m>.
- (28) Reardon, D.; Conan, F.; Gambarotta, S.; Yap, G.; Wang, Q. Life and Death of an Active Ethylene Polymerization Catalyst. Ligand Involvement in Catalyst Activation and Deactivation. Isolation and Characterization of Two Unprecedented Neutral and Anionic Vanadium(I) Alkyls. *J. Am. Chem. Soc.* **1999**, 121 (40), 9318–9325. <https://doi.org/10.1021/ja990263x>.
- (29) Scott, J.; Gambarotta, S.; Korobkov, I.; Budzelaar, P. H. M. Metal versus Ligand Alkylation in the Reactivity of the (Bis-Iminopyridinato)Fe Catalyst. *J. Am. Chem. Soc.* **2005**, 127 (37), 13019–13029. <https://doi.org/10.1021/ja054152b>.
- (30) Scott, J.; Gambarotta, S.; Korobkov, I. Ligand-Assisted Reduction of Co(II) to Co(I) and Subsequent Coordination of Dinitrogen. *Can. J. Chem.* **2005**, 83 (4), 279–285. <https://doi.org/10.1139/v05-010>.
- (31) Sugiyama, H.; Korobkov, I.; Gambarotta, S.; Möller, A.; Budzelaar, P. H. M. Preparation, Characterization, and Magnetic Behavior of the Ln Derivatives (Ln = Nd, La) of a 2,6-Diiminepyridine Ligand and Corresponding Dianion. *Inorg. Chem.* **2004**, 43 (18), 5771–5779. <https://doi.org/10.1021/ic049820t>.
- (32) Knijnenburg, Q.; Smits, J. M. M.; Budzelaar, P. H. M. Reaction of AlEt<sub>2</sub>Cl with the Diiminepyridine Ligand: An Unexpected Product. *Comptes Rendus Chim.* **2004**, 7 (8), 865–869. <https://doi.org/10.1016/j.crci.2004.03.012>.

- (33) Knijnenburg, Q.; Smits, J. M. M.; Budzelaar, P. H. M. Reaction of the Diimine Pyridine Ligand with Aluminum Alkyls: An Unexpectedly Complex Reaction. *Organometallics* **2006**, *25* (4), 1036–1046. <https://doi.org/10.1021/om050936m>.
- (34) Regenauer, N. I.; Settele, S.; Bill, E.; Wadepohl, H.; Roşca, D.-A. Bis(Imino)Pyrazine-Supported Iron Complexes: Ligand-Based Redox Chemistry, Dearomatization, and Reversible C–C Bond Formation. *Inorg. Chem.* **2020**, *59* (4), 2604–2612. <https://doi.org/10.1021/acs.inorgchem.9b03665>.
- (35) Hojilla Atienza, C. C.; Milsmann, C.; Semproni, S. P.; Turner, Z. R.; Chirik, P. J. Reversible Carbon–Carbon Bond Formation Induced by Oxidation and Reduction at a Redox-Active Cobalt Complex. *Inorg. Chem.* **2013**, *52* (9), 5403–5417. <https://doi.org/10.1021/ic400352r>.
- (36) Frazier, B. A.; Wolczanski, P. T.; Lobkovsky, E. B.; Cundari, T. R. Unusual Electronic Features and Reactivity of the Dipyritylazaallyl Ligand: Characterizations of (Smif)<sub>2</sub>M [M = Fe, Co, Co<sup>+</sup>, Ni; Smif = {(2-Py)CH<sub>2</sub>N}] and [(TMS)<sub>2</sub>NFe]<sub>2</sub>(Smif)<sub>2</sub>. *J. Am. Chem. Soc.* **2009**, *131* (10), 3428–3429. <https://doi.org/10.1021/ja8089747>.
- (37) Hulley, E. B.; Wolczanski, P. T.; Lobkovsky, E. B. Carbon–Carbon Bond Formation from Azaallyl and Imine Couplings about Metal–Metal Bonds. *J. Am. Chem. Soc.* **2011**, *133* (45), 18058–18061. <https://doi.org/10.1021/ja207638h>.
- (38) De Angelis, S.; Solari, E.; Floriani, C.; Chiesi-Villa, A.; Rizzoli, C. Oxidation of Metal-Meso-Octaethylporphyrinogen Complexes Leading to Novel Oxidized Forms of Porphyrinogen Other than Porphyrins. 1. The Redox Chemistry of Nickel(II)- and Copper(II)-Meso-Octaethylporphyrinogen Complexes Occurring with the Formation and Cleavage of a Cyclopropane Unit. *J. Am. Chem. Soc.* **1994**, *116* (13), 5691–5701. <https://doi.org/10.1021/ja00092a021>.
- (39) De Angelis, S.; Solari, E.; Floriani, C.; Chiesi-Villa, A.; Rizzoli, C. Oxidation of Metal-Meso-Octaethylporphyrinogen Complexes Leading to Novel Oxidized Forms of Porphyrinogen Other than Porphyrins. 2. The Redox Chemistry of Iron(II)- and Cobalt(II)-Meso-Octaethylporphyrinogen Complexes Occurring with the Formation and Cleavage of Two Cyclopropane Units. *J. Am. Chem. Soc.* **1994**, *116* (13), 5702–5713. <https://doi.org/10.1021/ja00092a022>.
- (40) Piarulli, U.; Solari, E.; Floriani, C.; Chiesi-Villa, A.; Rizzoli, C. Redox Chemistry Associated with the Complexation of Vanadium(V) and Tungsten(VI) by Meso-Octaethylporphyrinogen: Formation and Cleavage of Cyclopropane Units Functioning as Shuttles of Two Electrons. *J. Am. Chem. Soc.* **1996**, *118* (15), 3634–3642. <https://doi.org/10.1021/ja9543309>.
- (41) Crescenzi, R.; Solari, E.; Floriani, C.; Chiesi-Villa, A.; Rizzoli, C. One- and Two-Electron Oxidative Pathways Leading to Cyclopropane-Containing Oxidized Porphyrinogens and C–C-Coupled Porphyrinogens from Alkali Cation- and Transition Metal-meso-Octaethylporphyrinogen Complexes. *J. Am. Chem. Soc.* **1999**, *121* (8), 1695–1706. <https://doi.org/10.1021/ja982178f>.
- (42) Bachmann, J.; Nocera, D. G. Multielectron Redox Chemistry of Iron Porphyrinogens. *J. Am. Chem. Soc.* **2005**, *127* (13), 4730–4743. <https://doi.org/10.1021/ja043132r>.
- (43) Bailey, C. L.; Bereman, R. D.; Rillema, D. P. Redox and Spectral Properties of Cobalt(II) and Copper(II) Tetraazaannulene Complexes: {H<sub>2</sub>[Me<sub>4</sub>(RBzo)<sub>2</sub>[14]TetraeneN<sub>4</sub>]} (R = H, CO<sub>2</sub>CH<sub>3</sub>). Evidence for Superoxide Ligation and Reduction. *Inorg. Chem.* **1986**, *25* (18), 3149–3153. <https://doi.org/10.1021/ic00238a011>.
- (44) Balch, A. L.; Noll, B. C.; Reid, S. M.; Zovinka, E. P. Carbon-Carbon Bond Formation in the Dimerization of (Octaethyloxophlorin Radical)Nickel(II). *J. Am. Chem. Soc.* **1993**, *115* (6), 2531–2532. <https://doi.org/10.1021/ja00059a071>.
- (45) Adinarayana, B.; Kato, K.; Shimizu, D.; Tanaka, T.; Furukawa, K.; Osuka, A. Cyclophane-Type Chlorin Dimers from Dynamic Covalent Chemistry of 2,18-Porphyrinyl Dicyanomethyl Diradicals. *Angew. Chem. Int. Ed.* **2020**, *59* (11), 4320–4323. <https://doi.org/10.1002/anie.201914480>.

- (46) Liu, B.; Yoshida, T.; Li, X.; Stępień, M.; Shinokubo, H.; Chmielewski, P. J. Reversible Carbon-Carbon Bond Breaking and Spin Equilibria in Bis(Pyrimidinenorcorrole). *Angew. Chem. Int. Ed.* **2016**, *55* (42), 13142–13146. <https://doi.org/10.1002/anie.201607237>.
- (47) Dugan, T. R.; Bill, E.; MacLeod, K. C.; Christian, G. J.; Cowley, R. E.; Brennessel, W. W.; Ye, S.; Neese, F.; Holland, P. L. Reversible C–C Bond Formation between Redox-Active Pyridine Ligands in Iron Complexes. *J. Am. Chem. Soc.* **2012**, *134* (50), 20352–20364. <https://doi.org/10.1021/ja305679m>.
- (48) Lewis, R. A.; MacLeod, K. C.; Mercado, B. Q.; Holland, P. L. Geometric and Redox Flexibility of Pyridine as a Redox-Active Ligand That Can Reversibly Accept One or Two Electrons. *Chem. Commun.* **2014**, *50* (76), 11114–11117. <https://doi.org/10.1039/C4CC05495D>.
- (49) Huang, W.; Khan, S. I.; Diaconescu, P. L. Scandium Arene Inverted-Sandwich Complexes Supported by a Ferrocene Diamide Ligand. *J. Am. Chem. Soc.* **2011**, *133* (27), 10410–10413. <https://doi.org/10.1021/ja204304f>.
- (50) Moeller, T.; Martin, D. F.; Thompson, L. C.; Ferrús, R.; Feistel, G. R.; Randall, W. J. The Coordination Chemistry of Yttrium and the Rare Earth Metal Ions. *Chem. Rev.* **1965**, *65* (1), 1–50. <https://doi.org/10.1021/cr60233a001>.
- (51) Huang, W.; Diaconescu, P. L. Visible-Light-Induced Reversible C–C Bond Formation of an Imidazole-Derived Scandium Complex. *Inorganica Chim. Acta* **2012**, *380*, 274–277. <https://doi.org/10.1016/j.ica.2011.08.066>.
- (52) Monreal, M. J.; Diaconescu, P. L. Reversible C–C Coupling in a Uranium Biheterocyclic Complex. *J. Am. Chem. Soc.* **2010**, *132* (22), 7676–7683. <https://doi.org/10.1021/ja9109715>.
- (53) Camp, C.; Mougél, V.; Horeglad, P.; Pécaut, J.; Mazzanti, M. Multielectron Redox Reactions Involving C–C Coupling and Cleavage in Uranium Schiff Base Complexes. *J. Am. Chem. Soc.* **2010**, *132* (49), 17374–17377. <https://doi.org/10.1021/ja1089364>.
- (54) Camp, C.; Guidal, V.; Biswas, B.; Pécaut, J.; Dubois, L.; Mazzanti, M. Multielectron Redox Chemistry of Lanthanide Schiff-Base Complexes. *Chem. Sci.* **2012**, *3* (8), 2433–2448. <https://doi.org/10.1039/C2SC20476B>.
- (55) Berthet, J.-C.; Thuéry, P.; Baudin, C.; Boizot, B.; Ephritikhine, M. First Reductive Dimerization of a Polycyclic Azine. *Dalton Trans.* **2009**, No. 37, 7613–7616. <https://doi.org/10.1039/B909547K>.
- (56) Lam, O. P.; Anthon, C.; Heinemann, F. W.; O'Connor, J. M.; Meyer, K. Structural and Spectroscopic Characterization of a Charge-Separated Uranium Benzophenone Ketyl Radical Complex. *J. Am. Chem. Soc.* **2008**, *130* (20), 6567–6576. <https://doi.org/10.1021/ja801007q>.
- (57) Mullane, K. C.; Cheisson, T.; Nakamaru-Ogiso, E.; Manor, B. C.; Carroll, P. J.; Schelter, E. J. Reduction of Carbonyl Groups by Uranium(III) and Formation of a Stable Amide Radical Anion. *Chem. – Eur. J.* **2018**, *24* (4), 826–837. <https://doi.org/10.1002/chem.201703396>.
- (58) Duval, P. B.; Burns, C. J.; Clark, D. L.; Morris, D. E.; Scott, B. L.; Thompson, J. D.; Werkema, E. L.; Jia, L.; Andersen, R. A. Synthesis and Structural Characterization of the First Uranium Cluster Containing an Isopolyoxometalate Core. *Angew. Chem. Int. Ed.* **2001**, *40* (18), 3357–3361. [https://doi.org/10.1002/1521-3773\(20010917\)40:18<3357::AID-ANIE3357>3.0.CO;2-C](https://doi.org/10.1002/1521-3773(20010917)40:18<3357::AID-ANIE3357>3.0.CO;2-C).
- (59) Nugent, L. J.; Baybarz, R. D.; Burnett, J. L.; Ryan, J. L. Electron-Transfer and f-d Absorption Bands of Some Lanthanide and Actinide Complexes and the Standard (II-III) Oxidation Potential for Each Member of the Lanthanide and Actinide Series. *J. Phys. Chem.* **1973**, *77* (12), 1528–1539. <https://doi.org/10.1021/j100631a011>.
- (60) Mehdoui, T.; Berthet, J.-C.; Thuéry, P.; Ephritikhine, M. Clear-Cut Lanthanide(III)/Actinide(III) Differentiation in Coordination of Pyrazine to Tris(Cyclopentadienyl) Complexes of Cerium and Uranium, Involving Reversible U<sup>III</sup> → U<sup>IV</sup> Oxidation. *Eur. J. Inorg. Chem.* **2004**, *2004* (10), 1996–2000. <https://doi.org/10.1002/ejic.200400133>.
- (61) Formanuk, A.; Ortu, F.; Liu, J.; Nodaraki, L. E.; Tuna, F.; Kerridge, A.; Mills, D. P. Double Reduction of 4,4'-Bipyridine and Reductive Coupling of Pyridine by Two Thorium(III) Single-Electron Transfers. *Chem. – Eur. J.* **2017**, *23* (10), 2290–2293. <https://doi.org/10.1002/chem.201605974>.

- (62) Evans, W. J.; Drummond, D. K. Reductive Coupling of Pyridazine and Benzaldehyde Azine and Reduction of Bipyridine by Samarium Complex (C<sub>5</sub>Me<sub>5</sub>)<sub>2</sub>Sm(THF)<sub>2</sub>. *J. Am. Chem. Soc.* **1989**, *111* (9), 3329–3335. <https://doi.org/10.1021/ja00191a034>.
- (63) Coulson, C. A.; O'Leary, B.; Mallion, R. B. *Hückel Theory for Organic Chemists*; Academic Press, 1978.
- (64) Evans, W. J.; Gonzales, S. L.; Ziller, J. W. Reactivity of Decamethylsamarocene with Polycyclic Aromatic Hydrocarbons. *J. Am. Chem. Soc.* **1994**, *116* (6), 2600–2608. <https://doi.org/10.1021/ja00085a046>.
- (65) Berg, D. J.; Boncella, J. M.; Andersen, R. A. Preparation of Coordination Compounds of Cp\*<sub>2</sub>Yb with Heterocyclic Nitrogen Bases: Examples of Antiferromagnetic Exchange Coupling across Bridging Ligands. *Organometallics* **2002**, *21* (22), 4622–4631. <https://doi.org/10.1021/om020477e>.
- (66) Tilley, T. Don.; Andersen, R. A.; Spencer, Brock.; Zalkin, Allan. Crystal Structure of Bis(Pentamethylcyclopentadienyl)Bis(Pyridine)Ytterbium(II). *Inorg. Chem.* **1982**, *21* (7), 2647–2649. <https://doi.org/10.1021/ic00137a023>.
- (67) Nief, F.; Turcitu, D.; Ricard, L. Synthesis and Structure of Phospholyl- and Arsolylthulium(II) Complexes. *Chem. Commun.* **2002**, No. 15, 1646–1647. <https://doi.org/10.1039/B204337H>.
- (68) Gradoz, P.; Baudry, D.; Ephritikhine, M.; Lance, M.; Nierlich, M.; Vigner, J. Tetramethylphospholyluranium Complexes and Their Pentamethylcyclopentadienyl Analogues. *J. Organomet. Chem.* **1994**, *466* (1), 107–118. [https://doi.org/10.1016/0022-328X\(94\)88035-2](https://doi.org/10.1016/0022-328X(94)88035-2).
- (69) Jaroschik, F.; Nief, F.; Le Goff, X.-F.; Ricard, L. Synthesis and Reactivity of Organometallic Complexes of Divalent Thulium with Cyclopentadienyl and Phospholyl Ligands. *Organometallics* **2007**, *26* (14), 3552–3558. <https://doi.org/10.1021/om700316a>.
- (70) Fedushkin, I. L.; Nevodchikov, V. I.; Bochkarev, M. N.; Dechert, S.; Schumann, H. Reduction of 2,5-Di-Tert-Butylcyclopentadienone and Pyridine with Thulium Diiodide. Structures of the Complexes TmI<sub>2</sub>(THF)<sub>2</sub>[H<sup>5</sup>-But<sub>2</sub>C<sub>5</sub>H<sub>2</sub>O]TmI<sub>2</sub>(THF)<sub>3</sub> and [TmI<sub>2</sub>(C<sub>5</sub>H<sub>5</sub>N)<sub>4</sub>]<sub>2</sub>(M<sub>2</sub>-N<sub>2</sub>C<sub>10</sub>H<sub>10</sub>). *Russ. Chem. Bull.* **2003**, *52* (1), 154–159. <https://doi.org/10.1023/A:1022408717918>.
- (71) Labouille, S.; Nief, F.; Le Goff, X.-F.; Maron, L.; Kindra, D. R.; Houghton, H. L.; Ziller, J. W.; Evans, W. J. Ligand Influence on the Redox Chemistry of Organosamarium Complexes: Experimental and Theoretical Studies of the Reactions of (C<sub>5</sub>Me<sub>5</sub>)<sub>2</sub>Sm(THF)<sub>2</sub> and (C<sub>4</sub>Me<sub>4</sub>P)<sub>2</sub>Sm with Pyridine and Acridine. *Organometallics* **2012**, *31* (14), 5196–5203. <https://doi.org/10.1021/om300573z>.
- (72) Schultz, M.; Boncella, J. M.; Berg, D. J.; Tilley, T. D.; Andersen, R. A. Coordination of 2,2'-Bipyridyl and 1,10-Phenanthroline to Substituted Ytterbocenes: An Experimental Investigation of Spin Coupling in Lanthanide Complexes. *Organometallics* **2002**, *21* (3), 460–472. <https://doi.org/10.1021/om010661k>.
- (73) Veauthier, J. M.; Schelter, E. J.; Carlson, C. N.; Scott, B. L.; Re, R. E. D.; Thompson, J. D.; Kiplinger, J. L.; Morris, D. E.; John, K. D. Direct Comparison of the Magnetic and Electronic Properties of Samarocene and Ytterbocene Terpyridine Complexes. *Inorg. Chem.* **2008**, *47* (13), 5841–5849. <https://doi.org/10.1021/ic8001465>.
- (74) Molina, P.; Tárraga, A.; Otón, F. Imidazole Derivatives: A Comprehensive Survey of Their Recognition Properties. *Org. Biomol. Chem.* **2012**, *10* (9), 1711–1724. <https://doi.org/10.1039/C2OB06808G>.
- (75) Kaim, W.; Sarkar, B. Mixed Valency of a 5d Element: The Osmium Example. *Coord. Chem. Rev.* **2013**, *257* (9–10), 1650–1659. <https://doi.org/10.1016/j.ccr.2012.08.026>.
- (76) Haga, Masaaki.; Bond, A. M. Electrochemistry of Symmetrical and Asymmetrical Dinuclear Ruthenium, Osmium, and Mixed-Metal 2,2'-Bipyridine Complexes Bridged by 2,2'-Bibenzimidazolate. *Inorg. Chem.* **1991**, *30* (3), 475–480. <https://doi.org/10.1021/ic00003a023>.
- (77) Haga, Masaaki.; Ano, Tomoaki.; Kano, Kenji.; Yamabe, Shinichi. Proton-Induced Switching of Metal-Metal Interactions in Dinuclear Ruthenium and Osmium Complexes Bridged by 2,2'-Bis(2-Pyridyl)Bibenzimidazole. *Inorg. Chem.* **1991**, *30* (20), 3843–3849. <https://doi.org/10.1021/ic00020a014>.

- (78) Chen, Z.-Q.; Ding, F.; Bian, Z.-Q.; Huang, C.-H. Efficient Near-Infrared Organic Light-Emitting Diodes Based on Multimetallic Assemblies of Lanthanides and Iridium Complexes. *Org. Electron.* **2010**, *11* (3), 369–376. <https://doi.org/10.1016/j.orgel.2009.11.015>.
- (79) Haga, M.; Ishizuya, M.; Kanetsugi, T.; Yutaka, T.; Sakiyama, D.; Fees, J.; Kaim, W. Synthesis and Formation of Dinuclear Mixed-Valent Complexes of Ruthenium and Osmium Bridged by 2-(2-Pyrimidyl)Benzimidazolate. *Indian J. Chem.-Sect. A* **2003**, *42A* (9), 2290–2299.
- (80) Xu, H.; Diccianni, J. B.; Katigbak, J.; Hu, C.; Zhang, Y.; Diao, T. Bimetallic C–C Bond-Forming Reductive Elimination from Nickel. *J. Am. Chem. Soc.* **2016**, *138* (14), 4779–4786. <https://doi.org/10.1021/jacs.6b00016>.
- (81) Singh, P. K.; Silakari, O. Chapter 2 - Benzimidazole: Journey From Single Targeting to Multitargeting Molecule. In *Key Heterocycle Cores for Designing Multitargeting Molecules*; Silakari, O., Ed.; Elsevier, 2018; pp 31–52. <https://doi.org/10.1016/B978-0-08-102083-8.00002-9>.
- (82) Nocton, G.; Booth, C. H.; Maron, L.; Andersen, R. A. Influence of the Torsion Angle in 3,3'-Dimethyl-2,2'-Bipyridine on the Intermediate Valence of Yb in (C<sub>5</sub>Me<sub>5</sub>)<sub>2</sub>Yb(3,3'-Me<sub>2</sub>-Bipy). *Organometallics* **2013**, *32* (19), 5305–5312. <https://doi.org/10.1021/om400528d>.
- (83) Booth, C. H.; Walter, M. D.; Kazhdan, D.; Hu, Y.-J.; Lukens, W. W.; Bauer, E. D.; Maron, L.; Eisenstein, O.; Andersen, R. A. Decamethylterbocene Complexes of Bipyridines and Diazabutadienes: Multiconfigurational Ground States and Open-Shell Singlet Formation. *J. Am. Chem. Soc.* **2009**, *131* (18), 6480–6491. <https://doi.org/10.1021/ja809624w>.
- (84) Birmingham, J. M.; Wilkinson, G. The Cyclopentadienides of Scandium, Yttrium and Some Rare Earth Elements. *J. Am. Chem. Soc.* **1956**, *78* (1), 42–44. <https://doi.org/10.1021/ja01582a009>.
- (85) Liotta, C. L.; Harris, H. P. Chemistry of Naked Anions. I. Reactions of the 18-Crown-6 Complex of Potassium Fluoride with Organic Substrates in Aprotic Organic Solvents. *J. Am. Chem. Soc.* **1974**, *96* (7), 2250–2252. <https://doi.org/10.1021/ja00814a044>.
- (86) Allpress, C. J.; Arif, A. M.; Houghton, D. T.; Berreau, L. M. Photochemically Initiated Oxidative Carbon–Carbon Bond-Cleavage Reactivity in Chlorodiketonate Ni(II) Complexes. *Chem. – Eur. J.* **2011**, *17* (52), 14962–14973. <https://doi.org/10.1002/chem.201101962>.
- (87) Allpress, C. J.; Grubel, K.; Szajna-Fuller, E.; Arif, A. M.; Berreau, L. M. Regioselective Aliphatic Carbon–Carbon Bond Cleavage by a Model System of Relevance to Iron-Containing Acireductone Dioxygenase. *J. Am. Chem. Soc.* **2013**, *135* (2), 659–668. <https://doi.org/10.1021/ja3038189>.
- (88) Jaoul, A.; Clavaguéra, C.; Nocton, G. Electron Transfer in Tetramethylbiphosphinine Complexes of Cp\*<sub>2</sub>Yb and Cp\*<sub>2</sub>Sm. *New J. Chem.* **2016**, *40* (8), 6643–6649. <https://doi.org/10.1039/C6NJ00527F>.



## Redox-active tridentate nickel complexes with divalent lanthanides: planarity and reactivity

In the previous chapters, nickel complexes bearing redox-active bidentate ligands (bipym and bimpm) have been discussed in combination with  $[\text{Ni}(\text{CH}_3)_2]$  or  $[\text{Ni}(\text{CF}_3)_2]$  motifs. Their reactivity in the presence of divalent lanthanide fragments has also been investigated. Tridentate ligands such as redox-active terpyridine-based ones will be excellent candidates to extend our concept of “Ln-RAL-TM” frameworks.

The 2,2':6',2''-terpyridine (tpy) ligand and its derivatives are widely involved in diverse research areas from biomedical chemistry,<sup>1</sup> material science,<sup>2</sup> including supramolecular motifs,<sup>3</sup> to fundamental chemical transformations.<sup>4</sup> One of the practical applications of such ligands is in catalytic systems such as carbon-carbon cross-coupling reactions promoted by transition metals.<sup>5,6</sup> Besides, organometallic complexes supported by these ligands have great potentials in electro- and photoactive catalysis thanks to their excellent redox-active behavior.<sup>7,8</sup>

Within the series of terpyridine-based ligands bearing aromatic substituents in their 4'-position, 4'-(4-pyridyl)-2,2':6',2''-terpyridine, *viz.* pytpy, is not only an efficient linker in supramolecular chemistry highly used for self-assembly, but also an important ligand with great interest in building up binuclear complexes with different coordination environments.<sup>9</sup> In our case, a heterobimetallic nickel-based complex featuring a tridentate ligand system with a monochelated divalent lanthanide fragment is under consideration.

Hence, in the context of this chapter, the synthesis and characterization of a monomethyl nickel complex with the pytpy ligand will be presented and discussed in terms of its electron delocalization property over the tpy portion. The coordination of reductive divalent organolanthanides was attempted in order to induce reduction of the pyridyl moiety and facilitate the electron correlation through the whole ligand. Such an effect should impact the electronic structure of the corresponding complex and alter the reactivity of the nickel fragment. Furthermore, preliminary results on the reactivity toward borane derivatives point to possible applications in the formation of B-C bonds.

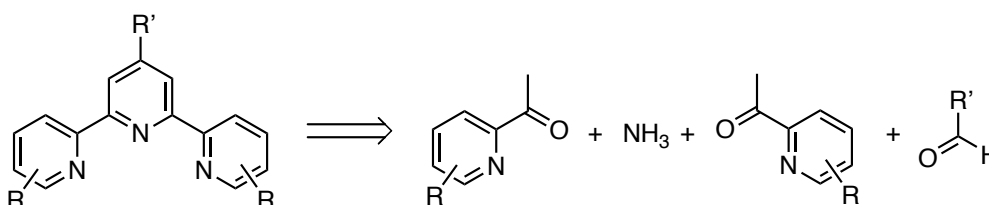


## 1. Introduction: electron delocalization in terpyridine-based ligands

### 1.1. Ligand-based redox effects in terpyridine complexes

The first reported terpyridine complex could be traced back to the 1930s: when Morgan and Burstall followed the precedented method of direct dehydrogenation of pyridine by anhydrous ferric chloride ( $\text{FeCl}_3$ ) to obtain 2,2'-bipyridine on a considerable scale, they isolated the 2,2':6',2''-terpyridine ligand as a by-product, associated as deep purple terpyridyl ferrous salts.<sup>10</sup> Numerous terpyridyl complexes with d-block metals were further obtained using similar strategies.<sup>11</sup>

Terpyridine-based ligands together with transition metals have then been an attractive area of research, especially in supramolecular chemistry, because of the relatively facile synthesis of versatile terpyridine derivatives to build multinuclear architectures (Scheme 64).<sup>12,13</sup> In terms of organometallic chemistry, the tpy ligand can be considered as a strong  $\pi$ -acceptor and is of particular interest in the design of molecules with unusual electronic structures, including mixed-valency, and for possible photo-, electro- and catalytic applications due to the strong  $\pi$ -conjugation.<sup>14</sup>



**Scheme 64.** A common versatile retrosynthetic analysis of the targeted terpyridine ligands.

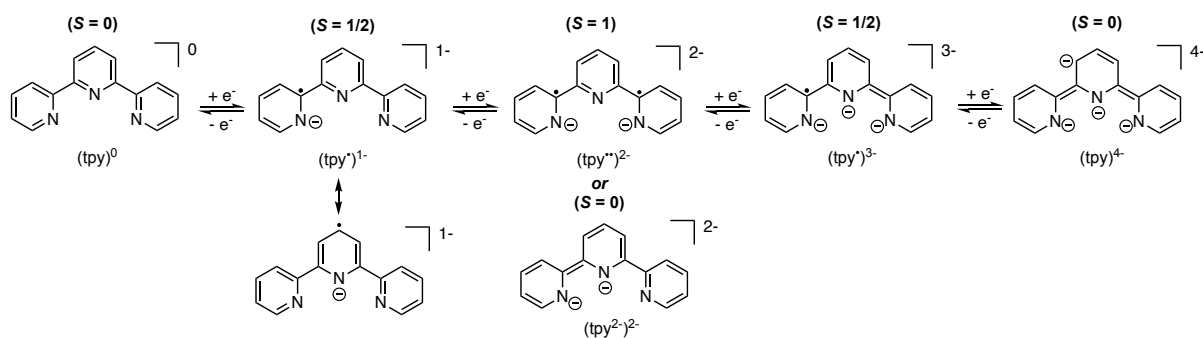
One of the representative examples in metal-tpy complexes was reported by Miskowski and Gray and corresponds to the chloro(terpyridine)platinum(II) complex  $[\text{Pt}(\text{tpy})\text{Cl}]^+$ , which behavior upon one-electron reduction was studied. Two reversible reduction waves were observed: in the first redox event, a  $\text{Pt}^{\text{II}}$  ion with a stable  $(\pi^*)^1$  radical state for the tpy ligand, corresponding to  $[\text{Pt}(\text{tpy})\text{Cl}]$ , was generated, and a presumably metal-centered reduction occurred in the second reduction event *via* formation of the mixed-valence dimer  $[(\text{Pt}(\text{tpy})\text{Cl})_2]^+$ .<sup>15</sup> Similar mixed-valency in dinuclear ruthenium complexes was achieved using bridging *bis*-tpy-based ligands and reported by Jean-Pierre Sauvage (Nobel Laureate in Chemistry, 2016) and co-workers.<sup>16</sup>

Comprehensively, Wieghardt and co-workers investigated the redox activity of terpyridyl chelates and the remarkable electronic structures of a series of original terpyridyl complexes in both experimental and theoretical studies. In these systems, the unpaired electron is more prone to residing in the tpy  $\pi^*$  orbital than on the metal center, since terpyridine behaves as an excellent extended  $\pi$ -system.<sup>17–23</sup> For example, the complex  $[\text{Ni}^{\text{II}}(\text{tpy})_2]^{2+}$  can be reversibly reduced in three steps, undergoing a  $[\text{Ni}^{\text{II}}(\text{tpy}^0)_2]^{2+} \rightarrow [\text{Ni}^{\text{II}}(\text{tpy}^{\cdot-})(\text{tpy}^0)]^+ \rightarrow [\text{Ni}^{\text{II}}(\text{tpy}^{\cdot-})_2]^0 \rightarrow [\text{Ni}^{\text{II}}(\text{tpy}^{2-})(\text{tpy}^{\cdot-})]^-$  sequence.<sup>24,25</sup> All the involved species were experimentally and computationally confirmed, and characterized as possessing ligand-centered unpaired electron(s) delocalized over the ligands. Interestingly, the four-coordinate, neutral diamagnetic  $[\text{Ni}^{\text{II}}(\text{tpy})_2]^0$  species ( $S = 0$ ) was better

elucidated as a compressed (or pseudo) tetrahedral structure ( $\eta^2$ -binding for the tpy) with a  $[\text{Ni}^{\text{I}}(\text{tpy}^{\cdot-})(\text{tpy}^0)]^0$  electronic configuration. Such an electronic behavior is attained through a strong antiferromagnetic coupling of the unpaired electron at the Ni(I) ion ( $d^9$ ,  $S_{\text{Ni}} = 1/2$ ) with the one centered on the  $\text{tpy}^{\cdot-}$  radical anion. However, the six-coordinate complexes  $[\text{Ni}^{\text{II}}(\text{tpy})_2]^{2+}$  and  $[\text{Ni}^{\text{II}}(\text{tpy})_2]^+$  solely contain a  $d^8$   $\text{Ni}^{\text{II}}$  ion, dominated by a ferromagnetic interaction between the unpaired spins on the ligands and at the metal center.<sup>20</sup>

The understanding of the structural changes within tpy complexes of redox-inert metal ions (e.g.,  $\text{Zn}^{2+}$  and  $\text{Al}^{3+}$ ) was computationally described in detail by the authors. They used  $(\text{tpy})^0$  for the neutral, diamagnetic ligand;  $(\text{tpy}^{\cdot})^{1-}$  for the  $\pi$  radical monoanion;  $(\text{tpy}^{\cdot\cdot})^{2-}$  for the triplet dianion or  $(\text{tpy}^{2-})^{2-}$  for its singlet form, and  $(\text{tpy}^{\cdot\cdot\cdot})^{3-}$  for the doublet ( $S = 1/2$ ) trianionic form (Scheme 65). The spin density distribution of  $(\text{tpy}^{\cdot})^{1-}$  is localized predominantly on the central pyridyl moiety (0.55 electrons), while the calculations show that in  $(\text{tpy}^{\cdot\cdot})^{2-}$ , which has, similarly, a single unpaired electron environment, only 17% of spin density is located on the central pyridine and approximately 0.4 electron is located on each terminal pyridyl fragment.

The resonance structures of  $(\text{tpy}^{2-})^{2-}$  reveal two forms, one diamagnetic and one paramagnetic. In the model complex  $[\text{Zn}^{\text{II}}(\text{tpy}^{2-})(\text{NH}_3)_2]^0$  ( $S = 0$  or  $S = 1$ ), the singlet diradical ground state is more stable than the triplet state with a small energy gap, which is in good agreement with the little calculated structural changes, showing that both the singlet ground state and low-lying excited triplet state may be accessible in energy. In contrast, the quartet state ( $S = 3/2$ ) of  $(\text{tpy}^{\cdot\cdot\cdot})^{3-}$  is 18.6  $\text{kcal}\cdot\text{mol}^{-1}$  higher in energy than the doublet state ( $S = 1/2$ ), explaining the higher stability and accessibility of the latter form.<sup>26</sup>

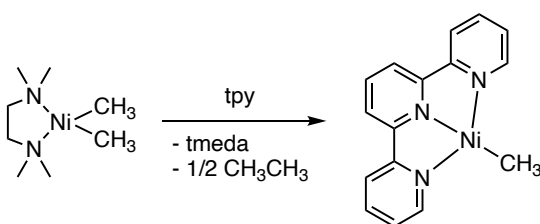


**Scheme 65.** Resonance structures of terpyridine ligand in hypothetical molecules of  $[\text{M}(\text{tpy})]$ .

Successive one-electron reductions of the uncoordinated tpy ligand, *i.e.*,  $(\text{tpy})^0 \rightarrow (\text{tpy}^{\cdot})^{1-} \rightarrow (\text{tpy}^{2-})^{2-}$ , were experimentally shown to occur at potentials ( $-2.55$  and  $-3.06$  V vs.  $\text{Fc}^+/\text{Fc}$ ,<sup>27</sup> respectively) very similar to those of the bipy ligand, as  $-2.60$  and  $-3.16$  V vs.  $\text{Fc}^+/\text{Fc}$ , respectively.<sup>28</sup> The reductions agree with sequential one-electron filling in the LUMO of the ligands within  $C_{2v}$  symmetry. However, a second pyridyl moiety, or a second  $\pi^*$  orbital for tpy, may be accessed in further reductions, in comparison with the bipy ligand. Wieghardt *et al.* therefore investigated the electronic structures of chromium complexes in a series of  $[\text{Cr}(\text{tpy})_2](\text{PF}_6)_n$  ( $n = 3-0$ ), in which the binding to the tpy ligand is regarded as weak covalence because of the high exchange energy of the Cr(III) ion, based on multiple electron transfer processes. Spectroscopic measurements and

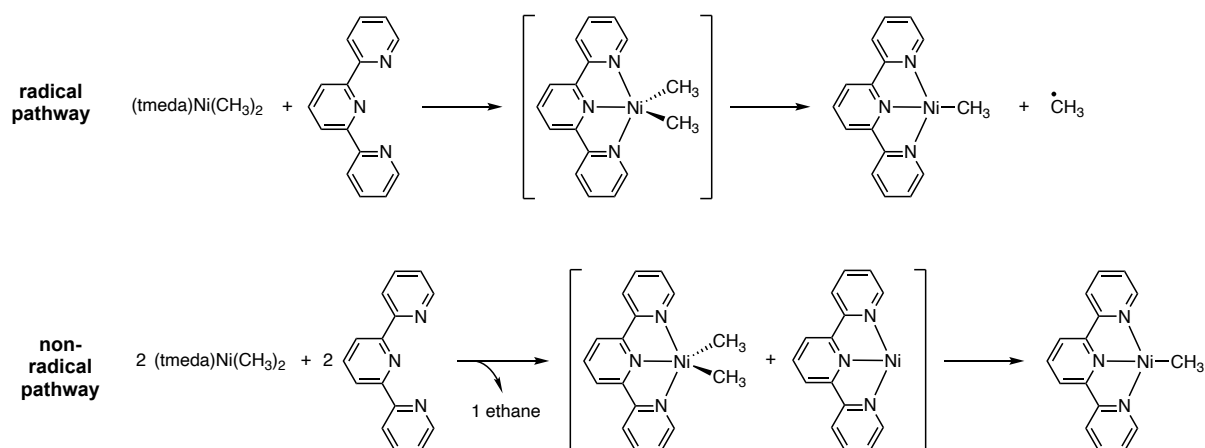
DFT calculations were used to assign the electronic structures of all the four well-defined complexes, which are  $[\text{Cr}^{\text{III}}(\text{tpy}^0)_2](\text{PF}_6)_3$  ( $S = 3/2$ ),  $[\text{Cr}^{\text{III}}(\text{tpy}^*)(\text{tpy}^0)](\text{PF}_6)_2$  ( $S = 1$ ),  $[\text{Cr}^{\text{III}}(\text{tpy}^{**})_2](\text{PF}_6)$  ( $S = 1/2$ ), and  $[\text{Cr}^{\text{III}}(\text{tpy}^{**})(\text{tpy}^*)]^0$  ( $S = 0$ ). In particular, the charge is delocalized on a single tpy ligand in the  $[\text{Cr}^{\text{III}}(\text{tpy}^*)(\text{tpy}^0)](\text{PF}_6)_2$  congener while the neutral diamagnetic  $[\text{Cr}^{\text{III}}(\text{tpy}^{**})(\text{tpy}^*)]^0$  complex has a full delocalization of the electrons through both tpy ligands.<sup>26</sup> This work by Wieghardt provides an example of accurate electronic structure elucidation of tpy complexes through experimental and theoretical studies.

Vicic *et al.* reported a remarkable study of an isolated “Ni<sup>I</sup>”-alkyl organometallic complex in their mechanistic investigation of the Negishi-type cross-coupling of alkyl electrophiles<sup>29</sup> (Scheme 66). This paramagnetic complex, namely  $(\text{tpy})\text{NiCH}_3$ , possesses one unpaired d-electron ( $\mu_{\text{eff}} = 1.64\mu_{\text{B}}$  in THF, Evans method).



**Scheme 66.** Synthesis of a “Ni(I)” complex, *viz.*  $(\text{tpy})\text{NiCH}_3$ , reported by Vicic.

The intriguing formation of the stable monomethyl product together with ethane led to subsequent analytical studies on a very related complex bearing a terpyridine ligand derivative, namely 4,4',4'-tri-*tert*-butylterpyridine ( $\text{tpy}'$ ), and using the isotopically labeled nickel-dimethyl precursor  $(\text{tmeda})\text{Ni}(\text{CD}_3)_2$ . The ethane formation upon addition of  $\pi$ -ligands to  $(\text{tmeda})\text{Ni}(\text{CH}_3)_2$  was already noted by Pörschke and co-workers, while the reaction pathway was not reported.<sup>30</sup> The addition of  $\text{tpy}'$  to a mixture of  $(\text{tmeda})\text{Ni}(\text{CH}_3)_2$  and  $(\text{tmeda})\text{Ni}(\text{CD}_3)_2$  did not generate  $\text{CH}_3\text{-CD}_3$  but only  $\text{CH}_3\text{-CH}_3$  and  $\text{CD}_3\text{-CD}_3$ , which ascertained a non-radical reaction pathway (Scheme 67). A ligand-based radical nature for  $(\text{tpy})\text{NiCH}_3$  rather than a metal-centered species was confirmed by EPR spectroscopy, implying a charge-transferred Ni(II)-methyl cation and a reduced radical anionic tpy ligand in a  $(d^8)(\pi^{*1})$  ground-state electronic configuration (Figure 78).<sup>31</sup> Similar results were also concluded by Klein and co-workers from electrochemical and spectroelectrochemical studies on tpy-based nickel-aryl complexes, demonstrating mainly terpyridine-centered reductions with only marginal metal contributions. These results show that a singly - or doubly - reduced ligand with a divalent nickel center should be considered, instead of a Ni(I) description.<sup>27</sup> DFT calculations showed that the majority of the spin density in this compound resides on the terpyridine ligand and, additionally, a large amount of radical character is located at the ortho- and para-carbons relative to the central nitrogen of the terpyridine ring.<sup>32</sup>



**Scheme 67.** Possible reaction pathways towards (tpy)NiCH<sub>3</sub> and its terpyridyl ligand derivatives.

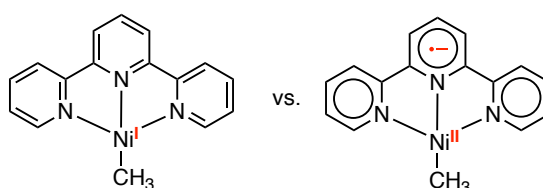
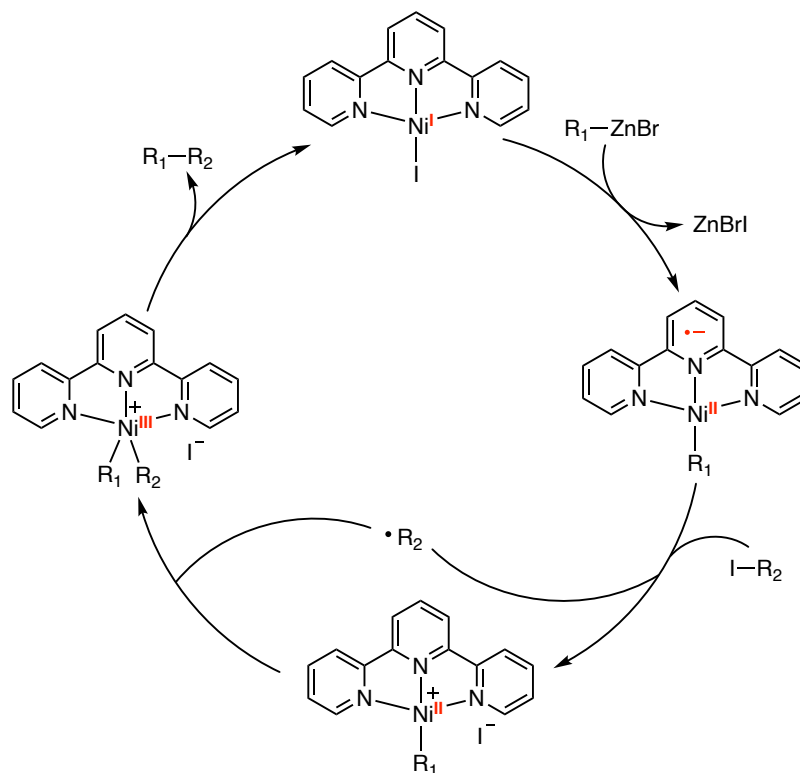


**Figure 78.** Representations of (tpy)NiCH<sub>3</sub> as a Ni(I)-methyl complex (left) and a charge-transfer state comprising a Ni(II)-methyl cation (right).

The (tpy)NiCH<sub>3</sub> complex exhibited one reversible oxidation wave in the cyclic voltammogram at  $-1.316 \text{ V vs. Ag/Ag}^+$  in THF solution,<sup>33</sup> which is rather close to that of Sml<sub>2</sub> ( $-1.55 \text{ V}$ ) as whose chemistry in organic synthesis was pioneeringly discovered by Kagan.<sup>34,35</sup> The latter reagent is known as an efficient catalyst to readily reduce alkyl iodides generating radical anion species.<sup>36</sup> The authors therefore performed a stoichiometric reaction at room temperature between (tpy)NiCH<sub>3</sub> and one equivalent of iodocyclohexane, which generated methylcyclohexane in a good yield (79%), without significant amount of olefinic by-products formed *via*  $\beta$ -H elimination processes. This stoichiometric reaction, in consistence with the catalytic version (5 mol% of (tpy)NiCH<sub>3</sub>), involves a bench-stable monovalent (tpy)NiI species, and a radical-mediated mechanism was speculated, since dicyclohexyl was detected as a minor product in the catalysis.<sup>29</sup> Mechanistic insights in such a transformation were later investigated by the same group.<sup>32</sup> The reaction of an alkylzinc reagent with a cationic Ni(II)-methyl complex, which was obtained *via* oxidative addition of iodomethane with Ni(COD)<sub>2</sub> in the presence of terpyridine, only yielded 8% of cross-coupled products. In contrast, the neutral Ni(II)-methyl complex could give up to 90% yield of the expected coupling product with the corresponding alkyl iodide. Interestingly, the reaction that formed the cationic Ni(II)-methyl complex could easily lead to a thermodynamically stable (tpy)NiI species when the reaction was kept for a longer time. All these results by Vicic indicated that this Negishi-like reaction does not undergo the classical Ni(0)/Ni(II) mechanism involving oxidative addition of alkyl halides, transmetalation generating nickel dialkyl intermediates and reductive elimination to form the coupling products.<sup>37</sup> The ability of the (tpy)NiCH<sub>3</sub> complex to reduce alkyl halides leads to a fundamentally different concept that involves an one-electron

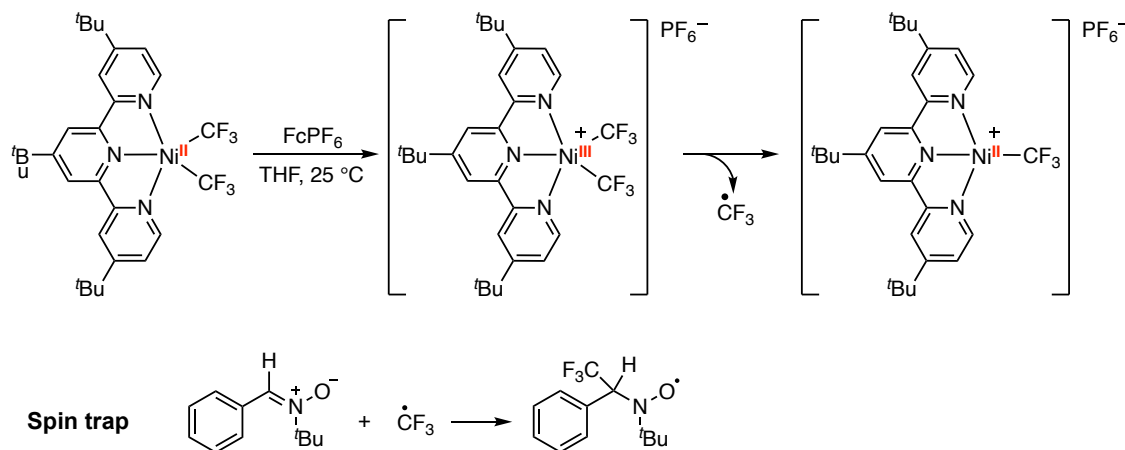
ligand-based redox system: an alkyl radical is released in close proximity to the nickel center by the reduction of the alkyl halide, which then reacts to afford a highly reactive Ni(III)-dialkyl intermediate *via* radical addition. The fast and facile coupling step, *i.e.*, reductive elimination of the newly formed alkane is followed by the formation of a metal-centered Ni(I) complex with a ( $d^8$ )( $d_{x^2-y^2}$ ) electronic configuration,<sup>31</sup> namely (tpy)NiI, which is also a viable precatalyst in this transformation (Scheme 68).<sup>38</sup> Related DFT calculations based on Vici's experimental mechanistic insights were explicitly explored by Phillips, demonstrating that the neutral (tpy)NiCH<sub>3</sub> complex can be favorably involved in this catalytic cycle in terms of the feasible free activation energy. In contrast, the transmetalation step of the cationic Ni(II)-alkyl iodide complex with alkylzinc reagents is highly unfavorable.<sup>39</sup> The iodine transfer step, which meanwhile generates a free alkyl radical, is also calculated as the rate-determining step in the presence of primary alkyl electrophiles. The result of the oxidative radical addition leads the Ni(III) intermediate undergoing the thermodynamically favorable reductive elimination over the kinetically favorable decomposition as a side reaction.



**Scheme 68.** Proposed catalytic cycle of alkyl-alkyl cross-coupling reaction in nickel-terpyridine system.

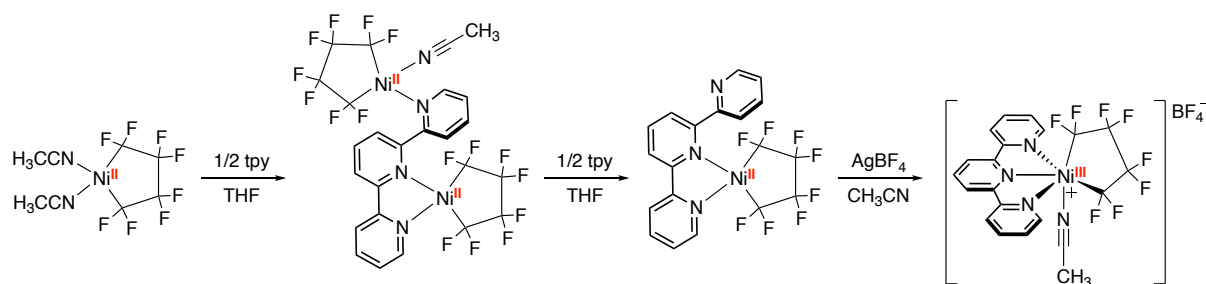
The series of high-valent Ni(III) species involved in the above-reported coupling mechanism are of particular interest to be fingerprinted due to their highly reactive nature. The group of Vici then isolated a five-coordinate terpyridyl nickel di-trifluoromethyl variant, [(tpy')Ni(CF<sub>3</sub>)<sub>2</sub>], which was found to be paramagnetic ( $\mu_{\text{eff}} = 2.59 \mu_{\text{B}}$ ). Chemical oxidation with [ferrocenium][PF<sub>6</sub>] salt generated a transient [Ni(III)(CF<sub>3</sub>)<sub>2</sub>] species, which was detected by EPR spectroscopy. Such a short-lived species then rapidly undergoes reductive homolysis of one trifluoromethyl radical, yielding a cationic, four-coordinate Ni(II) complex. Similar reaction behavior of (tpy')Ni(CF<sub>3</sub>)<sub>2</sub>

appeared using AgOTf as oxidant. In both cases, C<sub>2</sub>F<sub>6</sub> and CF<sub>3</sub>H were produced in 14 and 42% average yields, respectively, as confirmed by NMR analysis. In the presence of PBN (*N*-*tert*-butyl- $\alpha$ -phenylnitrone) as a spin trap, the oxidation of (tpy')Ni(CF<sub>3</sub>)<sub>2</sub> by EPR spectroelectrochemistry could be clearly traced to the generated CF<sub>3</sub>-PBN species, agreeing with the homolysis step of trifluoromethyl ligands<sup>40</sup> (Scheme 69).



**Scheme 69.** Oxidation-induced spectroscopically detectable Ni(III) species from a five-coordinate Ni(II) trifluoromethyl complex.

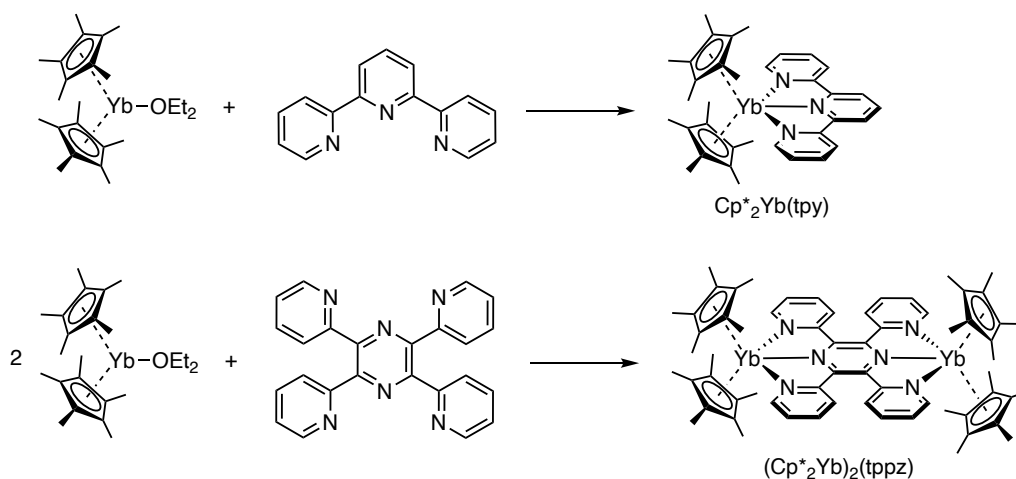
Fluoroalkyl moieties are good ligands to stabilize high-valent organometallic species, as already mentioned in *Chapter 3* about a number of isolated nickel complexes with high oxidation states. The Vici's group successively reported a new nickel complex bearing a [C<sub>4</sub>F<sub>8</sub>] functional group with terpyridyl ligand coordinated in a  $\eta^2$  fashion. This compound has a paramagnetic property and possesses an equilibrium between the  $\eta^2$  and  $\eta^3$  chelating modes. A different outcome in the synthesis of the complex was observed if 0.5 equivalent of terpyridine was used together with the [(MeCN)<sub>2</sub>Ni(C<sub>4</sub>F<sub>8</sub>)] precursor, leading to a stable, bimetallic species, which proves the lability of the acetonitrile ligands in this precursor. The oxidation of [( $\eta^2$ -tpy)Ni(C<sub>4</sub>F<sub>8</sub>)] with AgBF<sub>4</sub> yielded a stable, high-spin Ni(III) complex in an octahedral geometry with  $\eta^3$ -binding for the terpyridine without any fluoroalkyl radical formation (Scheme 70).<sup>41</sup> The use of the [C<sub>4</sub>F<sub>8</sub>] ligand provided an example for the successful isolation of high-valent metal complexes, especially nickel. Also, the cyclic voltammograms of this high-valent Ni(III) complex showed two redox couples with good reversibility, representing not only the Ni(II)/Ni(III) couple but also the Ni(III)/Ni(IV) one, which agrees with the accessibility of well-defined Ni(IV) complexes bearing fluoroalkyl [CF<sub>3</sub>] ligands as reported by Sanford.<sup>42</sup>



**Scheme 70.** Synthesis of terpyridyl nickel complexes bearing a readily attached [C<sub>4</sub>F<sub>8</sub>] ligand.

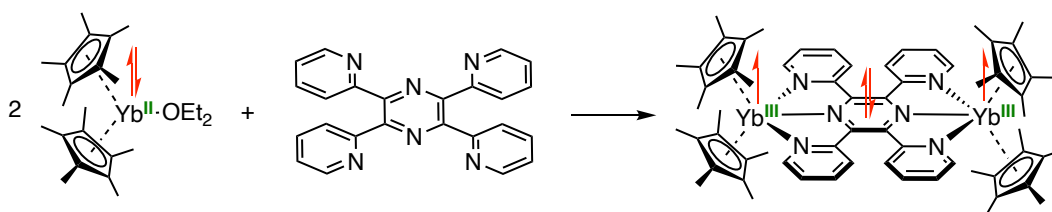
## 1.2. Redox activity in divalent lanthanide terpyridine-based complexes

In previous chapters, internal charge-transfer properties in divalent lanthanide complexes with *N*-aromatic heterocycle adducts have been explicated. A related study by Andersen and coworkers described monometallic and bimetallic ytterbocene adducts with versatile nitrogen bases.<sup>43</sup> A significant follow-up study based on divalent ytterbium polypyridyl complexes was also reported by Morris and John in 2003, demonstrating mixed-valent systems in ytterbocene terpyridine (tpy) and tetrapyridinylpyrazine (tppz) complexes<sup>44</sup> (Scheme 71). Both the Cp\*<sub>2</sub>Yb(tpy) complex and its samarium analogue, Cp\*<sub>2</sub>Sm(tpy), have a ligand-based radical and f<sup>n+1</sup> electronic structure. The electronic and magnetic behaviors of Cp\*<sub>2</sub>Yb(tpy) and Cp\*<sub>2</sub>Sm(tpy) have been studied and remarkable differences between these two complexes have been observed depending on the nature of the divalent lanthanide ions.<sup>45</sup> Strong temperature dependence for proton resonances in the radical anionic ligand, as  $\Delta\delta > 100$  ppm and  $> 50$  ppm for a single resonance in Cp\*<sub>2</sub>Yb(tpy) and Cp\*<sub>2</sub>Sm(tpy), respectively, indicates a more effective electron transfer from divalent samarium than from ytterbium metal centers to the tpy ligand. The same tendency was also observed by the authors in the oxidized congeners of these two compounds. UV-vis-NIR spectra of both complexes exhibit dominating  $\pi$ - $\pi^*$  and/or  $\pi^*$ - $\pi^*$  absorption bands localized on the ligand, which is different from the prominent characteristic of f-f bands in their formally trivalent Cp\*<sub>2</sub>Yb(tpy)<sup>+</sup> and Cp\*<sub>2</sub>Sm(tpy)<sup>+</sup> derivatives. More particularly, the visible spectra show a red-shift ( $\sim 400$  cm<sup>-1</sup>) in all of the bands of Cp\*<sub>2</sub>Sm(tpy) relative to those of Cp\*<sub>2</sub>Yb(tpy), revealing a slightly greater stabilization of the  $\pi^*$ -level(s) in the samarium(III) complex compared to that in the ytterbium(III) complex. In addition, the magnetic susceptibility of Cp\*<sub>2</sub>Sm(tpy) is relatively different than that of Cp\*<sub>2</sub>Yb(tpy). The latter possesses a multiconfigurational ground state and has been thoroughly investigated by Andersen.<sup>44,46-49</sup> In contrast, in the case of Cp\*<sub>2</sub>Sm(tpy), a very monotonic  $\chi T$  versus *T* plot is observed, suggesting with a non-magnetic ground state with thermally populated excited states (TIP).<sup>50</sup> The  $\chi T$  value of 0.61 emu K mol<sup>-1</sup> at 300 K is consistent with the presence of a Sm<sup>III</sup> ion with an uncoupled radical (*S* = 1/2) on the ligand. In consistence with the magnetic data, the spin-orbit coupling constant in Cp\*<sub>2</sub>Sm(tpy) measured by optical experiments is much smaller than that for Cp\*<sub>2</sub>Yb(tpy), revealing an evidence of the ground state difference between these two complexes.



**Scheme 71.** Synthesis of mixed-valent ytterbocene terpyridine complexes by Morris and John.

The binuclear (Cp\*<sub>2</sub>Yb)<sub>2</sub>(tppz) complex displays a similar feature, with an initial spontaneous electron transfer from the f<sup>14</sup> metal center into the lowest unoccupied ( $\pi^*$ ) molecular orbital (LUMO) of the polypyridyl ligand (tppz),<sup>51</sup> forming an [(f)<sup>13</sup>(tppz)<sup>2</sup>(f)<sup>13</sup>] ground-state electronic configuration (Scheme 72). The mixed valency of this complex has been observed and rationalized by several physicochemical characterizations such as cyclic voltammetry and electronic-absorption spectroscopy, which also revealed a reversible redox behavior, as a (tppz)<sup>-2/-1</sup>/Yb<sup>3+/2+</sup> pair of redox waves. One-electron reduction of (Cp\*<sub>2</sub>Yb)<sub>2</sub>(tppz) yields a mixed-valent (Yb<sup>II</sup>-Yb<sup>III</sup>) congener, in which the electron vacancy is delocalized through the doubly-reduced tppz ligand, different from the typical metal-centered mixed-valency observed in symmetrical bimetallic ruthenium Creutz-Taube systems involving metal-ligand-metal interactions.<sup>52,53</sup>



**Scheme 72.** Spontaneous double-electron transfer process in (Cp\*<sub>2</sub>Yb)<sub>2</sub>(tppz) complex.

Similar phenomena involving [(f)<sup>13</sup>( $\pi^*$ )<sup>2</sup>(f)<sup>13</sup>] electronic configurations in bimetallic ytterbocene-polypyridyl adducts were expanded by Morris and John upon double electron-transfer (one from each Yb<sup>II</sup> metal center) into the bridging ligand with a spin-paired configuration in the same ligand- $\pi^*$  orbital.<sup>54</sup> The authors explored a symmetrical 4'-substituted-terpyridine to facilitate the axially symmetric coordination environment, in order to study the electronic correlation influence of the increased Yb-Yb separation. Selected examples from their study have been shown in Figure 79. The qtp (*i.e.*, 6',6''-bis(2-pyridyl)-2,2':4',4''':2'',2'''-quaterpyridine) ligand as well as its derivatives with longer chains such as 1,4-dtb (*i.e.*, 1,4-di(terpyridyl)-benzene) ligand, can be easily twisted. The lack of crystallographic data on (Cp\*<sub>2</sub>Yb)<sub>2</sub>(qtp) and (Cp\*<sub>2</sub>Yb)<sub>2</sub>(1,4-dtb) could not enable precise insights into the corresponding solid-state structures. However, an almost planar qtp ligand was found by the authors in the analogous bimetallic (Cp\*<sub>2</sub>Yb)<sub>2</sub>(qtp) complex (*i.e.*,



$[(C_5EtMe_4)_2Yb]_2(qtp)$ , in which the torsion angle between the two terpyridine fragments is  $0.4^\circ$  in the solid-state structure. This planarity resembles that reported for metal oxide materials in which mixed-valent copper subunits are bridged by qtp ligands, leading to one-dimensional structures, studied by Zubieta and co-workers.<sup>55,56</sup> Similarly to the  $(Cp^*_2Yb)_2(qtp)$  compound, the  $(Cp^*_2Yb)_2(1,4-dtb)$  complex was observed to possess significant electronic interaction across the ligand between two  $\{Cp^*_2Yb(tpy)\}$  fragments by magnetic and electronic characterizations, plausibly indicating a nearly planar structure, which is also in a singlet dianion-bridged  $[(4f)^{13}(\pi^*)^2(4f)^{13}]$  ground-state electronic configuration.<sup>57</sup> Differently, when the bridging ligand changed from 1,4-dtb to 1,3-dtb (*i.e.*, 1-methyl-3,5-bis(2,2':6',2''-terpyridin-4'-yl)benzene), a diradical-bridged  $[(4f)^{13}(\pi^*_{tpy1})^1(\pi^*_{tpy2})^1(4f)^{13}]$  ground state was identified in the  $(Cp^*_2Yb)_2(1,3-dtb)$  complex as a result of the linking tolyl moiety free rotation. Such different spin states between two dtb derivatives are consistent with the related study on the nature of spin coupling of organic diradicals depending on the molecular geometry. Strong ferromagnetic spin coupling across a phenyl system can be achieved in the 1,3-geometry, while antiferromagnetic coupling can be promoted in the 1,4-geometry.<sup>58</sup> Such magnetic behavior was observed by the authors, as well as electronic measurements in agreement with those of the monometallic  $Cp^*_2Yb(tpy)$  analogue. A  $C_2$  symmetry, lower than the  $C_{2v}$  symmetry found in the  $(Cp^*_2Yb)_2(1,4-dtb)$  congener, was observed in the crystal structure, as the result of two torsion angles between each tpy group and the tolyl spacer of  $26$  and  $41^\circ$ , respectively.<sup>59</sup>

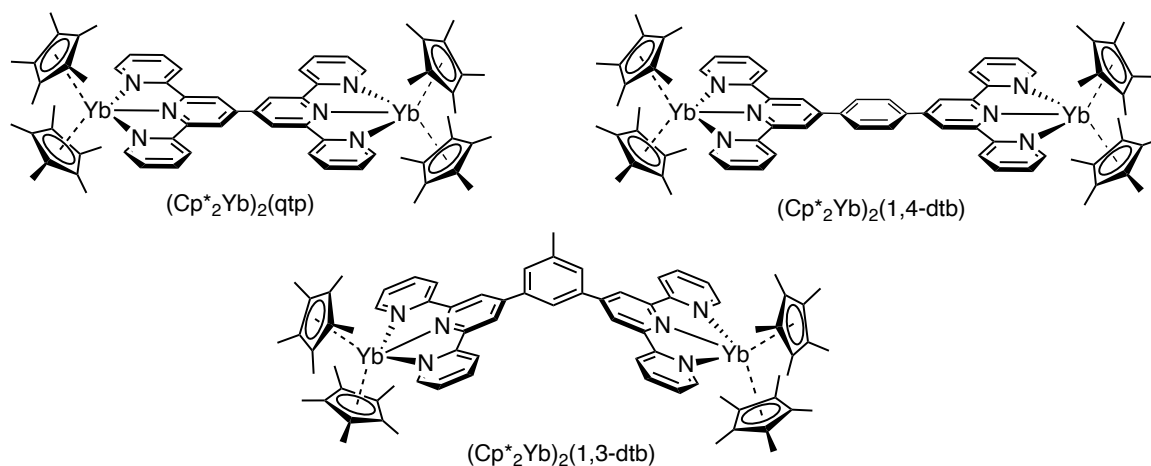


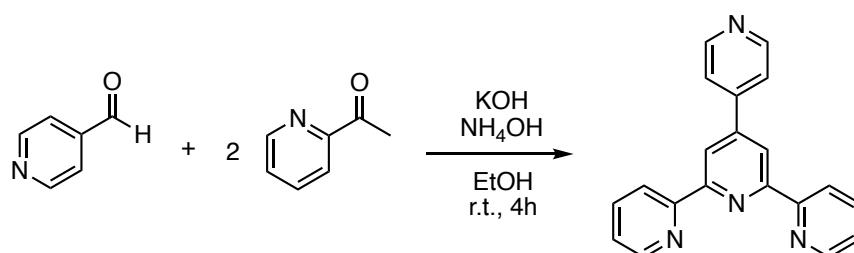
**Figure 79.** Selected examples on bimetallic ytterbocene terpyridine-based complexes by Morris and John.

Hence, an effective electron correlation across the overall metal-ligand system can be considered in the case of a planar bimetallic framework. The electronic structure of a highly reduced tpy-based complex can be affected by the ligand-centered radical(s), leading to a potential reactivity towards small molecule functionalization or enhanced catalytic activity.<sup>60</sup> In this work, the combination of an appropriate heterobimetallic framework with a freely rotating bridging ligand (pytpy) will be considered.

## 2. Towards the heterobimetallic framework: synthesis and structural analysis

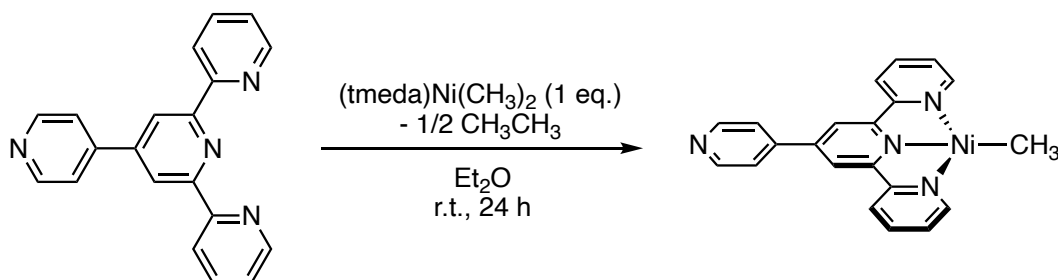
### 2.1. A new nickel complex with the pytpy ligand

The preliminary strategy in the synthesis of the pytpy linker has already been described by Hanan *et al.* in 2005.<sup>61</sup> This straightforward synthetic method successively involves enolate formation, aldol condensation, Michael addition and central pyridine ring formation using aqueous ammonia as nitrogen source, and proceeds smoothly at room temperature (Scheme 73).<sup>62</sup>



**Scheme 73.** One-pot synthesis of the 4'-(4-pyridyl)-2,2':6',2''-terpyridine ligand.

The synthesis of the desired (pytpy)NiCH<sub>3</sub> complex (**1**) was performed referring to the well-described synthetic methodology towards the (tpy)NiCH<sub>3</sub> analogue reported by Vicic and coworkers (Scheme 74). The 24-hour reaction in Et<sub>2</sub>O at room temperature between (tmeda)Ni(CH<sub>3</sub>)<sub>2</sub> and the pytpy ligand yielded a dark blue suspension. The resulting dark blue solid was separated *via* centrifugation, dried under reduced pressure and isolated in 76% yield. This compound has extremely poor solubility in many organic solvents at room temperature, yet dark colored X-ray suitable crystals could be grown *via* slow diffusion of *n*-pentane in a pyridine solution of the complex at -40 °C over several days (Figure 80).



**Scheme 74.** Synthesis of (pytpy)NiCH<sub>3</sub> (**1**).

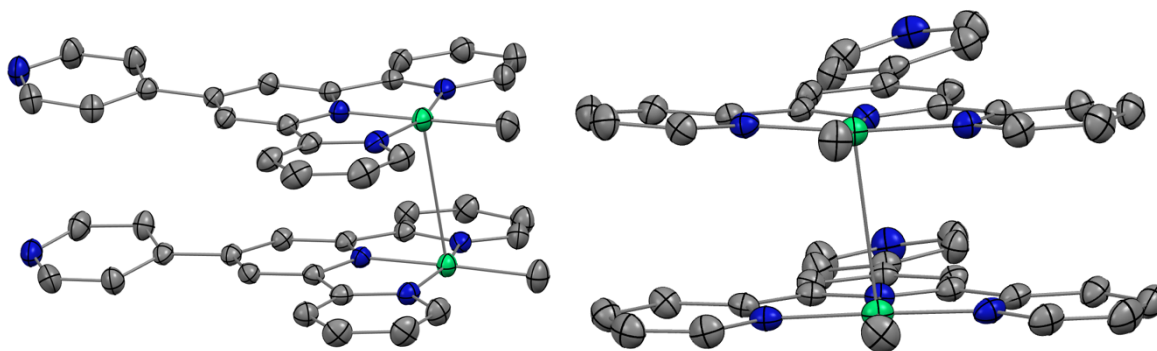


**Figure 80.** ORTEP of **1**. Thermal ellipsoids are at 50% level. Two different orientations of the structure are presented. Carbon atoms are in grey, nitrogen atoms in blue, nickel atoms are in green. Hydrogen atoms and co-crystallized solvate molecules of pyridine are removed for clarity.

In **1**, the average Ni-C bond length is 1.934(5) Å, in agreement with a divalent nickel coordination environment, whereas the average distance for Ni-alkyl bonds in reported isolated Ni(I) complexes is approximately 1.98 Å, depending on the nature of the chelating ligands.<sup>63–65</sup> The average distance of the C-C bond that links the pyridine ring and terpyridine plane is 1.470(5) Å. This metrical datum will be one of the crucial parameters to refer to, when studying further reduction of the pyridine moiety. The average torsion angle between the pyridine and terpyridine moieties is 10°, indicative of a non-planar system in the overall ligand. Importantly, a Ni–Ni interaction of 3.213 Å can be observed in the solid-state structure, which is likely induced by  $\pi$  stacking effects between two ligands. Similar intermolecular  $\pi$ -stacking interactions have been reported in several metal complexes bearing the 4'-phenyl-2,2':6',2''-terpyridine (Phtpy) ligand, in which edge-to-face and offset face-to-face stacking fashions were observed in the solid state.<sup>66</sup> Notably, a redox-active nickel system bearing a diiminobenzosemiquinonate ligand was found to display a weak Ni-Ni interaction of 2.800(1) Å,<sup>67</sup> yet the head-to-head interaction observed in **1** is rather rare. The molecular structure of **1** can be compared to that of the (tpy)NiCH<sub>3</sub> analogue prepared by Vicic, with a similar average Ni–C bond distance of 1.95(13) Å and short nickel–nickel contact of 3.18(12) Å. However, the crystallographic data of the latter compound were of limited quality (18.7% *R*-factor value) and care is necessary in comparing both solid-state structures.

A plausible Ni<sup>II</sup>-pytpy<sup>•-</sup> formulation could be explicitly postulated from the XRD data alone, in reference to the study of Vicic.<sup>32</sup> The further characterizations that were performed aimed at clarifying the electronic structure of **1** in the aforementioned context. Meanwhile, the reduction of the Ni-pytpy fragment by divalent lanthanides will be of great interest. Particularly, the reduction of pyridine moieties has been described by divalent lanthanides such as samarium and thulium complexes in *Chapter 4*. Upon electron transfer reactions, planarity between the pyridine and terpyridine rings should be allowed, eventually resulting in the formation of a doubly reduced terpyridine moiety and a dianionic ligand. Furthermore, since the (tpy)NiCH<sub>3</sub> compound is able to perform radical reactivity such as cross-coupling reactions,<sup>29</sup> it would be remarkable to explore the

potential reactivity of the newly formed heterobimetallic complexes obtained upon coordination of the pytpyNiCH<sub>3</sub> fragment to divalent lanthanide moieties.

## 2.2. Complexation with divalent organolanthanides

To begin with, divalent lanthanides were first considered as candidates to coordinate selectively to the pytpy ligand at the 4'-pyridyl site. Since ytterbocene, as well as samarocene, bearing Cp\* ligands are known to coordinate to the nitrogen atoms of terpyridine in a chelating  $\kappa^3$ -fashion,<sup>45</sup> more bulky organolanthanide fragments,<sup>68</sup> such as Cp<sup>ttt</sup><sub>2</sub>Yb and Cp<sup>ttt</sup><sub>2</sub>Sm (Cp<sup>ttt</sup> = 1,2,4-*t*Bu<sub>3</sub>C<sub>5</sub>H<sub>2</sub>) were applied in this step to possibly suppress coordination at the terpyridine site of the pytpy ligand.<sup>69</sup>

The complexation of pytpy with Cp<sup>ttt</sup><sub>2</sub>Yb in THF-d<sup>8</sup> at room temperature yielded a deep green, surprisingly paramagnetic species (Figure 81 and 82). The corresponding <sup>1</sup>H NMR spectrum nicely showed most of the proton signals of the coordinated pytpy ligand, highly shifted compared to the signals of free pytpy, as well as two non-equivalent Cp<sup>ttt</sup> ligands. This NMR spectrum is very similar to that of Cp\*<sub>2</sub>Yb(tpy) reported by Kevin D. John and colleagues.<sup>46</sup> However, due to the lack of crystallographic data on this new species, conclusive information about the structure of the obtained product are still elusive.

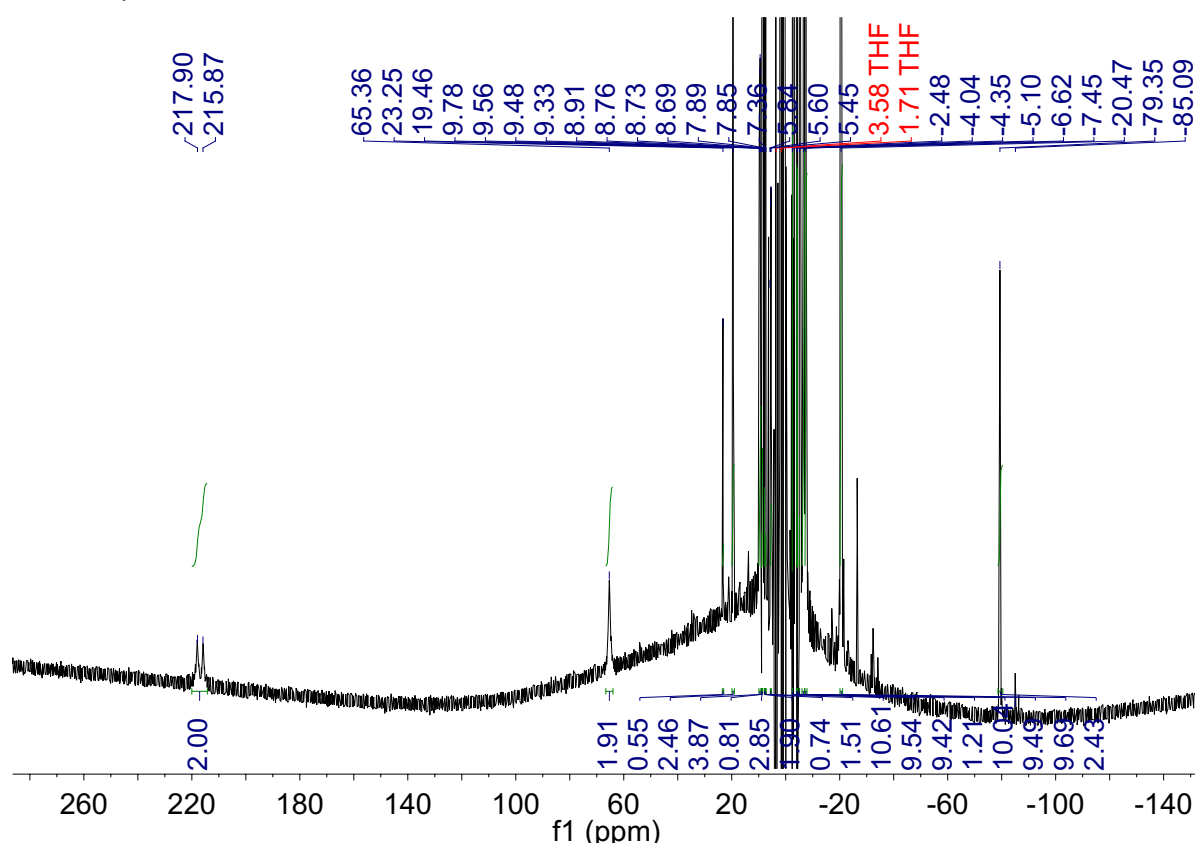
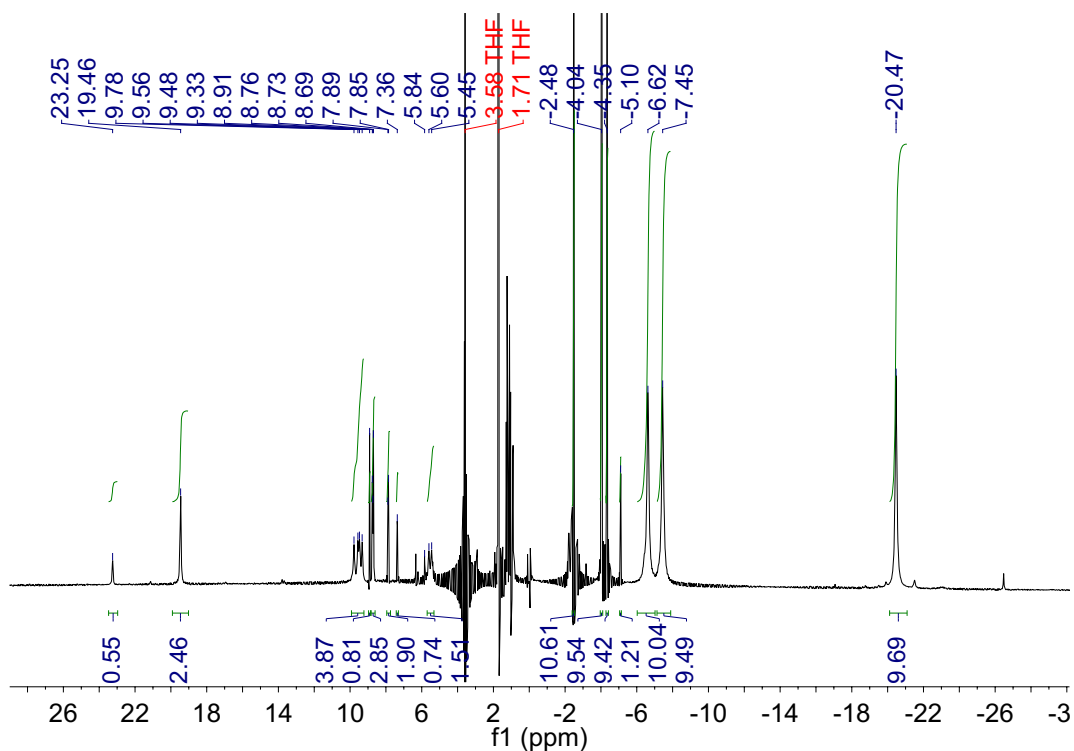
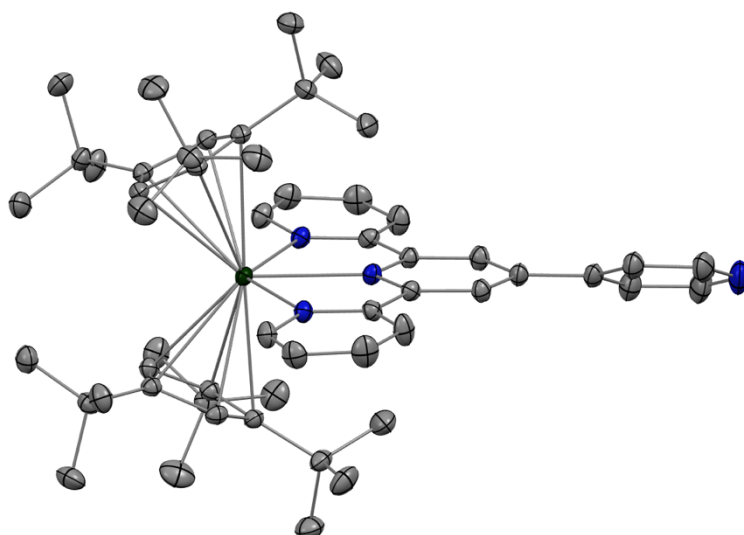


Figure 81. <sup>1</sup>H NMR of *in situ* complexation of pytpy with Cp<sup>ttt</sup><sub>2</sub>Yb in THF-d<sup>8</sup> at 20°C.



**Figure 82.**  $^1\text{H}$  NMR of *in situ* complexation of pytpy with  $\text{Cp}^{\text{ttt}}_2\text{Yb}$  in  $\text{THF-d}^8$  at  $20^\circ\text{C}$  (Zoom in).

No strong evidence about the coordination mode of the pytpy ligand towards a sterically hindered organolanthanide fragment featuring the relatively small Yb(II) ion could be obtained to date. The reactivity towards  $\text{Cp}^{\text{ttt}}_2\text{Sm}$  was then considered, taking into consideration of the lower reduction potential of the Sm(II) analogue. However, it should be noted that  $\text{Cp}^{\text{ttt}}_2\text{Sm}$  was found not to reduce pyridine, contrary to  $\text{Cp}^*_2\text{Sm}$ . This unexpected reactivity has been traced back to the large steric repulsion between the bulky *t*Bu substituents that would occur upon oxidation of the Sm(II) center to Sm(III), due to the corresponding decrease in the lanthanide ionic radius. Applying a similar reasoning, reduction of terpyridine by  $\text{Cp}^{\text{ttt}}_2\text{Sm}$  should be disfavored as the resulting Sm(III) ion bearing both tpy and  $\text{Cp}^{\text{ttt}}$  ligands would be too sterically crowded. The complexation between  $\text{Cp}^{\text{ttt}}_2\text{Sm}$  and pytpy was carried out by mixing stoichiometric equivalents of both compounds in  $\text{Et}_2\text{O}$ . Deep green crystals of **2** (72% yield) suitable for X-ray diffraction studies could be obtained upon storage of the  $\text{Et}_2\text{O}$  solution at  $-40^\circ\text{C}$  (Figure 83). In **2**, the  $\text{Cp}^{\text{ttt}}_2\text{Sm}$  fragment chelates to the tpy pocket instead of the expected terminal pyridine ring. The average Sm-Cp<sub>ctr</sub> and Sm-N distances are 2.58(7) and 2.53(2) Å, respectively, consistent with the presence of a divalent samarium ion. The distortion angle of the py-tpy linkage is  $25^\circ$ , with a C-C distance between the two N-heterocycles of 1.46(1) Å, which excludes electron correlation between the terpyridine and terminal pyridine moieties. The  $^1\text{H}$  NMR spectrum of **2** recorded in  $\text{C}_6\text{D}_6$  at  $20^\circ\text{C}$  shows paramagnetically shifted resonances, in agreement with a Sm(II) complex (Figure 84).



**Figure 83.** ORTEP of **2**. Thermal ellipsoids are at 50% level. Carbon atoms are in grey, nitrogen in blue, samarium in deep green. Hydrogen atoms and co-crystallized diethyl ether solvate molecules are removed for clarity.

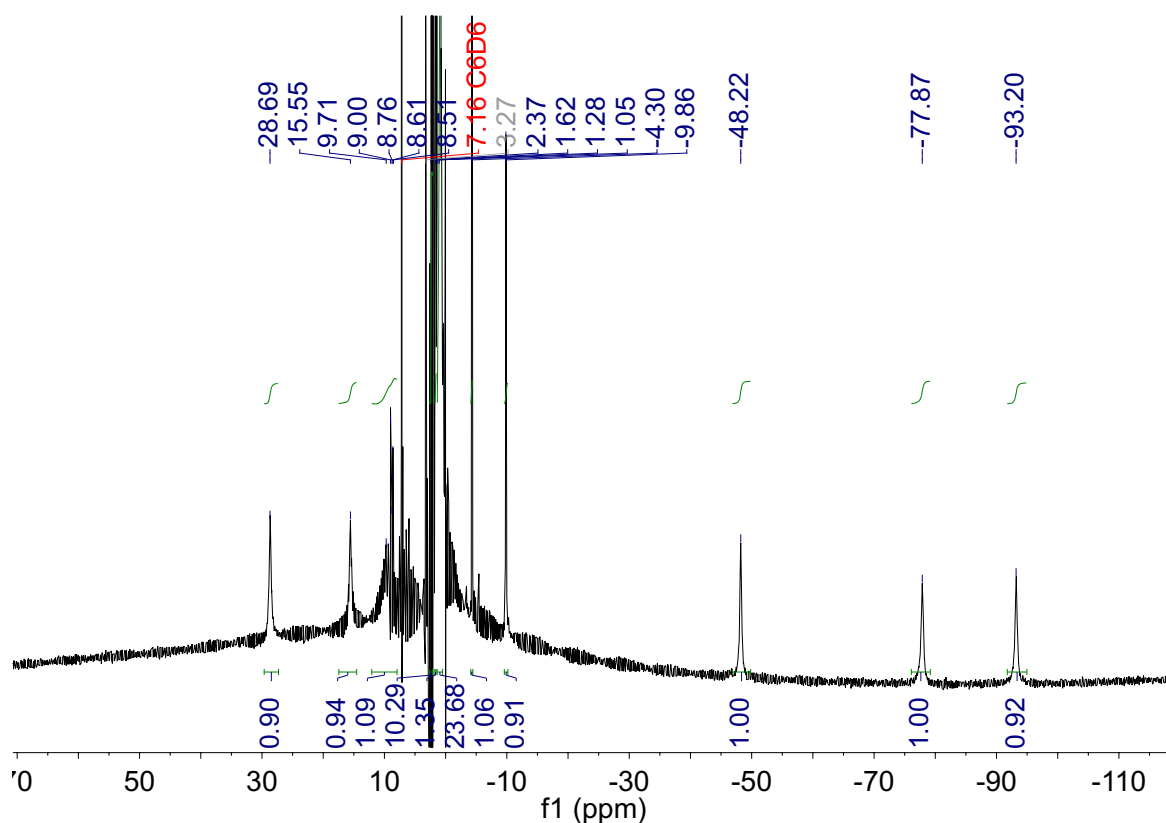


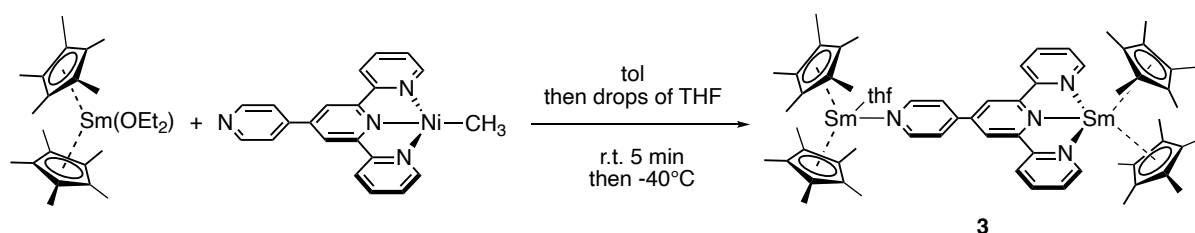
**Figure 84.** <sup>1</sup>H NMR of **2** in C<sub>6</sub>D<sub>6</sub> at 20°C. Et<sub>2</sub>O impurity from the synthesis is indicated in grey.

Therefore, to obtain the expected heterobimetallic motif, it is necessary to perform the synthesis starting from the precursor **1** with further addition of the divalent organolanthanide fragment. The first attempt to build up a hetero-binuclear compound was upon addition of the divalent Cp\*<sub>2</sub>Yb(OEt<sub>2</sub>) compound to pytpyNiCH<sub>3</sub> in different solvents including toluene, Et<sub>2</sub>O, THF and

pyridine. Although a color change was directly observed, it cannot be used as a sign of efficient electron transfer, as weak interaction between the ytterbium ion and pytpy ligand is possible. Indeed, facile dissociation of the  $\text{Cp}^*_2\text{Yb}$  and  $(\text{pytpy})\text{NiCH}_3$  fragments was observed by  $^1\text{H}$  NMR spectroscopy when recording the spectra in coordinating deuterated solvents such as  $\text{THF-d}^8$ . Besides,  $\text{Cp}^*_2\text{Yb}(\text{py})_2$  was isolated when using pyridine as reaction or NMR solvent. Even when performing the synthesis in  $\text{Et}_2\text{O}$ , green crystals of  $\text{Cp}^*_2\text{Yb}(\text{OEt}_2)$  were isolated in the end instead of the expected heterobimetallic complex. Yet, the reaction in toluene led to the most promising results but only a dark brown material was obtained and could not be successfully recrystallized due to a very poor solubility in suitable nonpolar solvents.

The ineffective reduction of the pyridyl fragment by divalent  $\text{Cp}^*_2\text{Yb}$  can be explained by the less negative reduction potential of the  $\text{Yb}^{\text{III}}/\text{Yb}^{\text{II}}$  couple compared to that of pyridine, which was already demonstrated by Andersen and Zalkin.<sup>70</sup> The subsequent attempt focused on the utilization of divalent samarium complexes, as their efficient reduction of pyridine and other *N*-aromatic heterocycles has already been reported.<sup>71–73</sup>

$\text{Cp}^*_2\text{Sm}(\text{OEt}_2)$  was therefore added to a dark toluene suspension of **1**, leading to a more soluble deep green solution. Recrystallization from concentrated solutions at  $-40^\circ\text{C}$  was not successful. However, upon addition of several drops of THF, deep green X-ray suitable crystals of **3** were isolated in a moderate yield of 47% (Scheme 75). An homobimetallic  $(\text{Cp}^*_2\text{Sm})_2(\text{pytpy})$  compound was unexpectedly obtained without presence of the  $-\text{NiCH}_3$  moiety (Figure 85). The reason for dissociation of the nickel center is still unclear. *In situ*  $^1\text{H}$  NMR monitoring of the reaction in  $\text{tol-d}^8$  could not confirm the potential formation of ethane, possibly due to overlapping signal with the broad resonances of  $\text{Et}_2\text{O}$ , nor that of  $\text{Ni}(0)$  species trapped by 1,5-cyclooctadiene (COD) molecules in the presence of free COD.



**Scheme 75.** Synthesis of **3** from  $\text{Cp}^*_2\text{Sm}(\text{OEt}_2)$  and **1** in toluene in the presence of drops of THF.

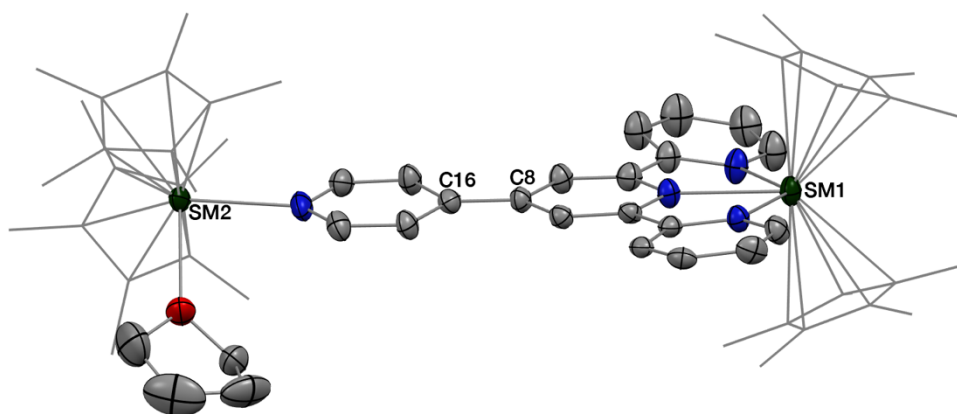


**Figure 85.** ORTEPs of homobimetallic  $(\text{Cp}^*_2\text{Sm})_2(\text{pytpy})$  compound (**3**). Thermal ellipsoids are at 50% level. Carbon atoms are in grey, nitrogen in blue, oxygen in red and samarium atoms in deep green. Hydrogen atoms are removed and  $\text{Cp}^*$  ligands on samarium are presented in wireframe style for clarity.

Although the mechanism leading to the formation of **3** remains ambiguous, the structural character of this homobimetallic complex is still very informative. The average  $\text{Sm}(1)\text{-Cp}^*$  (at the terpyridine site) and  $\text{Sm}(2)\text{-Cp}^*$  (at the pyridine site) distances are 2.516(5) and 2.45(7) Å, respectively. The solid-state crystallographic data are in good agreement with a ligand-based radical system ( $\text{Sm}^{\text{III}}\text{-tpy}^{\cdot-}$ ) and a pure trivalent samarium ion corresponding to the  $\text{Sm}(1)$  site,<sup>45</sup> while the reduction of the overall pytpy ligand is illustrated by a much shorter  $\text{C}_{\text{py}}\text{-C}_{\text{tpy}}$  distance (1.40(7) Å), compared to that in **1** (1.470(5) Å). In addition, a nearly planar pytpy ligand is observed with a torsion angle of 4°, in comparison to the one in **1** of 10°. Such structural features would be highly desirable for heterobimetallic Ln-Ni complexes owing to the particular ligand-radical delocalization.

While the  $\text{Cp}^*_2\text{Sm}$  fragment readily displaces the Ni center at the terpyridine unit and is coordinated in a chelating fashion, a similar behavior might be disfavored and avoided by the use of a bulkier metallocene, such as  $\text{Cp}^{\text{ttt}}_2\text{Sm}$ . Though the less reducing  $\text{Cp}^{\text{ttt}}_2\text{Sm}$  compound has been reported not competent to reduce pyridine molecules,<sup>71</sup> it can still help to get more insights into the possible nickel disassociation pathway.  $\text{Cp}^{\text{ttt}}_2\text{Sm}$  was then utilized to perform the complexation with **1**. *In-situ*  $^1\text{H}$  NMR experiment was carried out in  $\text{tol-d}^8$  at 20 °C by mixing stoichiometric equivalents of  $\text{Cp}^{\text{ttt}}_2\text{Sm}$  and **1**, showing a slightly different paramagnetic spectrum compared to that of **1** (Figure 86). The poor solubility of the formed species in toluene did not help the recrystallization *via* slow evaporation from a concentrated toluene solution; therefore, without solid-state structural information, it would be difficult to have more insights about this reaction. One of the hypotheses would be that  $\text{Cp}^{\text{ttt}}_2\text{Sm}$  coordinates at the pyridyl site, which could slightly influence the electron density and thus the chemical shifts of the paramagnetic **1**.



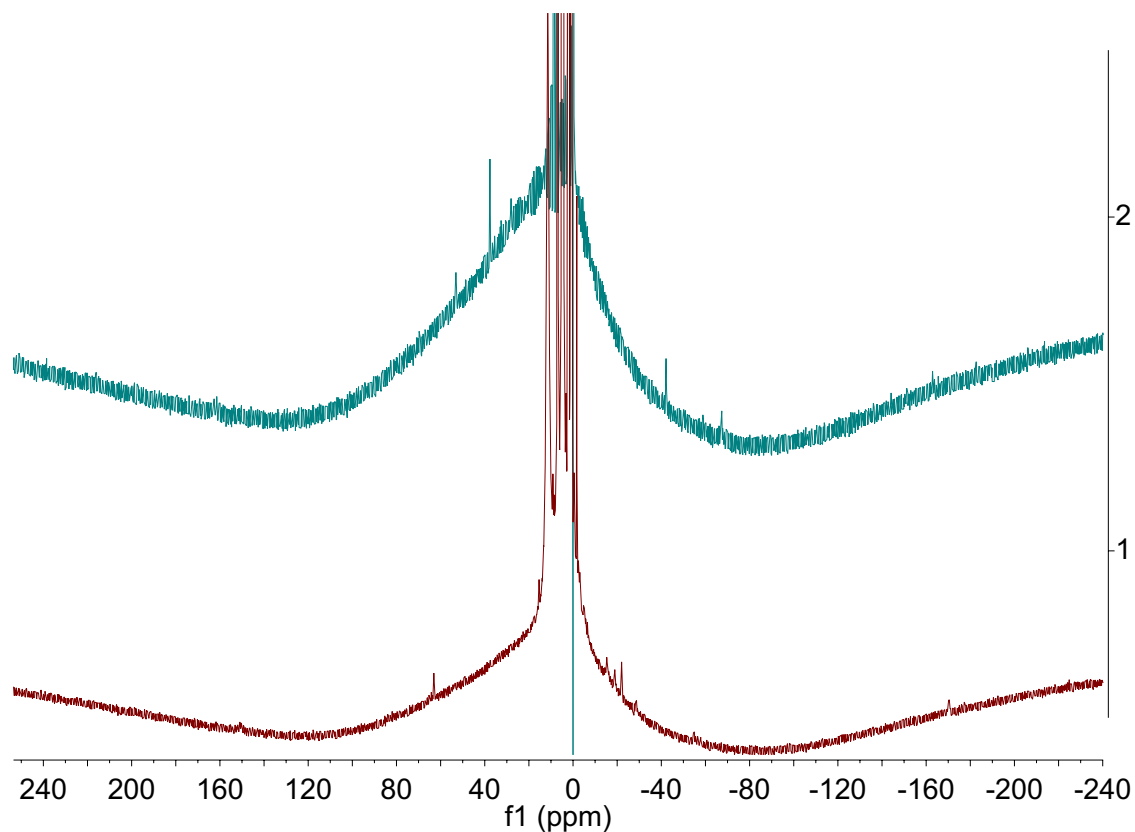
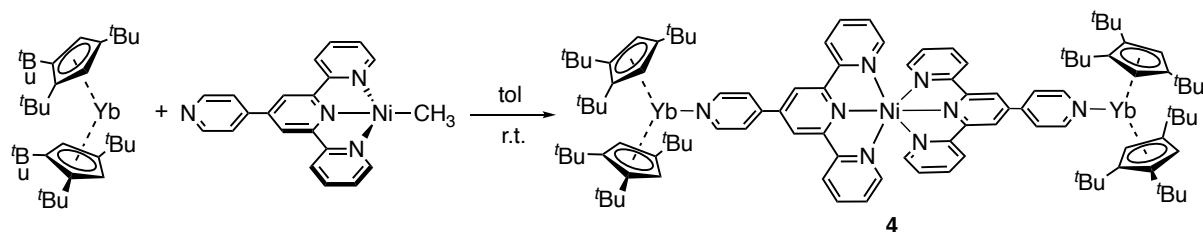


**Figure 86.**  $^1\text{H}$  NMR comparison of **1** (in green) and *in situ* experiment of  $\text{Cp}^{\text{ttt}}_2\text{Sm}$  with **1** (in red), in  $\text{tol-d}^8$  at  $20^\circ\text{C}$ .



**Scheme 76.** Synthesis of **4** from  $\text{Cp}^{\text{ttt}}_2\text{Yb}$  and **1** in toluene at room temperature.

Interestingly,  $\text{Cp}^{\text{ttt}}_2\text{Yb}$  was in parallel used to undergo the complexation with **1** in toluene- $d^8$  at room temperature, resulting in a much different paramagnetic system (Scheme 76). Dark green crystals of **4** were isolated from the toluene solution after several days, revealing a trinuclear species with a six-coordinated Ni subunit and two Yb fragments (Figure 87). The average Yb-N and Yb- $\text{Cp}_{\text{ctr}}$  distances are 2.50(1) and 2.47(1) Å, respectively, indicating that the Yb ions remain in the divalent oxidation state.<sup>68</sup> Also, a  $\text{C}_{\text{py}}-\text{C}_{\text{tpy}}$  distance of 1.441(5) Å, shorter than that in **1** (1.470(5) Å) indicates a higher electron density on the overall pytpy ligand. Yet, the distortion angle of the pytpy ligand of  $19^\circ$ , compared to the one in **1** of  $10^\circ$ , implies a lower electron correlation between the pyridine and terpyridine cycles in **4**. Furthermore, the average Ni-N distance of 2.070(8) Å is more consistent with a divalent nickel ion. The loss of the  $\text{CH}_3$  fragment on the nickel ion should facilitate the formation of a six-coordinated Ni center, however, the driving force of this Ni-C bond cleavage is unclear. The oxidation state of the newly formed Ni ion center can be either a formally zero-

valence or +2 valence with two radical-centered ligands. The Cp<sup>III</sup><sub>2</sub>Yb fragment might facilitate the (d<sup>8</sup>)(π\*<sup>1</sup>) → (d<sup>9</sup>)(π\*<sup>0</sup>) charger-transfer process in **1** followed by the elimination of a CH<sub>3</sub> radical. However, no obvious ethane formation was detected from *in situ* NMR experiments in tol-d<sup>8</sup> at 20 °C (Figure 88), and the redox potential of the Cp<sup>III</sup><sub>2</sub>Yb fragment should not be able to undergo a single-electron transfer in **1**. Clearly, further characterizations of **4** by different techniques such as EPR and magnetism studies are necessary in order to better understand the mechanism of the formation of this complex.

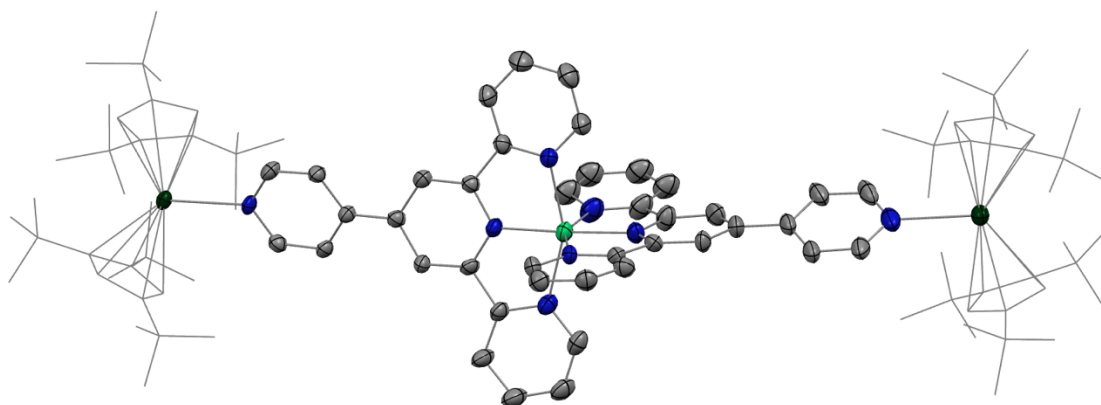


**Figure 87.** ORTEPs of the trinuclear **4**. Thermal ellipsoids are at 50% level. Carbon atoms are in grey, nitrogen in blue, nickel in bright green and ytterbium atoms in deep green. Hydrogen atoms and four co-crystallized toluene solvate molecules are removed and Cp<sup>III</sup> ligands are presented in wireframe style for clarity.

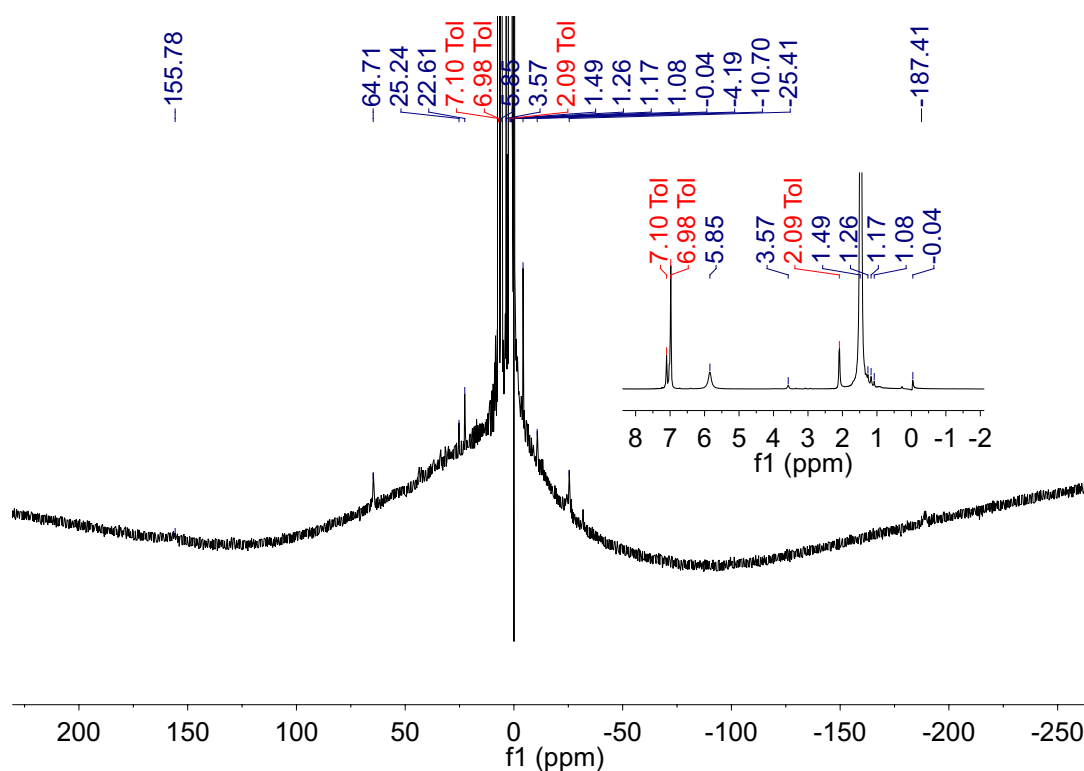
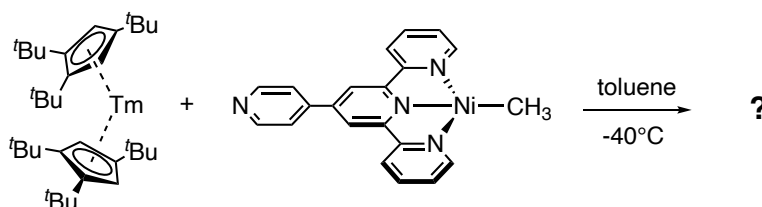


**Figure 88.** <sup>1</sup>H NMR of *in situ* experiment of Cp<sup>III</sup><sub>2</sub>Yb with **1** to synthesize **4** in tol-d<sup>8</sup> at 20 °C.

As discussed in the previous chapters, divalent thulium is well known to be very reductive. Since the less bulky Cp\*<sub>2</sub>Tm compound is highly reactive and can even react with dinitrogen,<sup>74</sup> the more stable Cp<sup>tt</sup><sub>2</sub>Tm was first selected to reduce the pyridyl moiety owing to its excellent reductive property towards the pyridine ligand.<sup>75</sup> The reaction instantly yielded a much more soluble deep green mixture when transferring a purple Cp<sup>tt</sup><sub>2</sub>Tm solution into the very dark green suspension of **1** in cold toluene (Scheme 77). After washing the resulting product with *n*-pentane, <sup>1</sup>H NMR studies in tol-d<sup>8</sup> at 20 °C showed a highly paramagnetic species, containing very broad resonances over a very wide range of chemical shifts, from 357 to -665 ppm (Figure 89). Despite large efforts to isolate crystals of this intriguing deep green species suitable for X-ray diffraction studies, only tiny and thin plate-type crystals poorly suitable for XRD analysis were obtained; moreover, the obtained deep green micro-crystalline plates were extremely reactive and rapidly decomposed outside the glovebox even when coated with Paratone-N oil. Nevertheless, the interesting highly reactive character of this complex deserves future investigations.



**Scheme 77.** Synthetic attempt of the complexation of **1** with Cp<sup>tt</sup><sub>2</sub>Tm in toluene at -40 °C.

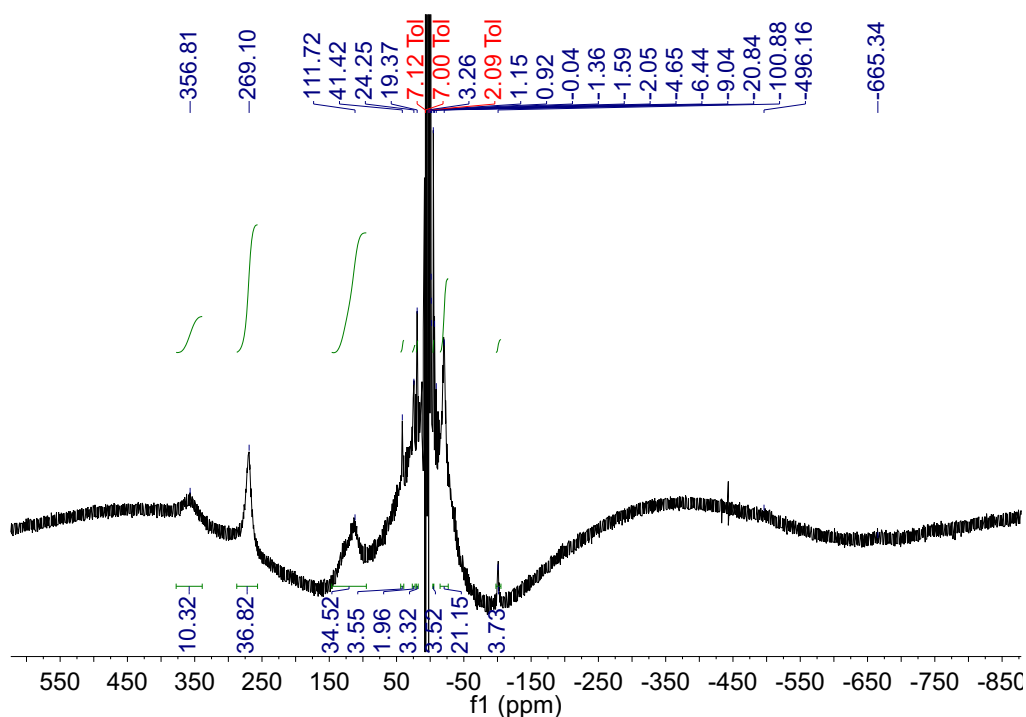


**Figure 89.** <sup>1</sup>H NMR of the deep green product from the reaction of Cp<sup>tt</sup><sub>2</sub>Tm with **1** in tol-d<sup>8</sup> at 20 °C.

The distinct outcomes in the complexation attempts of **1** with different reducing divalent organolanthanides triggered an interesting question: what compound would be obtained upon reaction of **1** with a strong reducing agent such as potassium graphite (KC<sub>8</sub>) instead of a reductive

divalent lanthanide? Accordingly, the reduction of **1** was performed using excess potassium graphite in THF at room temperature for a short reaction time (several seconds). After filtration and evaporation of the solvent, a deep green solid was eventually obtained and remained silent in  $^1\text{H}$  NMR analyses. Recrystallization of the compound was only successful in the presence of one equivalent of 18-crown-6, leading to XRD-suitable dark green crystals of **5**, isolated in 27% yield *via* slow diffusion of  $\text{Et}_2\text{O}$  into a THF solution of the complex at  $-35\text{ }^\circ\text{C}$  over several days. An ORTEP of **5** is presented in Figure 90.

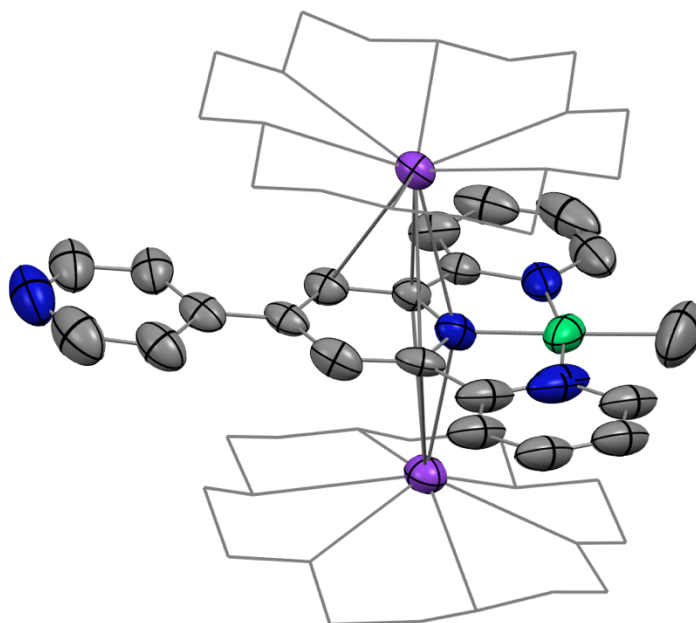


**Figure 90.** ORTEPs of **5** when each one position disorder of the carbons of one pyridyl ring on tpy as well as the atoms on one 18-crown-6, is allowed. Thermal ellipsoids are at 50 % level. Carbon atoms are in grey, nitrogen in blue, nickel in bright green and potassium in purple. Hydrogen atoms and one co-crystallized diethyl ether solvate molecule are removed and two 18c6 molecules are presented in wireframe style for clarity.

In **5**, the average Ni-N and Ni- $\text{CH}_3$  bond distances are 1.847(7) and 1.93 (5) Å, respectively, which are similar to those in **1** of 1.892(7) and 1.934(5) Å, respectively, indicating that the nickel center should stay in a divalent oxidation state. A remarkably shorter distance for the C-C linkage between the pyridine and terpyridine moieties of 1.42(4) Å, compared to that of 1.470(5) Å in **1**, and even shorter than that of 1.441(5) in **3**, indicates reduction of the overall ligand. The torsion angle between the pyridine-terpyridine rings is  $3^\circ$ , which is indicative of a nearly planar ligand moiety as a result of the effective reduction by  $\text{KC}_8$ . The presence of two potassium counter ions confirms the double reduction of **1** and the generation of a new Ni species, **5**, in a formally -1 oxidation state. Further work is needed to fully characterize this complex, elucidate its unusual electronic structure and to explore its potential high reactivity.

### 3. Characterizations in solution and discussions

Although **1** usually features a poor solubility in most aprotic solvents, the corresponding  $^1\text{H}$  NMR spectrum could still be recorded in  $\text{THF-d}^8$  for a very diluted solution (Figure 91 and 92) with a long acquisition time. A  $C_1$  symmetry of compound **1** in solution can be noticed due to the restricted

rotation of the neutral pyridyl fragment in the ligand. The  $^1\text{H}$  NMR spectrum of **1** shows only seven paramagnetically shifted resonances at 161.39, 55.57, 35.89, 21.87, -40.60, -61.38 and -172.17 ppm, integrating each for one proton, for the  $\pi$ -radical monoanionic terpyridine ring (10 protons). Four protons, attributed to the pyridine moiety, are observed in the diamagnetic aromatic region (8.91–7.40 ppm). The strong paramagnetism of **1** is in agreement with a central  $\text{Ni}^{\text{II}}$  ion and a  $\text{tpy}^-$  ligand system.

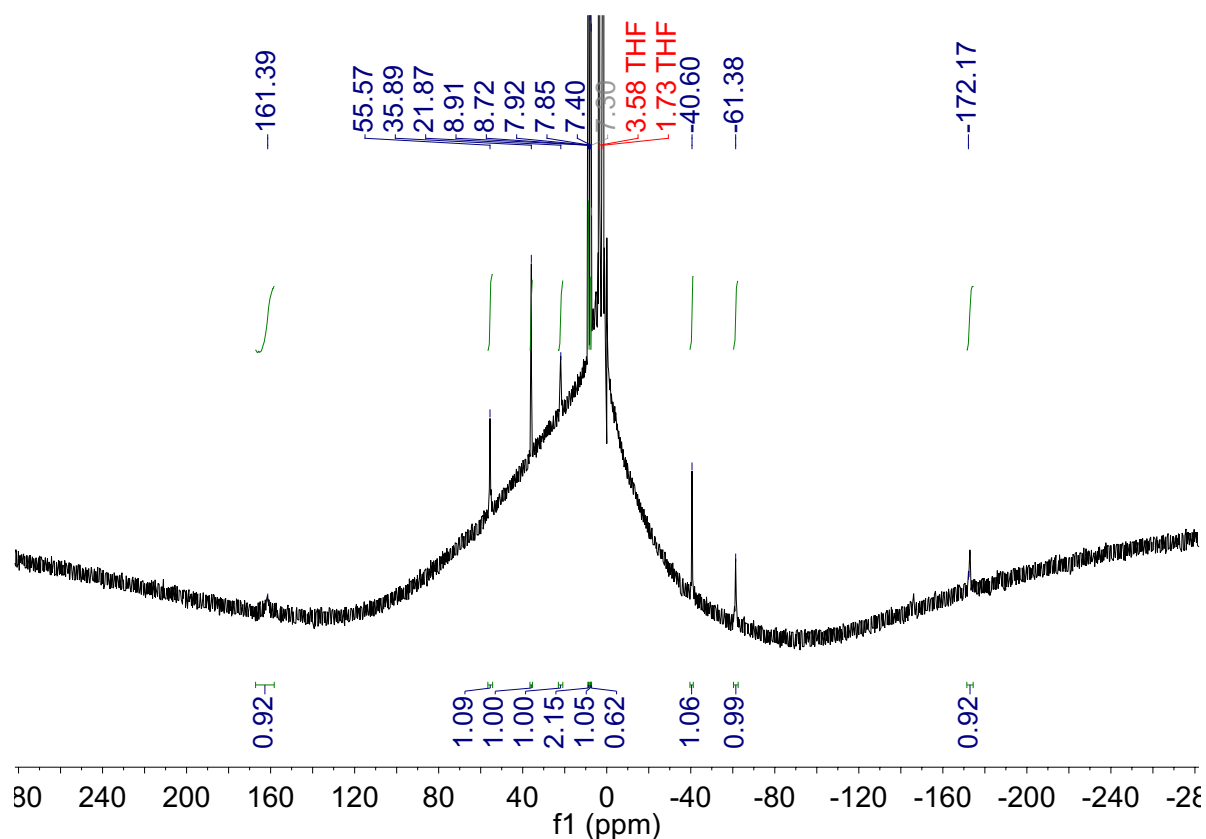


**Figure 91.**  $^1\text{H}$  NMR of  $(\text{pytpy})\text{Ni}(\text{CH}_3)$  (**1**) in  $\text{THF-d}_8$  at  $20^\circ\text{C}$ . Benzene impurity is indicated in grey.

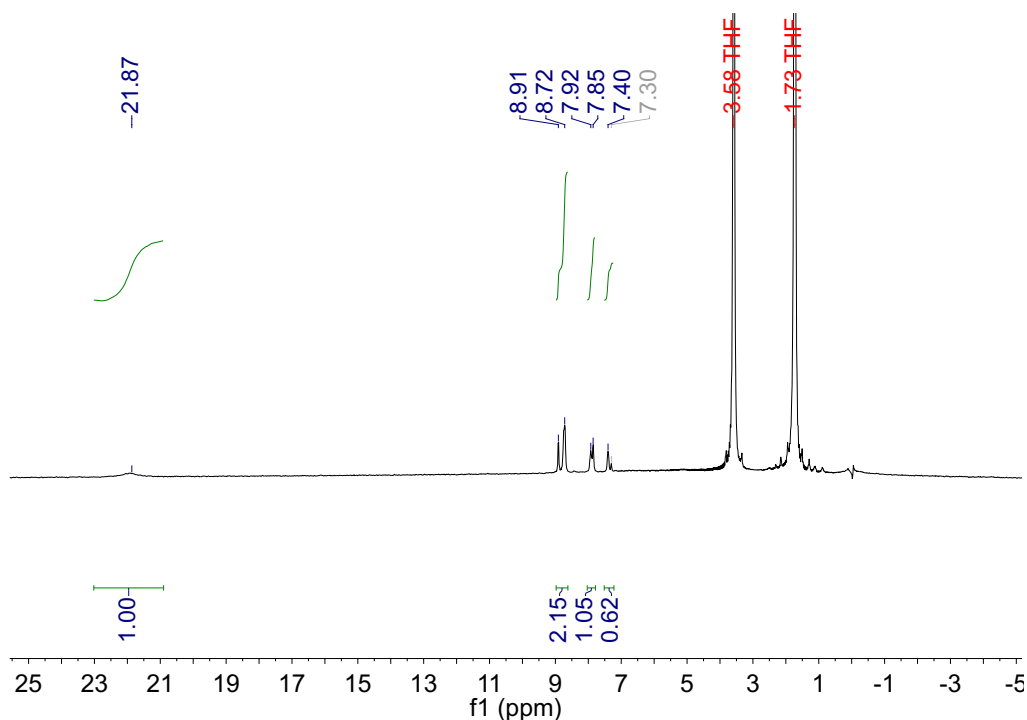


**Figure 92.**  $^1\text{H}$  NMR of (pytpy)Ni(CH<sub>3</sub>) (**1**) in THF-d<sup>8</sup> at 20 °C. Zoom in diamagnetic area. Benzene impurity is indicated in grey.

The variable-temperature  $^1\text{H}$  NMR of **1** was performed over the temperature range of -80 to 60 °C (Figure 93 and 94). The chemical shifts  $\delta$  of every observed signal of **1** are plotted versus  $1/T$ , revealing a Curie behavior, as the plot of  $\delta$  vs.  $1/T$  is linear (Figure 95).

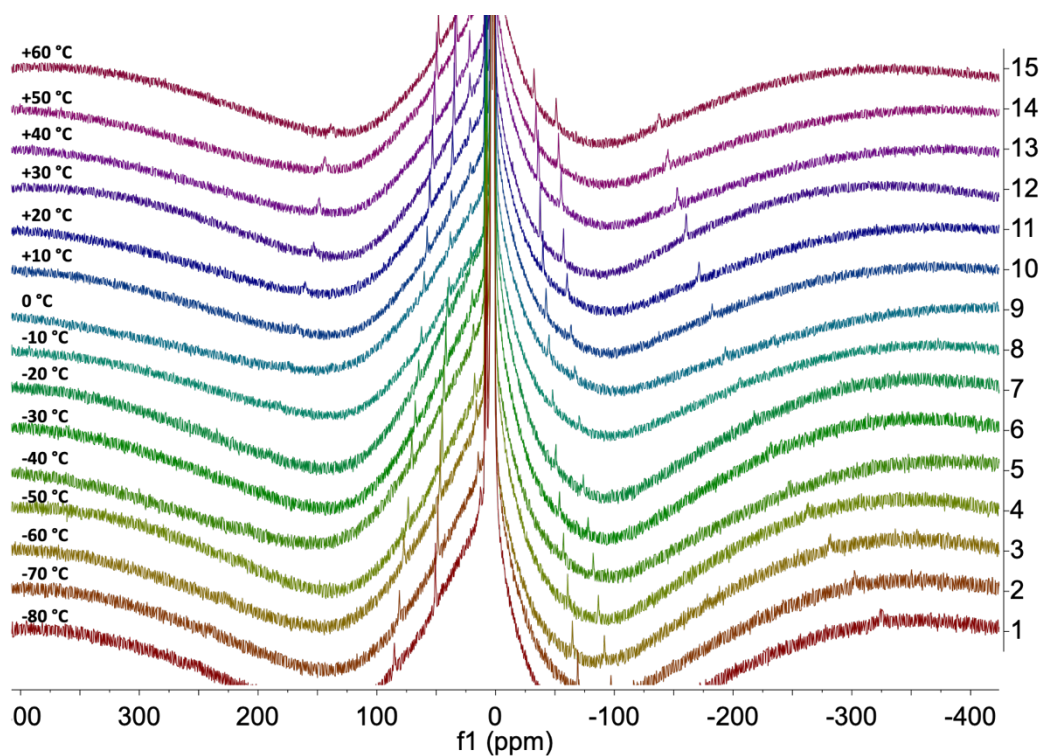


**Figure 93.** Variable Temperature  $^1\text{H}$  NMR of **1** in THF-d<sup>8</sup> from -80 °C to 60 °C:  $\delta$  vs T.

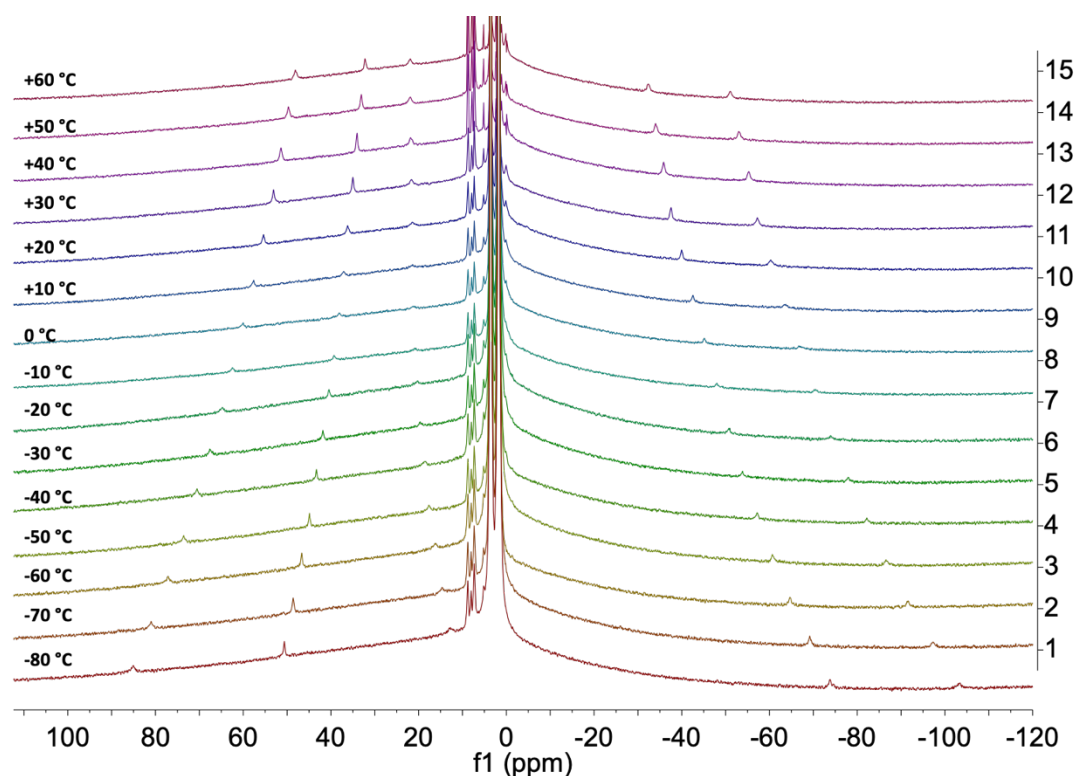


**Figure 94.** Variable Temperature  $^1\text{H}$  NMR of **1** in  $\text{THF-d}_8$  from  $-80\text{ }^\circ\text{C}$  to  $60\text{ }^\circ\text{C}$ :  $\delta$  vs  $T$  zoom.

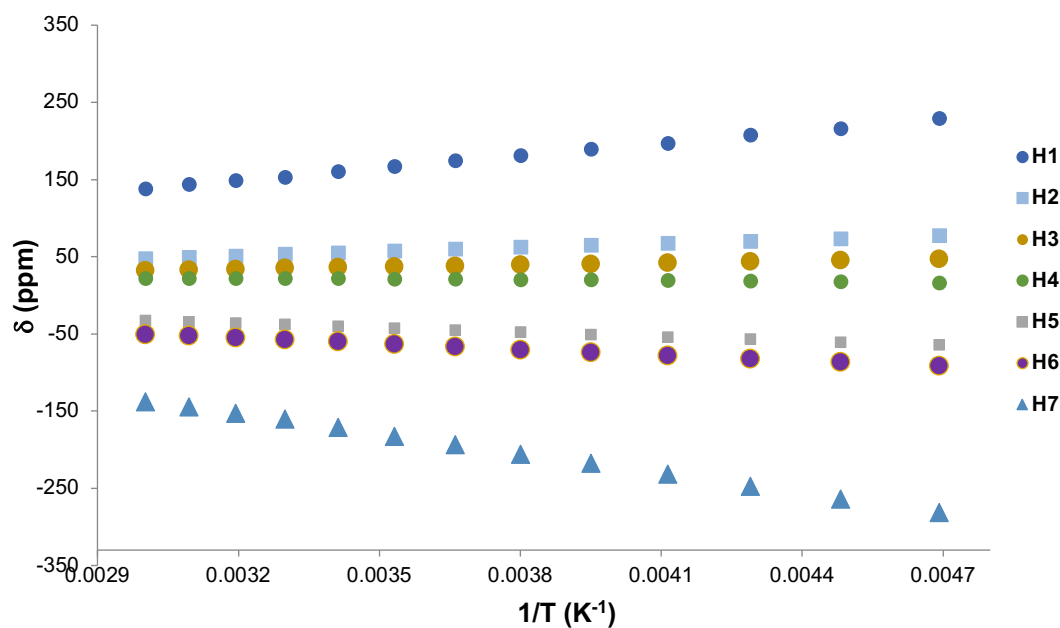


**Figure 95.** Variable Temperature  $^1\text{H}$  NMR of **1** in  $\text{THF-d}_8$  from  $-80\text{ }^\circ\text{C}$  to  $60\text{ }^\circ\text{C}$ :  $\delta$  vs  $1/T$ .

*Note: due to solubility issues, especially below 293 K, the signal of H1 cannot be effectively identified. Peak picking requires much care.*

The  $^1\text{H}$  NMR spectrum of **3** was recorded in  $\text{C}_6\text{D}_6$  at  $20\text{ }^\circ\text{C}$  (Figure 96). Even though some residual impurities remained in the solution, such as some unreacted  $\text{Cp}^*_2\text{Sm}(\text{OEt}_2)$  compound,<sup>76</sup> two signals at 2.45 and 2.19 ppm could be well identified, integrating each for 30 protons and corresponding to the two  $\text{Cp}^*$  ligands on each Sm ion. Six signals, integrating for two protons each,

can be attributed to the resonances of the pytpy protons; the seventh one is possibly overlapping with impurity signals in the range from -0.5 to 1.5 ppm, revealing that a more careful purification would be required for unambiguous assignment (Figure 97). The  $^1\text{H}$  NMR behavior is in good agreement with a  $C_{2v}$  symmetry of **3** in solution, consistent with a planar pytpy ligand system.

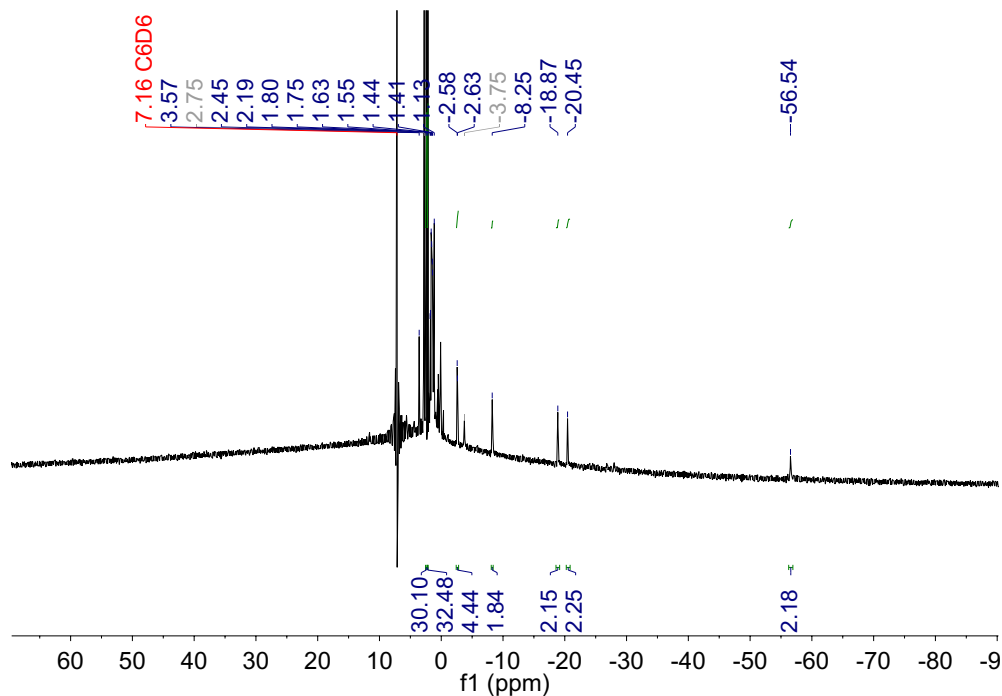


**Figure 96.**  $^1\text{H}$  NMR of **3** in  $\text{C}_6\text{D}_6$  at 20 °C. Traces of unreacted  $\text{Cp}^*\text{Sm}(\text{OEt})_2$  is indicated in grey.

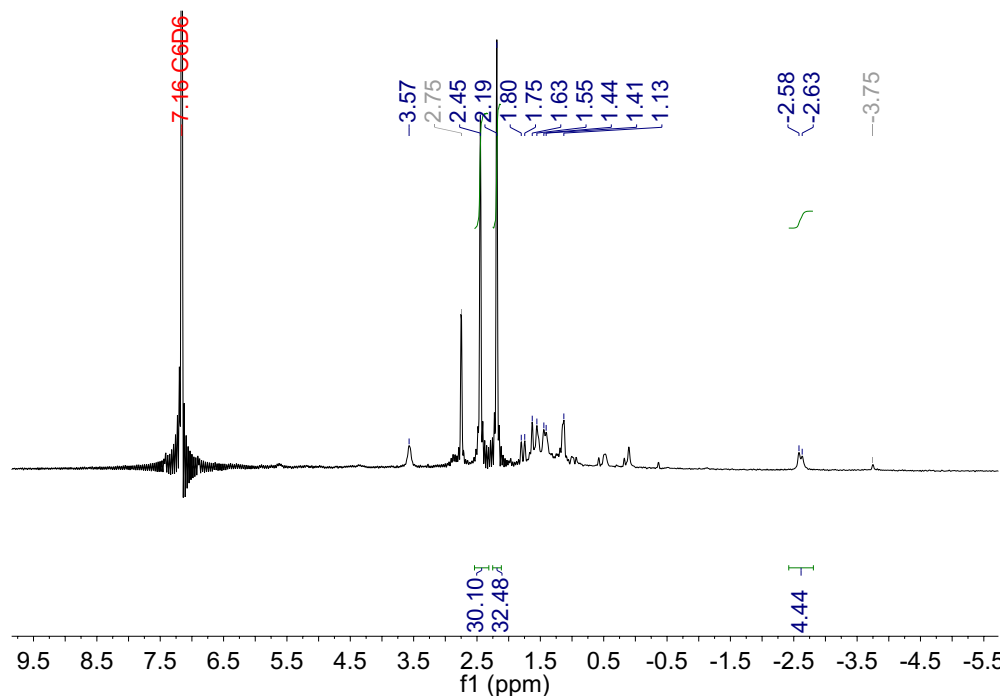


**Figure 97.**  $^1\text{H}$  NMR of **3** in  $\text{C}_6\text{D}_6$  at 20 °C (zoom in). Traces of unreacted  $\text{Cp}^*\text{Sm}(\text{OEt})_2$  is indicated in grey.



#### 4. Reactivity attempts

Different reactivity tests based on some experimental investigations described in the previous chapter were preliminarily performed on **1**, such as the addition of CO and alkyl iodides. The very poor solubility of **1** limits the scope of the reactivity attempts in terms of  $^1\text{H}$  NMR monitoring of the reaction as well as isolation of possible reaction products.

As it has been mentioned in the introduction, the (tpy)NiMe complex isolated by Vivic and co-workers was applied into an alkyl-alkyl cross-coupling reaction system. These carbon-carbon bond-formation reactions, which are considered as key steps in the design and building of various molecules and materials, are in many cases involving reactive organoborane species.<sup>77</sup> These important boronic precursors in the realm of cross-coupling reactions can mostly be obtained *via* metal-catalyzed hydroboration or borylation reactions of unsaturated derivatives or from alkyl or aryl halide derivatives.<sup>78–80</sup>

The transfer of a metal boryl species to organic feedstock can provide an efficient and facile route to important boronic derivatives.<sup>81</sup> The general synthesis of metal boryl complexes involves four aspects: (a) nucleophilic attack of anionic metal complexes on  $\text{X-BR}_2$  ( $\text{X} = \text{Cl}, \text{Br}, \text{I}$ ); (b) the use of metal hydride with  $\text{H-BR}_2$ ; (c)  $\sigma$ -bond metathesis reactions and (d) oxidative addition of  $\text{X-BR}_2$ ,  $\text{H-BR}_2$ , and  $\text{R}_2\text{B-BR}_2$  on the electron-rich metal centers.<sup>82</sup> It has been reported, though very rarely, that Ni(I) species can undergo cooperative H-B- and B-B-type bond cleavage reactions to generate Ni-boryl species.<sup>83</sup>

One equivalent of bis(pinacolato)diboron ( $\text{B}_2\text{pin}_2$ ) was preliminarily added to a  $\text{THF-d}^8$  suspension of **1** at room temperature. The mixture instantly turned deep greenish blue and the corresponding  $^1\text{H}$  NMR spectrum was silent. Expecting the formation of a Ni diboryl methyl species formed *via* homolytic cleavage of the B-B bond, or a monoboryl Ni product generated after a slow reductive elimination of MeBpin, the reaction mixture was filtered and stored at  $-40^\circ\text{C}$ . Surprisingly, deep green crystals of **6** were eventually isolated after several days in 42% yield (Figure 98).

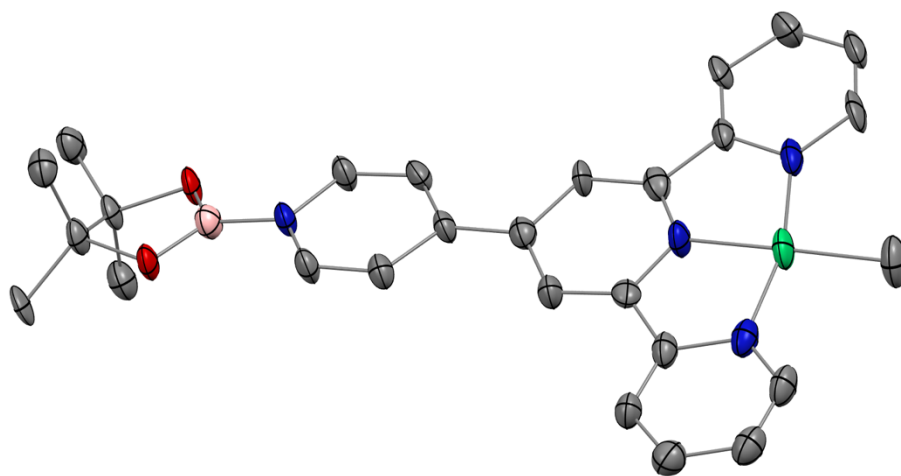


**Figure 98.** ORTEPs of **6**. Thermal ellipsoids are at 50% level. Carbon atoms are in grey, nitrogen in blue, boron in pink, oxygen in red and nickel in bright green. Hydrogen atoms are removed for clarity.

In **6**, the average Ni-N and Ni-CH<sub>3</sub> bond distances are 1.893(0) and 1.94 (7) Å, respectively, which are similar to those in **1** of 1.892(7) and 1.934(5) Å, respectively, indicating that the nickel center remains in the divalent oxidation state. An extremely shorter distance for the C-C linkage between the pyridine and terpyridine groups (1.40(6) Å) compared to that of 1.470(5) Å in **1**, and even shorter than that of 1.42(4) Å in the doubly-reduced species **5**, is found, which might indicate a distinct change of electron density on the ligand motif in **6**. The torsion angle between the pyridine-terpyridine cycles is surprisingly high, with a value of 10°, which overrules much electron correlation between the pyridine and terpyridine rings. Formation of the N-B bond implies a radical reaction pathway instead of a typical oxidative addition of B<sub>2</sub>pin<sub>2</sub> on the nickel center. More detailed mechanistic insights by other characterization methods such as <sup>11</sup>B NMR as well as EPR studies would be required in the future.

In parallel, pinacolborane (HBpin) was added to a THF-d<sup>8</sup> suspension of **1**, yielding a newly paramagnetic species identified by <sup>1</sup>H NMR spectroscopy (Figure 99). Without further structural information, unambiguous identification of this species remains difficult to date. Crystallization attempts are ongoing in order to get more information on this species.

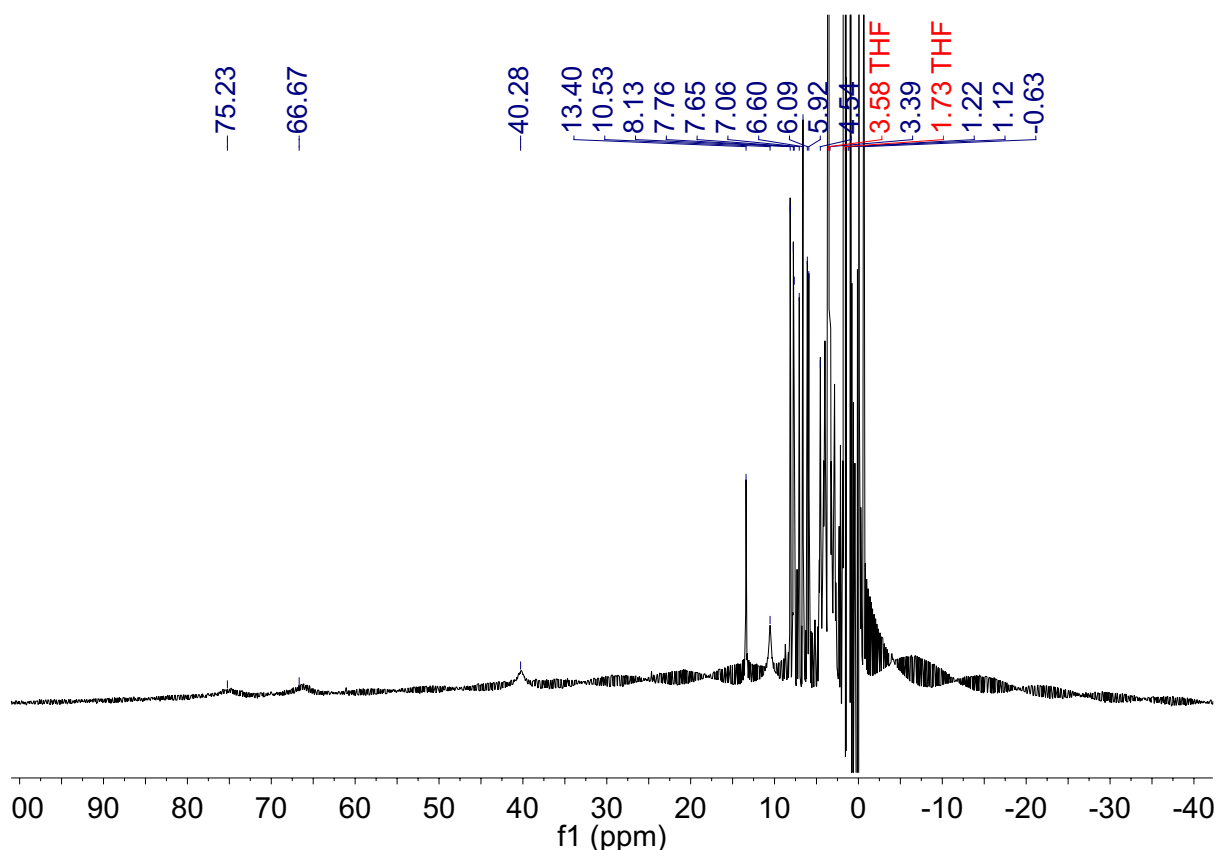


**Figure 99.** <sup>1</sup>H NMR of the *in situ* reaction mixture of **1** and HBpin (1.5 equiv.) in THF-d<sup>8</sup> at 20 °C.

## 5. Conclusion and perspectives

In this chapter, a formally Ni(I) complex with a tridentate ligand, pytpy, has been presented and is likely to be better described as a Ni(II) complex bearing a ligand-centered radical anion. However, further solid-state characterizations should be undertaken to determine the accurate electronic

structure of this complex. Magnetism (SQUID) and EPR analyses could especially be very informative for the further investigations.

The complexation of the ligand's pyridyl moiety with divalent organolanthanide fragments led to a variety of different binuclear or trinuclear complexes. The reactive Ni-CH<sub>3</sub> fragment is seemingly labile towards the coordination of lanthanide ions. However, due to the poor solubility of **1**, *in situ* monitoring of transformation processes is difficult. Therefore, subtle modifications on the pytpy ligand can be considered, such as adding lipophilic alkyl substituents, in order to increase the solubility of **1**. Meanwhile, further characterizations need to be carried out to understand the overall electronic configurations of the organometallic complexes obtained with lanthanide ion, in particular **4**. Importantly, due to the intriguing highly paramagnetic property of the formed reaction mixture, as well as the expected competency of Tm(II) species to reduce the pyridyl moiety, the challenging coordination of **1** to a divalent thulium fragment requires more endeavors.

The doubly-reduced **5** with a formally -1 oxidation state for the nickel center will be another interesting candidate in this topic. The reactivity of **5** towards the reduction of certain unsaturated derivatives is worth investigating. Besides, it will be very appealing to know if the addition of one equivalent of divalent lanthanide can further reduce **5** to form a triply-reduced molecule, *i.e.* a formally Ni<sup>2-</sup> species.

Last but not least, the potential activity of the boryl complex **6** and of the expected Ni-boryl species obtained upon reaction with HBpin should be studied in hydroboration or borylation reactions. The relative thermal stability of **6** may be advantageous for catalytic applications with unsaturated molecules, such as alkenes and alkynes. Some preliminary insights have already been obtained in the laboratory and the related work is under investigation.

## References

- (1) Hannon, M. J. Supramolecular DNA Recognition. *Chem. Soc. Rev.* **2007**, 36 (2), 280–295. <https://doi.org/10.1039/B606046N>.
- (2) Aribia, K. B.; Moehl, T.; Zakeeruddin, S. M.; Grätzel, M. Tridentate Cobalt Complexes as Alternative Redox Couples for High-Efficiency Dye-Sensitized Solar Cells. *Chem. Sci.* **2012**, 4 (1), 454–459. <https://doi.org/10.1039/C2SC21401F>.
- (3) Chakrabarty, R.; Mukherjee, P. S.; Stang, P. J. Supramolecular Coordination: Self-Assembly of Finite Two- and Three-Dimensional Ensembles. *Chem. Rev.* **2011**, 111 (11), 6810–6918. <https://doi.org/10.1021/cr200077m>.
- (4) Constable, E. C. 2,2':6',2"-Terpyridines: From Chemical Obscurity to Common Supramolecular Motifs. *Chem. Soc. Rev.* **2007**, 36 (2), 246–253. <https://doi.org/10.1039/B601166G>.
- (5) Winter, A.; Newkome, G. R.; Schubert, U. S. Catalytic Applications of Terpyridines and Their Transition Metal Complexes. *ChemCatChem* **2011**, 3 (9), 1384–1406. <https://doi.org/10.1002/cctc.201100118>.
- (6) Winter, A.; Schubert, U. S. Metal-Terpyridine Complexes in Catalytic Application – A Spotlight on the Last Decade. *ChemCatChem* **2020**, n/a (n/a). <https://doi.org/10.1002/cctc.201902290>.
- (7) Constable, E. C. The Coordination Chemistry of 2,2':6',2"-Terpyridine and Higher Oligopyridines. In *Advances in Inorganic Chemistry*; Emeléus, H. J., Ed.; Academic Press, 1986; Vol. 30, pp 69–121. [https://doi.org/10.1016/S0898-8838\(08\)60240-8](https://doi.org/10.1016/S0898-8838(08)60240-8).
- (8) Schubert, U. S.; Winter, A.; Newkome, G. R. *Terpyridine-Based Materials: For Catalytic, Optoelectronic and Life Science Applications*; John Wiley & Sons, Ltd, 2011.
- (9) Constable, E. C. Expanded Ligands—An Assembly Principle for Supramolecular Chemistry. *Coord. Chem. Rev.* **2008**, 252 (8), 842–855. <https://doi.org/10.1016/j.ccr.2007.10.020>.
- (10) Morgan, G. T.; Burstall, F. H. Dehydrogenation of Pyridine by Anhydrous Ferric Chloride. *J. Chem. Soc.* **1932**, No. 0, 20–30. <https://doi.org/10.1039/JR9320000020>.
- (11) Morgan, G.; Burstall, F. H. Researches on Residual Affinity and Co-Ordination. Part XXXVII. Complex Metallic Salts Containing 2 : 6-Di-2'-Pyridylpyridine (2 : 2' : 2"-Tripyridyl). *J. Chem. Soc.* **1937**, No. 0, 1649–1655. <https://doi.org/10.1039/JR9370001649>.
- (12) Heller, M.; Schubert, U. S. Syntheses of Functionalized 2,2':6',2"-Terpyridines. *Eur. J. Org. Chem.* **2003**, 2003 (6), 947–961. <https://doi.org/10.1002/ejoc.200390150>.
- (13) Hofmeier, H.; Schubert, U. S. Recent Developments in the Supramolecular Chemistry of Terpyridine–Metal Complexes. *Chem. Soc. Rev.* **2004**, 33 (6), 373–399. <https://doi.org/10.1039/B400653B>.
- (14) Wild, A.; Winter, A.; Schlütter, F.; Schubert, U. S. Advances in the Field of  $\pi$ -Conjugated 2,2':6',2"-Terpyridines. *Chem. Soc. Rev.* **2011**, 40 (3), 1459–1511. <https://doi.org/10.1039/C0CS00074D>.
- (15) Hill, M. G.; Bailey, J. A.; Miskowski, V. M.; Gray, H. B. Spectroelectrochemistry and Dimerization Equilibria of Chloro(Terpyridine)Platinum(II). Nature of the Reduced Complexes. *Inorg. Chem.* **1996**, 35 (16), 4585–4590. <https://doi.org/10.1021/ic960137j>.
- (16) Collin, J.-P.; Lainé, P.; Launay, J.-P.; Sauvage, J.-P.; Sour, A. Long-Range Coupling in a Mixed-Valence Diruthenium Complexes Containing Bis-Terpyridine Ligands of Various Lengths as Bridges. *J. Chem. Soc. Chem. Commun.* **1993**, No. 5, 434–435. <https://doi.org/10.1039/C39930000434>.
- (17) England, J.; Scarborough, C. C.; Weyhermüller, T.; Sproules, S.; Wieghardt, K. Electronic Structures of the Electron Transfer Series  $[M(\text{Bpy})_3]_n$ ,  $[M(\text{Tpy})_2]_n$ , and  $[\text{Fe}(\text{Tbpy})_3]_n$  ( $M = \text{Fe}, \text{Ru}$ ;  $n = 3+, 2+, 1+, 0, 1-$ ): A Mössbauer Spectroscopic and DFT Study. *Eur. J. Inorg. Chem.* **2012**, 2012 (29), 4605–4621. <https://doi.org/10.1002/ejic.201200232>.
- (18) Wang, M.; Weyhermüller, T.; England, J.; Wieghardt, K. Molecular and Electronic Structures of Six-Coordinate “Low-Valent”  $[M(\text{Mebpy})_3]_0$  ( $M = \text{Ti}, \text{V}, \text{Cr}, \text{Mo}$ ) and  $[M(\text{Tpy})_2]_0$  ( $M = \text{Ti}, \text{V}, \text{Cr}$ ), and Seven-Coordinate  $[\text{MoF}(\text{Mebpy})_3](\text{PF}_6)$  and  $[\text{MX}(\text{Tpy})_2](\text{PF}_6)$  ( $M = \text{Mo}, \text{X} = \text{Cl}$  and  $M = \text{W}, \text{X} = \text{F}$ ). *Inorg. Chem.* **2013**, 52 (21), 12763–12776. <https://doi.org/10.1021/ic402037e>.

- (19) Wang, M.; England, J.; Weyhermüller, T.; Wieghardt, K. Molecular and Electronic Structures of the Members of the Electron Transfer Series  $[\text{Mn}(\text{Bpy})_3]_n$  ( $n = 2+, 1+, 0, 1-$ ) and  $[\text{Mn}(\text{Tpy})_2]_m$  ( $m = 4+, 3+, 2+, 1+, 0$ ). An Experimental and Density Functional Theory Study. *Inorg. Chem.* **2014**, *53* (4), 2276–2287. <https://doi.org/10.1021/ic4029854>.
- (20) Wang, M.; England, J.; Weyhermüller, T.; Wieghardt, K. Electronic Structures of “Low-Valent” Neutral Complexes  $[\text{NiL}_2]_0$  ( $S = 0$ ;  $L = \text{Bpy}, \text{Phen}, \text{Tpy}$ ) – An Experimental and DFT Computational Study. *Eur. J. Inorg. Chem.* **2015**, *2015* (9), 1511–1523. <https://doi.org/10.1002/ejic.201403144>.
- (21) England, J.; Bill, E.; Weyhermüller, T.; Neese, F.; Atanasov, M.; Wieghardt, K. Molecular and Electronic Structures of Homoleptic Six-Coordinate Cobalt(I) Complexes of 2,2':6',2"-Terpyridine, 2,2'-Bipyridine, and 1,10-Phenanthroline. An Experimental and Computational Study. *Inorg. Chem.* **2015**, *54* (24), 12002–12018. <https://doi.org/10.1021/acs.inorgchem.5b02415>.
- (22) Wang, M.; Weyhermüller, T.; Bill, E.; Ye, S.; Wieghardt, K. Structural and Spectroscopic Characterization of Rhenium Complexes Containing Neutral, Monoanionic, and Dianionic Ligands of 2,2'-Bipyridines and 2,2':6',2"-Terpyridines: An Experimental and Density Functional Theory (DFT)-Computational Study. *Inorg. Chem.* **2016**, *55* (10), 5019–5036. <https://doi.org/10.1021/acs.inorgchem.6b00609>.
- (23) Wang, M.; Römel, C.; Weyhermüller, T.; Wieghardt, K. Coordination Modes, Oxidation, and Protonation Levels of 2,6-Pyridinediimine and 2,2':6',2"-Terpyridine Ligands in New Complexes of Cobalt, Zirconium, and Ruthenium. An Experimental and Density Functional Theory Computational Study. *Inorg. Chem.* **2019**, *58* (1), 121–132. <https://doi.org/10.1021/acs.inorgchem.8b01949>.
- (24) Arana, C.; Yan, S.; Keshavarz-K., M.; Potts, K. T.; Abruna, H. D. Electrocatalytic Reduction of Carbon Dioxide with Iron, Cobalt, and Nickel Complexes of Terdentate Ligands. *Inorg. Chem.* **1992**, *31* (17), 3680–3682. <https://doi.org/10.1021/ic00043a034>.
- (25) Elgrishi, N.; Chambers, M. B.; Artero, V.; Fontecave, M. Terpyridine Complexes of First Row Transition Metals and Electrochemical Reduction of  $\text{CO}_2$  to  $\text{CO}$ . *Phys. Chem. Chem. Phys.* **2014**, *16* (27), 13635–13644. <https://doi.org/10.1039/C4CP00451E>.
- (26) Scarborough, C. C.; Lancaster, K. M.; DeBeer, S.; Weyhermüller, T.; Sproules, S.; Wieghardt, K. Experimental Fingerprints for Redox-Active Terpyridine in  $[\text{Cr}(\text{Tpy})_2](\text{PF}_6)_n$  ( $n = 3-0$ ), and the Remarkable Electronic Structure of  $[\text{Cr}(\text{Tpy})_2]_1^-$ . *Inorg. Chem.* **2012**, *51* (6), 3718–3732. <https://doi.org/10.1021/ic2027219>.
- (27) Hamacher, C.; Hurkes, N.; Kaiser, A.; Klein, A.; Schüren, A. Electrochemistry and Spectroscopy of Organometallic Terpyridine Nickel Complexes. *Inorg. Chem.* **2009**, *48* (20), 9947–9951. <https://doi.org/10.1021/ic900753r>.
- (28) Du Bois, D. W.; Iwamoto, R. T.; Kleinberg, J. Electrochemical Investigation of Molybdenum(III)-Chloro Complexes with Pyridine, 2,2'-Bipyridine, and 1,10-Phenanthroline in Acetonitrile. *Inorg. Chem.* **1969**, *8* (4), 815–819. <https://doi.org/10.1021/ic50074a023>.
- (29) Anderson, T. J.; Jones, G. D.; Vicic, D. A. Evidence for a Nil Active Species in the Catalytic Cross-Coupling of Alkyl Electrophiles. *J. Am. Chem. Soc.* **2004**, *126* (26), 8100–8101. <https://doi.org/10.1021/ja0483903>.
- (30) Kaschube, W.; Pörschke, K. R.; Wilke, G. tmeda-Nickel-Komplexe: III. (N,N,N',N'-Tetramethylethylendiamin)-(dimethyl)nickel(II). *J. Organomet. Chem.* **1988**, *355* (1), 525–532. [https://doi.org/10.1016/0022-328X\(88\)89050-8](https://doi.org/10.1016/0022-328X(88)89050-8).
- (31) Ciszewski, J. T.; Mikhaylov, D. Y.; Holin, K. V.; Kadirov, M. K.; Budnikova, Y. H.; Sinyashin, O.; Vicic, D. A. Redox Trends in Terpyridine Nickel Complexes. *Inorg. Chem.* **2011**, *50* (17), 8630–8635. <https://doi.org/10.1021/ic201184x>.
- (32) Jones, G. D.; Martin, J. L.; McFarland, C.; Allen, O. R.; Hall, R. E.; Haley, A. D.; Brandon, R. J.; Konovalova, T.; Desrochers, P. J.; Pulay, P.; Vicic, D. A. Ligand Redox Effects in the Synthesis, Electronic Structure, and Reactivity of an Alkyl-Alkyl Cross-Coupling Catalyst. *J. Am. Chem. Soc.* **2006**, *128* (40), 13175–13183. <https://doi.org/10.1021/ja063334i>.

- (33) Anderson, T. J.; Jones, G. D.; Vivic, D. A. Evidence for a Nil Active Species in the Catalytic Cross-Coupling of Alkyl Electrophiles [J. Am. Chem. Soc. 2004, 126, 8100–8101]. *J. Am. Chem. Soc.* **2004**, 126 (35), 11113–11113. <https://doi.org/10.1021/ja040817i>.
- (34) Namy, J. L.; Girard, P.; Kagan, H. B. A New Preparation of Some Divalent Lanthanide Iodides and Their Usefulness in Organic Synthesis. *Nouv. J. Chim.* **1977**, 1 (1), 5–7.
- (35) Girard, P.; Namy, J. L.; Kagan, H. B. Divalent Lanthanide Derivatives in Organic Synthesis. 1. Mild Preparation of Samarium Iodide and Ytterbium Iodide and Their Use as Reducing or Coupling Agents. *J. Am. Chem. Soc.* **1980**, 102 (8), 2693–2698. <https://doi.org/10.1021/ja00528a029>.
- (36) Szostak, M.; Fazakerley, N. J.; Parmar, D.; Procter, D. J. Cross-Coupling Reactions Using Samarium(II) Iodide. *Chem. Rev.* **2014**, 114 (11), 5959–6039. <https://doi.org/10.1021/cr400685r>.
- (37) Jones, G. D.; McFarland, C.; Anderson, T. J.; Vivic, D. A. Analysis of Key Steps in the Catalytic Cross-Coupling of Alkyl Electrophiles under Negishi-like Conditions. *Chem. Commun.* **2005**, No. 33, 4211–4213. <https://doi.org/10.1039/B504996B>.
- (38) Budnikova, Y. H.; Vivic, D. A.; Klein, A. Exploring Mechanisms in Ni Terpyridine Catalyzed C–C Cross-Coupling Reactions—A Review. *Inorganics* **2018**, 6 (1), 18. <https://doi.org/10.3390/inorganics6010018>.
- (39) Lin, X.; Phillips, D. L. Density Functional Theory Studies of Negishi Alkyl–Alkyl Cross-Coupling Reactions Catalyzed by a Methylterpyridyl-Ni(I) Complex. *J. Org. Chem.* **2008**, 73 (10), 3680–3688. <https://doi.org/10.1021/jo702497p>.
- (40) Zhang, C.-P.; Wang, H.; Klein, A.; Biewer, C.; Stirnat, K.; Yamaguchi, Y.; Xu, L.; Gomez-Benitez, V.; Vivic, D. A. A Five-Coordinate Nickel(II) Fluoroalkyl Complex as a Precursor to a Spectroscopically Detectable Ni(III) Species. *J. Am. Chem. Soc.* **2013**, 135 (22), 8141–8144. <https://doi.org/10.1021/ja4030462>.
- (41) Yu, S.; Dudkina, Y.; Wang, H.; Kholin, K. V.; Kadirov, M. K.; Budnikova, Y. H.; Vivic, D. A. Accessing Perfluoroalkyl Nickel(II), (III), and (IV) Complexes Bearing a Readily Attached [C4F8] Ligand. *Dalton Trans.* **2015**, 44 (45), 19443–19446. <https://doi.org/10.1039/C5DT01771H>.
- (42) Camasso, N. M.; Sanford, M. S. Design, Synthesis, and Carbon-Heteroatom Coupling Reactions of Organometallic Nickel(IV) Complexes. *Science* **2015**, 347 (6227), 1218–1220. <https://doi.org/10.1126/science.aaa4526>.
- (43) Berg, D. J.; Boncella, J. M.; Andersen, R. A. Preparation of Coordination Compounds of Cp\*<sub>2</sub>Yb with Heterocyclic Nitrogen Bases: Examples of Antiferromagnetic Exchange Coupling across Bridging Ligands. *Organometallics* **2002**, 21 (22), 4622–4631. <https://doi.org/10.1021/om020477e>.
- (44) Kuehl, C. J.; Re, R. E. D.; Scott, B. L.; Morris, D. E.; John, K. D. Toward New Paradigms in Mixed-Valency: Ytterbocene–Terpyridine Charge-Transfer Complexes. *Chem. Commun.* **2003**, No. 18, 2336–2337. <https://doi.org/10.1039/B306484K>.
- (45) Veauthier, J. M.; Schelter, E. J.; Carlson, C. N.; Scott, B. L.; Re, R. E. D.; Thompson, J. D.; Kiplinger, J. L.; Morris, D. E.; John, K. D. Direct Comparison of the Magnetic and Electronic Properties of Samarocene and Ytterbocene Terpyridine Complexes. *Inorg. Chem.* **2008**, 47 (13), 5841–5849. <https://doi.org/10.1021/ic8001465>.
- (46) Veauthier, J. M.; Schelter, E. J.; Kuehl, C. J.; Clark, A. E.; Scott, B. L.; Morris, D. E.; Martin, R. L.; Thompson, J. D.; Kiplinger, J. L.; John, K. D. Ligand Substituent Effect Observed for Ytterbocene 4'-Cyano-2,2':6',2''-Terpyridine. *Inorg. Chem.* **2005**, 44 (16), 5911–5920. <https://doi.org/10.1021/ic050148p>.
- (47) Booth, C. H.; Walter, M. D.; Daniel, M.; Lukens, W. W.; Andersen, R. A. Self-Contained Kondo Effect in Single Molecules. *Phys. Rev. Lett.* **2005**, 95 (26), 267202. <https://doi.org/10.1103/PhysRevLett.95.267202>.
- (48) Booth, C. H.; Walter, M. D.; Kazhdan, D.; Hu, Y.-J.; Lukens, W. W.; Bauer, E. D.; Maron, L.; Eisenstein, O.; Andersen, R. A. Decamethylytterbocene Complexes of Bipyridines and

- Diazabutadienes: Multiconfigurational Ground States and Open-Shell Singlet Formation. *J. Am. Chem. Soc.* **2009**, *131* (18), 6480–6491. <https://doi.org/10.1021/ja809624w>.
- (49) Booth, C. H.; Kazhdan, D.; Werkema, E. L.; Walter, M. D.; Lukens, W. W.; Bauer, E. D.; Hu, Y.-J.; Maron, L.; Eisenstein, O.; Head-Gordon, M.; Andersen, R. A. Intermediate-Valence Tautomerism in Decamethylytterbocene Complexes of Methyl-Substituted Bipyridines. *J. Am. Chem. Soc.* **2010**, *132* (49), 17537–17549. <https://doi.org/10.1021/ja106902s>.
- (50) Nocton, G.; Ricard, L. N-Aromatic Heterocycle Adducts of Bulky [1,2,4-(Me<sub>3</sub>C)<sub>3</sub>C<sub>5</sub>H<sub>2</sub>]<sub>2</sub>Sm: Synthesis, Structure and Solution Analysis. *Dalton Trans* **2014**, *43* (11), 4380–4387. <https://doi.org/10.1039/C3DT52641K>.
- (51) Da Re, R. E.; Kuehl, C. J.; Brown, M. G.; Rocha, R. C.; Bauer, E. D.; John, K. D.; Morris, D. E.; Shreve, A. P.; Sarrao, J. L. Electrochemical and Spectroscopic Characterization of the Novel Charge-Transfer Ground State in Diimine Complexes of Ytterbocene. *Inorg. Chem.* **2003**, *42* (18), 5551–5559. <https://doi.org/10.1021/ic030069i>.
- (52) Creutz, Carol.; Taube, H. Binuclear Complexes of Ruthenium Ammines. *J. Am. Chem. Soc.* **1973**, *95* (4), 1086–1094. <https://doi.org/10.1021/ja00785a016>.
- (53) Kaim, W.; Klein, A.; Glöckle, M. Exploration of Mixed-Valence Chemistry: Inventing New Analogues of the Creutz-Taube Ion. *Acc. Chem. Res.* **2000**, *33* (11), 755–763. <https://doi.org/10.1021/ar960067k>.
- (54) Carlson, C. N.; Veauthier, J. M.; John, K. D.; Morris, D. E. Electronic and Magnetic Properties of Bimetallic Ytterbocene Complexes: The Impact of Bridging Ligand Geometry. *Chem. – Eur. J.* **2008**, *14* (2), 422–431. <https://doi.org/10.1002/chem.200700986>.
- (55) Koo, B.-K.; Bewley, L.; Golub, V.; Rarig, R. S.; Burkholder, E.; O'Connor, C. J.; Zubieta, J. Anion Influences on the Construction of One-Dimensional Structures of the Cu(II)–Bisterpy Family (Bisterpy=2,2':4',4":2",2"-Quarterpyridyl, 6',6"-Di-2-Pyridiine). *Inorganica Chim. Acta* **2003**, *351*, 167–176. [https://doi.org/10.1016/S0020-1693\(03\)00186-5](https://doi.org/10.1016/S0020-1693(03)00186-5).
- (56) Ouellette, W.; Golub, V.; O'Connor, C. J.; Zubieta, J. Solid State Coordination Chemistry of Metal Oxides: Structural Consequences of Fluoride Incorporation into the Oxovanadium–Copper–Bisterpy–{O3P(CH<sub>2</sub>)NPO3}4– System, n = 1–5 (Bisterpy = 2,2':4',4":2",2"-Quaterpyridyl-6',6"-Di-2-Pyridine). *Dalton Trans.* **2005**, No. 2, 291–309. <https://doi.org/10.1039/B412808G>.
- (57) Carlson, C. N.; Kuehl, C. J.; Da Re, R. E.; Veauthier, J. M.; Schelter, E. J.; Milligan, A. E.; Scott, B. L.; Bauer, E. D.; Thompson, J. D.; Morris, D. E.; John, K. D. Ytterbocene Charge-Transfer Molecular Wire Complexes. *J. Am. Chem. Soc.* **2006**, *128* (22), 7230–7241. <https://doi.org/10.1021/ja058667e>.
- (58) Rajca, A. Organic Diradicals and Polyradicals: From Spin Coupling to Magnetism? *Chem. Rev.* **1994**, *94* (4), 871–893. <https://doi.org/10.1021/cr00028a002>.
- (59) Carlson, C. N.; Scott, B. L.; Martin, R. L.; Thompson, J. D.; Morris, D. E.; John, K. D. Control of Electronic and Magnetic Coupling via Bridging Ligand Geometry in a Bimetallic Ytterbocene Complex. *Inorg. Chem.* **2007**, *46* (12), 5013–5022. <https://doi.org/10.1021/ic0702973>.
- (60) Lin, Z.; Thacker, N. C.; Sawano, T.; Drake, T.; Ji, P.; Lan, G.; Cao, L.; Liu, S.; Wang, C.; Lin, W. Metal–Organic Layers Stabilize Earth-Abundant Metal–Terpyridine Diradical Complexes for Catalytic C–H Activation. *Chem. Sci.* **2017**, *9* (1), 143–151. <https://doi.org/10.1039/C7SC03537C>.
- (61) Wang, J.; Hanan, G. S. A Facile Route to Sterically Hindered and Non-Hindered 4'-Aryl-2,2':6',2"-Terpyridines. *Synlett* **2005**, *2005* (08), 1251–1254. <https://doi.org/10.1055/s-2005-868481>.
- (62) Cargill Thompson, A. M. W. The Synthesis of 2,2':6',2"-Terpyridine Ligands — Versatile Building Blocks for Supramolecular Chemistry. *Coord. Chem. Rev.* **1997**, *160*, 1–52. [https://doi.org/10.1016/S0010-8545\(96\)01283-0](https://doi.org/10.1016/S0010-8545(96)01283-0).
- (63) Kitiachvili, K. D.; Mindiola, D. J.; Hillhouse, G. L. Preparation of Stable Alkyl Complexes of Ni(I) and Their One-Electron Oxidation to Ni(II) Complex Cations. *J. Am. Chem. Soc.* **2004**, *126* (34), 10554–10555. <https://doi.org/10.1021/ja047052z>.

- (64) Laskowski, C. A.; Bungum, D. J.; Baldwin, S. M.; Del Ciello, S. A.; Iluc, V. M.; Hillhouse, G. L. Synthesis and Reactivity of Two-Coordinate Ni(I) Alkyl and Aryl Complexes. *J. Am. Chem. Soc.* **2013**, *135* (49), 18272–18275. <https://doi.org/10.1021/ja4095236>.
- (65) Dicciani, J. B.; Hu, C. T.; Diao, T. Insertion of CO<sub>2</sub> Mediated by a (Xantphos)NiI–Alkyl Species. *Angew. Chem. Int. Ed.* **2019**, *58* (39), 13865–13868. <https://doi.org/10.1002/anie.201906005>.
- (66) Huang, T.-H.; Zhang, M.-H.; Gao, C.-Y.; Wang, L.-T. Synthesis, Structures and Characterization of Metal Complexes Containing 4'-Phenyl-2,2':6',2''-Terpyridine Ligands with Extended  $\pi\cdots\pi$  Interactions. *Inorganica Chim. Acta* **2013**, *408*, 91–95. <https://doi.org/10.1016/j.ica.2013.08.024>.
- (67) Herebian, D.; Bothe, E.; Neese, F.; Weyhermüller, T.; Wieghardt, K. Molecular and Electronic Structures of Bis-(*o*-Diiminobenzosemiquinonato)Metal(II) Complexes (Ni, Pd, Pt), Their Monocations and -Anions, and of Dimeric Dications Containing Weak Metal–Metal Bonds. *J. Am. Chem. Soc.* **2003**, *125* (30), 9116–9128. <https://doi.org/10.1021/ja030123u>.
- (68) Weber, F.; Schultz, M.; Sofield, C. D.; Andersen, R. A. Synthesis and Solid State Structures of Sterically Crowded d<sup>0</sup>-Metallocenes of Magnesium, Calcium, Strontium, Barium, Samarium, and Ytterbium. *Organometallics* **2002**, *21* (15), 3139–3146. <https://doi.org/10.1021/om0108705>.
- (69) Sitzmann, H.; Dezember, T.; Schmitt, O.; Weber, F.; Wolmershäuser, G.; Ruck, M. Metallocenes of Samarium, Europium, and Ytterbium with the Especially Bulky Cyclopentadienyl Ligands C<sub>5</sub>H(CHMe<sub>2</sub>)<sub>4</sub>, C<sub>5</sub>H<sub>2</sub>(CMe<sub>3</sub>)<sub>3</sub>, and C<sub>5</sub>(CHMe<sub>2</sub>)<sub>5</sub>. *Z. Für Anorg. Allg. Chem.* **2000**, *626* (11), 2241–2244. [https://doi.org/10.1002/1521-3749\(200011\)626:11<2241::AID-ZAAC2241>3.0.CO;2-0](https://doi.org/10.1002/1521-3749(200011)626:11<2241::AID-ZAAC2241>3.0.CO;2-0).
- (70) Tilley, T. Don.; Andersen, R. A.; Spencer, Brock.; Zalkin, Allan. Crystal Structure of Bis(Pentamethylcyclopentadienyl)Bis(Pyridine)Ytterbium(II). *Inorg. Chem.* **1982**, *21* (7), 2647–2649. <https://doi.org/10.1021/ic00137a023>.
- (71) Labouille, S.; Nief, F.; Le Goff, X.-F.; Maron, L.; Kindra, D. R.; Houghton, H. L.; Ziller, J. W.; Evans, W. J. Ligand Influence on the Redox Chemistry of Organosamarium Complexes: Experimental and Theoretical Studies of the Reactions of (C<sub>5</sub>Me<sub>5</sub>)<sub>2</sub>Sm(THF)<sub>2</sub> and (C<sub>4</sub>Me<sub>4</sub>P)<sub>2</sub>Sm with Pyridine and Acridine. *Organometallics* **2012**, *31* (14), 5196–5203. <https://doi.org/10.1021/om300573z>.
- (72) Evans, W. J.; Drummond, D. K. Reductive Coupling of Pyridazine and Benzaldehyde Azine and Reduction of Bipyridine by Samarium Complex (C<sub>5</sub>Me<sub>5</sub>)<sub>2</sub>Sm(THF)<sub>2</sub>. *J. Am. Chem. Soc.* **1989**, *111* (9), 3329–3335. <https://doi.org/10.1021/ja00191a034>.
- (73) Evans, W. J.; Gonzales, S. L.; Ziller, J. W. Reactivity of Decamethylsamarocene with Polycyclic Aromatic Hydrocarbons. *J. Am. Chem. Soc.* **1994**, *116* (6), 2600–2608. <https://doi.org/10.1021/ja00085a046>.
- (74) Evans, W. J.; Ulibarri, T. A.; Ziller, J. W. Isolation and X-Ray Crystal Structure of the First Dinitrogen Complex of an f-Element Metal, [(C<sub>5</sub>Me<sub>5</sub>)<sub>2</sub>Sm]N<sub>2</sub>. *J. Am. Chem. Soc.* **1988**, *110* (20), 6877–6879. <https://doi.org/10.1021/ja00228a043>.
- (75) Jaroschik, F.; Nief, F.; Le Goff, X.-F.; Ricard, L. Synthesis and Reactivity of Organometallic Complexes of Divalent Thulium with Cyclopentadienyl and Phospholyl Ligands. *Organometallics* **2007**, *26* (14), 3552–3558. <https://doi.org/10.1021/om700316a>.
- (76) Berg, D. J.; Burns, C. J.; Andersen, R. A.; Zalkin, Allan. Electron-Transfer Reactions of Divalent Ytterbium Metallocenes. Synthesis of the Series [(Me<sub>5</sub>C<sub>5</sub>)<sub>2</sub>Yb]<sub>2</sub>[ $\mu$ -E] (E = Oxygen, Sulfur, Selenium, or Tellurium) and Crystal Structure of [(Me<sub>5</sub>C<sub>5</sub>)<sub>2</sub>Yb]<sub>2</sub>[ $\mu$ -Se]. *Organometallics* **1989**, *8* (8), 1865–1870. <https://doi.org/10.1021/om00110a006>.
- (77) Suzuki, A. Cross-Coupling Reactions Of Organoboranes: An Easy Way To Construct C-C Bonds (Nobel Lecture). *Angew. Chem. Int. Ed.* **2011**, *50* (30), 6722–6737. <https://doi.org/10.1002/anie.201101379>.



- (78) Obligacion, J. V.; Chirik, P. J. Earth-Abundant Transition Metal Catalysts for Alkene Hydrosilylation and Hydroboration. *Nat. Rev. Chem.* **2018**, 2 (5), 15–34. <https://doi.org/10.1038/s41570-018-0001-2>.
- (79) Dudnik, A. S.; Fu, G. C. Nickel-Catalyzed Coupling Reactions of Alkyl Electrophiles, Including Unactivated Tertiary Halides, To Generate Carbon–Boron Bonds. *J. Am. Chem. Soc.* **2012**, 134 (25), 10693–10697. <https://doi.org/10.1021/ja304068t>.
- (80) Bheeter, L. P.; Wei, D.; Dorcet, V.; Roisnel, T.; Ghosh, P.; Sortais, J.-B.; Darcel, C. 1,2,4-Triazole-Based N-Heterocyclic Carbene Nickel Complexes – Synthesis and Catalytic Application. *Eur. J. Inorg. Chem.* **2015**, 2015 (31), 5226–5231. <https://doi.org/10.1002/ejic.201500852>.
- (81) Miyaura, Norio.; Suzuki, Akira. Palladium-Catalyzed Cross-Coupling Reactions of Organoboron Compounds. *Chem. Rev.* **1995**, 95 (7), 2457–2483. <https://doi.org/10.1021/cr00039a007>.
- (82) Tran, B. L.; Adhikari, D.; Fan, H.; Pink, M.; Mindiola, D. J. Facile Entry to 3d Late Transition Metal Boryl Complexes. *Dalton Trans.* **2009**, 39 (2), 358–360. <https://doi.org/10.1039/B912040H>.
- (83) Adhikari, D.; Mossin, S.; Basuli, F.; Dible, B. R.; Chipara, M.; Fan, H.; Huffman, J. C.; Meyer, K.; Mindiola, D. J. A Dinuclear Ni(I) System Having a Diradical Ni<sub>2</sub>N<sub>2</sub> Diamond Core Resting State: Synthetic, Structural, Spectroscopic Elucidation, and Reductive Bond Splitting Reactions. *Inorg. Chem.* **2008**, 47 (22), 10479–10490. <https://doi.org/10.1021/ic801137p>.

## General conclusion and perspectives

In the combination with redox-active *N*-heterocyclic ligands, divalent organolanthanides as *in situ* electron sources, are able to perform single-electron transfer processes. The resulting redox-active systems, exhibiting remarkable properties, can be used to construct heterometallic frameworks in the presence of reactive transition metal fragments. The electronic configurations can be subtly modulated by the transferred electron(s), resulting in altered reactivity behaviors on the transition metal fragments.

The unique electronic structure of  $\text{Cp}^*_2\text{Yb}(\text{bipym})\text{NiMe}_2$ , involving a multiconfigurational ground state, leads to a modulated reactivity of the nickel center towards the migratory insertion of carbon monoxide and subsequent reductive elimination of acetone. The resulting stabilization of the possible acyl intermediate generated *via* CO insertion allowed us to study the kinetics of the overall transformation. These intriguing results lead the way to further reactivity investigations in the presence of other unsaturated derivatives.

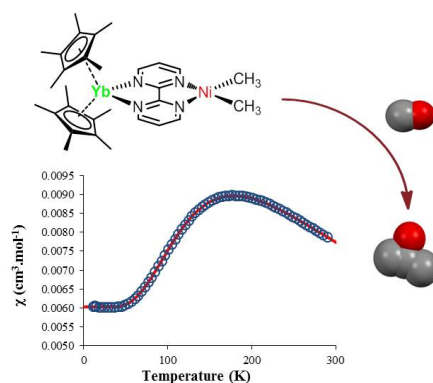


**Figure 100.** Graphical abstract for multiconfigurational bipym complex.

The attempts to stabilize high-valent Ni species by formally substituting the dimethyl functionality by perfluoroalkyl ligands revealed very challenging, which can be traced back to the relatively easy activation of C-F bonds induced by divalent lanthanides. However, on the one hand, the application of such a fluorine abstraction reaction can be considered for the synthesis of fluorocarbene species, and, on the other hand, more restrained functional motifs, such as cycloalkyl or cycloperfluoroalkyl groups, may be considered as alternative ligands, inspired by the pioneering work by Sanford, Mirica, Vicic and others. Indeed, the restrained ligands should induce a higher

stability on the corresponding complexes upon one- or two-electron oxidation processes. Alternatively, the reductive elimination products would be more easily identifiable *via* NMR spectroscopy, comparing to those arising from the dimethyl or di-trifluoromethyl complexes. Besides, radical coupling between two redox-active ligand fragments was found to occur, triggered by the single-electron transfer step from the divalent lanthanide moiety. Further investigations would be required to get more insights into the reversibility of this process. The idea would be to take advantage of the electron(s) stored in the ligand moiety for the further reactivity use, instead of the observed facile, intermolecular C-C bond formation. To this effect, subtle modifications of the ligand framework, such as the addition of bulky substituents to block the coupling site, may be helpful. Moreover, in order to better understand how the lanthanide ions impact the spin density of the redox-active ligand system, more sophisticated computational studies, such as CASSCF methods, should be applied in the future.

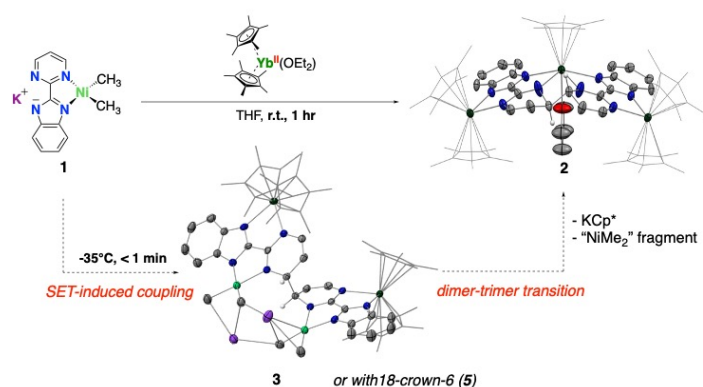


**Figure 101.** Graphical abstract for dissymmetric bimpm complex.

Finally, the use of a multidentate ligand scaffold is desirable to extend the “Ln-RAL-TM” framework. Interesting results have been obtained up to date, even though the very poor solubility of not only the pytpy ligand but also the formally Ni(I) compound, has to be overcome. Further insights into the electronic structure of the pytpyNiMe molecule could be obtained by the means of EPR and magnetic analyses. Modifications on the pytpy ligand by adding alkyl functional groups may help to increase the solubility and facilitate *in situ* spectroscopic monitoring of complexation reactions with divalent lanthanides. At the same time, preliminary results have shown promising catalytic activity of the pytpyNiMe complex in the hydroborylation of some terminal alkynes. This reactivity deserves further investigations from both stoichiometric and catalytic points of view in order to identify key intermediates and extend the scope of the complex in catalysis.

# *Appendices*



## Synthesis and characterization data

All reactions were conducted using standard Schlenk-line techniques or in argon- or nitrogen-filled gloveboxes (MBraun, Garching, Germany). All glassware was dried at 120 °C for at least 12 h prior to use. Tetrahydrofuran (THF), toluene, benzene (C<sub>6</sub>H<sub>6</sub>), pyridine, *n*-pentane, diethyl ether, THF-d<sup>8</sup>, toluene-d<sup>8</sup>, C<sub>6</sub>D<sub>6</sub>, and pyridine-d<sup>5</sup> were dried over sodium/benzophenone. Acetonitrile (CH<sub>3</sub>CN), dichloromethane (CH<sub>2</sub>Cl<sub>2</sub> or DCM), CD<sub>3</sub>CN, and CD<sub>2</sub>Cl<sub>2</sub> were dried over CaH<sub>2</sub>. All the solvents were degassed with Freeze-Pump-Thaw Cycling and then freshly distilled under reduced pressure prior to use.

<sup>1</sup>H, <sup>13</sup>C and <sup>19</sup>F NMR spectra were recorded in 5-mm tubes adapted with a J. Young valve on Bruker AVANCE II or III-300 MHz (Bruker, Billerica, MA, USA). <sup>1</sup>H chemical shifts were expressed relative to TMS (tetramethylsilane) in ppm.

Magnetic susceptibility measurements were made for all samples on a Quantum Design SQUID magnetometer (Cryogenic, London, GB). Diamagnetic corrections were made using Pascal's constants. Temperature dependent magnetic measurements were obtained in sealed quartz tube on a Quantum Design SQUID at 0.5 and 2 T.<sup>1</sup>

Elemental analyses were obtained from Mikroanalytisches Labor Pascher (Remagen, Germany). All calculations were performed using the ORCA 4.2.1 software.<sup>2</sup> The geometry optimizations were done at three different levels of theory (PBE,<sup>3</sup> PBE0,<sup>4</sup> and TPSSh<sup>5,6</sup>), using scalar relativistic ZORA Hamiltonian with ZORA-def2-TZVP basis set,<sup>7</sup> and SARC/J auxiliary basis set for Coulomb fitting.<sup>8-10</sup> Each time, dispersion corrections were added to the functional used in the D3 framework proposed by Grimme with the addition of the Becke-Johnson damping (D3BJ).<sup>11</sup> Frequencies were calculated (analytically for PBE and PBE0 and numerically for TPSSh) to ensure these structures corresponded to energy minima. Single-point energy calculations starting from PBE optimized geometry were then performed in gas phase at the PBE, PBE0,<sup>12</sup> TPSSh, and ωB97X-D3.<sup>13</sup>, and in a toluene *continuum* with the CPCM method.<sup>14</sup>

## Chapter II

(*tmeda*)NiMe<sub>2</sub>,<sup>15</sup> Cp\*<sub>2</sub>Yb(OEt)<sub>2</sub>,<sup>16</sup> and Cp\*<sub>2</sub>Sm(OEt)<sub>2</sub>,<sup>17</sup> were synthesized according to published procedures and recrystallized prior to use. 2,2'-Bipyrimidine was purchased from TCI EUROPE N.V. and sublimed before use.

**CO Migratory Insertion Studies.** Reactivity tests were conducted in 5 mm NMR tubes adapted with a J. Young valve by adding CO gas directly to a degassed frozen solution of **1** or **2** and letting it react at room temperature. Kinetic analysis was performed following the <sup>1</sup>H NMR resonances. The concentration of **1** was normalized by benzene residue (used as internal standard) in the deuterated solvent and complex **2** was referred to the toluene (used as internal standard), which crystallized in the cell. Integration of the NMR signals required care.

**Syntheses.** (*bipym*)Ni(Me)<sub>2</sub> (**1**). (*tmeda*)NiMe<sub>2</sub> (146 mg, 0.71 mmol, 1.0 equiv.) and bipyrimidine (113 mg, 0.71 mmol, 1.0 equiv.) were respectively dissolved in cold THF (−35 °C). Transferring the bipyrimidine solution dropwise into the greenish yellow nickel solution at ambient temperature gave a dark-colored mixture after stirring for several minutes. Then, the mixture was stirred for 2 h and was stored at −35 °C in order to crystallize. Black crystalline product was obtained after one night and isolated in 73% yield (105 mg, 0.42 mmol). <sup>1</sup>H NMR (300 MHz, 293 K, thf-d<sub>8</sub>): δ (ppm) = 9.32 (m, 2H, *bipym*), 9.12 (m, 2H, *bipym*), 7.67 (m, 2H, *bipym*), 0.06 (s, 6H, Ni–Me). <sup>13</sup>C NMR (75 MHz, 293 K, thf-d<sub>8</sub>): δ (ppm) = 162.0, 156.6, 154.6, 124.4, −5.2. **Anal. calcd.** for C<sub>10</sub>H<sub>12</sub>N<sub>4</sub>Ni: C, 48.64; H, 4.90; N, 22.69; found: C, 47.00; H, 4.59; N, 21.00.

(Cp\*)<sub>2</sub>Yb(*bipym*)Ni(Me)<sub>2</sub> (**2**). Cp\*<sub>2</sub>Yb(OEt)<sub>2</sub> (200 mg, 0.39 mmol, 1.0 equiv.) and (*bipym*)NiMe<sub>2</sub> (98 mg, 0.40 mmol, 1.02 equiv.) were dissolved in toluene, respectively, and cooled down to −35 °C. Transferring the green Cp\*<sub>2</sub>Yb solution dropwise into the Nickel solution at ambient temperature gave a dark-brown mixture once the addition was finished. Then, the mixture was stored at −35 °C in order to crystallize. Dark-brown crystals were obtained after several hours and were isolated after washing three times with *n*-pentane, in 58% yield (156 mg, 0.22 mmol). <sup>1</sup>H NMR (300 MHz, 293 K, thf-d<sub>8</sub>): δ (ppm) = 246.83 (s, 2H, *bipym*), 15.91 (s, 6H, −Me), 9.02 (s, 2H, *bipym*), 6.09 (s, 30H, Cp\*), −172.34 (s, 2H, *bipym*). **Anal. calcd** for C<sub>30</sub>H<sub>42</sub>N<sub>4</sub>NiYb: C, 52.19; H, 6.13; N, 8.11; found: C, 53.07; H, 6.06; N, 7.31.

Na(*bipym*)Ni(Me)<sub>2</sub> (**7**). (*bipym*)NiMe<sub>2</sub> (15 mg, 0.06 mmol, 1.0 equiv.) was dissolved in cold THF (−35 °C), and deep green, freshly prepared sodium naphthalenide (0.08 M) in cold THF (0.76 mL, 0.06 mmol, 1.0 equiv.) was transferred to the nickel solution at ambient temperature giving a dark-colored mixture after stirring for several minutes. <sup>1</sup>H NMR only showed the formation of naphthalene. Then, the mixture was concentrated and layered by cold *n*-pentane, then stored at −35 °C in order to crystallize. Dark needle-like crystals were obtained after one night and isolated in 47% yield (7.8 mg, 0.03 mmol).

Na<sub>2</sub>(Cp\*)<sub>2</sub>Yb(*bipym*)Ni(Me)<sub>2</sub> (**8**). Cp\*<sub>2</sub>Yb(*bipym*)NiMe<sub>2</sub> (21.5 mg, 0.03 mmol, 1.0 equiv.) was dissolved in cold THF (−35 °C), and deep green, freshly prepared sodium naphthalenide (0.08 M) in cold THF (0.78 mL, 0.06 mmol, 2.0 equiv.) was transferred to the dark brown solution at ambient

temperature giving a deep brownish mixture after stirring for several minutes.  $^1\text{H}$  NMR only showed the formation of naphthalene. Then, the mixture was concentrated and layered by cold *n*-pentane, then stored at  $-35\text{ }^\circ\text{C}$ . very deep green crystals were obtained after several days and isolated in 49% yield (11.2 mg, 0.015 mmol).

$(\text{Cp}^*)_2\text{Sm}(\text{bipym})\text{Ni}(\text{Me})_2$  (**9**).  $\text{Cp}^*_2\text{Sm}(\text{OEt}_2)$  (20 mg, 0.04 mmol, 1.0 equiv.) and  $(\text{bipym})\text{NiMe}_2$  (10 mg, 0.04 mmol, 1.0 equiv.) were dissolved in toluene, respectively, and cooled down to  $-35\text{ }^\circ\text{C}$ . Transferring the deep green  $\text{Cp}^*_2\text{Sm}$  solution dropwise into the Nickel solution at ambient temperature gave a dark mixture once the addition was finished. Then, the mixture was stored at  $-35\text{ }^\circ\text{C}$  in order to crystallize. Dark-brown crystals were obtained after several hours and were isolated after washing three times with *n*-pentane, in 76% yield (20.4 mg, 0.22 mmol).

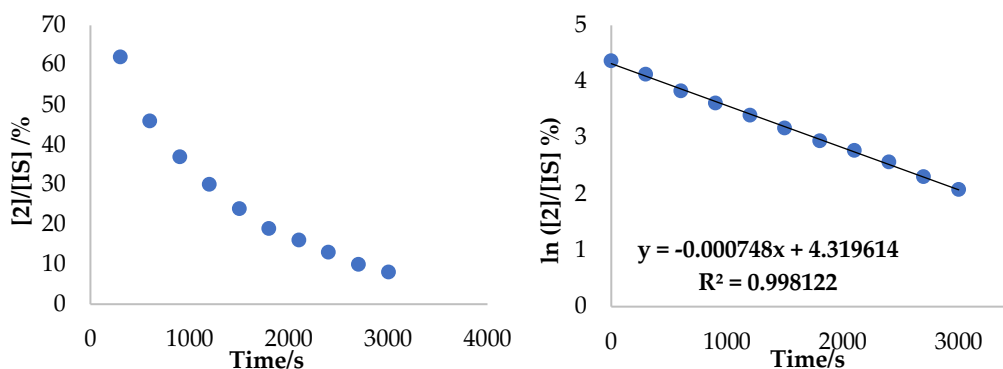


**Figure S102.** Kinetic data for **2** at  $35\text{ }^\circ\text{C}$ .  $t_{1/2} = 926.7\text{ s}$ .

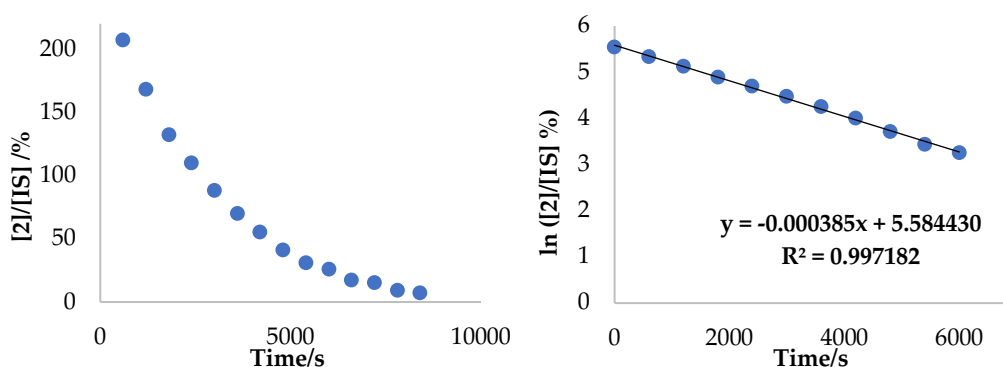


**Figure S103.** Kinetic data for **2** at  $30\text{ }^\circ\text{C}$ .  $t_{1/2} = 1800.4\text{ s}$ .

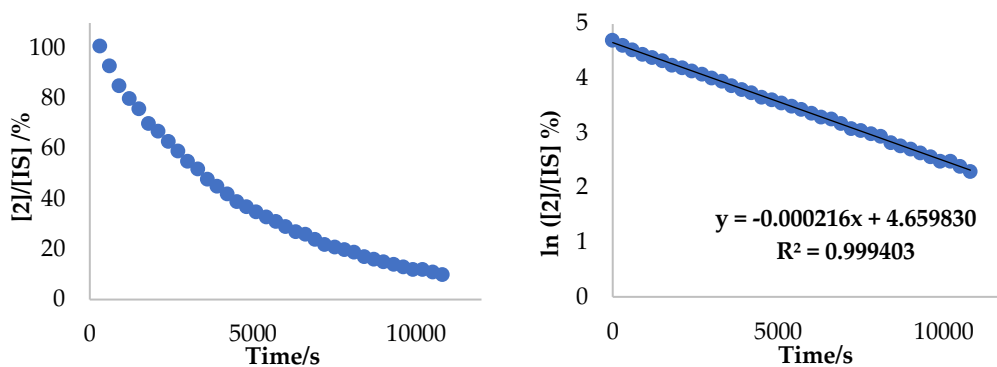


**Figure S104.** Kinetic data for **2** at  $25\text{ }^\circ\text{C}$ .  $t_{1/2} = 3209.0\text{ s}$ .



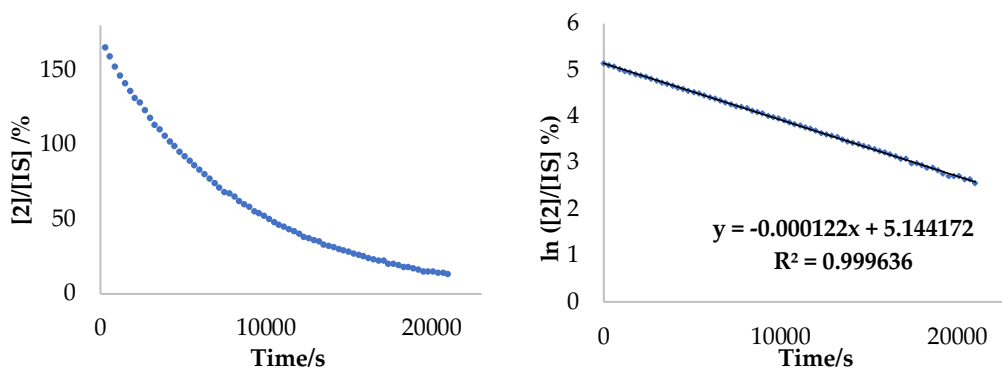


**Figure S105.** Kinetic data for **2** at 20 °C.  $t_{1/2} = 5681.5$  s.

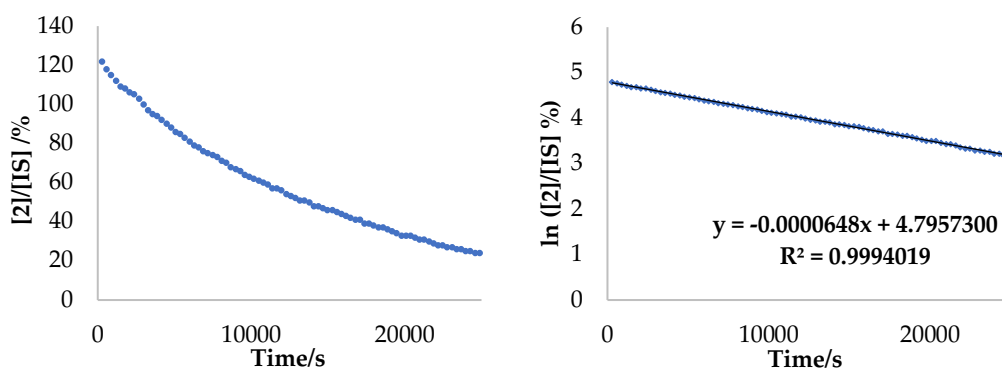
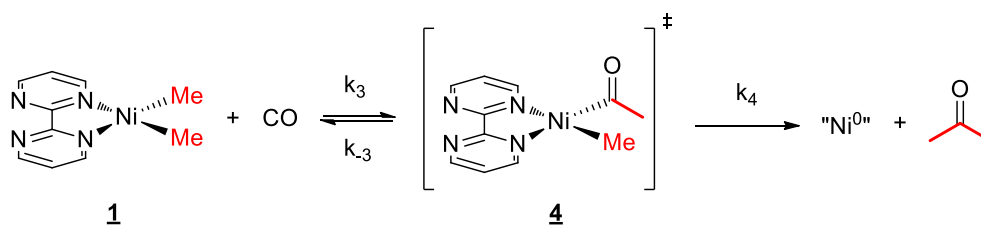


**Figure S106.** Kinetic data for **2** at 15 °C.  $t_{1/2} = 10696.7$  s

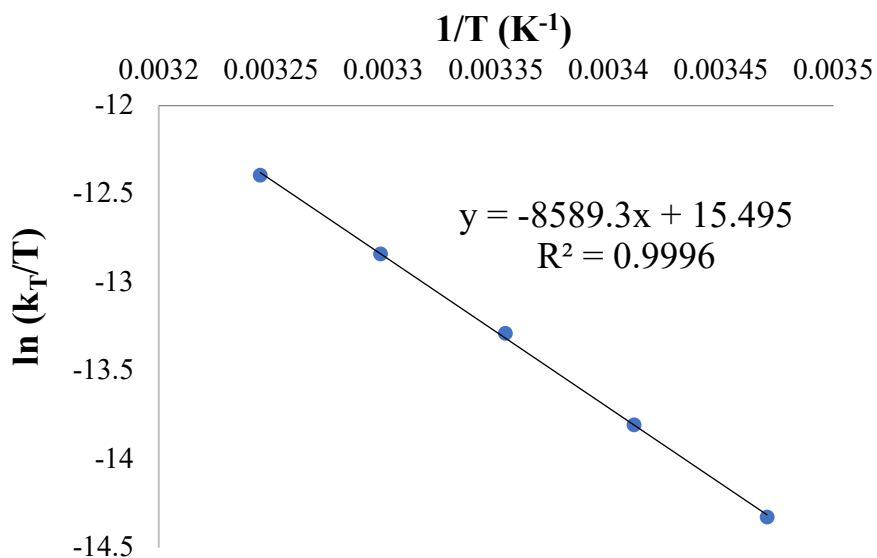


**Scheme S78.** Mechanism for the reaction of **1** with CO.

$$k_{obs} = \frac{k_3 k_4}{k_{-3} + k_4} [\text{CO}]$$

**Table S10.** Eyring Plot data for **1**.

T (°C)	T (K)	1/T (K <sup>-1</sup> )	k (s <sup>-1</sup> )	k/T (s <sup>-1</sup> K <sup>-1</sup> )	ln (k/T)	$t_{1/2}$ (s)
35	308.15	0.003245173	0.00128	4.15382E-06	-12.391482	541.5
30	303.15	0.003298697	0.000804	2.65215E-06	-12.840139	862.1
25	298.15	0.003354016	0.000506	1.69713E-06	-13.286571	1369.9
20	293.15	0.003411223	0.000296	1.00972E-06	-13.805836	2341.7
15	288.15	0.003470415	0.000173	6.00382E-07	-14.3257	4006.6



$$\Delta H^\ddagger = 71.41 \text{ kJ mol}^{-1} (17.06 \text{ kcal mol}^{-1})$$

$$\Delta S^\ddagger = -68.72 \text{ J mol}^{-1} \text{ K}^{-1} (-16.41 \text{ cal mol}^{-1} \cdot \text{K}^{-1})$$

**Figure S107.** Eyring Plot and resulting  $\Delta H^\ddagger$  and  $\Delta S^\ddagger$  for **1**.

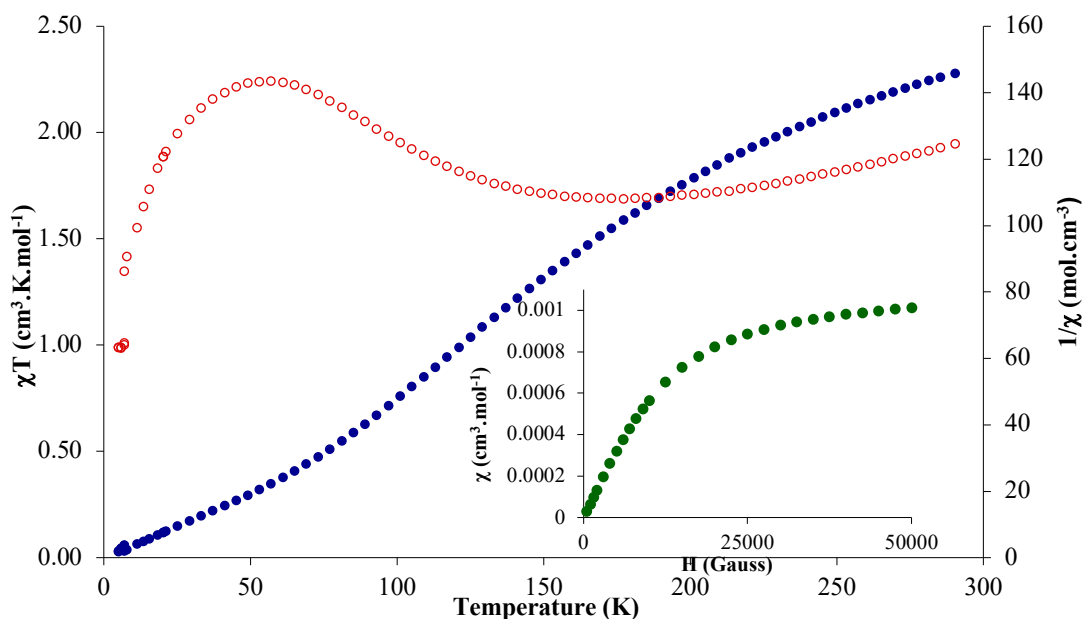


**Figure S108.** Temperature dependent magnetic data for **2** at 0.2T.  $1/\chi$  vs T is given as unfilled red dots,  $\chi T$  vs T as filled blue dots. Inset show magnetization vs H at 5K.

**Table S11.** Average main distances (Å) and angles (°) for (bipym)NiMe<sub>2</sub> (**1**) DFT optimized geometry with three different functional (PBE, PBE0 and TPSSH) vs XRD crystal structure.

Atoms	PBE	PBE0	TPSSH	XRD
Ni-C	1.916	1.899	1.911	1.930(3)
Ni-N	1.951	1.967	1.953	1.959(2)
C-C <sub>bipym</sub>	1.471	1.472	1.469	1.482(5) (avg)
Me-Ni-Me <sup>^</sup> N-Ni-N	9.41	16.90	13.11	5.34±0.24 (avg)
N-C-C <sup>^</sup> C-C-N <sub>bipym</sub>	4.65	12.80	7.64	2.63±1.04 (avg)

**Table S12.** Cartesian coordinates for the PBE optimized geometry

Ni	1.02122660532342	3.14409386460801	2.98955432851006
N	3.91360444234729	4.93868469680804	5.32137831697165
N	3.15486436792260	6.66722934684548	3.21831859757962
N	1.56176679775467	4.97442958846558	2.58837429646529
N	2.38962225339262	3.33566713372091	4.36642759969447
C	4.24033898716970	4.04773961720592	6.26366464340771
H	4.98635783793639	4.36428405231481	6.99768060213871
C	3.65817056844596	2.77731679180689	6.31420239951038
H	3.92285178249195	2.05589718569941	7.08704014023842
C	2.72935094484467	2.45760899158293	5.33507856458957
H	2.23548155386991	1.48667871576435	5.29492938935872
C	3.00803549169623	4.55670098436277	4.42293231353177
C	2.57243883180281	5.47874198663747	3.36302047684962
C	2.71837091578446	7.43387918165066	2.21363972299956
H	3.19828821478854	8.40933797760293	2.09967315768061
C	1.70361040797094	7.01292402540281	1.34882886595659
H	1.35468563617542	7.63796199984575	0.52717989197954
C	1.14453435266755	5.76481774611270	1.57551309124557
H	0.34351324663976	5.36335004401491	0.95438667140380
C	0.70410436388021	1.28121597496656	3.30689149168597
H	0.14641613697265	1.19840544311913	4.25767278362353
H	1.68857053585856	0.79228394014465	3.41559034905400
H	0.13895701126033	0.74582915917873	2.53447105491620
C	-0.44491390658014	3.12339516530584	1.75634308650510
H	-1.14860290574047	2.28621375428331	1.84072090323621
H	-0.02013525688884	3.11394692159549	0.73612381698628
H	-1.00372921778722	4.06404571095393	1.90861344388103

**Table 13.** Cartesian coordinates for the PBE0 optimized geometry.

N	1.02443198505548	3.15381408738126	2.98059621977688
N	3.73407525725889	5.00466505653483	5.43642947631058
N	3.18575891561773	6.63363577128596	3.19729907056606
N	1.55302893115246	5.00632272424439	2.62031668191389
N	2.45510586297498	3.33513723346412	4.32643779433853
C	4.06350802992681	4.11545020947509	6.36353847881887
H	4.69037321483515	4.47141138993181	7.17537347015335
C	3.63115049964051	2.79903385436962	6.30812635732142
H	3.91447565701858	2.07428781708130	7.05975021476159
C	2.81024627462597	2.44674676479416	5.25548582068772
H	2.41085318536828	1.44713263577522	5.13513904654961
C	2.95819026798853	4.57663390851985	4.45976699545082
C	2.55293522753717	5.48968112970821	3.37824140127253
C	2.80725810939503	7.35861677232767	2.15364199650896
H	3.33727808606635	8.29256317038145	1.99411869474128
C	1.79410256272804	6.95090265262687	1.29916782856216
H	1.49344416245264	7.54650925452393	0.44785272305163
C	1.17950335068019	5.74683079492121	1.57701659717732
H	0.37721104287126	5.34426999229061	0.97182426951632
C	0.83053440953936	1.27444589676548	3.13924331453817
H	0.31931136020791	1.01679031668262	4.07758537248421
H	1.83248223232069	0.82065452606085	3.15418392128216

H	0.27112600088362	0.80468916646153	2.32902257643419
C	-0.57913007981063	3.18784299600823	1.96021117695315
H	-1.32674752923950	2.47785926291177	2.31896414441347
H	-0.37627170464102	2.94575176395743	0.90816459300438
H	-1.02645531245451	4.19100085151452	2.01075176341074

**Table S14.** Cartesian coordinates for the TPSSh optimized geometry.

Ni	1.01605874053002	3.15477826488399	2.99669812615423
N	3.86704470965689	4.96096384452984	5.35497278496369
N	3.18150292980035	6.64880191416881	3.19967284837824
N	1.55160589242891	4.99333273570274	2.61596439052871
N	2.40366529576587	3.34566461877816	4.35973718090016
C	4.18560017616430	4.07078468599449	6.29410080051198
H	4.89601844054177	4.39665081628832	7.04686425276797
C	3.63532707385691	2.79221511867931	6.31671959706934
H	3.89780153567076	2.07335897009374	7.08190938885243
C	2.73770147724413	2.46427241142651	5.31772336778343
H	2.26524921009032	1.49320241870463	5.25392536773564
C	2.99522207905912	4.56722353687998	4.43585137475829
C	2.57047744793116	5.48372486845664	3.36989522093211
C	2.76167266368714	7.39843727167811	2.18167857584365
H	3.26654877516045	8.34855344900602	2.04168379070249
C	1.73499144951792	6.98764567244854	1.33580978436789
H	1.40251853856117	7.59990097728904	0.50789987016247
C	1.14669310547595	5.76353058017209	1.59210476045569
H	0.33963119896529	5.36641163604271	0.99090609782762
C	0.77469305113230	1.27388418459435	3.22721279053762
H	0.17945683952117	1.09200622496433	4.13321269253687
H	1.76443554620180	0.81246360283823	3.35449762963640
H	0.27557743695802	0.77326910405294	2.39630000065619
C	-0.50818958816696	3.14779017566527	1.84214773622614
H	-1.23430033281012	2.35989583898908	2.04821832267607
H	-0.16866493171474	3.02827840533922	0.80324943066894
H	-1.02055876122990	4.11563867233286	1.93929381636574

**Table S15.** Single point energy difference (kcal/mol) vs the PBE<sub>gas</sub> calculated one. All these single point energies were calculated starting from the PBE optimized geometry. Two environments are studied: in gas phase and with the presence of a toluene *continuum* (CPCM method).

	PBE <sub>gas</sub>	PBE0 <sub>gas</sub>	TPSSh <sub>gas</sub>	PBE <sub>Tol</sub>	PBE0 <sub>Tol</sub>	TPSSh <sub>Tol</sub>
$\Delta$ SPE(PBE <sub>gas</sub> ) – SPE	0	18.095	-636.954	-14.585	4.850	-649.198

**Table 16.** MO energy gaps (cm<sup>-1</sup>) calculated with three different functionals (PBE, PBE0 and TPSSh) starting from the PBE optimized geometry. Two environments are studied: in gas phase and with the presence of a toluene *continuum* (CPCM method).

MO	PBE <sub>gas</sub>	PBE0 <sub>gas</sub>	TPSSh <sub>gas</sub>	PBE <sub>Tol</sub>	PBE0 <sub>Tol</sub>	TPSSh <sub>Tol</sub>
HOMO => LUMO	7260.22	22324.96	13758.86	8072.28	23975.41	14856.24
LUMO => LUMO +1	4299.51	5366.15	4903.06	4378.52	5469.31	5006.216

## Chapter III

$(\text{CH}_3\text{CN})_2\text{Ni}(\text{CF}_3)_2$  and  $(\text{tmeda})\text{Ni}(\text{CF}_3)_2$ ,<sup>18</sup> were synthesized according to published procedures and carefully recrystallized prior to use.

**Syntheses.**  $(\text{bipym})\text{Ni}(\text{CF}_3)_2$  (**1**).  $(\text{tmeda})\text{Ni}(\text{CF}_3)_2$  (107 mg, 0.34 mmol) and bipym (54 mg, 0.34 mmol) were respectively dissolved in cold THF ( $-35\text{ }^\circ\text{C}$ ). Transferring the bipyrimidine solution dropwise into the orange yellow nickel solution at ambient temperature in THF and the reaction mixture was let stir overnight. Orange slurry mixture was then obtained, and the volatile materials were evaporated under reduced pressure. The orange yellow crude product was dissolved in DCM and layered by  $\text{Et}_2\text{O}$  at room temperature at room temperature. After several days, yellow crystals were isolated in 62% yield (75.4 mg, 0.21 mmol).  **$^1\text{H NMR}$**  (300 MHz, 293.15K,  $\text{CD}_2\text{Cl}_2$ ):  $\delta$  (ppm) = 9.04 (d, 6.6 Hz, 4H, bipym), 7.68 (t, 5.1 Hz, 2H, bipym).  **$^{19}\text{F NMR}$**  (282 MHz, 293.15K,  $\text{CD}_2\text{Cl}_2$ ):  $\delta$  (ppm) = -28.2.

$(\text{Hbimp})\text{Ni}(\text{CF}_3)_2$  (**2**).  $(\text{CH}_3\text{CN})_2\text{Ni}(\text{CF}_3)_2$  (63.0 mg, 0.22 mmol) was dissolved in THF and transferred to the white THF suspension of Hbimp (44.3 mg, 0.22 mmol) in THF at ambient temperature. The reaction mixture was stirred at ambient temperature for 2 hours, forming a brownish orange suspension gradually. The mixture was filtrated, concentrated and stored at  $-35\text{ }^\circ\text{C}$ . Yellow crystals were obtained after one night in 38% yield (39.2 mg, 0.08 mmol).  **$^1\text{H NMR}$**  (300 MHz, 293.15K,  $\text{THF-d}_8$ ):  $\delta$  (ppm) = 13.60 (s, 1H, H-bimp), 8.98 (d, 5.4 Hz, 1H, Hbimp), 8.93 (d, 5.6 Hz, 1H, Hbimp), 8.00 (d, 8.6 Hz, 1H, Hbimp), 7.67 (t, 5.3 Hz, 1H, Hbimp), 7.61 (d, 7.7 Hz, 1H, Hbimp), 7.39 (dt, 16.0, 7.2 Hz, 2H, Hbimp).  **$^{19}\text{F NMR}$**  (282 MHz, 293.15K,  $\text{THF-d}_8$ ):  $\delta$  (ppm) =  $\delta$  -24.0, -30.7.

$(\text{Kbimp})\text{Ni}(\text{CF}_3)_2$  (**3**).  $(\text{CH}_3\text{CN})_2\text{Ni}(\text{CF}_3)_2$  (89.8 mg, 0.32 mmol) was dissolved in THF and transferred to the white THF suspension of Kbimp (75.5 mg, 0.32 mmol) in THF at ambient temperature. The reaction mixture was stirred at ambient temperature for 4 hours, forming a brownish yellow suspension gradually. The mixture was filtrated, dried under reduced pressure and then dissolved in MeCN. Bright yellow crystals were obtained from MeCN/*n*-pentane vapor diffusion after several days in 36% yield (50.3 mg, 0.12 mmol).  **$^1\text{H NMR}$**  (300 MHz, 293.15K,  $\text{THF-d}_8$ ):  $\delta$  (ppm) = 8.64 (d, 4.9 Hz, 1H, Kbimp), 8.56 (d, 5.5 Hz, 1H, Kbimp), 7.73 (d, 8.6 Hz, 1H, Kbimp), 7.45 (d, 9.2 Hz, 1H, Kbimp), 7.10 (t, 5.0 Hz, 1H, Kbimp), 7.01 – 6.89 (m, 2H, Kbimp).  **$^{19}\text{F NMR}$**  (282 MHz, 293.15K,  $\text{THF-d}_8$ ):  $\delta$  (ppm) = -17.0, -24.6.

## Chapter IV

Hbimp<sup>19</sup> was synthesized according to published procedures and recrystallized prior to use. 18-crown-6 was purchased from Sigma-Aldrich and sublimed before use.

**Syntheses.** *K(bimp)Ni(CH<sub>3</sub>)<sub>2</sub>* (**1**). A 50 mL Schlenk was charged with Hbimp (283.6 mg, 1.44 mmol), KHMDS (317.2 mg, 1.59 mmol) in the glovebox. 20 mL of THF were added and the mixture was stirred at ambient temperature for 16 hours, remaining a milky suspension during the reaction time. The solvent was removed under reduced pressure and the residue was washed with diethyl ether for 3 times, allowing the removal of the slight excess of KHMDS, was dried under reduced pressure and used without further characterizations (298.3 mg, 1.27 mmol, 88%). (tmeda)Ni(CH<sub>3</sub>)<sub>2</sub> (174.1 mg, 0.85 mmol) was dissolved in cold THF (-40 °C) and transferred dropwise into a cold THF suspension of Kbimp (199.4 mg, 0.85 mmol) at ambient temperature. The suspension was stirred for 2 hours, resulting in a colour change from olive-green to night blue and was filtered. The solvent of the solution was removed under reduced pressure and K(bimp)Ni(CH<sub>3</sub>)<sub>2</sub> was isolated as a brown powder in 60% yield (163.6 mg, 0.51 mmol). *When CH<sub>3</sub>CN is used instead of THF, the yield is increased because the better solubility of **1** soluble in CH<sub>3</sub>CN. However, the necessary drying step is longer and traces of CH<sub>3</sub>CN may influence the further use with reactive divalent lanthanide.* Purple crystals were recrystallized *via* vapor diffusion by *n*-pentane on THF solution at ambient temperature after 24 hours and isolated in 40% yield (110.0 mg, 0.34 mmol). **<sup>1</sup>H NMR** (300 MHz, 293.15K, THF-d<sub>8</sub>): δ (ppm) = 8.63 (d, 5.0 Hz, 1H, Kbimp), 8.47 (d, 4.1 Hz, 1H, Kbimp), 7.92 (m, 1H, Kbimp), 7.39 (m, 1H, Kbimp), 6.86 (m, 3H), 0.02 (s, 3H, Ni-Me1), -0.40 (s, 3H, Ni-Me2). **<sup>13</sup>C NMR** (75 MHz, 293.15K, THF-d<sub>8</sub>): δ (ppm) = 163.08, 159.19, 153.97, 153.10, 149.88, 146.99, 120.54, 120.35, 119.63, 119.05, 119.01, -7.05, -12.23. **Anal. calcd** for C<sub>13</sub>H<sub>13</sub>KN<sub>4</sub>Ni: C, 48.33; H, 4.06; N, 17.34; found: C, 47.42; H, 4.20; N, 15.70.

*Cp\*Yb(thf)[Cp\*<sub>2</sub>Yb(bimp)]<sub>2</sub>* (**2**). Cp\*<sub>2</sub>Yb(OEt<sub>2</sub>) (94.4 mg, 0.18 mmol) and K(bimp)NiMe<sub>2</sub> (58.9 mg, 0.18 mmol) were dissolved in THF, respectively and cooled down to -35 °C. Transferring the red Cp\*<sub>2</sub>Yb THF solution dropwise into the blue Nickel solution at room temperature led to a dark red mixture immediately after the addition. The mixture was stirred at room temperature for one more hour, forming a red suspension. The solvent was removed under reduced pressure, yielding a brown-red solid that was extracted by Et<sub>2</sub>O (10 mL). Red crystals were obtained and isolated from slow evaporation of the Et<sub>2</sub>O solution in 51% yield (50.8 mg, 0.031 mmol). **<sup>1</sup>H NMR** (300 MHz, 293.15K, THF-d<sup>8</sup>): δ (ppm) = 213.6 (s, 1H, *v*<sub>1/2</sub> = 280 Hz, bimp), 205.9 (s, 1H, *v*<sub>1/2</sub> = 280 Hz, bimp), 196.8 (s, 1H, *v*<sub>1/2</sub> = 185 Hz, bimp), 186.5 (s, 1H, *v*<sub>1/2</sub> = 185 Hz, bimp), 175.7 (s, 1H, *v*<sub>1/2</sub> = 185 Hz, bimp), 110.3 (s, 1H, *v*<sub>1/2</sub> = 62 Hz, bimp), 70.6 (s, 1H, *v*<sub>1/2</sub> = 56 Hz, bimp), 63.9 (s, 1H, *v*<sub>1/2</sub> = 30 Hz, bimp), 55.8 (s, 1H, *v*<sub>1/2</sub> = 28 Hz, bimp), 54.6 (s, 1H, *v*<sub>1/2</sub> = 26 Hz, bimp), 46.5 (s, 1H, *v*<sub>1/2</sub> = 25 Hz, bimp), 45.4 (s, 1H, *v*<sub>1/2</sub> = 25 Hz, bimp), 33.5 (s, 1H, *v*<sub>1/2</sub> = 20 Hz, bimp), -0.8 (s, 15H, *v*<sub>1/2</sub> = 55 Hz, Cp\*), -5.5 (s, 15H, *v*<sub>1/2</sub> = 63 Hz, Cp\*), -6.6 (s, 15H, *v*<sub>1/2</sub> = 63 Hz, Cp\*), -10.6 (s, 15H, *v*<sub>1/2</sub> = 63 Hz, Cp\*), -12.8 (s, 15H, *v*<sub>1/2</sub> = 61 Hz, Cp\*), -25.2 (s, 1H, *v*<sub>1/2</sub> = 71 Hz,

bimpm). **Anal. calcd** for  $C_{76}H_{97}N_8OYb_3$ : C, 55.06; H, 5.90; N, 6.76; found: C, 54.41; H, 6.02; N, 6.61.

$[K(Cp^*_2Yb(bimpm)NiMe_2)_2]$  (**3**).  $Cp^*_2Yb(OEt_2)$  (42.6 mg, 0.08 mmol) and  $K(bimpm)NiMe_2$  (26.6 mg, 0.08 mmol) were dissolved separately in THF and cooled down to  $-35\text{ }^\circ\text{C}$ . Transferring the red  $Cp^*_2Yb$  THF solution into the deep blue Nickel solution at room temperature led to a dark brown-red solution immediately. The solution was kept under stirring at room temperature for only several seconds and the solvent was rapidly removed under reduced pressure to yield brown oil.  $Et_2O$  was then added, leading to a brown solution and an insoluble pale yellow solid. The mixture was filtered, concentrated and then kept at  $-35\text{ }^\circ\text{C}$  overnight to yield brown-red crystalline product as the first crop (24.3 mg, 0.031 mmol, 39% yield). *Further crops can be also collected but small amounts of 2 co-crystallized.*  **$^1H$  NMR** (300 MHz, 293.15K, THF- $d^8$ ):  $\delta$  (ppm) = 187.7 (s, 1H,  $v_{1/2}$  = 193 Hz, bimpm), 181.5 (s, 1H,  $v_{1/2}$  = 151 Hz, bimpm), 50.4 (s, 1H,  $v_{1/2}$  = 19 Hz, bimpm), 27.5 (s, 1H,  $v_{1/2}$  = 16 Hz, bimpm), 19.2 (s, 1H,  $v_{1/2}$  = 12 Hz, bimpm), 12.3 (s, 15H,  $v_{1/2}$  = 46 Hz,  $Cp^*$ ), 4.9 (s, 1H,  $v_{1/2}$  = 30 Hz, bimpm), 2.9 (s, 15H,  $v_{1/2}$  = 44 Hz,  $Cp^*$ ), -4.8 (s, 3H,  $v_{1/2}$  = 10 Hz, Ni-Me1), -8.3 (s, 1H,  $v_{1/2}$  = 18 Hz, bimpm), -18.2 (s, 3H,  $v_{1/2}$  = 12 Hz, Ni-Me2). **Anal. calcd** for  $C_{66}H_{86}K_2N_8Ni_2Yb_2$ : C, 51.71; H, 5.65; N, 7.31; found: C, 52.28; H, 6.04; N, 6.94.

$K(18-c-6)(bimpm)Ni(CH_3)_2$  (**4**). 18-crown-6 (47.8 mg, 0.18 mmol) was dissolved in cold THF ( $-40\text{ }^\circ\text{C}$ ) and transferred dropwise into a cold purple THF solution of  $K(bimpm)NiMe_2$  (55.6 mg, 0.17 mmol) at ambient temperature, immediately forming a deep blue solution that was stirred for 10 minutes. The solvent was then removed under reduce pressure, and the crude  $K(18-c-6)(bimpm)Ni(CH_3)_2$  complex (**4**) was obtained as deep blue oil. *The use of  $CH_3CN$  instead of THF as reaction solvent tends to increase the yield because the product is much more soluble in  $CH_3CN$ . However, the necessary drying step is longer and traces of  $CH_3CN$  may influence the further use with reactive divalent lanthanide.* Deep blue crystals were recrystallized via vapor diffusion by diethyl ether on THF solution at ambient temperature after 24 hours and isolated in 91% yield (91.0 mg, 0.15 mmol).  **$^1H$  NMR** (300 MHz, 293.15K,  $CD_3CN$ ):  $\delta$  (ppm) =  $\delta$  8.76 (dd,  $J$  = 4.7, 2.2 Hz, 1H,  $Kbimpm$ ), 8.67 (dd,  $J$  = 5.6, 2.2 Hz, 1H,  $Kbimpm$ ), 7.84 - 7.78 (m, 1H,  $Kbimpm$ ), 7.59 - 7.52 (m, 1H,  $Kbimpm$ ), 7.15 - 7.07 (m, 1H,  $Kbimpm$ ), 6.99 - 6.89 (m, 2H,  $Kbimpm$ ), 3.55 (s, 24H, 18-c-6), -0.10 (s, 3H, Ni-Me1), -0.54 (s, 3H, Ni-Me2).  **$^{13}C$  NMR** (75 MHz, 293.15K, THF- $d_8$ ):  $\delta$  (ppm) = 163.72, 159.55, 154.12, 153.62, 150.60, 147.22, 119.91, 119.72, 119.53, 118.73, 70.88, -7.07, -12.20. **Anal. calcd** for  $C_{25}H_{37}KN_4NiO_6$ : C, 51.12; H, 6.35; N, 9.54; found: C, 51.03; H, 6.30; N, 9.06.

$[K(18-c-6)Cp^*_2Yb(bimpm)NiMe_2]_2$  (**5**).  $Cp^*_2Yb(OEt_2)$  (42.7 mg, 0.08 mmol) and  $K(18-c-6)(bimpm)NiMe_2$  (48.5 mg, 0.08 mmol) were separately dissolved in THF and cooled down to  $-35\text{ }^\circ\text{C}$ . Transferring the red  $Cp^*_2Yb$  THF solution dropwise into the blue Nickel solution at room temperature led to a dark purple mixture immediately once the addition. The solution was stirred at room temperature for 10 minutes and the solvent was removed under reduced pressure, yielding a red microcrystalline product (82.3 mg, 0.078 mmol, 97% yield). Dark red crystals were obtained

and isolated from THF solution by vapor diffusion with Et<sub>2</sub>O, in 64% yield (54.4 mg, 0.051 mmol). **<sup>1</sup>H NMR** (300 MHz, 293.15K, CD<sub>3</sub>CN): δ (ppm) = 186.2 (s, 1H, *v*<sub>1/2</sub> = 131 Hz, bimpm), 176.1 (s, 1H, *v*<sub>1/2</sub> = 233 Hz, bimpm), 53.0 (s, 1H, *v*<sub>1/2</sub> = 22 Hz, bimpm), 30.6 (s, 1H, *v*<sub>1/2</sub> = 20 Hz, bimpm), 23.3 (s, 1H, *v*<sub>1/2</sub> = 17 Hz, bimpm), 7.9 (s, 15H, *v*<sub>1/2</sub> = 50 Hz, Cp\*), 3.5 (s, 24H, *v*<sub>1/2</sub> = 12 Hz, 18-c-6), 2.3 (s, 15H, *v*<sub>1/2</sub> = 45 Hz, Cp\*), -0.0 (s, 1H, *v*<sub>1/2</sub> = 10 Hz, bimpm), -0.9 (s, 3H, *v*<sub>1/2</sub> = 14 Hz, Ni-Me1), -4.5 (s, 1H, *v*<sub>1/2</sub> = 25 Hz, bimpm), -14.0 (s, 3H, *v*<sub>1/2</sub> = 13 Hz, Ni-Me2). (*Note: Another dissymmetric Cp\* signal at 2.29 ppm is largely overlapped by the solvent signal.*) **Anal. calcd** for C<sub>90</sub>H<sub>134</sub>K<sub>2</sub>N<sub>8</sub>Ni<sub>2</sub>O<sub>12</sub>Yb<sub>2</sub>: C, 52.43; H, 6.55; N, 5.43; found: C, 52.26; H, 6.50; N, 5.34.

**[K<sub>2</sub>(bimpm)NiMe<sub>2</sub>]<sub>2</sub> (6)**. K(bimpm)NiMe<sub>2</sub> (28.8 mg, 0.09 mmol) was dissolved in THF and cooled down to -35 °C. Then, cold potassium graphite (53.3 mg, 0.39 mmol) was added to the deep blue THF solution of **1** at room temperature, leading to a dark brown red mixture after stirring for a few seconds. The mixture was then filtered, and the solvent was removed under reduced pressure, yielding a brown-red crystalline product that was washed by Et<sub>2</sub>O (5 mL) in 69% yield (22.4 mg, 0.031 mmol). Brown orange, XRD suitable crystals of **6** were able to be obtained from slow diffusion of pentane into the THF solution at -35 °C. **<sup>1</sup>H NMR** (300 MHz, 293.15 K, THF-d<sup>8</sup>): δ (ppm) = 7.62 (d, *J* = 9.2 Hz, 1H), 7.26 (m, 1H), 6.91 (d, *J* = 7.8 Hz, 1H), 6.64 (m, 1H), 6.22 (d, *J* = 7.9 Hz, 1H), 4.09 (d, *J* = 9.0 Hz, 1H), -0.61 (s, 3H), -1.08 (s, 3H). **<sup>13</sup>C NMR** (75 MHz, 293.15K, THF-d<sup>8</sup>): δ (ppm) = 163.67, 161.42, 149.13, 146.71, 137.42, 118.55, 118.35, 117.85, 117.57, 101.14, -9.93, -14.35. *One of <sup>13</sup>C signals on the ligand was not observed due to the overlapping with the resonances of the hardly removable residue impurity.*

**[K(18-c-6)Cp\*<sub>2</sub>Sm(bimpm)NiMe<sub>2</sub>]<sub>2</sub> (7)**. Cp\*<sub>2</sub>Sm(OEt<sub>2</sub>) (19.7 mg, 0.03 mmol) and K(18-c-6)(bimpm)NiMe<sub>2</sub> (16.6 mg, 0.03 mmol) were separately dissolved in THF and cooled down to -35 °C. Transferring the bordeaux red Cp\*<sub>2</sub>Sm THF solution dropwise into the blue nickel solution at room temperature led to a dark purple-red mixture immediately once the addition. The solution was stirred at room temperature for 10 minutes and the solvent was removed under reduced pressure, yielding a red microcrystalline product. Dark red crystals were eventually obtained and isolated from THF solution by vapor diffusion with Et<sub>2</sub>O, in 31% yield (10.5 mg, 0.010 mmol).



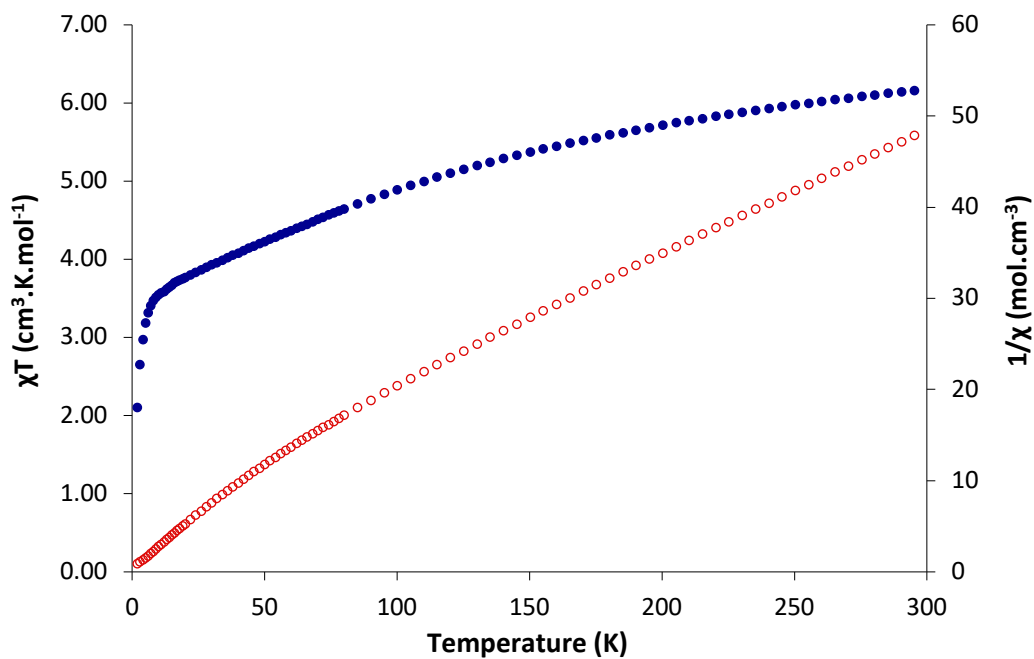


**Figure S109.** Temperature-dependent magnetic data for **2** at 2 T.  $1/\chi$  vs T is given as unfilled red dots, and  $\chi T$  vs. T as filled blue dots.

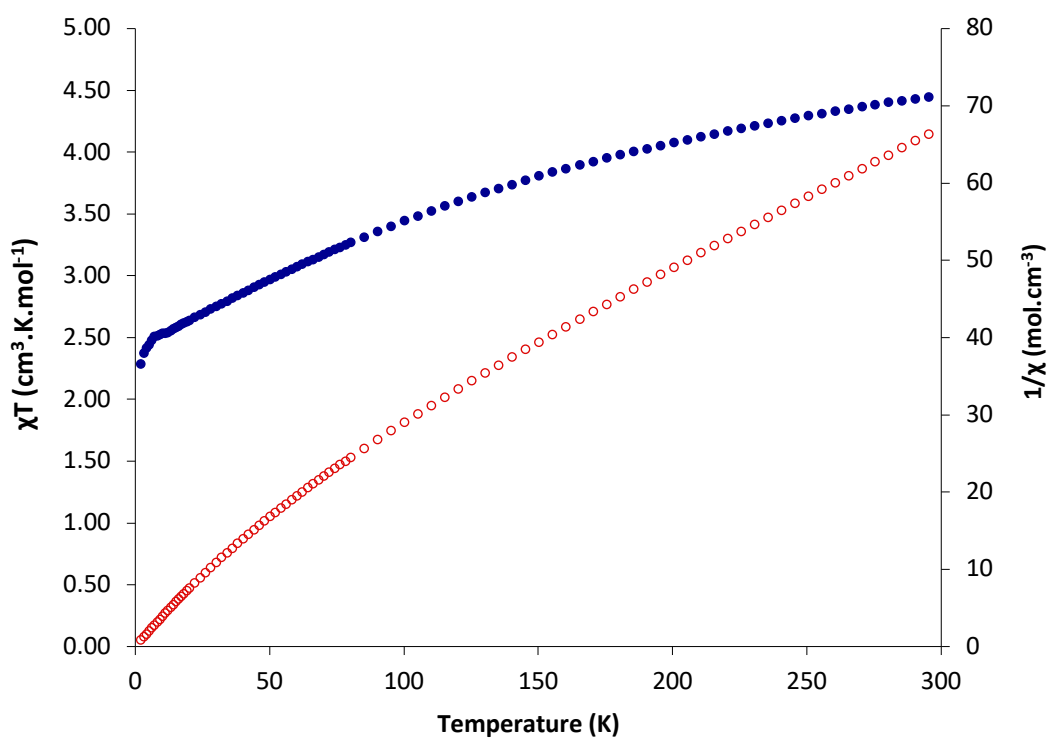


**Figure S110.** Temperature-dependent magnetic data for **3** at 2 T.  $1/\chi$  vs T is given as unfilled red dots, and  $\chi T$  vs. T as filled blue dots.

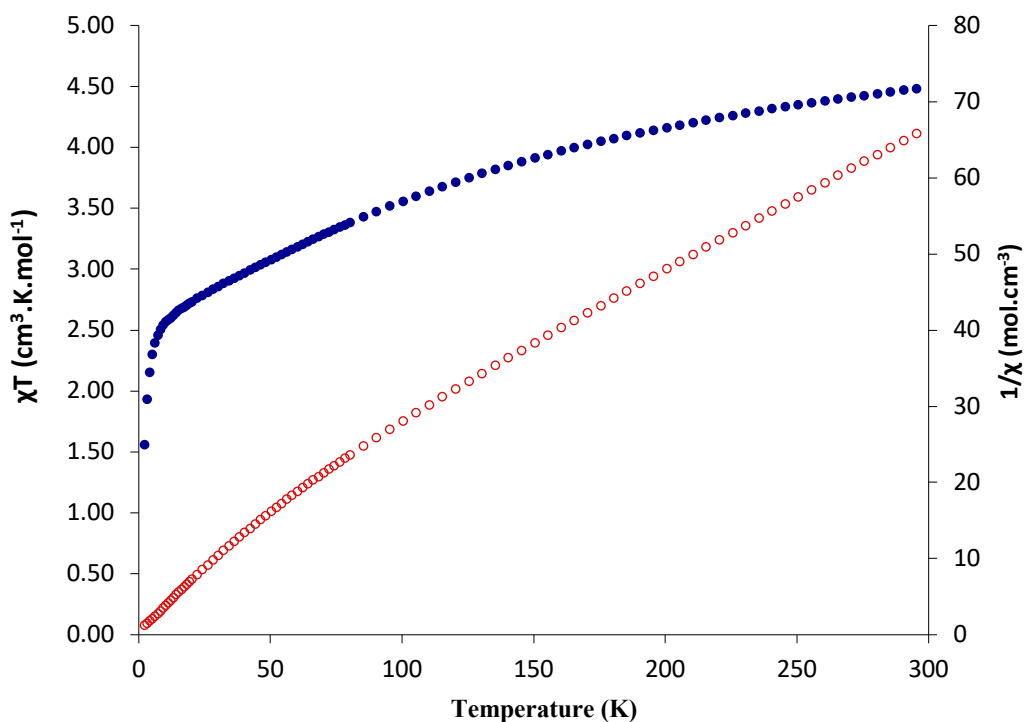


**Figure S111.** Temperature-dependent magnetic data for **5** at 2 T.  $1/\chi$  vs T is given as unfilled red dots, and  $\chi T$  vs. T as filled blue dots.

**Table S17.** Main average distances (Å) and angles (°) in the compounds  $[\text{bimpm}]^-$ ,  $[(\text{bimpm})\text{NiMe}_2]^-$  and  $[\text{Cp}^*_2\text{Yb}(\text{bimpm})\text{NiMe}_2]^-$ . Geometries were optimized with the PBE functional.

	$[\text{bimpm}]^-$	$[(\text{bimpm})\text{NiMe}_2]^-$	$[\text{Cp}^*_2\text{Yb}(\text{bimpm})\text{NiMe}_2]^-$
Ni-CH <sub>3</sub>	-	1.921	1.922
Ni-N	-	1.959	1,9725
Yb-N	-	-	2,39855
Yb-Cp* <sub>centr</sub>	-	-	2.379
Bridging C-C <sub>bimpm</sub>	1.46119	1.443	1.45(6)
Coupled C-C <sub>bimpm</sub>	-	-	1.40139
bimpm <sup>^</sup> NiMe <sub>2</sub>	-	1.56	13.55

**Table S18.** Cartesian coordinates for the PBE optimized geometry for compound  $[\text{bimpm}]^-$ .

N	10.96939429243430	5.56793491400100	8.32405298785742
N	9.10821178716916	7.59068238655870	8.92344824145940
N	9.12262317600363	8.30171024547728	6.69773453292266
N	10.96971838079360	6.29286313861084	6.02821040104677
C	11.85977850903180	5.34415616264287	5.75402181630087
H	12.19141900602610	5.28182791582472	4.70859015662691
C	12.36574418052770	4.46224082440688	6.71257247458056
H	13.10037667788650	3.69235299054774	6.46929205933975
C	11.86050112917730	4.63417621927497	8.00396943081854

H	12.19210804314950	3.98286470361457	8.82402266831438
C	10.54666927944640	6.38668323416213	7.32020110590324
C	9.58286705308764	7.43424232633364	7.65001927210445
C	8.26677362468822	8.65060610200981	8.79018263661858
C	7.46294972346363	9.31122181108609	9.74172660447988
H	7.45366013842814	8.97987397178864	10.78387879934960
C	6.69156747282486	10.38860770021320	9.32009696906957
H	6.06186904308575	10.91854340975720	10.04039035515020
C	6.70266557521504	10.82243616797390	7.96836269775326
H	6.08364731254276	11.67754091920770	7.68208304215277
C	7.48357548695074	10.18665211303540	7.00952980891279
H	7.49169368984768	10.52354490587110	5.96920900635484
C	8.27608641821909	9.09170783760120	7.41083493288330

**Table S19.** Cartesian coordinates for the PBE optimized geometry for compound [(bimpm)NiMe<sub>2</sub>].

Ni	-10.85795270488540	-2.45740262521130	-6.57935426882062
N	-12.16690938027450	-2.47617400645348	-8.02848767309177
N	-9.63104288187552	-0.98924629496297	-10.19297569602920
N	-9.72190513164585	-1.67784842361876	-7.97877934398171
N	-12.46603543931090	-1.87008588432823	-10.35303098582760
C	-10.35483787957940	-1.52205420376669	-9.19096651394813
C	-11.72804155261930	-1.96256742857989	-9.23842460493234
C	-8.41833447966368	-0.77438005535526	-9.59887705420482
C	-13.43898642383910	-2.91715654354570	-8.00446671102704
H	-13.78280493081610	-3.32493148992910	-7.05348346371986
C	-8.45849025645250	-1.19818253643805	-8.21929767910621
C	-7.23911396604844	-0.23336095848478	-10.14545110920170
H	-7.21816133290692	0.08499896421989	-11.19005705938840
C	-14.26708679409540	-2.85864896297681	-9.12068589740189
H	-15.29345282976310	-3.22425455654789	-9.07469775017968
C	-6.16597411403526	-0.53635024547288	-7.97167460508340
H	-5.26872830288447	-0.43039336329760	-7.35641269722556
C	-6.12418176307088	-0.11943702116715	-9.32462379430804
H	-5.19653391075010	0.29838548510648	-9.72395705729421
C	-13.72617664086060	-2.31585067378255	-10.28796512632440
H	-14.31955675621730	-2.23306177029168	-11.20537559305620
C	-7.31676040488315	-1.07487759059319	-7.40524923123936
H	-7.33371636792981	-1.39219404724718	-6.36440803125959
C	-9.51730015881202	-2.37213474562474	-5.20749482385873
H	-8.66106683383841	-2.97420385339203	-5.55934331431786
H	-9.80407210279150	-2.72512383352885	-4.20659008874281
H	-9.19618709629966	-1.31902674576451	-5.13163817508685
C	-12.08303369501440	-3.23157898342586	-5.31638360137583
H	-12.96604234310390	-2.56531401659679	-5.24312130412955
H	-11.71021274944740	-3.40299288536415	-4.29655101771715
H	-12.41863377628410	-4.20885870357825	-5.71782272811903

**Table S20.** Cartesian coordinates for the PBE optimized geometry for compound [Cp\*<sub>2</sub>Yb(bimpm)NiMe<sub>2</sub>].

Yb	2.39641272031517	6.15729270118101	2.17623539274325
Ni	5.86072236274985	8.61550105486300	6.03309031529828
N	4.11237202236377	9.08842011923908	5.19547893787800
N	5.71563672389365	7.01104788159994	4.93506825566606

N	2.48387516240986	8.12681684414460	3.62414364774130
N	4.36326531994733	5.88241491594803	3.43456679111152
C	4.54136719860743	6.98787997471363	4.21991992281914
C	1.71137087533012	9.19017889340959	3.81688174439116
H	0.78103974564572	9.22692173513074	3.24522255993999
C	3.66724710196465	8.07740751881191	4.33272936282232
C	2.05945456175369	10.22916801393730	4.70438084352796
H	1.40953707271138	11.08784260415250	4.85852450720239
C	3.36825109753380	8.03193116469782	0.52328658233750
C	3.29814949401944	10.12239074919770	5.36169038605642
H	3.64889984481953	10.90603609057970	6.03835193750379
C	5.51688322209105	5.14948120084789	3.63260872420609
C	1.07047736769470	5.14865045031667	4.25255626421903
C	7.17602242788496	3.42387181138627	3.42307661635628
H	7.51346149845632	2.48014550129935	2.99013124452023
C	3.54417898589444	5.84844897342900	-0.20267074690117
C	0.92346318428311	3.93028499704512	2.29679588397145
C	2.10415288491797	7.64273885842900	-0.01257621564896
C	2.21787107957549	6.29693508829315	-0.48013760040722
C	5.92335426665246	3.93893290491699	3.06233011328329
H	5.27790037074100	3.41440877006212	2.35424516845242
C	7.41643002350605	8.04898118182051	7.00686229010992
H	7.28328807187182	6.98093079639079	7.24095609771287
H	7.58798213636076	8.60574856580025	7.93916726488627
H	8.30007310946648	8.16863193748175	6.35578534230198
C	4.25757497661698	6.92445313919276	0.40594274555639
C	7.61332011183881	5.32159005453330	4.90662056304681
H	8.26972086883253	5.85120365875788	5.59478429262628
C	8.00360243484257	4.10566803658788	4.32701510300378
H	8.97770514897346	3.68399279593937	4.58333028729923
C	4.12447257781091	4.52639338340720	-0.61116575210817
H	4.95669276573238	4.22742325090820	0.04358016605098
H	4.52400283505917	4.55358276840978	-1.64162604834321
H	3.37372799109757	3.72157661955813	-0.58389318034125
C	2.58697781879088	3.04210121135381	4.09789344096194
H	3.13613014393777	2.52044122501607	3.30107477998948
H	2.09086919354623	2.26433332563434	4.70718061168830
H	3.33941440580214	3.52608849928554	4.73644761728281
C	5.71586213732072	6.94091667203119	0.74893462921725
H	5.91770431324628	7.49339863748183	1.67738645280602
H	6.30750032747332	7.42087000283874	-0.05135857144106
H	6.11550431842012	5.92840455077550	0.89085461674529
C	1.06992272524842	2.79926397732262	1.32196440054742
H	0.66735909715695	3.05438728868776	0.33111655930116
H	0.53273525843273	1.89582744016537	1.66266760130067
H	2.12151618113693	2.50564877875339	1.17992431556064

C	1.22639133945835	5.58154915635379	-1.34507019616007
H	0.20310059124306	5.94891344896402	-1.19087393465549
H	1.22004038132427	4.49619973526261	-1.16507892164361
H	1.46130402328226	5.72432312468086	-2.41706886853748
C	-0.83875281480479	6.87622075489877	3.81972147254907
H	-0.41749630536220	7.46958344226592	4.64309788328965
H	-1.82351933227440	6.50544361812122	4.15784196568667
H	-1.03553301921867	7.56425915450630	2.98154128887365
C	0.90523077201579	8.53267165200117	-0.16283986106713
H	0.93684459510962	9.11908389862296	-1.09977800668563
H	0.83024952241699	9.26192591395969	0.65946486086599
H	-0.03331291575853	7.95741456860572	-0.17921589023261
C	-1.10489655830724	5.17498883972956	1.19876904781476
H	-1.22666416968764	6.22408779624994	0.88617484112156
H	-2.08544242553667	4.84893292182627	1.59219013276248
H	-0.91038557245085	4.58503096703050	0.29347683911357
C	0.06810483038516	5.74776829058412	3.43341787314285
C	1.59531006602882	4.02345129097902	3.55125045074993
C	6.36206717604535	5.84707048353001	4.56227693222938
C	3.74830341105638	9.40049687177665	1.00114069746180
H	2.88319322612116	9.95957800171721	1.38431761057975
H	4.18937486397982	10.00160062434140	0.18541421681186
H	4.49102973912560	9.35914945206526	1.81186529118388
C	-0.02663332654978	4.99856984182425	2.22572926351211
C	1.47259294741769	5.58064266879634	5.63026205712258
H	2.55133314652206	5.44478219138609	5.79600208739841
H	0.94616258526837	5.00357695038904	6.41038748739249
H	1.25186419149996	6.64369529459219	5.80231364785171
C	6.09119399067120	10.36117578750750	6.81064540498873
H	7.10480848110940	10.59205380065770	7.16393738485188
H	5.79237331651299	11.11452246967220	6.06198970042898
H	5.39945612157676	10.41610773233380	7.67220496734523

## Chapter V

$\text{Cp}^{\text{III}}_2\text{Yb}$  and  $\text{Cp}^{\text{III}}_2\text{Sm}$ ,<sup>20</sup> as well as  $\text{Cp}^{\text{III}}_2\text{Tm}$ ,<sup>21</sup> were synthesized according to published procedures and recrystallized prior to use. 18-crown-6 and  $\text{B}_2\text{pin}_2$  were purchased from Sigma-Aldrich and sublimed before use.

**Syntheses.** *(pytpy)Ni(CH<sub>3</sub>) (1).* (tmeda)Ni(CH<sub>3</sub>)<sub>2</sub> (86.5 mg, 0.42 mmol, 1.0 equiv.) in cold Et<sub>2</sub>O at -40 °C was combined with a cold Et<sub>2</sub>O suspension of pytpy (131.0 mg, 0.42 mmol, 1.0 equiv.), namely 4'-(4"-pyridyl)-2,2':6',2"-terpyridine, at ambient temperature. The yellowish suspension turned to olive then deep green gradually during stirring. The suspension kept stirring for 24 hours at ambient temperature. Sequentially, dark blue solid was separated *via* centrifugation, washed with Et<sub>2</sub>O and *n*-pentane several times, and dried under vacuum, isolated in 76% yield (123.0 mg, 0.32 mmol). Furthermore, dark green crystals could be recrystallized *via* slow diffusion of pyridine solution with *n*-pentane at -40 °C after several days. <sup>1</sup>H NMR (300 MHz, 293.15K, THF-d<sup>8</sup>): δ (ppm) = 161.39 (s, 1H, terpyridine-pytpy), 55.57 (s, 1H, terpyridine-pytpy), 35.89 (s, 1H, terpyridine-pytpy), 21.87 (s, 1H, terpyridine-pytpy), 8.91-7.40 (m, 4H, pyridyl-pytpy), -40.60 (s, 1H, terpyridine-pytpy), -61.38 (s, 1H, terpyridine-pytpy), -172.17 (s, 1H, terpyridine-pytpy). *The rest of proton resonances cannot be detected with the best effort, probably because of the high paramagnetism of 1 with bad solubility.* **Anal. calcd** for C<sub>21</sub>H<sub>17</sub>N<sub>4</sub>Ni: C, 65.67; H, 4.46; N, 14.59; found: C, 65.40; H, 4.20; N, 14.9.

*(pytpy)SmCp\*<sub>2</sub> (2).*  $\text{Cp}^{\text{III}}_2\text{Sm}$  (13.9 mg, 0.02 mmol) was dissolved in Et<sub>2</sub>O and cooled down to -35 °C, then transferred into the dark Et<sub>2</sub>O suspension of (pytpy)Ni(CH<sub>3</sub>) (7.0 mg, 0.02 mmol) at room temperature led to a green mixture immediately. The suspension was filtrated and concentrated, and the mixture was then kept at -40°C. Dark green crystals were eventually obtained and isolated in 72% yield (14.6 mg, 0.016 mmol).

*Cp\*<sub>2</sub>Sm(thf)(pytpy)SmCp\*<sub>2</sub> (3).*  $\text{Cp}^*_2\text{Sm}(\text{OEt}_2)$  (27.4 mg, 0.06 mmol) was dissolved in toluene and cooled down to -35 °C. Transferring deep green  $\text{Cp}^*_2\text{Sm}$  solution dropwise into the dark toluene suspension of (pytpy)Ni(CH<sub>3</sub>) (21.3 mg, 0.06 mmol) at room temperature led to a dark green mixture immediately. The suspension was stirred at room temperature for 10 minutes and filtrated and concentrated. Several drops of THF were added into the obtained deep green solution and the mixture was then kept at -40°C. Dark green crystals were eventually obtained and isolated in 51% yield (15.9 mg, 0.014 mmol).

*Cp<sup>III</sup><sub>2</sub>Yb(pytpy)Ni(pytpy)YbCp<sup>III</sup><sub>2</sub> (4).*  $\text{Cp}^{\text{III}}_2\text{Yb}$  (10.7 mg, 0.02 mmol) was dissolved in toluene and cooled down to -35 °C. Transferring brown  $\text{Cp}^{\text{III}}_2\text{Yb}$  solution into the dark toluene suspension of (pytpy)Ni(CH<sub>3</sub>) (6.4 mg, 0.02 mmol) at room temperature led to a dark green mixture immediately. The suspension was filtrated and concentrated, and the mixture was then kept at -40°C. Dark green crystals were eventually obtained and isolated in 40% yield (6.7 mg, 0.003 mmol).

*[K(18-c-6)]<sub>2</sub>(pytpy)Ni(CH<sub>3</sub>) (5).* (pytpy)Ni(CH<sub>3</sub>) (19.3 mg, 0.05 mmol) and potassium graphite (13.7 mg, 0.10 mmol) were kept at -40 °C, then cold THF was added at ambient temperature. The obtained deep green suspension was kept stirring for 10 min at ambient temperature, and 18-

crown-6 (13.3 mg, 0.05 mmol) in THF was added to reaction mixture during the stirring. Sequentially, the dark green suspension was filtrated, and dark green crystals were recrystallized *via* slow diffusion of THF solution with diethyl ether at -40 °C after several days in 27% yield (13.6 mg, 0.014 mmol).

*pinB(pytpy)Ni(CH<sub>3</sub>) (6)*. B<sub>2</sub>pin<sub>2</sub> (3.3 mg, 0.013 mmol) was dissolved in THF and transferred to the dark THF suspension of (pytpy)Ni(CH<sub>3</sub>) (5.0 mg, 0.013 mmol) at room temperature led to a deep blue mixture immediately. The suspension was filtrated and concentrated, and the mixture was then kept at -40°C. Dark green crystals were eventually obtained and isolated in 42% yield (2.8 mg, 0.0055 mmol).

## Crystallographic data

Single crystals were coated in Paratone-N oil and mounted on a Kapton loop. A BRUKER APEX-II CCD detector and a graphite Mo-K $\alpha$  monochromator (Nonius, Delft, Netherlands) were used for the data acquisition. All data were measured at 150 K under a nitrogen stream and a refinement method was used for solving the structure. The structure resolution was accomplished using the SHELXS-97 and SHELXT program,<sup>22</sup> and the refinement was done with the SHELXL program.<sup>23,24</sup> The structure solution and the refinement were achieved with the PLATON,<sup>25</sup> and Olex2 softwares.<sup>26</sup> During the refinement steps, all atoms - except hydrogen atoms - were refined anisotropically. The position of the hydrogen atoms was determined using residual electronic densities. Finally, in order to obtain a complete refinement, a weighting step followed by multiples loops of refinement was done. ORTEP drawings of the compound structures were obtained using the MERCURY software.

### Chapter II

**Table S21.** Crystallographic data for **1**, **2**, **7**, **8** and **9**.

	<b>1</b>	<b>2</b>	<b>7</b>	<b>8</b>	<b>9</b>
Molecular formula	C <sub>10</sub> H <sub>12</sub> N <sub>4</sub> Ni	C <sub>30</sub> H <sub>42</sub> N <sub>4</sub> Ni Yb, C <sub>7</sub> H <sub>8</sub>	C <sub>18</sub> H <sub>28</sub> N <sub>4</sub> Na Ni O <sub>2</sub>	C <sub>54</sub> H <sub>90</sub> N <sub>4</sub> Na <sub>2</sub> Ni O <sub>6</sub> Yb, (C <sub>4</sub> H <sub>8</sub> O) <sub>2</sub>	C <sub>30</sub> H <sub>42</sub> N <sub>4</sub> Ni Sm, C <sub>7</sub> H <sub>8</sub>
Molecular weight	246.95	782.56	414.14	1205.08	758.86
Crystal habit	black needle	red purple plate	black needle	dark green block	black needle
Crystal dimensions(m m)	0.300x0.040x0.020	0.280x0.140x0.100	0.520x0.300x0.200	0.300x0.200x0.140	0.180x0.100x0.060
Crystal system	monoclinic	triclinic	monoclinic	triclinic	triclinic
Space group	C 2/c	P -1	P 2 <sub>1</sub> /n	P -1	P -1
a(Å)	9.5916(10)	9.4362(7)	9.3714(5)	13.5226(11)	9.5054(9)
b(Å)	33.666(3)	10.7558(7)	19.4868(8)	13.8481(12)	10.9145(9)
c(Å)	13.3219(13)	17.0271(12)	11.0351(5)	17.2604(14)	16.8808(15)
$\alpha$ (°)	90	103.204(2)	90	108.274(2)	102.075(3)
$\beta$ (°)	105.255(3)	94.650(2)	101.532(2)	91.973(3)	94.212(3)



$\gamma(^{\circ})$	90	93.872(2)	90	98.645(3)	94.230(3)
$V(\text{\AA}^3)$	4150.2(7)	1670.3(2)	1974.53(16)	3022.9(4)	1700.8(3)
Z	16	2	4	2	2
$d(\text{g}\cdot\text{cm}^{-3})$	1.581	1.556	1.393	1.324	1.482
F(000)	2048	796	876	1260	778
$m(\text{cm}^{-1})$	1.839	3.377	1.024	1.912	2.294
Absorption corrections	multi-scan; 0.6496 min, 0.7456 max	multi-scan; 0.6046 min, 0.7456 max	multi-scan; 0.6347 min, 0.7456 max	multi-scan;	multi-scan;
Diffractometer	Kappa APEX II	Kappa APEX II	Kappa APEX II	Kappa APEX II	Kappa APEX II
X-ray source	MoK $\alpha$	MoK $\alpha$	MoK $\alpha$	MoK $\alpha$	MoK $\alpha$
$\lambda(\text{\AA})$	0.71069	0.71069	0.71073	0.71069	0.71069
Monochromator	graphite	graphite	graphite	graphite	graphite
T (K)	150.0(1)	150.0(1)	150.0(1)	150.0(1)	150.0(1)
Scan mode	phi and omega scans	phi and omega scans	phi and omega scans	phi and omega scans	phi and omega scans
Maximum $q$	25.68	26.369	27.500	27.761	27.558
HKL ranges	-11 11 ; -40 40 ; -13 16	-11 11 ; -13 13 ; -21 21	-12 12 ; -25 25 ; -14 14	-17 17 ; -18 18 ; -22 22	-12 12 ; -14 14 ; -21 21
Reflections measured	13457	26666	22085	81992	47095
Unique data	3910	6781	4536	14057	7841
Rint	0.0379	0.045	0.0438	0.0735	0.0524
Reflections used	3204	6241	3695	11914	7102
Criterion	$I > 2(I)$	$I > 2\sigma(I)$	$I > 2\sigma(I)$	$I > 2\sigma(I)$	$I > 2\sigma(I)$
Refinement type	Fsqd	Fsqd	Fsqd	Fsqd	Fsqd
Hydrogen atoms	constr	constr	constr	constr	constr
Parameters refined	275	404	236	695	427
Reflections / parameter	11	15	15	17	16
wR2	0.0793	0.0588	0.0893	0.1009	0.0884
Flack's parameter	0.0308	0.0236	0.0348	0.0337	0.0246
Weights a, b	0.0391 ; 2.5054	0.0346 ; 0.1167	0.0401 ; 1.0318	0.0611 ; 1.5090	0.1000 ; 0.0000
GoF	1.038	0.945	1.030	1.025	0.722
difference peak / hole ( $e \text{\AA}^{-3}$ )	0.376(0.062) / - 0.244(0.062)	0.538(0.092) / - 0.427(0.092)	0.410(0.059) / - 0.369(0.059)	1.247(0.092) / - 0.851(0.092)	0.509(0.081) / - 0.410(0.081)

## Chapter III

**Table S22.** Crystallographic data for **1**.

	<b>1</b>
Molecular formula	'C <sub>10</sub> H <sub>6</sub> F <sub>6</sub> N <sub>4</sub> Ni'
Molecular weight	354.9
Crystal habit	yellow needle

Crystal dimensions(mm)	0.520x0.140x0.100
Crystal system	monoclinic
Space group	P 2 <sub>1</sub> /c
a(Å)	7.8265(3)
b(Å)	10.2257(4)
c(Å)	14.5532(6)
a(°)	90
b(°)	98.879(1)
g(°)	90
V(Å <sup>3</sup> )	1150.76(8)
Z	4
d(g-cm <sup>-3</sup> )	2.048
F(000)	704
m(cm <sup>-1</sup> )	1.764
Absorption corrections	multi-scan; 0.6091 min, 0.7456 max
Diffractometer	Kappa APEX II
X-ray source	MoKa
I(Å)	0.71069
Monochromator	graphite
T (K)	150.0(1)
Scan mode	phi and omega scans
Maximum q	27.605
HKL ranges	-10 7 ; -13 13 ; -18 18
Reflections measured	19484
Unique data	2658
Rint	0.042
Reflections used	2453
Criterion	I > 2σI)
Refinement type	Fsqd
Hydrogen atoms	constr
Parameters refined	190
Reflections / parameter	12
wR2	0.0568
R1	0.0213
Weights a, b	0.0239 ; 0.6802
GoF	1.057
difference peak / hole (e Å <sup>-3</sup> )	0.359(0.055) / -0.285(0.055)

**Table S23.** Crystallographic data for **2** and **3**.

	<b>2</b>	<b>3</b>
Empirical formula	C <sub>17</sub> H <sub>16</sub> F <sub>6</sub> N <sub>4</sub> NiO	C <sub>15</sub> H <sub>10</sub> F <sub>6</sub> KN <sub>5</sub> Ni
Formula weight	465.05	472.09
Temperature/K	150.01	150.0
Crystal system	triclinic	monoclinic
Space group	P-1	P2 <sub>1</sub> /c
a/Å	9.072(2)	10.9337(17)
b/Å	9.323(2)	7.6373(11)
c/Å	10.604(3)	20.781(3)

$\alpha/^\circ$	88.427(8)	90
$\beta/^\circ$	88.169(8)	91.825(4)
$\gamma/^\circ$	78.873(8)	90
Volume/ $\text{\AA}^3$	879.4(4)	1734.5(4)
Z	2	4
$\rho_{\text{calc}}/\text{g/cm}^3$	1.756	1.808
$\mu/\text{mm}^{-1}$	1.182	1.431
F(000)	472.0	944.0
Crystal size/ $\text{mm}^3$	$0.3 \times 0.1 \times 0.06$	$0.2 \times 0.11 \times 0.02$
Radiation	MoK $\alpha$ ( $\lambda = 0.71073$ )	MoK $\alpha$ ( $\lambda = 0.71073$ )
2 $\theta$ range for data collection/ $^\circ$	5.742 to 57.396	5.496 to 52.042
Index ranges	$-12 \leq h \leq 12, -12 \leq k \leq 12, -14 \leq l \leq 14$	$-13 \leq h \leq 13, -9 \leq k \leq 9, -24 \leq l \leq 25$
Reflections collected	23794	26118
Independent reflections	4541 [ $R_{\text{int}} = 0.0722, R_{\text{sigma}} = 0.0615$ ]	3430 [ $R_{\text{int}} = 0.1163, R_{\text{sigma}} = 0.0835$ ]
Data/restraints/parameters	4541/0/266	3430/0/254
Goodness-of-fit on $F^2$	1.079	1.015
Final R indexes [ $ I  > 2\sigma(I)$ ]	$R_1 = 0.0567, wR_2 = 0.1543$	$R_1 = 0.0429, wR_2 = 0.0815$
Final R indexes [all data]	$R_1 = 0.0832, wR_2 = 0.1699$	$R_1 = 0.0924, wR_2 = 0.0962$
Largest diff. peak/hole / $e \text{\AA}^{-3}$	1.19/-0.69	0.51/-0.58

## Chapter IV

**Table S24.** Crystallographic data for compounds **1 - 6**.

	<b>1</b>	<b>2</b>	<b>3</b>	<b>4</b>	<b>5</b>	<b>6</b>
Empirical formula	$\text{C}_{17}\text{H}_{21}\text{KN}_4\text{Ni}$	$\text{C}_{84}\text{H}_{117}\text{N}_8\text{O}_3\text{Y}$	$\text{C}_{100}\text{H}_{161}\text{K}_3\text{N}_8\text{N}$	$\text{C}_{50}\text{H}_{73}\text{K}_2\text{N}_8\text{N}$	$\text{C}_{94}\text{H}_{144}\text{K}_2\text{N}_8\text{Ni}$	$\text{C}_{62}\text{H}_{98}\text{K}_4\text{N}_8\text{Ni}_2$
Formula weight	395.19	1805.97	2152.16	1173.78	2135.86	1373.3
Temperature/K	150.15	150.0	150.01	150.0	150.0	150.0
Crystal system	monoclinic	tetragonal	triclinic	triclinic	triclinic	monoclinic
Space group	$P2_1/n$	$I4/m$	P-1	P-1	P-1	$P2_1/n$
a/ $\text{\AA}$	13.7210(7)	26.3931(15)	15.4720(13)	13.9055(13)	17.575(6)	14.7527(11)
b/ $\text{\AA}$	7.1655(4)	26.3931(15)	18.3028(16)	14.5462(13)	17.768(6)	17.6187(14)
c/ $\text{\AA}$	18.9082(8)	22.8754(13)	20.4081(17)	16.4926(15)	18.319(6)	26.226(2)
$\alpha/^\circ$	90	90	98.073(2)	93.346(3)	111.847(7)	90
$\beta/^\circ$	106.036(5)	90	102.959(2)	104.115(3)	101.994(9)	96.607(2)
$\gamma/^\circ$	90	90	99.279(3)	118.509(3)	95.118(10)	90
Volume/ $\text{\AA}^3$	1786.68(16)	15935(2)	5463.8(8)	2782.5(4)	5106(3)	6771.5(9)
Z	4	8	2	2	2	4
$\rho_{\text{calc}}/\text{g/cm}^3$	1.469	1.506	1.308	1.401	1.389	1.347
$\mu/\text{mm}^{-1}$	1.330	3.544	2.200	0.892	2.319	0.86
F(000)	824.0	7288.0	2236.0	1238.0	2204.0	2920
Crystal size/ $\text{mm}^3$	$0.32 \times 0.2 \times 0.1$	$0.34 \times 0.25 \times 0.12$	$0.22 \times 0.1 \times 0.04$	$0.32 \times 0.32 \times 0.15$	$0.12 \times 0.12 \times 0.04$	$0.26 \times 0.18 \times 0.12$

Radiation	MoK $\alpha$ ( $\lambda$ = 0.71073)	MoK $\alpha$ ( $\lambda$ = 0.71069)	MoK $\alpha$ ( $\lambda$ = 0.71073)	MoK $\alpha$ ( $\lambda$ = 0.71073)	MoK $\alpha$ ( $\lambda$ = 0.71073)	MoK $\alpha$ ( $\lambda$ = 0.71073)
2 $\theta$ range for data collection/ $^{\circ}$	4.482 to 60.054	4.712 to 60.154	2.294 to 54.97	2.602 to 61.998	2.41 to 52.044	3.888 to 52.044
Index ranges	-19 $\leq$ h $\leq$ 19, -10 $\leq$ k $\leq$ 10, -26 $\leq$ l $\leq$ 26	-37 $\leq$ h $\leq$ 37, -37 $\leq$ k $\leq$ 37, -32 $\leq$ l $\leq$ 32	-20 $\leq$ h $\leq$ 20, -23 $\leq$ k $\leq$ 23, -26 $\leq$ l $\leq$ 26	-20 $\leq$ h $\leq$ 20, -21 $\leq$ k $\leq$ 21, -23 $\leq$ l $\leq$ 23	-21 $\leq$ h $\leq$ 20, -21 $\leq$ k $\leq$ 21, -22 $\leq$ l $\leq$ 22	-18 $\leq$ h $\leq$ 17, -21 $\leq$ k $\leq$ 21, -32 $\leq$ l $\leq$ 30
Reflections collected	85107	326142	188869	117733	55476	75848
Independent reflections	5228 [R <sub>int</sub> = 0.0586, R <sub>sigma</sub> = 0.0263]	11978 [R <sub>int</sub> = 0.1064, R <sub>sigma</sub> = 0.0343]	25047 [R <sub>int</sub> = 0.0902, R <sub>sigma</sub> = 0.0600]	17709 [R <sub>int</sub> = 0.0609, R <sub>sigma</sub> = 0.0431]	20057 [R <sub>int</sub> = 0.1761, R <sub>sigma</sub> = 0.2547]	13329 [R <sub>int</sub> = 0.0899, R <sub>sigma</sub> = 0.0738]
Data/restraints/parameters	5228/36/238	11978/54/487	25047/307/126	17709/0/671	20057/598/1071	13329/892/1000
Goodness-of-fit on F <sup>2</sup>	1.081	1.167	1.055	1.036	1.055	1.117
Final R indexes [ $>=2\sigma$ (I)]	R <sub>1</sub> = 0.0535, wR <sub>2</sub> = 0.1330	R <sub>1</sub> = 0.0376, wR <sub>2</sub> = 0.0788	R <sub>1</sub> = 0.0411, wR <sub>2</sub> = 0.0836	R <sub>1</sub> = 0.0460, wR <sub>2</sub> = 0.1094	R <sub>1</sub> = 0.1174, wR <sub>2</sub> = 0.3150	R <sub>1</sub> = 0.0672, wR <sub>2</sub> = 0.1401
Final R indexes [all data]	R <sub>1</sub> = 0.0667, wR <sub>2</sub> = 0.1429	R <sub>1</sub> = 0.0738, wR <sub>2</sub> = 0.0992	R <sub>1</sub> = 0.0777, wR <sub>2</sub> = 0.1013	R <sub>1</sub> = 0.0786, wR <sub>2</sub> = 0.1276	R <sub>1</sub> = 0.2209, wR <sub>2</sub> = 0.3805	R <sub>1</sub> = 0.1160, wR <sub>2</sub> = 0.1589
Largest diff. peak/hole / e $\text{\AA}^{-3}$	1.84/-0.58	2.59/-2.00	2.45/-1.37	2.55/-0.68	4.70/-2.54	0.72/-0.45

**Table S25.** Crystallographic data for **7**.

<b>7</b>	
Empirical formula	C <sub>94</sub> H <sub>144</sub> K <sub>2</sub> N <sub>8</sub> Ni <sub>2</sub> O <sub>13</sub> Sm <sub>2</sub>
Formula weight	2090.48
Temperature/K	150.0
Crystal system	triclinic
Space group	P-1
a/ $\text{\AA}$	17.715(2)
b/ $\text{\AA}$	17.832(2)
c/ $\text{\AA}$	18.341(2)
$\alpha$ / $^{\circ}$	111.868(3)
$\beta$ / $^{\circ}$	102.060(3)
$\gamma$ / $^{\circ}$	95.076(4)
Volume/ $\text{\AA}^3$	5169.2(11)
Z	2
$\rho_{\text{calc}}$ /cm <sup>3</sup>	1.343
$\mu$ /mm <sup>-1</sup>	1.617
F(000)	2172.0
Crystal size/mm <sup>3</sup>	0.38 $\times$ 0.2 $\times$ 0.14
Radiation	MoK $\alpha$ ( $\lambda$ = 0.71073)
2 $\theta$ range for data collection/ $^{\circ}$	2.478 to 52.044
Index ranges	-21 $\leq$ h $\leq$ 21, -22 $\leq$ k $\leq$ 22, -22 $\leq$ l $\leq$ 22

Reflections collected	141065
Independent reflections	20326 [ $R_{\text{int}} = 0.0898$ , $R_{\text{sigma}} = 0.0606$ ]
Data/restraints/parameters	20326/372/1093
Goodness-of-fit on $F^2$	1.113
Final R indexes [ $I \geq 2\sigma(I)$ ]	$R_1 = 0.0869$ , $wR_2 = 0.2043$
Final R indexes [all data]	$R_1 = 0.1370$ , $wR_2 = 0.2453$
Largest diff. peak/hole / $e \text{ \AA}^{-3}$	2.99/-1.85

Comments on the way the structures were solved:

A solvent mask was used for the structures of **2**, **3** and **5**.

In **2**, 422 electrons were found in a volume of  $1064 \text{ \AA}^3$  in 3 voids per unit cell. This is consistent with the presence of 1.5  $[\text{C}_4\text{H}_{10}\text{O}]$  per asymmetric unit, which account for 504 electrons per unit cell.

In **3**, 28 electrons were found in a volume of  $477 \text{ \AA}^3$  in 2 voids per unit cell. This is consistent with the presence of 0.333  $[\text{C}_4\text{H}_{10}\text{O}]$  per asymmetric unit, which account for 28 electrons per unit cell.

In **5**, 152 electrons were found in a volume of  $476 \text{ \AA}^3$  in 2 voids per unit cell. This is consistent with the presence of 2  $[\text{C}_4\text{H}_{10}\text{O}]$  per asymmetric unit, which account for 168 electrons per unit cell.

Moreover, after several crystallization and acquisition tries, no better data set was recorded for compound **5**. We choose however to present it as a qualitative characterization while taking care not to expect too much precision on the distances observed. Two A alerts and three B alerts are signaled by checkcif and are all resulting from the lack of data at high angle.

## Chapter V

**Table S26.** Crystallographic data for **1**, **2**, **3**, **4**, **5** and **6**.

	<b>1</b>	<b>2</b>	<b>3</b>	<b>4</b>	<b>5</b>	<b>6</b>
Empirical formula	$\text{C}_{27.25}\text{H}_{23.25}\text{N}_{5.25}$ Ni	$\text{C}_{66}\text{H}_{102}\text{N}_4\text{O}_3$ Sm	$\text{C}_{136}\text{H}_{176}\text{N}_8\text{Ni}$ Yb <sub>2</sub>	$\text{C}_{85}\text{H}_{106}\text{N}_4\text{OS}$ m <sub>2</sub>	$\text{C}_{49}\text{H}_{75}\text{K}_2\text{N}_4\text{Ni}$ O <sub>13</sub>	$\text{C}_{27}\text{H}_{29}\text{BN}_4\text{Ni}$ O <sub>2</sub>
Formula weight	482.97	1149.86	2327.63	1500.43	1065.04	511.06
Temperature/K	150.0	150.0	150.01	150.0	150.0	149.99
Crystal system	triclinic	triclinic	triclinic	triclinic	monoclinic	triclinic
Space group	P-1	P-1	P-1	P-1	P2 <sub>1</sub> /n	P-1
a/Å	8.6656(9)	14.3037(10)	15.9987(14)	14.3925(17)	12.0484(11)	6.448(3)
b/Å	14.7651(14)	14.5048(10)	21.3236(19)	15.4233(18)	24.786(2)	11.804(6)
c/Å	18.2785(18)	16.7050(12)	24.457(2)	20.161(2)	17.9579(12)	16.532(8)
$\alpha^\circ$	70.879(3)	80.151(2)	77.224(3)	73.604(4)	90	97.780(15)
$\beta^\circ$	84.748(3)	68.232(2)	71.562(3)	88.206(4)	93.667(4)	99.494(14)
$\gamma^\circ$	87.200(3)	89.719(2)	69.920(2)	63.953(3)	90	105.117(14)
Volume/Å <sup>3</sup>	2200.0(4)	3164.8(4)	7374.5(11)	3834.9(8)	5351.8(8)	1176.9(10)
Z	4	2	2	2	4	2

$\rho_{\text{calc}}/\text{cm}^3$	1.458	1.207	1.048	1.299	1.322	1.442
$\mu/\text{mm}^{-1}$	0.909	0.973	1.427	1.562	0.582	0.858
F(000)	1006.0	1224.0	2432.0	1552.0	2268.0	536.0
Crystal size/ $\text{mm}^3$	$0.31 \times 0.25 \times 0.05$	$0.76 \times 0.21 \times 0.12$	$0.28 \times 0.22 \times 0.08$	$0.48 \times 0.05 \times 0.01$	$0.32 \times 0.18 \times 0.12$	$0.24 \times 0.06 \times 0.02$
Radiation	MoK $\alpha$ ( $\lambda = 0.71073$ )	MoK $\alpha$ ( $\lambda = 0.71073$ )	MoK $\alpha$ ( $\lambda = 0.71073$ )	MoK $\alpha$ ( $\lambda = 0.71073$ )	MoK $\alpha$ ( $\lambda = 0.71073$ )	MoK $\alpha$ ( $\lambda = 0.71073$ )
2 $\theta$ range for data collection/ $^\circ$	4.684 to 60.068	5.196 to 68.676	1.77 to 55.318	5.32 to 55.238	2.804 to 50.054	4.03 to 50.054
Index ranges	$-12 \leq h \leq 12,$ $20 \leq k \leq 20,$ $25 \leq l \leq 25$	$-22 \leq h \leq 22,$ $-23 \leq k \leq 23,$ $-26 \leq l \leq 26$	$-20 \leq h \leq 20,$ $-27 \leq k \leq 27,$ $-31 \leq l \leq 31$	$-18 \leq h \leq 18,$ $-20 \leq k \leq 20,$ $-26 \leq l \leq 26$	$-14 \leq h \leq 14,$ $28 \leq k \leq 29,$ $18 \leq l \leq 21$	$-7 \leq h \leq 7,$ $-9 \leq k \leq 14,$ $-19 \leq l \leq 19$
Reflections collected	76196	99700	199803	106413	51334	17883
Independent reflections	12857 [ $R_{\text{int}} = 0.0761,$ $R_{\text{sigma}} = 0.0481]$	26452 [ $R_{\text{int}} = 0.0880,$ $R_{\text{sigma}} = 0.0818]$	34110 [ $R_{\text{int}} = 0.0851,$ $R_{\text{sigma}} = 0.0710]$	17711 [ $R_{\text{int}} = 0.0961,$ $R_{\text{sigma}} = 0.0859]$	9454 [ $R_{\text{int}} = 0.1345,$ $R_{\text{sigma}} = 0.1058]$	4143 [ $R_{\text{int}} = 0.1479,$ $R_{\text{sigma}} = 0.1486]$
Data/restraints/parameters	12857/0/618	26452/80/720	34110/780/1602	17711/288/934	9454/816/832	4143/0/321
Goodness-of-fit on $F^2$	1.017	1.021	1.025	1.013	0.964	0.995
Final R indexes [ $l > 2\sigma(l)$ ]	$R_1 = 0.0376,$ $wR_2 = 0.0853$	$R_1 = 0.0415,$ $wR_2 = 0.0867$	$R_1 = 0.0573,$ $wR_2 = 0.1347$	$R_1 = 0.0438,$ $wR_2 = 0.0967$	$R_1 = 0.0763,$ $wR_2 = 0.1842$	$R_1 = 0.0732,$ $wR_2 = 0.1556$
Final R indexes [all data]	$R_1 = 0.0630,$ $wR_2 = 0.0982$	$R_1 = 0.0651,$ $wR_2 = 0.0980$	$R_1 = 0.0925,$ $wR_2 = 0.1528$	$R_1 = 0.0906,$ $wR_2 = 0.1142$	$R_1 = 0.1603,$ $wR_2 = 0.2447$	$R_1 = 0.1438,$ $wR_2 = 0.1902$
Largest diff. peak/hole / $e \text{ \AA}^{-3}$	0.47/-0.43	1.65/-1.57	2.11/-1.55	0.81/-1.87	0.59/-0.43	1.04/-0.82

## Reference

- (1) Walter, M. D.; Schultz, M.; Andersen, R. A. Weak Paramagnetism in Compounds of the Type Cp<sup>2</sup>Yb(Bipy). *New J. Chem.* **2006**, *30* (2), 238–246. <https://doi.org/10.1039/B512865J>.
- (2) Neese, F. The ORCA Program System. *WIREs Comput. Mol. Sci.* **2012**, *2* (1), 73–78. <https://doi.org/10.1002/wcms.81>.
- (3) Perdew, J. P.; Burke, K.; Ernzerhof, M. Generalized Gradient Approximation Made Simple [Phys. Rev. Lett. 77, 3865 (1996)]. *Phys. Rev. Lett.* **1997**, *78* (7), 1396–1396. <https://doi.org/10.1103/PhysRevLett.78.1396>.
- (4) Adamo, C.; Barone, V. Toward Reliable Density Functional Methods without Adjustable Parameters: The PBE0 Model. *J. Chem. Phys.* **1999**, *110* (13), 6158–6170. <https://doi.org/10.1063/1.478522>.
- (5) Tao, J.; Perdew, J. P.; Staroverov, V. N.; Scuseria, G. E. Climbing the Density Functional Ladder: Nonempirical Meta-Generalized Gradient Approximation Designed for Molecules and Solids. *Phys. Rev. Lett.* **2003**, *91* (14), 146401. <https://doi.org/10.1103/PhysRevLett.91.146401>.
- (6) Vydrov, O. A.; Scuseria, G. E. Assessment of a Long-Range Corrected Hybrid Functional. *J. Chem. Phys.* **2006**, *125* (23), 234109. <https://doi.org/10.1063/1.2409292>.
- (7) Weigend, F.; Ahlrichs, R. Balanced Basis Sets of Split Valence, Triple Zeta Valence and Quadruple Zeta Valence Quality for H to Rn: Design and Assessment of Accuracy. *Phys. Chem. Chem. Phys.* **2005**, *7* (18), 3297–3305. <https://doi.org/10.1039/B508541A>.
- (8) Weigend, F. Accurate Coulomb-Fitting Basis Sets for H to Rn. *Phys. Chem. Chem. Phys.* **2006**, *8* (9), 1057–1065. <https://doi.org/10.1039/B515623H>.
- (9) Pantazis, D. A.; Chen, X.-Y.; Landis, C. R.; Neese, F. All-Electron Scalar Relativistic Basis Sets for Third-Row Transition Metal Atoms. *J. Chem. Theory Comput.* **2008**, *4* (6), 908–919. <https://doi.org/10.1021/ct800047t>.
- (10) Pantazis, D. A.; Neese, F. All-Electron Scalar Relativistic Basis Sets for the Lanthanides. *J. Chem. Theory Comput.* **2009**, *5* (9), 2229–2238. <https://doi.org/10.1021/ct900090f>.
- (11) Grimme, S.; Antony, J.; Ehrlich, S.; Krieg, H. A Consistent and Accurate Ab Initio Parametrization of Density Functional Dispersion Correction (DFT-D) for the 94 Elements H–Pu. *J. Chem. Phys.* **2010**, *132* (15), 154104. <https://doi.org/10.1063/1.3382344>.
- (12) Adamo, C.; Barone, V. Toward Reliable Density Functional Methods without Adjustable Parameters: The PBE0 Model. *J. Chem. Phys.* **1999**, *110* (13), 6158–6170. <https://doi.org/10.1063/1.478522>.
- (13) Chai, J.-D.; Head-Gordon, M. Systematic Optimization of Long-Range Corrected Hybrid Density Functionals. *J. Chem. Phys.* **2008**, *128* (8), 084106. <https://doi.org/10.1063/1.2834918>.
- (14) Marenich, A. V.; Cramer, C. J.; Truhlar, D. G. Universal Solvation Model Based on Solute Electron Density and on a Continuum Model of the Solvent Defined by the Bulk Dielectric Constant and Atomic Surface Tensions. *J. Phys. Chem. B* **2009**, *113* (18), 6378–6396. <https://doi.org/10.1021/jp810292n>.
- (15) Kaschube, W.; Pörschke, K. R.; Wilke, G. tmeda-Nickel-Komplexe: III. (N,N,N',N'-Tetramethylethylendiamin)-(dimethyl)nickel(II). *J. Organomet. Chem.* **1988**, *355* (1), 525–532. [https://doi.org/10.1016/0022-328X\(88\)89050-8](https://doi.org/10.1016/0022-328X(88)89050-8).
- (16) Tilley, T. D.; Boncella, J. M.; Berg, D. J.; Burns, C. J.; Andersen, R. A.; Lawless, G. A.; Edelman, M. A.; Lappert, M. F. Bis[Bis(Trimethylsilyl)Amido]Bis(Diethyl Ether)Ytterbium and (Diethyl Ether)Bis(H5-Pentamethylcyclopentadienyl)Ytterbium. In *Inorganic Syntheses*; John Wiley & Sons, Ltd, 2007; pp 146–150. <https://doi.org/10.1002/9780470132586.ch27>.
- (17) Tilley, T. D.; Andersen, R. A.; Spencer, B.; Ruben, H.; Zalkin, A.; Templeton, D. H. Divalent Lanthanide Chemistry. Bis (Pentamethylcyclopentadienyl) Europium(II) and -Ytterbium(II) Derivatives: Crystal Structure of Bis (Pentamethylcyclopentadienyl) (Tetrahydrofuran Ytterbium(II) -Hemitoluene at 176 K. *Inorg. Chem.* **1980**, *19* (10), 2999–3003. <https://doi.org/10.1021/ic50212a031>.

- (18) Zhang, C.-P.; Wang, H.; Klein, A.; Biewer, C.; Stirnat, K.; Yamaguchi, Y.; Xu, L.; Gomez-Benitez, V.; Vivic, D. A. A Five-Coordinate Nickel(II) Fluoroalkyl Complex as a Precursor to a Spectroscopically Detectable Ni(III) Species. *J. Am. Chem. Soc.* **2013**, *135* (22), 8141–8144. <https://doi.org/10.1021/ja4030462>.
- (19) Haga, M.; Ishizuya, M.; Kanetsugi, T.; Yutaka, T.; Sakiyama, D.; Fees, J.; Kaim, W. Synthesis and Formation of Dinuclear Mixed-Valent Complexes of Ruthenium and Osmium Bridged by 2-(2-Pyrimidyl)Benzimidazolate. *Indian J. Chem.-Sect. A* **2003**, *42A* (9), 2290–2299.
- (20) Dehmlow, E. V.; Bollmann, C. Verbesserte Präparative Darstellung von Polyisopropyl- Und Poly-Tert-Butylcyclopentadienen / Improved Preparation of Polyisopropyl- and -Tert-Butylcyclopentadienes. *Z. Für Naturforschung B* **1993**, *48* (4), 457–460. <https://doi.org/10.1515/znb-1993-0410>.
- (21) Jaroschik, F.; Nief, F.; Ricard, L. Synthesis of a New Stable, Neutral Organothulium(II) Complex by Reduction of a Thulium(III) Precursor. *Chem. Commun.* **2006**, No. 4, 426–428. <https://doi.org/10.1039/B514818A>.
- (22) Sheldrick, G. M. SHELXT– Integrated Space-group and Crystal-structure Determination. *Acta Crystallogr. Sect. Found. Adv.* **2015**, *71*, 3–8. <https://doi.org/10.1107/S2053273314026370>.
- (23) Sheldrick, G. M. A Short History of SHELX. *Acta Crystallogr. A* **2008**, *64*, 112–122. <https://doi.org/10.1107/S0108767307043930>.
- (24) Sheldrick, G. M. Crystal Structure Refinement with SHELXL. *Acta Crystallogr. Sect. C Struct. Chem.* **2015**, *71*, 3–8. <https://doi.org/10.1107/S2053229614024218>.
- (25) Spek, A. L. Single-Crystal Structure Validation with the Program PLATON. *J. Appl. Crystallogr.* **2003**, *36*, 7–13. <https://doi.org/10.1107/S0021889802022112>.
- (26) Dolomanov, O. V.; Bourhis, L. J.; Gildea, R. J.; Howard, J. a. K.; Puschmann, H. OLEX2: A Complete Structure Solution, Refinement and Analysis Program. *J. Appl. Crystallogr.* **2009**, *42* (2), 339–341. <https://doi.org/10.1107/S0021889808042726>.







C

## Published articles



Article

# Reactive Heterobimetallic Complex Combining Divalent Ytterbium and Dimethyl Nickel Fragments

Ding Wang, Jules Moutet, Maxime Tricoire, Marie Cordier  and Grégory Nocton \* 

LCM, CNRS, Ecole Polytechnique, IP Paris, Route de Saclay, 91128 Palaiseau, France; ding.wang@polytechnique.edu (D.W.); jules.moutet@polytechnique.edu (J.M.); maxime.tricoire@polytechnique.edu (M.T.); marie.cordier@polytechnique.edu (M.C.)

\* Correspondence: greg.nocton@polytechnique.edu; Tel.: +33-1-6933-4402

Received: 8 March 2019; Accepted: 17 April 2019; Published: 26 April 2019



**Abstract:** This article presented the synthesis and characterization of original heterobimetallic species combining a divalent lanthanide fragment and a divalent nickel center bridged by the bipyrimidine ligand, a redox-active ligand. X-ray crystal structures were obtained for the Ni monomer (bipym)NiMe<sub>2</sub>, **1**, as well as the heterobimetallic dimer compounds, Cp\*<sub>2</sub>Yb(bipym)NiMe<sub>2</sub>, **2**, along with <sup>1</sup>H solution NMR, solid-state magnetic data, and DFT calculations only for **1**. The reactivity with CO was investigated on both compounds and the stoichiometric acetone formation is discussed based on kinetic and mechanistic studies. The key role of the lanthanide fragment was demonstrated by the relatively slow CO migratory insertion step, which indicated the stability of the intermediate.

**Keywords:** divalent lanthanides; redox non-innocent ligand; magnetism; CO insertion

## 1. Introduction

Heterometallic complexes are important objects of study because both metallic fragments have a role to play in the chemical reaction and/or properties of interest [1–3]. In nature, the active sites of many enzymes are bimetallic, and the understanding of the role of each metallic part is crucial to the design of appropriate models [4–7]. In some cases, the role of one fragment is purely structural and only facilitates the reaction at the other metal center, while in most cases, both fragments have a role and either participate in the fate of the chemical reaction or complete it [8]. This particular case was extensively studied in terms of the tandem-reaction catalysts, where, for example, one metal is the source of one reaction, the other of a second one, and the substrate undergoes two chemical transformations in one pot [9–12]. Another elegant use of the bimetallic complexes is found in the chemical cooperation between both metal fragments, allowing a reactivity that would not occur efficiently with only one of these taken separately [13]. The recent interest in photochemically active bimetallic complexes is witness to these developments [14,15].

In our group, we designed bimetallic complexes with a slightly different approach. We combined a reductive divalent lanthanide fragment with a transition metal fragment, which possessed a ligand that could be eventually reduced or oxidized upon coordination. These studies have recently led us to develop a system with Pd and the bipyrimidine ligand (bipym) in which the palladium can be stabilized at the Pd<sup>IV</sup> for several hours at room temperature [16]. This result was rendered possible using divalent ytterbium, which can reduce the palladium/bipym complex and have an impact on the overall electronic structure of the bimetallic assembly. Thus, the two metallic fragments cooperate by means of their electronic correlation. The use of divalent lanthanide is purposeful, since as they are strong single electron reductants [17–20], the divalent lanthanides adapt their electronic structures depending on the ligand that is used and form multiconfigurational electronic states [21–23], which allow the tuning of their properties with the redox-active ligand [24–29].

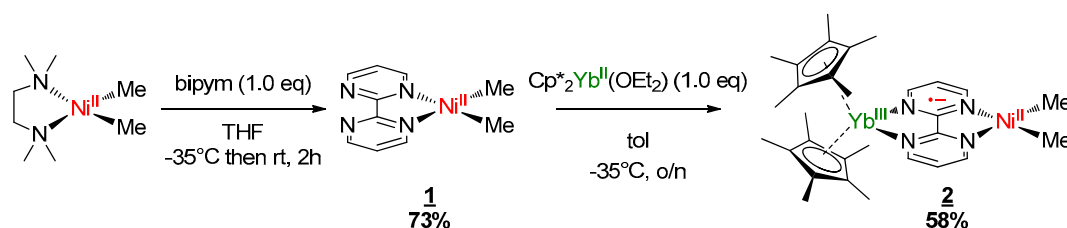
High oxidation states such as Pd<sup>IV</sup> or Ni<sup>IV</sup> are actively sought after because of their scarcity, but also because they allow important reactions [30–34]. Notably, the oxidative addition from Pd<sup>II</sup> or Ni<sup>II</sup> centers is an important step because it may avoid the difficult use of low-valence Pd and Ni species as catalysts, and their electrophilic character could also prevent the use of other electrophile metal fragments which have less-abundant resources, such as Rh, Ir, or Pt [35,36]. For example, methanol is transformed to acetic acid using carbon monoxide (CO) in a reaction that uses Ir (Cativa) [37,38] or Pt (Monsanto) [39] catalysts. In these reactions, the crucial step of CO insertion is performed after the oxidative addition at the high oxidation state of the metal center [40].

In this work, we developed a new complex that possesses a Ni metal center and bipym as the ligand and combined it with the Cp\*<sub>2</sub>Yb divalent lanthanide fragment. The synthesis and characterization of the bimetallic complex is presented, as well as reactivity studies implying CO insertion.

## 2. Results and Discussions

### 2.1. Synthesis and X-ray Diffraction

Complexes **1** and **2** were synthesized according to similar published procedures for similar Pd complexes (Scheme 1) [16]. The (tmeda)NiMe<sub>2</sub> [41] was suitable for the ligand exchange in THF with bipyrimidine (bipym) and the reaction yielded (bipym)NiMe<sub>2</sub> (**1**) as dark X-ray-suitable crystals in good yield after the solution was cooled to −35 °C. Note that this synthesis method avoided the formation of the (bipym)(NiMe<sub>2</sub>)<sub>2</sub> dimer as well as free bipym, which are both very problematic for the next step. An Oak Ridge Thermal Ellipsoid Plot (ORTEP) of **1** is shown in Figure 1, and the main metric parameters are available in Supplementary Materials. Complex **1** was dissolved in toluene and cooled down to −35 °C and the addition of a room temperature toluene solution of the Cp\*<sub>2</sub>Yb(OEt<sub>2</sub>) complex led to a dark-brown solution, which yielded X-ray-suitable dark-brown crystals of the heterobimetallic dimer Cp\*<sub>2</sub>Yb(bipym)NiMe<sub>2</sub>, **2**, when cooled down to −35 °C. An ORTEP is shown in Figure 1, and the main metric parameters are available in the Supplementary Materials. Comparing the solid-state structures of **1** and **2**, the first noteworthy feature is the C4–C5 distance, which was strongly reduced in **2** (1.403(4) Å) compared to that in **1** (1.482(5) Å). This is similar to the observation made with the Pd complex [16] and is due to an electron transfer from the ytterbium center that reduced the bipyrimidine ligand. Accordingly, the average Cp centroid–Yb distance was 2.31(1) Å, which is lower than that when the fragment is divalent and similar to that when it is trivalent [25]. The Ni–N (1.959(2) and 1.956(3) Å) and Ni–C (1.930(3) and 1.925(1) Å) average distances were similar in both **1** and **2**, respectively, which is indicative of a similar oxidation state in both complexes.



**Scheme 1.** Synthesis of the bimetallic complex. bipym: bipyrimidine ligand.

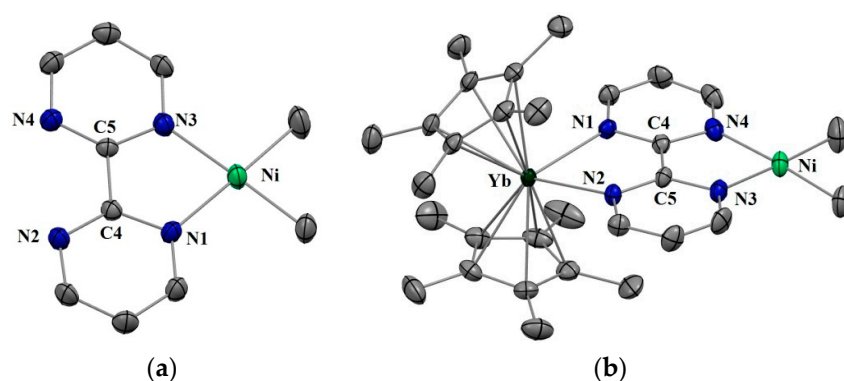


**Figure 1.** (a) Oak Ridge Thermal Ellipsoid Plot (ORTEP) of (bipym)NiMe<sub>2</sub> (**1**) (only one of the molecules of the cell is shown) (b) ORTEP of Cp\*<sub>2</sub>Yb(bipym)NiMe<sub>2</sub> (**2**). Hydrogen atoms have been removed for clarity and thermal ellipsoids are at the 50% level.

## 2.2. Solution NMR and Solid-State Magnetism

The <sup>1</sup>H NMR of **1** showed only four signals: three for the bipym ligand, integrating each for two protons, and one for the methyl fragments, integrating for six protons, in good agreement with a C<sub>2v</sub> symmetry in solution. In **1**, all signals were found in the typical diamagnetic range. The <sup>1</sup>H NMR of **2** at 253 K in tol-*d*<sub>8</sub> was very different: three signals integrated for two protons at 272.67, 5.39, and −160.45 ppm, one signal integrated for six protons at 15.03 ppm, and one for 30 protons at 6.59 ppm (Figure 2). The latter signal was easily attributed to the protons of the Cp\* fragments, while the former were attributed to the bipym ligand and the methyl fragments, respectively. The spectrum is in agreement with a C<sub>2v</sub> symmetry in solution, and the clear paramagnetism of the signals agrees with an electron transfer from the divalent ytterbium to the bipym ligand. In such a situation, the ytterbium metal center becomes trivalent and is f<sup>13</sup> (one hole on the f-shell) while the bipym is a radical anion.

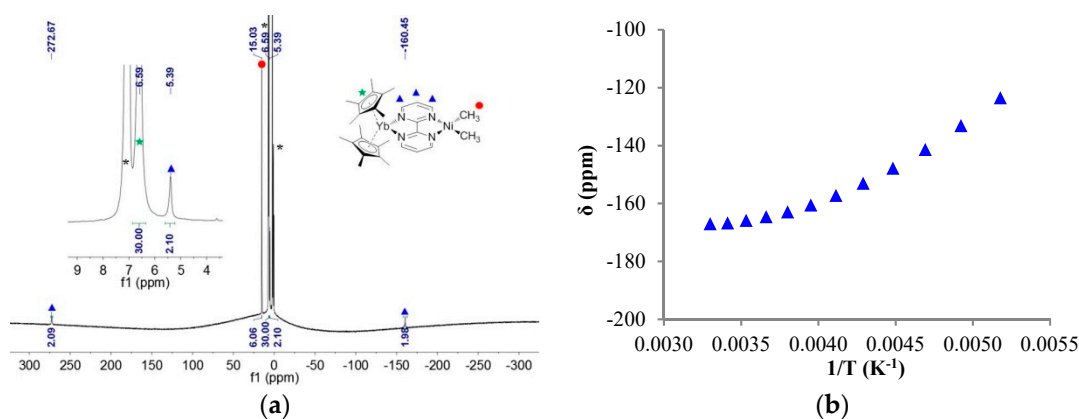


**Figure 2.** (a) <sup>1</sup>H NMR of **2** at 253 K, solvent and grease impurities are indicated by an asterisk (\*); (b) Variable temperature <sup>1</sup>H NMR chemical shifts (δ) versus 1/T (K<sup>-1</sup>) of the proton at −160.5 ppm on the previous spectrum.

Considering the paramagnetism measured by NMR, multiple possibilities arise for the electronic ground state of **2**: a triplet state or a singlet state with a low-lying triplet state. The chemical shifts of each resonance were plotted versus 1/T (Figure S5), and an example is given in Figure 2. It is clear from these plots that the behavior did not strictly follow Curie's law, since the plots are curved. Two reasons may explain this behavior: (i) the bipym ligand in **2** was in exchange with free bipym and the chemical shift depended on the equilibrium thermodynamics at a given temperature, or (ii) the magnetic behavior of **2** did not follow Curie's law because of a magnetic exchange coupling between the two single electrons. To test these two propositions, the solid-state magnetism was measured.

The temperature-dependent magnetic data were recorded and  $\chi$  and  $\chi T$  were plotted versus  $T$  and are represented in Figure 3. The  $\chi T$  value decreased gradually with decreasing temperature until the value approached zero, with two inflection points around 65 and 170 K. The near-zero value at low temperature indicates a singlet ground state while the value of  $2.3 \text{ emu}\cdot\text{K}\cdot\text{mol}^{-1}$  is close to the theoretical value obtained by the sum of a  $^2F$  state ( $f^{13}$ ) and a  $^2S$  state ( $\text{bipym}^-$ ). The  $\chi$  value versus the temperature is more indicative of the magnetic behavior of **2**: a maximum was obtained at 170 K while the low-temperature data was low and independent of the temperature (temperature-independent paramagnetism (TIP) or Van Vleck paramagnetism) [42,43]. Such a behavior can be explained by an anti-ferromagnetic coupling between the single electron located on the ytterbium center and that on the bipym ligand. The TIP was indicative of a low-lying triplet state above the singlet ground state. The  $\chi T$  value at room temperature agrees with a substantial population of the triplet at this temperature and therefore a low-lying triplet excited state. Using a modified version of the Bleaney–Bowers equation (Equation (1)) [44], the data were fitted using an average  $g$ -value of 3.78, a TIP of  $0.00602 \text{ emu}\cdot\text{mol}^{-1}$ , and a  $2J$  value of  $-275.2 \text{ cm}^{-1}$ . The average  $g$ -value that was used was relatively close to the one measured for the similar trivalent ytterbium complexes, that is, 3.315 for  $\text{Cp}^*_2\text{Yb}(\text{bipy})^+$  [45]. The red curve is the fit of the data with the Equation (1), and is very satisfactory. However, the value of both TIP and  $g$ -average are in very high agreement with a high anisotropy in this system. In order to account for the anisotropy, we used another model from Lukens et al. that is more adapted to highly anisotropic compounds such as the lanthanide complexes [46]. Assuming the  $c_1^2$  is close to 1 in **2** (which means that the oxidation state is close to purely trivalent) and using the  $g$ -value of the similar  $\text{Cp}^*_2\text{Yb}(\text{bipy})^+$  complex [45], the  $2J$  value was estimated to be  $-245.65 \text{ cm}^{-1}$ —a similar value to that found with the simple Bleaney–Bowers model (Equation (1)). It indicates that the exchange coupling was rather strong, compares well with the value found in the literature for the  $\text{Cp}^*_2\text{Yb}$  fragment and other N-aromatic heterocycles [46], and is typical for this type of species [47].

$$\chi = \frac{2N\beta^2 g_{\text{ave}}^2 e^x}{kT(1 + 3e^x)}, \quad x = \frac{2J}{kT} \quad (1)$$

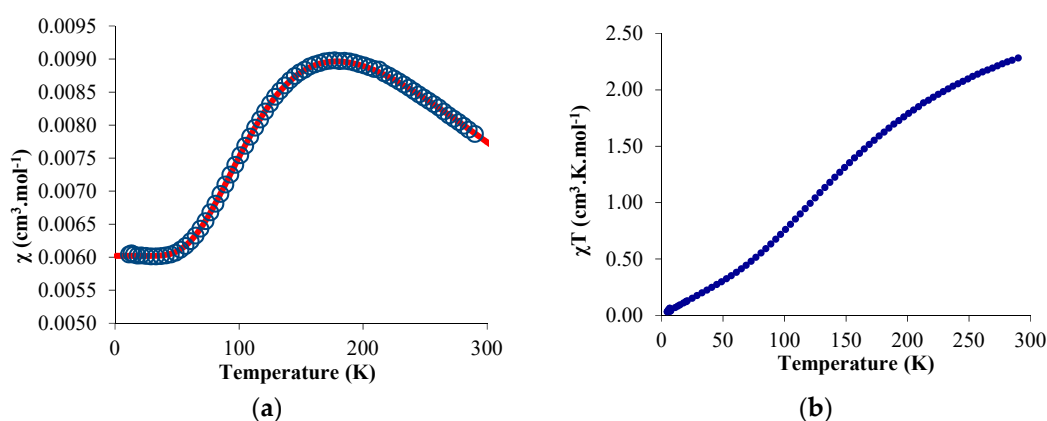


**Figure 3.** Solid-state temperature-dependent magnetic data at 0.5 T: (a) plot of  $\chi$  versus  $T$  and of (b)  $\chi T$  versus  $T$ . The solid line represents the fit of the magnetic data (see text).

The magnetism as well as the  $^1\text{H}$  solution NMR spectroscopy agreed with a singlet ground state and a triplet state that is substantially populated. Strong spin density was located on the bipym ligand as indicated by the X-ray crystallography, and the exchange coupling was monitored by the solid-state magnetism. However, in order to probe the reactivity at the nickel center, it is important to quantify how the electronic density is organized on the transition metal. For this, we turned to theoretical computations on **1**.

### 2.3. Theoretical Computations on **1**

Theoretical computations were performed on **1** at the DFT level with three different functionals: PBE, PBE0, and TPSSh (see the Materials and Methods section for more information). The difference in geometry is given in the Supplementary Materials, and the differences were minor compared to the X-ray data (see Table S7). The HOMO was clearly the  $dz_2$  of the nickel center, while the LUMO and LUMO +1 were orbitals located in the bipym ligand with the  $b_1$  symmetry (in  $C_{2v}$ ) (Figure 4). The LUMO possessed much density on the C–C bond that linked the two pyrimidine rings, the LUMO +1 had a node at these positions. The density on the nickel center was only residual, and the estimated atomic orbital Mulliken contribution from the nickel to these two MOs were 8.3% for the LUMO and 4.6% for the LUMO +1.

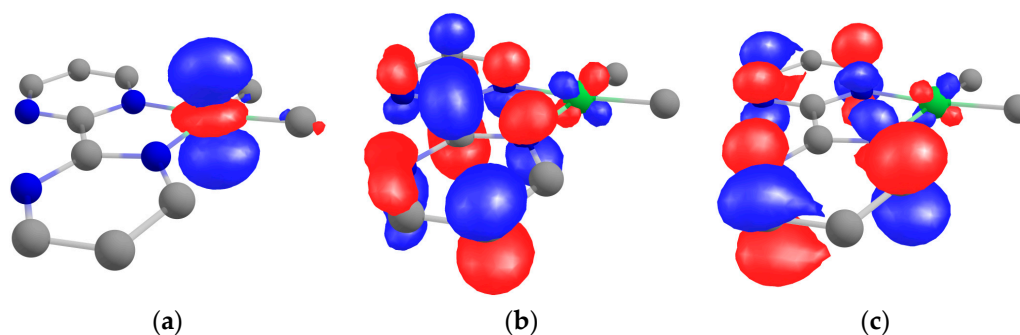


**Figure 4.** Kohn–Sham orbitals of **1** at the TPSSh level of theory calculated taking PBE optimized geometry: (a) HOMO, (b) LUMO, and (c) LUMO +1.

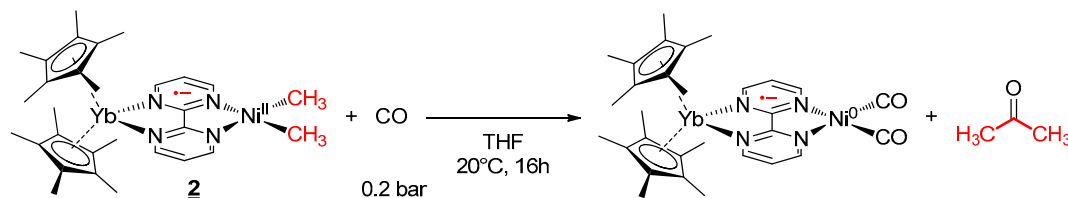
According to the magnetism, the ground state of **2** was a singlet state while the triplet state was low in energy. We did not perform DFT computations on **2** because the electronic state was likely to be multiconfigurational considering the previous data published on similar compounds [21–25,27] and the multi-referential calculations are more difficult considering the number of atoms. However, the magnetism and the X-ray crystal structure were indicative of spin density localized on the C–C bond that linked the two pyrimidine rings, which was in agreement with an electron transfer from the  $Cp^*_2Yb$  fragment to the LUMO of **1**. Another interesting feature was the high-energy  $dz^2$  located on the Ni center that is ready for reactivity. However, the addition of MeI or MeOTf on **1** and **2** only led to the very fast formation of ethane, even at low temperature. If it is indicative of some reactivity, the lack of intermediates observed in the course of the reaction does not allow the drawing of any conclusions on the possible mechanism. Therefore, we turned to the reaction of **1** and **2** with CO.

### 2.4. Reactivity with Carbon Monoxide

The reactivity with CO and group 10 alkyl complexes has been well investigated over the years. We were interested in knowing whether the presence of the lanthanide fragment in **2** influenced the mechanism of such a reaction. Thus, the reactivity at a low concentration of CO (0.2 bar) was investigated in both complexes **1** and **2** in THF. The reaction occurred rapidly and was followed by  $^1H$  NMR spectroscopy. After a few minutes of reaction, in the case of complex **2**, new signals appeared at 259.9, 12.4, and  $-0.1$  ppm, while the starting material concentration decreased slowly (see Figure S12). As the reaction time evolved, the intensity of these new signals increased then dropped until the end of the reaction. Similar to **2**, in the complex **1** system, new signals appeared at 9.2 and 2.2 ppm with time, and the rapid formation of acetone was clearly observed (see Figure S19). These new signals were attributed to the acyl intermediate after the CO migratory insertion in the Ni–C bond. The prior coordination of the CO on the nickel center through the loaded  $dz^2$  orbital was not observed. The formation of acetone (Scheme 2) was monitored with time. The apparition of this ketone indicates a reductive elimination from the acyl-methyl divalent nickel center to form  $Ni^0$  species. Considering the presence of CO in excess, the formation of bis-CO  $Ni^0$  species is likely.



At the end of the reaction, the signals of the intermediates disappeared, and unfortunately, at this point, the reduced complex could not be isolated. Instead, the formation of a small amount of free bipym ligand as well as the  $\text{Cp}^*\text{Yb}(\text{bipym})\text{YbCp}^*$  [48] dimer was observed, indicating the disassociation of the reduced  $\text{Ni}^0$  complex.



**Scheme 2.** Reactivity of **2** with carbon monoxide.

The reaction kinetics was followed by analysis with  $^1\text{H}$  NMR spectroscopy, using the decrease of the signal of **2**. A mono-exponential variation decrease of the concentration of **2** was recorded at  $35^\circ\text{C}$  (Figure 5a). The variation of the concentration of **2** did not modify the observed rate of the reaction at the same temperature at moderate concentrations of **2** (0.0073–0.029 mol/L). At higher concentrations, there was no longer a large excess of CO and the rate evolved. This information indicates that the rate overall order was pseudo first-order in **2** only when CO was in excess. The mechanism as well as the rate law can be written accordingly (Scheme 3 and Equation (2)):

$$r = \frac{k_1 k_2 [\mathbf{2}] [\text{CO}]}{k_{-1} + k_2} \quad (2)$$

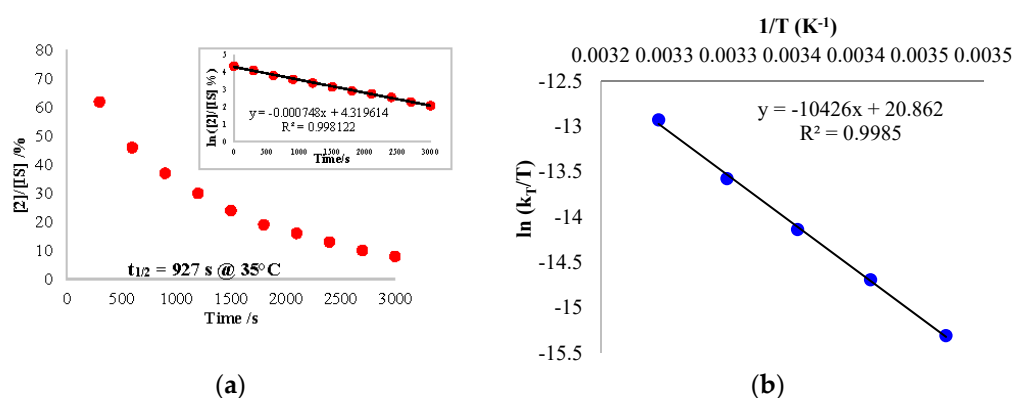
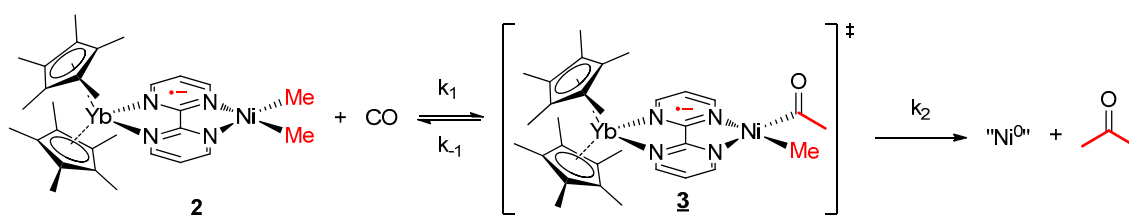


**Figure 5.** (a) Plot of the concentration of **2**/IS (normalized) over the reaction time at  $35^\circ\text{C}$ . The insert shows the kinetics order. (b) Eyring plot analysis for the reaction of **2** with carbon monoxide. The internal standard (IS) used was the toluene molecules crystallized in the cell.

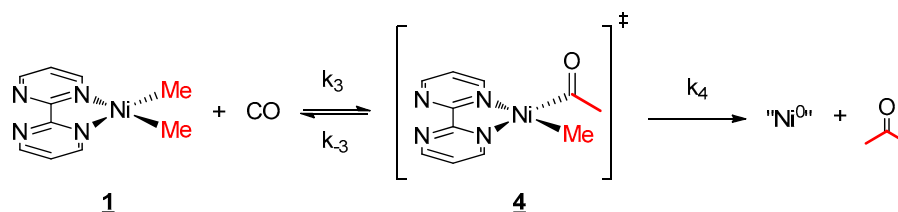


**Scheme 3.** Mechanism for the reaction of **2** with CO.

Using the rate law, the same analysis over a temperature range from 15 to  $35^\circ\text{C}$  allowed us to perform an Eyring analysis (Figure 5b). The activation parameters obtained were  $20.7 \text{ kcal}\cdot\text{mol}^{-1}$  and  $-5.75 \text{ cal}\cdot\text{mol}^{-1}\cdot\text{K}^{-1}$ . The moderate  $\Delta H^\ddagger$  is in agreement with a rather slow reaction at room

temperature while the small negative  $\Delta S^\ddagger$  indicates that the reductive elimination (entropically favorable) was not the rate-determining step (RDS) or it was balanced with a step with similar rate that was not favorable in entropy. On the other hand, the migratory insertion had a more modest effect on the entropy and could correspond to the RDS in this case. Without the information on the C coordination, it is not possible to conclude at this stage.

The kinetics of the reaction with CO and **1** were also monitored over time by  $^1\text{H}$  NMR spectroscopy in order to estimate the influence of the divalent lanthanide fragment. Having discovered that the overall reaction was also following a pseudo first-order kinetics (Scheme 4), an Eyring plot was constructed with the same temperature range as the one with **2** and CO, revealing the activation parameters  $\Delta H^\ddagger$  and  $\Delta S^\ddagger$  as  $17.06 \text{ kcal mol}^{-1}$  and  $-16.41 \text{ cal mol}^{-1} \text{ K}^{-1}$ , respectively (see Table S2 and Figure S18). The decent negative  $\Delta S^\ddagger$  value explains that the RDS is likely to be the reductive elimination, or more precisely, the entropically favorable rate  $k_4$  was much larger than  $k_3$  (see Supplementary Materials). Besides, the lesser  $\Delta H^\ddagger$  than the one of **2** indicates that there was a decreased barrier in the reaction without the organolanthanide fragment. This conclusion can also be proved with the much higher half-life time of complex **2** at  $20^\circ\text{C}$  (94.7 min) compared to the one of **1** (39.0 min, see Tables S1 and S2). The comparison of these data allows the deduction that the CO migratory insertion intermediate will be much more stable in the presence of lanthanide fragments.



Scheme 4. Mechanism for the reaction of **1** with CO.

### 3. Materials and Methods

All reactions were performed using standard Schlenk-line techniques or in argon- or nitrogen-filled gloveboxes (MBraun, Garching, Germany). All glassware was dried at  $140^\circ\text{C}$  for at least 12 h prior to use. Tetrahydrofuran (THF), THF- $d_8$ , toluene, and toluene- $d_8$  were dried over sodium, degassed, and transferred under reduced pressure in a cold flask.

$^1\text{H}$  NMR spectra were recorded in 5-mm tubes adapted with a J. Young valve on Bruker AVANCE II or III-300 MHz (Bruker, Billerica, MA, USA).  $^1\text{H}$  chemical shifts were expressed relative to TMS (Tetramethylsilane) in ppm. Magnetic susceptibility measurements were made for all samples on powder in sealed quartz tubes at 0.5 and 20 kOe in a 7 T Cryogenic SX600 SQUID magnetometer (Cryogenic, London, UK). Diamagnetic corrections were made using Pascal's constants. Elemental analyses were obtained from Mikroanalytisches Labor Pascher (Remagen, Germany).

(Tmeda)NiMe<sub>2</sub> [41] and Cp\*<sub>2</sub>Yb(OEt<sub>2</sub>) [49] complexes were synthesized according to published procedures. The bipyrimidine from TCI (Tokyo, Japan) was sublimated prior to use.

#### 3.1. Synthesis of (bipym)Ni(Me)<sub>2</sub> (**1**)

(tmeda)NiMe<sub>2</sub> (146 mg, 0.71 mmol, 1.0 equiv.) and bipyrimidine (113 mg, 0.71 mmol, 1.0 equiv.) were respectively dissolved in cold THF ( $-35^\circ\text{C}$ ). Transferring the bipyrimidine solution dropwise into the greenish yellow nickel solution at ambient temperature gave a dark-colored mixture after stirring for several minutes. Then, the mixture was stirred for 2 h and was stored at  $-35^\circ\text{C}$  in order to crystallize. Black crystalline product was obtained after one night and isolated in 73% yield (105 mg, 0.42 mmol). Yield: 73%.  $^1\text{H}$  NMR (300 MHz, 293 K, thf- $d_8$ ):  $\delta$  (ppm) = 9.32 (m, 2H, bipym), 9.12 (m, 2H, bipym), 7.67 (m, 2H, bipym), 0.06 (s, 6H, Ni–Me).  $^{13}\text{C}$  NMR (75 MHz, 273 K, thf- $d_8$ ):  $\delta$  (ppm) = 162.0, 156.6, 154.6, 124.4,  $-5.2$ . Anal. calcd. for C<sub>10</sub>H<sub>12</sub>N<sub>4</sub>Ni: C, 48.64; H, 4.90; N, 22.69; found: C, 47.00; H, 4.59; N, 21.00.

### 3.2. Synthesis of $(Cp^*)_2Yb(bipym)Ni(Me)_2$ (**2**)

$Cp^*_2Yb(OEt)_2$  (200 mg, 0.39 mmol, 1.0 equiv.) and  $(bipym)NiMe_2$  (98 mg, 0.40 mmol, 1.02 equiv.) were dissolved in toluene, respectively, and cooled down to  $-35\text{ }^\circ\text{C}$ . Transferring the green  $Cp^*_2Yb$  solution dropwise into the Nickel solution at ambient temperature gave a dark-brown mixture once the addition was finished. Then, the mixture was stored at  $-35\text{ }^\circ\text{C}$  in order to crystallize. Dark-brown crystals were obtained after several hours, and were isolated after washing three times with *n*-pentane, in 58% yield (156 mg, 0.22 mmol). Yield: 58%.  $^1\text{H NMR}$  (300 MHz, 293 K,  $thf-d_8$ ):  $\delta$  (ppm) = 246.83 (s, 2H,  $bipym$ ), 15.91 (s, 6H,  $-Me$ ), 9.02 (s, 2H,  $bipym$ ), 6.09 (s, 30H,  $Cp^*$ ),  $-172.34$  (s, 2H,  $bipym$ ). Anal. calcd for  $C_{30}H_{42}N_4NiYb$ : C, 52.19; H, 6.13; N, 8.11; found: C, 53.07; H, 6.06; N, 7.31.

### 3.3. Theoretical Calculations

All calculations were performed using the ORCA 4.0.0.2 software [50]. The geometry optimizations were done at three different levels of theory (PBE [51], PBE0 [52], and TPSSh [53,54]) using scalar relativistic ZORA Hamiltonian with ZORA-def2-TZVP basis set [55] and SARC/J auxiliary basis set for Coulomb fitting [56–58]. Each time, dispersion corrections were added to the functional used in the D3 framework proposed by Grimme [59] with the addition of the Becke–Johnson damping (D3BJ) [41]. Frequencies were calculated (analytically for PBE and PBE0 and numerically for TPSSh) to ensure these structures corresponded to energy minima. Single-point energy calculations starting from PBE optimized geometry were then performed in gas phase and in a toluene *continuum* with the CPCM method [60].

### 3.4. Crystal Structure Determinations

The structure resolution was accomplished using the SHELXS-97 and SHELXT [61] programs, and the refinement was done with the SHELXL program [62,63]. The structure solution and the refinement were achieved with the PLATON software [64]. Pictures of the compound structure were obtained using the MERCURY software. During the refinement steps, all atoms except hydrogen atoms were refined anisotropically. The position of the hydrogen atoms was determined using residual electronic densities. Finally, in order to obtain a complete refinement, a weighting step followed by multiple loops of refinement was done. The structures have been deposited in the CCDC with #1901938 (**1**) and 1901939 (**2**).

### 3.5. CO Migratory Insertion Studies

Reactivity tests were conducted in 5 mm NMR tubes adapted with a J. Young valve by adding CO gas directly to a degassed frozen solution of **1** or **2** and letting it react at room temperature. Kinetic analysis was performed following the  $^1\text{H NMR}$  resonances. The concentration of **1** was normalized by benzene residue (used as internal standard) in the deuterated solvent and complex **2** was referred to the toluene (used as internal standard), which crystallized in the cell. Integration of the NMR signals required care.

## 4. Conclusions

We successfully synthesized an original molecule with full characterizations containing reductive divalent lanthanide and reactive  $NiMe_2$  fragments with a redox-active bridging ligand. The strong electron correlation occurred due to the lanthanide fragment and therefore largely influenced the reactivity behavior in carbon monoxide migratory insertion. Complex **2** had a singlet ground state and a substantially populated triplet state. It was also shown that due to the electron transfer, strong spin density was on the *N*-heteroatom ligand to the reactive metal center. These considerations led to the increased stability of the CO migratory insertion step, forming an acyl-methyl intermediate. This work provides us with a new strategy for the further mechanistic study of carbonylation reactions.

**Supplementary Materials:** The following are available online at <http://www.mdpi.com/2304-6740/7/5/58/s1>. <sup>1</sup>H NMR characterization (Figures S1–S5), Kinetic analysis (Figures S6–S19 and Tables S1 and S2), Magnetism (Figure S20), Crystallographic data (Figures S21–S23 and Tables S3–S6), DFT Calculation data (Figures S24 and S25; Tables S7–S12).

**Author Contributions:** D.W. synthesized and characterized both compounds and studied the reactivity. M.T. realized the theoretical computations. M.C. realized the X-ray diffraction analysis. J.M. conducted the magnetic measurements and analyzed all the data with D.W. and G.N. G.N. had the original idea, managed all aspects of the project, and wrote the structure of the manuscript. All authors contributed to the editing of the manuscript.

**Funding:** This work is part of a project that has received funding from the European Research Council (ERC) under the European Union's Horizon 2020 research and innovation program under grant agreement No. 716314.

**Acknowledgments:** CNRS and École polytechnique are thanked for funding.

**Conflicts of Interest:** The authors declare no conflict of interest.

## References

1. Buchwalter, P.; Rosé, J.; Braunstein, P. Multimetallic catalysis based on heterometallic complexes and clusters. *Chem. Rev.* **2015**, *115*, 28–126. [[CrossRef](#)] [[PubMed](#)]
2. Sil, A.; Ghosh, U.; Mishra, V.K.; Mishra, S.; Patra, S.K. Synthesis, structure, electrochemical, and spectroscopic properties of hetero-bimetallic Ru(II)/Fe(II)-alkynyl organometallic complexes. *Inorg. Chem.* **2019**, *58*, 1155–1166. [[CrossRef](#)] [[PubMed](#)]
3. Murata, K.; Saito, K.; Kikuchi, S.; Akita, M.; Inagaki, A. Visible-light-controlled homo- and copolymerization of styrenes by a bichromophoric Ir–Pd catalyst. *Chem. Commun.* **2015**, *51*, 5717–5720. [[CrossRef](#)]
4. Dobbek, H.; Gremer, L.; Kiefersauer, R.; Huber, R.; Meyer, O. Catalysis at a dinuclear [CuSMo(O)OH] cluster in a CO dehydrogenase resolved at 1.1-Å resolution. *Proc. Natl. Acad. Sci. USA* **2002**, *99*, 15971–15976. [[CrossRef](#)] [[PubMed](#)]
5. Hollingsworth, T.S.; Hollingsworth, R.L.; Lord, R.L.; Groysman, S. Cooperative bimetallic reactivity of a heterodinuclear molybdenum–copper model of Mo–Cu CODH. *Dalton Trans.* **2018**, *47*, 10017–10024. [[CrossRef](#)] [[PubMed](#)]
6. Schilter, D.; Camara, J.M.; Huynh, M.T.; Hammes-Schiffer, S.; Rauchfuss, T.B. Hydrogenase enzymes and their synthetic models: The role of metal hydrides. *Chem. Rev.* **2016**, *116*, 8693–8749. [[CrossRef](#)] [[PubMed](#)]
7. Bouchard, S.; Bruschi, M.; De Gioia, L.; Le Roy, C.; Pétilion, F.Y.; Schollhammer, P.; Talarmin, J. FeMo heterobimetallic dithiolate complexes: Investigation of their electron transfer chemistry and reactivity toward acids, a density functional theory rationalization. *Inorg. Chem.* **2019**, *58*, 679–694. [[CrossRef](#)]
8. Ogo, S.; Mori, Y.; Ando, T.; Matsumoto, T.; Yatabe, T.; Yoon, K.-S.; Hayashi, H.; Asano, M. One model, two enzymes: Activation of hydrogen and carbon monoxide. *Angew. Chem. Int. Ed.* **2017**, *56*, 9723–9726. [[CrossRef](#)]
9. Mankad, N.P. Selectivity effects in bimetallic catalysis. *Chem. Eur. J.* **2016**, *22*, 5822–5829. [[CrossRef](#)]
10. Pye, D.R.; Mankad, N.P. Bimetallic catalysis for C–C and C–X coupling reactions. *Chem. Sci.* **2017**, *8*, 1705–1718. [[CrossRef](#)] [[PubMed](#)]
11. Ajamian, A.; Gleason, J.L. Two birds with one metallic stone: Single-pot catalysis of fundamentally different transformations. *Angew. Chem. Int. Ed.* **2004**, *43*, 3754–3760. [[CrossRef](#)]
12. Mata, J.A.; Hahn, F.E.; Peris, E. Heterometallic complexes, tandem catalysis and catalytic cooperativity. *Chem. Sci.* **2014**, *5*, 1723–1732. [[CrossRef](#)]
13. Lorber, C.; Vendier, L. Imido–titanium/molybdenum heterobimetallic systems. Switching from  $\eta^6$ -arene to fischer-type aminocarbene complexes by tuning reactivity conditions. *Organometallics* **2010**, *29*, 1127–1136. [[CrossRef](#)]
14. Stark, H.S.; Altmann, P.J.; Sproules, S.; Hess, C.R. Structural characterization and photochemical properties of mono- and bimetallic Cu–Mabiq complexes. *Inorg. Chem.* **2018**, *57*, 6401–6409. [[CrossRef](#)] [[PubMed](#)]
15. Mori, K.; Kawashima, M.; Yamashita, H. Visible-light-enhanced suzuki–miyaura coupling reaction by cooperative photocatalysis with an Ru–Pd bimetallic complex. *Chem. Commun.* **2014**, *50*, 14501–14503. [[CrossRef](#)]

16. Goudy, V.; Jaoul, A.; Cordier, M.; Clavaguéra, C.; Nocton, G. Tuning the Stability of Pd(IV) Intermediates using a redox non-innocent ligand combined with an organolanthanide fragment. *J. Am. Chem. Soc.* **2017**, *139*, 10633–10636. [[CrossRef](#)]
17. Goudy, V.; Xémard, M.; Karleskind, S.; Cordier, M.; Alvarez Lamsfus, C.; Maron, L.; Nocton, G. Phenylacetylene and carbon dioxide activation by an organometallic samarium complex. *Inorganics* **2018**, *6*, 82. [[CrossRef](#)]
18. Xémard, M.; Cordier, M.; Louyriac, E.; Maron, L.; Clavaguéra, C.; Nocton, G. Small molecule activation with divalent samarium triflate: A synergistic effort to cleave O<sub>2</sub>. *Dalton Trans.* **2018**, *47*, 9226–9230. [[CrossRef](#)]
19. Evans, W.J.; Ulibarri, T.A.; Ziller, J.W. Isolation and x-ray crystal structure of the first dinitrogen complex of an f-element metal, [(C<sub>5</sub>Me<sub>5</sub>)<sub>2</sub>Sm]<sub>2</sub>N<sub>2</sub>. *J. Am. Chem. Soc.* **1988**, *110*, 6877–6879. [[CrossRef](#)]
20. Jaroschik, F.; Momin, A.; Nief, F.; Le Goff, X.F.; Deacon, G.B.; Junk, P.C. Dinitrogen reduction and C–H activation by the divalent organoneodymium complex [(C<sub>5</sub>H<sub>2</sub>tBu<sub>3</sub>)<sub>2</sub>Nd(μ-I)K([18]crown-6)]. *Angew. Chem. Int. Ed.* **2009**, *48*, 1117–1121. [[CrossRef](#)] [[PubMed](#)]
21. Booth, C.H.; Walter, M.D.; Kazhdan, D.; Hu, Y.-J.; Lukens, W.W.; Bauer, E.D.; Maron, L.; Eisenstein, O.; Andersen, R.A. Decamethylterbocene complexes of bipyridines and diazabutadienes: Multiconfigurational ground states and open-shell singlet formation. *J. Am. Chem. Soc.* **2009**, *131*, 6480–6491. [[CrossRef](#)] [[PubMed](#)]
22. Booth, C.H.; Kazhdan, D.; Werkema, E.L.; Walter, M.D.; Lukens, W.W.; Bauer, E.D.; Hu, Y.-J.; Maron, L.; Eisenstein, O.; Head-Gordon, M.; et al. Intermediate-valence tautomerism in decamethylterbocene complexes of methyl-substituted bipyridines. *J. Am. Chem. Soc.* **2010**, *132*, 17537–17549. [[CrossRef](#)] [[PubMed](#)]
23. Nocton, G.; Lukens, W.L.; Booth, C.H.; Rozenel, S.S.; Melding, S.A.; Maron, L.; Andersen, R.A. Reversible sigma C–C bond formation between phenanthroline ligands activated by (C<sub>5</sub>Me<sub>5</sub>)<sub>2</sub>Yb. *J. Am. Chem. Soc.* **2014**, *136*, 8626–8641. [[CrossRef](#)]
24. Nocton, G.; Booth, C.H.; Maron, L.; Andersen, R.A. Thermal dihydrogen elimination from Cp\*<sub>2</sub>Yb(4,5-diazafluorene). *Organometallics* **2013**, *32*, 1150–1158. [[CrossRef](#)]
25. Nocton, G.; Booth, C.H.; Maron, L.; Andersen, R.A. Influence of the torsion angle in 3,3'-dimethyl-2,2'-bipyridine on the intermediate valence of Yb in (C<sub>5</sub>Me<sub>5</sub>)<sub>2</sub>Yb(3,3'-Me<sub>2</sub>-bipy). *Organometallics* **2013**, *32*, 5305–5312. [[CrossRef](#)]
26. Jacquot, L.; Xémard, M.; Clavaguéra, C.; Nocton, G. Multiple one-electron transfers in bipyridine complexes of Bis(phosphohyl) thulium. *Organometallics* **2014**, *33*, 4100–4106. [[CrossRef](#)]
27. Nocton, G.; Booth, C.H.; Maron, L.; Ricard, L.; Andersen, R.A. Carbon–hydrogen bond breaking and making in the open-shell singlet molecule, Cp\*<sub>2</sub>Yb(4,7-Me<sub>2</sub>phen). *Organometallics* **2014**, *44*, 6819–6829. [[CrossRef](#)]
28. Nocton, G.; Ricard, L. Reversible C–C coupling in phenanthroline complexes of divalent samarium and thulium. *Chem. Commun.* **2015**, *51*, 3578–3581. [[CrossRef](#)] [[PubMed](#)]
29. Jaoul, A.; Clavaguera, C.; Nocton, G. Electron transfer in tetramethylbiphosphinine complexes of Cp\*<sub>2</sub>Yb and Cp\*<sub>2</sub>Sm. *New J. Chem.* **2016**, *40*, 6643–6649. [[CrossRef](#)]
30. Dick, A.R.; Kampf, J.W.; Sanford, M.S. Unusually stable palladium(IV) Complexes: Detailed mechanistic investigation of C–O bond-forming reductive elimination. *J. Am. Chem. Soc.* **2005**, *127*, 12790–12791. [[CrossRef](#)] [[PubMed](#)]
31. Shabashov, D.; Daugulis, O. Auxiliary-assisted palladium-catalyzed arylation and Alkylation of sp<sup>2</sup> and sp<sup>3</sup> carbon–hydrogen bonds. *J. Am. Chem. Soc.* **2010**, *132*, 3965–3972. [[CrossRef](#)] [[PubMed](#)]
32. Rovira, M.; Roldán-Gómez, S.; Martin-Diaconescu, V.; Whiteoak, C.J.; Company, A.; Luis, J.M.; Ribas, X. Trifluoromethylation of a well-defined square-planar aryl–Ni<sup>II</sup> complex involving Ni<sup>III</sup>/CF<sub>3</sub>· and Ni<sup>IV</sup>–CF<sub>3</sub> intermediate species. *Chem. Eur. J.* **2017**, *23*, 11662–11668. [[CrossRef](#)] [[PubMed](#)]
33. Camasso, N.M.; Sanford, M.S. Design, synthesis, and carbon–heteroatom coupling reactions of organometallic nickel(IV) complexes. *Science* **2015**, *347*, 1218–1220. [[CrossRef](#)] [[PubMed](#)]
34. D'Accrisio, F.; Borja, P.; Saffon-Merceron, N.; Fustier-Boutignon, M.; Mézailles, N.; Nebra, N. C–H bond trifluoromethylation of arenes enabled by a robust, high-valent nickel(IV) complex. *Angew. Chem. Int. Ed.* **2017**, *56*, 12898–12902. [[CrossRef](#)] [[PubMed](#)]
35. Gandeepan, P.; Müller, T.; Zell, D.; Cera, G.; Warratz, S.; Ackermann, L. 3d transition metals for C–H activation. *Chem. Rev.* **2018**. [[CrossRef](#)] [[PubMed](#)]
36. Han, F.-S. Transition-metal-catalyzed Suzuki–Miyaura cross-coupling reactions: A remarkable advance from palladium to nickel catalysts. *Chem. Soc. Rev.* **2013**, *42*, 5270–5298. [[CrossRef](#)]



37. Peng, J.-B.; Wu, F.-P.; Wu, X.-F. First-row transition-metal-catalyzed carbonylative transformations of carbon electrophiles. *Chem. Rev.* **2018**. [[CrossRef](#)] [[PubMed](#)]
38. Maitlis, P.M.; Haynes, A.; Sunley, G.J.; Howard, M.J. Methanol carbonylation revisited: Thirty years on. *J. Chem. Soc. Dalton Trans.* **1996**, 2187–2196. [[CrossRef](#)]
39. Paulik, F.E.; Roth, J.F. Novel catalysts for the low-pressure carbonylation of methanol to acetic acid. *Chem. Commun.* **1968**, 1578a. [[CrossRef](#)]
40. Haynes, A.; Maitlis, P.M.; Morris, G.E.; Sunley, G.J.; Adams, H.; Badger, P.W.; Bowers, C.M.; Cook, D.B.; Elliott, P.I.P.; Ghaffar, T.; et al. Promotion of iridium-catalyzed methanol carbonylation: Mechanistic studies of the cativa process. *J. Am. Chem. Soc.* **2004**, *126*, 2847–2861. [[CrossRef](#)]
41. Kaschube, W.; Pörschke, K.R.; Wilke, G. tmeda-Nickel-Komplexe: III. (*N,N,N',N'*-Tetramethylethylendiamin)-(dimethyl)nickel(II). *J. Organomet. Chem.* **1988**, *355*, 525–532. [[CrossRef](#)]
42. Nocton, G.; Ricard, L. N-aromatic heterocycle adducts of bulky [1,2,4-(Me<sub>3</sub>C)<sub>3</sub>C<sub>5</sub>H<sub>2</sub>]<sub>2</sub>Sm: Synthesis, structure and solution analysis. *Dalton Trans.* **2014**, *43*, 4380–4387. [[CrossRef](#)] [[PubMed](#)]
43. Van Vleck, J.H. *The Theory of Electric and Magnetic Susceptibilities*; Oxford University Press: London, UK, 1932.
44. O'Connor, C.J. Magnetochemistry—advances in theory and experimentation. In *Progress in Inorganic Chemistry*; Lippard, S.J., Ed.; Wiley: Hoboken, NJ, USA, 1982; Chapter 4.
45. Lukens, W.W.; Walter, M.D. Quantifying exchange coupling in f-ion pairs using the diamagnetic substitution method. *Inorg. Chem.* **2010**, *49*, 4458–4465. [[CrossRef](#)]
46. Lukens, W.W.; Magnani, N.; Booth, C.H. Application of the hubbard model to Cp\*<sub>2</sub>Yb(bipy), a model system for strong exchange coupling in lanthanide systems. *Inorg. Chem.* **2012**, *51*, 10105–10110. [[CrossRef](#)]
47. Scarborough, C.C.; Wieghardt, K. Electronic structure of 2,2'-bipyridine organotransition-metal complexes. Establishing the ligand oxidation level by density functional theoretical calculations. *Inorg. Chem.* **2011**, *50*, 9773–9793. [[CrossRef](#)] [[PubMed](#)]
48. Berg, D.J.; Boncella, J.M.; Andersen, R.A. Preparation of coordination compounds of Cp\*<sub>2</sub>Yb with heterocyclic nitrogen bases: Examples of antiferromagnetic exchange coupling across bridging ligands. *Organometallics* **2002**, *21*, 4622–4631. [[CrossRef](#)]
49. Tilley, T.D.; Boncella, J.M.; Berg, D.J.; Burns, C.J.; Andersen, R.A.; Lawless, G.A.; Edelman, M.A.; Lappert, M.F. Bis[Bis(Trimethylsilyl)Amido]Bis(Diethyl Ether)Ytterbium and (Diethyl Ether)Bis(η<sup>5</sup>-Pentamethylcyclopentadienyl)Ytterbium. In *Inorganic Syntheses*; Ginsberg, A.P., Ed.; Wiley: Hoboken, NJ, USA, 2007; Chapter 27, pp. 146–150. [[CrossRef](#)]
50. Neese, F. The ORCA program system. *Wiley Interdiscip. Rev. Comput. Mol. Sci.* **2012**, *2*, 73–78. [[CrossRef](#)]
51. Perdew, J.P.; Burke, K.; Ernzerhof, M. Generalized gradient approximation made simple. *Phys. Rev. Lett.* **1997**, *78*, 1396. [[CrossRef](#)]
52. Adamo, C.; Barone, V. Toward reliable density functional methods without adjustable parameters: The PBE0 model. *J. Chem. Phys.* **1999**, *110*, 6158–6170. [[CrossRef](#)]
53. Tao, J.; Perdew, J.P.; Staroverov, V.N.; Scuseria, G.E. Climbing the density functional ladder: Nonempirical meta-generalized gradient approximation designed for molecules and solids. *Phys. Rev. Lett.* **2003**, *91*, 146401. [[CrossRef](#)]
54. Vydrov, O.A.; Scuseria, G.E. Assessment of a long-range corrected hybrid functional. *J. Chem. Phys.* **2006**, *125*, 234109. [[CrossRef](#)] [[PubMed](#)]
55. Weigend, F.; Ahlrichs, R. Balanced basis sets of split valence, triple zeta valence and quadruple zeta valence quality for H to Rn: Design and assessment of accuracy. *Phys. Chem. Chem. Phys.* **2005**, *7*, 3297–3305. [[CrossRef](#)] [[PubMed](#)]
56. Weigend, F. Accurate Coulomb-fitting basis sets for H to Rn. *Phys. Chem. Chem. Phys.* **2006**, *8*, 1057–1065. [[CrossRef](#)] [[PubMed](#)]
57. Pantazis, D.A.; Chen, X.-Y.; Landis, C.R.; Neese, F. All-electron scalar relativistic basis sets for third-row transition metal atoms. *J. Chem. Theo. Comput.* **2008**, *4*, 908–919. [[CrossRef](#)] [[PubMed](#)]
58. Pantazis, D.A.; Neese, F. All-electron scalar relativistic basis sets for the lanthanides. *J. Chem. Theo. Comput.* **2009**, *5*, 2229–2238. [[CrossRef](#)]
59. Grimme, S.; Antony, J.; Ehrlich, S.; Krieg, H. A consistent and accurate *ab initio* parametrization of density functional dispersion correction (DFT-D) for the 94 elements H-Pu. *J. Chem. Phys.* **2010**, *132*, 154104. [[CrossRef](#)]

60. Marenich, A.V.; Cramer, C.J.; Truhlar, D.G. Universal solvation model based on solute electron density and on a continuum model of the solvent defined by the bulk dielectric constant and atomic surface tensions. *J. Phys. Chem. B* **2009**, *113*, 6378–6396. [[CrossRef](#)] [[PubMed](#)]
61. Sheldrick, G. SHELXT—Integrated space-group and crystal-structure determination. *Acta Crystallogr. A* **2015**, *71*, 3–8. [[CrossRef](#)]
62. Sheldrick, G. Crystal structure refinement with SHELXL. *Acta Crystallogr. C* **2015**, *71*, 3–8. [[CrossRef](#)]
63. Sheldrick, G.M. A short history of SHELX. *Acta Crystallogr. A* **2008**, *64*, 112–122. [[CrossRef](#)]
64. Spek, A. Single-crystal structure validation with the program PLATON. *J. App. Crystallogr.* **2003**, *36*, 7–13. [[CrossRef](#)]



© 2019 by the authors. Licensee MDPI, Basel, Switzerland. This article is an open access article distributed under the terms and conditions of the Creative Commons Attribution (CC BY) license (<http://creativecommons.org/licenses/by/4.0/>).

## RESEARCH ARTICLE

View Article Online  
View Journal

Cite this: DOI: 10.1039/d0qi00952k

## Redox activity of a dissymmetric ligand bridging divalent ytterbium and reactive nickel fragments†

Ding Wang, Maxime Tricoire, Valeriu Cemortan, Jules Moutet and Grégory Nocton \*

The reaction of a reactive nickel dimethyl **1** bearing a redox-active, dissymmetric ligand, which is obtained by deprotonation of 2-pyrimidin-2-yl-1H-benzimidazole (Hbimpm) with a divalent lanthanide complex, Cp\*<sub>2</sub>Yb(OEt<sub>2</sub>), affords an unprecedented, trimeric **2** with C(sp<sup>3</sup>)–C(sp<sup>3</sup>) bond formation between two ligands in an *exo* position. Meanwhile, the transient, dimeric species **3** can be isolated with the same ligand coupling fashion, however, with a drastic distortion angle of the bimpm ligand and reactive NiMe<sub>2</sub> fragment, revealing the possible mechanism of this rearrangement. A much more stable dimeric congener, **5**, with an *exo* ligand coupling, is synthesized in the presence of 18-crown-6, which captures the potassium counter ion. The C–C coupling formation between two bimpm ligands results from the effective electron transfer from divalent lanthanide fragments. Without the divalent lanthanide, the reductive coupling occurs on a different carbon of the ligand, nicely showing the modulation of the spin density induced by the presence of the lanthanide ion. The electronic structures of these complexes are investigated by magnetic study (SQUID), indicating a <sup>2</sup>F<sub>7/2</sub> ground state for each ytterbium in all the heterometallics. This work firstly reports ligand coupling reactivity in a redox-active, yet dissymmetric system with divalent organolanthanides, and the reactive nickel moiety can impact the intriguing transition towards a stable homoleptic, trinuclear lanthanide species.

Received 10th August 2020,  
Accepted 29th October 2020

DOI: 10.1039/d0qi00952k

rsc.li/frontiers-inorganic

## Introduction

Electron transfer behaviour in organometallic complexes has been well documented over decades. In these complexes, when the electron is accessibly transferred to an empty ligand orbital while the metal centre remains stable, the ligand is regarded as redox-active.<sup>1</sup> Generally, N-heterocyclic ligands are excellent candidates as redox-active ligands because of their large delocalization extent added to a low-lying π\*-system.<sup>2</sup> In redox-active ligand–metal systems, the electron(s) (or hole(s)) can be stored on the ligand, therefore affecting the ground spin state of the complex and ultimately leading to unusual chemical transformation(s) at the metal site,<sup>3–5</sup> but also at the ligand site. For the latter situation, a cooperative effect of the ligand is invoked and can develop with or without a redox event.<sup>6,7</sup>

In the extensive studies of complexes with redox active ligands, divalent organolanthanides are of specific interest because of the formation of strongly correlated systems.<sup>8–21</sup> In the latter, an important question is the role of the symmetry orbitals and the geometry of the ligand in the electronic structure and the subsequent reactivity of the overall complex. For instance, the electronic configurations of decamethyl-ytterbocenes with 2,2'-bipyridine (bpy) and phenanthroline (phen) are drastically different: Cp\*<sub>2</sub>Yb(bpy) has multiconfigurational singlet ground states, in which Yb is intermediate valent, composed of an open-shell (f<sup>13</sup>, bpy<sup>•-</sup>) and a closed-shell (f<sup>14</sup>, bpy<sup>0</sup>) state<sup>9</sup> and is stable in solution; while Cp\*<sub>2</sub>Yb(phen) is a ground state triplet (f<sup>13</sup>, phen<sup>•-</sup>), which dimerizes reversibly to form a C–C σ bond at the 4,4'-positions on the phen ligands.<sup>13</sup> This reversible coupling has been also observed with Sm and Tm analogues<sup>14,22</sup> and other low-valent metal ions.<sup>22–26</sup> The chemical correlation between the ligand design and the reactivity of the complex provides a strategic framework for the usage of this type of complex in further reactivity. Our group has recently taken advantage of this work to develop the synthesis of a series of complexes combining a divalent lanthanide (Ln) fragment with a transition metal (TM) fragment bridged by N-heterocyclic aromatics.<sup>27–29</sup>

However, these examples remained based on neutral symmetrical N-aromatics. Thus, furthering the study on these het-

LCM, CNRS, École Polytechnique, Institut Polytechnique de Paris, Route de Saclay, 91128 Palaiseau, France. E-mail: gregory.nocton@polytechnique.edu;  
Tel: +33-1-6933-4402

† Electronic supplementary information (ESI) available: NMR data, magnetism measurements, DFT computation data and X-ray crystallography details. CCDC 2021801–2021805 2034256. For ESI and crystallographic data in CIF or other electronic format see DOI: 10.1039/d0qi00952k





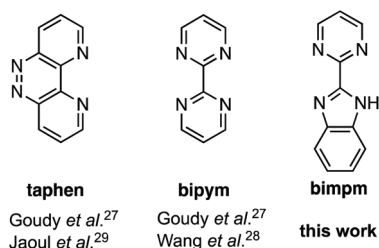


**Chart 1** Ligands used with divalent lanthanides in previous and this study, containing 4,5,9,10-tetraazaphenanthrene (taphen), 2,2'-bipyrimidine (bipym), and 2-pyrimidin-2-yl-1H-benzimidazole (Hbimpm).

erometallic frameworks by using dissymmetric redox active ligands, such as LX-type ones (Chart 1), is worthy of interest. Particularly, LX-type ligands are widely used in Nickel-catalysed cross-coupling reactions to enhance catalytic efficiency.<sup>30–33</sup> They are considered to allow significantly facile activation of unreactive carbon-halogen bonds.<sup>34</sup> Inspired by recent work by Diao and co-workers which highlighted the complexity of high-valent nickel-mediated  $sp^3$ - $sp^3$  and  $sp^2$ - $sp^2$  C-C bond formation using spectroscopic and computational methods,<sup>35</sup> we thought that imidazole-based linkers, such as 2-pyrimidin-2-yl-1H-benzimidazole, namely Hbimpm,<sup>36</sup> would be good candidates to construct original bimetallic Ln-TM complexes and study the electronic modulation within these systems. In addition, the bite angle and the dissymmetry of the ligand<sup>37</sup> are proved to be key parameters for varying the electronic structures and reactivity of metal complexes.<sup>38</sup>

In this article, we present the synthesis and characterization of original organometallic frameworks with the dissymmetric bimpm ligand, which combines a divalent organolanthanide and a dimethyl nickel fragment. Dimerization between two bimpm ligands occurs in an *exo* position. The lack of stability of the nickel fragment in the dimeric species is demonstrated by the evolution of dimer to a trimer with the identical *exo* coupling formation, in which the nickel fragment has been replaced by a Cp\*Yb fragment.

## Results and discussion

### Synthesis and structural characterization

The first attempt at combining the nickel precursor, (tmeda)NiMe<sub>2</sub>, and Hbimpm in chelating solvents such as pyridine or acetonitrile at room temperature led to insoluble solids that were difficult to characterize. Heating up the mixture to higher temperature only yielded decomposition products, which were hardly identifiable, probably due to the temperature sensitivity of the precursor, (tmeda)NiMe<sub>2</sub>. However, when the Hbimpm pro-ligand was deprotonated beforehand with a strong base (potassium hexamethyldisilane) prior to an addition of (tmeda)NiMe<sub>2</sub> in THF, dark red microcrystalline solid K(bimpm)NiMe<sub>2</sub> (**1**) was isolated in good yield (60%). The solid can be further re-crystallized from THF-pentane vapor diffusion in moderate yield (40%) as purple crystals. The crys-

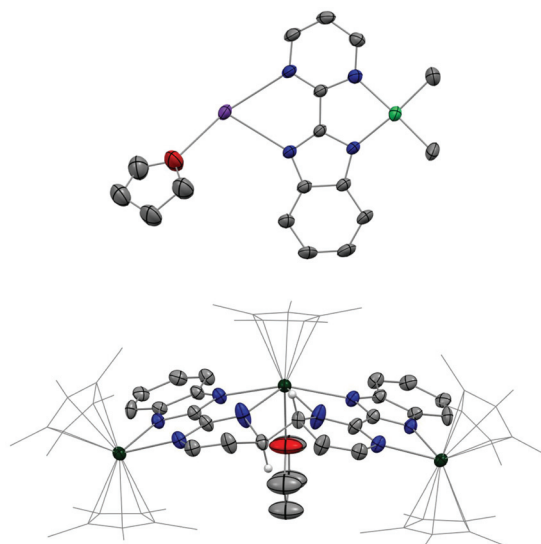
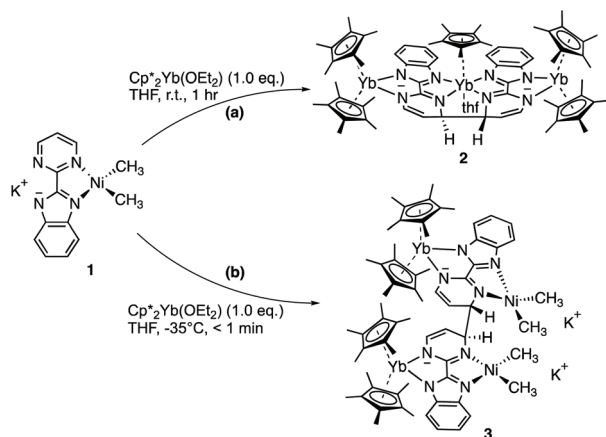


**Fig. 1** ORTEP of **1**(THF) (top) and **2** (bottom). Thermal ellipsoids are at 50% level. Carbon atoms are in grey, hydrogen atoms are in white and have been removed for clarity except the ones on the coupled carbons of the ligands, potassium in purple, nitrogen in blue, nickel in bright green and ytterbium atoms in deep green. Co-recrystallized solvent molecules of Et<sub>2</sub>O in **2** are omitted. Cp\* ligands on ytterbium are presented in wireframe style for clarity.

tals of **1**(THF) were suitable for X-ray diffraction (XRD) (Fig. 1). The addition of a stoichiometric amount of Cp\*<sub>2</sub>Yb(OEt<sub>2</sub>) in THF led to the formation of a red suspension after 1 h. After evaporation of the volatiles, the red residue is extracted in Et<sub>2</sub>O and bright red crystals can be crystallized *via* slow evaporation at -35 °C of the Et<sub>2</sub>O solution in moderate yield (51%). Interestingly, instead of forming the expected dimeric Yb-bimpm-Ni anionic complex, a homo-trimetallic neutral Yb-bimpm compound (**2**) was generated. In **2**, the ligand bimpm is coupled as in other *N*-heteroaromatic ligands<sup>13,14,39</sup> including pyrazine<sup>23</sup> and pyridazine;<sup>22</sup> in *exo*-position, which is the contrary to the bulkier acridine adduct.<sup>40</sup> A third ytterbium metal centre is coordinated in the pocket formed by four of the nitrogen atoms from two bimpm ligands. Only one pentamethylcyclopentadienyl ligand remained on the ytterbium metal centre (Scheme 1a). ORTEP of **1** and **2** and main distances and angles are shown in Fig. 1 and in Table 1.

In **2**, the average distance between Cp\* centroid and ytterbium atom is in the range of 2.33–2.34 Å. It is lower than the typical values (2.43–2.50 Å) found in divalent Yb complexes with Cp ligands.<sup>41</sup> This indicates the trivalent oxidation state of Yb,<sup>8,9,11–13</sup> which means that the Yb-ligand fragment undergoes the transition from Yb<sup>II</sup>(f<sup>14</sup>, L<sup>0</sup>) to Yb<sup>III</sup>(f<sup>13</sup>, L<sup>-</sup>) before coupling. The C-C  $\sigma$  bond coupling takes place between the same *meso*-position of pyrimidine cycles on bimpm ligands, causing the dearomatization of pyrimidine and forming a new C(sp<sup>3</sup>)-C(sp<sup>3</sup>) bond. This behaviour is explained by the efficient electron transfer from ytterbium fragment to the LUMO of pyrimidine heterocycle, which then undergoes the radical coupling process. The latter has been investigated by Haga *et al.* on the bimpm ligand system *via ab initio* molecular





**Scheme 1** Synthetic routes for **2** and **3**.

orbital calculations.<sup>36</sup> Such coupling was already reported with pyridine and pyrimidine moieties.<sup>23,39,40</sup> The effective reduction of the ligand also features a longer C–C distance linking the pyrimidine and benzimidazole heterocycles in **2** (1.476 Å) than in **1** (1.451 Å). This is indicative of a loss of good conjugation in the ligand and charge localization on the nitrogen of the pyrimidine.

This surprising compound, **2**, obtained in rather good yield could be the result of the easy formation of KCP\*, which is soluble in THF and not in Et<sub>2</sub>O, the solvent of extraction. The formation of the salt could be explained by the ionic bonding nature of the lanthanide to the Cp ring.<sup>42</sup> It also demonstrates the relative lability of the nickel dimethyl fragment. As such, **2** is likely to be the thermodynamic product of the reaction by rearrangement of the expected heterobimetallic dimer. In order to get some insights in this singular rearrangement, another reaction was performed in a similar fashion but that was reacted only for several seconds at room temperature before it was dried, dissolved in Et<sub>2</sub>O and cooled to –35 °C. A brown solution formed without any precipitate. The crystallization of this brown solution yield brown X-ray suitable crystals of an anionic Yb-bimpm-Ni fragment in which two bimpm ligands are coupled (**3**) and one molecule of KCP\* that co-crystallized (see ESI† for more details). The same reaction performed in Et<sub>2</sub>O, no matter the reaction time, only yielded the red crystalline product of rearrangement (**2**) (Scheme 1b). ORTEP of **3** and main distances and angle are shown in Fig. 2 and Table 1.

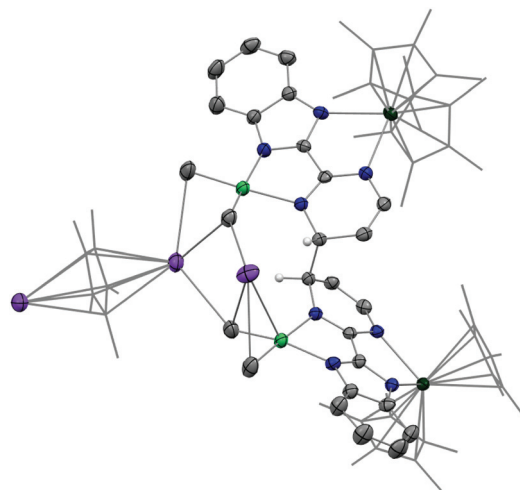
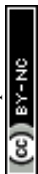


**Fig. 2** ORTEP of **3**. Thermal ellipsoids are at 50% level. Carbon atoms are in grey, hydrogen atoms are in white and have been removed for clarity except the ones on the coupled carbons of the ligands, potassium in purple, nitrogen in blue, nickel in bright green and ytterbium atoms in deep green. Co-recrystallized solvate molecules of Et<sub>2</sub>O are removed and pentamethylcyclopentadienyl ligands on ytterbium are presented in wireframe style for clarity.

The average Yb–Cp\* and Yb–N distances in **3** are 2.33(2) and 2.330(8) Å, respectively, which are slightly shorter than the ones in **2** as 2.342(2) and 2.364(2) Å. The data agree well with a trivalent Yb fragment. A longer bimpm bridging distance of 1.459(5) Å is observed in **3** in comparison to that in **1** (1.451 Å). This follows a similar trend of the ligand reduction. The distance of the coupled  $\sigma$  bond (1.56 Å) between two pyrimidine cycles is much longer than the one in **2** (1.520 Å). It could be due to the less compressed coordination environment in dimeric **3** than in **2**. Moreover, in comparison with **1**, the average distances in **3** of the Ni–N (1.987(2) Å in **3**, 1.97(5) in **1** Å) and Ni–CH<sub>3</sub> bonds (1.928(5) Å in **3**, 1.922(5) Å in **1**) are rather similar. It indicates that **1** and **3** possess a similar divalent coordination system around the nickel centre. The presence of one co-crystallized KCP\* molecule is an undoubtedly important part of the dimeric to trimeric transition from **3** to **2**, given that the KCP\* formation in solution can be regarded as a clear driving force leading to the rearrangement. Another interesting observation in **3** is the noticeable distortion of the nickel fragment (Fig. 3). The nearly planar angle (2°) between the bimpm ligand plane and NiMe<sub>2</sub> fragment in **1** became

**Table 1** Main distances (Å) and angles (°) for **1–6**

	<b>1</b>	<b>4</b>	<b>2</b>	<b>3</b>	<b>5</b>	<b>6</b>
Ni–CH <sub>3</sub>	1.922(5)	1.92(4)	—	1.928(5)	1.92(2)	1.930(5)
Ni–N	1.97(5)	1.970(5)	—	1.987(2)	2.01(4)	1.973(5)
Yb–N	—	—	2.364(2)	2.330(8)	2.32(2)	—
Yb–Cp* <sub>centr</sub>	—	—	2.342(2)	2.33(2)	2.38(3)	—
Bridging C–C <sub>bimpm</sub>	1.451	1.45(6)	1.476	1.459(5)	1.46(3)	1.46(8)
Coupled C–C <sub>bimpm</sub>	—	—	1.520	1.56	1.56(3)	1.537
bimpm^NiMe <sub>2</sub>	2	12	—	31	19	17



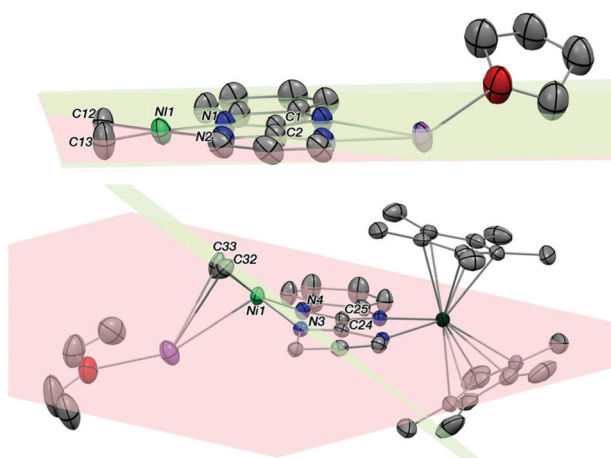
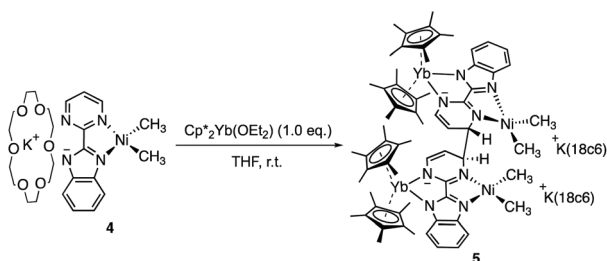


**Fig. 3** Comparison of distortion of the NiMe<sub>2</sub> fragment in **1** (top) and **3** (bottom) presented by ORTEP. N–C–N is regarded as the overall ligand plane (red) and atoms are labelled; C–Ni–C is NiMe<sub>2</sub> plane (green) and also labelled. Thermal ellipsoids are at 50% level. Carbon atoms are in grey, potassium in purple, nitrogen in blue, nickel in bright green and ytterbium atoms in deep green. Half structure of the coupled **3** is presented. Hydrogen atoms have been removed for clarity.

largely bent (31°) in **3**. This is clearly indicative of the liable dissociation of the NiMe<sub>2</sub> moiety in the coupled ligand system. It is also shown by the facile decomposition of **3** under the inert atmosphere in solid-state at room temperature compared to **2**, which is stable in these conditions. This probably indicates that the dimethyl-nickel moiety is ready for dissociation from the bimpm ligand to generate ethane and Ni(0) species (Fig. S11–12†).

In the reaction forming **2**, the fate of the nickel dimethyl fragment remains uncertain while it is clear that the formation of KCp\* helps the rearrangement from **2** to **3**. Accordingly, the addition of crown ether (18-crown-6) in solution was considered to capture the active potassium ion.<sup>43</sup> The analogous nickel precursor K(18-c-6)(bimpm)NiMe<sub>2</sub> (**4**) was synthesized as deep blue crystalline product in good yield (91%). The combination with Cp\*<sub>2</sub>Yb(OEt<sub>2</sub>) was performed in both THF and Et<sub>2</sub>O with different reaction times at room temperature, yielding indifferently an anionic heterobimetallic species containing the Yb–bimpm–Ni fragment, in which two pyrimidine cycles on bimpm ligands are also coupled in *exo*-position (**5**). The potassium counter ions are captured by 18-crown-6 (Scheme 2). ORTEP of **4**



**Scheme 2** Synthesis of **5** from **4**.

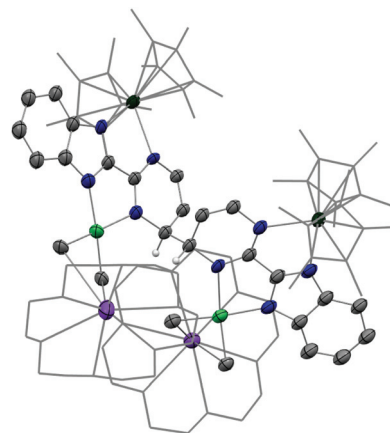


**Fig. 4** ORTEP of **5**. Thermal ellipsoids are at 50% level. Carbon atoms are in grey, hydrogen atoms are in white and have been removed for clarity, except the ones on the coupled carbons of the ligands, potassium in purple, nitrogen in blue, nickel in bright green and ytterbium atoms in deep green. Co-recrystallized solvate molecule of Et<sub>2</sub>O is removed and pentamethylcyclopentadienyl ligands on ytterbium are presented in wireframe style for clarity.

and **5** are shown in ESI† and Fig. 4, respectively and main distances and angles in Table 1.

The average distance Yb–Cp<sub>ctr</sub> in **5** is 2.340(2) Å indicating an Yb<sup>III</sup> fragment. A reduction has taken place in the ligand, which can be noticed by typical longer ligand linker distance (1.464(5) Å) comparing to the one in **4** as 1.45(6) Å. Similar parameters based on the comparison in Ni–CH<sub>3</sub> and Ni–N distances of **4** and **5** indicate that the nickel ion remains at its divalent oxidation state. The distortion angle of bimpm and NiMe<sub>2</sub> difference in **4** and **5** is only 7°, indicating a more stable coordination environment, compared to the one found in **3**.

As discussed before, it is interesting to compare the angles between the bimpm ligand plane and the dimethyl nickel fragment plane in **3** and **5** (Fig. 5). In **5**, the average angle is 19°, which is similar to that of 12° in **4**. Thus, the small increase in **5** compare to **1** is likely due to steric hindrance because of the 18-crown-6. Additionally, **5** was found to be stable at room temperature in the solid-state, unlike **3**. Thus, the fast decomposition of the nickel fragment in **3** is likely to be the reason for the easy formation of **2** as a thermodynamically stable trimer.

In order to estimate the impact of the single-electron transfer system without the lanthanides ion, a reduction was performed on **1** using potassium graphite (in excess) in THF instead of the divalent lanthanide ion reductant. XRD-suitable brown-orange crystals of the reaction product, **6**, were isolated *via* slow diffusion of pentane into THF solution at –35 °C after several days. An ORTEP of **6** and main distances and angle are presented in Fig. 6 and Table 1.

In **6**, the average distances of the Ni–N and Ni–CH<sub>3</sub> bonds are 1.973(5) and 1.930(5) Å, respectively, indicating that the nickel centre remains in a divalent oxidation state. A longer



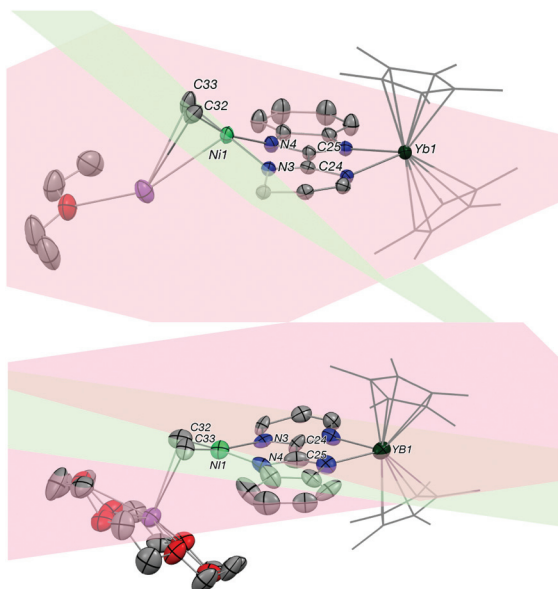


**Fig. 5** Comparison of the bimpm-NiMe<sub>2</sub> distortion angle between **3** and **5**. ORTEPs of **3** (top), **5** (bottom). Thermal ellipsoids are at 50% level. Carbon atoms are in grey, potassium in purple, nitrogen in blue, nickel in bright green and ytterbium atoms in deep green. Half structures of **3** and **5** are presented. Hydrogen atoms and co-recrystallized solvate molecules of Et<sub>2</sub>O in both complexes have been removed and penta-methylcyclopentadienyl ligands on ytterbium are presented in wireframe style for clarity.

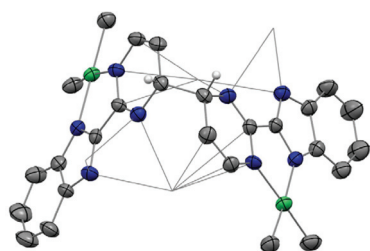


**Fig. 6** ORTEP of **6**. Thermal ellipsoids are at 50% level. Carbon atoms are in grey, hydrogen atoms are in white and have been removed for clarity except the ones on the coupled carbons of bimpm ligands, nitrogen in blue and nickel in bright green. Co-recrystallized solvate molecules of THF have been omitted and potassium atoms are presented in wireframe style for clarity.

distance of C–C linkage between pyrimidine and benzimidazole of 1.46(8) Å compared to that of 1.451 Å in **1**, is indicative of an efficient reduction on the ligand moiety. The torsion angle between the ligand plane and the NiMe<sub>2</sub> fragment is 17°, which is similar to the one in **5** (19°). Correspondingly, **6** was found to be thermally stable for several days in solution at room temperature under inert atmosphere. Interestingly, a coupled C–C bond between two pyrimidine rings was also observed but in a different position than that in **2**, **3** and **5**. In **6**, the coupling occurs at the *para* position of the Ni-coordinated nitrogen atom, while in other structures with the

divalent lanthanide, the coupling occurs at the *ortho* site. The length of the coupled C(sp<sup>3</sup>)-C(sp<sup>3</sup>) bond is 1.537 Å, which is similar to the ones in **2**, **3** and **5**.

This difference in the coupling fashion on bimpm ligand in **3** and **6** is intriguing and it is then plausible that the coordination of the divalent lanthanide ions could subtly modulate the electron density on the redox-active ligand fragment because of strong electron correlation. Additionally, the steric hinderance effect of the Cp\* ligands on the lanthanide moiety might also participate in regulating the position at which the coupling occurs. Thus computational investigations were performed at the DFT level.

### Theoretical studies

Computational investigations were performed on the anionic bimpm ligand, **1** and the monomeric anion of **3** at the DFT level. The corresponding geometries were optimised using the PBE density functional and Kohn–Sham orbitals are depicted in the ESI†.

The optimised geometry of the anionic ligand yields a symmetrical species, in which the LUMO is delocalised equally across the C<sub>2</sub> axis of ligand while the density is more localised in the pyrimidine part. The addition of the Ni fragment significantly modifies the electronic density of the LUMO with strong density located on the pyrimidine nitrogen atom that coordinates the nickel ion and on the carbon in *para* position to the latter. On the other hand, the *ortho* position to that coordinated nitrogen atom possesses very little density. Thus, an electron transfer that would occur on this species would definitely strongly localise spin density in the *para* position, which is consistent with the coupling observed in **6**.

Now, the addition of the ytterbocene fragment is accompanied by an electron transfer to the ligand and the SOMO is now delocalised on the ligand while the LUMO is principally centred on the pyrimidine moiety. In the SOMO, the spin density has virtually no contribution on the carbon atoms where the coupling is observed in **6** (*para* to the nickel-coordinated pyrimidine nitrogen atom) while it has little contribution on the carbon atoms where the coupling is observed in **2**, **3** and **5**. Additionally, the presence of the lanthanide ion may enforce a multiconfigurational energy state allowing the LUMO to contribute significantly<sup>11,13</sup> to the spin delocalization and thus explaining the distinct position of the coupling between **6** and **2**, **3** and **5**. This could be verified by a proper CASSCF computation that was not possible to handle in our hands.

### Solution studies

The dissymmetry of the ligand imposes a C<sub>s</sub> symmetry in the precursor **1** and **4**. <sup>1</sup>H NMR of **1** in THF-d<sup>8</sup> shows seven resonances in total, two for the methyl (6 protons) at 0.02 and -0.40 ppm, and five for the bimpm ligands (7 protons), found in 8.6–6.8 range. The spectrum of **4** recorded in CD<sub>3</sub>CN shows six resonances for the bimpm ligands (7 protons), found in 8.8–6.9 ppm range, one signal for 18-crown-6 (24 protons) at 3.55 ppm, as well as two for the methyl (6 protons) at -0.10





and  $-0.54$  ppm. The addition of the ytterbium fragment drastically shifts these protons, in agreement with the presence of a paramagnetic  $\text{Yb}^{\text{III}}$  centre. **2** recorded in  $\text{THF-d}_8$  at 293 K nicely shows 14 signals, integrating for 1 proton each and 5 signals, integrating for 15 protons each. This spectrum is in good agreement with a coupled ligand and no symmetry, other than the identity, *i.e.* a  $C_1$  symmetric molecule in solution. The strong paramagnetism of the complex indicates the presence of at least one trivalent ytterbium.

The  $^1\text{H}$  NMR spectra of **3** and **5** (in bracket) present similar spectra in  $\text{THF-d}_8$  at 293 K, with seven protons at 187.66 (186.25), 181.49 (176.11), 50.43 (53.04), 27.46 (30.55), 19.17 (23.32), 4.91 ( $-0.03$ ) and  $-8.27$  ( $-4.50$ ) ppm. Additionally, two non-equivalent  $\text{Cp}^*$  signals are found at 12.28 (7.91) and 2.93 (2.29) ppm and two non-equivalent methyl signals at  $-4.81$  ( $-0.86$ ) and  $-18.17$  ( $-14.03$ ) ppm. The presence of only seven signals for the ligand but two different signals for the methyl and  $\text{Cp}^*$  moieties is in agreement with a dimeric species with a  $C_2$ , an inversion centre at the centre position of the *exo* C–C bond that was formed or a plane of symmetry cutting the C–C bond that was formed. Thus, the NMR spectra are not informative as to the stereochemical nature of the coupling, but allow identifying its formation. Because both **3** and **5** have very similar coordination environment, their NMR chemical shifts are very close to each other. Again, the paramagnetism of **3** and **5** is indicative of an effective electron transfer from the divalent lanthanide to the redox-active ligand-transition metal fragment with bimpm.

The paramagnetic shift of the signals in **2**, **3** and **5** were followed by variable temperature  $^1\text{H}$  NMR. The chemical shifts of each resonance in these complexes respectively are plotted versus  $1/T$  (see ESI†). A linear  $\delta$  vs.  $1/T$  plot over the set-up temperature range for each, revealing typical Curie behaviour under this temperature range. This is in good agreement with the recorded solid-state temperature-dependent magnetic data.

The possibility of a reversible C–C transfer was studied. This occurred in multiple occasions after electron transfer from divalent lanthanides.<sup>13,14,44</sup> Compared to the relatively stable nature of the  $\text{Cp}^*_2\text{Yb}(\text{phen})$ , **2**, **3** and **5** are rather thermosensitive. The eventual dimer-monomer equilibrium was not efficiently observed when dissolving the crystals of **2**, **3** and **5** in  $\text{THF-d}_8$  at room temperature. It might take place at higher temperatures, such as at 60 °C, however, the concomitant decomposition of the dimers occurred when heating up the solutions for extended periods of time, resulting in a number of newly formed, hardly identifiable signals (Fig. S19–24†). Thus, the reversibility of C–C coupling in **2**, **3** and **5** remains equivocal.

### Magnetism solid-state studies

The organometallic products were analysed by solid-state magnetism using a SQUID (Fig. 7). When the divalent ytterbium is coordinated to the bimpm ligand, one electron is transferred, which allow the coupling to occur. Thus, in **2**, **3** and **5**, it is expected that Yb centres are at the trivalent state. This was

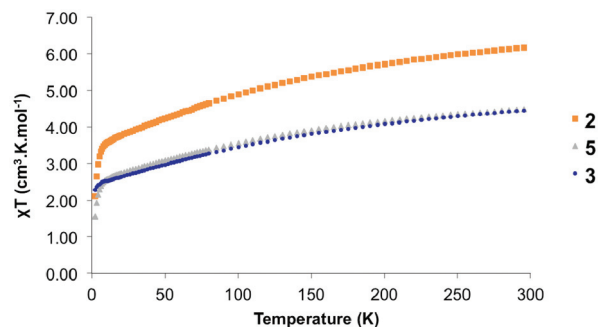


Fig. 7 Temperature dependent magnetic data for **2**, **3** and **5**.

notably indicated by the paramagnetic NMR as well as the  $\text{Cp}^*\text{-Yb}$  distance (see previous paragraphs). The solid-state data indicate 300 K  $\chi_T$  values of 6.17, 4.45 and 4.45  $\text{emu K mol}^{-1}$  for **2**, **3** and **5**, respectively. These values agree with the theoretical values of 2.54  $\text{emu K mol}^{-1}$  for uncorrelated  $^2\text{F}_{7/2}$  ground-states for each ytterbium centre, that is three ytterbium centres in **2** and two ytterbium centres in **3** and **5**. The  $\chi_T$  value decreases monotonously up to 6 K with respective values of 3.32, 2.42 and 2.44  $\text{emu K mol}^{-1}$  for **2**, **3** and **5**. The decrease is due to the depopulation of the higher energy crystal-field states. Note that the very similar decrease of **3** and **5** indicate a very similar crystal field, in agreement with their very similar structural nature. The decrease below 6 K is associated with a mixture of dipolar coupling contributions, while only the ground crystal-field state is populated.

## Conclusions

In this article, we have successfully synthesized original redox-active, dissymmetric hetero- or homometallic complexes containing divalent organolanthanides,  $\text{Cp}^*_2\text{Yb}$ , which allows effective single electron transfer process and leads to the intermolecular  $\text{C}(\text{sp}^3)\text{-C}(\text{sp}^3)$  coupling formation between two bridging ligands. The stereochemistry of this ligand coupling is identified as an *exo* formation, and the dimer-trimer transition is affected by a reactive  $\text{NiMe}_2$  fragment, which impacts the torsion angle between the bridging ligand and dimethyl functional group. The solid-state explanation of such a rearrangement is provided by the XRD study of the isolated transient *exo* species. Magnetic measurements show that **2**, **3** and **5** possess triplet ground states. This work implements a new redox-active system of divalent lanthanides, in the presence of a dissymmetric ligand, yielding an intermolecular ligand coupling reactivity, yet the reversibility of this bond formation remains ambiguous. This study provides us with a new avenue for the design of our heterometallic architectures with other transition metals using this dissymmetric ligand system, which may lead to different reactivity behaviours compared to the one observed for nickel. The related work is currently under investigation.



## Experimental section

### General considerations

All reactions were performed using standard Schlenk-line techniques or in argon- or nitrogen-filled gloveboxes (MBraun, Garching, Germany). All glassware was dried at 120 °C for at least 12 h prior to use. Tetrahydrofuran (THF), THF-d<sup>8</sup>, toluene, and toluene-d<sup>8</sup> were dried over sodium, degassed; CD<sub>3</sub>CN was dried over CaH<sub>2</sub>, degassed. All the solvents were transferred under reduced pressure in a cold flask.

<sup>1</sup>H NMR spectra were recorded in 5 mm tubes adapted with a J. Young valve on Bruker AVANCE II or III-300 MHz (Bruker, Billerica, MA, USA). <sup>1</sup>H chemical shifts were expressed relative to TMS (tetramethylsilane) in ppm. Magnetic susceptibility measurements were made for all samples on a SQUID. Diamagnetic corrections were made using Pascal's constants. Temperature dependent magnetic measurements were obtained in sealed quartz tube<sup>45</sup> on a SQUID at 0.5 and 2 T. Elemental analyses were obtained from Mikroanalytisches Labor Pascher (Remagen, Germany).

All calculations were performed using the ORCA 4.2.1 software.<sup>46</sup> The geometry optimizations were done at the PBE level of theory,<sup>47</sup> using scalar relativistic ZORA Hamiltonian with ZORA-def2-TZVP basis set,<sup>48</sup> and SARC/J auxiliary basis set for Coulomb fitting.<sup>49–51</sup> Each time, dispersion corrections were added to the functional used in the D3 framework proposed by Grimme<sup>52</sup> with the addition of the Becke–Johnson damping (D3BJ). Frequencies were calculated numerically to ensure these structures corresponded to energy minima. Single-point energy calculations starting from PBE optimized geometry were then performed in gas phase at the PBE, PBE0,<sup>53</sup> TPSSH,<sup>54,55</sup> and ωB97X-D3.<sup>56</sup>

Single crystals of the compounds **1–6** were coated in Paratone-N oil and mounted on a Kapton loop. A BRUKER APEX-II CCD detector and a graphite Mo-K<sub>α</sub> monochromator (Nonius, Delft, Netherlands) were used for the data acquisition. All data were measured at 150 K under a nitrogen stream and a refinement method was used for solving the structure. The structure resolution was accomplished using the SHELXS-97 and SHELXT<sup>57</sup> program, and the refinement was done with the SHELXL program.<sup>58,59</sup> The structure solution and the refinement were achieved with the PLATON<sup>60</sup> and Olex2 softwares.<sup>61</sup> During the refinement steps, all atoms except hydrogen atoms were refined anisotropically. The position of the hydrogen atoms was determined using residual electronic densities. Finally, in order to obtain a complete refinement, a weighting step followed by multiples loops of refinement was done. ORTEPs of the compound structures were obtained using the MERCURY software. The structures have been deposited in the CCDC with 2021801–2021805 and 2034256 for **1–5** and **6**, respectively.†

(tmeda)NiMe<sub>2</sub>,<sup>62</sup> Cp\*<sub>2</sub>Yb(OEt<sub>2</sub>),<sup>63</sup> and HBimp<sub>m</sub><sup>36</sup> were synthesized according to published procedures and recrystallized prior use. 18-crown-6 was purchased from Sigma-Aldrich and sublimed before use.

### Syntheses

**K(bimp<sub>m</sub>)Ni(CH<sub>3</sub>)<sub>2</sub> (1).** A 50 mL Schlenk was charged with Hbimp<sub>m</sub> (283.6 mg, 1.44 mmol), KHMDS (317.2 mg, 1.59 mmol) in the glovebox. 20 mL of THF were added and the mixture was stirred at ambient temperature for 16 hours, remaining a milky suspension during the reaction time. The solvent was removed under reduced pressure and the residue was washed with diethyl ether for 3 times, allowing the removal of the slight excess of KHMDS, was dried under reduce pressure and used without further characterizations (298.3 mg, 1.27 mmol, 88%). (tmeda)Ni(CH<sub>3</sub>)<sub>2</sub> (174.1 mg, 0.85 mmol) was dissolved in cold THF (−40 °C) and transferred dropwise into a cold THF suspension of Kbimp<sub>m</sub> (199.4 mg, 0.85 mmol) at ambient temperature. The suspension was stirred for 2 hours, resulting in a colour change from olive-green to night blue and was filtered. The solvent of the solution was removing solvent under reduced pressure and K(bimp<sub>m</sub>)Ni(CH<sub>3</sub>)<sub>2</sub> was isolated as a brown powder in 60% yield (163.6 mg, 0.51 mmol). When CH<sub>3</sub>CN is used instead of THF, the yield is increased because the better solubility of **1** soluble in CH<sub>3</sub>CN. However, the necessary drying step is longer and traces of CH<sub>3</sub>CN may influence the further use with reactive divalent lanthanide. Purple crystals were recrystallized *via* vapor diffusion by *n*-pentane on THF solution at ambient temperature after 24 hours and isolated in 40% yield (110.0 mg, 0.34 mmol). <sup>1</sup>H NMR (300 MHz, 293.15 K, THF-d<sub>8</sub>): δ (ppm) = 8.63 (d, 5.0 Hz, 1H, Kbimp<sub>m</sub>), 8.47 (d, 4.1 Hz, 1H, Kbimp<sub>m</sub>), 7.92 (m, 1H, Kbimp<sub>m</sub>), 7.39 (m, 1H, Kbimp<sub>m</sub>), 6.86 (m, 3H), 0.02 (s, 3H, Ni–Me1), −0.40 (s, 3H, Ni–Me2). <sup>13</sup>C NMR (75 MHz, 293.15 K, THF-d<sub>8</sub>, q is for quaternary carbon): δ (ppm) = 163.08 (C<sub>q</sub>, bimp<sub>m</sub>), 159.19 (C<sub>q</sub>, bimp<sub>m</sub>), 153.97 (C<sub>sp2</sub>, bimp<sub>m</sub>), 153.10 (C<sub>sp2</sub>, bimp<sub>m</sub>), 149.88 (C<sub>q</sub>, bimp<sub>m</sub>), 146.99 (C<sub>q</sub>, bimp<sub>m</sub>), 120.54 (C<sub>sp2</sub>, bimp<sub>m</sub>), 120.35 (C<sub>sp2</sub>, bimp<sub>m</sub>), 119.63 (C<sub>sp2</sub>, bimp<sub>m</sub>), 119.05 (C<sub>sp2</sub>, bimp<sub>m</sub>), 119.01 (C<sub>sp2</sub>, bimp<sub>m</sub>), −7.05 (C<sub>sp3</sub>, Ni–Me2), −12.23 (C<sub>sp3</sub>, Ni–Me1). **Anal. calcd** for C<sub>13</sub>H<sub>13</sub>KN<sub>4</sub>Ni: C, 48.33; H, 4.06; N, 17.34; found: C, 47.42; H, 4.20; N, 15.70.

**Cp\*Yb(thf)[Cp\*<sub>2</sub>Yb(bimp<sub>m</sub>)]<sub>2</sub> (2).** Cp\*<sub>2</sub>Yb(OEt<sub>2</sub>) (94.4 mg, 0.18 mmol) and K(bimp<sub>m</sub>)NiMe<sub>2</sub> (58.9 mg, 0.18 mmol) were dissolved in THF, respectively and cooled down to −35 °C. Transferring the red Cp\*<sub>2</sub>Yb THF solution dropwise into the blue Nickel solution at room temperature led to a dark red mixture immediately after the addition. The mixture was stirred at room temperature for one more hour, forming a red suspension. The solvent was removed under reduced pressure, yielding a brown-red solid that was extracted by Et<sub>2</sub>O (10 mL). Red crystals were obtained and isolated from slow evaporation of the Et<sub>2</sub>O solution in 51% yield (50.8 mg, 0.031 mmol). <sup>1</sup>H NMR (300 MHz, 293.15 K, THF-d<sub>8</sub>): δ (ppm) = 213.6 (s, 1H, ν<sub>1/2</sub> = 280 Hz, bimp<sub>m</sub>), 205.9 (s, 1H, ν<sub>1/2</sub> = 280 Hz, bimp<sub>m</sub>), 196.8 (s, 1H, ν<sub>1/2</sub> = 185 Hz, bimp<sub>m</sub>), 186.5 (s, 1H, ν<sub>1/2</sub> = 185 Hz, bimp<sub>m</sub>), 175.7 (s, 1H, ν<sub>1/2</sub> = 185 Hz, bimp<sub>m</sub>), 110.3 (s, 1H, ν<sub>1/2</sub> = 62 Hz, bimp<sub>m</sub>), 70.6 (s, 1H, ν<sub>1/2</sub> = 56 Hz, bimp<sub>m</sub>), 63.9 (s, 1H, ν<sub>1/2</sub> = 30 Hz, bimp<sub>m</sub>), 55.8 (s, 1H, ν<sub>1/2</sub> = 28 Hz, bimp<sub>m</sub>), 54.6 (s, 1H, ν<sub>1/2</sub> = 26 Hz, bimp<sub>m</sub>), 46.5 (s, 1H, ν<sub>1/2</sub> = 25 Hz,



bimpm), 45.4 (s, 1H,  $\nu_{1/2}$  = 25 Hz, bimpm), 33.5 (s, 1H,  $\nu_{1/2}$  = 20 Hz, bimpm), -0.8 (s, 15H,  $\nu_{1/2}$  = 55 Hz, Cp\*), -5.5 (s, 15H,  $\nu_{1/2}$  = 63 Hz, Cp\*), -6.6 (s, 15H,  $\nu_{1/2}$  = 63 Hz, Cp\*), -10.6 (s, 15H,  $\nu_{1/2}$  = 63 Hz, Cp\*), -12.8 (s, 15H,  $\nu_{1/2}$  = 61 Hz, Cp\*), -25.2 (s, 1H,  $\nu_{1/2}$  = 71 Hz, bimpm). **Anal. calcd** for  $C_{76}H_{97}N_8OYb_3$ : C, 55.06; H, 5.90; N, 6.76; found: C, 54.41; H, 6.02; N, 6.61.

**[K(Cp\*)<sub>2</sub>Yb(bimpm)NiMe<sub>2</sub>]<sub>2</sub>** (3). Cp\*<sub>2</sub>Yb(OEt<sub>2</sub>) (42.6 mg, 0.08 mmol) and K(bimpm)NiMe<sub>2</sub> (26.6 mg, 0.08 mmol) were dissolved separately in THF and cooled down to -35 °C. Transferring the red Cp\*<sub>2</sub>Yb THF solution into the deep blue Nickel solution at room temperature led to a dark brown-red solution immediately. The solution was kept under stirring at room temperature for only several seconds and the solvent was rapidly removed under reduced pressure to yield brown oil. Et<sub>2</sub>O was then added, leading to a brown solution and an insoluble pale yellow solid. The mixture was filtered, concentrated and then kept at -35 °C overnight to yield brown-red crystalline product as the first crop (24.3 mg, 0.031 mmol, 39% yield). Further crops can be also collected but small amounts of 2 co-crystallized. <sup>1</sup>H NMR (300 MHz, 293.15 K, THF-d<sub>8</sub>):  $\delta$  (ppm) = 187.7 (s, 1H,  $\nu_{1/2}$  = 193 Hz, bimpm), 181.5 (s, 1H,  $\nu_{1/2}$  = 151 Hz, bimpm), 50.4 (s, 1H,  $\nu_{1/2}$  = 19 Hz, bimpm), 27.5 (s, 1H,  $\nu_{1/2}$  = 16 Hz, bimpm), 19.2 (s, 1H,  $\nu_{1/2}$  = 12 Hz, bimpm), 12.3 (s, 15H,  $\nu_{1/2}$  = 46 Hz, Cp\*), 4.9 (s, 1H,  $\nu_{1/2}$  = 30 Hz, bimpm), 2.9 (s, 15H,  $\nu_{1/2}$  = 44 Hz, Cp\*), -4.8 (s, 3H,  $\nu_{1/2}$  = 10 Hz, Ni-Me1), -8.3 (s, 1H,  $\nu_{1/2}$  = 18 Hz, bimpm), -18.2 (s, 3H,  $\nu_{1/2}$  = 12 Hz, Ni-Me2). **Anal. calcd** for  $C_{66}H_{86}K_2N_8Ni_2Yb_2$ : C, 51.71; H, 5.65; N, 7.31; found: C, 52.28; H, 6.04; N, 6.94.

**K(18-c-6)(bimpm)Ni(CH<sub>3</sub>)<sub>2</sub>** (4). 18-crown-6 (47.8 mg, 0.18 mmol) was dissolved in cold THF (-40 °C) and transferred dropwise into a cold purple THF solution of K(bimpm)NiMe<sub>2</sub> (55.6 mg, 0.17 mmol) at ambient temperature, immediately forming a deep blue solution that was stirred for 10 minutes. The solvent was then removed under reduced pressure, and the crude K(18-c-6)(bimpm)Ni(CH<sub>3</sub>)<sub>2</sub> complex (4) was obtained as deep blue oil. The use of CH<sub>3</sub>CN instead of THF as reaction solvent tends to increase the yield because the product is much more soluble in CH<sub>3</sub>CN. However, the necessary drying step is longer and traces of CH<sub>3</sub>CN may influence the further use with reactive divalent lanthanide. Deep blue crystals were recrystallized via vapor diffusion by diethyl ether on THF solution at ambient temperature after 24 hours and isolated in 91% yield (91.0 mg, 0.15 mmol). <sup>1</sup>H NMR (300 MHz, 293.15 K, CD<sub>3</sub>CN):  $\delta$  (ppm) =  $\delta$  8.76 (dd,  $J$  = 4.7, 2.2 Hz, 1H, Kbimpm), 8.67 (dd,  $J$  = 5.6, 2.2 Hz, 1H, Kbimpm), 7.84–7.78 (m, 1H, Kbimpm), 7.59–7.52 (m, 1H, Kbimpm), 7.15–7.07 (m, 1H, Kbimpm), 6.99–6.89 (m, 2H, Kbimpm), 3.55 (s, 24H, 18-c-6), -0.10 (s, 3H, Ni-Me1), -0.54 (s, 3H, Ni-Me2). <sup>13</sup>C NMR (75 MHz, 293.15 K, THF-d<sub>8</sub>, q is for quaternary carbon):  $\delta$  (ppm) = 163.72 (C<sub>q</sub>, bimpm), 159.55 (C<sub>q</sub>, bimpm), 154.12 (C<sub>sp2</sub>, bimpm), 153.62 (C<sub>sp2</sub>, bimpm), 150.60 (C<sub>q</sub>, bimpm), 147.22 (C<sub>q</sub>, bimpm), 119.91 (C<sub>sp2</sub>, bimpm), 119.72 (C<sub>sp2</sub>, bimpm), 119.53 (C<sub>sp2</sub>, bimpm), 118.73 (C<sub>sp2</sub>, bimpm), 70.88 (C<sub>sp3</sub>, 18-c-6), -7.07 (C<sub>sp3</sub>, Ni-Me2), -12.20 (C<sub>sp3</sub>, Ni-Me1).

**Anal. calcd** for  $C_{25}H_{37}KN_4NiO_6$ : C, 51.12; H, 6.35; N, 9.54; found: C, 51.03; H, 6.30; N, 9.06.

**[K(18-c-6)Cp\*<sub>2</sub>Yb(bimpm)NiMe<sub>2</sub>]<sub>2</sub>** (5). Cp\*<sub>2</sub>Yb(OEt<sub>2</sub>) (42.7 mg, 0.08 mmol) and K(18-c-6)(bimpm)NiMe<sub>2</sub> (48.5 mg, 0.08 mmol) were separately dissolved in THF and cooled down to -35 °C. Transferring the red Cp\*<sub>2</sub>Yb THF solution dropwise into the blue Nickel solution at room temperature led to a dark purple mixture immediately once the addition. The solution was stirred at room temperature for 10 minutes and the solvent was removed under reduced pressure, yielding a red microcrystalline product (82.3 mg, 0.078 mmol, 97% yield). Dark red crystals were obtained and isolated from THF solution by vapor diffusion with Et<sub>2</sub>O, in 64% yield (54.4 mg, 0.051 mmol). <sup>1</sup>H NMR (300 MHz, 293.15 K, CD<sub>3</sub>CN):  $\delta$  (ppm) = 186.2 (s, 1H,  $\nu_{1/2}$  = 131 Hz, bimpm), 176.1 (s, 1H,  $\nu_{1/2}$  = 233 Hz, bimpm), 53.0 (s, 1H,  $\nu_{1/2}$  = 22 Hz, bimpm), 30.6 (s, 1H,  $\nu_{1/2}$  = 20 Hz, bimpm), 23.3 (s, 1H,  $\nu_{1/2}$  = 17 Hz, bimpm), 7.9 (s, 15H,  $\nu_{1/2}$  = 50 Hz, Cp\*), 3.5 (s, 24H,  $\nu_{1/2}$  = 12 Hz, 18-c-6), 2.3 (s, 15H,  $\nu_{1/2}$  = 45 Hz, Cp\*), -0.0 (s, 1H,  $\nu_{1/2}$  = 10 Hz, bimpm), -0.9 (s, 3H,  $\nu_{1/2}$  = 14 Hz, Ni-Me1), -4.5 (s, 1H,  $\nu_{1/2}$  = 25 Hz, bimpm), -14.0 (s, 3H,  $\nu_{1/2}$  = 13 Hz, Ni-Me2). (Note: Another dissymmetric Cp\* signal at 2.29 ppm is largely overlapped by the solvent signal.) **Anal. calcd** for  $C_{90}H_{134}K_2N_8Ni_2O_{12}Yb_2$ : C, 52.43; H, 6.55; N, 5.43; found: C, 52.26; H, 6.50; N, 5.34.

**[K<sub>2</sub>(bimpm)NiMe<sub>2</sub>]<sub>2</sub>** (6). K(bimpm)NiMe<sub>2</sub> (28.8 mg, 0.09 mmol) was dissolved in THF and cooled down to -35 °C. Then, cold potassium graphite (53.3 mg, 0.39 mmol) was added to the deep blue THF solution of 1 at room temperature, leading to a dark brown red mixture after stirring for a few seconds. The mixture was then filtered, and the solvent was removed under reduced pressure, yielding a brown-red crystalline product that was washed by Et<sub>2</sub>O (5 mL) in 69% yield (22.4 mg, 0.031 mmol). Brown orange, XRD suitable crystals of 6 were able to be obtained from slow diffusion of pentane into the THF solution at -35 °C. <sup>1</sup>H NMR (300 MHz, 293.15 K, THF-d<sub>8</sub>):  $\delta$  (ppm) = 7.62 (d,  $J$  = 9.2 Hz, 1H), 7.26 (m, 1H), 6.91 (d,  $J$  = 7.8 Hz, 1H), 6.64 (m, 1H), 6.22 (d,  $J$  = 7.9 Hz, 1H), 4.09 (d,  $J$  = 9.0 Hz, 1H), -0.61 (s, 3H), -1.08 (s, 3H). <sup>13</sup>C NMR (75 MHz, 293.15 K, THF-d<sub>8</sub>, q is for quaternary carbon):  $\delta$  (ppm) = 163.67 (C<sub>q</sub>, bimpm), 161.42 (C<sub>q</sub>, bimpm), 149.13 (C<sub>q</sub>, bimpm), 146.71 (C<sub>q</sub>, bimpm), 137.42 (C<sub>sp2</sub>, bimpm), 118.55 (C<sub>sp2</sub>, bimpm), 118.35 (C<sub>sp2</sub>, bimpm), 117.85 (C<sub>sp2</sub>, bimpm), (C<sub>sp2</sub>, bimpm) 117.57 (C<sub>sp2</sub>, bimpm), 101.14 (C<sub>sp3</sub>, bimpm-coupled), -9.93 (C<sub>sp3</sub>, Ni-Me2), -14.35 (C<sub>sp3</sub>, Ni-Me1). One <sup>13</sup>C was missing due to low solubility.

## Conflicts of interest

There are no conflicts to declare.

## Acknowledgements

The acknowledgements come at the end of an article after the This project has received funding from the H2020 European Research Council (ERC) under the European Union' Horizon





H2020 research program (grant agreement No. 716314). CNRS and Ecole Polytechnique are thanked for funding.

## Notes and references

- P. J. Chirik and K. Wieghardt, Radical Ligands Confer Nobility on Base-Metal Catalysts, *Science*, 2010, **327**, 794–795.
- A. I. O. Suarez, V. Lyaskovskyy, J. N. H. Reek, J. I. van der Vlugt and B. de Bruin, Complexes with Nitrogen-Centered Radical Ligands: Classification, Spectroscopic Features, Reactivity, and Catalytic Applications, *Angew. Chem., Int. Ed.*, 2013, **52**, 12510–12529.
- P. J. Chirik, Preface: Forum on Redox-Active Ligands, *Inorg. Chem.*, 2011, **50**, 9737–9740.
- V. Lyaskovskyy and B. de Bruin, Redox Non-Innocent Ligands: Versatile New Tools to Control Catalytic Reactions, *ACS Catal.*, 2012, **2**, 270–279.
- D. L. J. Broere, L. L. Metz, B. de Bruin, J. N. H. Reek, M. A. Siegler and J. I. van der Vlugt, Redox-Active Ligand-Induced Homolytic Bond Activation, *Angew. Chem., Int. Ed.*, 2015, **54**, 1516–1520.
- C. Gunanathan and D. Milstein, Metal–Ligand Cooperation by Aromatization–Dearomatization: A New Paradigm in Bond Activation and “Green” Catalysis, *Acc. Chem. Res.*, 2011, **44**, 588–602.
- J. R. Khusnutdinova and D. Milstein, Metal–Ligand Cooperation, *Angew. Chem., Int. Ed.*, 2015, **54**, 12236–12273.
- M. Schultz, J. M. Boncella, D. J. Berg, T. D. Tilley and R. A. Andersen, Coordination of 2,2′-Bipyridyl and 1,10-Phenanthroline to Substituted Ytterbocenes: An Experimental Investigation of Spin Coupling in Lanthanide Complexes, *Organometallics*, 2002, **21**, 460–472.
- C. H. Booth, M. D. Walter, D. Kazhdan, Y.-J. Hu, W. W. Lukens, E. D. Bauer, L. Maron, O. Eisenstein and R. A. Andersen, Decamethylytterbocene Complexes of Bipyridines and Diazabutadienes: Multiconfigurational Ground States and Open-Shell Singlet Formation, *J. Am. Chem. Soc.*, 2009, **131**, 6480–6491.
- C. H. Booth, D. Kazhdan, E. L. Werkema, M. D. Walter, W. W. Lukens, E. D. Bauer, Y.-J. Hu, L. Maron, O. Eisenstein, M. Head-Gordon and R. A. Andersen, Intermediate-Valence Tautomerism in Decamethylytterbocene Complexes of Methyl-Substituted Bipyridines, *J. Am. Chem. Soc.*, 2010, **132**, 17537–17549.
- G. Nocton, C. H. Booth, L. Maron and R. A. Andersen, Thermal Dihydrogen Elimination from Cp\*2Yb(4,5-diazafluorene), *Organometallics*, 2013, **32**, 1150–1158.
- G. Nocton, C. H. Booth, L. Maron, L. Ricard and R. A. Andersen, Carbon–Hydrogen Bond Breaking and Making in the Open-Shell Singlet Molecule Cp\*2Yb(4,7-Me2phen), *Organometallics*, 2014, **33**, 6819–6829.
- G. Nocton, W. W. Lukens, C. H. Booth, S. S. Rozenel, S. A. Medling, L. Maron and R. A. Andersen, Reversible Sigma C–C Bond Formation Between Phenanthroline Ligands Activated by (C5Me5)2Yb, *J. Am. Chem. Soc.*, 2014, **136**, 8626–8641.
- G. Nocton and L. Ricard, Reversible C–C coupling in phenanthroline complexes of divalent samarium and thulium, *Chem. Commun.*, 2015, **51**, 3578–3581.
- J. Andrez, G. Bozoklu, G. Nocton, J. Pécaut, R. Scopelliti, L. Dubois and M. Mazzanti, Lanthanide(II) Complexes Supported by N,O-Donor Tripodal Ligands: Synthesis, Structure, and Ligand-Dependent Redox Behavior, *Chem. – Eur. J.*, 2015, **21**, 15188–15200.
- A. Jaoul, C. Clavaguéra and G. Nocton, Electron transfer in tetramethylbiphosphinine complexes of Cp\*2Yb and Cp\*2Sm, *New J. Chem.*, 2016, **40**, 6643–6649.
- M. Xémard, S. Zimmer, M. Cordier, V. Goudy, L. Ricard, C. Clavaguéra and G. Nocton, Lanthanidocenes: Synthesis, Structure, and Bonding of Linear Sandwich Complexes of Lanthanides, *J. Am. Chem. Soc.*, 2018, **140**, 14433–14439.
- C. A. P. Goodwin, N. F. Chilton, L. S. Natrajan, M.-E. Boulon, J. W. Ziller, W. J. Evans and D. P. Mills, Investigation into the Effects of a Trigonal-Planar Ligand Field on the Electronic Properties of Lanthanide(II) Tris (silylamide) Complexes (Ln = Sm, Eu, Tm, Yb), *Inorg. Chem.*, 2017, **56**, 5959–5970.
- C. J. Kuehl, R. E. D. Re, B. L. Scott, D. E. Morris and K. D. John, Toward new paradigms in mixed-valency: ytterbocene–terpyridine charge-transfer complexes, *Chem. Commun.*, 2003, 2336–2337.
- F. Jaroschik, A. Momin, A. Martinez, D. Harakat, L. Ricard, X. F. Le Goff and G. Nocton, Synthesis and Characterization of 1,1′-Diphosphaplumbocenes: Oxidative Ligand Transfer Reactions with Divalent Thulium Complexes, *Organometallics*, 2016, **35**, 2032–2038.
- T. P. Gomba, N. Jiang, J. Bacsá and H. S. La Pierre, Synthesis of homoleptic, divalent lanthanide (Sm, Eu) complexes via oxidative transmetalation, *Dalton Trans.*, 2019, **48**, 16869–16872.
- W. J. Evans and D. K. Drummond, Reductive coupling of pyridazine and benzaldehyde azine and reduction of bipyridine by samarium complex (C5Me5)2Sm(THF)2, *J. Am. Chem. Soc.*, 1989, **111**, 3329–3335.
- D. J. Berg, J. M. Boncella and R. A. Andersen, Preparation of Coordination Compounds of Cp\*2Yb with Heterocyclic Nitrogen Bases: Examples of Antiferromagnetic Exchange Coupling across Bridging Ligands, *Organometallics*, 2002, **21**, 4622–4631.
- P. L. Holland, R. A. Andersen and R. G. Bergman, Synthesis, Characterization, Isomerization, and Reactivity of Dimeric Cyclopentadienylnickel Amido Complexes, *J. Am. Chem. Soc.*, 1996, **118**, 1092–1104.
- T. R. Dugan, E. Bill, K. C. MacLeod, G. J. Christian, R. E. Cowley, W. W. Brennessel, S. Ye, F. Neese and P. L. Holland, Reversible C–C Bond Formation between Redox-Active Pyridine Ligands in Iron Complexes, *J. Am. Chem. Soc.*, 2012, **134**, 20352–20364.
- C. C. H. Atienza, C. Milsmann, S. P. Semproni, Z. R. Turner and P. J. Chirik, Reversible Carbon–Carbon Bond





- Formation Induced by Oxidation and Reduction at a Redox-Active Cobalt Complex, *Inorg. Chem.*, 2013, **52**, 5403–5417.
- 27 V. Goudy, A. Jaoul, M. Cordier, C. Clavaguéra and G. Nocton, Tuning the Stability of Pd(IV) Intermediates Using a Redox Non-innocent Ligand Combined with an Organolanthanide Fragment, *J. Am. Chem. Soc.*, 2017, **139**, 10633–10636.
- 28 D. Wang, J. Moutet, M. Tricoire, M. Cordier and G. Nocton, Reactive Heterobimetallic Complex Combining Divalent Ytterbium and Dimethyl Nickel Fragments, *Inorganics*, 2019, **7**, 58.
- 29 A. Jaoul, M. Tricoire, J. Moutet, M. Cordier, C. Clavaguéra and G. Nocton, Reversible electron transfer in organolanthanide chemistry, *Chem. Squared*, 2019, **3**, 1.
- 30 R. Ghosh and A. Sarkar, Bidentate P, N–P Ligand for Nickel-Catalyzed Cross-Coupling of Aryl or Benzyl Chlorides with ArMgX, *J. Org. Chem.*, 2010, **75**, 8283–8286.
- 31 J. Magano and J. R. Dunetz, Large-Scale Applications of Transition Metal-Catalyzed Couplings for the Synthesis of Pharmaceuticals, *Chem. Rev.*, 2011, **111**, 2177–2250.
- 32 S. Handa, Y. L. N. Mathota Arachchige and L. M. Slaughter, Access to 2'-Substituted Binaphthyl Monoalcohols via Complementary Nickel-Catalyzed Kumada Coupling Reactions under Mild Conditions: Key Role of a P,O Ligand, *J. Org. Chem.*, 2013, **78**, 5694–5699.
- 33 F.-S. Han, Transition-metal-catalyzed Suzuki–Miyaura cross-coupling reactions: a remarkable advance from palladium to nickel catalysts, *Chem. Soc. Rev.*, 2013, **42**, 5270–5298.
- 34 N. Yoshikai, H. Mashima and E. Nakamura, Nickel-Catalyzed Cross-Coupling Reaction of Aryl Fluorides and Chlorides with Grignard Reagents under Nickel/Magnesium Bimetallic Cooperation, *J. Am. Chem. Soc.*, 2005, **127**, 17978–17979.
- 35 H. Xu, J. B. Diccianni, J. Katigbak, C. Hu, Y. Zhang and T. Diao, Bimetallic C–C Bond-Forming Reductive Elimination from Nickel, *J. Am. Chem. Soc.*, 2016, **138**, 4779–4786.
- 36 M. Haga, M. Ishizuya, T. Kanetsugi, T. Yutaka, D. Sakiyama, J. Fees and W. Kaim, Synthesis and formation of dinuclear mixed-valent complexes of ruthenium and osmium bridged by 2-(2-pyrimidyl)benzimidazolates, *Indian J. Chem. Sect. A*, 2003, **42A**, 2290–2299.
- 37 P. W. N. M. van Leeuwen, P. C. J. Kamer, J. N. H. Reek and P. Dierkes, Ligand Bite Angle Effects in Metal-catalyzed C–C Bond Formation, *Chem. Rev.*, 2000, **100**, 2741–2770.
- 38 M. Kranenburg, P. C. J. Kamer, P. W. N. M. van Leeuwen, D. Vogt and W. Keim, Effect of the bite angle of diphosphine ligands on activity and selectivity in the nickel-catalysed hydrocyanation of styrene, *J. Chem. Soc. Chem. Commun.*, 1995, 2177–2178.
- 39 F. Jaroschik, F. Nief, X.-F. Le Goff and L. Ricard, Synthesis and Reactivity of Organometallic Complexes of Divalent Thulium with Cyclopentadienyl and Phospholyl Ligands, *Organometallics*, 2007, **26**, 3552–3558.
- 40 S. Labouille, F. Nief, X.-F. Le Goff, L. Maron, D. R. Kindra, H. L. Houghton, J. W. Ziller and W. J. Evans, Ligand Influence on the Redox Chemistry of Organosamarium Complexes: Experimental and Theoretical Studies of the Reactions of (C<sub>5</sub>Me<sub>5</sub>)<sub>2</sub>Sm(THF)<sub>2</sub> and (C<sub>4</sub>Me<sub>4</sub>P)<sub>2</sub>Sm with Pyridine and Acridine, *Organometallics*, 2012, **31**, 5196–5203.
- 41 G. Nocton, C. H. Booth, L. Maron and R. A. Andersen, Influence of the Torsion Angle in 3,3'-Dimethyl-2,2'-bipyridine on the Intermediate Valence of Yb in (C<sub>5</sub>Me<sub>5</sub>)<sub>2</sub>Yb(3,3'-Me<sub>2</sub>-bipy), *Organometallics*, 2013, **32**, 5305–5312.
- 42 J. M. Birmingham and G. Wilkinson, The Cyclopentadienides of Scandium, Yttrium and Some Rare Earth Elements, *J. Am. Chem. Soc.*, 1956, **78**, 42–44.
- 43 C. L. Liotta and H. P. Harris, Chemistry of naked anions. I. Reactions of the 18-crown-6 complex of potassium fluoride with organic substrates in aprotic organic solvents, *J. Am. Chem. Soc.*, 1974, **96**, 2250–2252.
- 44 T. Cheisson, L. Ricard, F. W. Heinemann, K. Meyer, A. Auffrant and G. Nocton, Synthesis and Reactivity of Low-Valent f-Element Iodide Complexes with Neutral Iminophosphorane Ligands, *Inorg. Chem.*, 2018, **57**, 9230–9240.
- 45 M. D. Walter, M. Schultz and R. A. Andersen, Weak paramagnetism in compounds of the type Cp'<sub>2</sub>Yb(bipy), *New J. Chem.*, 2006, **30**, 238–246.
- 46 F. Neese, The ORCA program system, *Wiley Interdiscip. Rev.: Comput. Mol. Sci.*, 2012, **2**, 73–78.
- 47 J. P. Perdew, K. Burke and M. Ernzerhof, Generalized Gradient Approximation Made Simple, *Phys. Rev. Lett.*, 1997, **78**, 1396–1396.
- 48 F. Weigend and R. Ahlrichs, Balanced basis sets of split valence, triple zeta valence and quadruple zeta valence quality for H to Rn: Design and assessment of accuracy, *Phys. Chem. Chem. Phys.*, 2005, **7**, 3297.
- 49 F. Weigend, Accurate Coulomb-fitting basis sets for H to Rn, *Phys. Chem. Chem. Phys.*, 2006, **8**, 1057.
- 50 D. A. Pantazis, X.-Y. Chen, C. R. Landis and F. Neese, All-Electron Scalar Relativistic Basis Sets for Third-Row Transition Metal Atoms, *J. Chem. Theory Comput.*, 2008, **4**, 908–919.
- 51 D. A. Pantazis and F. Neese, All-Electron Scalar Relativistic Basis Sets for the Lanthanides, *J. Chem. Theory Comput.*, 2009, **5**, 2229–2238.
- 52 S. Grimme, J. Antony, S. Ehrlich and H. Krieg, A consistent and accurate ab initio parametrization of density functional dispersion correction (DFT-D) for the 94 elements H–Pu, *J. Chem. Phys.*, 2010, **132**, 154104.
- 53 C. Adamo and V. Barone, Toward reliable density functional methods without adjustable parameters: The PBE0 model, *J. Chem. Phys.*, 1999, **110**, 6158–6170.
- 54 J. Tao, J. P. Perdew, V. N. Staroverov and G. E. Scuseria, Climbing the Density Functional Ladder: Nonempirical Meta-Generalized Gradient Approximation Designed for Molecules and Solids, *Phys. Rev. Lett.*, 2003, **91**, 146401.



- 55 O. A. Vydrov and G. E. Scuseria, Assessment of a long-range corrected hybrid functional, *J. Chem. Phys.*, 2006, **125**, 234109.
- 56 J.-D. Chai and M. Head-Gordon, Systematic optimization of long-range corrected hybrid density functionals, *J. Chem. Phys.*, 2008, **128**, 084106.
- 57 G. M. Sheldrick, SHELXT- Integrated space-group and crystal-structure determination, *Acta Crystallogr. Sect. Found. Adv.*, 2015, **71**, 3–8.
- 58 G. M. Sheldrick, A short history of SHELX, *Acta Crystallogr. A*, 2008, **64**, 112–122.
- 59 G. M. Sheldrick, Crystal structure refinement with SHELXL, *Acta Crystallogr., Sect. C: Struct. Chem.*, 2015, **71**, 3–8.
- 60 A. L. Spek, Single-crystal structure validation with the program PLATON, *J. Appl. Crystallogr.*, 2003, **36**, 7–13.
- 61 O. V. Dolomanov, L. J. Bourhis, R. J. Gildea, J. a. K. Howard and H. Puschmann, OLEX2: a complete structure solution, refinement and analysis program, *J. Appl. Crystallogr.*, 2009, **42**, 339–341.
- 62 W. Kaschube, K. R. Pörschke and G. Wilke, tmeda-Nickel-Komplexe: III. (N,N,N',N'-Tetramethylethylendiamin)-(dimethyl)nickel(II), *J. Organomet. Chem.*, 1988, **355**, 525–532.
- 63 T. D. Tilley, J. M. Boncella, D. J. Berg, C. J. Burns, R. A. Andersen, G. A. Lawless, M. A. Edelman and M. F. Lappert, in *Inorganic Syntheses*, John Wiley & Sons, Ltd, 2007, pp. 146–150.





# Résumé Général

---

Ce travail doctoral se concentre sur les stratégies synthétiques et diverses caractérisations spectroscopiques des complexes hétérométalliques originaux ainsi que sur leurs structures électroniques uniques. Le cadre général de cette série de molécules hétérométalliques contient un fragment de lanthanide divalent, qui possède une propriété prometteuse de transfert d'un seul électron et pourrait donc être la source d'électrons; un hétérocycle *N*-aromatique reliant, autrement dit un ligand redox non innocent, afin de recevoir, stocker et transférer l'électron de lanthanide, comme un "*dimmer switch*" (interrupteur de gradateur) dans le système entier ; et un métal de transition afin d'effectuer des transformations chimiques. Précisément, la synthèse et la caractérisation de complexes originaux de nickel, hautement réactifs avec trois différents systèmes de ligands redox-actifs sont présentées dans ce manuscrit, et la chimie de coordination de ces complexes synthétisés avec des lanthanides divalents (ytterbium, samarium et thulium) est également montrée, ce qui conduit à des propriétés électroniques intéressantes et des comportements de réactivité modulés par le transfert d'électrons uniques.

Dans le premier chapitre, l'essentiel du projet global est décrit, en introduisant spécifiquement les trois composants importants (catalyseurs à base de métal de transition, ligands redox-actifs et lanthanides) dans le cadre hétérométallique. Le concept original du projet est introduit, qui était de la compréhension globale vers les propriétés électroniques des organolanthanides divalents. Par exemple, un état multiconfigurationnel, composé de configurations  $f^{13}(\pi^*)^1$  et  $f^{14}(\pi^*)^0$ , est révélé dans l'adducteur bipyridine du complexe  $Cp^*_2Yb$ . L'exemple de preuve de concept sur l'exploration du système hétérométallique est introduit. Le fragment réactif de palladium a été appliqué à l'assemblage avec l'adduit bipyrimidine de  $Cp^*_2Yb$ , et du fait de la modulation de la propriété électronique par corrélation électronique, un complexe stable et rare de palladium tétravalent peut être isolé par l'addition oxydante simple de l'iodométhane.

Dans le deuxième chapitre, des travaux d'extension du système de ligand bipyrimidine (bipym) avec des espèces de nickel diméthyle sont présentés. Le complexe bimétallique  $Cp^*_2Yb(bipym)NiMe_2$  s'est entièrement caractérisé par la solution RMN et DRX à cristaux simples, montrant une nature paramagnétique, et l'analyse du magnétisme à l'état solide indique une structure électronique multiconfigurationnelle, due à la corrélation des électrons. La réactivité de l'activation de monoxyde de carbone sur le centre de nickel et la cinétique de la réaction correspondante de couplage de C-C est étudiée, montrant l'impact de l'unité de lanthanide.

Le troisième chapitre montre une série de complexes de nickel trifluorométhyle basés sur l'intérêt général dans la littérature pour l'isolement des espèces de Ni(IV) de haute valence. La poursuite

de la synthèse vers des molécules hétérométallique reste difficile due à l'activation inattendue de liaison de C-F induite par des lanthanides divalent.

Dans le quatrième chapitre, un système dissymétrique de ligand pyrimidine-benzimidazole (bimpm) est rapporté. À la suite d'un transfert unique d'électrons, un couplage réducteur de liaison C-C se forme de façon intermoléculaire dans les complexes lanthanides-nickel hétérométalliques. Les caractéristiques structurales par l'analyse spectroscopique, ainsi que les investigations théoriques sont décrites dans ce chapitre. Ce qu'il faut souligner, c'est une transition structurale par l'isolement réussi de différentes molécules multimétalliques, y compris une espèce intermédiaire transitoire, qui peuvent être soigneusement synthétisées ou stabilisées par l'éther couronne (éther 18-couronne-6). En outre, l'impact des ions de lanthanide dans la densité électronique du système de ligand est discuté, selon une mode différente de couplage du précurseur de nickel en présence d'un réducteur fort (graphite de potassium), ainsi que les données computationnelles connexes.

Dans le cinquième chapitre, un nouveau système redox en utilisant ligand pyridine-terpyridine (pytpy) est présenté. Un complexe formel Ni(I)-méthyle est synthétisé, qui devrait mieux être décrit comme une molécule Ni(II) avec un ligand anionique radical. La coordination avec les lanthanides divalents pour obtenir les complexes bimétalliques idéaux reste un défi. Cependant, certains aspects intéressants du complexe de nickel sont montrés, par exemple, un composé doublement réduit (ou un système de ligand triplement réduit) est isolé, offrant une espèce formelle Ni(-I), ce qui peut ouvrir certaines possibilités de réactivité réductrice dans la poursuite de l'étude. En plus, l'activation du lien borane en pinacolborane est également observée, ce qui conduit à des applications de réactivité telles que l'hydroboration ou la borylation de substrats insaturés à l'avenir.

En conclusion, cette thèse de doctorat démontre que, en combinaison avec de ligands *N*-hétérocycliques redox-actifs (bipym, bimpm et pytpy), les organolanthanides divalent (Yb, Sm et Tm) comme sources d'électrons in situ, sont capables de réaliser des processus de transfert d'électrons. Les systèmes redox-actifs qui en résultent, présentant des propriétés remarquables, peuvent être utilisés pour construire des cadres hétérométalliques en présence de fragments de nickel réactifs. Les structures électroniques peuvent être subtilement modulées par l'électron transféré, ce qui entraîne des comportements de réactivité modifiés sur le centre de nickel ou le système de ligand(s). Les connaissances approfondies de ces complexes synthétisés par des méthodes spectroscopiques et théoriques peuvent potentiellement non seulement aider à poursuivre les recherches sur les comportements de réactivité, mais aussi fournir des perspectives intrigantes sur le système hétérométallique unique.



**Titre :** La réactivité rédox des complexes originaux de nickel combinant avec des lanthanides divalents

**Mots clés :** Ligands rédox-actifs ; Complexes hétérobimétaboliques ; Transfert mono-électronique

**Résumé :** Le but de ce travail a été de concevoir des structures hétérobimétaboliques combinant une espèce réactive de nickel et un fragment organolanthanide divalent. Au sein de celles-ci, d'une part, le fragment lanthanide divalent joue le rôle crucial de réducteur mono-électronique. D'autre part, les propriétés de non-innocence rédox du ligand permettent de transférer une partie de la densité électronique vers le second centre métallique, et ainsi de moduler sélectivement la réactivité du métal de transition. Dans ce contexte, l'activation du monoxyde de carbone a été étudiée en utilisant un complexe hétérobimétabolique particulier, dont les deux centres métalliques sont liés à l'aide d'un ligand 2,2'-bipyridimine pontant. Dans son état fondamental, ce complexe présente un comportement multiconfigurationnel. Une étude cinétique minutieuse a d'ailleurs montré que cette configuration électronique particulière était responsable de la stabilisation des espèces acyles intermédiaires.

Diverses espèces de trifluorométhyle de nickel ont été étudiées, permettant une activation de la liaison C-F facilitée par la présence de l'ion lanthanide. Par la suite, cette réactivité a pu être appliquée à l'étude de complexes métalliques de type difluorocarbènes. Par ailleurs, l'utilisation d'un ligand dissymétrique, a permis de dévoiler une réaction de couplage radicalaire entre deux ligands, induite par la présence du fragment lanthanide réducteur. En particulier, une transformation inhabituelle entre une forme dimère et trimère a été observée. Le couplage entre deux unités de complexe de nickel a ensuite été réalisé par réduction avec du potassium-graphite. Dans ce composé couplé, une modulation de la densité de spin au niveau du système rédox-actif est induite par le fragment lanthanide divalent. Enfin, des travaux préliminaires à partir d'un ligand tridenté ont été entrepris de façon à étudier des complexes de nickel possédant des états d'oxydation peu communs, et laissant entrevoir une réactivité intéressante impliquant des processus radicalaires.

**Title :** Redox reactivity of original nickel complexes combined with divalent lanthanides

**Keywords :** Redox activity; Heterometallic coordination chemistry; Single-electron transfer

**Abstract :** This work aimed at designing a heterobimetallic framework combining a reactive nickel species and a divalent organolanthanide fragment. The crucial role of the divalent lanthanide moiety is to act as a single-electron transfer reductant. As redox non-innocent ligands are able to allow strong electron correlation, the reactivity of the reactive transition metal center can be selectively modulated.

In this context, carbon monoxide activation was investigated using a special heterobimetallic complex bridged by a 2,2'-bipyridimine ligand. A multiconfigurational ground state behavior was observed and found responsible for the stabilization of the intermediate acyl species, as evidenced by kinetic analysis.

Trifluoromethyl nickel species were studied, yielding a facile C-F bond activation triggered by the lanthanide ion, and such reactivity could be further applied to study difluorocarbene metal complexes. A dissymmetric, redox-active ligand was used afterwards, resulting in a radical coupling between two ligands in the presence of the reductive lanthanide fragment. A dimer-trimer transition was observed. The coupled nickel species was isolated by strong reduction, revealing a modulation of the spin density on the redox-active system induced by the divalent lanthanide fragment. Finally, a tridentate ligand scaffold was investigated to study redox-active nickel complexes with uncommon oxidation states, which led to interesting reactivity insights involving radical processes.